DTIC FILE COPY

LEVEL

INVENTORY

AD-A229 200

DTIC ACCESSION NUMBER

AFOSR-TR 90 1056

DOCUMENT IDENTIFICATION

21 NOV 90

DISTRIBUTION STATEMENT

ACCESSION FOR

NTIS	GRA&I
DTIC	TRAC
UNANNOUNCED	
JUSTIFICATION	

BY

DISTRIBUTION/
AVAILABILITY CODES

DISTRIBUTION	AVAILABILITY AND/OR SPECIAL

A-1

DISTRIBUTION STAMP

D5349

ORPV
INSPECTED

DTIC
ELECTE
NOV 19 1990
S E D
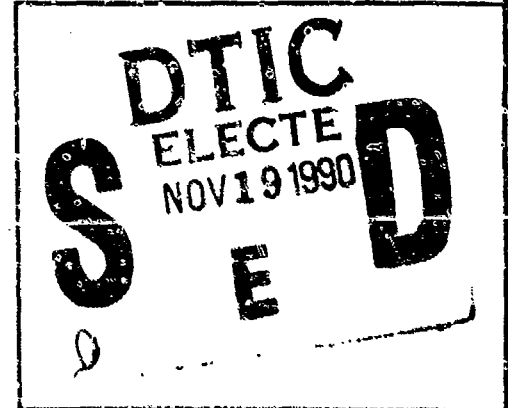
DATE ACCESSIONED

DATE RETURNED

90 11 15 118

DATE RECEIVED IN DTIC

REGISTERED OR CERTIFIED NUMBER

VOLUME 170

Interfaces in Composites

EDITORS

Carlo G. Pantano

Eric J.H. Chen

REPORT DOCUMENTATION PAGE

1. AGENCY USE ONLY (Leave blank)	2. REPORT DATE	3. REPORT TYPE AND DATES COVERED
		Final Report 22 Nov 89–21 Nov 90

4. TITLE AND SUBTITLE

1989 Materials Research Society Fall Meeting

5. FUNDING NUMBERS

2306/A2

6. AUTHOR(S)

Dr John Ballance

7. PERFORMING ORGANIZATION NAME(S) AND ADDRESS(ES)

Material Research Society
9800 McKnight Road, Suite 327
Pittsburgh, PA 15237-6005

8. PERFORMING ORGANIZATION REPORT NUMBER

AFOSR-TR· 90 1056

9. SPONSORING / MONITORING AGENCY NAME(S) AND ADDRESS(ES)

AFOSR/NE
Bldg 410
Bolling AFB DC 2033206448

10. SPONSORING / MONITORING AGENCY REPORT NUMBER

AFOSR-90-0081

11. SUPPLEMENTARY NOTES

12a. DISTRIBUTION / AVAILABILITY STATEMENT

UNLIMITED

12b. DISTRIBUTION CODE

13. ABSTRACT (Maximum 200 words)

CONFERENCE WAS HELD ON THE FOLLWING AREA
(158)   In Situ Patterning: Selective Area Deposition and Etching
(161)   Properties of II-VI Semiconductors: Bulk Crystals, Expitaxial Films,
Quantum Well Structures, and Dilute Magnetic Systems
(163)   Impurties, Defects and Diffusion in Semiconductors: Bulk and Layered
Structures
(168)   Chemical Vapor Deposition of Refractory Metals and Ceramics
(170)   Tailored Interfaces in Composite Materials.

14. SUBJECT TERMS

15. NUMBER OF PAGES

16. PRICE CODE

17. SECURITY CLASSIFICATION OF REPORT	18. SECURITY CLASSIFICATION OF THIS PAGE	19. SECURITY CLASSIFICATION OF ABSTRACT	20. LIMITATION OF ABSTRACT
UNCLASS	UNCLASS	UNCLASS	UNLIMITED

AFOSR-TR- 90 1056

90 11 15 118

Interfaces in Composites

Interfaces in Composites

Symposium held November 27-29, 1989, Boston,
Massachusetts, U.S.A.

EDITORS:

Carlo G. Pantano
The Pennsylvania State University, University Park, Pennsylvania, U.S.A.

Eric J.H. Chen
E.I. DuPont DeNemours and Company, Wilmington, Delaware, U.S.A.

Contents

v

PART II: CHARACTERIZATION OF INTERFACES

PART V: INTERFACE EFFECTS IN
POLYMER MATRIX COMPOSITES

ix

Preface

This volume contains the proceedings of the Materials Research Society Symposium on Tailored Interfaces In Composite Materials which was held November 27-29, 1989 in Boston, Massachusetts, at the 1989 MRS Fall Meeting.

This symposium, which was funded by the Air Force Office of Scientific Research and E.I. du Pont de Nemours & Co., Inc., brought together over 80 international researchers from government laboratories, universities, and industry, with diverse backgrounds ranging from physics and chemistry to engineering mechanics, and with interests in a wide variety of materials including polymers, metals and ceramics.

The central theme of the symposium focused on tailoring of an interface to optimize the adhesion or transfer of load between reinforcing phases and the matrix, to enhance crack deflection through debonding, or to control interface reactivity. The symposium was designed to be interdisciplinary. Thus, some of the sessions addressed the micromechanics, chemistry, and characterization of interfaces in general.

Eighty papers were presented either orally or as posters. Fifty of the presented papers appear in this volume. All papers were subjected to peer review after which authors had an opportunity to respond to the reviewer's comment. Because a primary goal of the editors was rapid publication, the revised papers reflect the views and standards of the authors, and not necessarily those of the editors.

January 22, 1990   Carlo G. Pantano
                                                  Eric J.H. Chen

MATERIALS RESEARCH SOCIETY SYMPOSIUM PROCEEDINGS

MATERIALS RESEARCH SOCIETY SYMPOSIUM PROCEEDINGS

MATERIALS RESEARCH SOCIETY MONOGRAPH

Earlier Materials Research Society Symposium Proceedings listed in the back.

Micromechanics of Interfaces

SURFACE FORCES AND ADHESION BETWEEN DISSIMILAR MATERIALS MEASURED IN VARIOUS ENVIRONMENTS

Douglas T. Smith and Roger G. Horn
National Institute of Standards and Technology, Gaithersburg, MD 20899.

ABSTRACT

The Israelachvili surface force apparatus has been used extensively over the past decade to make detailed measurements of surface forces and adhesion between very smooth solids in various liquid and vapor environments. Most of those measurements have been made with mica surfaces, but we have recently developed a method of preparing smooth silica surfaces for use in place of the mica. The silica surfaces adhere in dry and humid atmospheres, but do not adhere when immersed in water.

The use of a second material not only broadens the scope of the Israelachvili technique, but also enables studies of forces and adhesion between dissimilar materials. In this work, we present the results of measurements of adhesion in air and forces in aqueous solution between two silica surfaces; we also report preliminary results of the adhesion between a mica surface and a silica surface.

INTRODUCTION

The surface forces which contribute to the adhesion between materials can be investigated in detail using a direct measurement apparatus developed by Israelachvili [1]. By measuring the force as a function of surface separation, and studying its dependence on various conditions such as surface preparation and the nature of the medium between the surfaces, it is generally possible to determine the origin of various components of the force, for example electrostatic and van der Waals terms. This has been demonstrated very clearly and comprehensively by a range of measurements made with the Israelachvili apparatus using mica surfaces [2].

The inherent smoothness of mica makes it an excellent model material for these studies, and we have now learned a great deal about its interactions and behavior in various environments, but clearly it would be highly desirable to extend these techniques to other materials of greater practical interest. One approach to this goal is to coat the mica surfaces with other materials such as surfactants [3], polymers [4] and thin metal films [5][6], hopefully maintaining a good degree of smoothness while modifying the surface chemistry and consequent surface forces. Another is to replace the mica altogether. With the Israelachvili technique, the requirements for alternative materials are that they be transparent, thin, and of course smooth. Recently ways have been found to prepare two important alternative materials in suitable form: sapphire [7] and silica [8]. In this symposium, Thakkar, Tirrell and David [9] report results obtained with Pyrex glass prepared by a technique similar to that used for silica.

In this report we present measurements of the adhesion between two silica surfaces in air measured as a function of relative humidity. With the surfaces immersed in aqueous electrolyte solutions we find, in addition to classical electrical double-layer forces, a repulsion at short range which prevents the surfaces from adhering.

The advent of alternative substrates to mica also makes it possible to measure surface forces and adhesion between dissimilar materials. Aside from obvious practical applications, we believe that these studies will aid us in identifying the origin and

importance of different contributions to the adhesion (or lack of it). An example emerges in the final set of data which we present, namely the first measurements of adhesion between silica and mica in dry air.

EXPERIMENTAL

The Surface Force Apparatus

A detailed description of the surface force apparatus can be found in Ref. 1. Briefly, two thin sheets of optically transparent material, silvered on their outer faces, are formed into cylindrical form by bending them over two cylindrical silica lenses and gluing them down. The cylinders are mounted in a chamber with their axes crossed, so that the surfaces meet at a point, which is a practical geometry from the experimental viewpoint because problems of parallelism and edge effects are avoided. Furthermore, the interpretation of the forces is less difficult than one might suppose; according to the Derjaguin approximation, the force F between gently curved cylindrical surfaces, divided by their radius of curvature R, is 2π times the interaction energy per unit area E_f between corresponding flat surfaces at the same separation D. (This is included on the right-hand axis of Figure 3.)

The two silver layers on the outer surfaces form an optical interferometer, whose thickness can be determined by measuring the wavelengths of "fringes of equal chromatic order" (FECO) transmitted through the system when white light is used as the illumination source. The unusually smooth reflecting surfaces, coupled with multiple beam interference, lead to a precise measurement of the separation between the inner surfaces (after the thickness of the two sheets is subtracted from the total); a resolution of 0.1 - 0.2 nm is achievable in practice.

One of the two surfaces is mounted on a cantilever spring, and the deflection of this spring as the surfaces are moved towards each other is used to measure the force between them. Because very small spring deflections can be detected, correspondingly small forces can be measured - the resolution is better than 10^{-7} N.

Silica Surface Preparation and Characterization

The method of preparing silica in a form sufficiently thin and smooth for deployment in the Israelachvili apparatus is to melt one end of a tube of high-purity silica to close it, then rapidly blow it out into a large bubble. Thakkar et al. [9] employ the same technique in their study of Pyrex glass. Wall thicknesses down to a few micrometers are readily prepared in this way, and the surface is expected to be smooth since it is formed by rapid setting of a liquid under tension. Surface profilometry measurements made in this laboratory using a Talystep stylus machine confirm this [10]: the average surface roughness over a 30 μm trace is less than 0.5 nm. The advancing contact angle of water on freshly-prepared surfaces is about 45°, indicating a low degree of hydroxylation of siloxane groups on the surface.

Because two silica sheets prepared in this manner are not in general of equal thickness, the computation of surface separation from the measured wavelengths of fringes of equal chromatic order is more complex than for the usual symmetrical interferometer obtained with mica sheets. A summary of that computation is given below.

The Three-Layer Non-symmetrical Interferometer

In order to use fringes of equal chromatic order to determine the separation of two surfaces in an arbitrary medium, the relationship between the FECO wavelengths and the surface separation must be known. Consider the case of two smooth transparent substrates, not necessarily of the same material, with thicknesses Y_1 and Y_2 and indices of refraction μ_1 and μ_2, separated by an intervening fluid of thickness D and index of refraction μ_3. If this general three-layer interferometer is taken to have highly-reflecting films on the two outside surfaces, the resulting system will transmit only those wavelengths which meet the appropriate interference condition. Deriving an expression for the transmitted wavelengths as a function of Y_1, Y_2 and D is relatively straightforward [11]; what we require is an analytic expression for D as a function of the transmitted wavelength. Israelachvili [12] has solved this problem for the special case $Y_1=Y_2$ and $\mu_1=\mu_2$, which is typically the case for mica experiments. We have solved the problem for the more general situation of dissimilar substrates, allowing for the fact that the indices of refraction of the three layers are in general functions of wavelength, and allowing also for the correction of phase shift errors introduced by the highly-reflective external coatings. Details of the calculation are given elsewhere [13].

The relationship we find between the surface separation D and the vacuum wavenumber $k=2\pi/\lambda$ is given by

$$\tan(k\mu_3 D) = \frac{(\rho_1 - \rho_2)\sin(k\Delta) + (\rho_1 + \rho_2)\sin(k\Sigma)}{(\rho_1\rho_2 - 1)\cos(k\Delta) - (\rho_1\rho_2 + 1)\cos(k\Sigma)} \quad , \tag{1}$$

where $\Sigma=\mu_1 Y_1+\mu_2 Y_2$ and $\Delta=\mu_1 Y_1-\mu_2 Y_2$ represent respectively the sum and difference of the substrate optical thicknesses, and $\rho_i=\mu_i/\mu_3$ (i=1,2). If the two substrates are of the same material ($\mu_1=\mu_2$, $\rho_1=\rho_2=\rho$), but are not of equal thickness, the result reduces to

$$\tan(k\mu_3 D) = \frac{2\rho\sin[k\mu_1(Y_1 + Y_2)]}{(\rho^2 - 1)\cos[k\mu_1(Y_1 - Y_2)] - (\rho^2 + 1)\cos[k\mu_1(Y_1 + Y_2)]} \quad . \tag{2}$$

If the two substrates are the same material and also of equal thickness ($Y_1=Y_2=Y$), the result reduces further, to that obtained by Israelachvili [12]:

$$\tan(k\mu_3 D) = \frac{2\rho\sin(2k\mu_1 Y)}{(\rho^2 - 1) - (\rho^2 + 1)\cos(2k\mu_1 Y)} \quad . \tag{3}$$

The procedures for calculating Y_1, Y_2 and D from observed interference fringe positions have been developed and are also reported elsewhere [13].

6

RESULTS

Adhesion Between Silica Surfaces in Air

To measure the strength of adhesion between two silica surfaces in both dry and humid air, silica samples were prepared and mounted in the surface force apparatus using the techniques described above. They were then brought into contact, where they spontaneously flattened over a contact diameter of typically 50 - 100 μm without any externally-applied load. This adhesive flattening, the result of elastic deformation of the glue supporting the silica, indicates an attractive force between the surfaces comparable to that observed with mica surfaces, and is also strong evidence that the silica surfaces are reasonably smooth at the atomic level. Rough surfaces, being held apart by asperities, are not able to come into intimate enough contact for the short-range forces to produce a strong adhesion.

After bringing the surfaces into adhesive contact, the pull-off force F_ρ required to separate them was measured. In the absence of a condensed meniscus around the contact area (i.e., for dry N_2 gas or air at 0% relative humidity), F_ρ can be related to the surface energy of the solid, γ_s, using the theory of Johnson, Kendall and Roberts [14]; they find that $F_\rho/R=3\pi\gamma_s$. When a condensed meniscus is present, however, the contribution to the pull-off force from that meniscus is given [15] by $F_\rho/R=4\pi\gamma_L\cos(\theta)$, where γ_L is the surface tension of the condensed liquid and θ is the wetting angle of the liquid on the surface. If there is no other force between the surfaces, the surface tension term is the only contribution to the pull-off force.

The observed pull-off forces between two silica surfaces, normalized by R, are shown in Figure 1 for five values of relative humidity. With the exception of the peak observed at 50% relative humidity (RH), the data are not unlike those seen with mica substrates [16]. The right axis is normalized by $4\pi R\cos(45°)$ so that it represents the surface tension γ_L of a meniscus of water if one is present (the wetting angle of water on these silica substrates was observed to be approximately 45°). Note that the data for high RH approach the correct value γ_L=72 mJ/m for the surface tension of water. This implies that there is no other strong attractive interaction between the silica surfaces when a macroscopic meniscus of water is present; in the next section we report

Figure 1. Pull-off force between two silica surfaces in air as a function of relative humidity. The right axis is in units of the surface tension of a condensed meniscus with a wetting angle of 45°.

measurements of the forces between silica surfaces in bulk water which are consistent with this conclusion. It is however possible that the peak observed at 50% RH is the result of a combination of solid-solid attraction and surface tension, albeit from a relatively small meniscus.

Forces Between Silica Surfaces in Aqueous Solutions

The forces measured in different aqueous concentrations of NaCl are shown in Figures 2 and 3. In Figure 2 we see the electrical double-layer forces found at comparatively large separations, their range depending on electrolyte concentration as expected from Derjaguin-Landau-Verwey-Overbeek (DLVO) theory. Numerical solutions of the Poisson-Boltzmann equation [17], which describes the electric double layer repulsion, are also shown for the appropriate experimental concentrations. The surface potential at infinite separation was chosen in each case to get the best fit to the data; the values used, in order of increasing concentration, are -40, -32, -28 and -23 mV. At separations greater than 3 nm the data generally lie between the solutions for constant-charge (solid lines) and constant-potential (not shown, for clarity) boundary conditions.

DLVO theory predicts that at short range, van der Waals attraction should exceed the double-layer repulsion, leading to an adhesive minimum as $D \to 0$. However, as Figure 3 shows, in the case of silica we find that the repulsion continues to increase as separation decreases: over and above the double-layer repulsion there is an additional, short-range component to the force, which we ascribe to a "hydration repulsion" akin to that found between hydrophilic surfaces such as mica [18] and various surfactant and lipid layers [3][19]. A similar force was observed between silica surfaces by Rabinovich et al. [20] and Peschel et al. [21] using different apparatuses to measure force and different methods to prepare the surfaces; our results are comparable in magnitude to these earlier measurements. We observe this repulsion even with pure water, which from analysis of the long-range double-layer force was found to have an ion concentration of 8×10^{-6} M. The short-range force prevented any adhesion between the silica sheets. When the surfaces were forced together under a large load ($F/R > 40$ mN/m) there was an extremely steep repulsion (see Fig. 3); we used this hard-wall contact position to define our "zero" of separation.

One feature of the silica surface is that — in contrast to mica — it can readily be modified by chemical reaction, allowing us to explore the effect of surface chemistry on surface forces. As a simple demonstration of this, we made a set of measurements with silica surfaces which had been exposed for 10 minutes to ammonia vapor. It was found
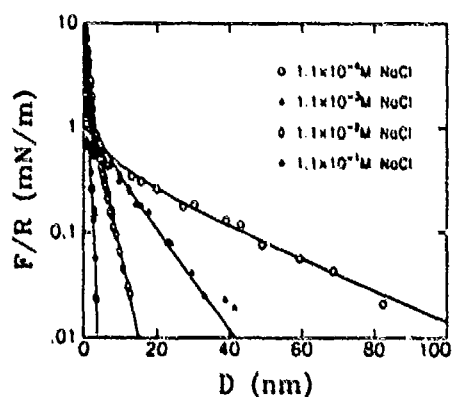
Figure 2. The repulsive force F measured between silica surfaces immersed in aqueous NaCl solutions at various concentrations, plotted as a function of the surface separation D. The solid lines are theoretical fits (see text).
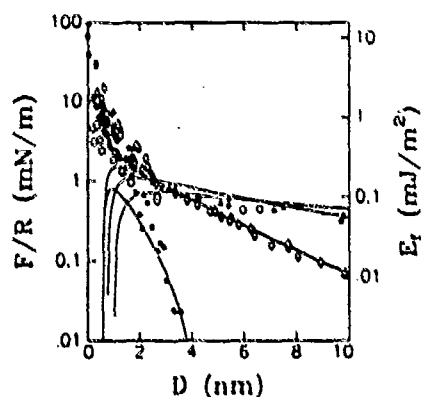
Figure 3. Amplification of the data of Fig. 2 to show the forces at short range. A strong short-range repulsion was observed at all concentrations studied. E_f is defined in the text.

that the double-layer forces were considerably stronger than those seen with the untreated surfaces, with potentials of -200 mV, -165 mV, -150 mV and -115 mV for NaCl concentrations of 7×10^{-6} M (pure water), 2×10^{-5} M, 1.2×10^{-4} M and 1.1×10^{-3} M respectively. The short-range repulsion was again observed at all NaCl concentrations.

Adhesion Between a Silica Surface and a Mica Surface

In addition to the results reported above for a pair of silica substrates, we have also made preliminary measurements of the adhesion in air between a silica surface and a mica surface. In dry air or nitrogen, we observe an unusually strong time- and history-dependent attractive force between the two surfaces. This force is not observed when the surfaces first approach each other, but is seen when the surfaces are separated.

The effect is illustrated in Figure 4, which shows the profile of the surface separation determined from analysis of the interference fringes [22] before (A), during (B) and after being brought into contact (C). Note that the magnification along the vertical axis is approximately 10^{-3} times that along the horizontal. Curve A shows the original, undeformed shape of the surfaces. When in contact, short-range adhesive forces pull the surfaces together, and a hard-wall repulsion causes them to flatten over a certain area (Curve B), as discussed above [14][22]. After separation, we observe a very marked deformation (C) caused by a strong attractive force, which by a strong attractive force, which evidently has a long range, and was not present on the initial approach.

Figure 4. Surface profiles for the silica-mica system recorded (A) before, (B) during, and (C) after contact. Note the difference in scale of ~1000 between the X and Y axes.

We attribute this post-contact force to an electrostatic attraction resulting from charge transferring from one surface to the other when they are in contact. At this stage we do not know the exact mechanism, but evidence in support of this idea comes from the observations that (a) the strength of the attractive force, and the concomitant deformation, decrease with increasing surface separation, (b) both of these diminish with time out of contact, (c) the effect is not seen in humid air, and (d) it is only seen with dissimilar materials.

The phenomenon is presumably related to other charging effects such as static electricity and triboelectricity. In the present context it contributes a large term to the adhesion between these two materials, which is significantly stronger than that seen between two sheets of the same material.

CONCLUSIONS

We have presented data obtained using the Israelachvili surface force apparatus with silica glass surfaces. In air the adhesion between two such surfaces is comparable to that between mica surfaces; at high humidity it is determined by the surface tension of a

condensed water capillary. In aqueous solutions there is no adhesion, the surfaces being kept apart by a hydration repulsion.

When a mica surface and a silica surface come into contact, charge transfers from one to the other so that when they are subsequently separated (in dry air) there is a very strong electrostatic attraction between them. This contributes significantly to their adhesion. It may be that similar charge transfer effects are an important factor in determining the strength of other interfaces between dissimilar materials.

ACKNOWLEDGMENTS

REFERENCES

1. J.N. Israelachvili and G.E. Adams, J. Chem. Soc. Faraday Trans. I 74 (1978) 975.
2. R.G. Horn and D.T. Smith, J. Non-Cryst. Solids, in press.
3. R.M. Pashley and J.N. Israelachvili, Colloids and Surfaces 2 (1981) 169.
4. S.S. Patel and M. Tirrell, Annu. Rev. Phys. Chem. 40 (1989) 597.
5. C.P. Smith, M. Maeda, L. Atanasoska, H.S. White and D.J. McClure, J. Phys. Chem. 92 (1988) 199.
6. J.L. Parker and H.K. Christenson, J. Chem. Phys. 88 (1988) 8013.
7. R.G. Horn, D.R. Clarke and M.T. Clarkson, J. Mater. Res. 3 (1988) 413.
8. R.G. Horn, D.T. Smith and W. Haller, Chem. Phys. Lett. 162 (1989) 404.
9. B. Thakkar, M. Tirrell and D.J. David, Proceedings of this symposium.
10. R.G. Horn, K.W. Schantz, D.T. Smith, J.F. Song and V. Elings, in preparation.
11. M. Born and E. Wolf, Principles of Optics (Pergamon, Oxford, 1965).
12. J.N. Israelachvili, J. Colloid Interface Sci. 44 (1973) 259.
13. R.G. Horn and D.T. Smith, submitted to Applied Optics.
14. K.L. Johnson, K. Kendall and A.D. Roberts, Proc. R. Soc. London A324 (1971) 301.
15. L.R. Fisher and J.N. Israelachvili, Colloids Surf. 3 (1981) 303.
16. H.K. Christenson, J. Colloid Interface Sci. 121 (1987) 170.
17. D.Y.C. Chan, R.M. Pashley and L.R. White, J. Colloid Interface Sci. 77 (1980) 283.
18. R.M. Pashley, J. Colloid Interface Sci. 83 (1981) 531.
19. V.A. Parsegian, N. Fuller and R.P. Rand, Proc. Natl. Acad. Sci. USA 76 (1979) 2750.
20. Ya.I. Rabinovich, B.V. Derjaguin and N.V. Churaev, Adv. Colloid Interface Sci. 16 (1982) 63.
21. G. Peschel, P. Belouschek, M.M. Müller, M.R. Müller and R. König, Colloid Polymer Sci. 260 (1982) 444.
22. R.G. Horn, J.N. Israelachvili and F. Pribac, J. Colloid Interface Sci. 115 (1986) 480.

MEASUREMENT OF INTERFACIAL FRACTURE ENERGY

L.G. Rosenfeld, J.E. Ritter, T.J. Lardner
Mechanical Engineering Department, University of Massachusetts,
Amherst, MA 01003

ABSTRACT

The contact stresses resulting from indentation of a compliant coating on a
rigid substrate cause debond cracks to initiate and propagate along the
interface. The indentation debonding behavior of four polymer coatings on
glass substrates is investigated. A model is developed for calculating
interfacial fracture energy based on data of indenter load vs. debond crack
size. Based on the experimental observations and the data for the four
coating systems, the limitations of the model are discussed.

INTRODUCTION

An indentation based adhesion test consists of loading a coated surface
with an indenter such as a ball or Vickers. The indenter load at which
debonding initiates is a measure of the interfacial strength [1,2] while the
debond crack size as a function of indenter load is a measure of interfacial
fracture energy [3-5]. In a previous paper by the present authors an
indentation model was presented for calculating interfacial fracture energy
in systems consisting of a compliant coating on a rigid substrate [5]. The
purpose of this paper is to extend our previous model to account for the
possibility of coating buckling and to study the indentation debonding
behavior of four different polymer coatings on glass substrates.

EXPERIMENTAL

The coating materials for this study were epoxy (DGEBA resin/polyamide
hardener), polyimide (Dupont Pyre-M.L. RK-692), epoxy acrylate (DeSoto 950-
008) and urethane acrylate (DeSoto 950-133). The substrates were soda-lime
glass plates. Prior to deposition of the coatings, the substrates were

annealed at 520° C for 24 hours and cleaned in an ultrasonic methanol bath.
The coatings were deposited by a doctor blade technique. The epoxy and the
two acrylate coatings had thicknesses ranging from 20 to 200 µm and the
polyimide coatings had thicknesses less than 20 µm.

The indentation experiments were performed with a Vickers indenter.
The indenter was attached to a load cell which was bolted to the crosshead
of a universal testing machine. The specimens were placed with the coating
side up on the stage of an inverted microscope that was positioned
underneath the indenter. This permitted in-situ viewing of the indentation-
induced debonding through the backside of the substrate. To obtain data on
the debond crack size as a function of indenter load, the specimens were
loaded with a crosshead speed of 0.5 mm/minute and the indentation events
were recorded with a video camera that was attached to the microscope.
During playback of the video tape on a video monitor, the debond crack
sizes were measured at a variety of indenter loads.

RESULTS AND DISCUSSION

Figure 1 contains micrographs of the initiation and growth of a debond
crack in a 98 µm epoxy coating. It is evident that the debond crack forms
in an annular region surrounding the contact zone and extends stably during
the loading portion of the indentation cycle. This type of behavior is
typical of epoxy and epoxy acrylate coatings. In these coatings the debond
crack initiates prior to the indenter penetrating the substrate and extends
out to 2 to 3 times the contact diameter. It should be noted that the

deformations underneath the indenter were predominantly plastic and debonding did not occur underneath the indenter.

Figure 1. Micrographs of a 98 μm epoxy coating being subjected to Vickers indentation. (a) P = 15 N, (b) P = 30 N.

Based on these observations, Fig. 2a contains a schematic of the indentation-induced debond crack. The debond crack has an annular configuration with an outer radius of c and an inner radius of b. This inner radius corresponds to the half diagonal length of the contact zone between the indenter and the coating. The portion of the coating within the central contact zone is plastically deformed and the coating thickness is h. To obtain an expression for the strain energy release rate associated with the debond crack, the debonded portion of the coating was modelled as an annular plate with plane stress conditions in the axial direction as shown in Fig. 2b. The stress distribution in the plate was determined by
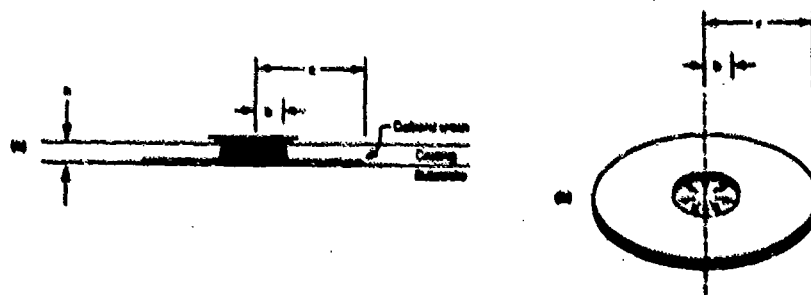
Figure 2(a). Schematic of a typical debond crack; (b) schematic of the annular plate model.

applying the Lame' equations to the plate with a zero displacement boundary condition at the outer edge of the plate (r=c) and a fixed radial stress condition ($\sigma = \sigma_{rb}$) at the inner edge of the plate (r=b). The stresses were integrated over the volume of the plate to determine the strain energy in the plate. Differentiation of the strain energy with respect to the crack area gave an expression for the strain energy release rate [5]:

$$G = \frac{2(1-\nu^2)\sigma_{rb}^2 h}{E} \frac{1}{[1+\nu+2(1-\nu)c^2/b^2]^2} \qquad (1)$$

where E is the elastic modulus of the coating and v is Poissons ratio. Note that if G and σ_{rb} are independent of crack size, Eq. (1) predicts that the ratio of the crack size over the indenter half diagonal length will be constant.

In reference 5 the validity of the above analysis was confirmed with finite element analysis. The finite element work also indicated that the mode I (opening) and mode II (shearing) stress intensity factors at the crack tip were approximately equal. Therefore the phase angle, defined as $\tan^{-1}(K_{II}/K_{I})$, was between 45° and 55° depending on the debond crack size.

Due to the constraint imposed by the surrounding bonded coating, the debonded portion of the coating is in a state of biaxial compression and as a result, buckling is possible. Buckling will occur if the radial compressive stress at the outer edge of the debonded section, σ_{o} is greater than a critical value, σ_{c}. From the Lame' equations [5], σ_{o} is:

$$\sigma_{o} = 2\sigma_{rb}/[1+v+(1-v)(c/b)^2] \qquad (2)$$

The critical buckling stress for a circular plate with a constraint in its center, similar to the constraint provided by the indenter is, [6]:

$$\sigma_{c} = 3.6Eh^2/(1-v^2)c^2 \qquad (3)$$

The decrease in the strain energy in the debonded portion of the coating due to buckling can be determined by assuming linear post-buckling behavior in the debonded portion of the coating [7]. By differentiating the change in the strain energy with respect crack area and subtracting it from Eq. (1), the following equation for the strain energy release rate in the buckled coatings is obtained:

$$G = [(\sigma_{o}-\sigma_{c})(d\sigma_{o}/dc-d\sigma_{c}/dc)\chi-(\sigma_{o}-\sigma_{c})^2(d\chi/dc)](1-\alpha)h/2c \qquad (4)$$

where χ is $[c^2b^2(1+v)+c^4(1-v)]/E(c^2-b^2)$.

To determine whether buckling occurred in the epoxy and epoxy acrylate coatings, σ_{o} and σ_{c} were estimated using Eqs. (2) and (3). E was assumed to be 3.6 GPa for the epoxy coatings and 1.54 GPa for the epoxy acrylate coatings, v for both materials was taken to be 0.38 and b and σ_{rb} were determined as discussed below. It was found that σ_{o} was always less than σ_{c} and thus, buckling is not likely and Eq. (1) can be used to calculate G for these coatings.

Figure 3 contains a plot of the hardness of the epoxy coatings as a function of indenter load where hardness is defined as:

$$H = P/2b^2 \qquad (5)$$

with P being the indenter load. It is seen that the hardness of the epoxy coatings to good approximation is independent of indenter load and coating thickness with the average value being 238 MPa. Since the hardness of the coating is constant, Eq. (5) can be used to replace b in Eq. (1) with $(P/2H)^{1/2}$. This results in the debond crack radius, c being proportional to the indenter load to the 1/2 power. Figure 4 shows a plot of the measured debond crack sizes as a function of the indenter load and indicates

that the data is in good agreement with this trend. To determine σ_{rb} it will be assumed that the indenter contact pressure is constant across the contact zone and equal to the coating hardness. By applying the Tresca yield criteria [1] to the central contact zone, it can be shown that the radial stress σ_{rb} is equal to the yield stress of the material in uniaxial
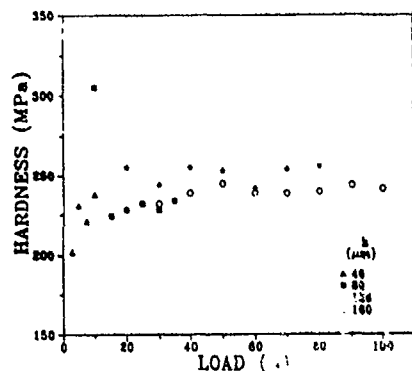
Figure 3. Hardness vs. indenter load for epoxy coatings.
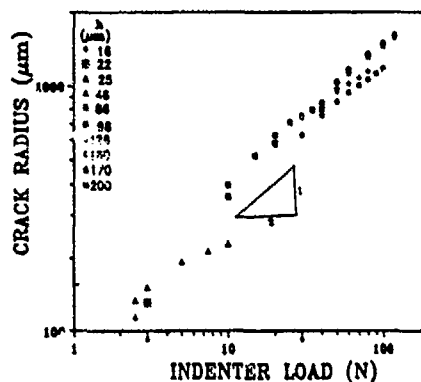
Figure 4. Debond crack radius vs. indenter load for epoxy coatings.

loading, Y, minus the vertical stress or the hardness. If the hardness of the coating is taken to be 2.25Y [1], σ_{rb} is then .56H. Thus:

$$G = \frac{.627(1-v^2)H^2h}{E} \frac{1}{[1+v+4(1-v)Hc^2/P]^2} \tag{6}$$

Values of the interfacial fracture energy for each data point in Fig. 4 were calculated with Eq. 6. For all thicknesses the elastic modulus of the coatings was taken to be 3.6 GPa, Poisson's ratio 0.38, and the coating hardness 238 MPa. The average and 95% confidence limits of the interfacial fracture values for each thickness are shown in Fig. 5. As expected, the
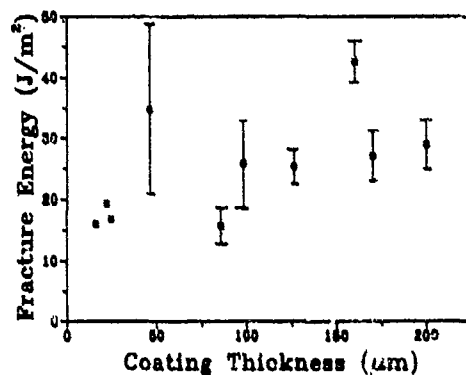
Figure 5   Interfacial fracture energy vs. coating thickness for epoxy coatings.

interfacial fracture energies are independent of coating thickness within experimental scatter with an average value of 25.2 (8.7) J/m^2. For comparative purposes, four point flexure and double cantilever beam tests were also done on the glass/epoxy system. With the double cantilever beam test, which has a phase angle of $0°$ (pure tension), G_c was 8.1(1.7) J/m^2.

With the four point flexure test, which has a phase angle of $41°$, G_c was 15(0.4) J/m^2. This increase in measured interfacial fracture energy with increasing phase angle is similar to that found by other authors [7].

Figure 6 contains a plot of hardness vs indenter load for 49 and 106 μm epoxy acrylate coatings. Unlike the epoxy coatings, the hardness of the epoxy acrylate coatings varies with both indenter load and coating thickness. As indicated by the line in Fig. 6, the hardness of the epoxy acrylate coatings can be approximated by functions of the form $H = A\ P^{1/3}$ where A is a constant which depends on the coating thickness. By substituting $A\ P^{1/3}$ for H in Eq. (5) and using Eq. (5) to replace b in Eq. (1), the following equation is obtained for the strain energy release rate in terms of debond crack length and indenter load:

$$G = \frac{2(1-v^2)\sigma_{rb}^2 h}{E} \frac{1}{[1+v+4(1-v)Ac^2/P^{2/3}]^2} \quad (7)$$

Due to the fact that the hardness of the epoxy acrylate coatings increases with increasing indenter loads, the assumption of a constant contact stress across the contact zone is not valid; however, it is believed that the stresses at the outer edge of the contact zone are still independent of the indenter load. This is because the edge of the contact zone is at the edge of the plastic zone where the material has just begun to yield and thus the plastic strains will always be small. The stress increase which accounts for the increasing hardness occurs at the center of the contact zone where the plastic strain continuously increases. Based on assumptions that G and σ_{rb} are independent of indenter load, Eq. (7) predicts that the debond crack radius will be proportional to the indenter load to the 1/3 power. In Fig. 7 the debond crack radius is plotted as a function of the indenter
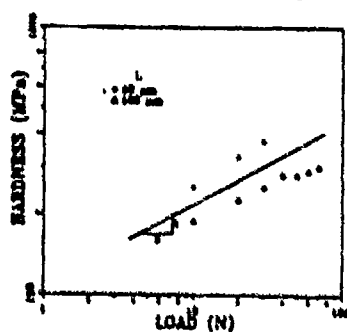
Figure 6. Hardness vs. indenter load   Figure 7. Debond crack radius
          for epoxy acrylate coatings.   vs. indenter load for
                                                        epoxy acrylate coatings.

load. It is seen that there is moderately good agreement between the predicted slope, 1/3 and the data. However, a calculation of the

interfacial fracture energy is not possible due to the lack of knowledge of the exact value of σ_{rb}.

Figure 8 shows the initiation and growth of debond a crack in a 7 μm polyimide coating. The behavior seen in Fig. 8 is typical of polyimide and urethane acrylate coatings. It is seen that the debond crack initiates during the loading portion of the indentation cycle but with further increases of the indenter load, the outer radius of the debond crack does not become much larger than the contact radius. As a result, the annular plate model cannot be applied to the data for the polyimide and urethane acrylate coatings. The limited debond crack growth in the polyimide and urethane acrylate coatings is due to the debond crack initiating after the indenter penetrates into the substrate. Once the indenter has penetrated into the substrate, most of the indenter load is supported by the substrate since the glass substrate is more than an order of magnitude harder than the polymer coatings. Thus, most of the work done by the indenter goes into plastic deformation of the substrate rather than debonding of the coating.
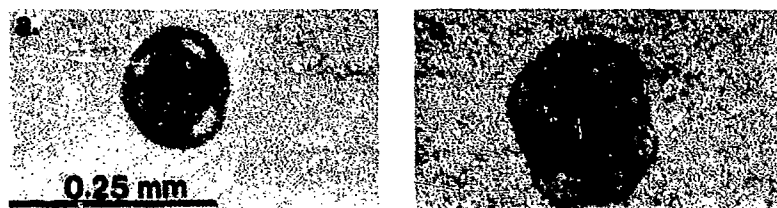
Figure 8. Micrographs of a 7 μm polyimide coating being subjected to Vickers indentation. (a) $P = 12$ N, (b) $P = 25$ N.

In summary, it has been shown that the indentation method can be used to determine the interfacial fracture energy associated with polymer coating systems in which well developed debond cracks form and strain hardening of the coating does not occur. Well developed debond cracks form in systems where debonding occurs prior to penetration of the substrate by the indenter. To determine the interfacial fracture energy in systems where strain hardening of the coating occurs, a more sophisticated approach to modelling the plastic deformation underneath the indenter is needed.

ACKNOWLEDGMENT

REFERENCES

1. J.E. Ritter, T.J. Lardner, L. Rosenfeld, and M.R. Lin, J. Appl. Phys., 66, (8), 3626-3634, (1989).
2. N.J. Matthewson, Appl. Phys. Lett., 49, 1426-1428, (1986).
3. D.B. Marshall and A.G. Evans, J. Appl. Phys., 56, 2632-2638, (1984).
4. C. Rossington, A.G. Evans, D.B. Marshall and B.T. Khuri-Yakub, J. Appl. Phys., 56, 2639-2644 (1984).
5. L.G. Rosenfeld, J.E. Ritter, T.J. Lardner and M.R. Lin, Submitted to J. Appl. Phys.
6. S. Timoshenko and J.M. Gere, Theory of Elastic Stability, 2nd. Edition, McGraw Hill, New York, (1973).
7. M.C. Lu, B.J. Dagleish, A.G. Evans, Closed Loop, 17, 13-27, (1989).

INTERFACE PROPERTIES FOR CERAMIC COMPOSITES FROM A SINGLE-FIBER PULL-OUT TEST

ELIZABETH P. BUTLER*, EDWIN R. FULLER, JR.*, AND HELEN M. CHAN**
*Ceramics Division, Nat'l Inst. of Standards & Tech., Gaithersburg, MD 20899
**Dept. of Materials Science & Eng., Lehigh University, Bethlehem, PA 18015

ABSTRACT

An experimental approach has been developed using a single-fiber pull-out test to measure intrinsic interface properties for ceramic composites. The properties are determined from a pull-out, force-displacement curve, which is directly related to reinforcement toughening via fiber/matrix debonding and frictional pull-out. They were evaluated for a model composite system of continuous SiC fibers with various surface treatments in a borosilicate glass matrix. For the processing conditions used, the interface fracture toughness and the interface frictional shear resistance were found to be 1.0 ± 0.5 J/m^2 and 3.3 ± 0.6 MPa, respectively, for as-received fibers. Experiments conducted with long embedded fiber lengths allowed the shear resistance to be deconvolved into an interface friction coefficient of 0.05 ± 0.01 and an initial fiber-clamping pressure of 65 ± 6 MPa. Nitric acid-washed fibers gave an increased interface toughness of 3.6 ± 0.1 J/m^2 and friction coefficient of 0.08 ± 0.02, but nearly the same initial clamping pressure, 72 ± 12 MPa. Calculations of the clamping pressure from the fiber/matrix thermal expansion mismatch and from stress birefringence measurements in the glass were in general agreement with this value.

INTRODUCTION

Major improvements in the fracture resistance behavior of brittle ceramics have been made in the last decade by developing microstructures which lead to the phenomenon of crack shielding. In such systems, elements of the microstructure shield the crack tip from the applied mechanical load. A notable example of this phenomenon is the incorporation of ceramic fibers or whiskers into brittle matrices to enhance their toughness [1]. Advantages of reinforcement toughening over other shielding mechanisms are that a variety of reinforcements (fibers, whiskers, platelets, etc.) can be incorporated into a wide range of host materials, directional properties can be obtained, and toughening increments may be retained at elevated temperatures. However, fundamental understanding of reinforcement-toughening mechanisms has yet to be established. Furthermore, the links between ceramic processing, toughening mechanisms, and structural performance are equally vague. Such understanding will most readily be attained via a micromechanics description of reinforcement toughening, relating microstructure and interfacial properties to processing and structural performance.

The toughening attributes that fibers produce in brittle ceramics arise from several phenomena, which are critically dependent on the properties of the fiber/matrix interface. The toughening increment via fiber bridging is simply the product of the volume fraction of fibers, V_f, and the integral of the force-displacement curve for fiber debonding and frictional pull-out. In terms of the J-integral [2], this toughening increment is:

$$J_r = V_f \cdot \int T(\delta) \, d\delta, \tag{1}$$

where $T(\delta)$ is the force-displacement relation for a single-fiber pull-out. The important parameters for fiber toughening lie in this force-displacement relation. These parameters are amenable to direct experimental measurement via a single-fiber pull-out test. This test was initially developed for testing polymeric composites [3], but is now widely applied to all composite materials. Furthermore, this test provides a systematic way for

investigating the influence of fiber/matrix materials' properties and processing conditions on the toughness of the final manufactured composite.

THEORY

Single Fiber Pull-Out Test

The analysis of fiber debonding and subsequent frictional pull-out is treated here as an interfacial fracture problem [4,5] with frictional wake tractions [6,7]. A simplistic analysis [8], i.e., one with no Poisson's contractions, is illustrated schematically in Fig. 1. A cylindrical crack of radius R (also the fiber radius) is propagated down the fiber/matrix interface as a pure Mode II crack. The axial stress σ is transferred from the fiber to the matrix along the flanks of the debonded crack by interfacial friction. The differential stress transfer with axial distance z is:

$$d\sigma/dz = -2\tau/R, \tag{2}$$

where τ is the frictional shear stress on the interface. Assuming a Coulomb friction law for τ with a friction coefficient of μ, this shear stress is:

$$\tau = \mu \cdot \sigma_{rr}, \tag{3}$$

where σ_{rr} is the radial matrix (clamping) stress. With no Poisson's effects, σ_{rr} is only the initial clamping pressure, q_o, that results from the thermal expansion mismatch strains that occur during fabrication. τ is accordingly independent of z, so that the axial fiber stress decreases linearly in z, as depicted in Fig. 1, as this stress is transferred to the matrix.

The interface is presumed to be cohesively bonded at the crack tip. Accordingly, the axial fiber stress does not fall entirely to its average composite value of σ_c at the crack tip, but rather has a stress discontinuity.[1] To determine the magnitude that this stress discontinuity can reach before equilibrium crack propagation ensues, we use a strain-energy-release-rate analysis similar to that of Marshall and Oliver [6] and Gao et al. [7]. We first calculate the elastic strain energy, U_{SE}, the external work, W_{ext}, and the frictional work, W_{fric}, and then differentiate $(U_{SE} - W_{ext} + W_{fric})$ with respect to crack area, $2\pi Rc$, to obtain a strain-energy-release rate, G. Equating this G to a critical interface toughness, G_{ic}, we obtain the following relation between external stress, σ_a, and debond crack length, c, for equilibrium crack propagation:

$$\sigma_a = \sigma_i + 2\tau c/Re_m. \tag{4}$$

where $e_m = m/(m+f)$, $m = E_m/E_f$ (the ratio of the Young's modulus of the matrix to that of the fiber), and $f = V_f/(1-V_f)$ (the volume fraction ratio). The "frictionless debond" stress, σ_i, is related the interface toughness, G_{ic}, through the relation: $\sigma_i = [4E_f G_{ic}/Re_m]^{1/2}$.

Eqn. (4) is effectively a fracture resistance curve (R-curve) for the interfacial fracture problem. Multiplying Eqn. (4) by $[Re_m/4]^{1/2}$, puts it in units of stress intensity factor: $\sigma_i[Re_m/4]^{1/2} = [E_f G_{ic}]^{1/2}$ is the critical stress intensity factor for the interface and $\tau c/[Re_m]^{1/2}$ is the rising fracture resistance with crack extension that results from frictional tractions across the crack flanks. When Poisson's effects are included, the resulting contractions reduce the radial clamping pressure and accordingly the crack length over which frictional shear stresses can be transferred. This phenomenon results in an asymptotic, or steady-state value for the fracture

---

1. A rigorous analysis should include the crack-tip stress singularity and a non-frictional shear-stress transfer to σ_f beyond the crack tip.
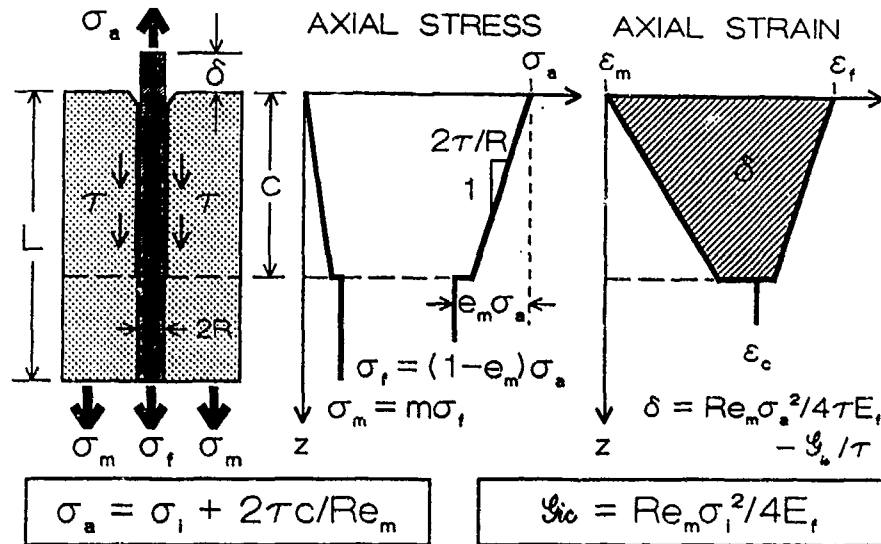
Fig. 1. Schematic drawing of a simplistic analysis of fiber debonding (i.e., one with no Poisson's contractions) and subsequent frictional fiber pull-out: an interfacial fracture problem with frictional wake tractions.

resistance, and debond stress. An analysis that includes fiber-debonding, frictional pull-out, and Poisson's contractions is that of Gao et al. [7]. Although their treatment is a plane-strain approximation to the exact problem, it is fully analytical and expressed in terms of materials', interface and processing parameters. Their generalization of Eqn. (4), is:

$$\sigma_a = \sigma_i e^{-\lambda \cdot c} + \bar{\sigma}(1 - e^{-\lambda \cdot c}), \tag{5}$$

where λ is a reciprocal length giving the effective frictional shear-stress transfer distance and $\bar{\sigma}$ is the asymptotic pull-out stress for long crack lengths. The experimentally determined parameters σ_i, λ, and $\bar{\sigma}$ are related, respectively, to the interface fracture toughness, G_{ic}, the fiber-matrix friction coefficient, μ, and the initial fiber-clamping pressure, q_0, by:

$$\sigma_i = [(4E_f G_{ic}/R)[1+(f/m)\cdot(1-2k\nu_m)/(1-2k\nu_f)]/(1-2k\nu_f)]^{1/2} \tag{6}$$
$$\lambda = 2\mu k/R \tag{7}$$
$$\bar{\sigma} = q_0 \cdot [1 + (f/m)\cdot(\nu_m/\nu_f)]/k \tag{8}$$

where $k = (m\nu_f + f\nu_m)/[m(1-\nu_f) + 1+\nu_m + 2f]$, and ν_m and ν_f are the matrix and fiber Poisson's ratio, respectively. These results reduce to the simplistic analysis of Fig. 1, when $\nu_m = \nu_f = 0$.

Thermal Expansion Mismatch Stresses

When the thermal expansion coefficient of the matrix is greater than that of the fibers, the matrix contracts on the fibers upon cooling from the fabrication temperature. The residual (biaxial) clamping pressure on the fiber, q_0, that results from a cooling differential of ΔT is [9]:

$$q_o = [E_{fz}(\alpha_m - \alpha_{fz}) + E_{fr}(\alpha_m - \alpha_{fr})] \cdot \Delta T \tag{9}$$

where α_m is the thermal expansion coefficient of the matrix, and α_{fz} and α_{fr} are, respectively, the axial and transverse thermal expansion coefficients of the fiber. α_{fz} and α_{fr} are here assumed to be the same. The effective elastic moduli E_{fz} and E_{fr} are given by:

$$E_{fz} = E_m k/[m+f + 2kf(\nu_f - \nu_m)] \quad \text{and} \quad E_{fr} = E_{fz} \cdot (m+f)/(m\nu_f + f\nu_m) \tag{10}$$

where the parameters m, f, and k are defined above.

EXPERIMENTAL PROCEDURE

Single Fiber Pull-Out Test

Specimens for the single-fiber pull-out test were fabricated from SiC fibers sandwiched between two plates of borosilicate glass.[2] The fibers were first degreased by washing them in 1,1,1-tri-chloroethelyne, followed by rinsing them in acetone and then ethanol. The sandwich assembly was diffusionally bonded by hot pressing in vacuo at a temperature of 725°C and under a stress of 3.4 MPa. The bonded assembly with fiber protruding from both ends was then cut to give two specimens of different embedded fiber lengths. To enhance fiber/matrix bonding, some fibers were washed with a 50 volt nitric acid solution following the degreasing procedure to remove the carbon-rich surface layers [10].

Fibers were pulled from the matrix using an universal testing machine with a 5 kg load cell. The sample/grip arrangement is shown in Fig. 2. The crosshead displacement speed was 1 cm/min, a rate fast enough to prevent environmentally assisted fracture,[3] but slow enough for the response time of the strip-chart recorder and the load cell. Effects of the testing system's compliance on experimental results were evaluated and found to be negligible.

A principal experimental difficulty in many fracture mechanics measurements is the determination of the crack length. This difficulty is particularly pronounced for the fiber/matrix debond crack due to its 3-dimensional nature. A simple stratagem was used in the current experiments to resolve this difficulty. The debond crack was propagated to the end of the specimen, at which point the crack length is known explicitly, namely the embedded fiber length, L. See Figs. 1 and 2. Since the applied stress, σ_a, increases with crack length, c, according to Eqn. (5), i.e., the "rising fracture resistance" behavior of the micromechanic pull-out problem, this "break-through" fracture condition corresponds to a maximum fiber-debond stress, σ_d:

$$\sigma_d = \sigma_i e^{-\lambda \cdot L} + \bar{\sigma}(1 - e^{-\lambda \cdot L}), \tag{11}$$

After "break-through", the interface toughness no longer contributes to Eqn. (11), i.e., $\sigma_i = 0$, and the applied stress drops to that of the maximum frictional stress, σ_f:

$$\sigma_f = \bar{\sigma}(1 - e^{-\lambda \cdot L}). \tag{12}$$

---

2. The SiC fibers (AVCO SCS-6) are 140 μm diameter monofilaments of chemically vapor-deposited SiC on a carbon core and have two carbon-rich surface layers. The matrix material is Corning borosilicate glass #7740. (Product names are used to identify the materials used. Such identification does not imply recommendation or endorsement by NIST, nor does it imply that they are the best available for the purpose.)

3. Studies examining effects of loading rate on debond stress indicate possible environmental influences at the lowest loading rates [8].
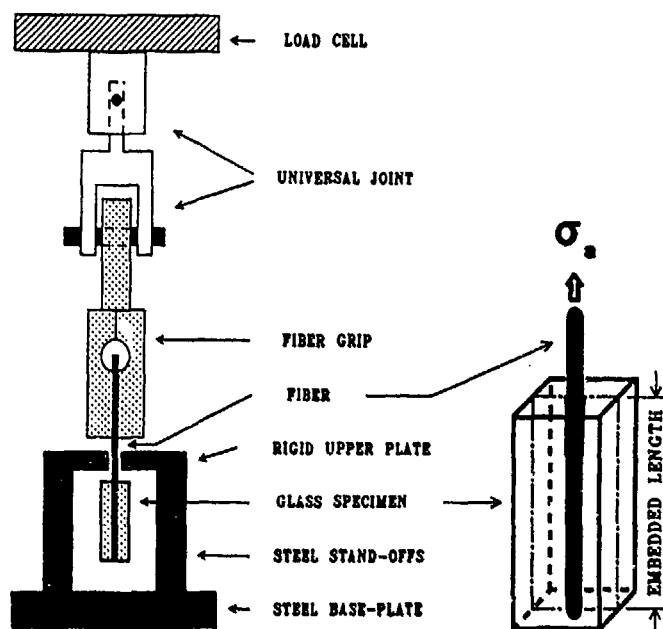
Fig. 2. Schematic diagram of the single-fiber pull-out test geometry.

Accordingly, by using specimens of varying embedded fiber lengths, empirical relations can be developed between σ_d and c=L, and between σ_t and c=L. The stress drop upon "break-through" is an accurate way to determine, σ_i, or G_{i_0}:

$$\Delta\sigma = (\sigma_d - \sigma_t) = \sigma_i e^{-\lambda \cdot L}. \tag{13}$$

Upon continued loading after the stress drop, the applied stress decreases linearly to zero as the fiber pulls from the matrix.

Clamping Pressure from Stress-Induced Birefringence

Under stress, glass becomes optically birefringent. This stress-induced retardation of light travelling through glass is directly proportional to the difference in principal stresses, $(\sigma_{rr} - \sigma_{\phi\phi})$, through the stress optical law

$$\Delta = Ct(\sigma_{rr} - \sigma_{\phi\phi}), \tag{14}$$

where Δ is the relative phase shift of light waves polarized along the radial and tangential directions, C is the stress optic coefficient for the material, and t is the axial specimen thickness (and the optic path length). The principal stress difference in the matrix, $(\sigma_{rr} - \sigma_{\phi\phi})$, is related to the initial clamping pressure on the fiber, q_0, by the elasticity relation [7]

$$(\sigma_{rr} - \sigma_{\phi\phi}) = 2q_0 \cdot (1+f)(R^2/r^2), \tag{15}$$

where R is the fiber radius, r is the polar coordinate measured from the fiber axis, and f is the volume fraction ratio, $V_f/(1-V_f)$. Thus, the initial clamping pressure is related to the relative phase shift, Δ, by

$$q_0 = \Delta \cdot (r/R)^2/[2Ct(1+f)]. \tag{16}$$

In the current study the phase shift Δ was measured by the Tardy method [11] using a polariscope with both the polarizer and analyzer and the two quarter-wave plates in the crossed arrangement.

RESULTS AND DISCUSSION

The maximum debond stress and the maximum frictional stress were both measured as a function of embedded fiber length. The results are presented in Fig. 3 for as-received fibers and nitric acid-washed fibers in a borosilicate glass matrix. For each fiber treatment, both the debond and frictional stress data show an initial linear behavior and then turn over into a common asymptotic stress, $\tilde{\sigma}$, at long embedded fiber lengths. The debond stress is always greater than the frictional stress at a given L. In the linear region of the debond curve, the initial gradient is equal to $\lambda(\tilde{\sigma} - \sigma_i)$ and the stress-axis intercept is the frictionless debond stress, σ_i.

The σ_d and σ_ℓ data for each fiber treatment were fitted simultaneously to Eqns. (11) and (12), respectively, using a non-linear least squares analysis to determine the three independent parameters: σ_i, λ, and $\tilde{\sigma}$. Since the value for σ_i was typically very small, this simultaneous fit was not an accurate way to determine σ_i (i.e., this procedure occasionally gave a negative value for σ_i, which is not physical, since experimentally the stress differences in Eqn. (13) were all greater than or equal to zero). Accordingly, both data sets were initially fit to Eqn. (12) to give a common value of λ and $\tilde{\sigma}$. The difference between the debond stress and the frictional stress at each value of L was then fit to Eqn. (13) with the known value of λ to determine σ_i. The values for the parameters thus determined are given in
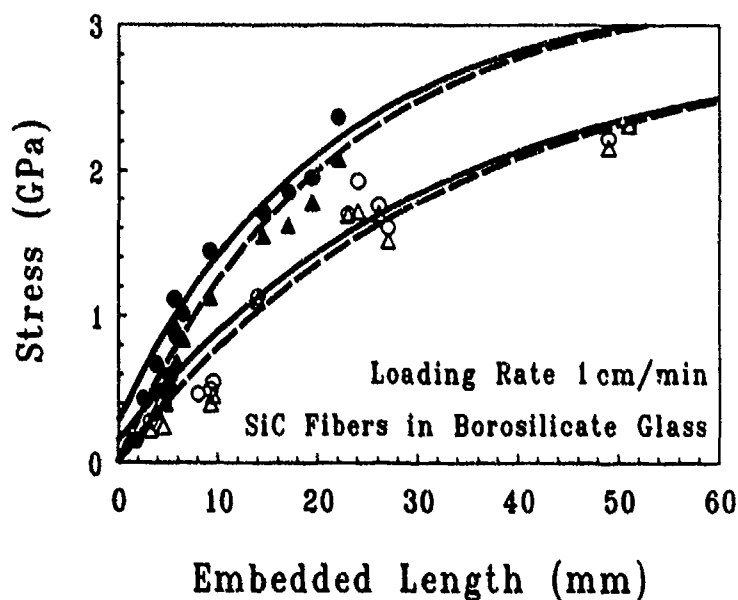
Fig. 3. Debond stress (circles) and maximum frictional stress (triangles) as a function of embedded fiber length for as-received fibers (open symbols) and nitric acid-washed fibers (filled symbols) in a borosilicate glass matrix. The solid and dashed lines are graphs of Eqns. (11) and (12), respectively, with the parameters σ_i, λ, and $\tilde{\sigma}$ determined from the least squares fit.

Table I. Single-fiber pull-out parameters and intrinsic interface properties
of a SiC fiber-reinforced, borosilicate glass matrix composite system

SINGLE-FIBER PULL-OUT PARAMETERS AND INTRINSIC COMPOSITE INTERFACE PROPERTIES	Surface Treatment of SiC Fiber	
	As-Received	Acid-Washed
Frictionless Debond Stress, σ_i (MPa) Asymptotic Pull-Out Stress, $\tilde{\sigma}$ (GPa) Inverse Stress Transfer Length, λ (m^{-1})	149 $\pm$ 36 2.9 $\pm$ 0.3 31 $\pm$ 5	285 $\pm$ 52 3.3 $\pm$ 0.6 48 $\pm$ 12
Interface Toughness, G_{i_o} (J/m^2)	1.0 $\pm$ 0.5	3.6 $\pm$ 0.1
Frictional Shear Resistance, τ (MPa) * Friction Coefficient, μ * Initial Clamping Pressure, q_o (MPa)	3.3 $\pm$ 0.6 0.05 $\pm$ 0.01 65 $\pm$ 6	5.5 $\pm$ 0.2 0.08 $\pm$ 0.02 72 $\pm$ 12

Table I for both the as-received and nitric acid-washed fibers. The error
given for each parameter represents only that error resulting from the least
squares fit. The intrinsic interface properties, G_{i_o}, μ, and q_o, were calcu-
lated from these parameters using Eqns. (6), (7), and (8), respectively.
These results are also given in Table I. Pull-out measurements at long
embedded lengths are required to deconvolve the interfacial shear resistance,
τ, into its components, μ and q_o. However, τ by itself can be determined
from the initial slope, $\lambda \cdot \tilde{\sigma}$, of the frictional pull-out curve:

$$\tau = \mu \cdot q_o = (\lambda \tilde{\sigma} R/2)/[1 + (f/m) \cdot (\nu_m/\nu_\ell)]. \tag{17}$$

The initial clamping stress on the fiber, as well as the stress distri-
bution in the matrix away from the interface, can be independently calculated
from the known processing conditions. Using the thermal expansion coeffi-
cient for borosilicate glass, 3.2×10^{-6}/°C, and that for the fiber (manufac-
turer's data sheet [12]), 2.0×10^{-6}/°C, q_o was determined to be 47 MPa, in
good general agreement with the value determined from the pull-out experi-
ments. However, using the axial expansion coefficient of 2.63×10^{-6}/°C
measured by Goettler and Faber [13], this value drops to 22 MPa.

The clamping stress can also be measured from the radial stress distri-
bution in the matrix using the stress-induced birefringence properties of
borosilicate glass. This was done, but a value of the stress optical coeffi-
cient, C, is needed to calculate q_o. Values for C in borosilicate glass have
been reported in the range of 1.6 to 2.91 TPa^{-1} [14]. Values of q_o deter-
mined from this range of values are 160 MPa to 90 MPa for the as-received
fiber composite. These values are higher than the pull-out results, but a
final comparison awaits an experimental determination of C for the borosili-
cate glass used in the present experiments. These measurements are underway.

Comparing the results of the as-received and nitric acid-washed fiber
pull-out tests, we observe that the fiber/matrix bond, as characterized by
the interface toughness, and the friction coefficient were both enhanced by
the nitric acid treatment. Little change was observed in the initial clamp-
ing pressure within the estimated errors. The acid wash facilitated the
removal or etching of the outermost carbon layer(s) of the SCS-6 fibers [10].
These layers are important in two ways: as an interlayer to prevent strong
fiber/glass bonding and as a frictional lubricant at the interface. Thus,
removal of these layers would cause an increase in both the interface bonding
and the interface friction. The initial clamping stress is only dependent on
the processing temperature and difference in linear expansion coefficients
between the fiber and matrix. As these parameters are not affected by the
nitric acid wash, no change is expected in the clamping stress.

CONCLUSIONS

The single-fiber pull-out test is an excellent technique for determining fundamental interface properties and pull-out force/displacement relations. Long crack lengths, or rather long embedded fiber lengths, are required to deconvolute the interfacial shear resistance into a coefficient of friction and an initial fiber-clamping stress. The interfacial properties measured in this study for a model SiC fiber/borosilicate glass system are of similar magnitude to those reported by other authors working on similar systems.

The initial clamping stress on the fiber is amenable to determination by three different techniques which yield similar results. However, the stress birefringence measurements to date are only preliminary results and await an experimental determination of the stress optical coefficient.

The overall experimental procedure provides an effective way to determine micromechanical properties of composite interfaces, to infer composite toughening increments resulting from fiber reinforcement, and to monitor influences of processing variations on composite properties.

ACKNOWLEDGEMENTS

REFERENCES

1. D.B. Marshall and J.E. Ritter, "Reliability of Advanced Structural Ceramics and Ceramic Matrix Composites," Am. Ceram. Soc. Bull., 66 (2), 309-317 (1987).
2. J.R. Rice, "A Path Independent Integral and the Approximate Analysis of Strain Concentration by Notches and Cracks," J. Appl. Mech., 35, 379-386 (1968).
3. L.J. Broutman, "Measurement of the Fiber-Polymer Matrix Interfacial Strength," in Interfaces in Composites, edited by M.J. Salkind, STP 452, Am. Soc. for Testing and Materials, Philadelphia, 1969, pp. 27-41.
4. C. Gurney and J. Hunt, Proc. Roy. Soc. (London), A299, 508 (1967).
5. H. Stang and S.P. Shah, J. Mater. Sci., 21, 953 (1986).
6. D.B. Marshall and W.C. Oliver, "Measurement of Interfacial Mechanical Properties in Fiber Reinforced Ceramic Composites," J. Am. Ceram. Soc., Vol. 70, [8], 542-48 (1987).
7. Y.-C. Gao, Y.-W. Mai and B. Cotterell, "Fracture of Fiber-Reinforced Materials," J. Appl. Math. and Phys. (ZAMP), 39, 550-572 (1988).
8. E.P. Butler, E.R. Fuller, Jr., and H.M. Chan, to be published.
9. M. Vedula, R.N. Pangborn and R.A. Queeney, "Fiber Anisotropic Thermal Expansion and Residual Thermal Stress in a Graphite/Aluminum Composite," COMPOSITES, Vol. 19, [1], 55-60 (1988).
10. J.H. Cranmer, C.C. Tesoro, and D.R. Uhlmann, "Chemical Modification of Carbon Fiber Surfaces with Organic Polymer Coatings," Ind. Eng. Chem. Prod. Res. Dev., 21, 185-190 (1982).
11. Photoelastic Stress Analysis, by A. Kuske and G. Robertson, (John Wiley & Sons, New York, 1974), pp. 111-114.
12. Technical Data Sheet for Textron Silicon Carbide Fibers, TEXTRON Specialty Materials, Lowell, MA, March 1988.
13. R.W. Goettler and K.T. Faber, "Interfacial Shear Stresses in Fiber-Reinforced Glasses," Composites Science & Technology, (1989), in press.
14. J.W. Fleming "Optical Glasses," in CRC Handbook of Laser Science & Technology, Volume 4: Optical Materials, Part 2, edited by M. J. Weber, CRC Press, Inc., 1986, pp. 69-83.

BRIDGING PROCESSES IN METAL-REINFORCED CERAMICS

M. C. SHAW*,** D.B. MARSHALL* AND A. G. EVANS**
*Structural Ceramics Department, Rockwell International Science Center, 1049 Camino Dos
Rios, Thousand Oaks, California 91360
**Materials Department, University of California, Santa Barbara, California, 93106

ABSTRACT

In situ observations of fracture mechanisms and crack bridging effects in model copper-glass
laminated composites are described and compared with measured resistance curves.

INTRODUCTION

Toughening of brittle materials by ductile reinforcements may involve either crack bridging
or process zone contributions. However, a systematic study of their relative effects, and of the
role of the interfacial bond strength in a geometry conducive to accurate analysis is lacking. The
current investigation was initiated to address this deficiency through experiments conducted
with model copper/glass laminate composite systems.

The steady-state increase in toughness ΔG_b due to crack bridging is:

$$\Delta G_b = f \int_0^{u^*} \sigma(u)\, du \qquad (1)$$

where $\sigma(u)$ is the stress in the metal ligaments between the crack faces, u is the local crack
opening displacement, u^* is the maximum plastic stretch of the metal and f is the volume
fraction of metal phase. The influence of the metal/ceramic interfacial bond strength on ΔG_b
has been analyzed by Mataga [1]. For well-bonded ductile ligaments, the high degree of elastic
constraint exerted by the uncracked matrix increases the peak stress above the uniaxial flow
stress (Figure 1) [1]. However, the corresponding small amount of plastic stretching before
rupture restricts the overall toughening. On the other hand, if debonding occurs at the
metal/ceramic interface on either side of the crack, then plastic stretching (i.e. u^*) is larger but
the constraint (and hence the peak stress) is smaller. Consequently, the increase in toughness is
predicted to depend on the extent of debonding [1] (Figure 2), with the interfacial
characteristics strongly influencing the overall mechanical characteristics of the composite.

SPECIMEN PREPARATION

Copper/glass composite laminates were selected as the model system. These were prepared
by diffusion bonding at temperatures ranging from 450° C, to 700° C, in a vacuum of
$\leq 2 \times 10^{-6}$ Torr, with an applied pressure of 2 MPa. Copper was introduced between glass
cover slips† by two different methods. First, thin films (300-500 nm) of 99.999% pure
copper were electron-beam evaporated on both sides of pre-cleaned glass cover slips.
Diffusion bonding occurred between mating copper surfaces, resulting in laminates with
approximately 1%, by volume, of metal. In the second technique, sheets of copper-silver alloy
foil†, nominally 35μm thickness, were used. In this case, bonding occurred between the foil
and the glass surfaces, resulting in a composite with approximately 25% metal.

---

† The composition (wt %) of the glass cover slips was: 64% SiO_2, 9% B_2O_3, 7% Z_nO, 7% K_2O
7% Na_2O, 3% TiO_2 and 3% Al_2O_3. The alloy foil contained 27.5% Cu, 59.2% Ag, 12% In, 1.2%
Ti, and <0.01% Al, Ca, Fe, Mn, Ni, Si and Mo.
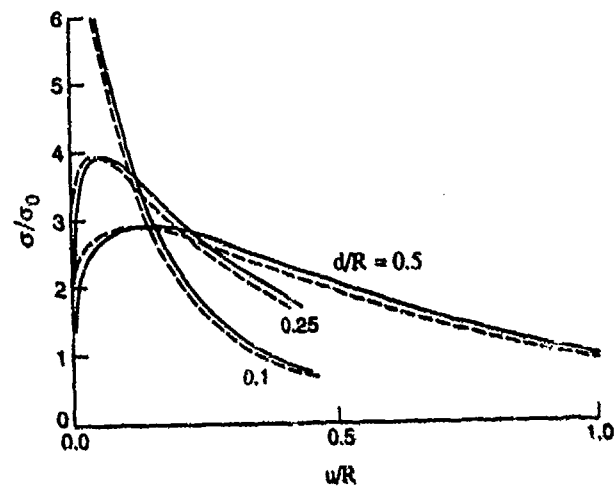
Figure 1. Effect of elastic constraint on the bridging ligament stress/displacement relationship. σ_0 is the uniaxial yield stress, R the ligament radius, and d the debond length. From Ref. 1.
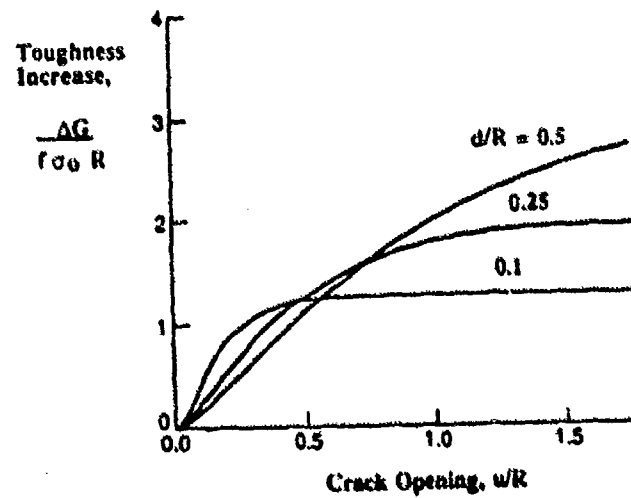
Figure 2. Effect of debond zone size on the steady-state toughness increase. From Ref. 1.

MECHANICAL TESTING

Each laminate was machined into a compact tension (C(T)) specimen with geometry specified by ASTM E 399 - 83, and a final prenotch width of ~200 microns. The C(T) specimens were tested under displacement control in a fixture which permitted high magnification optical monitoring of the crack. During a typical test, the specimen was completely unloaded after initial, stable, crack pop-in from the notch root. The specimen was then reloaded to failure, with the crack growing stably with increasing displacement of the loading points. After final fracture, the fracture surfaces were examined in a scanning electron microscope.

EXPERIMENTAL RESULTS

Copper Film Laminates

An example of the fracture resistance (R-curve) measured for a C(T) specimen, comprising 5 glass and 4 copper film layers diffusion bonded at 550° C, is shown in Figure 3. The fracture resistance, K_R, increased from 0.4 MPa.m$^{1/2}$ to a near-steady-state value of ~0.8 MPa.m$^{1/2}$ over an increment of crack growth of approximately 3 mm. Scanning electron microscopy of the fracture surfaces revealed that the copper had locally debonded and plastically deformed to a knife edge (Figure 4). The plastic stretch of the copper was 1 - 2 μm, approximately the same as the film thickness. The debonding that governs the plastic stretch is influenced by the interfacial fracture energy. One method of raising the interfacial fracture energy is to increase the roughness of the interface [2]. Preliminary results suggest that this may be accomplished by diffusion bonding above the annealing point of the glass (~550° C). The scanning electron micrograph of Figure 5 from a debonded region of a laminate specimen diffusion bonded at 600° C confirmed close contact between the copper film and the glass, with the glass surface adjacent to the copper deforming during diffusion bonding to conform to the grain boundary grooves of the copper.
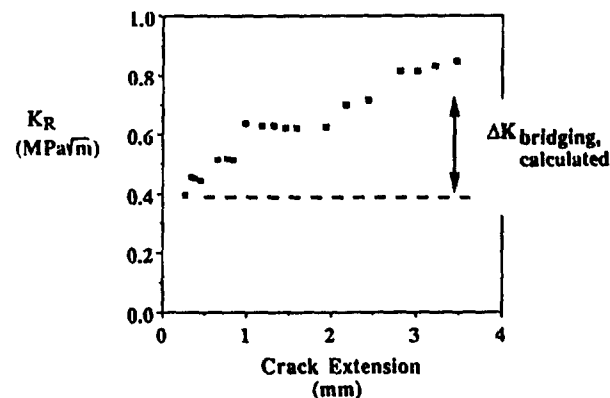
Figure 3. R-curve measured from a copper film laminate C(T) specimen diffusion bonded at 550° C.
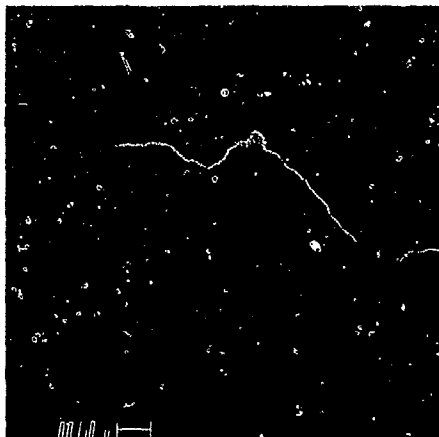
Figure 4. Scanning electron micrograph of the fracture surface from the copper film laminate, revealing debonding between the copper and the glass, plastic stretch of the copper, and failure by deformation to a knife edge.
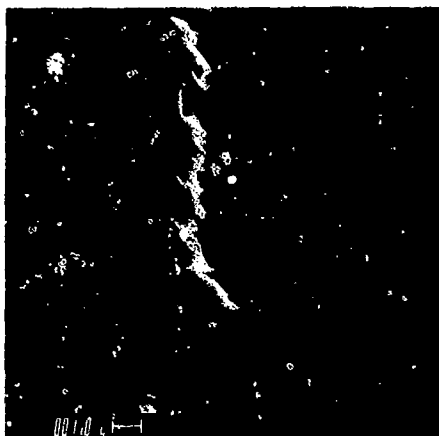
Figure 5. Interfacial morphology in a laminate diffusion bonded at 600° C: outer glass sheet removed and the copper film (left) peeled away to expose the debonded glass surface (right).

Copper Alloy Foil Laminates

The copper foil C(T) specimens revealed a different fracture mode. Multiple cracks nucleated from both the root of the prenotch, and the sides of cracks that formed during the test, with initial trajectories inclined to the prenotch crack plane. After some extension, these multiple cracks became oriented parallel each other, and to the prenotch crack plane (Figure 6). Although the existence of parallel, multiple cracks precluded the measurement of a meaningful fracture energy, it is possible to estimate a "nominal" toughness of approximately 12 MPa.m$^{1/2}$, based on the length of the leading crack. This value indicates substantial toughening.
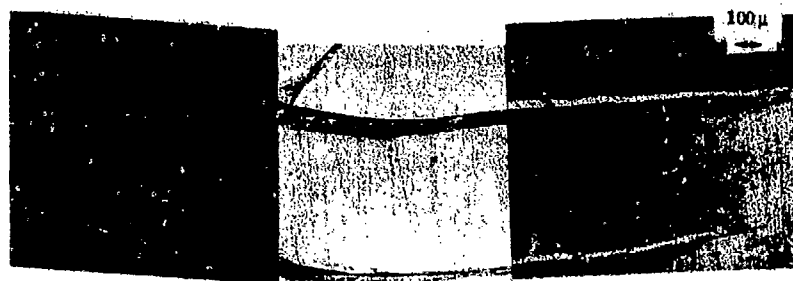
Figure 6. In situ optical micrographs from a copper foil laminate, viewed through the outer glass sheet and focused on the interface. The root of the prenotch is to the left of the field of view.

Debonding is also apparent along the metal-ceramic interface on both sides of the cracks, with debond lengths of up to 3-4 times the foil thicknesses (Fig. 6). The width of the debonded zone at the root of the prenotch continued to increase during the test, indicating that the crack remained completely bridged by the foil. In contrast to this extensive wake debonding, no debonding was observed ahead of the crack tip. Plastic deformation of the copper alloy foil within the bridged zone was observed (Figure 7) with failure occurring by microvoid coalescence.
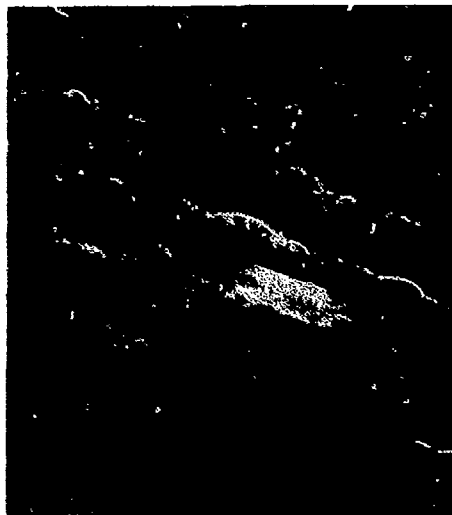
Figure 7. Scanning electron micrograph of the fracture surface of the foil laminate C(T) specimen. Debonding, plastic stretching and failure of the foil by microvoid coalescence are evident.

The existence of crack bridging ligaments modifies the opening displacements within the crack. Recent analysis has shown that it is possible to use high-accuracy measurements of crack profiles to determine the stress-displacement relationship for the bridging ligaments [3]. Preliminary measurements of the opening profile of a bridged crack in the copper foil laminate are shown in Figure 8. The effect of crack bridging is clearly evident as a zone of reduced crack opening within approximately 2.5 mm of the crack tip. At point A in Fig. 8 the crack opening is ~8μm (u/R~ 0.3) and the length of the interfacial debond, d, is ~ 80μm (d/R ~2).
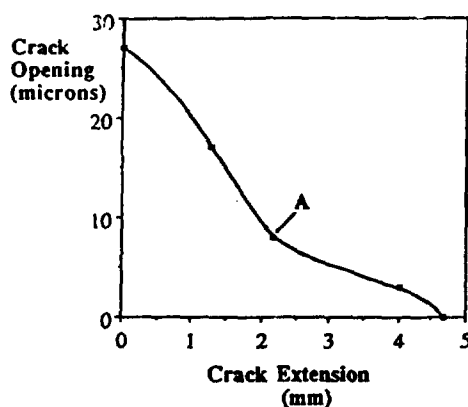
Figure 8. Crack opening displacements of a bridged crack in a copper foil C(T) laminate.

DISCUSSION AND CONCLUSIONS:

In both of the copper/glass model laminate composites, substantial toughening was observed. However, the fracture modes differed: in the film system, failure involved propagation of a single crack, whereas in the foil system, multiple cracking occurred. Direct observations confirmed that debonding occurred in both systems. However, in the copper foil system, where debonding could be readily observed in situ, significant debonding occurred only in the crack wake, with debond lengths of up to 3-4 times the foil thickness. Preliminary measurements of the opening profile of the bridged crack in the copper foil system show the greatest effects of bridging at crack openings up to ~ u/R ~ 0.3, corresponding approximately to the expected position of the peak in the stress-displacement relationship for the bridging ligaments (Fig. 1). Thus, crack opening measurements provide valuable insight into the distribution of bridging tractions within the crack. Similar, higher accuracy measurements of bridged crack profiles in these and other metal-reinforced ceramic composites are the subject of ongoing research.

Comparison of the observed toughness increases with those predicted from preliminary calculations of crack bridging is possible. If the $\sigma(u)$ relation of the copper is approximated as being perfectly plastic, with yield stress σ_0 and rupture stretch u^*, then the increase in fracture energy is (Eq. 1),

$$\Delta G_b \sim f \sigma_0 u^* \qquad (2)$$

With σ_0 taken as the uniaxial ultimate stress (~200 MPa), and u^* measured from the fracture surfaces, increases in toughnesses of ~ 5 - 8 J/m^2, and ~1750 J/m^2 were obtained from Eq. 2 for the copper film and copper foil laminates, respectively. With a composite modulus, E, calculated by rule-of-mixtures, these fracture energies can be expressed in terms of critical stress intensity factors:

$$G_0 + \Delta G_b = (K_0 + \Delta K_b)^2 / E \qquad (3)$$

where G_o is the fracture energy of unreinforced glass, K_o is the critical stress intensity factor for unreinforced glass, and ΔK_b is the increase in stress intensity factor due to crack bridging. With the fracture energy of unreinforced glass $\sim 3 - 4$ J/m^2 (0.5 MPa.m$^{1/2}$), the toughness increases become $\Delta K_b \sim 0.1 - 0.3$ MPa.m$^{1/2}$ and ~ 11 MPa.m$^{1/2}$ for the copper film and copper foil laminates respectively. These values are consistent with the observed increases in toughness.

REFERENCES

1) P. Mataga, "Deformation of Crack-Bridging Ductile Reinforcements in Toughened Brittle Materials," UCSB, 1988

2) A.G. Evans and J.W. Hutchinson, "Effects of Non-Planarity on the Mixed Mode Fracture Resistance of Bimaterial Interfaces, UCSB URI, 1988

3) B.N. Cox and D.B. Marshall, "The Determination of Crack Bridging Forces," Int. J. Fracture, in press.

TOUGHENING OF INTERMETALLICS BY
COATED DUCTILE REINFORCEMENTS.

H.E. DEVE, A. G. EVANS, R. MEHRABIAN.
Materials Department, University of California, Santa Barbara, California 93106.

ABSTRACT

The effects of reinforcement debonding and work hardening on ductile reinforcement toughening of γ-TiAl have been examined. Debonding has been varied by either the development of a brittle reaction product layer or by depositing a thin oxide coating between the reinforcement and matrix. The role of work hardening has been explored by comparing Nb reinforcements that exhibits high work hardening with solution hardened Ti-Nb alloy that exhibits negligible work hardening. It is demonstrated that a high work of rupture is encouraged by extensive debonding when the reinforcement exhibits high work hardening. Conversely, debonding is not beneficial when the reinforcement exhibits low work hardening.

INTRODUCTION

Substantial toughening of intermetallics and ceramics by ductile reinforcements has been established.[1-5] It has also been demonstrated that the toughening due to bridging, $\Delta\mathcal{G}_C$, has a steady-state magnitude given by[6,7];

$$\Delta\mathcal{G}_c = \sigma_o f R \chi \qquad (1)$$

where σ_0 is the uniaxial yield strength, f is the area fraction of reinforcements, 2R is the reinforcement thickness and χ is a work of rupture parameter that can vary between $\sim 1/2$ and ~ 6, depending upon the extent of interface debonding and the reinforcement work hardening.[1-3,8] Furthermore, the magnitude of χ is reflected in the non-dimensional stress-stretch relationship

$$\chi = \int_0^{\alpha^*} (\sigma/\sigma_o) \, d\alpha \qquad (2)$$

where, $\alpha = u/R$, with u being the crack opening displacement and α^* is the value of α at the rupture displacement, u^*. The principal intent of the present study is to examine the specific, yet coupled, effects of debonding and work hardening on χ, including the role of the interface/coating properties.

The systems selected for investigation consist of γ-TiAl reinforced with Nb and Ti-Nb alloys. These systems have been demonstrated to exhibit appreciable toughening in composite form [4,9] and also are susceptible to interface debonding when a brittle reaction product (e.g., σ phase) forms between the reinforcement and the matrix.[3] Furthermore, extremes of work hardening behavior, as well as a substantial range of flow strength, are accessible in this system.[3]

Tests that reflect toughening characteristics may be conducted using either composite cylinders[2,3] or laminates[10,11] (Fig. 1). Test specimens are more readily produced for the latter geometry, by direct diffusion bonding. Furthermore, this geometry is typical of that used for ductile phase reinforced intermetallics.[4]

Consequently, a test procedure based on a plane strain laminate geometry (Fig. 1) is devised and used to evaluate the toughening potential, based on Eqn. (2).

The degree of debonding can be independently varied by introducing a non-reactive coating between the matrix and the reinforcement. For this purpose, the potential for thin oxide coatings is given explicit consideration, with the extent of debonding assessed in terms of the fracture properties of the oxide material.
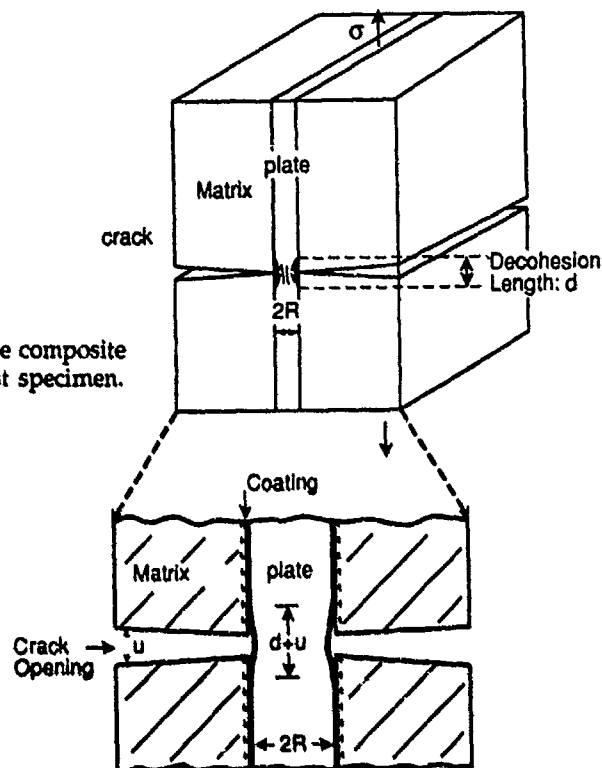
Figure 1: Sketch of the composite laminate test specimen.

MATERIALS

Matrix plates (1.5 mm thickness) of TiAl (Ti-50.5 at%Al) have been prepared from HIPed and forged billets by electro-discharge machining (EDM), followed by a homogenization heat treatment at 1000°C for 20 hrs. The resultant microstructure consists of predominantly equiaxed grains of γ-TiAl (grain size 100 μm) with small amounts of α_2 in a $(\alpha_2 + \gamma)$-lath structure. Thin reinforcement plates (from 0.12 to 0.17 mm thickness) of either pure Nb or Ti-33 at%Nb produced by hot rolling have been annealed in vacuum at 1066°C for 4 h. This material consists of single-phase β with equiaxed grains. Some of the reinforcement plates are coated on both sides with ~2 μm of either Al_2O_3 or Y_2O_3. The coatings are produced by physical vapor deposition.

Laminates suitable for testing (Fig. 1) are produced by diffusion bonding. To achieve representative microstructures, the TiAl plates are carefully polished to provide good planarity and inserted into a bonding fixture. The diffusion bonding is carried in vacuum at 1066°C for times varying between 1 hr. for the Ti-Nb alloys to 4 hrs. for the pure Nb.

MICROSTRUCTURES

The bonded laminates have been investigated by both scanning (SEM) and transmission (TEM) electron microscopy on sections normal to the interface. Analytical electron microscopy has indicated the following general features. In the absence of oxide coatings, both SEM and TEM investigation showed that the Nb reacts with the TiAl to form T_2 and σ intermediate phases[3]; whereas Ti-33%Nb produces α_2, and a duplex α/β layer[3]. Coatings of Y_2O_3 are found to be essentially inert and also prevent the formation of reaction products between the reinforcements and the matrix[11].

The Al_2O_3 coating was subject to extensive reaction with the Ti-Nb reinforcement and fully reacted during diffusion bonding to form a complex multiphase reaction product zone[11]. These specimens were not subjected to mechanical testing. Conversely, little reaction occurred upon bonding with the Nb reinforcement[11]. The incidence of reactions in the presence of Al_2O_3 is consistent with previous studies, which have revealed that high purity Nb bonds to Al_2O_3 without reaction product formation,[12] whereas Ti reacts with Al_2O_3 to form a multiphase Ti aluminide layer.[13]

MECHANICAL PROPERTIES.

The mechanical properties of the laminates were evaluated by conducting uniaxial tensile tests, using the geometry indicated on Fig. 1. Symmetric precracking of the TiAl outer layers prior to tensile testing was an essential feature of the experiment. Some tests were conducted in a servohydraulic machine with displacements monitored from an axial extensometer. Other tests were conducted *in situ* in the scanning electron microscope. Tests were also conducted on the reinforcements, without bonding to the TiAl. Tensile stress/stretch characteristic obtained on the unbonded Nb and Ti-Nb reinforcements confirm previous studies[3,11] which revealed that appreciable work hardening occurs in the Nb, but that Ti-Nb has a low work hardening and exhibits early plastic instability. The yield stress is 430 MPa for Ti-Nb and 140 MPa for Nb. Tests on laminates indicate marked differences in behavior between the Nb and Ti-33 at%Nb reinforcements and between specimens with and without oxide coatings, (Figs 2,3).

The presence of oxide coatings encouraged extensive debonding, which initiated with minimal plastic deformation of the reinforcement at stresses of the order of the uniaxial yield strength σ_0 . The debonding occurred primarily between the oxide and the reinforcement. Detailed investigation[11] revealed that the debond lengths, d, for the Nb reinforcements coated with either Y_2O_3 or Al_2O_3 were substantially larger than those for uncoated reinforcements. The largest debonds occurred for Y_2O_3, d = ∼ 1R, while the Al_2O_3 coating gave, d = 7-10R, and the uncoated reinforcements gave, d ≈ 5R. Furthermore, for oxide coated Nb reinforcements, the rupture stretch, u*, is found to be proportional to the debond length, d. Accordingly, the work of rupture χ is largest with Y_2O_3 coatings (χ ≈ 8) and of intermediate magnitude for Al_2O_3 coatings (χ ≈ 4), such that χ exhibits a linear dependence on either d/R (Fig. 4) or u*/R.

In the absence of oxide coatings, the behavior has similar features to that noted in previous studies on composite cylinders[3] and on actual composites.[4,5] Notably, the σ phase that forms with the Nb behaves as a debond layer, and debonding extends primarily in the brittle σ phase. Necking then initiates and rupture occurs at a stretch u ∼ 2R, such that the work of rupture is of intermediate magnitude, χ ≈ 2.5. Consequently, it is apparent that the σ phase is not as effective a debond
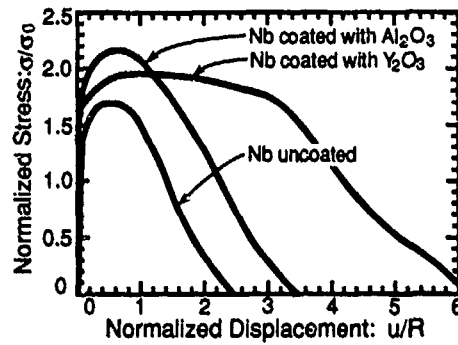
Fig 2:.   Tensile stress-stretch curves for the TiAl/Nb laminates.
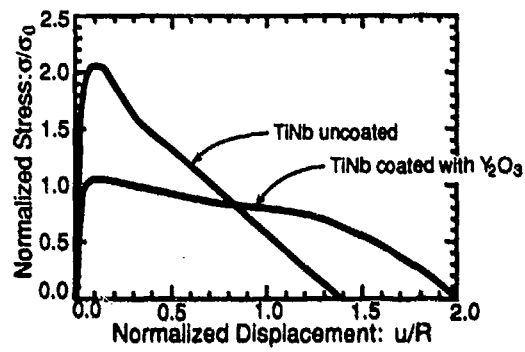
Fig 3:   Tensile stress-stretch curves for the TiAl/Ti-Nb laminates.
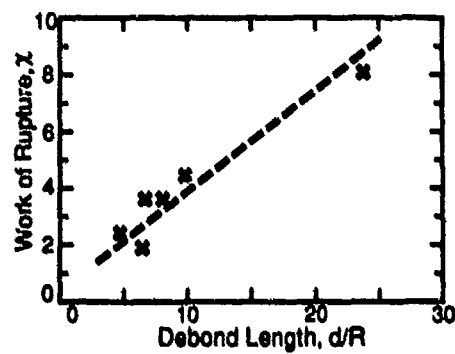
Fig 4:.   Trend in the work of rupture χ with the debond length d/R, for Nb reinforcements.

medium as either the Y_2O_3 or Al_2O_3 coatings. The Ti-33 at%Nb reinforcement does not form a brittle reaction product.[3] However, the present observations indicate that the TiAl matrix can crack parallel to the interface. Such cracks inhibit the development of full constraint and apparently encourage the formation of shear bands that lead to reinforcement rupture. The work of rupture $\chi \approx 1.5$ is comparable than that apparent when the Y_2O_3 coating is used, although some constraint ($\sigma \approx 2\sigma_0$) develops before the matrix cracks nucleate.

IMPLICATIONS

Debonding

Debonding in ductile reinforcement toughened intermetallics is strongly influenced by the fracture properties of the phases that exist between the reinforcement and the matrix. The fracture energies of some of the interfacial layers have been measured using the UCSB flexural test[13]. Tests conducted on specimens with Y_2O_3 coatings gave $\Gamma_i \approx 25$ Jm^{-2}, with crack propagation occurring primarily between the Y_2O_3 and the reinforcement[11]. This value is typical of the fracture energy found for polycrystalline oxides. Tests conducted on the TiAl/Nb specimens with a σ reaction product phase gave $\Gamma_i \approx 45$ Jm^{-2}, with crack growth occurring primarily within the σ phase[11].

Oxide coatings that have a small fracture energy ($\Gamma_i \approx 25$ Jm^{-2} for Y_2O_3) debond extensively prior to significant plastic deformation of the reinforcement. Simple elastic calculations would suggest steady-state energy release rates[14] and predict unlimited symmetric debonding at a critical stress. In practice, the debond is found to arrest. The actual extent of debonding is thus influenced by other factors, such as frictional sliding and bridging ligaments along the debond surface. Additionally, the somewhat larger debond resistance of the σ-phase ($\Gamma \approx 45$ Jm^{-2}) is apparently sufficient to substantially stabilize the debonding. Finally, it is noted that matrix cracking is possible with high strength Ti-Nb reinforcements. This occurs, albeit erratically, subject to a fracture energy[4], $\Gamma \approx 200$ Jm^{-2}.

Toughening

The present experiments provide a definite rationale for the attainment of an optimum steady-state toughness, as manifest in the work of rupture, χ. The largest values of χ (≈ 8) occur for reinforcements that work harden substantially and for interfaces that debond readily. *The work hardening coefficient applicable to Nb (n = 0.3) coupled with an interface fracture energy typical of that for oxides, ($\Gamma_i \approx 25$ Jm^{-2}) satisfies these requirements.* Conversely, a fracture energy applicable to the σ-phase reaction product ($\Gamma_i \approx 45$ Jm^{-2}) is apparently too large to allow the requisite debonding.

The behavior typified by the Ti-Nb reinforcement provides an important contrast. This reinforcement gives a desirably large work of rupture without debonding. Seemingly, in this case, when debond cracking of the matrix is suppressed, moderate constraint accompanied by appreciable plastic dissipation within shear bands is possible.

To further comprehend the significance of the above results, an important duality in behavior is noted, based on related research[16]. The work of rupture provided by the coated Nb reinforcements can only be partially utilized to give *composite toughness*. This limitation arises because of resistance curve and large scale bridging issues, which become accentuated as the debond length increases.[15,16] Consequently, strictly on the basis of toughness, the Ti-Nb reinforcements, which do not debond and have a high yield stress, are superior.

However, the full plastic dissipation allowed by debonding of the reinforcement can be utilized in loading situations that sample the complete range of material resistance, such as *Charpy tests*[16]. Consequently, when the criterion used for material selection is based on the Charpy energy, oxide debond coatings, and high work hardening reinforcements are preferred. The duality in behavior associated with debonding suggests that, in some cases, when both high Charpy energy and a high toughness are needed, a dual reinforcement scheme may be required: One reinforcement debonds and contributes to the Charpy energy, whereas the other bonds well and has the strength needed to provide a large toughness.

CONCLUDING REMARKS

The present set of experiments clarify the influence of debonding on the work of rupture, χ, of intermetallics toughness with reinforcements that exhibit a large work hardening, such as Nb. In particular, for such reinforcements, it has been established that χ exhibits a linear dependence on the debond length, d. It is also apparent that inert oxide coatings emplaced between the reinforcement and the matrix have a sufficiently low fracture energy that extensive debonding is induced, leading to enhanced values of χ. However, it remains to explicitly relate the debond length to the specific fracture energy of the coatings. Furthermore, it has been demonstrated that debonding is not beneficial when the reinforcements have limited ductility, caused by an absence of work hardening, as exemplified by Ti-Nb reinforcements.

References.

[1] L. S. Sigl, A. G. Evans, P. Mataga, R. M. McMeeking and B. J. Dagleish, *Acta Metall.*, 36, 946, (1988).
[2] M. F. Ashby, F. J. Blunt and M. Bannister, *Acta Metall.*, 37, 1847, (1989).
[3] H. C. Cao, B. J. Dalgleish, H. E. Dève, C. Elliott, A. G. Evans, R. Mehrabian and G. R. Odette, (in press), *Acta Metall.*
[4] C. K. Elliott, G. R. Odette, G. E. Lucas and J. W. Sheckard, *MRS Proceedings*, vol 120, p. 95, (1988).
[5] V. D. Krstic, *Phil Mag.*, A 48, 695, (1983).
[6] B. Budiansky, J. C. Amazigo and A. G. Evans, *J. Mech. Phys. Solids*, 36, 167, (1988).
[7] A. G. Evans and R. M. McMeeking, *Acta Metall.*, 34, 2435, (1986).
[8] P. A. Mataga, *Acta Metall.*, (in press).
[9] G. R. Odette, C. K. Elliott, G. E. Lucas and J. W. Sheckhard, to be published.
[10] B. J. Dalgleish, K. Trumble and A. G. Evans, Acta Metall., 37, 1923, (1989).
[11] H.E. Dève, A.G. Evans, G.R. Odette, R. Mehrabian, M.L. Emiliani, R. Hecht, to be published.
[12] W. Mader and M. Rühle, *Acta Metall.*, 37, 853, (1989).
[13] R. E. Tressler, T. L. Moore and R. L. Crane, *J. of Mat. Sci.*, 151, (1973).
[14] P. G. Charalambides, J. Lund, A. G. Evans and R. M. McMeeking, *J. of Appl. Mech.*, 56, 77, (1989).
[15] F. Zok and C. Hom, to be published.
[16] F. Zok, S. Jansson, A. G. Evans and V. Nardonne, to be published.

PLASTICITY DURING FRACTURE OF THE Au/Al$_2$O$_3$ INTERFACE

IVAR E. REIMANIS
Materials Department, University of California, Santa Barbara, CA   93106

Abstract

Au/Al$_2$O$_3$ interfaces are created by bonding highly textured Au films (25μm thick) to single crystal Al$_2$O$_3$. Mechanical tests are done under the optical microscope to examine the effect of plastic deformation on the energy of fracture of the interface. Fracture occurs at the interface and is accompanied by plastic deformation in the Au. The relatively large value for the fracture energy measured (50-70J/m^2) is attributed to the plastic deformation in the Au. It is also observed that fracture occurs subcritically due to stress corrosion at fracture energies from 10-20J/m^2. Topographic features on the fracture surfaces are characterized and discussed briefly.

Introduction

The fracture energy of metal/ceramic interfaces is controlled by interfacial chemical segregation [1], interphase formation [2], interfacial roughness and morphology [3], and plasticity in the metal [4]. The present work reports preliminary results from a fundamental study on plasticity effects during fracture of interfaces. Fracture energies are measured to be several orders of magnitude larger than the measured work of adhesion for Au/Al$_2$O$_3$. Au and single crystal Al$_2$O$_3$ (sapphire) produce an experimentally desired interface: the interface is clean and non-reactive [5] and there is negligible segregation of aluminum and oxygen in Au resulting in a well behaved flow stress. A further advantage for this system is the ability to observe fracture *in situ* in the optical microscope due to the transparancy of the sapphire. Fracture tests can be done using a mixed mode 4-point bending specimen such that the fracture energy for the interface crack is measured [6]. For this specimen when the crack is between the inner loading points, the strain energy release rate is crack length independent [6].

Experimental Procedure

Interfaces are made by diffusion bonding Au and sapphire in a sandwich geometry to produce specimens as shown in Figure 1. Basal (0001) plane sapphire is bonded to highly textured (001) poycrystalline Au foil of thickness 25μm. Materials are carefully cleaned and annealed

at 1000°C in air before bonding. Bonding is done at 3-5MPa, 1040°C, for 2-48h, in air or vacuum. Residual voids in the Au become isolated and facetted in the later stages of bonding and remain at the interface even after 48h. Typical voids are 1μm deep and 3-10μm wide as shown in the fracture surface in Figure 2.

Fracture testing is done in two stages during which load and displacement are monitored. First, the beam is placed in 3-point bending similar to the geometry shown in Figure 1. A Vicker's indent on the tensile face of the beam then propagates a crack through the sapphire to the interface where it symmetrically debonds the interface and subsequently arrests. The arrest load is used to estimate the critical energy release rate. The second stage of testing is carried out by allowing crack growth while the specimen is loaded in 4-pt bending. The phase angle of loading for this geometry is ~52°. The crack growth is monitored *in situ* by optical observation through the tensile face of the sapphire.

It was noted during the testing that when distilled water is injected into the crack front the crack velocities increase compared with tests done in air. Subsequently, all tests were done by allowing the penetration of water into the crack front.
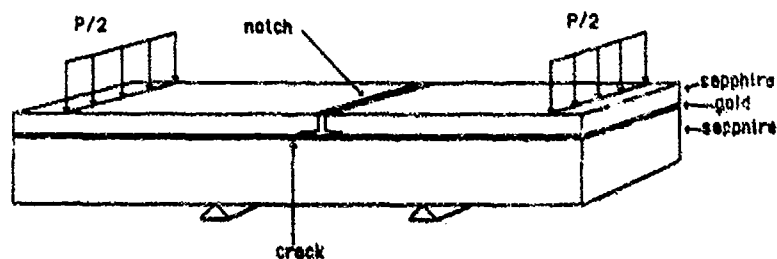
Figure 1. Specimen geometry for flexure testing.

Results and Characterization

It was observed that interface fracture occurs subcritically at crack velocities as low as 10^{-7}m/s. Higher fracture energies correspond to higher values for crack velocities. During subcritical crack growth fracture energies range from 10-20J/m^2. During rapid crack growth (velocity > 10^{-2}m/s) fracture energies range from 50-70J/m^2. The differences in fracture energies between rapid crack growth and slow crack growth are explored by examination of the fracture surfaces shown in Figure 3. During fast fracture the Au surface shows distortions and striations, features indicative of substantial plasticity. During subcritical growth the Au fracture surface is relatively featureless (Figure 3). Steps are generated in the Au surface when a load change occurs (Figure 3). These steps are indicative of crack tip blunting in the

Au during fracture: a mode of energy dissipation. Because of their shallow nature, the step heights could not be measured using conventional scanning electron microscope techniques. However, more detailed characteriztion using profilometry revealed that typical step heights are 70-100nm (Figure 4).
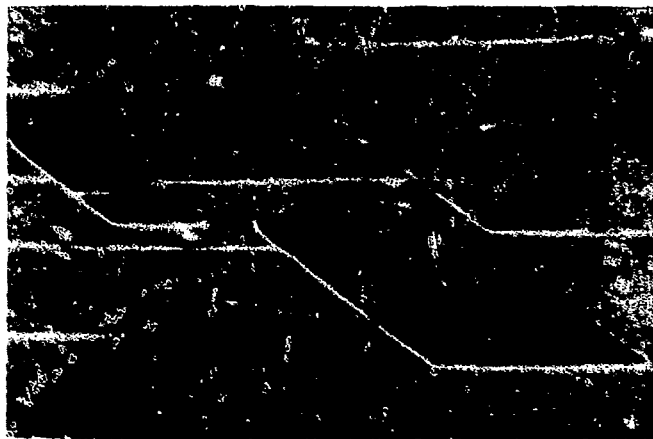
Figure 2. Scanning electron micrograph of fracture surface of gold showing facetted voids. Slip steps produced during fracture are evident.
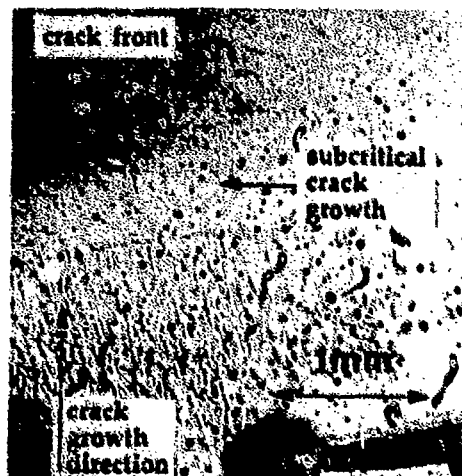
Figure 3. *In situ* optical micrograph (through sappphire layer) showing differences between fracture surfaces for subcritical crack growth and fast crack growth.

Direction of crack propagation

180nm

150µm
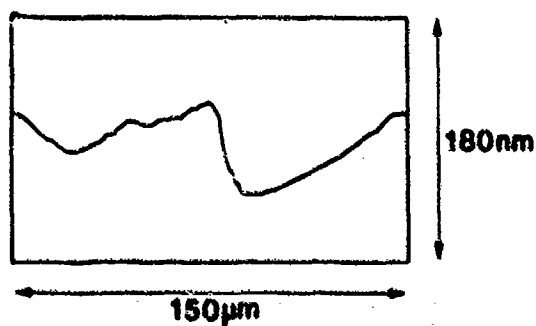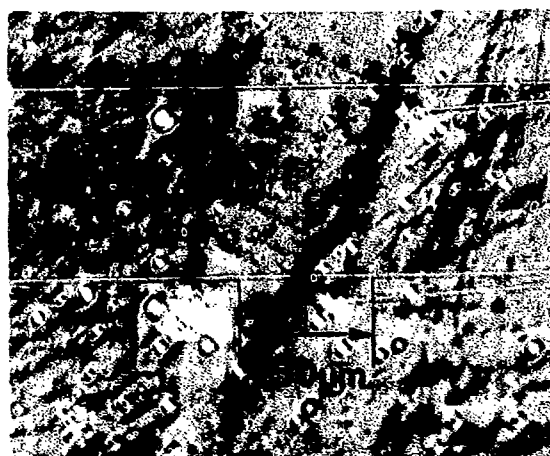
Figure 4. Optical micrograph of fracture surface on Au side showing the residual plastic trough resulting from profilometry. The corresponding trace is also shown.

Further characterization of fracture surfaces using EDAX in the scanning electron microscope revealed that within the resolution limits of EDAX there is no evidence of Au on the sapphire and no Al on the gold. This is indicative of fracture occuring by interfacial bond rupture at the crack tip. It can be contrasted to ductile interface fracture which occurs by void nucleation and coalescence ahead of the crack tip. Thus, a brittle mode of fracture occurs despite plasticity in the Au. The

topography of the Au fracture surface was further investigated using a
tilting technique in the SEM. Lines of electron beam damage were
created while the specimen surface is oriented normal to the electron
beam [7]. The specimens were then tilted 60-80° so that the features
become more apparent as shown in Figure 5. This technique confirmed
that the height of blunting steps measured by profilometry are on the
order of 0.1μm. This technique was also used to make measurements
on the angle which a void wall makes with the surface (Figure 5). The
angles were in the range 140-150°, giving an estimate for the work of
adhesion as 0.3-0.5J/m^2.

Figure 5. Scanning electron micrograph, specimen tilted 60° such
that shape of void becomes apparent. Electron beam damage line
(arrowed) was deposited under 0° tilt.

Conclusions

The large value of the fracture energy (50-70J/m^2) compared
with the work of adhesion (0.3-0.5J/m^2) is indicative of plastic
dissipation in the metal. Plasticity occurs despite the brittle nature of
interface fracture. Also, subcritical crack growth occurs in accordance
with stress corrosion concepts, at fracture energies as low as 10-20J/m^2.
Though subcritical crack growth yields relatively featureless fracture

44

surfaces, blunting steps generated upon load changes indicate that plastic dissipation is involved. Further research will address the issue of plastic dissipation and its connection to the fracture energy through the work of adhesion.

References

1. M. Rühle, M. Backhaus-Ricoult, K. Burger, and W. Mader in Ceramic Microstructures '86: Role of interfaces Materials Science Research, edited by J. A. Pask, A. G. Evans (Plenum Pres., New York 1987) p.307.

2. J. T. Klomp, in Fundamentals of Diffusion Bonding, edited by Y. Ishida (Elsevier, New York 1987) p.3.

3. H. C. Cao and A. G. Evans, Mechanics of Materials, 7, (1989) p.295.

4. R. M. Cannon, V. Jayaram, B. J. Dalgleish, R. M. Fisher, in Ceramic Microstructures '86: Role of Interfaces Materials Science Research, edited by J. A. Pask, A. G. Evans (Plenum Press, New York 1987) p.959.

5. I. E. Reimanis, B. J. Dalgleish, M. Brahy, M. Rühle, A. G. Evans, to be published.

6. P. G. Charalambides, J. Lund, R. M. McMeeking and A. G. Evans, J. Appl. Mech., 111 (1989) p.77.

7. R. A. Hoover, Journal of Physics E: Scientific Instruments, 1971 Volume 4, p.747.

A NEW THEORY FOR THE DEBONDING OF DISCONTINUOUS
FIBERS IN AN ELASTIC MATRIX

CHRISTOPHER K.Y. LEUNG AND VICTOR C. LI,
Department of Civil Engineering, Massachusetts Institute of Technology, Cambridge, MA 02139

ABSTRACT

The mechanical properties of fiber composites are strongly influenced by the debonding of
fibers. When an embedded fiber is loaded from one end, debonding can occur at both the loaded
end and the embedded end. Existing theories neglect the possibility of debonding from the
embedded end and are thus limited in applications to cases with low fiber volume fraction, low
fiber modulus, high interfacial strength/interfacial friction ratio or short fiber length. A new two-
way fiber debonding theory, which can extend the validity of one-way debonding theories to all
general cases, has recently been developed. In this paper, the physical reason for the occurrence
of two-way debonding is discussed. The limit of validity for one-way debonding theories is
considered. One-way and two-way debonding theories are then compared with respect to the
prediction of composite behaviour. The determination of interfacial parameters from the fiber
pull-out test will also be described.

INTRODUCTION

Brittle materials usually fail by the unstable propagation of an inherent flaw. When fibers are
added to the matrix, the first-cracking strength (i.e., the applied stress at which unstable crack
propagation occurs) can be greatly increased due to bridging of the crack by the fibers. If we
assume a penny-shaped inherent crack under a remote uniform tensile field, the first cracking
strength σ_{fc} is given by:-

$$\sigma_{fc} = 0.5 \ (r_f/c)^{1/2} \ (K_c + K_{bridg}) \qquad (1)$$

Here, K_c is the fracture toughness without bridging, K_{bridg} is the contribution of bridging
fibers to crack resistance and c is the size of the inherent flaw. K_{bridg} is a function of the
bridging stress versus crack opening (p-u) relation of the composite. The p-u relation is
associated with the stress versus displacement (displacement of loaded fiber end relative to matrix
surface) relation (σ_p-u relation) for a fiber pulled from the matrix through $p = V_f \sigma_p$, where V_f is
the volume fraction of fiber [1,2]. Hence, a model for the debonding of fiber pulled from the
matrix is required for prediction of composite behaviour.

In this paper, a new two-way debonding model for the debonding of discontinuous fibers
will be described. This is a strength-based theory in which debonding occurs when the
interfacial stress reaches the interfacial strength τ_s. The debonded interface is then assumed to be
under a uniform frictional stress τ_i. Details of derivation and applications of the new theory can

be found elsewhere [3,4]. Here, the physical reasons for the occurrence of two-way debonding, the conditions under which two-way debonding is important and the problems associated with unlimited use of traditional one-way debonding theories are discussed. Since τ_s and τ_i are important parameters in strength-based theories, the experimental determination of τ_s and τ_i are also described.

PHYSICAL REASONS FOR THE OCCURRENCE OF TWO-WAY DEBONDING

Debonding theories for a discontinuous fiber pulled at one end have been derived by several investigators [5-8]. In all existing debonding theories, only debonding from the loaded end is considered. However, as derived in [8], the interfacial shear stress distribution has maxima at the loaded end as well as the embedded end (Fig.1). Depending on fiber volume fraction and relative stiffness of fiber and matrix, fiber debonding can start from one or the other fiber end. Moreover, after debonding starts from one end, the continuation of debonding at that side is accompanied by increasing shear stress at the other end and eventually, the other end will also debond. A two-way debonding theory is therefore necessary.

While it is well accepted that debonding can occur at the loaded end of the fiber, the possibility of debonding from the embedded end can be most easily explained by considering a fiber of significant length being loaded at one end (Fig.2). For discussion purpose, axial strain and displacement are assumed to be uniform in the matrix although in reality they decrease with distance from the fiber/matrix interface. At $z=0$, matrix axial stress (and strain) is equal to zero. As z increases, stress transfer by shear between fiber and matrix leads to continued decrease in fiber axial strain and increase in matrix axial strain. On continuing stress transfer along the interface, a point will eventually be reached where the longitudinal displacement in the matrix is higher than that in the fiber, which is physically impossible (Fig. 2a). What really happens is shown in Figs 2b and 2c. When the fiber and matrix reach the same axial strain, the transfer of stress from one to the other is essentially terminated. The rest of the composite is under an applied constant strain (Fig. 2c). In a continuous fiber system, this constant strain will be sustained until the surface of the specimen is approached. In a discontinuous fiber composite with very little bond or anchorage at its embedded end, the stress at that end is zero. Hence, stress has to be transferred back into the fiber from the matrix. If the applied strain in Fig. 2c is high enough, debonding at the embedded end will take place.

Fig. 1 Fiber/Matrix Interfacial Shear Stress Distribution

(a)

u = v

u > v   u < v, physically impossible

Applied
Stress

v

u

(b)

u > v   u ≈ v

Applied
Stress

Zero Stress at Fiber End

(c)

Constant
Strain

High Interfacial Shear to
Transfer Stress Back into Fiber
(May Lead to Debonding)
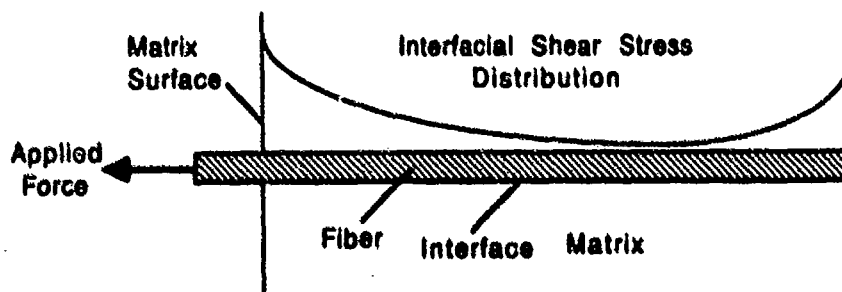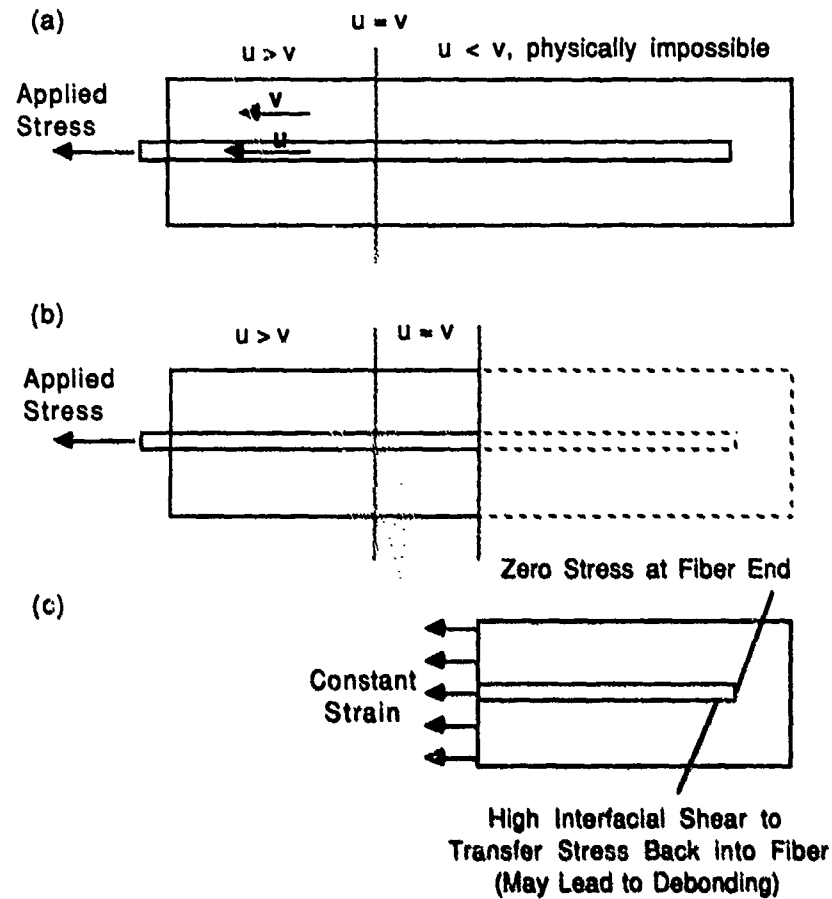
Fig. 2   Illustration of the Physical Reason for Two-Way Debonding to Occur

LIMIT OF VALIDITY FOR ONE-WAY DEBONDING THEORIES

A Typical σ_p-u relation is shown in Fig.3. After point A is reached, the theoretical curve shows a snap-back to point B. In reality, the snap-back cannot be obtained and the stress simply drops unstably to the pull-out branch BCD. If some stable two-way debonding occurs before peak stress is reached, two-way debonding has to be considered. Otherwise, two-way debonding occurs at the snap-back part and only slightly affects the position of point B. Since BCD is very flat compared with OA, the change in the position of B will not have any significant effect on the overall σ_p-u relation.
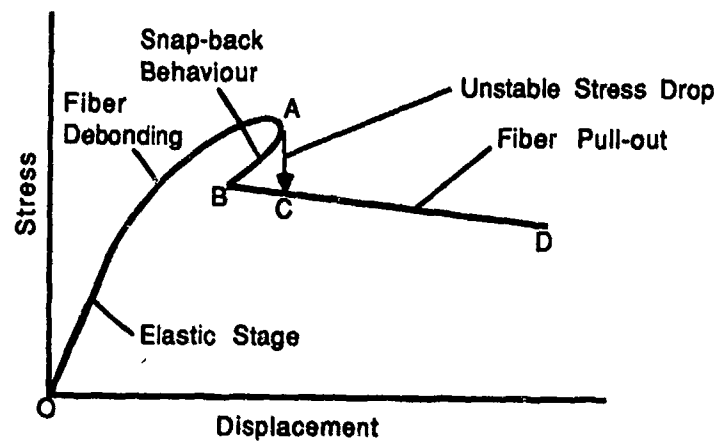
Fig.3 Various Parts of the Stress-Displacement Curve

With the occurrence of two-way debonding at or before peak stress as a criterion for one-way debonding theories to be inapplicable, the transition aspect ratio L^{tr}/r_f beyond which two-way debonding theories have to be employed is given by:

$$\rho \, L^{tr}/r_f = \cosh^{-1}(\tau_s/\tau_i) + [\,(1-2\alpha)/\alpha\,]\,[\,(\tau_s/\tau_i - 1)\,(\tau_s/\tau_i)\,]/\sqrt{[\,(\tau_s/\tau_i)^2 - 1\,]} \quad (2)$$

for $\alpha < 0.5$. Here, $\alpha = E_f V_f / E_c$ is the contribution of fibers to composite modulus, τ_s/τ_i is the ratio of interfacial strength to interfacial friction and ρ is a parameter depending on modulus of fiber (E_f), modulus of matrix (E_m) as well as V_f. For $\alpha > 0.5$, debonding always start from the embedded end of the fiber and traditional one-way debonding theories are never applicable.

$\rho \, L^{tr}/r_f$ is plotted against τ_s/τ_i for α from 0.01 to 0.4 in Fig. 4. For each α, if the aspect ratio lies in the region above the line, two-way debonding theories have to be employed. It is obvious that one-way debonding theories are only good for low V_f, low E_f, low fiber aspect ratio or high τ_s/τ_i.

Eqn (2) as well as Fig.4 show that the longer the fiber, the more likely will two-way debonding theory be required. This is the case only if the possibility of fiber breakage is neglected. In practice, if the fiber is too long, breakage may occur before two-way debonding occurs and use of two-way debonding theory is not necessary.

The transition aspect ratios for two practical composite systems are shown in Figs 5a and b. It is assumed here that the fibers are either perpendicular to the crack plane or strong and flexible enough to bend across the crack without breaking. For steel fiber reinforced concrete, one-way debonding theories are good for volume fractions up to about 1 to 1.5 %, depending on fiber aspect ratio. (Note: SIFCON is a high volume fraction steel fiber reinforced mortar made by slurry infiltration.) For carbon fiber reinforced glass, one-way debonding theories are never applicable for practical volume fractions.
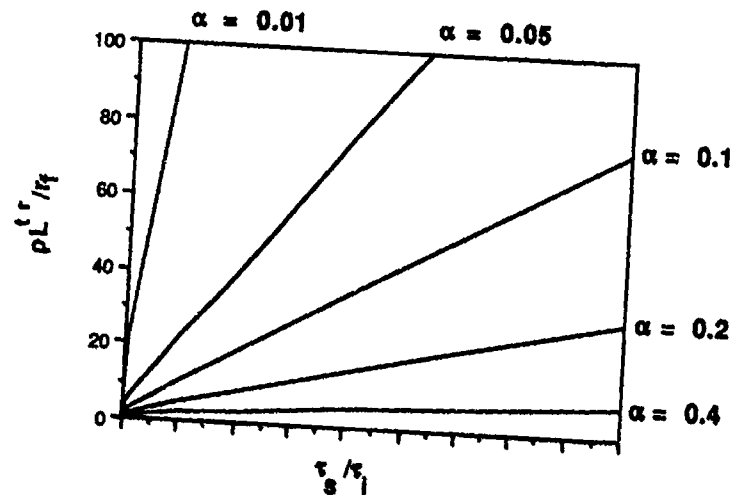
Fig. 4   Curves of Transition Aspect Ratio Beyond which Two-Way Debonding Theories have to be Employed

(a)

Steel Fiber Reinforced Concrete

(b)

Carbon Fiber Reinforced Glass
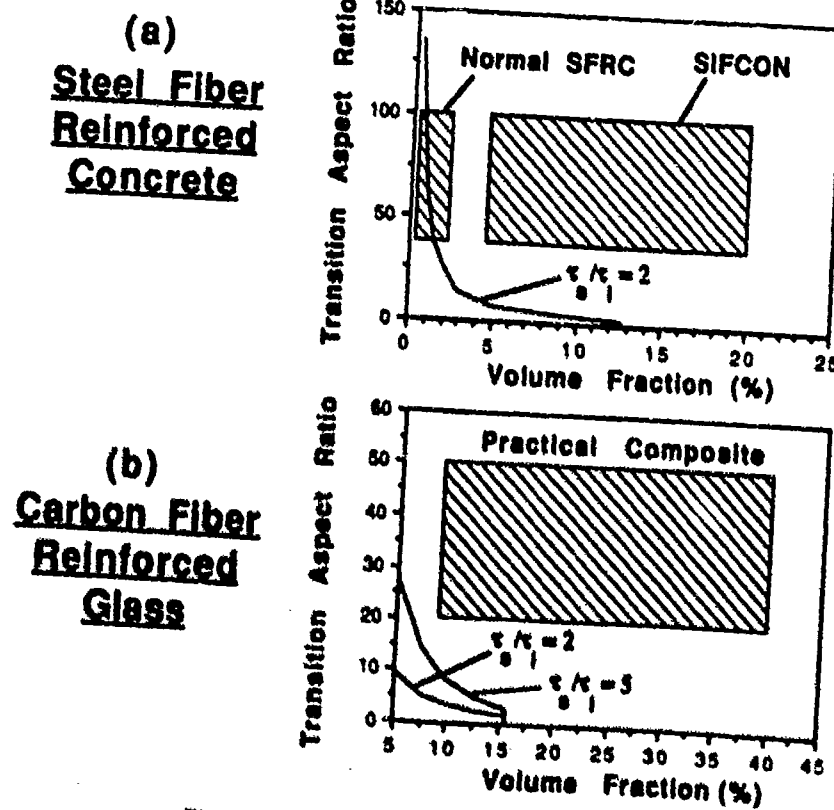
Fig. 5 Transition Aspect Ratios for Two Practical Systems

PROBLEMS WITH THE UNLIMITED USE OF ONE-WAY DEBONDING THEORIES

σ_p-u curves for various cases have been numerically simulated with one-way and two-way debonding theories and compared[3]. For cases where two-way debonding is important, it is found that the unlimited use of one-way debonding theories leads to extension of the σ_p-u curve to a higher load (Fig. 6). This may be expected because the neglecting of two-way debonding is equivalent to assuming an extremely high shear strength at the embedded fiber end, which tends to overestimate the load-carrying capacity of the fiber. If the σ_p-u relation predicted by one-way debonding theory is used instead of the correct relation (predicted by two-way debonding theories) in the computation of K_{bridg} in eqn(1), the first-cracking strength will be overestimated for any inherent flaw size (Fig. 7). Moreover, the rate of change of strength with flaw size also decreases if one-way debonding theory is used. The variability of strength from specimen to specimen (due to different sizes of inherent flaws) is therefore underestimated. In other words, material reliability is being overestimated.
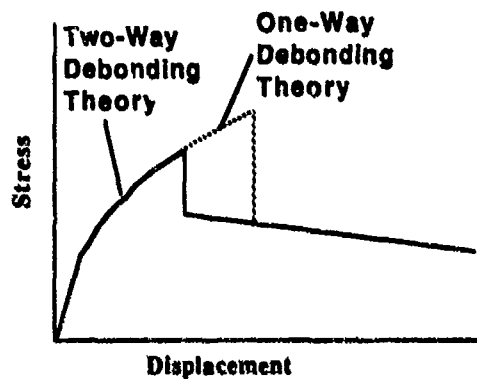
Fig. 6 Stress-Displacement Curves Predicted by One-Way and Two-Way Debonding Theories
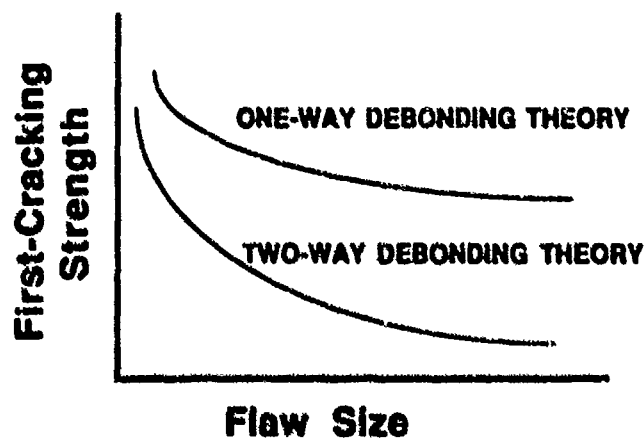
Fig. 7 Composite Behaviour Predicted by One-Way and Two-Way Debonding Theories

DETERMINATION OF INTERFACIAL PARAMETERS

In strength-based theories (traditional one-way theories or the new two-way theory), composite behaviour is strongly affected by the interfacial parameters τ_s and τ_i. The experimental determination of these parameters is thus very important. The fiber pull-out test is a very common technique for the determination of interfacial properties. A typical pull-out test data is shown in Fig. 8. The interfacial friction τ_i can be obtained by simply dividing $P_{postpeak}$ by the net interfacial area $(2\pi r_f)L_e$, where r_f is the fiber radius and L_e the embedded length. The determination of τ_s is not so straight forward. To obtain τ_s, one need to know the size of debonded zone (l_d) when peak load (P_{peak}) is reached. It should be noticed that for the small volume fraction of fiber in the pull-out specimen, a one-way debonding theory which only considers debonding from the pulled fiber end is good enough. With a one-way debonding theory, l_d is obtained and $P_{peak}/P_{postpeak}$ is then computed for various values of τ_s/τ_i and $\rho(L_e/r_f)$. The results are shown in the form of a chart in Fig.9. ρ depends on the fiber volume fraction in the pull-out specimen as well as fiber and matrix moduli. For a certain pull-out specimen (with known fiber radius and embedded length), $\rho(L_e/r_f)$ is fixed. τ_s/τ_i can then be obtained from $P_{peak}/P_{postpeak}$. With τ_i determined from $P_{postpeak}$, τ_s can be deduced.
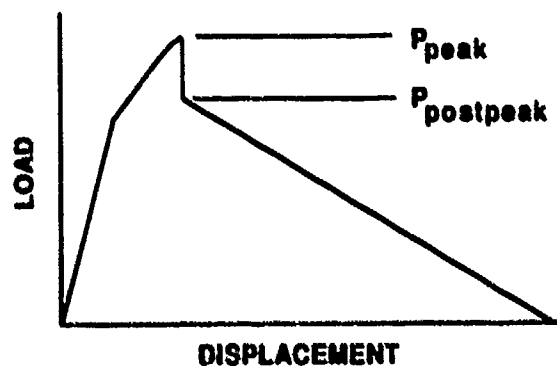
Fig. 8 A Typical Fiber Pull-Out Test Result
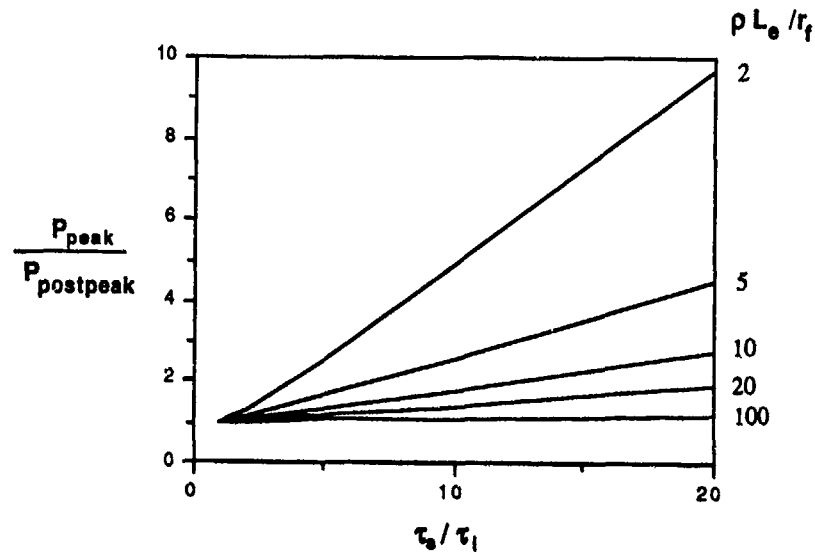
Fig. 9 Chart for the Determination of Interfacial Shear Strength

CONCLUSIONS

Traditional one-way debonding theories are only applicable to cases with small fiber volume fraction, small fiber modulus, small fiber aspect ratio or large ratio of interfacial strength/interfacial friction. For example, one-way debonding theories can be employed to extract τ_s from the result of a fiber pull-out test, where fiber volume fraction is very small. However, in more general cases, such as in many practical composite systems, debonding from the embedded end have to be considered and two-way debonding theories have to be employed. In cases where two-way debonding is important, the unlimited use of one-way debonding theories will lead to overestimation of both composite first-cracking strength and composite reliability.

REFERENCES

1. Marshall, D.B., Cox, B.N. & Evans, A.G., "The Mechanics of Matrix Cracking in Brittle-Matrix Fiber Composites", Acta Metall. Vol 33, No 11, p.2013-2021 (1985)
2. Majumdar, B.S., Newaz, G.M. and Rosenfield, A.R., "Yielding Behavior of Ceramic Matrix Composites", Proceedings of the Seventh International Conference on Fracture, Vol. 4, p.2805-2814 (1989)

3. Leung, C.K.Y. and Li, V.C., "A New Strength-Based Model for the Debonding of Discontinuous Fibers in an Elastic Matrix", submitted to J. Mat. Sci. (1989)

4. Leung, C.K.Y. and Li, V.C., "Applications of a Two-Way Debonding Theory to Short Fiber Composites", submitted to Composites (1989)

5. Greszczuk, L.B., "Theoretical Studies of the Mechanics of the Fiber-Matrix Interface in Composites", ASTM STP 452, p.42-58 (1969)

6. Takaku, A. and Arridge, R.G.C., "The Effect of Interfacial Radial and Shear Stress on Fiber Pull-out in Composite Materials", J. Phys. D: Appl. Phys., Vol. 6, p.2038-2047 (1973).

7. Lawrence, P., "Some Theoretical Considerations of Fiber Pull-out from an Elastic Matrix", J. Mat.Sci., Vol. 7, p.1-6 (1972)

8. Gopalaratnam, V.S. and Shah, S.P., "Tensile Fracture of Steel Fiber Reinforced Concrete", ASCE J. Eng. Mech., Vol. 113, No.5, p.635-653 (1987)

DETERMINATION OF FLEXIBLE INTERLAYER THICKNESS FOR FIBER REINFORCED COMPOSITES

KING H. LO, ROBERT W. SCHMITZ, AND WILLIAM G. GOTTENBERG
Shell Development Company, P.O.Box 1380, Houston, Texas 77251-1380

ABSTRACT

The influence of flexible interlayers/interphases on the performance of unidirectional fiber reinforced composites is studied. Micromechanical analysis based on the embedded composite cylinders model is used to study the stiffness as well as the internal stress distributions within the matrix phase of composites. Based on the results of the analysis, a criterion is proposed for the selection of optimal interlayer thickness for fiber composites. The proposed criterion gives results which seem to correlate well with the experimental data published in the literature.

INTRODUCTION

In recent years, many researchers attempted to improve the performance of composites by incorporating a soft interlayer between the fiber and the resin matrix. References [1,2] reported that substantial increases in transverse tensile strength, interlaminar shear strength, torsional fatigue life, and moisture resistance were obtained for glass fiber composites. However, only moderate improvement in impact resistance was obtained for carbon fiber composites [3-5]. It has long been recognized that the performance of a composite could strongly be influenced by both the thickness and the stiffness of the interlayer. But no apparent rational approach has been proposed to guide the selection of interlayer. In this paper, an attempt is made to develop a simple method for selecting proper combinations of interlayer thickness and stiffness for composites. This is achieved by correlating the stress distributions in the matrix phase of glass fiber composites with the experimental results given in [1,2].

EMBEDDED COMPOSITE CYLINDERS MODEL

In this study, the stiffness and internal stress distributions in a composite with interlayer were determined using the embedded composite cylinders model (Figure 1). Mathematical formulation of the model followed the same approach as that discussed in [6,7] and will not be given here. With the exception of the longitudinal modulus and major Poisson's ratio, the addition of a soft interlayer between the fiber and the matrix will lead to reduction in the stiffness of the composite.

EFFECT OF INTERLAYER THICKNESS AND STIFFNESS ON STRESS DISTRIBUTIONS

Figure 2 shows the radial stress distributions (along the 2-axis) in the matrix phase of four glass fiber composites subjected to unit transverse tension in the 2-direction (Figure 1). Three different interlayer thicknesses (1%, 2% and 4% fiber diameter) were studied. The Young's moduli of the glass fiber, matrix, and interlayer used in the simulations were assumed to be 10500 ksi, 360 ksi, and 110 ksi, respectively. The corresponding Poisson's ratios were assumed to be 0.22, 0.35, and 0.4. For correlating with the experimental results given in [1,2], the radius of the glass fiber was assumed to be 0.002 inch and the volume fraction of glass fiber was assumed to be 50%. It is important to point out that the radial

stresses along the 2-axis are the dominating stress components in the matrix phase of the composites under consideration. They are plotted as function of distances from the matrix/interlayer interface.

It can be seen from Figure 2 that the magnitudes of the radial stress in the matrix are not significantly changed by the presence of the interlayer. The only noticeable difference is the shifting of the location of maximum radial stress from within the matrix to the matrix/interlayer interface. Assuming that failure initiation in a composite under transverse tension is associated with the maximum stress in the matrix, the presence of the interlayer could change the mode of failure initiation from matrix cracking to debonding at the matrix/interlayer interface. This change in failure initiation mode could be responsible for the improvement in the transverse tensile strengths reported in [1,2] for these composites.

Reference [1] also reported that the largest increase in transverse tensile strength (at room temperature) was obtained for the composite with a 2% fiber diameter thick interlayer. When correlating this finding with the location and magnitude of the maximum radial stress for these composites (Figure 2), it is not surprising that the composite with a 2% fiber diameter thick interlayer had the largest increase in transverse tensile strength. It thus appears that the optimal interlayer thickness for improving the transverse tensile strength of glass fiber composites is the one that results in the lowest maximum radial stress at the matrix/interlayer interface.

To show the effect of interlayer stiffness on composite performance, the stress distributions in the matrix phase of composites with a very soft interlayer (Young's modulus of 5 ksi) under unit transverse tension were again evaluated. Figure 3 shows the radial stress distributions along the 2-axis and Figure 4 shows the circumferential stress distributions along the 3-axis (Figure 1). It can be seen from the figures, even though the maximum radial stresses all occur at the matrix/interlayer interface, the circumferential stresses are the dominating stress components that control the failure of these composites. Since the magnitudes of the induced circumferential stresses are significantly higher for the composites with the soft interlayer, it is logical that their transverse tensile strengths be lower than that of the composite with no interlayer. This correlates with the experimental results given in [1] when the composites were tested at temperatures close to the glass transition temperature of the interlayer.
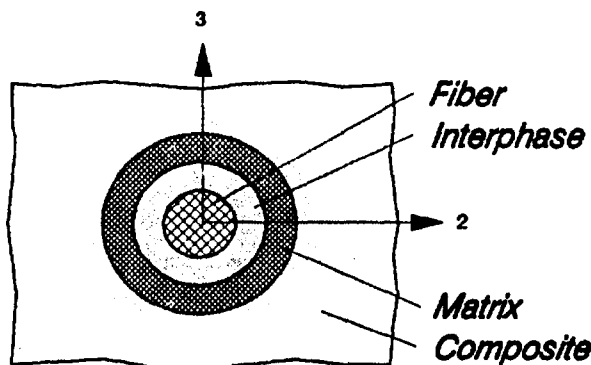
Figure 1. Embedded Composite Cylinders Model

Figure 3. Radial Stress Distributions
in the Matrix Phase (E-interlayer − 5 ksi)

Figure 5. Optimal Interlayer Thickness
for C-Glass Fiber Composites (v_f = 50%)

Figure 2. Radial Stress Distributions
in the Matrix Phase (E-interlayer − 5 ksi)

Figure 4. Circumferential Stress Distributions
in the Matrix Phase (E-interlayer − 5 ksi)
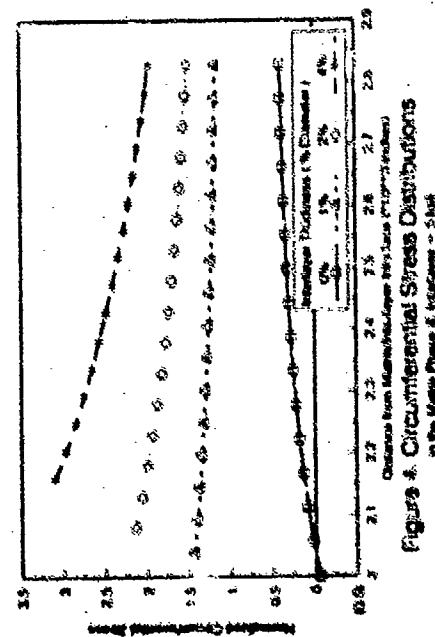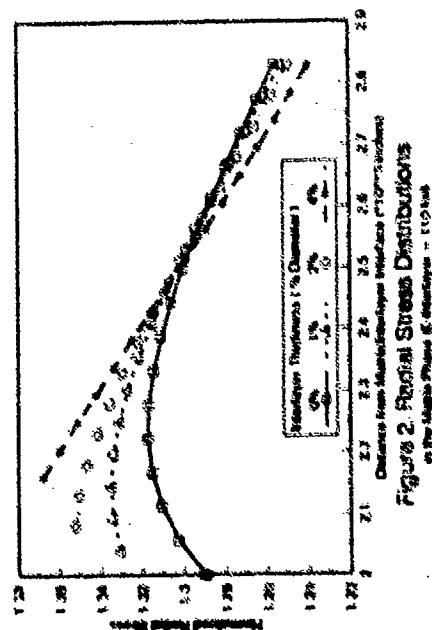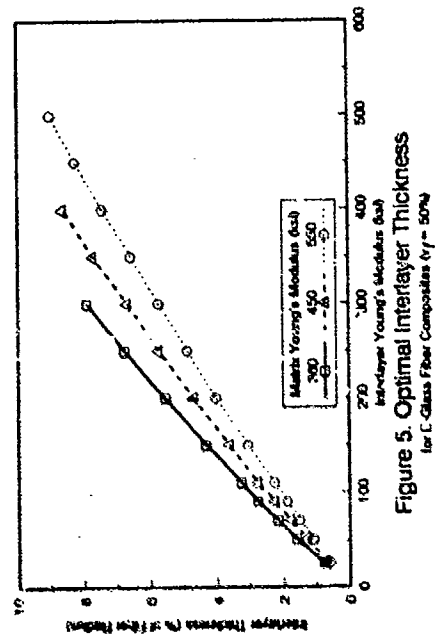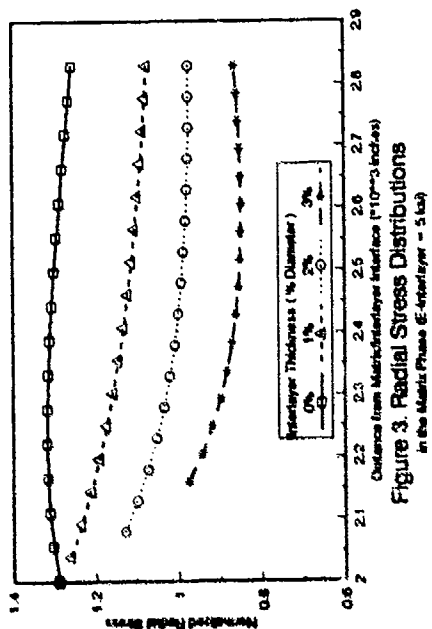
DISCUSSION

The above discussion demonstrated that it is possible to relate the effect of interlayer on composite performance to the stress distributions in the matrix phase of the composite. Although the discussion given here is related to glass fiber composites, similar results (stress distributions) have also been obtained for carbon fiber composites. Using the hypothesis that the optimal interlayer thickness for transverse tensile strength improvement is the one that will cause the lowest maximum radial stress to develop at the matrix/interlayer interface, the appropriate relationship between optimal interlayer thickness and stiffness is illustrated in Figure 5 for some 50% volume fraction glass fiber composites. It can be seen from the figure that the stiffness of the matrix will influence the selection of optimal interlayer thickness for fiber composites.

As mentioned earlier, incorporating a soft interlayer between fiber and matrix will lead to reduction in the transverse stiffness of composites. With the appropriate interlayer thickness, an increase in transverse tensile strength coupled with a reduction in transverse stiffness will lead to significant improvement in the transverse deformation capability of a composite. This could contribute to the improvement in the impact resistance of composites with soft interlayer.

REFERENCES

1. R. E. Lavengood and M. J. Michno, Jr., Proc. Div. Tech. Conf., Engrg. Props. and structure Div., SPE, (1975), 127.

2. L. D. Tryson and J. L. Kardos, Proc. 36th Annual Conference, SPI, (1981), 2-E.

3. L. Ying, Proc. 38th Annual Conference, SPI, (1983), 12-F.

4. J. Chang, J. P. Bell and R. Joseph, SAMPE Quarterly, (1987), 39.

5. J. Kawamoto, F. J. McGarry and J. F. Mandell, Impact Resistance of Rubber Modified Carbon Fiber Composite, MIT, PFST-85-5, (1985).

6. Z. Hashin, Theory of Fiber Reinforced Materials, NASA CR - 1974.

7. R. M. Christensen, Mechanics of Composite Materials, John Wiley & Sons, (1979).

EFFECTS OF A FRICTIONAL INTERFACE ON THE LOAD DIFFUSION FROM A BROKEN FILAMENT IN A FIBROUS COMPOSITE

BULENT AKSEL[*], DIMITRIS C. LAGOUDAS[**] and CHUNG-YUEN HUI[*]
*Theoretical and Applied Mechanics Department
Cornell University, Ithaca, NY 14853
**Department of Civil Engineering
Rensselaer Polytechnic Institute, Troy, NY 12180

ABSTRACT

The effects of a frictional interface on the load diffusion from a broken fiber to the surrounding matrix material and the extent of debonding near the fiber break in a single–fiber reinforced composite of infinite extent are studied by using the finite element method. The normal and shear stresses on the interface, the extent of the slip zone and the axial load of the fiber are evaluated for different frictional coefficients and material parameters for both the fiber and the matrix. A shear–lag analysis is also carried out to obtain a closed form approximate solution of the fiber load diffusion problem. The extent of the slip zone and the stresses predicted by the shear–lag model are compared with the finite element method results.

1. INTRODUCTION

The problem of load diffusion from a broken fiber into its surrounding matrix has been considered by many authors in various degrees of sophistication. Starting with a simple shear–lag analysis in the work of Cox [1], more elaborate analyses have appeared over the years with a recent attempt by Whitney and Drzal [2] that uses approximate stress fields only close to the fiber break. Muki and Sternberg [3] solve the load diffusion problem as an exact 3–D elasticity problem for the surrounding matrix but they consider the fiber to have a rod–like behavior. The exact solution to the load diffusion problem when both the fiber and matrix are taken to be isotropic linearly elastic and with perfectly bonded interface is given by Ford [4]. Due to the difference in the stress singularity near the fiber break, Ford's solution in the crack tip region significantly differs from that of Muki and Sternberg.

Experimental evidence (i.e., Netravali et al [5]) points out that for a wide range of material parameters, the high stresses near the crack tip are relaxed by the failure of the interface, leading to interface crack growth. The growth of interface cracks contributes significantly to the fracture toughness of the composite. On the negative side, interface failure is the principle cause of stiffness reduction in composites. To quantify this phenomenon, one must deviate from the assumption of a perfectly bonded interface adopted in the work of Muki and Sternberg and Ford mentioned above, and explicitly include the interface constitutive description in the stress analysis. Such an analysis was carried out by Dollar and Steif [6], who investigated the problem of interface failure near a fiber break using a Coulomb frictional interface model. To simplify their analysis, they solve a two dimensional plane strain contact problem where both the matrix and the fiber have the same material properties. In this work we will remove these restrictions and consider the axial symmetric problem of a broken fiber embedded in an infinite matrix under the action of transverse normal pressure with a uniform axial strain applied far away from the fiber break. There are no restrictions placed on the material properties of the fiber and the matrix, which for the purposes of this work will be assumed to be linearly elastic and isotropic. Instead of using the integral equation formulation as in Dollar and Steif, the above stated problem is analyzed by using the finite element

method. An analytic result, based on the shear–lag model is then developed to gain insight on how the various material parameters affect the deformation and stress fields (in the average sense) near the fiber break. These analytic results are then compared with the numerical results obtained by the finite element method.

2. FORMULATION OF THE PROBLEM

The configuration of the problem to be studied consists of an infinitely long broken fiber imbedded in an infinitely extended matrix under transverse pressure and axial tension. The broken fiber is a circular cylinder of radius a and is assumed to be isotropic linearly elastic with Young modulus E_f and Poisson ratio ν_f. The z axis of the cylindrical coordinate system (r, θ, z) coincides with the symmetry axis of the fiber with the origin located at the center of the circular crack, which lies on the plane z=0. The infinite matrix surrounding the fiber is also assumed to be linearly elastic with Young's modulus E_m and Poisson ratio ν_m.

As in Dollar and Steif [6], the fiber is free to slide along the interface r = a were it not for an applied pressure at infinity, i.e., $\sigma_{rr}^m(r \to \infty, z) = -p$ where p>0 and the superscript m refers to matrix. After the application of the compressive stress $-p$, an uniaxial strain $\epsilon_{zz} = \epsilon_\infty$ is applied monotonically at $z \to \infty$ to both the fiber and the matrix.

Continuity of tractions is enforced on the fiber–matrix interface at r=a. However, displacement discontinuity is allowed to exist according to the Coulomb frictional model, with frictional coefficient μ.

3. NUMERICAL RESULTS AND DISCUSSION

The following normalized variables are introduced to expedite the analysis:

$$\hat{r} = r/a \ , \quad \hat{z} = z/a \ , \quad \hat{u}_i = u_i/(a \ \epsilon_\infty) \ , \quad \hat{\sigma}_{ij} = \sigma_{ij}/p \ , \tag{1}$$

where a " $\hat{\ }$ " denotes a normalized quantity. From dimensional considerations, the normalized $\hat{u}_i$ and $\hat{\sigma}_{ij}$ depend only on $\hat{r}$, $\hat{z}$, μ, ν_f, ν_m, $\lambda = E_m \epsilon_\infty/p$ and $\beta = E_f/E_m$.

Due to axisymmetry, the solution of the problem is a function of r and z. Symmetry in the geometry and boundary conditions allows us to analyze only one quadrant with the appropriate boundary conditions. Axisymmetric Q8 elements (quadratic interpolation in both directions) are used throughout the analysis. Although it is impossible to duplicate the singular behavior in the stress fields of a crack ending on a bimaterial interface by using quadratic interpolations, we found, by careful selection of element sizes, that it is possible to localize inaccuracies to a very small region compared with a. For this reason the smallest element at $\hat{r}=1$, $\hat{z}=0$ on both fiber and matrix sides is chosen to be a square of size 0.006a. The element size in the matrix increases geometrically by a constant factor of 1.65 in the r direction, whereas the element size in the fiber increases geometrically by a constant factor of 1.43 in the negative r direction. The element size in the z direction increases geometrically by a constant factor of 1.55 for both the fiber and matrix. As a result of the geometric increase of the element size in both r and z directions, a fine mesh near the fiber break and the interface is generated. The outer limits of the region to be analyzed are chosen as $\hat{r}_\infty = 25$, $\hat{z}_\infty = 25$. The choice of these finite length dimensions to simulate infinity has been verified by examining the far field stress state after the analysis. To summarize: there are 12 elements in the fiber in the r

direction and 20 elements in the z direction. In the matrix, there are 18 elements in the r direction and 20 elements in the z direction. Finally, there are 20 interface elements at the fiber—matrix interface. In total, the program consists of 620 elements, 1983 nodes and 3966 degrees of freedom.

Interface elements, based on Coulomb friction with stiff elastic response before sliding, are used for representing the interface between the fiber and the matrix. A frictional interface element is a 1—D element composed of two sides, each having three nodes. An initial distance, which is zero in this case, between the two sides of the element, and a coefficient of friction need to be defined. If the normal component of stress (σ_{rr}) acting on the sides of the element is tensile, the two sides separate and no traction (no normal stress, as well as no shear stress) is carried by the element. If the normal component of stress acting on the sides of the element is compressive, the program checks whether the shear stress applied is higher than the shear limit, that is normal stress applied at that specific point times the coefficient of friction. If the shear stress is higher than the shear limit, the shear stress transferred by the element is taken to be equal to the shear limit. If it is less than the shear limit, the element transfers the shear stress.

ABAQUS commercial finite element code is chosen as the analysis tool.

Figures 1, 2, 3 and 4 show selected numerical results for the shear and normal stresses along the interface, the axial load carried by the fiber as a function of the distance away from the fiber break and the normal stress in the matrix on the plane of the fiber break, respectively. From the many different cases that have been tested, we present the results that correspond to $\nu_f = \nu_m = 0.25$, $\beta = 5$, $\mu = 0.1$ and for two values of the loading parameter λ as indicated in the figures.

The above results show that, in the presence of a frictional interface, stress gradients are much smaller than in the perfect bond case. Even though there is a stress concentration close to the crack tip, the stress singularity is relaxed by the loss of constraint due to the interface slip (i.e., Fig. 4). For this reason, extremely refined mesh is not necessary for reliable results. An important outcome of this study is that the broken fiber carries less load in the region close to the fiber break, with a longer ineffective length as the frictional coefficient decreases. Therefore, neighboring intact fibers will be overstressed over larger lengths than they will be overstressed in the case of perfect bonding. This result is important for the determination of the composite strength based on micromechanical models.

A shear—lag model has also been developed in which the normal stress on any cross—section A_f of the fiber is taken to be constant and the reaction to normal and shear stresses in the matrix is decoupled (more details are given in [7]). The length of the slip zone l_s is found to be

$$\dot{l}_s \equiv l_s/a = -\beta \lambda/(2\dot{\tau}_s) - 1/\xi \ , \tag{2}$$

while the normal stress σ_f in the fiber (the axial load carried by the fiber is $P = \sigma_f A_f$) is given by:

$$\dot{\sigma}_f(\dot{z}) \equiv \sigma_f(\dot{z})/\mu = -2\dot{z}\dot{\tau}_s \ , \ 0 \leq \dot{z} < \dot{l}_s \ , \tag{3a}$$

$$\dot{\sigma}_f(\dot{z}) = -(2\dot{l}_s\dot{\tau}_s + \beta \lambda) \exp[-\xi(\dot{z} - \dot{l}_s)] + \beta\lambda \ , \ \dot{l}_s \leq \dot{z} < \infty \ . \tag{3b}$$

The dimensionless constants ξ and $\dot{\tau}_s$ have the evaluations

$$\xi = \left[\frac{4}{\beta(1+\nu_m) \ln(\beta+1)}\right]^{1/2} \ , \ \dot{\tau}_s \equiv \mu\dot{\sigma}_{rr}^t = \frac{2(1-\nu_m^2) - (\nu_f - \nu_m)\lambda}{\nu_f(1+\nu_m) + (1+\nu_f)(1-2\nu_f)/\beta} \cdot \tag{4}$$
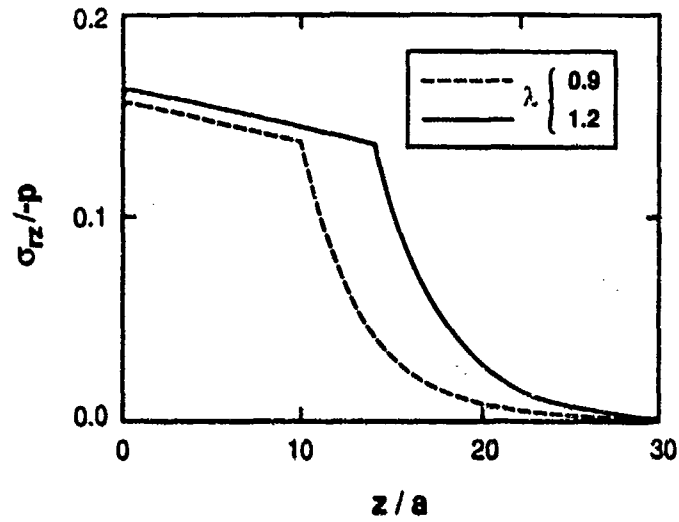
Fig. 1 Interface shear stress vs axial distance for various values of $\lambda = E_m c_o / p$ and for $\beta = E_f / E_m = 5$, $\mu = 0.1$, $\nu_f = \nu_m = 0.25$.
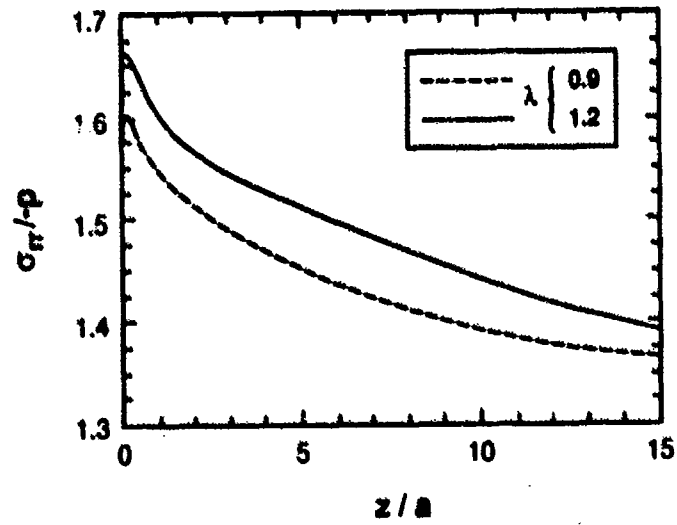
Fig. 2 Interface normal stress vs axial distance for various values of $\lambda = E_m c_o / p$ and for $\beta = E_f / E_m = 5$, $\mu = 0.1$, $\nu_f = \nu_m = 0.25$.
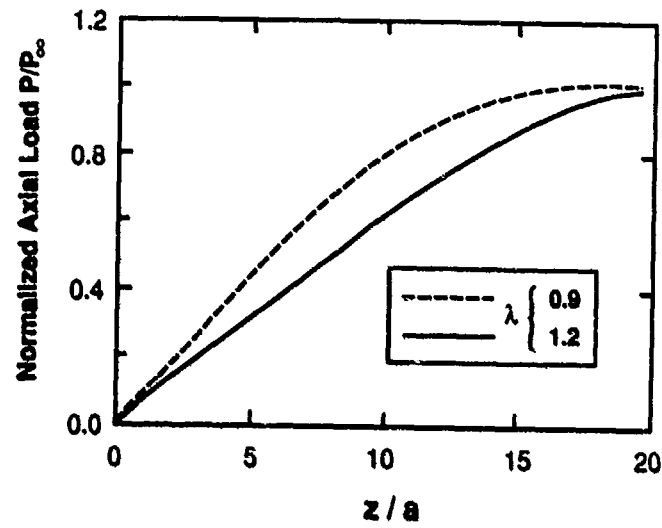
Fig. 3 Normalized axial load in the fiber vs axial distance for various values of
$\lambda = E_m \epsilon_\infty / p$ and for $\beta = E_f / E_m = 5$, $\mu = 0.1$, $\nu_f = \nu_m = 0.25$.
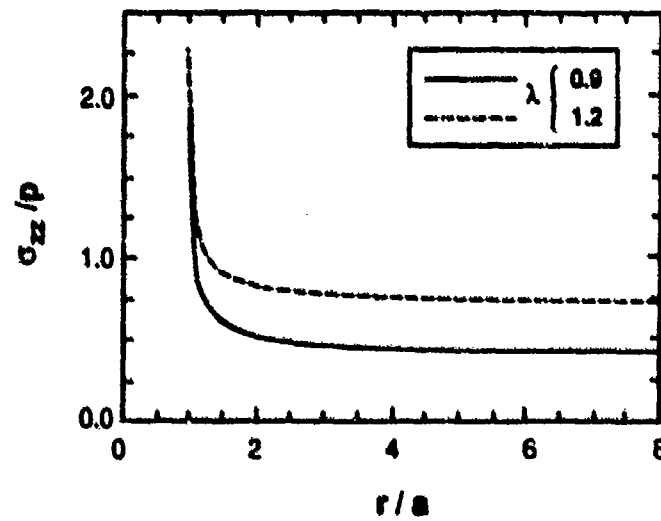
Fig. 4 Normal stress σ_{zz}^m in the matrix ahead of the fiber break for various values of
$\lambda = E_m \epsilon_\infty / p$ and for $\beta = E_f / E_m = 5$, $\mu = 0.1$, $\nu_f = \nu_m = 0.25$.

We note that the above shear–lag analysis results have been given in terms of the nondimensional parameters β, λ and μ introduced earlier.

It is of interest to compare the predictions of the simple shear–lag analysis results, namely equations (2) and (3), with the finite element calculations. The extent of the slip zone calculated by the finite element method is found in the plot of the interface shear stress, i.e. Fig. 1, as the value of z at which the shear stress changes slope. The prediction of the shear–lag model for the slip zone length $\hat{l}_s$ from (2) is 20.321 for the case shown in Fig. 1 and for applied loading $\lambda=1.2$. There is an overestimate of the slip–zone length prediction by the shear–lag model due to the underestimate of the shear stress along the interface in the slip zone. If the shear stress τ_s is corrected according to the results of the finite element analysis, then the predictions of $\hat{l}_s$ from the shear–lag model become closer to the finite element calculations (if we substitute $\nu_f=\nu_m=0.25$ into (4), we obtain the evaluation $\hat{\tau}_s=-1.364\mu$ or $-\sigma_{rz}=0.1364$ for $\mu=0.1$).

Another test for the shear–lag model is the comparison of its prediction for the axial load in the fiber with the finite element calculations. The basic characteristic of the shear–lag model is that in the slip zone the axial load varies linearly with the distance, which is equivalent with the assumption that the shear stress is constant in the slip zone. It is evident from Fig. 3 that this assumption is justified for large slip zones. The value of σ_f/σ_f^∞ (or P/P_∞) at $z=\hat{l}_s=20.321$ is 0.924 from (3) for $\lambda=1.2$ and it is very close to the finite element method result as indicated in Fig. 3.

In summary, the shear–lag analysis predicts accurately the interface shear stress and the axial load in the fiber for small frictional coefficients or large applied strains that lead to relatively large slip zone lengths ($\hat{l}_s > 5$).

ACKNOWLEDGEMENT

REFERENCES

[1] H.L. COX, British J. Applied Phys. 3, 72 (1952).
[2] J.M. WHITNEY and L.T. DRZAL in Toughened Composites, edited by N.J. Johnston (ASTM STP 937, Philadelphia, PA 1987) pp. 179–196.
[3] R. MUKI and E. STERNBERG, Z. Angew. Math. Phys. 22, 809 (1971).
[4] E.F. FORD, Technical Report No. 1, NSF Grant GH–33578, Div. of Applied Sciences, Harvard University (1973).
[5] A.N. NETRAVALI, R.B. HENSTENBURG, S.L. PHOENIX and P. SCWARTZ, Polymer Composites (in print).
[6] A. Dollar and P. S. Steif, Report SM 88–i, Carnegie–Mellon University (1988).
[7] B. AKSEL, D.C. LAGOUDAS and C.–Y. HUI, Int. J. Solids Structures (submitted).

FILAMENT FRAGMENTATION PHENOMENA

JUAN C. FIGUEROA#, LINDA S. SCHADLER* , and CAMPBELL LAIRD*,
#E.I.DuPont Experimental Station, P.O.Box 80304, Wilmington, DE
19880-0304.
*University of Pennsylvania, Dept. of Materials Science and
Engineering, Philadelphia, PA 19104.

ABSTRACT

The effect of fiber surface treatments on the relationship between the
tensile strength of a filament and the shear strength of its interphase is one of the
central issues facing composite materials technologists today. We demonstrate here
that analysis of fragmentation phenomena in monofilament composites can
simultaneously yield information about these two parameters. Characterization of
shear stress transfer zones in non-critical fragments has led us to the
determination of interphase strength.

A phenomenological treatment that highlights the role of the matrix in the
fragmentation process is presented here. This analysis considers issues such as the
strain energy exchange between a failing fiber and the matrix, as well as
interphase relaxation due to the viscoelastic nature of the matrix. Our observations
of the fragmentation phenomena in AU4/polycarbonate monofilament composites
indicate that the fiber/matrix interaction in this system is governed by
micromechanical locking.

INTRODUCTION

Interphase design is playing an increasing role in the development of
advanced composite materials. Monofilament composites are very useful in this
regard as they not only highlight interphase behaviour, but also provide the
researcher with a system that is superior in controllability, reproducibility, and
costeffectiveness than multifilamentary media. On this basis, the testing of
monofilament composites is widely practiced in the field, with particular emphasis
on analysis of critical fragment populations for the determination of interphase
strength [1].

We have extended this practice to include the monitoring of the evolution of
the entire fragmentation process to extract data not only on interphase strength
but on filament strength. In addition, we have attempted to identify the relative
role of fiber vs. matrix on interphase behaviour in a carbon/ polycarbonate
composite system.

EXPERIMENTAL

Unsized PAN-derived carbon fibers (Hercules AU4, 33Msi tensile modulus)
were surface treated for increasing amounts of time. Treatment time effects on
fiber surface topography (density of surface asperities) were assessed via
scanning electron microscopy (SEM). Similarly, the evolution of fiber surface
energetics was calculated from advancing wettability forces measured on single
filaments immersed in water and glycerol [2]. Specimen fabrication (hot
compression molding) and fragmentation testing procedures have already been
reported [3]. Highlights include: (1) filaments with different surface treatments
were simultaneously molded in an attempt to reduce molding and testing artifacts,
(2) as molded filaments were in a state of residual compression, (3) the exact
filament strain was assumed to be the applied composite strain.

RESULTS & DISCUSSION

We have postulated that the mechanical strength of a monofilament composite system is determined by two stress parameters, $\sigma^*_{zz}(r)$ and $\sigma^*_{rz}(r)$, which represent upper limit values for every point r in the composite (z represents the axial direction of the composite).

Our fragmentation evolution data can be conveniently represented in terms of the average fragment aspect ratio <L/d> (with L and d denoting fragment length and diameter respectively) as a function of applied strain [4], and Figure 1 schematically illustrates some of our observations for three filaments A, B, and C.
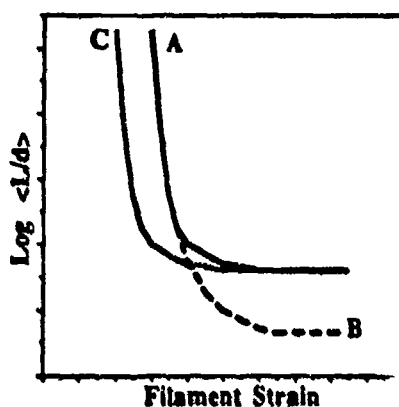
Figure 1. Schematic representation of average fragment aspect ratio as a function of applied strain for three filaments with different tensile strength and interface properties.

By resorting to a shear lag representation of σ_{zz} along a fragment, where L is depicted as composed of a central Lg region with uniform stress (defined as filament gage length) bounded by two stress transfer zones of length λ as illustrated in Figure 2, we have determined σ^*_{zz} data by painstakingly correlating Lg for every fragment with its failure strain [2]. During the early descending portion of a <L/d> curve, Lg – L because Lg >> λ and, therefore, this sector of the <L/d> curve can be thought of as representing the Lg dependence of σ^*_{zz}. In particular, the relative impact of surface treatments on σ^*_{zz} for a given fiber can be ascertained by the position of these curves along the abscissa axis. On this basis, a quick look at Figure 1 indicates that $\sigma^*_{zz}(A) = \sigma^*_{zz}(B) > \sigma^*_{zz}(C)$. The attainment of the critical state is clearly depicted by the <Lc/d> asymptotes in Figure 1, with Lc denoting lengths of critical fragments. Many workers have demonstrated that

$$\sigma^*_{rz} \propto \frac{\sigma^*_{zz}}{<Lc/d>} \qquad (1)$$

making $<L/d>$ curves very handy for quick qualitative comparisons for σ^*_{rz} between different filaments. However, we believe that quantitative determination of σ^*_{rz} based on critical fragment populations demands a statistical description of the entire fragmentation process up to the critical state.

$$\sigma^{\approx}_{rz} = \frac{E \cdot d \cdot \varepsilon}{4 \cdot \lambda}$$

E : Fiber Modulus
d : Fiber diameter
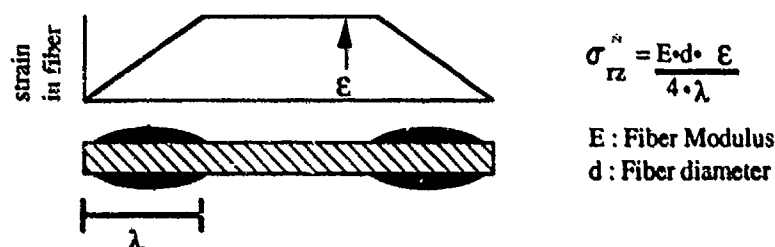
Figure 2.   Schematic of a filament fragment in cross polarization to define the Stress Transfer Zone, STZ (filled region), and its length, λ.

This task, although achievable, is enormously challenging as our observations and those of others clearly indicate [5-8]. The use of $<L/d>$ data precisely avoids key statistical aspects of the phenomenology, making their use inadequate for σ^*_{rz} determination. In view of these considerations, we have measured λ for fragments with $L > 2\lambda$ (see Figure 2) to yield σ^*_{rz} data.

Figure 3 presents our results for ε^*_{zz} (at one inch gage length), σ^*_{rz}, fiber surface energy (γ), and fiber surface roughness (R). The following observations are worth highlighting: (a) ε^*_{zz} was progressively reduced by the treatment, (b) there was a treatment time that maximized σ^*_{rz}, (c) γ increased earlier than σ^*_{rz} to a steady state level independent of treatment time, and (d) the evolution of R (density of surface asperities) paralleled that of σ^*_{rz}, and reflected a nucleation-growth-coalescence phenomena. In addition, critical state specimens were carefully sectioned to extract critical fragments for SEM analysis. Micrographs presented in Figure 4 indicate that fiber surfaces treated at increasing times were covered with more matrix material. A similar σ^*_{rz} evolution has recently been reported for an electrochemically treated carbon fiber embedded in epoxy [9].

Our interpretation for the evidence presented in the last two Figures is as follows: (a) weakly bound layers were present on the surface of the AU4 fiber, (b) as these layers were removed by the surface treatment, a quick saturation in surface chemistry was achieved, (c) the maximum in σ^*_{rz} reflects the complete removal of these layers and the increased participation of the polymeric matrix in

the interphase failure process, (d) fiber/matrix interaction is primarily governed by micromechanical locking, which in turn reflects the residual fiber surface roughness. These conclusions are consistent with earlier observations of Drzal for an AU4/epoxy system [10].
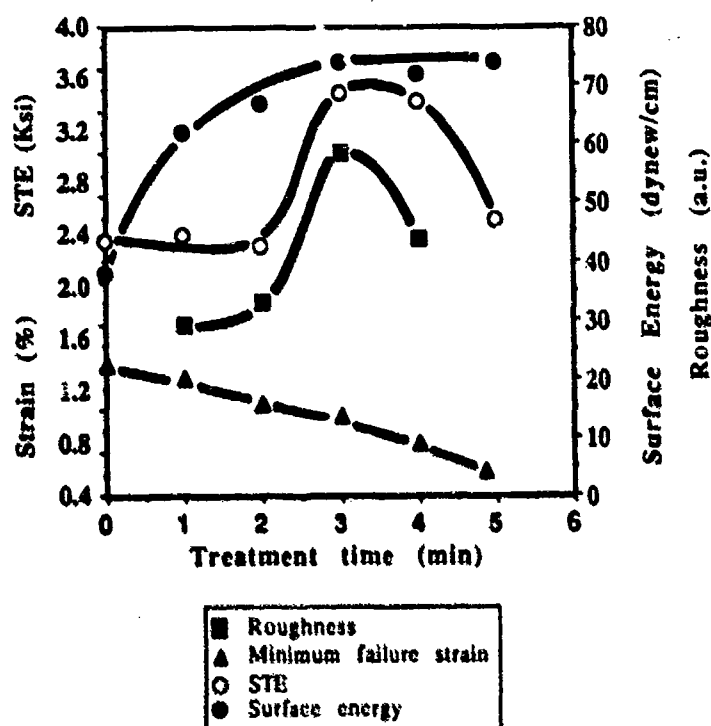
Figure 3. Treatment time effects on filament and interphase properties.

To ascertain the degree of participation of the matrix in the failure behaviour of the interphase, we carried out fragmentation tests directly up to the critical state but at different strain rates ($\dot{\epsilon}$), and Figure 5 shows <Lc/d> results for an as-received filament and another one that had been treated for a period of time longer than that required for maximum σ^{*}_{fz}. The as received filament showed the $\dot{\epsilon}$ dependency in spite of the fact that σ^{*}_{fz} was determined by the fiber at high $\dot{\epsilon}$. We feel that the treated filament did not show $\dot{\epsilon}$ dependency because of two considerations: (a) the entire fragmentation process in this specimen took place at a much lower $\dot{\epsilon}$ range than that of the untreated one, and (b) the fragmentation temperature was too low. If the fragmentation test had been carried out at a higher temperature, then <Lc/d> for the treated filament would have also been $\dot{\epsilon}$ sensitive [11,12].

As Received | Treated 1 min | Treated 3 min

Figure 4. SEM micrographs showing surface topography of extracted critical fragments. Marker denotes 1um.
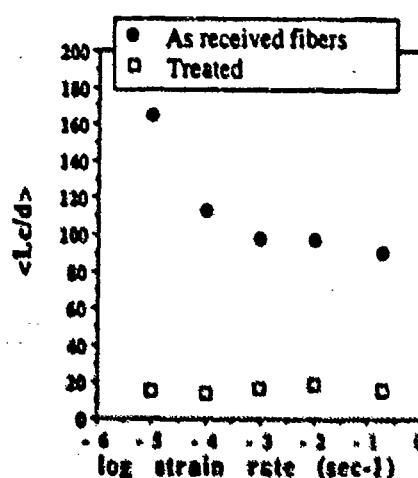
Figure 5. Effect of strain rate on critical aspect ratio.

In closing, our observations of the fragmentation process, which have paralleled those of others [4-10], have encouraged us to postulate a filament fragmentation phenomenology in composites as described in Figure 6. When a loaded filament fails, a considerable fraction of its stored strain energy is released to the matrix, and a stress transfer zone is almost suddenly formed. This zone reflects the response of the matrix to the enormously high strain rates imposed on it (the temporal modulus in this region increases accordingly) making the interphase region to expand into a region that was considered matrix phase before the burst. Viscoelastic relaxation mechanisms are the natural consequence to the initial violent exchange the kinetics of which scale with temperature. These mechanisms, driven by an overall reduction of strain energy in the transfer zone, lead to a localization of deformational energy right along the fiber/interphase boundary which, in the worst of cases, may result in a crack extending transversely across the matrix and/or along the interphase itself. The central issue of the stress transfer problem, then, is one of micromechanical energy exchange and redistribution in the transfer zone.
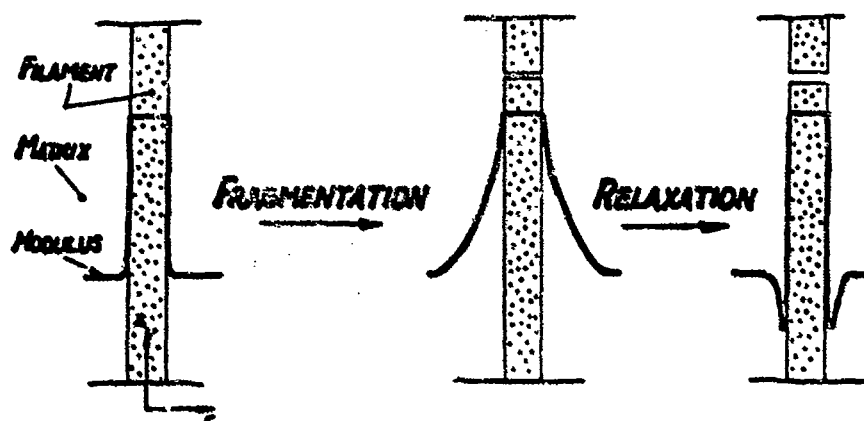
Figure 6.   Phenomenological model of micromechanical energy exchange and redistribution in the STZ following carbon filament fragmentation.

CONCLUSION

Fragmentation phenomena in monofilament composites yields simultaneous data on filament and interphase strengths. The lowest shear strength between the fiber (outer layers) and the matrix determines the interphase stress transfer effectiveness; in all cases, however, the matrix mediates the role of the weakest link. Fiber/matrix interaction in AU4/polycarbonate is governed by micromechanical locking.

REFERENCES

1. M.Narkis, E.J.H.Chen, R.B.Pipes, Polymer Composites, 9, 245 (1988), and references cited herein.

2. S. Wu, Polymer Interface and Adhesion, Marcel Decker (1982)

3. L.S.Schadler, J.C.Figueroa, C.Laird, B.T.Ma, paper presented at the 1989 Advanced Materials Conference, Golden, Colorado, March 1989 (in press).

4. N.Ikuta, Z.Maekawa, H.Hamada, S.Yoshioka, E.Nishio, T.Hirashima in Interfaces in Polymer, Ceramic, and Metal Matrix Composites, edited by H.Ishida (Proc. 3rd International Conference on Composite Interfaces, 1988) pp. 611.

5. L.T.Drzal, Adv. Polym. Sci., 75, 1 (1986).

6. W.D.Bascom, R.M.Jensen, J. Adhesion, 19, 219 (1986)

7. L.Dilandro, A.T.Dibenedetto, J.Groeger, Polymer Composites, 9(3), 209 (1988).

8. A.N.Netravali, R.B.Henstenburg, S.L.Phoenix, P.Schwartz, Polymer Composites, 10(4), 226 (1989).

9. J.Donnet, S.Dong, G.Gellpain, M.Brandle in Interfaces in Polymer, Ceramic, and Metal Matrix Composites, edited by H.Ishida (Proc. 3rd International Conference on Composite Interfaces, 1988) pp. 35.

10. L.T.Drzal, M.J.Rich, P.F.Lloyd, J. Adhesion, 16, 1 (1982).

11. T.Ohsawa, A.Nakayama, M.Miwa, A.Hasegawa, J. Appl. Polym. Sci., 22, 3203 (1978).

12. E.L.M.Asloun, M.Nardin, J.Schultz, J. Materials Sci., 24, 1835 (1989).

A CRITICAL EVALUATION OF THE USE OF THE MICROBOND METHOD FOR DETERMINATION OF COMPOSITE INTERFACIAL PROPERTIES

REBECCA A. HAAKSMA AND MARILYN J. CEHELNIK
Alcoa Laboratories, Alcoa Center, PA, 15069

ABSTRACT

The microbond method has been applied with increased frequency to characterize interfacial adhesion in fiber reinforced composites. Nevertheless, a number of serious questions remain regarding the interpretation of experimental data. This paper addresses material and experimental variables in the microbond test procedure including the cure behavior of thermoset test specimens, matrix heterogeneity, locus of failure in test specimens and load application techniques. The theoretical basis for the method is examined by viewing experimental results in terms of existing theoretical interpretations of interfacial failure. Conclusions are presented regarding the limitations and the potential of the microbond method for determining fiber/matrix adhesive bond strength.

INTRODUCTION

The properties of the interphase region resulting from the interaction of a polymeric matrix with a reinforcing fiber play a crucial role in determining composite performance. Effective utilization of the strength and stiffness of reinforcement materials depends on efficient load transfer through the interphase region. Development of a basic understanding of the chemistry, microstructure and mechanics of the composite interphase region is of potential value for optimizing the design of new composite materials and applications.

One important interfacial parameter in composite materials is the bond strength between the reinforcing fiber and the matrix resin. Chemical modification of a fiber surface through the use of sizings and surface treatments is a tool which may be used to alter fiber/matrix interactions. A reliable, readily interpretable experimental test for determining fiber/matrix adhesive bond strength is needed to assess the effects of interphase chemical modification. The method must be experimentally feasible and a theoretical basis must exist to provide a framework for interpretation of experimental results.

The goal of this paper is to evaluate the limitations and the potential of the microbond method for measurement of interfacial bond strength.[1-4]

EXPERIMENTAL PROCEDURE

The microbond test, first reported in 1987 by Miller,[1] fits into the general class of single filament pull-out tests which have been used to investigate interfacial properties in composite materials and reinforced concrete for more than two decades.[5-10] The basic test procedure involves pulling a single filament from a small volume of cured matrix while measuring the force required to detach the filament.

Sample preparation for the microbond test is carried out by applying two or three droplets of resin to individual single fibers which are mounted to an aluminum frame by tabs bonded to both fiber ends. In a typical microbond experiment, a fiber is hung from one end tab on a 1000 g load cell in an Instron machine; the load cell is fitted with a hook as depicted in Figure 1. A precision vise, modified to produce flush grip areas, is employed to debond the resin beads. The fiber is positioned between the two vise plates with a resin bead situated just below the opening in the vise. The proper test configuration is attained by carefully narrowing the vise gap utilizing a shim slightly larger than the fiber diameter while checking to ensure that the fiber continues to hang freely.

A debonding experiment is conducted by moving the Instron crosshead at a rate of 1 mm/min such that the resin bead is displaced upward to make contact with the edges of the vise. Load is transferred to the specimen until a critical value is reached and fiber pull-out occurs. A typical force versus time trace for a microbond experiment, illustrated in Figure 1, shows the peak debonding load corresponding to fiber pull-out followed by a sharp dropoff to an erratic, small frictional force arising from bead displacement along the fiber axis.
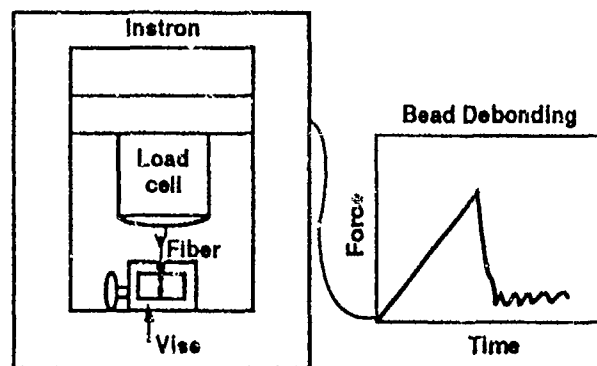
Fig. 1. Schematic diagram representing the microbond test configuration and a typical force versus time trace obtained in a debonding experiment.

The application of the microbond method to measure fiber/matrix adhesive bond strength on small diameter engineering fibers presents some experimental difficulties related to microscale testing. A limited experimental range and minute sample sizes are two features of the technique. The range of bead sizes which may be tested on small diameter carbon, glass and aramid fibers (7-12 μm) is bounded by a lower limit of about 40 μm due to the existence of a critical bead volume to fiber diameter ratio for droplet formation and an upper limit which is reached when fiber fracture occurs before fiber pull-out. The strength of engineering fibers establishes a clear upper limit for the test. The experimental range accessible to most fibers is less than one order of magnitude in terms of bead diameter. Corresponding weights of microbond resin droplets which are applied to small diameter fibers for measurement of interfacial shear strength range from hundredths of micrograms to a few micrograms for the larger bead diameters.

The microbond test was developed by Miller to overcome an additional experimental problem inherent in the application of conventional single fiber pull-out methods to small diameter engineering fibers. The tendency for formation of a meniscus, often larger than the embedment depth, exists when a fiber is embedded in a polymer sample which wets the fiber surface. The microbond procedure minimizes but does not completely eliminate this problem. [1]

EXPERIMENTAL OBSERVATIONS

The potential of the microbond technique for measurement of interfacial shear strength was evaluated by examining material and experimental variables identified as critical in the interpretation of test results and comparing the results with existing theoretical interpretations of interfacial failure. The variables investigated include the cure behavior of small thermoset test specimens, matrix heterogeneity, locus of failure in test specimens and load application techniques.

Thermoset Cure Behavior

A striking effect, uncovered early in this work, was that the microbond test configuration influenced the cure behavior of a thermoset epoxy resin system. The material system (EPON 828, meta-phenylenediamine (mPDA)/AS-4 carbon fiber) was selected for an initial investigation since the interfacial shear strength value for this system had been previously measured by the single fiber composite method.[11] It was impossible to obtain an interfacial shear strength value for this system employing the same cure cycle conditions (75°C, 2 hours; 125°C, 2 hours) used to prepare single fiber composite test specimens because the matrix droplets placed on the fibers did not cure.

The cure behavior of this resin system was investigated as a function of degree of mixing, resin/curing agent ratio, cure cyle conditions, reinforcement surface properties, specimen size and specimen geometry. Degree of cure was qualitatively evaluated using Fourier Transform Infrared Spectroscopy (FT-IR). FT-IR microscopy was conducted on droplets of resin placed on sodium chloride plates demonstrating the presence of curing agent and unreacted resin before the specimens were exposed to cure cyle conditions . After heating, specimens were again examined spectroscopically and evidence was obtained for unreacted resin with complete loss of curing agent. Incomplete cure was observed for small droplets placed on all types of surfaces (carbon, glass and aramid fibers; aluminum and sodium chloride plates). The extent of cure was the lowest for the smallest droplets, but even beads greater than 1 mm (1000 µm) in diameter remained tackier than cured tensile specimens. The spectroscopic results and the inverse relationship between degree of cure and bead size both suggest that evaporation of curing agent from test specimens is a critical factor which must be controlled in the microbond test procedure.

Drzal and coworkers independently observed the thermoset curing phenomenon and have recently completed a quantitative study correlating degree of cure with droplet size and curing agent volatility.[12]

The implications of the thermoset curing behavior observed in the microbond test are significant since a new requirement for application of the method is indicated. Prediction of adhesive performance at the fiber/matrix interphase in a composite requires a test specimen configuration which produces resin properties which are similar to resin properties in an actual composite. Our results suggest that prior to conducting the microbond test an independent method must be used to determine the extent of cure in resin droplets. Moreover, use of the microbond method to discern effects of systematic chemical modification will not be possible until sample preparation conditions are identified which produce cured test specimens.

The test specimen cure requirement actually represents a minimum requirement for modeling full composite properties using as input results from a single filament test. Valid questions exist concerning the relationship between matrix properties in all types of single fiber test specimens and matrix properties in the composite interphase region. Resin properties in the vicinity of the composite fiber/matrix interphase likely differ significantly from bulk resin properties and have not yet been well-characterized.

Matrix Heterogeneity

Another material variable explored was the effect of matrix heterogeneity on the scatter in microbond test results. Experimental precision in all single fiber tests is usually about 20%.[3] The microbond results obtained in our laboratory were consistent this observation. However, one experimental system investigated, a commercial epoxy resin formulation containing at least five components, exhibited much poorer precision, on the order of 40%, when tested with Kevlar 49. An investigation was conducted on this resin system replicating the cure cycle on a hotstage placed under an optical microscope. Photomicrographs, taken periodically throughout the cure cycle and after the test specimens had been cooled to room temperature, showed the presence of heterogeneities in the matrix greater than 50 µm in size which is the same order of magnitude as the diameter of matrix droplets in the smaller microbond test specimens. This observation indicates that structural inhomogeneities in the matrix resin are capable of seriously influencing test results. The experimental precision observed in the microbond test includes uncertainty in the measurement as well as intrinsic material variations.

Locus of Failure

The locus of failure must be evaluated in all interfacial testing in order to interpret experimental results, be it a full composite or a microbond specimen. Generally, tested microbond specimens which were examined microscopically appeared to fail at the fiber/matrix interface but the details of the failure mechanism are unknown. The most common example of tested specimen appearance, illustrated in Figure 2a, indicates adhesive failure at the fiber/matrix interface. Figure 2b is an example of a complex failure mode in which the sample displays both fibrillation of the outer layers of Kevlar 49 fiber and matrix failure. The interpretation of microbond results will differ in these two examples, and only in the former case can an interpretation hope to include consideration of the resin-fiber interaction at the molecular level. Characterization of the failure mode must be an integral part of the microbond test procedure and application of the method must be limited to cases with documented interface failure.
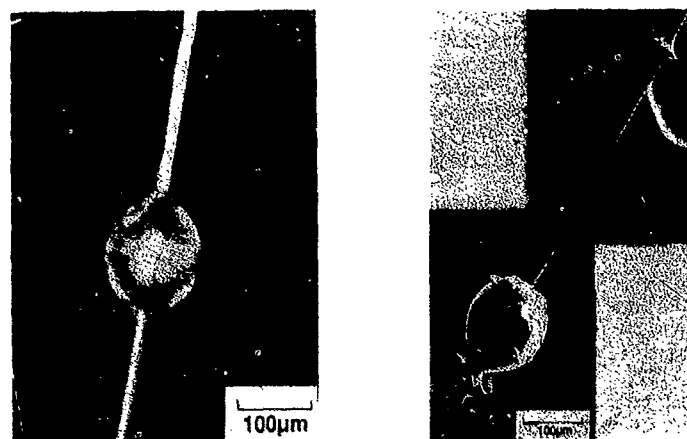
Fig. 2. (a) Photomicrograph of a tested microbond specimen (Epoxy/Kevlar 49) exhibiting interfacial failure. (b) Photomicrograph of a tested microbond specimen (Epoxy/Kevlar 49) showing a complex mode of failure.

Load Application Techniques

The microbond technique has been applied in our laboratories to thermose: epoxy resins with glass, carbon and aramid fibers and a thermoplastic polycarbonate resin with a glass fiber. The simplest experimental definition for the microbond test, shown in equation 1, follows from a strength of materials model which relates the measured peak debonding force, F, to a shear stress, τ, applied uniformly across the interface. In this expression, d corresponds to fiber diameter and l is the resin embedded length.

$$\tau = F/\pi dl \qquad (1)$$

Interpretation of microbond experimental data is facilitated by plotting peak debonding force versus embedded length for fiber/resin combinations of interest. Examination of these plots for the material systems under investigation showed a consistent trend in the experimental data. An example(epoxy resin/tetraethylene tetramine/Kevlar 49) represented in Figure 3a indicates that linear extrapolation to zero embedded length produces an apparent negative value of load. Lower interfacial shear strength values are calculated from equation (1) for smaller size resin specimens. The relevant question is whether the extrapolation is a valid operation related to the mechanism of failure or if the apparent negative load is an experimental artifact. Several experimental variables were investigated to determine possible origins of the effect including material properties, load measurement techniques, test speed and load application techniques.

The variable which exhibited the largest influence on experimental results was the load application method. An analysis of the microbond test design suggested that the ideal loading condition would be achieved using a circular area of contact.[13] A standard experiment, depicted in Figure 1, is characterized by point loading which occurs as the resin droplet contacts the edges of the vise. The data shown in Figure 3b were obtained for the epoxy/aramid system by pulling the fibers up through a hole made with a laser, corresponding to a circular area of contact. Although the characteristics of the hole were not ideal and only one experimental system was investigated, the results demonstrate the sensitivity of the measured debonding load to the detailed geometry of contact which develops during a debonding event.

KEVLAR 49/ EPOXY

a)

KEVLAR 49/ EPOXY
(circular area of contact)

b)
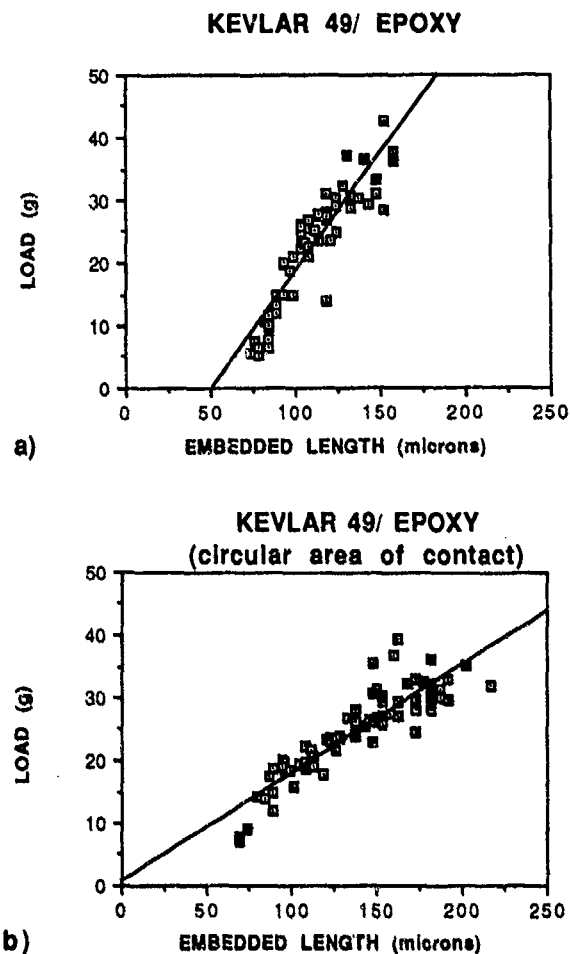
Fig. 3. (a) Microbond results for point loading of (Epoxy/Kevlar 49)test specimens.
(b) Microbond results for (Epoxy/Kevlar 49) specimens using a circular area of contact.

INTERPRETATION OF TEST RESULTS

The failure processes which occur as fibers are debonded and pulled out of a resin matrix are extremely important in building an understanding of composite performance and are not yet well understood despite considerable experimental and theoretical investigation. The two principal strategies applied in analytical investigations of single fiber pull-out tests are a strength of materials approach and a fracture mechanics approach.[10] The first approach assumes that failure takes place when the stress between the fiber and the matrix exceeds the interfacial shear strength and is the origin of equation 1. The second approach is based on the concept that the interfacial failure mechanism is crack propogation at the interface rather than simultaneous debonding.

Experimental results for single fiber tests including the microbond test have shown that for certain material systems the measured debonding force appears to increase with specimen size to a specific value and then remains unchanged as the embedded length continues to increase. This trend in microbond data has been reported by Miller and Penn for epoxy/aramid systems.[1,3]

Recently, Penn and coworkers applied a fracture mechanics approach to analyze the microbond test and predicted that the relationship between measured load and embedded length is not linear but should exhibit the dual behavior of rising load at low l and constant load at high l.[3]

Our experimental results were examined in terms of the strength of materials and fracture mechanics interpretations of interfacial failure. Due to experimental artifacts, a limited experimental range and relatively large experimental uncertainty, it was not possible to use our data to discriminate between these models and unambiguously establish a theoretical basis for the method.

CONCLUSIONS

An important interfacial parameter in composite materials is the bond strength between the reinforcing fiber and the matrix resin. The microbond test provides a method with potential for direct measurement of fiber/matrix interfacial properties. However, the current level of understanding of the method and the failure processes associated with fiber pull-out does not allow a straightforward interpretation of experimental results.

Examination of material and experimental variables in the microbond test procedure has clarified the limitations of the method. These limitations can be sufficiently severe as to impact the use of the method for systematic investigation of the effects of chemical modification on interfacial bond strength.

Prior to use of the microbond test for investigation of interfacial strength properties, the following conditions must be satisfied: independent determination of the extent of cure of the thermoset matrix droplet, identification of the locus of failure and investigation of the influence of the contact geometry developed during the debonding event.

Investigation of the potential application of the microbond method should continue despite the problems associated with the technique. To date, no single method has been identified for unambiguous delineation of interfacial bond strength for all material systems and the importance of the problem warrants continued experimental and theoretical investigation.

ACKNOWLEDGMENTS

REFERENCES

1. Bernard Miller, Pierre Muri and Ludwig Rebenfeld, *Comp. Sci. Tech.* 28, 17 (1987).
2. Umesh Gaur and Bernard Miller, *Comp. Sci. Tech.* 34, 35 (1989).
3. Lynn S. Penn and Shaw M. Lee, *J. Comp. Tech. Res.* 11(1), 23 (1989).
4. Kevin P. McLea and Gregory J. Besio, *Poly. Comp.* 9(4), 285 (1988).
5. L. S. Penn and S. M. Lee, *Fiber Science and Technology* 17, 91 (1982).
6. Michael R. Piggott and Ping S. Chua, *Ind. Eng. Chem. Res.* 27, 672 (1987).
7. L. J. Broutman in American Society for Testing and Materials, edited by M. J. Salkind, (Philadelphia, 1969), p. 27.
8. G. D. Andreevska and Y. A. Gorbatkina, *Ind.Eng. Chem., Prod. Res. Develop.* 11, 24 (1972).
9. D. B. Eagles, B. F. Blumentritt and S. L. Cooper, *J. Appl. Poly. Sci.* 20 435 (1976).
10. Jill K. Morrison, Surenda P. Shah and Yeou-Shang Jenq, *J. Engineering Mechanics* 114 (2) 277 (1988).
11. Lawrence T. Drzal, Michael J. Rich and Pamela F. Lloyd, *J. Adhesion* 16 1 (1982).
12. L. T. Drzal (private communication).
13. J. Y. Yeh, Letter to R. L. Rolf, Alcoa Laboratories, 1989.

Characterization of Interfaces

TRANSMISSION ELECTRON MICROSCOPY STUDIES OF SILICON NITRIDE / SILICON CARBIDE INTERFACES

H.-J. KLEEBE*, N. CORBIN**, C. WILLKENS**, and M. RÜHLE*,+
*UCSB, Materials Dept., Eng. III, Santa Barbara, CA;
**Norton Co., Northboro, MA.
+Now at MPI für Metallforschung, Stuttgart, FRG.

ABSTRACT

Microstructural investigations of HIP'ed silicon nitride reinforced with silicon carbide whiskers were performed using a 400 kV high resolution analytical transmission electron microscope. Two different whisker sources as well as uncoated and carbon coated whiskers were evaluated for their effectiveness in improving mechanical properties.

This paper focuses on microstructural and microchemical analysis of interface and grain boundary regions within the composites. Combined HREM and AEM investigations reveal that variations in fracture toughness are mainly influenced by the microstructural and chemical development of the interface. Fracture toughness can be related to the surface chemistry of the reinforcements.

INTRODUCTION

Silicon nitride is one of the leading candidate engineering ceramic materials for structural applications at elevated temperatures. This is a result of its good mechanical and thermo-mechanical properties (high strength, good corrosion resistance, and thermal shock resistance). Its rather low fracture toughness, a general problem for ceramic materials, is a concern for a variety of potential applications. One of the most effective concepts for improving toughness is the incorporation of SiC whiskers as a reinforcing phase.[1-3] Silicon carbide's favorable combination of properties such as high strength, high elastic modulus, and good thermal stability make it a very promising material for reinforcement in different ceramic systems. Furthermore, its compatibility with most oxide and non-oxide ceramic materials led to the formation of a variety of new ceramic composite materials with improved mechanical properties. Although the reported data for Si_3N_4/SiC whisker reinforced ceramics are not as promising as for Al_2O_3/SiC composites, there is a rather high potential for its use in engineering structural applications.[4,5]

The major toughening mechanisms for silicon nitride based whisker reinforced composites were identified as crack bridging, crack deflection, and crack branching. Unlike fiber reinforced materials, whisker pull-out is less pronounced when observed.[6] The resulting toughening mechanisms are mainly determined by the interfacial properties of the reinforcement/matrix interface, although toughness is also governed by whisker shape, strength, radius, and volume fraction.[7] The role of residual stress at interfaces due to different thermal expansion mismatches of SiC and Si_3N_4 are expected to be important. Therefore, a chemical and microstructural characterization of the interfacial regions combined with a general characterization of microstructural features gives valuable information for a deeper understanding of resulting mechanical behavior of the composites.

In this paper four different Si_3N_4/SiC whisker reinforced ceramics were investigated. The materials varied in whisker source and whisker coating. The investigation emphasized both general microstructural characterization of the composites and high resolution imaging of interfacial regions between whisker and host material. The goal was to correlate resulting mechanical properties to characteristic microstructural features of the composite materials.

EXPERIMENTAL PROCEDURES

Composite blends were prepared by mixing 30 vol.% SiC whiskers with a matrix of Si_3N_4 plus 4 wt.% Y_2O_3. Carbon coated and uncoated SiC whiskers supplied by American Matrix Incorporated (AMI)* and Tokai Carbon Co. J.td.** were used in this study. The composite blends were formed into 7.5x7.5x0.6 cm tiles by uniaxial die-pressing. This forming results in random alignment of the SiC whiskers in the Si_3N_4 matrix. Composites were hot isostatically pressed to full density using the ASEA glass encapsulation method.

Flexural strength was determined on 3x4x50 mm test specimens machined and tested according to the recommended MIL-STD procedures.[8] Fracture toughness values were determined using the controlled flaw method described by Chantikul et al.[9] A 10 kg vickers indent was inserted into the tension side of the test specimen. The same geometry and fixturing configuration used for strength testing was used for fracture toughness determination. Average strength and fracture toughness values were obtained from results on two to five test specimens. Because of the many concerns over the accuracy of fracture toughness techniques a well documented Si_3N_4 material (NC-132) was evaluated for comparison. The obtained value of 4.6 +/- 0.1 MPa(m)$^{1/2}$ for NC-132 is in good agreement with literature values of 4.7 MPa(m)$^{1/2}$ by chevron notch[10] and 5.0 MPa(m)$^{1/2}$ for controlled flaw method.[9]

TEM specimens were prepared following standard procedures. Dimpling and subsequent ion thinning with an argon dual-beam at 2.5 kV to 5 kV at 1.0 mA to perforation was the final step of specimen preparation. Microstructural and analytical analysis of amorphous phase regions included energy dispersive x-ray spectroscopy (EDS-Tracor, Northern), and parallel electron energy loss spectroscopy (PEELS-Gatan). Structural and analytical work was performed using a 400 kV JEOL instrument (Model 4000 FX) with the outlined analytical equipment attached. During all investigations a double tilting specimen holder operating at liquid N_2 temperature to reduce contamination was used .

* American Matrix Inc., Knoxville TN., Generation 4, Grade 1A SiC, Diameter 0.5-2.0 μm

** Tokai Carbon Co. Ltd., JAPAN, Grade 400 uncoated, 400C coated, Diameter 1.0-1.4 μm

RESULTS AND DISCUSSION

- Mechanical properties

Table I lists the mechanical property results on the four composites evaluated along with a monolithic representative of the matrix material. Optical microscope analysis of fracture surfaces of the composite materials have shown that the observed large variations in fracture strengths are mainly related to residual SiC grit with particle sizes >30 μm associated with the silicon carbide whiskers. Although different whiskers and coatings were utilized in the composites the fracture toughness results do not show large varia-

Tab. 1 Fracture strength and fracture toughness of monolithic and SiC whisker reinforced composites

Material	Whisker Source	Coating	Fracture * Strength [MPa]	Fracture * Toughness [MPam$^{1/2}$]
A	-	..	939 ∓ 85(9)	5.5 ∓ 0.2(3)
B	Tokai	-	464 ∓ 136(5)	6.4 ∓ 0.9(2)
C	Tokai	carbon	632 ∓ 43(3)	6.0 ∓ 0.5(3)
D	AMI	-	280 ∓ 64(3)	4.8 ∓ 0.2(3)
E	AMI	carbon	583 ∓ 59(5)	5.7 ∓ 0.2(5)

* Number of specimens in parenthesis

tions. The monolithic material A (see Table 1) and composites B, C, and E are all similar considering the standard deviations observed. Only composite material D is significantly different from the others. In this case it is the lowest toughness material.

- Microstructural characterization

TEM studies of the composites revealed, besides large SiC-particles, a non-uniform distribution of metallic contaminations as well as carbon clusters, which may also contribute to variations in fracture strength data. Materials B and C containing Tokai whiskers showed Co-rich particles as a major metallic contamination. They are described in the manufacture's patent as a possible catalyst during processing.[11] In contrast, combined EDS and PEELS analysis verified similar sized and shaped WC-particles in materials D and E, incorporated during powder processing from the milling media. Carbon clusters in the matrix were observed in composites reinforced with uncoated and carbon coated whiskers. The observation of carbon-rich clusters using uncoated SiC-reinforcements was unexpected. Residual carbon clusters in Tokai whisker reinforced composites were mainly found in the vicinity of the Co-rich particles. This can be related to excess carbon used during whisker synthesis. The AMI whisker, although labeled as uncoated, revealed a rather thin (10-20 nm) discontinous carbon layer at the surface. This coating showed a tendency to peel off and form clusters in the matrix.

Fig. 1   Uncoated SiC whiskers in Si_3N_4 based composites; a) Tokai whisker (beam direction close to [111]), b) AMI whisker (incident beam parallel to [110]).

Low magnification TEM images in Fig. 1 depict uncoated Tokai and AMI whiskers incorporated into the silicon nitride matrix material. All composites contained both smooth and contorted or irregular shaped whiskers with average diameter variations between 50 and 500 nm. Some of the Tokai whiskers appeared to be hexagonal and a minor amount triangular shaped when viewed parallel to the [111] growth direction. It is interesting to note that the Tokai whiskers are partly embedded in a Si-rich Y-containing secondary glassy phase (Fig. 1a), while no amorphous grain boundary phase was observed adjacent to AMI whiskers. The majority of the AMI reinforcements exhibited small impurities and/or cavities near the core regions as reported elsewhere[12,13] for rice-hull derived SiC whiskers and numerous stacking faults perpendicular to the whisker axis, indicated by typical contrast bands in the bright field images or intensive streaking in the corresponding diffraction pattern. No discrete SiC-polytype could be identified. Moreover, it is shown that some of the AMI reinforcements did not preserve morphological integrity during powder processing (see arrows in Fig. 1b), which indicates that less severe processing techniques like slip casting are required to reduce whisker damage during composite synthesis.

In general the carbon coatings in composite materials C and E are homogeneous with a varying thickness of 100-200 nm for Tokai whiskers and 25-50 nm for AMI reinforcements, respectively, as shown in Fig. 2. However, a continuous carbon coating is not present on all whiskers and peeled-off coatings forming an increased number of carbon clusters in the composites were observed. These results indicate again the problematic nature of processing and demonstrate that the carbon coatings 'survive' the processing route. Most coatings reveal a layered structure and can be compared to stress-graphitized films observed by Yamamoto et al[14] in a spinel matrix composite when carbon coated Tokai SiC whiskers were used.
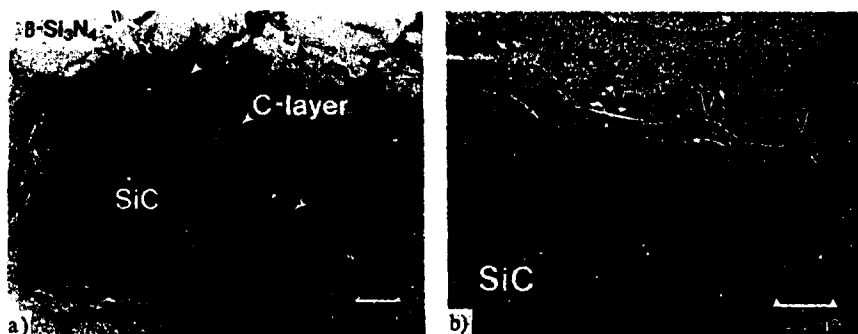
Fig. 2   Bright field images of carbon coated SiC whiskers; a) Tokai, b) AMI whisker in Si_3N_4 based composites.

- Interfacial characterization

Mechanical properties of ceramic components are strongly affected by grain boundary and interfacial characteristics. The composite toughness is expected to be critically dependant on the chemical and microstructural properties of the whisker/matrix interface. Residual strain due to different thermal expansion coefficients of matrix and reinforcement are detrimental to fracture resistance.[7] The structure of the interface will control debonding, crack branching and pull-out mechanisms for toughness enhancement.

Fig. 3a depicts the overall feature found in the silicon nitride matrix of the composites. A thin amorphous grain boundary film covers the silicon nitride particles intersecting at triple point junctions. The presence of a silicon oxynitride amorphous film along grain boundaries is well established for large angle boundaries in Si_3N_4 materials.[15,16] No crystalline secondary phases were observed in any of the composites investigated. EDS analysis at triple points showed a Y-containing Si-rich secondary phase, while additional PEELS data exhibited a high amount of oxygen, but only a minor quantity of nitrogen. No carbon was detected in any of the analyzed secondary glassy phase regions. As the interfacial structure and chemical composition of the matrix material in all composites show only negligible variations, it can be concluded that deviations in fracture resistance are closely related to differences in the Si_3N_4/SiC whisker interface.

Focussing on materials containing carbon coated reinforcements (Fig. 3b), it can be assumed that above a specific carbon-film thickness, which is below the observed thickness of 50-200 nm, a carbon coating has certain advantages regarding fracture toughness. The step-like nature of the whisker surface ({111} growth facets on close-packed planes) and the generally rough morphology of the reinforcement is reduced. Moreover, the propagating crack front will run along the whisker/matrix interface, because the graphitized carbon coating with its laminar structure parallel to the whisker axis will debond easily (weak interfacial bonding). Both reduced roughness and increased debond length contribute to an increase in fracture resistance of the composite. On the other hand, a random orientation of the reinforcements will reduce this effect, because the quantity of whiskers perpendicular to the crack plane is greatly reduced. Recent work has shown that maximum toughness occurs when whiskers are perpendicular to the crack plane.[17] Subsequent results demonstrated that the quantity of whiskers perpendicular to the crack plane is very sensitive to the bulk whisker orientation produced during processing.[18,20] Therefore, a significant increase in fracture toughness between composites with coated and uncoated whiskers was not to be expected (compare Table 1). Hence, material B (uncoated Tokai whiskers) with a continous glassy phase layer along the whisker/matrix interface (see Fig. 3c) shows only a minor deviation in fracture resistance compared to that of a material with carbon coated reinforcements.
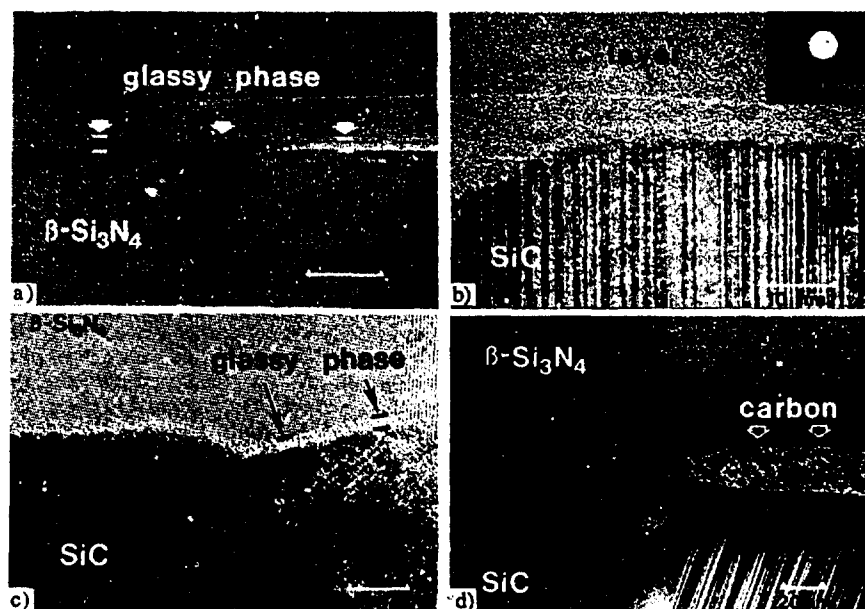
Fig. 3   HREM images; a) amorphous phase along Si_3N_4 grains, b) SiC/C-coating interface, and Si_3N_4/SiC whisker interface with c) uncoated Tokai, d) uncoated AMI whisker.

In contrast to the composites discussed above, an inhomogeneous interface structure is present in material D (see Fig. 3d). Areas with graphitized carbon layers in the form of a thin interfacial film adjacent to interface regions without any amorphous glassy phase were observed. Surface composition measurements via Auger analysis of as-received AMI whiskers shown in Tab. 2 confirm the TEM observations. The surface composition of the whiskers varies from whisker to whisker. On some surfaces additional Ca- and Cl-impurities were detected. Moreover, one of the AMI whiskers with a carbon-rich surface area was sputtered for about two minutes with only minor changes in composition. This indicates that the as received AMI whiskers exhibit an inhomogeneous surface chemistry and local carbon enrichments, respectively. Considering

Tab. 2   Auger analysis of as received AMI whisker surfaces

Whisker	Si [at.%]	O [at.%]	C [at.%]
1	11.1	54.9	33.9
2	28.8	13.8	57.4
3	30.4	34.4	35.2

HREM results and Auger analysis the formation of a non-uniform interface can be understood, but the question remains, why no amorphous secondary phase is present adjacent to the whisker. Both the formation of a continuous amorphous glassy phase as well as no amorphous interface film present along the whisker/matrix interface has been reported.[7,13,19] Assuming a silica-rich liquid film is formed along the whisker/matrix interface during densification, local carbon enrichments may promote the following reactions:

$$SiO_2 + C \rightarrow SiO + CO \quad (1) \quad \text{and} \quad SiC + 2\,SiO_2 \rightarrow 3\,SiO + CO \quad (2)$$
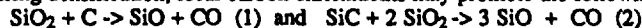
Thus, removing the SiO_2 constituents via CO or SiO vapor phase reactions in the early stage of composite densification when there is remaining open porosity. Therefore, the glassy phase formation along the whisker/matrix interface can be reduced and/or suppressed. Varying thickness of the carbon layer on the as-received whiskers leads to carbon and glassy phase free areas adjacent to residual graphitized layers depicted in Fig. 3d. Furthermore, with respect to fracture resistance, debonding will occur along the

interface where the whisker surface is covered with residual carbon. When the crack propagates and intersects the area where Si_3N_4 and SiC are directly bonded together the crack will kink into the whisker. Therefore, the rather low fracture resistance of material D, compared to the composites discussed earlier, can be related to the formation of a non-uniform interfacial structure due to the surface chemistry of the whisker starting material.

SUMMARY

This investigation characterized Si_3N_4 based SiC whisker reinforced composites. A homogeneous amorphous interfacial film was typically present along Si_3N_4 grains of the matrix for all composites. A uniform interface film was observed at the whisker/matrix interface for carbon coated and uncoated Tokai SiC whisker reinforced and carbon coated AMI SiC whisker reinforced composites. No significant difference in fracture toughness was measured for these composites. This is consistent with the low quantity of reinforcement perpendicular to the crack plane in these materials due to their random whisker orientation. An inhomogeneous interfacial structure formed in the carbon coated AMI whisker containing composite can be related to marked variations in whisker surface chemistry limiting fracture resistance. In this case it is the lowest toughness composite.

ACKNOWLEDGEMENTS

REFERENCES

1. K.T. Faber, A.G. Evans, Acta Metall. 31 565 (1933).
2. G.C. Wei, P.F. Becher, Am. Ceram. Soc. Bull 64 298 (1985).
3. M. Rühle, B.J. Dalgleish, A.G. Evans, Scripta Met. 21 689 (1987).
4. P.D. Shalek, J.J. Petrovic, G.F. Hurley, F. Gac, Am. Ceram. Soc. Bull. 65 351 (1986).
5. J.R. Porter, F.F. Lange, A.H. Chokshi, Mat. Res. Soc. Symp. Proc. 78 289 (1987).
6. T.N. Tiegs, P.F. Becher, L.A. Harris, ORNL Report #CONF-86-0714-3 (1986).
7. G. Campbell, M. Rühle, B. Dalgleish, A.G. Evans, subm. to J. Am. Ceram. Soc. (1989).
8. MIC-STD-1942 (MR), Department of Army, Nov. (1983).
9. P. Chantikul G. Anstis, B. Lawn, D.B. Marshall, J. Am. Ceram. Soc. 64 539 (1981).
10. I.A. Salem, I.L. Shannon Jr., J. Mater. Sci. 22 321 (1987).
11. M. Yamamoto, US Patent 4 500 504 (1985).
12. S. R. Nutt, J. Am. Ceram. Soc. 71 149 (1988).
13. V.K. Sarin, M. Rühle, Composites 18 129 (1987).
14. M. Yamamoto, T. Kida, K. Sugihara, in: Proc. of Int. Conf. on "Whisker and Fiber Toughened Ceramics", publ. by ASM Int., Oak Ridge, TN., June (1988).
15. D.R. Clarke, Ultramicroscopy 4 33 (1979).
16. H. Schmidt, M. Rühle, J. Mater. Sci. 19 615 (1984).
17. C.A. Willkens, N.D. Corbin, V.K. Pujari, R.L. Yeckley, M.I. Mangaudis, in Cer. Eng. and Sci. Proc., Vol. 9, 9/10, 1362 (1988).
18. N.D. Corbin, C.A. Willkens, V.K. Pujari, R.L. Yeckley, M.I. Mangaudis, in Proc. of Int. Conf. on "Whisker and Fiber Toughened Ceramics", publ. by ASM Int., Oak Ridge, June (1988).
19. W. Braue, R.W. Carpenter, D.J. Smith, submitted to J. Mater. Sci. (1989).
20. N.D. Corbin, C.A. Willkens, C.L. Chong, J.L. Hammarstrom, J.S. Hansen, U.K. Pujari, G.A. Rossi, K.N. Siebein; in Proc. of 26th Automotive Technology Development Contractor's Coordination Meeting, publ. by SAE, Dearborn, MI, 235 (1988).

FIBRE-MATRIX REACTION ZONES IN MODEL SILICON CARBIDE-TITANIUM ALUMINIDE METAL-MATRIX COMPOSITES

D.R.Baker*, P.J.Doorbar**, and M.H.Loretto***. *School of Metallurgy and Materials Science, University of Birmingham, Birmingham B15 2TT, UK, **Manufacturing Technology, Rolls-Royce plc, Derby DE2 8BJ, UK, *** IRC in Materials for High Performance Applications, University of Birmingham, Birmingham B15 2TT, UK.

ABSTRACT

The reactions between coated SiC continuous fibres and TiAl, Ti3Al, or Ti3Al + β matrices, have been investigated using optical metallography, scanning electron microscopy (SEM), and transmission electron microscopy (TEM), with chemical information obtained by energy dispersive x-ray analysis (EDX) and electron energy loss spectroscopy (EELS).

Similar sequences of phases were found in all the composites; carbides based on TiC and Ti_xAlC (x=2,3) and titanium silicides based on Ti_5Si_3 forming in narrow bands outside of the complex carbides. The occurrence of individual phases can be related to published phase diagram information. However, the sequences in which the reaction products occur within the reaction zones cannot be fully rationalised from the present results.

INTRODUCTION

Titanium aluminide metal matrix composites are being evaluated for possible high temperature aerospace applications. As part of this process, it is necessary to understand the reactions between the reinforcements (fibres, whiskers, or particles) and the matrices. The reaction products are believed to control or influence the mechanical properties of the composites[1].

This paper describes the results of investigations into the nature and extent of the reaction between coated SiC fibres, and three different titanium aluminide matrices -TiAl (γ - $tP4$), Ti3Al (α_2 - $hP8$), and α_2 + bcc solid solution (β - $cI2$).

EXPERIMENTAL

Sectioned as-cast Ti - 50at%Al, Ti - 25at%Al, and Ti - 24at%Al - 11at%Nb button melts supplied by IMI Titanium Ltd., were used to sandwich single layers of AVCO SCS-6 SiC fibres in a series of test specimens prepared by Rolls-Royce. Impurity levels (O,N)

in the as-cast material were <0.2 wt%. The composites were hot isostatically pressed for 2h at 1100°C and 103.4MPa. Optical, SEM, and TEM specimens were prepared from the composites. Qualitative and semi-quantitative EDX and EELS analyses were obtained from thin foils. Selected area and convergent beam electron diffraction (SAD and CBED) were used to determine crystal structures and lattice constants. The composites were identified as MT1149 (50Al), MT1150 (25Al), and MT1151 (24Al-11Nb).

RESULTS

Optical and SEM results revealed some evidence of cracking between closely spaced fibres but generally diffusion bonding was considered satisfactory since grain growth was seen across the bond line. β - depleted regions, adjacent to fibres, were present in the 24-11 matrix composite.

Extensive radial cracking in the fibre-matrix reaction zones and adjacent matrix was observed in all the composites. Cracks in the matrix had propogated only to the outer limit of the β - depleted regions in the Ti-24Al-11Nb matrix composite.

A TEM secondary electron image of a Ti-50Al matrix composite reaction zone (RZ) is shown in Fig.1. It is possible to distinguish between three separate regions. These regions correspond to phases which were identified using EDX/EELS and diffraction information. The innermost phase had an EDX spectrum which showed only Ti K peaks. Ring patterns from this fine grained region, however, could be indexed as cubic with $a = 0.43\pm0.01$nm. This is close to the lattice parameter of stoichiometric TiC. The middle phase was Al-rich and had an EDX-based composition of Ti-33Al. The presence of C was suggested by the asymmetry in the Ti L UTW-EDX peak and from EELS. SAD information suggested an ordered hexagonal structure consistent with lattice parameters $a = 0.30\pm0.01$nm and $c = 1.36\pm0.01$nm. This phase was identified as Ti_3AlC.

The outer phase was Si-rich with an EDX-based composition of Ti-39Si (+Al). SAD analysis revealed an ordered hexagonal structure with $a = 0.75\pm0.01$nm and $c = 0.52\pm0.01$nm. On this basis the phase was identified as Ti_5Si_3 (+Al).

It was also observed that Al enrichment of the matrix adjacent to the outer silicide phase had occurred. The enrichment of ~10% fell to near the nominal matrix value over a distance of ~30μm from the outer silicide layer (Fig.2).

The Ti-25Al matrix composite RZ appeared very similar to that of the Ti-50Al composite. The inner and outer RZ phases were again based on TiC_{1-x} and Ti_5Si_3 respectively, but the middle (and most extensive) phase had an ordered cubic structure with $a = 0.40\pm0.02$nm. The approximate EDX composition was Ti-21Al-1Si and it is likely that the

Figure 1. Secondary electron image of TiAl - SiC composite
reaction zone. The Al content of the matrix between 'A' and 'B'
varied as shown in Fig.2.
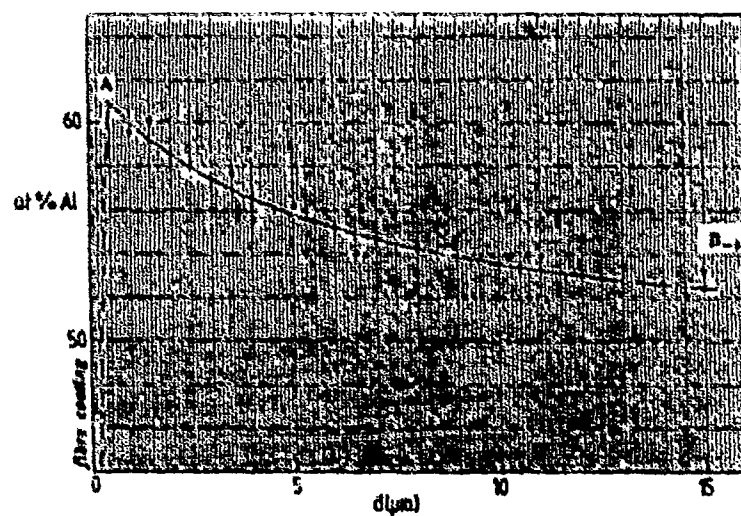
Fig.2 EDX result showing Al enrichment of the matrix adjacent to
the fibre-matrix reaction zone in the TiAl matrix composite
(between points 'A' and 'B' in Fig.1).

phase corresponded to Ti_3AlC (see phase diagram Fig.3) with dissolved Si although the presence of C could not be confirmed directly due to the reluctance of the phase to thin sufficiently during ion beam milling. No significant Al enrichment of the matrix outside the RZ was found.

The Ti-24Al-11Nb matrix composite had a complex RZ with five distinguishable phases. The inner two phases were based on TiC_{1-x} and $(TiNb)C_{1-x}$ and the outer phase was identified as $(TiNb)_5(AlSi)_3$ in a single grain thick band. The most extensive phase was a $(TiNb)_3AlC$ layer between the $(TiNb)C_{1-x}$ and the outer silicide. There was also a narrow (one grain thick) phase with EDX-based composition Ti-12Nb-12Si-11Al between the $(TiNb)C_{1-x}$ and $(TiNb)_3AlC$, which could not be identified from the limited diffraction information available. Further work is needed to identify this phase.

In all of the composites, $1 - 2\mu m$ of the outer C-rich fibre coating remained unreacted - often during TEM specimen preparation the fibre separated from the matrix by cracking through this coating rather than through the RZ itself. In each specimen the presence of Ti in the fibre adjacent to the RZ, and of Si in the matrix beyond the RZ, was detected by EDX.

The results are summarised in Fig 4.

DISCUSSION

The most obvious features of the fibre-matrix reactions are that at $1100°C$ processing the RZ widths are extensive and that several phases form as reaction products in well-defined bands within the RZ. The amount of retained C-rich fibre coating suggests that the RZ grows both towards and away from the fibre (i.e. on two fronts).

The sequences of RZ phases for the different composites were similar. In all cases the innermost phase was based on TiC_{1-x} sometimes with Nb substituting, presumably, for the Ti. Further out the complex carbides of the type $(TiNb)_xAlC$ (x=2,3) dominate the RZs. The sequence of phase formation is difficult to deduce from the present results although the presence of Ti in the fibres and the presence of Si in the matrix outside of the RZs confirms the inwards diffusion of Ti and the outwards diffusion of Si.

In the 24-11 matrix composite, it is possible that the initial reaction between Ti_3Al and C - rich SiC is to produce TiC_{1-x}. The Si which does not participate in this phase may diffuse through the TiC_{1-x} to the outer RZ/matrix boundary. Continued diffusion of Ti from the matrix, through the TiC_{1-x}, and into the fibre, could allow continued growth of TiC_{1-x}. The formation of Ti_3AlC could result from the diffusion of excess C from the fibre into
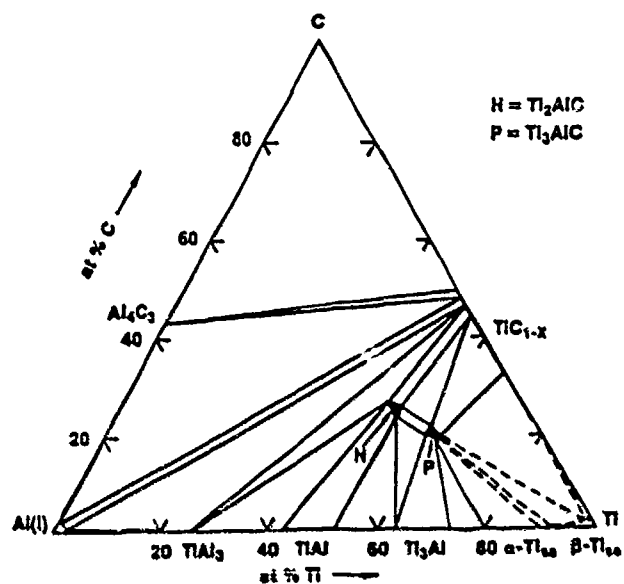
Fig.3 Ti-Al-C 1000°C ternary isotherm. (Schuster et al.)[2]
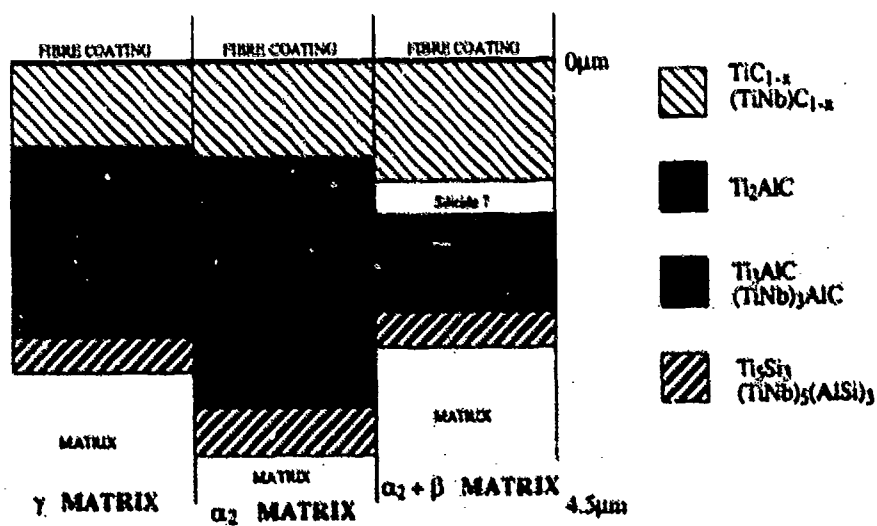
Figure 4. Summary of reaction zone phases.

the matrix - it is likely that the diffusivity of C in TiC_{1-x} is much higher than that of Ti [3]. In this case, the silicon (or silicide) present at the outer RZ would form a moving front as the Ti_3AlC continued to grow. Eventually precipitation of a silicide (with dissolved Al) could occur at the outer RZ edge. The presence of excess Al in the matrix could cause the formation of a β - depleted zone as observed. In the case of the TiAl matrix composite, the presence of Ti_2AlC in the RZ requires a much greater rejection of Al into the matrix as observed. The present results for the $Ti_3Al + \beta$ matrix composite are not entirely consistent with those of Baumann et al.[4] in so far as no microporosity was observed in this investigation nor could the presence of an inner Ti_5Si_3 phase between the carbide and complex carbide be confirmed.

The full elucidation of the reactions in these systems requires continued investigation via thermal processing experiments.

REFERENCES

1. P.Soumelidis, J.M.Quenisset, R.Naslain, N.S.Stoloff, J. Mat. Sci. 21 895 (1986)
2. J.C.Schuster, H.Nowotny, C.Vacarro, J. Sol. Stat. Chem. 32 213 (1980)
3. F.J.J. van Loo, G.F.Bastin, Met. Trans. 20A 403 (1987)
4. S.F.Baumann, P.K.Brindley, S.D.Smith, Proc. TMS Fall Meeting (1988)

ACKNOWLEDGEMENTS

THE STUDY OF THE DISLOCATION STRUCTURE AND ENERGY OF NiO-Pt INTERFACES

F.-S. SHIEU and S. L. SASS
Department of Materials Science and Engineering, Cornell University, Ithaca, NY 14853-1501

ABSTRACT

The dislocation structure of Pt-(001)NiO interfaces was studied using electron microscopy and electron diffraction techniques. Specimens were produced by hot pressing polycrystalline Pt films on to thin NiO single crystals, and bulk Pt single crystals on to bulk NiO single crystals. The polycrystalline Pt specimens were used to determine the favored orientation relationships between the NiO and Pt, while the bulk NiO-Pt specimens were used to study the detailed structure of the interface. Three categories of orientation relationships were identified: exact epitaxy with $(001)_{Pt} \parallel (001)_{NiO}$, $[110]_{Pt} \parallel [110]_{NiO}$; small rotations away from exact epitaxy about the common [001] direction; high index planes of Pt parallel to (001) of NiO. Theoretical calculations of the expected dislocation structures of interfaces with the first two orientation relationships were made using a Bollmann-type analysis. The experimental observations and theoretical predictions were shown to be in good agreement. The energies of the interfaces having the first two orientation relationships were shown to be similar which is believed to be the reason why they both occur.

INTRODUCTION

The importance of metal-ceramic systems comes from their applications in technology, for example, in electronic packaging, coatings and composites. For composite materials, the interface is a necessary link between the matrix and the reinforcement to accomplish load transfer as well as a site of dislocation generation. An understanding of the structure of metal-ceramic interfaces, and its relationship to mechanical, thermal and electrical properties, is, therefore, of both scientific and technological interest.

Although interactions at metal-ceramic interfaces can be quite complicated, in general the bonding can be classified into two categories: "reactive" where compounds are formed, and "non-reactive" where compounds are not formed. The latter case is the simplest to consider since it involves only physical interactions between atoms or ions. It must be realized that some systems may fit into either category depending upon the equilibrium state of the species, which is determined by whether the atmosphere is oxidizing or reducing, or the presence of compounds in the phase diagram.

Three questions are of interest with respect to metal-ceramic interfaces where compounds are not present.

(1) What kinds of orientation relationships and interface planes between metals and ceramics are favored, i.e. have low energy?

(2) What are the structures of these interfaces?

(3) Why do the favored structures have lower energy?

In order to answer these questions, experiments were performed on NiO-Pt interfaces which are in the "non-reactive" class and were produced by hot pressing polycrystalline Pt thin films on to thin NiO single crystals, and bulk Pt single crystals on to bulk NiO single crystals. To examine only those interfaces with relatively high bond strength, advantage was taken of the experimental observation that the chemical etching used to dissolve the MgO from the specimen and the ion thinning used to produce the electron microscope specimens, both eliminate weak interfaces. The structure and crystallographic orientations of the interfaces that survived the preparation procedure were studied by transmission electron microscopy and the observations were compared to predictions from an analysis based on Bollmann's O-lattice theory [1]. In addition, the energy of interfaces was examined and correlated to the bonding strength.

EXPERIMENTAL PROCEDURE

Thin single crystals of NiO were produced by the thermal decomposition of $NiBr_2$, following the method of Cech and Alessandrini [2]. The reaction

$$NiBr_2 + H_2O \longrightarrow NiO + 2HBr \qquad (1)$$

is catalyzed on a MgO surface in an atmosphere of water vapor. The Pt with a thickness of ~70 nm was produced in the form of thin films by sputtering on to freshly cleaved MgO. Bulk single crystals of Pt obtained by growing from the melt were mechanically polished to flat {001} surfaces. The bulk NiO single crystals were grown by the Verneuil process in an arc image furnace at Argonne National Laboratory.

The metal-ceramic interface was formed by hot pressing together in air the NiO and Pt films, still mounted on their substrates, at a temperature of $1200°C$ for between 2 and 8 hours. The MgO was dissolved in a 15% H_2SO_4-H_2O solution at a temperature of $70°C$, leaving the Pt and NiO bilayer with a typical thickness of 20 μm. The dissolution process occasionally resulted in separation of the Pt film from the NiO crystal. During the hot pressing procedure Mg^{++} ions dissolve in the NiO, and most likely a NiO-MgO solid solution is present.

The thin polycrystalline Pt-single crystal NiO specimens were used to determine the orientation relationships of those interfaces which are relatively strong. In order to study the dislocation structure of interfaces with special orientation relationships, bicrystals were produced by hot pressing together macroscopic NiO and Pt single crystals using conditions similar to those applied to the thin crystals. Details of the experimental procedure are addressed in reference [3].

EXPERIMENTAL RESULTS

After ion thinning of the polycrystalline Pt-NiO sandwich, typically only a few patches of Pt are left on the NiO single crystal. Selected area diffraction (SAD) was used to determine the orientation relationships that existed between the two crystals. Table 1 lists the observed orientation relationships which were divided into three categories. Category I involves exact matching of crystallographic planes and directions in both crystals, and is termed the exact epitaxial orientation. Category II is similar to I, but with deviations away from exact matching consisting of small rotations about the common [001] axis, and is termed a twist-misfit orientation. Category III involves the matching of different crystallographic planes in the Pt to the (001) plane in the NiO.

Table 1. The experimentally observed orientation relationships.

I	$(001)_{Pt} \parallel (001)_{NiO}$	$[110]_{Pt} \parallel [110]_{NiO}$
II	$(001)_{Pt} \parallel (001)_{NiO}$	Rotation about [001] of NiO by $0.5° \sim 3°$ away from category I orientation
III	$(\bar{1}23)_{Pt} \parallel (001)_{NiO}$	$[210]_{Pt}$ 12° away from $[\bar{1}\bar{1}0]_{NiO}$
	$(\bar{1}14)_{Pt} \parallel (001)_{NiO}$	$[110]_{Pt}$ 8° away from $[100]_{NiO}$

Fig. 1(a) shows a SAD pattern for Category I. Near the exact (001) pole, the diffraction pattern contains very strong double diffraction effects in the form of square arrays of satellite reflections around matrix reflections. In order to minimize the influence of the double diffraction reflections on the image, which would result in interference fringes, it was necessary to tilt the specimen slightly away from the orientation in Fig. 1(a) until the satellites disappeared. Fig. 1(b) is a bright field (BF) image taken under these conditions and shows the presence of a square dislocation network. The dislocations have line directions along <110> of the NiO and Pt, with a spacing between the dislocations, $S_D = 5.2 \pm 0.5$nm. Moire fringes with spacing of $S_D/\sqrt{2}$ are also observed along <100> directions. Based on the f.c.c. space lattice of NiO and Pt, the Burgers vector, b, of the misfit dislocations is expected to be a/2<110>. The expected misfit dislocation spacing was determined to be 4.6 nm, using either the well known relationship, $S_D = |b|/\alpha$, where α is the magnitude of the fractional misfit based on the NiO and Pt lattice parameters, or the O-
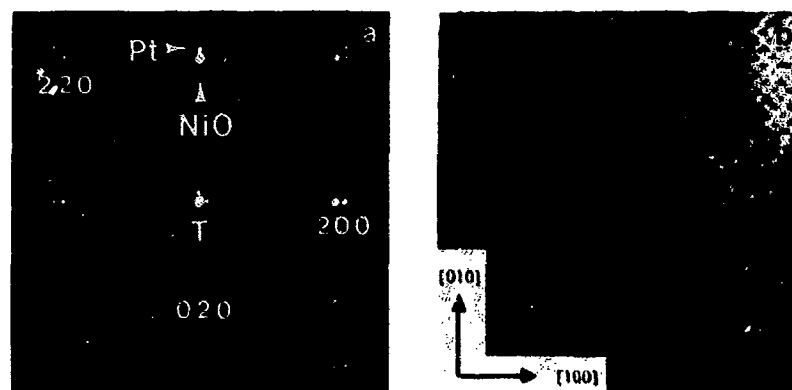
Fig. 1 Observations on a NiO-Pt interface. (a) Selected area diffraction pattern showing the $(001)_{Pt} \| (001)_{NiO}$; $[110]_{Pt} \| [110]_{NiO}$ orientation relationship. (b) Bright field image taken with a small tilt in orientation away from that in (a).

lattice theory discussed in the next section. Since both the experimental dislocation line direction and spacing are in reasonable agreement with prediction, the dislocations in Fig. 1(b) are believed to be misfit type.

The structure of the interfaces showing the Category II orientation relationship was studied in detail using specimens produced by hot pressing macroscopic NiO and Pt single crystals. Examination of the boundary oriented 30° away edge-on in Fig. 2(a), shows periodic diffraction contrast with a spacing of 3.0nm. In order to confirm that there is a periodic boundary structure present, diffraction patterns were taken from the boundary in Fig. 2(a), using a well defocussed second condenser lens. Fig. 2(b) shows enlarged portions of the 200 and 400 regions, and the extra reflections indicated by the arrows demonstrate that a periodic structure is present in the boundary. The position of the reflections relative to the matrix reflection is consistent with the observed periodic dislocation structure in the interface.

Fig. 2. Observations on a NiO-Pt interface which deviates from the exact (001) epitaxial orientation relationship by a rotation of 3° about the [001] axis. (a) Dark field image of the interface in (a) which is tilted ~30° away from edge-on. (b) Selected area diffraction pattern from the boundary in (b) with enlarged portions of the 200 and 400 regions.

THEORETICAL CALCULATIONS

According to Bollmann [1] the structure of a crystal interface is determined by two sets of parameters. The first set is related to the crystal structures and the relative orientation of the two crystals, and following Bollmann's analysis these determine the O-lattice that is present. The second set of parameters is given by the path of the boundary, i.e. the boundary plane. The intersections of the boundary plane with the O-lattice cell walls, i.e. the Wigner-Seitz cell, are dislocations, with the translation vector attributed to the respective cell wall being their Burgers vector. Any transformation which relates the position vectors in the two crystal spaces can be represented by a sequence of transformation matrices.

This paper is mainly concerned with the structure of Pt -NiO (001) interfaces. Therefore, the O-lattice construction which is used to predict the dislocation structure can be done in two dimensions, instead of the three dimensional construction usually needed for a general interface (see reference [3] for the more complete analysis). The transformation matrix which relates the position vectors in Pt and NiO can be represented by the product of two matrices. One is an expansion-contraction matrix, which can be written as:

$$E = \begin{pmatrix} 1+\alpha & 0 \\ 0 & 1+\alpha \end{pmatrix} \tag{2}$$

where α is the fractional lattice parameter mismatch between Pt and NiO,

$$\alpha = \frac{(a_{Pt} - a_{NiO})}{a_{NiO}} \tag{3}$$

and a_{Pt} = lattice constant of Pt; a_{NiO} = lattice constant of NiO.

The other matrix describes the rotation about the [001] axis through an angle θ, and has the form

$$R = \begin{pmatrix} \cos\theta & -\sin\theta \\ \sin\theta & \cos\theta \end{pmatrix} \tag{4}$$

The resultant transformation matrix, A, is

$$A = R\,E = \begin{pmatrix} \cos\theta & -\sin\theta \\ \sin\theta & \cos\theta \end{pmatrix} \begin{pmatrix} 1+\alpha & 0 \\ 0 & 1+\alpha \end{pmatrix} = \begin{pmatrix} (1+\alpha)\cos\theta & -(1+\alpha)\sin\theta \\ (1+\alpha)\sin\theta & (1+\alpha)\cos\theta \end{pmatrix} \tag{5}$$

If the Burgers vector is of the type a/2 <110> in the interface plane, and is represented in two dimensions as

$$b = \begin{pmatrix} \frac{1}{2} & \frac{-1}{2} \\ \frac{1}{2} & \frac{1}{2} \end{pmatrix} \tag{6}$$

the O-lattice, taking the NiO unit cell basis vectors as reference, then becomes

$$X^{(o)} = (I-A^{-1})^{-1}b = \begin{pmatrix} \dfrac{1+\alpha\cdot\cos\theta+\sin\theta}{2((1+\alpha)^2-2(1+\alpha)\cos\theta+1)} & \dfrac{-1-\alpha+\cos\theta+\sin\theta}{2((1+\alpha)^2-2(1+\alpha)\cos\theta+1)} \\[4mm] \dfrac{1+\alpha\cdot\cos\theta-\sin\theta}{2((1+\alpha)^2-2(1+\alpha)\cos\theta+1)} & \dfrac{1+\alpha\cdot\cos\theta+\sin\theta}{2((1+\alpha)^2-2(1+\alpha)\cos\theta+1)} \end{pmatrix} \tag{7}$$

which is a square "lattice". The two primitive vectors of the O-lattice are orthogonal independent of rotation angle θ. The dislocation structure can now be obtained by drawing the two dimensional Wigner-Seitz cell about each O-lattice point, which gives a square network. The dislocation spacing is equal to the shortest distance between O-lattice points, i.e. the length of the column matrices of $X^{(o)}$, and is

$$S_D = \frac{a_{Pt}\, a_{NiO}}{\sqrt{2(a_{Pt}^2 + a_{NiO}^2 - 2a_{Pt}a_{NiO}\cos\theta)}} \qquad (8)$$

Based on the above calculations, the plot of S_D vs θ in Fig. 3(a) is obtained, and it is seen that S_D decreases rapidly with increasing θ. The dislocation character can be obtained by considering the angle σ between the Burgers vector and the dislocation line. Taking the inner product, σ is found to be

$$\sigma = \frac{\pi}{2} - \tan^{-1}\left(\frac{a_{NiO}\sin\theta}{a_{NiO}\cos\theta - a_{Pt}}\right) \qquad (9)$$

The variation of σ with θ is given in Fig. 3(b). Starting with the exact epitaxial orientation ($\sigma = 90°$), the change of σ with θ is initially very rapid, and then σ slowly approaches the value of σ_0, where σ_0 depends on the difference in lattice parameters and the choice of reference axes. In other words, the dislocation network changes from pure edge towards more screw-type as θ increases.

Jesser and Kuhlmann-Wilsdorf [4] treated the same problem, but from a different approach, and obtained similar expressions for S_D and σ except for a different choice of reference axes. Hwang, Laughlin, and Bernstein [5] first demonstrated the validity of the approach of Jesser and Kuhlmann-Wilsdorf in their study of the dislocation structure of metal-metal phase boundaries.
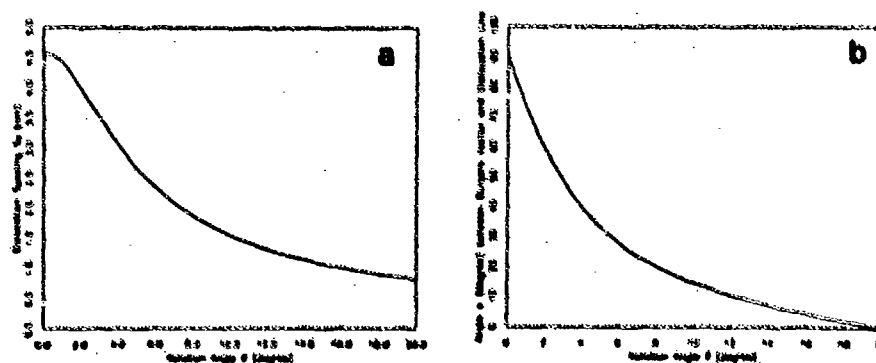

Fig. 3.The dependence of (a) S_D, the dislocation spacing, and (b) σ, the angle between the dislocation line and Burgers vector, on θ, the twist angle in a twist-misfit interface.

DISCUSSION

For an interphase interface, misfit dislocations are needed to accommodate the difference in lattice parameters. By substituting the lattice parameter of Pt, 0.3924nm and NiO, 0.4177nm, into eq. (8) for the exact (001) epitaxial orientation, i.e. $\theta = 0°$, the ideal dislocation spacing S_D was calculated to be 4.6nm, which is the period in the <110> direction to accommodate the lattice mismatch between Pt and NiO. The Burgers vectors and dislocation lines are along orthogonal <110> directions. All the misfit dislocations are expected to be pure edge-type, i.e. with Burgers vector perpendicular to the dislocation line. The measured dislocation spacing from Fig. 1(b) for the exact (001) epitaxial orientation is 5.2nm, which is slightly larger than the theoretical value. Mader [6], in his studies of Nb/Al$_2$O$_3$ interfaces formed by internal oxidation, found that the observed misfit dislocation spacing was 16-20% larger than predicted. It is believed that the elastic strain in the thin Pt layer may play an important role in determining the dislocation spacing in the interface.

Deviation from the (001) epitaxial orientation by a rotation about [001] is observed to decrease the dislocation spacing, while still maintaining the square network. From Figs. 3(a) and (b), it is seen that a rotation of 3° is expected to give a dislocation spacing of 3.5nm, while the angle between the dislocation line and <110> direction is expected to be 39°. That is, the dislocations should now be almost parallel to the <100> direction of NiO. Fig. 2(b) shows that the visible set of dislocations for such a boundary is approximately parallel to the [010] direction, and the dislocation spacing is 3.0nm; both observations are in reasonable agreement with the theoretical predictions.

Further information on the dislocation structure that is present comes from the diffraction pattern. According to Balluffi, Sass and Schober [7], a periodic structure in the grain boundary gives extra spots in the diffraction pattern. The square network in a twist-misfit boundary is expected, therefore, to show extra spots corresponding to the periodic structure. Fig. 4 shows a schematic diffraction pattern for the case when the electron beam is perpendicular to the interface plane. Each matrix reflection is surrounded by an array of extra reflections some of which are related to the periodic dislocation network. Possible sites for double diffraction are indicated by open circles, while reflections from the periodic dislocation network are indicated by small solid circles. Taking specimen tilt into account the agreement between the prediction in Fig. 4 and the appearance of the $\bar{4}00$ region in Fig. 2(b) is good. A detailed analysis of the observations in Fig. 2(b) also shows that the dislocation lines are not exactly along the [100] direction, which agrees with the prediction that they should be rotated ~6° away from this direction. As the dislocation spacing gets smaller, the electron diffraction pattern becomes a useful source of information on the periodic structure of the interface.

The experimental results of this study indicate that interfaces with the category II relationship can co-exist with the category I relationship even under severe testing conditions, suggesting that they have similar energy. In order to understand this result, it is of interest to examine the energy of the interface for the two cases.

The boundary between two crystals with the same crystal structure but different lattice parameters was treated in one dimension by Frank and van der Merwe [8] by employing the sinusoidal potential field introduced by Peierls [9] and Nabarro [10]. Van der Merwe [11] then extended this model to three dimensions, and calculated the stresses and energy for the boundary between crystals with the same structure and different lattice parameters. Van der Merwe [12] also discussed the structure and energy of the twist-misfit boundary in terms of the superposition of pure misfit dislocations and screw dislocations which are needed to accommodate the twist component. The energy of the interface based on this model was thought to increase rapidly as the twist component increased.

The energy of a twist-misfit boundary was calculated by Jesser and Kuhlmann-Wilsdorf [4] by applying the dislocation model based on their geometrical analysis. Instead of superimposing two sets of dislocation networks with pure edge and pure screw character as Van der Merwe suggested, the dislocation structure of the twist-misfit boundary was considered as a square dislocation network with mixed-type Burgers vector. The interfacial energy, E_i, is the sum of the dislocation network energy, E_d, and a constant energy, E_o, which depends on the bonding energy between the two crystals and the surface energy of the two crystals, and is independent of misfit or misorientation. The energy, E_d, due to the edge and screw components of the mixed-type Burgers
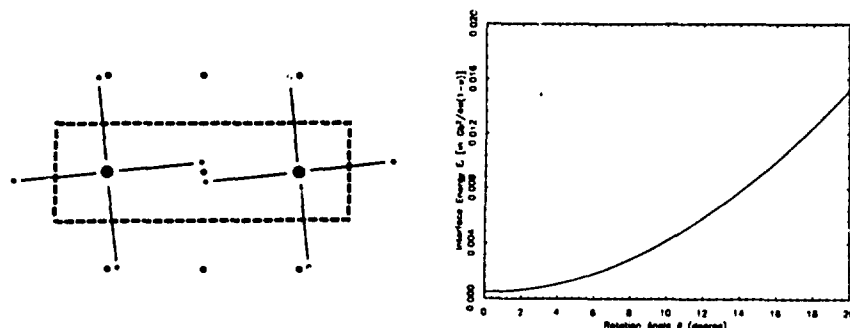
Fig. 4. A schematic diffraction pattern of the region in the vicinity of the $\bar{4}00$ reflections for the twist-misfit boundary with rotation of 3°, viewed at normal incidence. Matrix reflections represented by large solid circles, are surrounded by a square array of small solid circles corresponding to the periodic dislocation network. Possible sites for double diffraction reflections are indicated by open circles.

Fig. 5. The dependence of E_i, the interfacial energy, on θ for twist-misfit interfaces.

vector was taken from the result of van der Merwe [12], which involved a very complex formula for the calculation of boundary energy.

An even simpler and more straightforward method to calculate the energy of the interface, i.e. the energy of the dislocation network, which basically follows the idea of Jesser and Kuhlmann-Wilsdorf [4], is to multiply the dislocation density, which is proportional to the area density of the O-lattice and can be obtained from eq. (8), with the strain energy [13] associated with each dislocation. This calculation gives a similar result to that obtained by Jesser and Kuhlmann-Wilsdorf [4] which was a slowly varying minimum in energy centered around the exact epitaxy orientation. A plot of Ei vs θ is given in Fig. 5. The interface energy increases very slow with θ at first, since the energy increase due to the increase in the dislocation density is compensated by the reduction in energy when the dislocations alter their character from pure edge to mixed type. As the dislocations become more screw-like, the interface energy rises rapidly because of the increase in the dislocation density. This variation of the interface energy with θ is different from that of a small angle grain boundary, where a cusp minimum occurs at $\theta = 0°$. Fig. 5 demonstrates that the interface energy is approximately the same for both pure-misfit and small angle twist-misfit boundaries, which explains why both types occur.

Mulder and Klomp [14] used the hot pressing technique to study the Cu/Al_2O_3 interface, where Al_2O_3 was a single crystal with its surface parallel to (0001). They found that $(111)_{Cu} \parallel (0001)_{Al_2O_3}$ is a preferred orientation, as might be expected because both planes are close-packed, however, the closed-packed directions were misoriented by a rotation of 11° about [111] of Cu. The existence of small rotations away from exact epitaxy was also reported by Hoel, Habermeier, and Ruhle [15] for the case of Au islands on MgO, and Merkle and Shao [16] for Pt on NiO. It is believed, therefore, that the variation of the interface energy with θ shown in Fig. 5 is qualitatively correct.

SUMMARY AND CONCLUSIONS

For the NiO-Pt interfaces studied here with a fixed (001) NiO interface plane, three categories of orientation relationships were identified: exact epitaxy; a small rotation away from exact epitaxy about an axis normal to the interface, and high index Pt planes parallel to the (001) plane. The co-existence of the first two orientation relationships can be understood based on a calculation of the energy of the dislocation networks making up the interface.

Misfit dislocations, which accommodate the lattice mismatch between Pt and NiO, occur in

the exact (001) epitaxial interface, where the orientation relationship involves planes and directions being parallel in both crystals. The Burgers vectors are the type a/2<110>, with dislocation line direction along <110>, as predicted by a Bollmann O-lattice type analysis.

For a small deviation from the exact (001) epitaxy, the dislocations change direction and decrease in spacing relative to the epitaxial case, while the square network is still maintained. In order to confirm the detailed dislocation structure at such small spacing, information from both images and diffraction patterns are needed. The experimental observations of the dislocation structure are consistent with predictions based on the O-lattice analysis.

ACKNOWLEDGEMENTS

REFERENCE

1 W. Bollmann, *Crystal Defects and Crystalline Interfaces*, Springer, New York, 1970
2 R.E. Cech and E.I. Alessandrini, Trans. Am. Soc. Metals, 51 (1959) 150.
3 F.-S. Shieu and S.L. Sass, submitted to Acta Metall.
4 W.A. Jesser and D. Kuhlmann-Wilsdorf, Physica Status Solidi, 31 (1976) 533.
5 M. Hwang, D.E. Laughlin and I.M. Bernstein, Acta Metall., 28 (1980) 621.
6 W. Mader, Mat. Res. Soc. Symp. Proc., 82 (1987) 403.
7 R.W. Balluffi, S.L. Sass and T. Schober, Phil. Mag., 26 (1972) 585.
8 F.C. Frank and J.H. Van Der Merwe, Proc. Roy. Soc. A, 189 (1949) 205.
9 R. Peierls, Proc. Phys. Soc., 59 (1940) 256.
10 F.R.N. Nabarro, Proc. Phys. Soc., London, 59 (1947) 256.
11 J.H. Van Der Merwe, Proc. Phys. Soc. (London) A, 63 (1950) 616.
12 J.H. Van Der Merwe, in M.H. Francombe and H. Sato (ed.), *Single Crystal Films*, Macmillan Co., New York 1964, p. 139.
13 A.H. Cottrell, *Dislocations and Plastic Flow in Crystals*, Oxford University Press, Amen House, London 1961, p. 51.
14 C.A.M. Mulder and J. T. Klomp, J. de Physique, Colloque C4 (1985) 111.
15 R. Hoel, H.U. Habermeier and M. Ruhle, J. de Physique, Colloque C4 (1985) 141.
16 K.L. Merkle and B. Shao, Mat. Res. Soc. Symp. Proc., 122 (1988) 69.

SOLID STATE BONDING OF Si_3N_4 AND Ni

JIAN-YIH WANG[*], SHU-EN HSU[*], TADATOMO SUGA[**],
AND YOICHI ISHIDA[***]
*Chung Shun Institute of Science and Technology, P.O.Box 90008-8,
Taiwan, Republic of China
**Dept. of Precision Engineering, University of Tokyo, 7 Hongo,
Bunkyoku, Tokyo, Japan
***Institute of Industrial Science, University of Tokyo, 7
Roppongi, Minadoku, Tokyo, Japan

ABSTRACT

Solid state bonding of Si_3N_4 and Ni is considered to be a
simple ceramic/metal diffusion bonding as the case of Al_2O_3/Nb.
There are two kinds of bonding interfaces observed by
transmission electron microscope(TEM). In addition to the
directly bonded interface, an amorphous-like phase was found in
some regions of the Si_3N_4/Ni interface. It is responsible for
the degradation of bonding strength. In view of the experimental
results, the existence of the amorphous-like phase in bonding
interface results from the formation of SiO_2 and accumulation of
Al_2O_3 and Y_2O_3, which were used as sintering binders of Si_3N_4,
via intergranular diffusion during the bonding process.

INTRODUCTION

Since the solid state bonding of Si_3N_4 and Ni may possess
great applicability in the future, it becomes one of the most
attractive topics in the research field of ceramic/metal bonding.
According to the phase diagram, nickle can dissolve a fair amount
of silicon and nitrogen at the bonding temperature to avoid
forming any compound in the interface. Therefore, the Si_3N_4/Ni
bonding interface might be an ideal one without the formation of
reaction phases like the case of Al_2O_3/Nb bonding[1,2].

Although there are lots of research reports on the diffusion
bonding of Si_3N_4 and Ni, the conclusions regarding the
microstructure of bonding interface are different. Nakahashi et
al[3] found the formation of Ni_5Si_2 on the bonding interface,
whereas others declared that the Si_3N_4/Ni interface should be a
compound-free, directly bonded interface[4]. Furthermore,
according to the microstructure study of Si_3N_4/Ni interface in a
former experiment[5], the present authors noticed the existence
of amorphous-like phase.

Under an environment of high temperature and low pressure,
Si_3N_4 may partly decompose into Si and N atoms, which then can
be dissolved into Ni. In the subsequent cooling process, Si and
N will back-precipitate in the interface due to the decreased
solubility of Si and N in Ni at lower temperature. At the same
time, Al_2O_3 and Y_2O_3 as the sintering binders of Si_3N_4, can
diffuse to the interface. Consequently, the microstructure of
interface might be affected by the sintering binder in the
cooling step of diffusion bonding process.

In previous works concerning the study of ceramic/metal
bonding, the characterization of microstructure and composition
was mostly limited in the utilization of EPMA and SEM-EDX,
instead of TEM, due to the difficulty of preparing thin foils.

This article, however, shows that TEM is a powerful tool for the understanding of the ceramic/metal bonding mechanisms and predicting the performance of the bonding.

MATERIALS AND EXPERIMENTAL

The Toshiba-made pressureless sintering Si_3N_4, containing a small amount of Y_2O_3 and Al_2O_3 as the sintering binder, and a commercial grade Ni with purity 99.9% were used in this study. The surfaces of specimens were baff polished and then cleaned by acetone. Solid state bonding was achieved by applying a compressive load of 12MPa on a Si_3N_4-Ni(1mm thick)-Si_3N_4 sandwich and heating at 1223K for one hour in vacuum of 10^{-6} torr. After bonding, the specimen was cooled slowly at a rate of 20K/min to room temperature. Thin slices of thickness 200um were first cut from the bonded specimen along the direction perpendicular to the bonding interface by a diamond cutter, thinned by a diamond grinder down to 100um in thickness, and then dimpled until the thickness in the central part of disc was reduced down to 50-80um. The final thinning process was performed by 4KeV argon ion beams. JEM-1250 high voltage electron microscope(HVEM), JEM-2000EX high resolution electron microscope(HREM), and JEM-4000FX analytical electron microscope(AEM) were used for the observation and composition analysis of bonding interface.

RESULTS

The 4-point bonding strength of Si_3N_4/Ni in this research is about 200 MPa. Considering the difficulty of bonding a non-oxide ceramic and metal, it is a nice weldment. However the strength level is still not high enough for practical applications. Photo 1 is a low magnification TEM image of Si_3N_4/Ni bonding interface. Because of ion milling rate of Ni is higher than that of Si_3N_4, most of the remains are Si_3N_4. Some voids can be easily found in Ni due to the different diffusivities of Ni and Si, which is the so-called Kirkendall effect. However, the bonding interface is not compound-free and directly bonded as described in the work of Hirotsu et al[4]. On the other hand, the bonding interface is a mixture of directly bonded and amorphous-like regions, and thickness of the latter varied in a wide range. Photo 2 is an example of directly bonded interface of Si_3N_4 and Ni, and indicates a good epitaxial relationship between Si_3N_4 and Ni, which is just like what Hirotsu has observed. Photo 3 is a high resolution TEM image of this kind of interface. Photo 4 gives an example of amorphous-like phase interface between silicon nitride and Ni. In order to characterize the amorphous-like phase, techniques of selected area diffraction and micro-area analysis were conducted. Besides the spot patterns of crystalline Si_3N_4 and Ni, diffused halo rings of amorphous phase were found in the lower left of Photo 4. The X-ray energy spectra in Figure 1 qualitatively represent the chemical compositions of Si_3N_4, amorphous interface, and Ni, respectively. As can be seen in Figure 1 the amorphous phase contains elements of Si, Ni, Al, O, C, but no N. Especially, Oxygen is the major element. It can be inferred that this area is a solid solution of glassy phase which comprises SiO_2, Al_2O_3, or NiO_2 and so on. Carbon is usually found in amorphous-like phase[6].
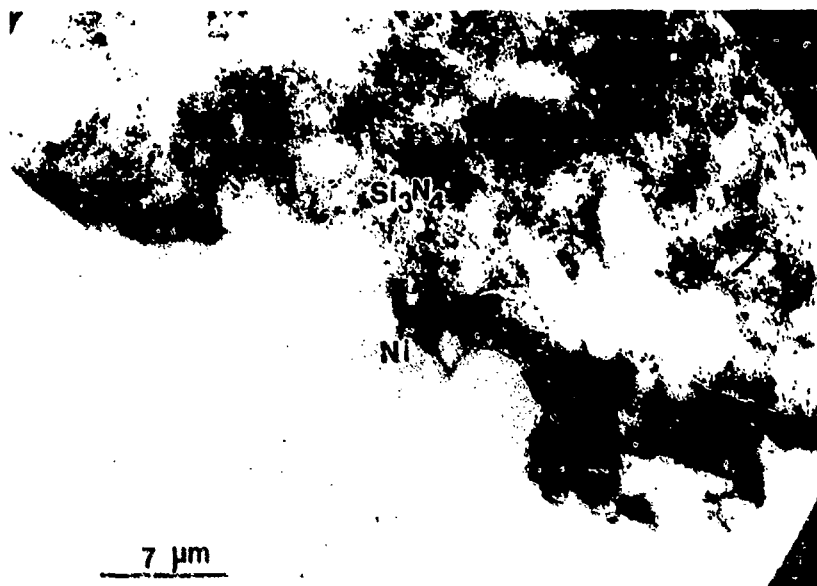
Photo 1 Transmission electron microscope image of
Si_3N_4/Ni interface

Photo 2 An example of directly bonded interface
of Si_3N_4/Ni
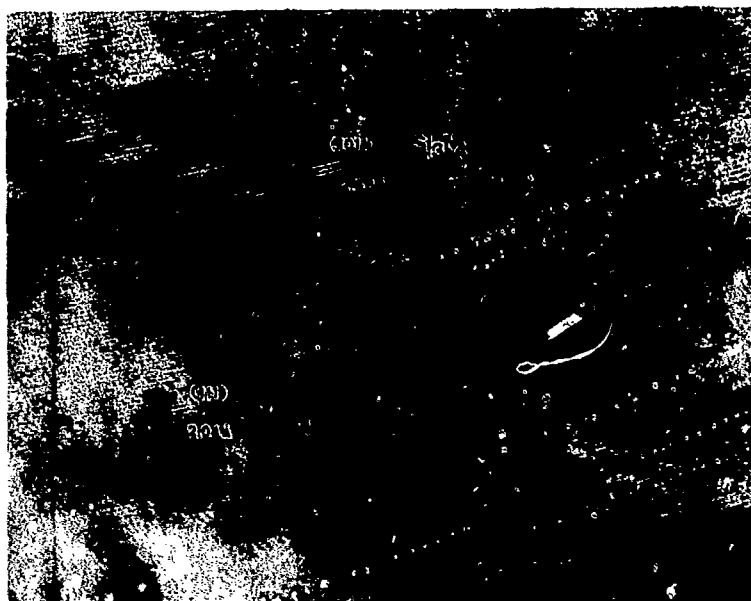
Photo 3 High resolution TEM image of directly bonded interface
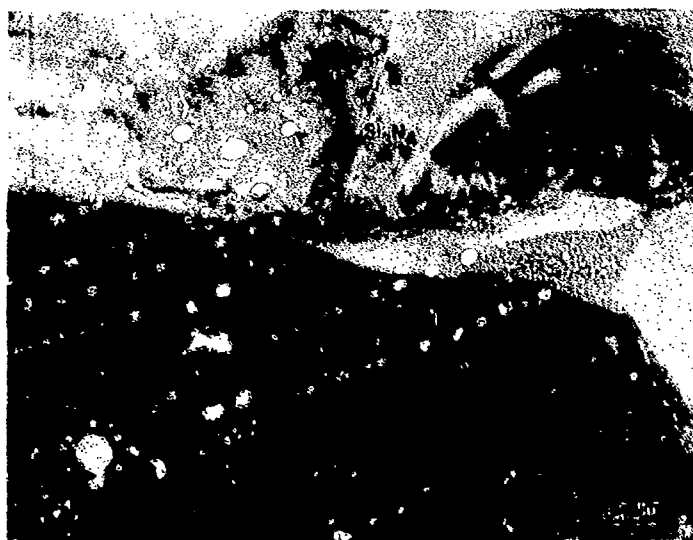
Photo 4 TEM image and electron diffraction pattern of Si_3N_4/Ni interface containing amorphous phase
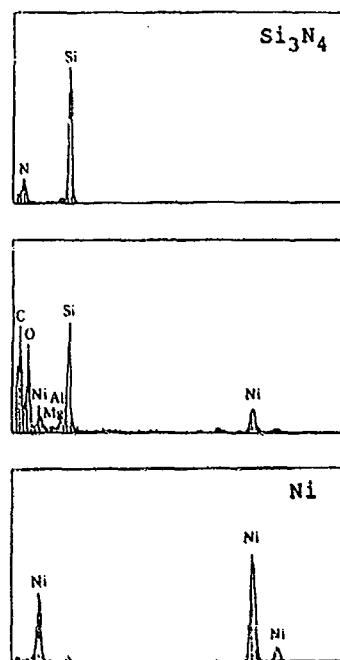
Figure 1 X-ray energy dispersive spectra of Si_3N_4, amorphous, and Ni

DISCUSSION

Both the directly bonded regions without any reaction product and the amorphous-like regions were observed in the bonding interface of Si_3N_4 and Ni. At the bonding temperature, Si_3N_4 will decompose into Si, and N. Part of Si atoms reacted with oxygen pre-existing in sintering binders, to form SiO_2, whereas the others diffused into Ni. In the mean time, the sintering binders Al_2O_3 and Y_2O_3 distributed on the grain boundaries of Si_3N_4 will move to the bonding interface via the preferential paths for diffusion, i.e., grain boundaries. After long exposure at high temperature, the interface finally gathered a large amount of the Al_2O_3, Y_2O_3, and SiO_2 sufficient to form the amorphous layer on the basis of glassy structure of SiO_2. This can explain the formation of amorphous interface. On the other hand, when the initial contact region of Si_3N_4 and Ni included no grain boundaries of Si_3N_4, directly bonded interface appeared on account of no sintering binders. In view of the composition analysis result, the amorphous phase comprises mostly Si and O, therefore it can be further known as a solid solution of oxides-SiO_2, Al_2O_3, and Y_2O_3 and so on.

According to Hirotsu's results, only compound-free directly bonded inteface is present. This could be due to the less content of sindering binders in Si_3N_4 or due to the preparation of TEM thin foils, in which the amorphous phase interface is easier to be milled and only directly bonded interface was seen.

In the study done by Nakahashi et al., the surfaces of Si_3N_4 were first metallized by a layer of Ni through CVD method . Since the bonding temperature in their experiment was 400K higher than the present work, Si_3N_4 could react with Ni and form a reaction phase on the interface.

The amorphous phase usually appears around the ion-thinned hole of TEM foil. Hence, the formation of amorphous phase might be considered as a result of ion striking. However, the amorphous phase primarily consists of SiO_2 glass from the results of composition analysis and thus exists before ion milled.

SUMMARY

From the above results, conclusions can be made as the follows:

(1) Sintering binders of Si_3N_4 tremendously affect the nature of Si_3N_4/Ni bonding interface.

(2) Two types of bonded interfaces were found. One is directly bonded interface without reaction phase and the other is amorphous phase interface. Directly bonded interface appears in the regions without sintering binders, whereas the amorphous phase interface exists in the place where the sintering binder is located.

(3) The bonding mechanism of Si_3N_4 and Ni is proposed in the following:

Si_3N_4 and Ni are placed together for solid state bonding. At the bonding temperature, Si_3N_4 decomposes into Si and N, which diffused toward Ni side. In the mean time, the sintering binders Y_2O_3, Al_2O_3 and oxygen on the grain boundaries of Si_3N_4 also diffused to the bonding interface. During the cooling process, back-precipitation of Si and N occurred because of the decreased solubility of Si and N in Ni. But the sintering binder remained in the interface can't back-precipitate again. Therefore, the directly bonded interface was formed in the regions without sintering binders. And the amorphous phase was formed in the regions containing sintering binders.

ACKNOWLEDGEMENT

REFERENCES

(1)N. Florjanic, W. Mader, M. Rühle and M.T urwitt: J.de Physique 46 c4 129(1985)
(2)Y. Ishida, J. Y. Wang and T. Suga: Proceeding of Asia MRS. Tokyo(1988)(to be published from Elsevier)
(3)N. Nakahashi, M. Shiragane and H. Takeda: Surface 24 10 595(1986)
(4)Y. Hirotsu and M. E. Brito: Proceeding of Symposium of Japan Institute of Metal 33(1988)(in Japanese)
(5)J. Y. Wang Y. Ishida H. Ichinose and Y. Bando: Proceeding of Annual Lecture Meeting of Japan Institute of Metal 24(1988,4)(in Japanese)
(6)Y. Bando (private communication)

CHARACTERIZATION OF INTERFACES IN SiC PARTICULATE-REINFORCED
Al ALLOYS BY AEM

BRIAN W. ROBERTSON, CHANDRA HOLM*, YANG-PI LIN, STEPHEN F.J. CORBIN and DAVID
S. WILKINSON
McMaster University, Department of Materials Science and Engineering,
1280 Main St W, Hamilton, Ontario, Canada, L8S 4L7.
*Permanent address: Martinsbergstrasse 49, CH 5400 Baden, Switzerland.

ABSTRACT

As a preliminary step to detailed study of the interfaces in SiC particulate-
reinforced Al alloys, a number of methods of sample preparation have been
explored ; the resultant artefacts on the thinned foils observed in transmis-
sion electron microscopes are discussed and improvements to the preparation
procedures are suggested. Initial observations of the microstructure of two
alloys differing significantly in their matrix silicon content are presented.

INTRODUCTION

Metal-matrix composite materials constitute a class of materials which are
extremely difficult to prepare for detailed examination of their micro-
structure and microchemistry since techniques which work well for ceramics and
metals individually are difficult to apply to composite materials, particular-
ly when the metal matrix is aluminum and the damage existing in that matrix in
the bulk needs to be preserved during specimen preparation for transmission
electron microscopy. We are studying the mechanical behaviour of particulate-
reinforced aluminum alloys and the importance of the interface regions between
particles and matrix as one of the major controlling factors in failure beha-
viour. In this paper, we present work done on the important, but often ne-
glected, area of sample preparation and some preliminary analysis of the
interfaces in two rather different alloys.

EXPERIMENT

Two commercial Si-C particulate-reinforced aluminum alloys, provided by Alcan
Research Laboratories, Kingston, Ontario, Canada, have been used in the
present work. These are: (1) 2014 alloy with 20% SiC particles by volume and
(2) A356 alloy with 10% SiC particles by volume. These differ most signifi-
cantly in their content of Si and Cu; the nominal compositions of the alloys
are, by weight: for 2014, 0.8% Si, 4.4% Cu, 0.5% Mg, the rest being Al; for
A356, 6% Si, <0.20% Cu, 0.35% Mg, <0.20% Fe, <0.10% Zn, the rest being Al.
Machined rods of each material 3mm in diameter were heat-treated to obtain the
T6 condition for the alloy in the same manner as the specimens used in mechan-
ical testing by Corbin and Wilkinson [1].

Disks 0.4 to 0.8 mm thick were then cut from the rods by spark-cutting with
very low spark energy to minimise damage. Both sides of the disks were wet
ground on 320, 400 and 600 grit SiC abrasive paper to a final thickness of 175
to 200 microns. Samples which were to be ion-thinned were then polished flat
on one side and polished to produce a spherical dimple on the other side using
a Gatan Model 656 Dimple Grinder; 6, 3 and finally 1 micron diamond paste was
employed for all polishing steps, with kerosene for dilution of the paste.

Samples were then either ion-milled or electropolished to perforation. Initial
attempts to prepare samples by ion-milling at room temperature resulted in the
introduction of substantial ion damage, as observed in subsequently in the
transmission electron microscope. All ion milling for samples discussed later
in this paper was performed only with samples cooled to near liquid nitrogen

temperatures in a Gatan model 600 Dual Ion Mill. An accelerating voltage of 4kV and an incident angle of 15 degrees to both surfaces was used for milling with argon ions before perforation of each sample; after perforation, milling was continued for a further 10 minutes but with the accelerating voltage reduced to 1.5 or 2.0 kV and the angle of incidence to 10 degrees. The vacuum chamber window was cleaned every 6 to 8 hours in order to allow setting of the laser optical detection system of the Ion Mill for best sensitivity to the smallest perforation to maximise the electron transparent region.

For samples which were electropolished, two different solutions and sets of polishing conditions were used: (1) 250ml nitric acid to 750ml methanol at about -20 C and 15 to 20 V applied voltage in a jet polishing unit; and (2) the solution designated BK2 (Kestel [3]) at about -30 C and 15 to 20 V. Since BK2 seemed to yield little, if any, improvement over the results of nitric/methanol electropolishing, the use of BK2 was discontinued.

Samples were examined with a scanning electron microscope (Philips 515 SEM), a transmission electron microscope (Philips CM12 TEM/STEM) and a dedicated scanning transmission electron microscope (VG HB5 STEM) as well as with light microscopes.

RESULTS

Specimen preparation

Diamond polish has generally been used for the final mechanical polishing step in preference to other abrasives because of its hardness compared with both matrix and particles in metal-matrix composites; its use helps minimise the protrusion of SiC particles from the sample surface which otherwise occurs. It is therefore commonly employed before ion-milling since ion bombardment tends to increase surface roughness, particularly if the angle of incidence of the ions is high enough to yield acceptable thinning rates. From one sample of the 2014 composite, it was observed however that, even after sputtering away much of the thickness of the sample remaining after the diamond polishing step of specimen preparation, some SiC particles appeared cracked or associated with voids. It remains to be determined whether this is typical of the bulk material in the state before electron microscope specimen preparation or is evidence of mechanical damage introduced in the diamond polishing step.

In areas thinned partially to electron transparency by ion-milling, it was usually observed that SiC particles were thinned most near their centres and that the metal matrix was thinned much less, resulting in a rapidly varying thickness near the metal / SiC interface. It was however frequently observed that SiC particles found in the thickest matrix regions visible in the TEM were less electron transparent than the surrounding matrix even under large variations of the angle of electron beam incidence to the specimen.

Specimens which, after dimple polishing, were only ion-milled at close to liquid nitrogen temperatures invariably showed high dislocation densities (figure 1), in contrast to electropolished samples which showed little evidence of dislocations in the matrix (see figure 2). However, the range of specimen features which could be examined in ion milled samples was considerably greater, extending from precipitates several microns away from a SiC particle through the interface region to near the centre of the SiC particle.

Samples of 2014 composite which had been electropolished in nitric / methanol solution to perforation were examined in the SEM. The images obtained showed that, as expected, there was little, if any, attack of the precipitates and SiC particles compared with the matrix. In some cases, connected series of

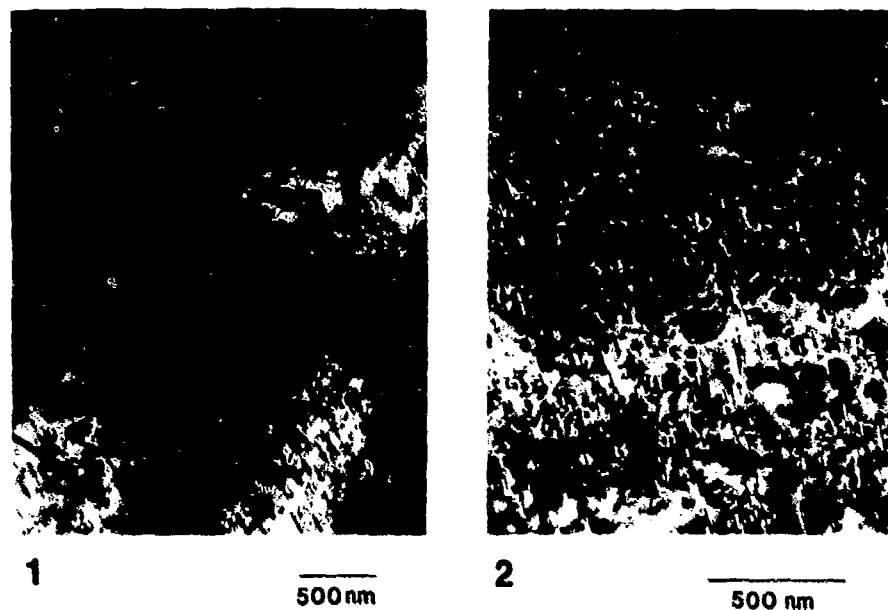**1** — 500 nm **2** — 500 nm

Figure 1. Ion-milled 2014-SiC composite, showing a high density of dislocations.

Figure 2. Matrix region of electropolished 2014-SiC composite, showing absence of dislocations.
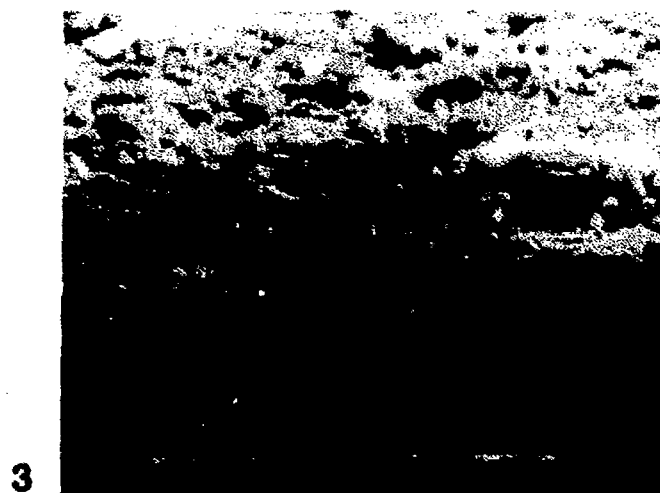

3

Figure 3. SEM image of an electropolished 2014-SiC sample, showing SiC particles protruding from the matrix thin film.

precipitates and particles were found to be left protruding from the sample surface, but minor etching resulting from slight reduction of the applied voltage during electropolishing was sufficient to reduce these to the level seen in figure 3.

Microstructure
In samples prepared from 2014 composite, precipitates were observed at several places on each matrix / SiC particle interface; in those cases in which sample thickness was lower than about 0.1 micron, the x-ray spectra obtained from analysis in the TEM and STEM were consistent with the phases $CuAl_2$ and $Cu_2Mg_8Si_6Al_5$ observed for example by Dignard-Bailey et al [2] and listed as equilibrium phases in [4]. On many SiC particles, an Al-rich phase (possibly Al_4C_3), which ion thinned much less readily than matrix or SiC, was observed to form a partial shell but no evidence for any serration of its interface with the SiC was found. A region of greatly reduced precipitate number density (precipitate-free zone) was observed near a large fraction of the larger precipitates and SiC particles (figure 4) in the 2014 composite. However, no precipitate-free zone was observed adjacent to any Al-rich shell on the SiC particles. In the matrix, $(Mn,Fe)_3SiAl_{12}$ precipitates were also observed.

In samples of A356 composite, several differences were observed from the 2014 material. Firstly, no precipitate-free zone was detected near the SiC particles (figure 5). Secondly, the interfaces between the SiC particles and metal showed virtually no evidence of reaction resulting in interfacial precipitation (figure 5). In fact, the alloy is intentionally high in Si content to inhibit such a reaction between the metal and the SiC particles. Thirdly, apart from a low number density of Mg-rich precipitates, only eutectic Si precipitates were detected in the metal matrix.

DISCUSSION

It was observed that the usual problem in any examination of inhomogeneous materials -- that of sampling only a small and certainly not necessarily representative part of the original bulk material -- was greatly increased in the case of the SiC particulate-reinforced aluminum alloys studied. Our results from these materials so far are only the preliminary ones; however, from our work on development of the necessary transmission electron microscope sample preparation techniques and from observations of composites 1 and 2, the following points are notable.

As the final preparation technique, electropolishing was clearly unsuitable for transmission electron examination of SiC particle interiors and, except in a very few cases, for x-ray microanalysis of the region near the interface. The presence of electron opaque material within a micron of a thin region whose elemental composition is to analysed may be acceptable for electron energy loss spectroscopy but can lead to major alteration of x-ray spectra through x-ray fluorescence, x-ray absorption and additional x-ray generation by electrons scattered from the beam by the region of interest.

Electropolishing has the two great advantages over any thinning process involving only mechanical polishing and then ion-milling. Firstly, the artefacts introduced into the matrix seem to be much fewer and, secondly, the speed of thinning is so great that there is no advantage in thinning the sample mechanically by dimple or flat polishing to less than 0.1mm thick before electropolishing. This final mechanical polishing may be the major cause of the high density of matrix dislocations observed in ion-milled samples. We are currently preparing samples by ion-milling disks which are at least 0.1mm thick to examine this possibility.

The observation of high dislocation densities in material ion-milled at low

temperature may also be linked to the repeated cycling of the sample temperature between room temperature and near liquid nitrogen temperatures when the material is still sufficiently thick for high stresses to develop as a result of the large difference in thermal expansion coefficients between the alloy and SiC. (This cycling occurs partially as a result of needing to clean sputtered deposits from the vacuum window to assist in early detection of sample perforation.) We have already found, by TEM observation of thin areas of the matrix, that there is no significant influence of temperature cycling on samples thinned to perforation by electropolishing. However, in this case, the stresses which could develop are expected to be much lower than in the bulk material because of relaxation near the free surfaces.

From consideration of the points discussed above, it seems that a potentially satisfactory transmission specimen preparation procedure may involve: 1) spark slicing of disks, 2) mechanical grinding and polishing to 0.1mm disk thickness, 3) electropolishing close to perforation, 4) final thinning by ion-milling at low temperature with very low angle of incidence to minimise thickness variations in the finished sample.

CONCLUSIONS

Sample preparation
Mechanical polishing of samples to reduce their thickness so that ion-milling is shortened to a reasonable duration may be unacceptable when the damage state of the matrix is to be studied but is probably quite satisfactory when only precipitate distributions and types are to be determined.

Thermal cycling of samples to near liquid nitrogen temperature may be a significant contributor of matrix dislocations if the sample is thick enough for the stress state due to differential thermal expansion of the metal matrix with respect to the SiC particles to be close to that in bulk material similarly cycled.

As a substitute step for final mechanical thinning before ion-milling, electropolishing may be useful in avoiding much of the damage observed in mechanically polished, ion-milled samples.

Work is in progress to test these possibilities.

Microstructure
In composite 2014, in addition to the Cu_2Al precipitates in high number density in the matrix, we have observed precipitates which can be identified as $Cu_2Mg_8Si_6Al_5$, $(Mn,Fe)_3SiAl_{12}$ and possibly Al_4C_3. The precipitate-free zone observed near some precipitate and particle interfaces is expected to have an influence on the local stress state and therefore on the mechanical properties of the composite.

The SiC interfaces in composite A356 show little evidence of reaction with the matrix, in agreement with expectations based on the high Si content; no precipitate-free zones have been observed.

4
200 nm

5
200 nm
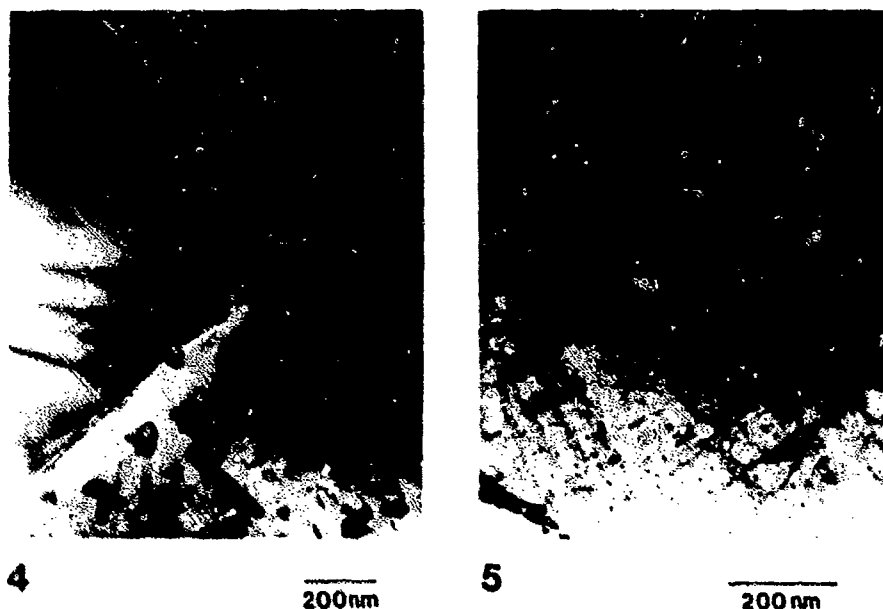
Figure 4. Precipitate free zone (PFZ) adjacent to a SiC particle in ion-milled 2014-SiC composite in the T6 condition. Note that some precipitates are also formed at the interface.

Figure 5. SiC-matrix interface in A356-SiC composite, showing absence of interfacial precipitates. Note that the matrix contains only small Mg-rich precipitates and the absence of PFZ.

REFERENCES
1. S.F. Corbin and D.S. Wilkinson, in Proceedings of the International Symposium on Processing of Ceramic and Metal Matrix Composites, edited by M. Mostaghaci (Proceedings of the Metallurgical Society of the Canadian Institute of Mining and Metallurgy 17, Pergamon Press, New York, 1989) pp. 401-411.

2. L.M. Olgnard-Bailey, T.F. Malis, J.D. Boyd and J.D. Embury, in Proceedings of the International Symposium on Advanced Structural Materials, edited by D.S. Wilkinson (Proceedings of the Metallurgical Society of the Canadian Institute of Mining and Metallurgy 5, Pergamon Press, New York, 1989) pp. 87-99.

3. B.J. Kestel, Ultramicroscopy 19, 205 (1986).

4. Aluminum: Properties and Physical Metallurgy, edited by J.E. Hatch (American Society for Metals, Metals Park, Ohio, 1984).

A TEM STUDY OF AN ADHESIVE / SHEET MOLDING COMPOUND INTERFACE

EDUARDO A. KAMENETZKY AND RAYMOND S. FARINATO
American Cyanamid, Chemical Research Division, 1937 West Main
St., P. O. Box 60, Stamford, CT 06904

ABSTRACT

The interface between an epoxy adhesive and sheet molding
compound (SMC) was studied by TEM. The interface width is less
than 20 nm where it is sharp, and on the order of 40 nm where it
is more diffuse. The interfacial area in the TEM sample is
located first by the difference between adhesive and SMC
microstructures. Where there are no microstructural features we
can investigate further the location of the interface by using
the Mg Kα peak from magnesia thickener in the polyester matrix
of the SMC. Calcium carbonate crystals in the SMC extend to
within less than 25 nm of the interface. Measurements of
interface extent and roughness indicate that there is intimate
contact and good mechanical bonding between the adhesive and
SMC. The surface and interfacial energetics of this epoxy-SMC
system were evaluated using sessile drop advancing contact
angles. Good mechanical bonding observed by TEM is consistent
with a small advancing contact angle of 20° for the epoxy
adhesive on the SMC at 121 °C which shows a good thermodynamic
driving force for the intimate contact during the bonding
process.

INTRODUCTION

Steel parts in auto frames and bodies are being steadily
replaced by glass fiber reinforced composites, specifically
SMC. Lower tooling costs and lead times for diversified model
lines is the driving force behind the increasing use of SMC.
Automotive SMC is typically composed of a filled (glass + CaCO$_3$)
styrene-crosslinked polyester resin. In addition, the polyester
resin will usually contain a phase separated thermoplastic
polymer which absorbs cure shrinkage stresses and creates a
smoother top surface. The SMC used in this study also contained
MgO/Mg(OH)$_2$, which was present to thicken the SMC resin in its
uncured state via physical crosslinks with residual carboxylate
groups in the polyester. A mold release agent (Zn stearate)
was also part of the formulation. Adhesives are the preferred
mode of joining SMC parts because they distribute stresses
uniformly over the bonded surface and are capable of good
surface finishes. An epoxy with good adhesive properties for
bonding SMC to SMC was selected for this study. Lap shear joint
testing results in cohesive fracture of the SMC. The adhesive
contains talc (magnesium silicate), silica, aluminum and titania
fillers.

The strength of an adhesive-SMC joint depends on the
microstructure of the interphase as well as on the nature of the
bonding of the adhesive to the polyester matrix of the SMC. The
formation of this interphase region will be driven
thermodynamically and be limited by the chemorheology of the
curing adhesive. The thermodynamics of adhesion can be
quantified by contact angle measurements which are used for the

tailoring of good composite mechanical properties. The microstructure at the interphase is studied here by transmission electron microscopy (TEM).

EXPERIMENTAL

Ultramicrotomy and ion milling were used for preparing thin film samples of the interface. The bulk samples were cut and thinned by mechanical means making sure that the interface remains centered in the specimen at all times. For example, for ion milling, a 2-mm strip with the interface at the center was cut and mechanically thinned to 20 μm before dimpling and ion milling. A section of the strip was then mounted on a Be grid for analytical electron microscopy (AEM). In order to eliminate differential milling at the edges, the thin sections were placed so as to cover the hole in the Be grid. Argon ion milling was carried out at 5 kV 18° and 1 mA total current until perforation and then at 4 kV 12° and 1 mA total gun current for 1/2 hr for surface finish. The resulting sample has two thin (electron transparent) regions of interface at the perforation which is centered at the interface. Although thinning was carried out at low angles to minimize the differential milling rates of the different components, the SMC matrix and the adhesive are thinner than the glass fibers and carbonate particles. Otherwise, the microstructure is well preserved and in particular, the interfacial area can be studied. The SMC matrix microstructure shows the formation of microgel particles which is typical of styrene - unsaturated polyester copolymerization [1]. Ultramicrotomy was not successful because when sectioned, the SMC fizzled away in the trough containing the water. Sections that looked good optically when examined in the TEM show that during microtomy the knife displaced the large glass and calcium carbonate crystals tearing the SMC polymer matrix. These results are in agreement with recent studies of C/C composites which indicate that the better TEM samples are produced by grinding, dimpling and ion-milling [2].

An atlas of microstructures of inorganic fillers in the adhesive and SMC were obtained by imaging, diffraction and EDX microanalysis. The ultra-thin window (UTW) in our energy-dispersive x-ray (EDX) detector allows the detection of light elements heavier than Be. However, the quantification of light element concentrations should be carried out with special consideration to absorption of light element x-rays and peak shape. A computer program was written to obtain mass absorption coefficients for our detector geometry and the different microstructures based on the mass absorption coefficients for light elements of Henke, et. al., [2]. The calculations show that for the thicker (1 μm) carbonate crystals the C K peak is lost, as is observed experimentally. In order to account for low-energy tailing of the light-element peaks, their intensities were quantified by fitting to standard peaks acquired from oxides, carbon and nitrides.

The surface and interfacial energetics of this epoxy-SMC system were evaluated using sessile drop advancing contact

angles. Averaged water and methylene iodide contact angles at 22 $\pm$ 2 °C were used to compute the dispersion, γ^d, and

non-dispersion, γ^{nd}, (acid-base or hydrogen bonding) contributions to the surface energy of the cured epoxy and the SMC. The harmonic mean method was used for the calculation assuming $\gamma^d(CH_2I_2)$ = 44.1 dynes/cm, $\gamma^{nd}(CH_2I_2)$ = 6.7 dynes/cm, $\gamma^d(H_2O)$ = 22.1 dynes/cm and $\gamma^{nd}(H_2O)$ = 50.7 dynes/cm.

RESULTS AND DISCUSSION

Using the atlas of microstructures and EDX the interfacial area in the TEM sample is located first by the difference between adhesive and SMC microstructures. Where there are no microstructural features we can investigate further the location of the interface by using the Mg Kα peak from magnesia thickener in the polyester matrix of the SMC (Fig. 1). The Mg peak is unique to the SMC matrix if precautions are taken not to fluoresce the talc particles on the epoxy side which are sometimes observed in the vicinity of the interface. However, we are then limited on the precise location of the interface by the beam diameter used (250 nm) in order to get good count rates. Typical electron micrographs of interfacial areas are shown in Figs. 2 and 3. The area of interface to the lower left in Fig.
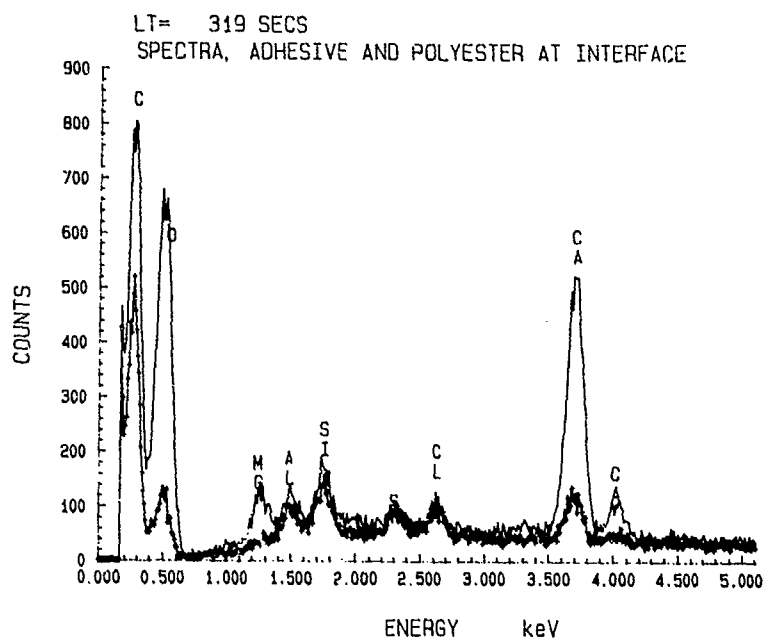
FIG. 1.--EDX spectra of adhesive and polyester at the interface. The Mg peak in the polyester matrix is due to a thickener. Peaks other than C and O are due to other fillers.

Fig. 3.--Another area of adhesive/ SMC interface. A glass fiber runs parallel and 2 um below the interface.
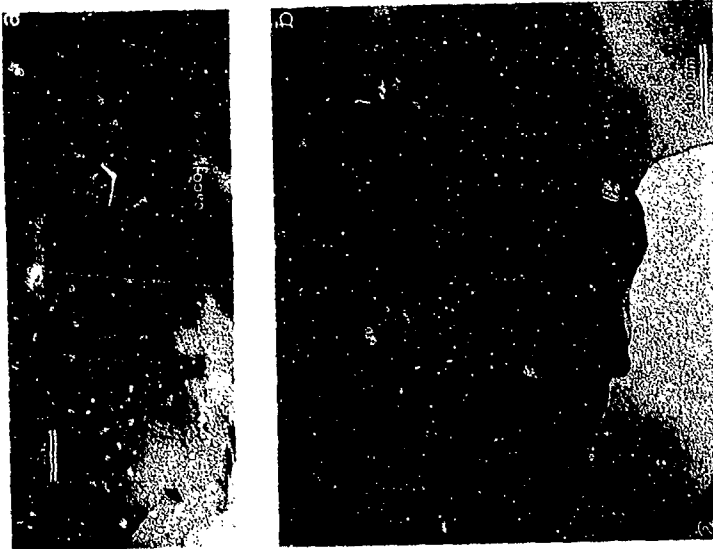
Fig. 2.--a) and b) are, respectively, low and high magnification images of an adhesive/SMC interface. The arrowheads indicate $CaCO_3$. The interface is indicated by arrows.

2a is shown at higher magnification in Fig. 2b. In some regions
of Fig. 2b the interface is less than 20 nm in extent while in
other regions it appears more diffuse on the order of 40 nm.
Tilting experiments indicate that this is not an effect due to
the interface being inclined at an angle to the beam. The $CaCO_3$
particles extend to within less than 25 nm of the interface.
However, in the thin area of Fig. 3 and in the region that
separates the titania crystal from the carbonate particle the
interface is not visible, suggesting that an extended diffuse
interface has formed. After examination of different areas it is
observed that the interface is rough at two different scales.
There are steps and penetrating terraces with dimension on the
order of 1 μm and there is local roughness with steps and
penetrating terraces with dimension on the order of 50 nm. The 1
μm range topography was also clearly seen in profilometer traces
of the SMC surface.

The results of the contact angle measurements are shown in
Table 1. The advancing contact angle of the liquid epoxy
adhesive on the SMC at the cure temperature of 121 °C was 20° ($\pm$
2°). This small contact angle of epoxy on SMC indicated a good
thermodynamic driving force for intimate contact during the
bonding process. Calculations of pore penetration using a
modified Washburn equation for a curing liquid indicated
complete wetting of a surface with the surface energy and
profilometry discussed above.

Table 1. Surface Energy of Components

Surface Energy (dynes/cm)* at 22 $\pm$ 2 °C		
	SMC	Epoxy
γd	27	25
γnd	16	14
γtotal	43	39

* standard deviation $\approx$ 2 dynes/cm

CONCLUSIONS

The measurements of interface extent and roughness indicate that there was intimate contact and good mechanical bonding between the adhesive and SMC. This was consistent with the contact angle data.

In tailoring the adhesive to a particulate-filled composite, additional consideration should be given to wetting of fillers which are exposed at the surface. In SMC by design the glass fibers are below the surface. However, we have seen that the calcium carbonate particles are in close proximity to the interface. TEM observations show that there is wetting of the carbonate particles by the epoxy when the filler is exposed. Otherwise, poor bonding between epoxy and carbonate could result in favorable sites for microcrack initiation.

REFERENCES

[1] Y. S. Yang and L. James Lee, Polymer 29, 1793 (1988).

[2] C. P. Ju and J. Don, Materially Speaking 5, No. 3 (1988).

[3] B. L. Henke, Atomic Data and Nuclear Data Tables 27, 1 (1982)

STUDY OF TRANSCRYSTALLIZATION IN POLYMER COMPOSITES

BENJAMIN S. HSIAO AND ERIC J. H. CHEN
E. I. du Pont de Nemours & Company, Inc., Fibers Department, Pioneering
Research Laboratory, Experimental Station, P.O. Box 80302, Wilmington,
Delaware   19880-0302

ABSTRACT

Transcrystallization of semicrystalline polymers, such as PEEK, PEKK
and PPS, in high performance composites has been investigated. It is found
that PPDT aramid fiber and pitch-based carbon fiber induce a transcrystalline
interphase in all three polymers, whereas in PAN-based carbon fiber and glass
fiber systems, transcrystallization occurs only under specific circumstances.
Epitaxy is used to explain the surface-induced transcrystalline interphase in
the first case. In the latter case, transcrystallization is probably not
due to epitaxy, but may be attributed to the thermal conductivity mismatch.
Plasma treatment on the fiber surface showed a negligible effect on inducing
transcrystallization, implying that surface-free energy was not important.
A microdebonding test was adopted to evaluate the interfacial strength be-
tween the fiber and matrix. Our preliminary results did not reveal any effect
on the fiber/matrix interfacial strength of transcrystallinity.

INTRODUCTION

It is known that, in a composite, the fiber surface can induce nucleation
of a crystalline matrix. This induced crystallization depends on the nucle-
ating activity of the fiber surfaces and thermal conditions. If the fiber
surface nucleates a large number of nuclei, impingement between the neighbor-
ing nuclei will force the nucleation growth direction normal to the fiber
surface. Such a process is referred to as transcrystallization or sometimes
row nucleation. A schematic diagram of the transcrystalline interphase is
illustrated in Figure 1. Though the direction of nucleation growth is normal
to the surface, molecules lie parallel to the fiber axis for maximum reduction
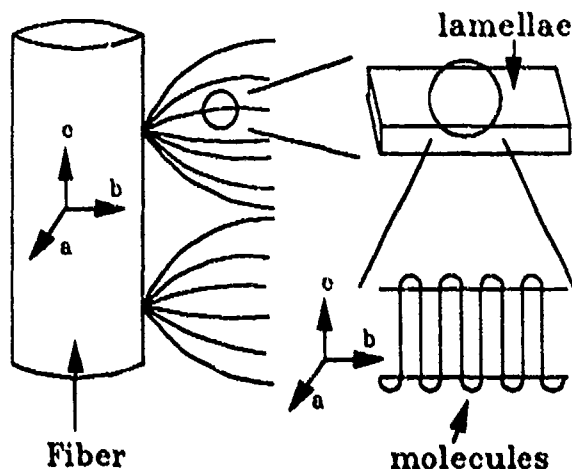of free energy of nucleation [1].

Figure 1. Schematic Diagram of the Transcrystalline Interphase

It has been reported that the physical properties of the transcrystalline interphase are different from those of the neat resin [2,3]. Such behavior is due to the distinct morphology of the transcrystalline structure. In the case of composites, many high performance thermoplastic systems exhibit a transcrystalline interphase, such as PAN-based carbon/PEEK (polyetheretherketone) [4,5], carbon/PEK (polyetherketone), carbon/PPS (polyphenylene-sulfide) [6], and aramid/PPS [7], yet none of these systems have clearly shown an effect of the transcrystalline interphase on the mechanical performance of composites. Findings in this area have often been contradictory, as seen for example, Porter et al., suggested that transcrystallization improved the transverse properties in an AS-4/PEEK composite [4]; Hardwich et al., concluded that transcrystalline interphase increased general mechanical properties in glass/polypropylene systems [8]; Hagenson et al., showed that transcrystalline interphase did not change mechanical properties in fiber/PPS composites [9]; and Bessel et al., reported that transcrystalline morphology led to a poor interfacial bonding [10]. Therefore, in this work, we attempt to study the attributes of transcrystalline interphase in high performance thermoplastic composites and also to investigate the interfacial shear strength of such composites via a microdebonding method.

EXPERIMENTAL

Materials and Preparation

The chosen fibers included four types: E-glass (Dow Corning), PAN-based AU-4 carbon (Hercules), PPDT aramid (Du Pont Company), and pitch-based carbon (Du Pont Company). Two of these fibers, AU-4 and aramid, were additionally plasma treated in an oxygen environment. Resins used were: polyphenylene-sulfide (PPS, from Phillips Chemical), polyetheretherketone (PEEK, from ICI) and polyetherketoneketone (PEKK, from Du Pont Company). All of these resins were vacuum dried at 120°C for 24 hours prior to use.

Thin films of polymer resin containing the chosen fibers were produced by heating small amounts of polymer and fiber on microscope slides. A typical temperature used for preparing the specimens was approximately 40°C above the melting temperature of the resin.

For the microdebonding test, unidirectional composites were prepared by compression molding the stacked wound fiber layers and polymer films under heat and pressure. The thermal processing conditions, similar to those of thin films, yielded 60% fiber volume content. Several types of composite were prepared; they were AS-4/PEEK (APC-2, from ICI), AU-4/PEKK, and aramid/PEKK.

Characterization Techniques

Thermal optical analysis (TOA), consisting of a Nikon Optiphot-Pol polarizing microscope equipped with a Mettler FP82 hot stage, was used to investigate the transcrystalline interphase. The maximum operating temperature of this hot stage was 400°C. The specimen was first equilibrated above the melting temperature for 30 minutes to eliminate the previous thermal history and subsequently dropped to a lower temperature for isothermal crystallization.

The microdebonding test, details of which have been reported elsewhere [11], was used to measure the in-situ fiber/matrix interfacial shear strength in a composite. Typical experimental procedures are as follows: a stepwise compressive loading is applied to an individual fiber end until debonding occurs (identified by a microscope); the measured normal force is then converted into an interfacial shear strength through a boundary element analysis using a micromechanics model; six to twelve fiber ends are tested for each specimen to obtain acceptable statistics.

RESULTS AND DISCUSSION

Our findings on transcrystallization in various fiber/resin systems are summarized in Table I. In the case of pitch-based carbon fiber and aramid fiber, a transcrystalline interphase was always observed, whereas in the case of PAN-based AU-4 carbon fiber and glass fiber, transcrystallization occurred only in some circumstances. Optical micrographs of the transcrystalline interphase in a few systems are illustrated in Figure 2.

It is conceivable that, in pitch-based carbon fiber and aramid fiber systems, a surface lattice match is responsible for transcrystallization. This argument is quite obvious in the PPDT system, where similar crystal unit cell dimensions are observed between the fiber substrate and resin. Comparison of unit cell dimensions between aramid fiber and various polymers is listed in Table II. The crystal structure of all six polymers is known to be orthorhombic with the c-axis along the chain directions [6]. In aramid fiber, the c-axis is also the fiber axis, and the fiber surface contains both the a-axis and the b-axis. As seen in Figure 1, resin molecules are aligned parallel to the fiber axis with their b-axis in the direction of transcrystallization growth. This suggests that the close match of unit cell dimension in the a-axis and/or c-axis between fiber and resin may be responsible for transcrystallization. Generally, it is believed that epitaxy can be observed as the lattice mismatch is less than approximately 20% between the substrate and resin, though some gross anomalies exist [12].

In the case of pitch-based carbon fiber, the epitaxial effect is again plausible. While previous investigators have concluded that the surface of the pitch-based carbon fiber is constituted of basal planes, there is recent evidence of presence of a significant number of edge planes [13], where a surface-topography match is again permissible for inducing nucleation [14]. However, in the PAN-based carbon fibers, transcrystallization occurs only under certain conditions, which are not fully characterized. This behavior may be because the surface of a PAN-based carbon fiber contains mostly the defect-free Basal planes [15], where resin molecules are difficult to match to such topography.

Table I. Transcrystalline Interphase Observation

Fiber/Resin	PPS	PEEK	PEKK
PAN-Based AU-4 Carbon	+/-	+/-	+/-
Pitch-Based Carbon	+	+	+
Glass	+/-	+/-	+/-
PPDT Aramid	+	+	+

+ Represents positive finding.
- Represents negative finding.

Table II. Unit Cell Dimensions (nm) of Various Polymers

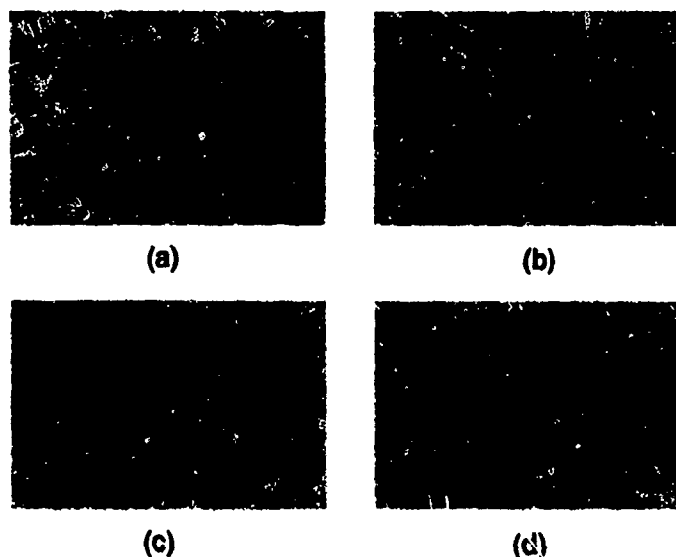|	a	b	c
PEEK [6]	0.775	0.586	1.00
PEK [6]	0.763	0.596	1.00
PPS [6]	0.867	0.561	1.026
PPO [6]	0.807	0.554	0.972
PEKK [18]	0.769	0.606	1.016
PPDT [18]	0.78	0.52	1.29

Figure 2. Optical Micrographs of Transcrystalline Interphase in (a) Aramid/
PEEK (b) Pitch-Based Carbon/PEEK (c) AU-4/PEEK (without trans-
crystalline interphase) (d) AU-4/PEEK (with transcrystalline
interphase)

In addition to the surface topography, another possible source of in-
ducing transcrystallization is the mismatch of thermal conductivity. If a
temperature gradient results from such a mismatch near the interface of a
fiber (with large thermal conductivity), the fiber surface can be cooler than
the resin and increase the supercooling. A large supercooling on the fiber
surface increases the nucleation rate and results in transcrystallization [2].
However, this phenomenon would depend on both the overall degree of super-
cooling and nucleating ability of the neat resins. If the overall degree of
supercooling is large, transcrystallization is difficult to occur, whereas
small degree of supercooling usually promotes transcrystallinity. Transcrys-
talline interphases observed in the PAN-based fiber and the amorphous glass
fiber systems may be partially due to this phenomenon.

Plasma treatment of the AU-4 fiber showed a negligible effect on induc-
ing transcrystallization. The surface free energy of the plasma-treated
carbon fiber is almost two times that of the untreated one [16]. Therefore,
this finding verifies our previous belief that the surface-free energy has
little influence on the surface-induced nucleation [16].

Microdebonding test results from several composites do not reveal any
difference in interfacial bond strength between the systems possibly having
transcrystalline interphase and the one without transcrystallinity. One pos-
sible explanation is that transcrystallinity may not change the fiber/matrix
interfacial adhesion. Though transcrystallinity is proven to enhance the resin
properties, high fiber content in the composites significantly restricts the
available space for transcrystallization growth, therefore, the effect of
transcrystallinity on composite properties may not be profound.

REFERENCES

1. B. Wunderlich, Macromolecular Physics, Vol. 2, Academic Press, NY (1973)

2. T.K. Kwei, H. Schonhorn and H.L. Frisch, J. Appl. Phys., 38, 2512 (1967)

3. H.L. Frisch and H. Schonhorn, J. Elastoplast., 3, 214 (1971)

4. Y.G. Lee and R.S. Porter, Polymer Eng. Sci., 26 (9), 633 (1986)

5. H.X. Nguyen, Ph.D. Thesis, Case Western Reserve University (1986)

6. A.J. Waddon, M.J. Hill, A. Keller and D.J. Blundell, J. Mat. Sci., 22, 1773 (1987)

7. G.P. Desio, Textile Research Institute, Notes of Research, No. 417 (1988)

8. S.T. Hardwich, Ph.D. Thesis, Brunel University, UK (1987)

9. R.L. Haganson, et al., SAMPE, Vol. 34, Book 2, 1255 (1989)

10. T. Bassell, D. Hull and J.B. Shortall, Faraday Spec. Disc., Chem. Soc., 2, 137 (1972)

11. J.F. Mandell, E.J.H. Chen and F.J. McGarry, Intl. J. Adhesion and Adhesives, 1, 40 (1980)

12. A.C. Zettlemoyer, Nucleation, Marcel Dekker, Inc., NY (1969)

13. J.G. Lavin, Private Communication (Nov., 1989)

14. E. Baer, J.L. Koenig, J.B. Lando and M.H. Litt, SPI, 26th Annual Technical Conference, 20-E, 1 (1971)

15. A. Oberlin, Carbon, 22 (6), 521 (1984)

16. Surface energy of AU-4 is 42.4 dyne/cm, plasma-treated AU-4 is 72.6 dyne/cm, measured by contact angle method.

17. S.H. Wu, Polymer Interface and Adhesion, Marcel Dekker, Inc., NY (1982)

18. K. Gardner, Private Communication (October, 1989)

THE INFLUENCE OF WATER ON THE EPOXY-RESIN-GLASS INTERPHASES

T. Marzi, U. Schröder, M. Heß, R. Kosfeld*
University of Duisburg, Department of Physical Chemistry
D-4100 Duisburg, FRG

ABSTRACT

The absorption of water in glass fiber reinforced epoxy resins is a complex process. With dynamic-mechanical measurements it is possible to distinguish locations of water in the resin-glass interphase, in micro-cracks of the resin, and diluted in the bulk polymer. The dominant mechanism of incorporation depends on the resin/hardener system, the surface treatment of the glass fabrics, and the sorption temperature.

INTRODUCTION

The knowledge of the water content of a glass fiber reinforced epoxy resin does not allow to predict its influence on the mechanical properties of the laminate. For such a prediction it is important to distinguish different states of water in the sample, namely water in the polymer matrix, and water in the interphase.

Water sorption of the glass fibers can be neglected. Water in the polymer- glass interphase is responsible for the decrease of the mechanical properties of the laminate. With dynamic-mechanical measurements it is possible to discriminate water in the resin-glass interphase from water in the bulk polymer and in micro-cracks of the resin.

EXPERIMENTAL

As laminating resin, an epoxy system of Bakelite, Duisburg, FRG (trade-name 0166 S20) was used. Its main component is bisphenol-A-diglycidether (DGEBA). The curing agents were bis (4-amino-3-methyl-cyclohexyl)methane (PACM) (trade-name SL), triethylene-tetramine (TETA) (trade- name VE 2896), and diethylene-triamine (DETA) (trade-name VE 2778), respectively.

Resin and hardener were added in stoichiometric proportions. The surface treatments of the glass fabrics (glass fabric style 92111 of Interglas, Ulm, FRG) were Finish I 550, and textile size, respectively. The test specimens were prepared by wet lamination of four glass fabric styles. The resin was cured 24 hours at room temperature and subsequently annealed for 17 h at 120 °C.

The conditioning was carried out in distilled water of 21 °C and 70 °C.
The dynamic-mechanical measurements were performed with an automatic torsional pendulum ATM3 of Myrenne, Roetgen, FRG at a frequency of constantly 1 Hz.
The water concentrations are detected by the weight change of the samples.

RESULTS AND DISKUSSION

The effect of water as plasticizing agent can be detected by the depression of the glass-transition temperature (Tg). Water clusters trapped in micro-voids show no influence on Tg. A significant increase of the relative damping factor ($\tan\delta_{rel}$) is observed instead. It is defined as the quotient of the loss tangent of each sample ($\tan\delta$) and the loss tangent of the dry sample ($\tan\delta_0$) at a given temperature:

124

$$\tan\delta_{rel} \equiv \frac{\tan\delta}{\tan\delta_o}$$

Fig. 1 shows the dependence of these relative values at 0 °C on the amount of incorporated water. The water conditioning has been done at 70 °C.
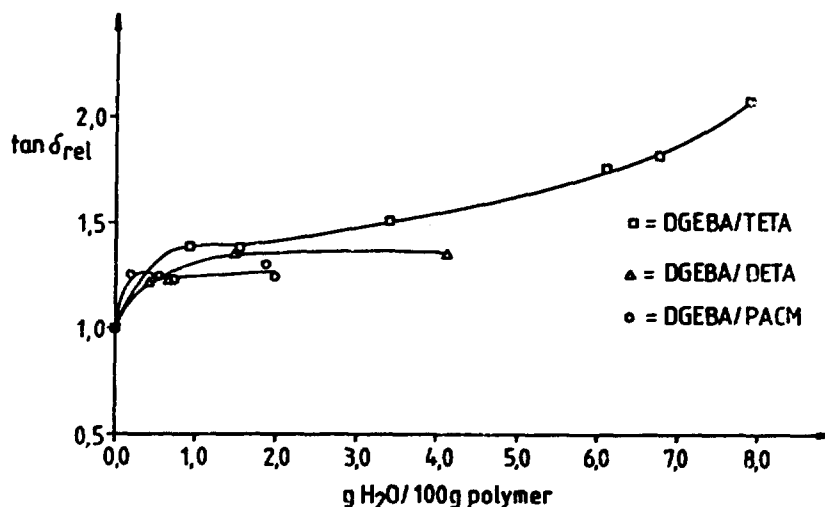

Fig. 1: Relative loss tangent at 0 °C versus water content

All resin systems show an increasing relative loss tangent due to incorporation of a first small amount of water. Two of them approach a constant value. Only the system DGEBA/TETA shows an additional increase in the relative loss tangent with increasing water absorption. Using a method of Apicella [1] it was calculated, that this system contain significantly higher amounts of water in micro–voids compared to the other resin systems. These water filled micro–voids disturb the energy transfer within sample and the damping increases.

Fig. 2 shows the watersorption of the unreinforced in comparison with the reinforced system (DGEBA/TETA) at 70 °C. The water concentrations are related to the resin content. The square root of time is related to the thickness of the samples (d). In this figure, the water sorption of the composite was lower than the sorption of the unreinforced material. Later the curves cross over and the water content of the laminate becomes higher than that of the pure resin system. This suggests that an additional mechanism of water sorption is active in the composite and it is probable that the additional water is located in the region of the interphase. This water sorption causes an additional relaxation in the damping characteristics of the composite (Fig. 3), which was not observed in the unreinforced material.
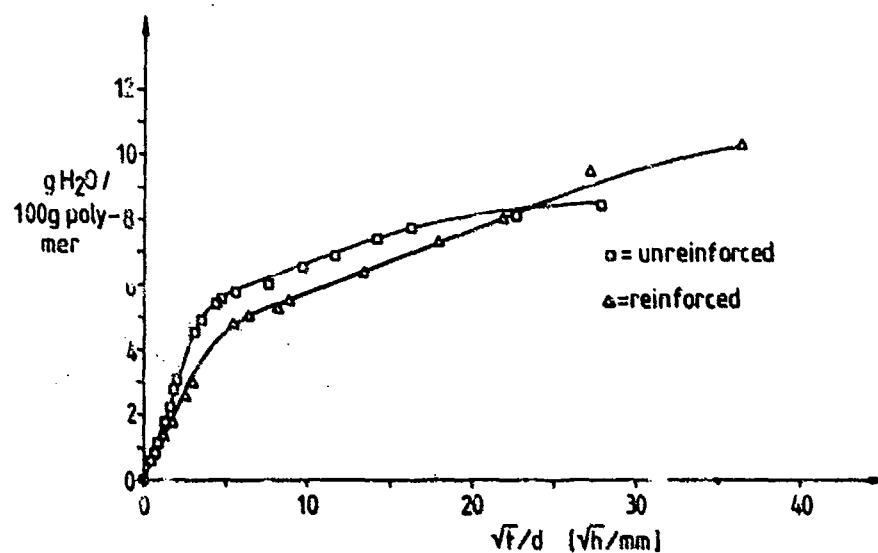
Fig. 2: Sorption of water of the reinforced and unreinforced resin system DGEBA/TETA at 70 °C (reinforcement: 92111 Finish I 550)
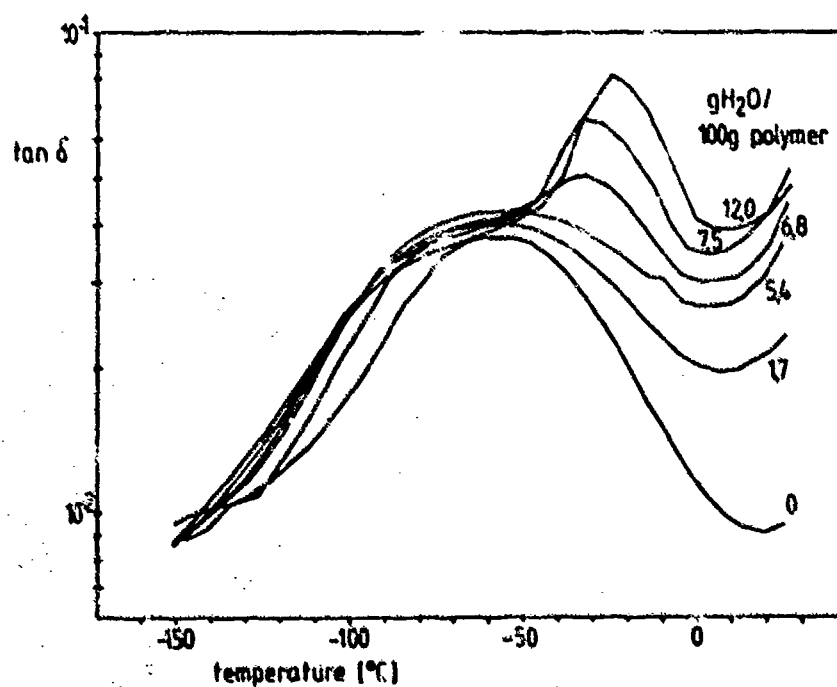

Fig. 3: Damping characteristics of the reinforced system DGEBA/TETA at different water contents (conditioning at 70 °C, reinforcement: 92111 Finish I 550)

The intensity of the new relaxation grows with increasing concentration of water and is shifted to higher temperatures. The relaxation temperature in addition depends on the surface treatment of the glass fibers. The relaxation was also observed by Williams [2] at glass reinforced epoxy resins by conditioning in boiling water. It may be explained by an interaction of glyceryl units in the vicinity of the glass surface with water. These hydrated units may cause the new relaxation observed in the damping curve [2].

If water sorption is performed at 21 °C the additional relaxation only can be observed if a glass fibre with a hydrophilic surface treatment (e.g. textile–size) is used as reinforcing material. Other surface treatments require a higher sorption temperature. After drying, the additional relaxation has vanished. Its appearence may indicate the incorporation of water in the polymer–glass interphase.

Fig. 1 has shown, that water in micro–voids increases the relative loss tangent. This effect must be enhanced if water is incorporated in the interphase or at the interface because the energy transfer from the resin to the fiber would be disturbed.

Fig. 4 shows the relative loss tangent of the composite of DGEBA/PACM at 0 °C depending on the water concentration at different temperatures of conditioning.

Fig. 4: Relative loss tangent at 0 °C in dependence of the water content of the reinforced resin–system DGEBA/PACM at different water conditioning temperatures

The appertaining unreinforced system shows only a small formation of micro–voids. Therefore the significant increase of the damping at later stages of the water sorption at 70 °C must be caused by the disturbance of the interphase. This disturbance can also be prove by an optical method [3]. The water concentrations, estimated from both methods for the occurence of interphase disturbance are equal.

The absorption of water at room temperature (21 °C) causes no incorporation of water in the interphase. The damping at 0 °C has the same origin as in the unreinforced material. This fact is also supported by results from the optical method.

Other systems already show a disturbance of the interphase by water sorption at room temperature. Fig. 5 represents the dependence of the relative loss tangent of the reinforced system DGEBA/TETA to the sorbed moisture.
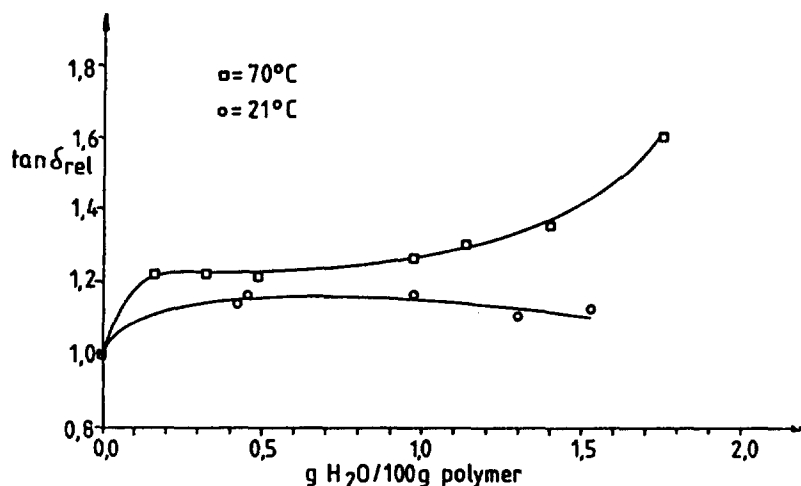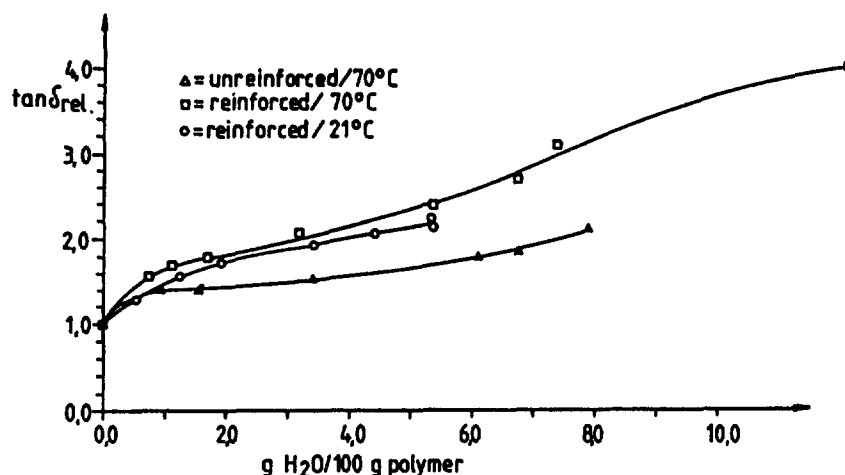
Fig. 5:   Relative loss tangent at 0 °C in dependence of the water content of the reinforced resin system DGEBA/TETA at different water conditioning temperatures

It's pointed out that this system shows significant deviations from the behaviour of the unreinforced material, even at water conditioning at 21 °C. The reinforced system DGEBA/DETA shows a qualitative equivalent nature. This means that in these systems the incorporation of water into the interphase can occur at even moderate conditions, whereas for the PACM–crosslinked system more drastical conditions are neccesary.

It is known from other investigations [4] that the interphase of the reinforced systems DGEBA/TETA and DGEBA/DETA have interrupted adhesion features. On the contrary the system DGEBA/PACM shows a strong interaction between polymer and reinforcing material, with a high immobilization of the polymeric chains in the interphase. This can be shown by the shift of the glass transition temperature of the reinforced system to higher temperatures in comparison with the unreinforced material [4]. Therefore further influences of the interphase caused by water are more easily in the reinforced systems DGEBA/TETA and DGEBA/DETA, whereas incorporation of water in the interphase needs stronger conditions in the DGEBA/PACM–system.

REFERENCES

[1]   A. Apicella, L. Nicolais, G. Astarita, E. Drioli
       Polymer 20 (1979) 459

[2]   J.G. Williams
       Journal of Materials Science 17 (1982) 1427

[3]   T. Marzi, U. Schröder, M. Heß, R. Kosfeld
       "Wasserbestimmung in glasfaserverstärkten Epoxidharzen"
       GIT–Verlag Tagungsband zur InCom 1990, in press

[4]   U. Schröder, T. Marzi, M. Heß, R. Kosfeld
       "The influence of annealing on the behaviour of epoxy–glass interphases"
       MRS–Fall–meeting Boston (1989)

THE INFLUENCE OF ANNEALING ON THE
BEHAVIOUR OF EPOXY–GLASS INTERPHASES

U. Schröder, T. Marzi, M. Heß, R. Kosfeld°
Department of Physical Chemistry, University of Duisburg
D–4100 Duisburg, FRG

ABSTRACT

Dynamic–mechanical measurements were used to study the properties of the interphase in glass fibre reinforced epoxy resins. The immobilisation of the polymer chains in the interphase is determined by the curing system, the annealing process, and the surface treatment of the glass fibres.

INTRODUCTION

Incorporation of filler into a polymer matrix is accompanied by changes in mechanical and thermal properties. These are mainly due to:
- a partial substitution of volume by the filler, which in general consists of a high–modulus material (volume effect)
- an increasing inner surface and thus an enhanced interaction on the microscopic scale (surface effect)
- interactions between polymer and filler (adhesion effect)

The dynamic–mechanical experiment is an excellent tool to analyze the properties of reinforced polymers.

Of great importance is the structure of the interphase which leads from the surface of the filler to the polymer with bulk properties.

The behaviour of this interlayer does influence the elastic properties of the whole system to a not negligible extent [2].

MATERIALS AND METHODS

- resin: Rütapox 0166/S20 (trade–name), Bakelite GmbH, Duisburg, FRG
                main component: bisphenol–A–diglycidether (DGEBA)
- curing agent:
                Rütapox SL (trade–name) main component:
                bis(p–amino–2–methyl–cyclohexyl)methane (PACM)
                Rütapox VE2896 (trade–name) main component: triethylene–tetramine (TETA)
- reinforcing material:
                glass fabrics (92111, weave type linen and 91945, weave type atlas 1/7) from Interglas, Ulm, FRG with different surface treatments
                a)   finished with I 550 (trade–name)
                b)   equipped with a textile size
                c)   textile size thermally removed

The reinforced specimen were prepared at room temperature from four layers of glass fabrics by hand–laminating. The unreinforced samples were molded in a silicone rubber mould. Sample size: 57 mm x 6 mm x 1 mm. After 12 h curing at room temperature the samples were subsequently kept at 120 °C for 17 h.

A torsional pendulum working at 1 Hz constantly, Fa. Myrenne, Roetgen, FRG, was used to measure the dynamic-mechanical behaviour in the temperature range from –150 °C to 200 °C with an angle of torsion of 1° and heating rates of 1K/min and 3K/min, respectively [2].

The inflection point of the G'(T) trace was chosen as a measure for the glass—transition temperature (Fig. 1).

The reproducibility of the glass—transition temperature was ± 1K (heating rate: 3K/min) resp. ± 0,5 K (heating rate: 1K/min).

RESULTS AND DISCUSSION
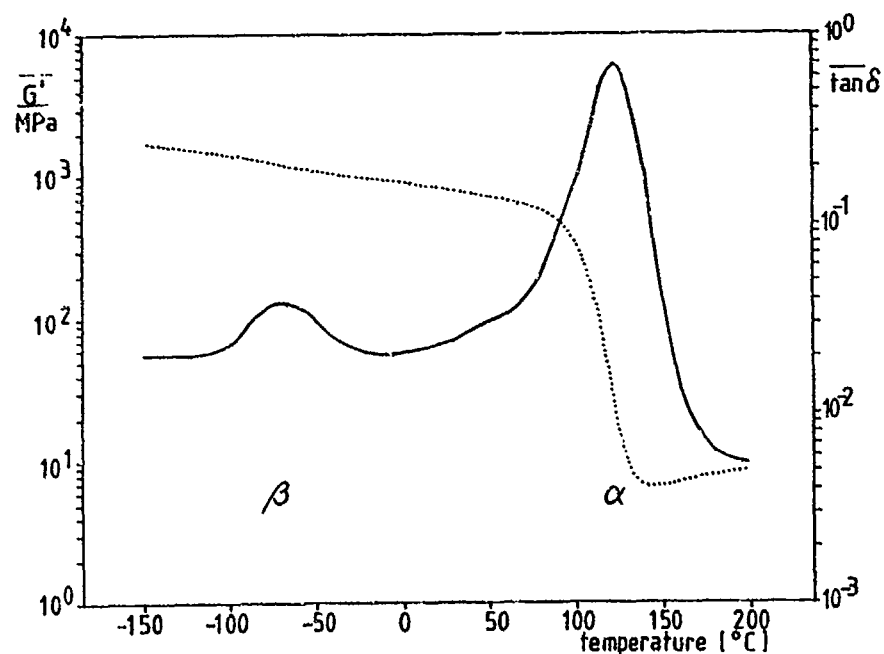
Fig. 1   Dependence of G' and tanδ as a function of temperature for the system DGEBA/PACM

Upon heating the region of the β–relaxation indicates the beginning motion of hydroxyether and diphenylpropane segments [1]. The region of the α–relaxation is identified with the glass–transition where the motion of longer chain segments begins.

Table 1 and 2 show the glass–transition temperatures of the resin after curing with the two different types of amines with and without reinforcing glass fabrics.

Table 1: Glass–transition temperature of the system DGEBA/PACM with and without reinforcing glass fabrics

reinforcement	Tg [°C]
unreinforced	115.5
92111+finish	124
92111+textile size thermally removed	124
92111+textile size	123
91945+finish	124
91945+textile size	122

Table 2: Glass–transition temperature of the system DGEBA/TETA with and without reinforcing glass fabrics

reinforement	Tg [°C]
unreinforced	98.5
92111+finish	98
92111+textile size thermally removed	95.5
92111+textile size	92
91945+finish	96
91945+textile size	93

Comparing the reinforced systems with the unreinforced ones, the particularity of the cycloaliphatic curing agent PACM becomes obvious:

The glass–transition temperatures of the reinforced samples are higher with PACM, which indicates a stronger interaction of the glass surface with the PACM than with the TETA cured system.

The fact that physical and/or chemical interactions, which decrease chain mobilities in the vicinity of a filler lead to a rise of the glass–transition temperature, is well known [3,4]. An interphase connecting glass–surface and bulk polymer, which shows thermal and viscoelastic properties different from the bulk polymer is discussed.

One possible way to investigate such a complex multiphase structure is to examine the mechanical relaxation process influenced by annealing. Fig. 2 shows the temperature dependence of the α–transition (glass–transition) of the pure cured resin compared to the reinforced material with PACM as curing agent.

In order to avoid further annealing during the measurement, the heating rate was enhanced to 3K/min. These values are slightly shifted to those measured at 1K/min.

It is obvious, that annealing increases crosslinking density. This can be deduced from the trace of the unreinforced sample, as the temperature of the α–transition is shifted to higher values with increasing annealing time. Compared to reinforced material there remains a clear difference, even after 17 h of annealing. These differences are only found after such a subsequent thermal treatment and indicates that the interaction between the polymer and the glass surface is strongly influenced by the thermal history of the sample. This is quite in contrast to the behaviour of the glass transition temperature which can be detected in the TETA–cured system after annealing (fig. 3).

Fig. 2: Dependence of the glass–transition temperature as a function of the annealing time at 120 °C of the system DGEBA/PACM with and without glass fabrics
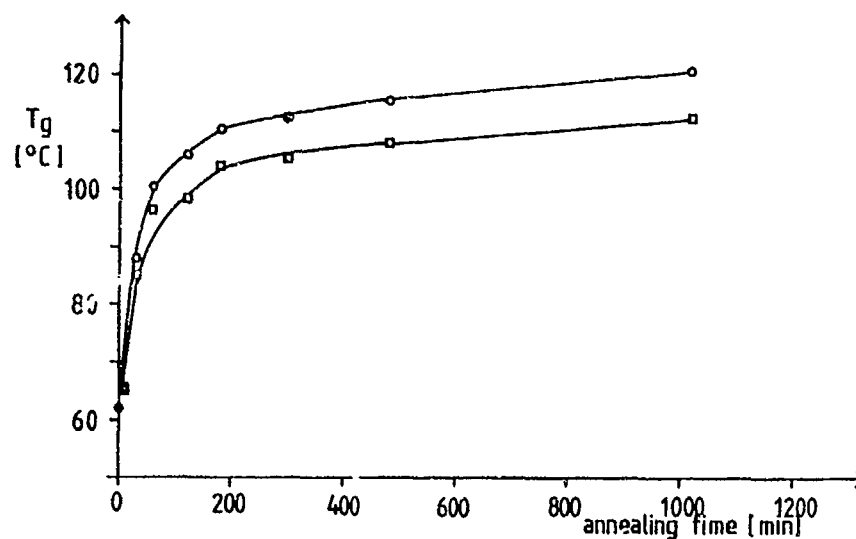□ = without glass fabric; o = with glass fabric (92111+finish)

Fig. 3: Dependence of the glass–transition temperature as a function of the annealing time at 120 °C of the system DGEBA/TETA with and without glass fabrics
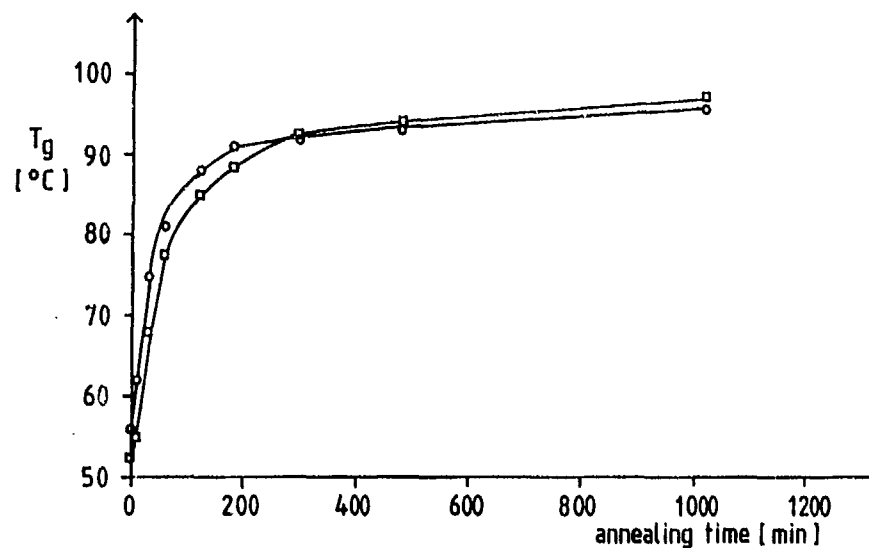□ = without glass fabric; o = with glass fabric (92111+finish)

In this case, on the contrary, just the unreinforced sample shows a higher characteristic temperature for the α-relaxation than the reinforced material shows after the subsequent thermal treatment.

The difference in behaviour becomes more pronounced if

$$\Delta Tg = Tg(\text{reinforced}) - Tg(\text{unreinforced})$$

is plotted versus annealing time, as shown in fig. 4.
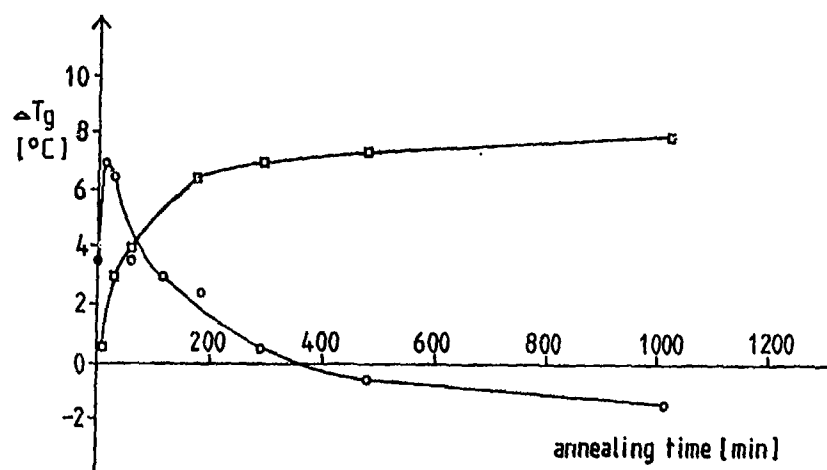
Fig. 4:   Dependence of ΔTg as a function of annealing time
□ = DGEBA/PACM;   o = DGEBA/TETA

There are basically different effects observable. As the type of the resin and the type of the glass fabrics are identical the effects are caused by different structures of the curing resin. In the PACM system the fixation of stresses which occur during crosslinking and annealing are able to relax to a high extent.

As this is not the case in the TETA cured system, these stresses, which will be mainly concentrated at the interphase, lead to partial delamination. This is due to steric hinderance caused by the closer vicinity of the reacting groups compared to PACM. This was supported by sorption measurements with water [5].

Thermally induced subsequent crosslinking increase crosslink density, and this supports the building up of stress areas. The delamination is further enhanced if the surface itself shows no optimum conditions for an interaction with the resin as this is the case if there is a textile size of the fibre. Fig. 5 shows the effects for differently pretreated fibre surfaces.

134
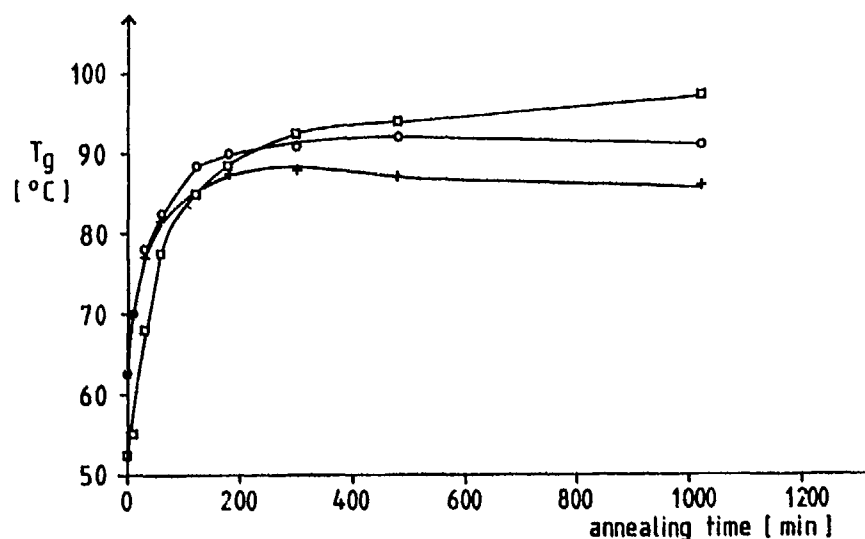
Fig. 5: Dependence of the glass—transition temperature as a function of annealing time at 120 °C of the system DGEBA/TETA with and without glass fabric
□ = without glass fabric; o = with glass fabric (92111+textile size thermally removed); + = with glass fabric (92111+textile size)

Insufficient interaction with the surface is reported by clearly lower Tg—values of the reinforced material compared to the unreinforced. In the case of a texile size treated surface there is even a further decrease of Tg after 5 h observable indicating increasing defects which lead to more flexible chains.

LITERATURE

[1]   M. Schrager, J. Carey
      Polymer Engineering and Science 10 (1970) 568

[2]   K.H. Illers, H. Breuer
      Koll. Zeitschrift 176 (1961) 110

[3]   H. Ishida, J.L. Koenig
      Polymer Engineering and Science 18 (1978) 128

[4]   T.B. Lewis, L.E. Nielsen
      Journal of Applied Polymer Science 14 (1970) 1449

[5]   T. Marzi
      Dissertation Universität –GH– Duisburg in press

ACID/BASE INTERACTIONS WITH SILICON CARBIDE FIBER

SHELDON P. WESSON* AND RONALD E. ALLRED**
*TRI/Princeton, P.O. Box 625, Princeton, NJ 08542
**PDA Engineering, Materials Development Department, 3754 Hawkins NE, Albuquerque, NM 87109

ABSTRACT

Silicon carbide fiber surfaces were analyzed by programmed thermal desorption and inverse gas chromatography, using Lewis acids and bases as probe adsorbates to compare the effect of RF glow discharge plasma and thermal treatment on surface energetics. Changes in surface acid/base character were correlated with wetting data, surface titrations, and surface chemical composition deduced from x-ray photoelectron spectroscopy. Thermal treatment did not alter fiber surface energetics significantly. Plasma treatment rendered the surface more acidic and more basic. XPS and thermal desorption analysis indicate that the plasma removed strongly adsorbed organic contaminants, exposing and activating the underlying glassy surface.

BACKGROUND

Silicon carbide fiber is manufactured by spinning, curing and pyrolyzing a polycarbosilane precursor [1]. These surfaces exhibit poor interfacial bonding with polymeric matrices [2]. This study is a survey of surface properties of silicon carbide fiber, and describes efforts to activate the surface prior to chemical modification. Unsized Dow Corning NICALON^{tm} filament was characterized as received, after applying an oxidative plasma (designated XA1, PDA Engineering), and after thermal treatment.

MATERIALS AND METHODS

XPS

X-ray photoelectron spectra were obtained by Rocky Mountain Laboratories, Inc., Golden, CO, using a Surface Sciences SSX-100 spectrometer with an Al Kα source. High resolution C$_{1s}$ peaks were averaged over 10 to 15 scans using a spot size of 300 μm^2 with the flood gun at 1 eV. Gaussian curve fitting was used to deconvolute high resolution photopeaks into components based on binding energy references from model compounds.

Titrations

Fiber specimens were dried under vacuum (5 kPa) for one hour at 50°C prior to titration in toluene with 1,2-diphenylguanidine for acid groups, and diphenyl phosphate for basic groups [3]. Fibers were reacted for 15 to 30 minutes with the appropriate acid or base solution prior to back titration. The indicator range of bromophthalein Magenta E (pH 3.0 to 4.4) was corrected with blank titrations.

Wetting

Fiber wettability was measured by the Wilhelmy technique using methylene iodide (nonpolar oil), formamide (Lewis base), and ethylene glycol (Lewis acid). Monofilaments were glued to metal hooks and suspended vertically from the working arm of a Cahn 2000 microbalance, while a precision elevator raised and lowered a liquid surface along 15 mm of fiber. The method and analysis were described previously [3].

Programmed Thermal Desorption

Desorption polytherms were obtained by loading a nickel column (55 cm by 1/4" i.d.) with 4g to 5g of fiber, a quantity that provides about 0.4 square meters of surface for investigation, with no pressure drop across the column. Nitrogen carrier gas was maintained at a flow rate of 24 cc/min in an HP 5880 gas chromatograph fitted with a flame ionization detector (FID). Thermal desorption polytherms were obtained by collecting signals from the FID and oven thermometer at 2 Hz as columns were subjected to linear temperature ramping from 30° C to 300° C at 5° C per minute. Detector response was monitored at zero attenuation. Thermal desorption polytherms are presented as FID response normalized for total surface area in the column *versus* column temperature.

Inverse Gas Chromatography

Chromatograms were obtained at the minimum attenuation required to maintain the detector signal below saturation at peak maximum; zero attenuation was implemented after the signal fell below 0.02% of saturation, permitting measurement of desorption at low coverage with maximum resolution. Chromatograms using t-butylamine and t-butanol were collected over periods of 3000 seconds. The method for transforming chromatograms to isotherms was described previously [3].

RESULTS

XPS

Concentrations of surface constituents for the two fiber specimens are listed in Table I. Components of the high resolution C_{1s} envelope are presented in Table II.

Table I. Surface Composition of Silicon Carbide Fiber

Species	Untreated, at%	XA1 plasma, at%
O	44.06	36.89
Na	0.61	0.65
N	2.12	2.14
Ca	0.52	——
C	28.54	34.80
Cl	1.53	1.12
Si	22.62	24.39

Table II. Components of C_{1s} Photopeaks

Binding Energy, eV	Species	Untreated	XA1 plasma
		percent of C_{1s} photopeak	
283.4	SiC	28.6	27.3
284.8	primary carbon	50.9	59.9
286.3	hydroxyl, ether, ester single bond	14.8	9.5
288.6	carboxyl, ester double bond	5.7	3.3

Titrations

Values listed in Table III are averages from titrations performed in triplicate.

Table III. Surface Site Titrations

Substrate	Acid Sites/nm^2	Basic Sites/nm^2
Untreated	1.6 ± 0.6	———
XA1 plasma	3.8 ± 1.3	———

Wetting

Advancing work of adhesion for methylene iodide, formamide, and ethylene glycol on the two silicon carbide specimens is presented in Table IV.

Table IV. Silicon Carbide Fiber Wettability, mN/m

Substrate	CH_2I_2		$HCONH_2$		$HOCH_2CH_2OH$	
	W	γ_s^d	W	$W^{a/b}$	W	$W^{a/b}$
Untreated	76.9	29.5	107.7	39.4	96.3 †	37.5
XA1 plasma	79.4	31.4	111.6	41.2	93.1	32.3

† probe spread on fiber

Programmed Thermal Desorption

Figure 1 shows thermal desorption from untreated silicon carbide fiber. The dotted curve shows evolution of adsorbed contaminants when no probe was placed on the column. The solid curve shows desorption of t–butylamine and contaminants from a fresh charge of fiber. The chemisorptive capacity of the substrate is taken as twice the area under the solid curve from 30°C to the maximum at 60°C. Figure 2 displays thermal desorption of t–butylamine and contaminants from plasma treated fiber. Table V lists chemisorptive capacities of substrates before and after thermal treatment.

Table V. Chemisorptive Properties of Silicon Carbide Fiber

Substrate	Moles Desorbed, volt·°C/m^2	
	As Received	300°C
	t–butylamine	
Untreated	4.0 [1]	7.3 [2]
XA1 plasma	13.0 [3]	12.7 [3]
	t–butanol	
Untreated	0.3 [4]	0.8 [4]
XA1 plasma	2.1 [5]	1.4 [5]

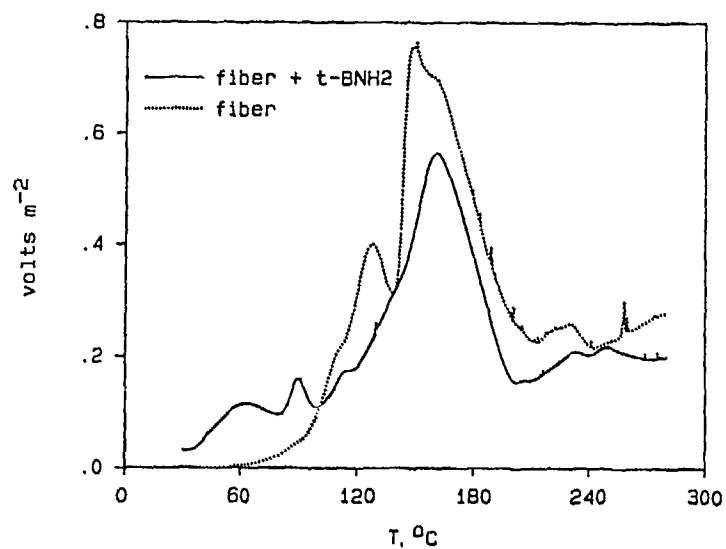T_{max} = ([1]) 60°C, ([2]) 70°C, ([3]) 75°C, ([4]) 50°C, ([5]) 52°C

Figure 1.   Thermal desorption from untreated silicon carbide fiber.   Dotted curve
denotes evolution from fiber without probe. Solid line shows evolution after
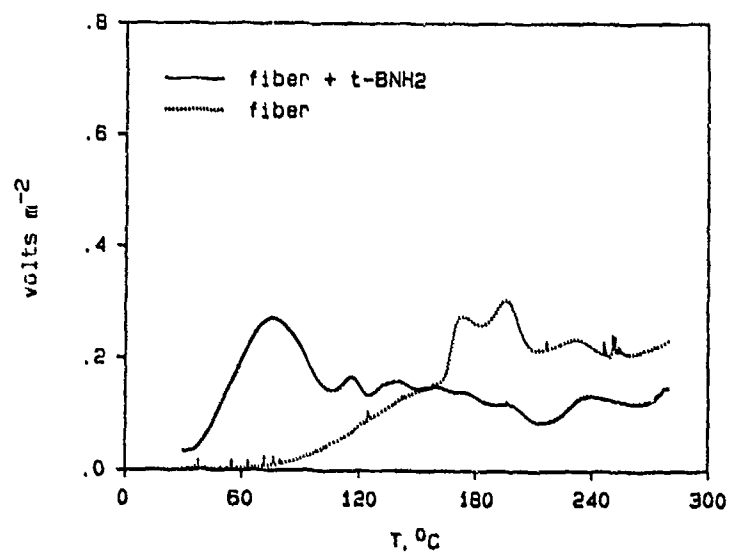injection of *t*-butylamine.

Figure 2.   Thermal desorption from silicon carbide fiber after oxidative plasma
treatment. Dotted curve denotes evolution from fiber without probe. Solid
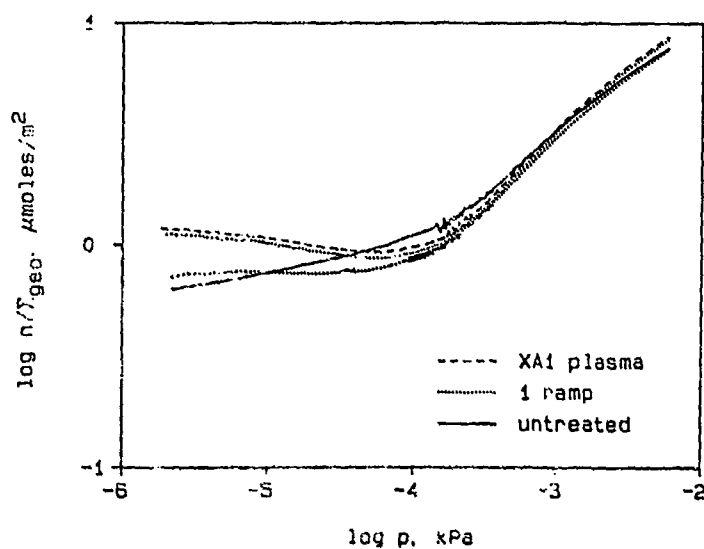line shows evolution after injection of *t*-butylamine.

Figure 3. Physical adsorption isotherms for *t*–butylamine on silicon carbide fiber at 30°C. Solid line denotes adsorption on untreated fiber. Dashed line shows adsorption on plasma treated surface. Dotted curves indicate isotherms for both specimens after thermal treatment to 300°C.

Figure 4. Physical adsorption isotherms for *t*–butanol on silicon carbide fiber at 30°C. Solid line denotes adsorption on untreated fiber. Dashed line shows adsorption on plasma treated surface. Dotted curves indicate isotherms for both specimens after thermal treatment to 300°C.
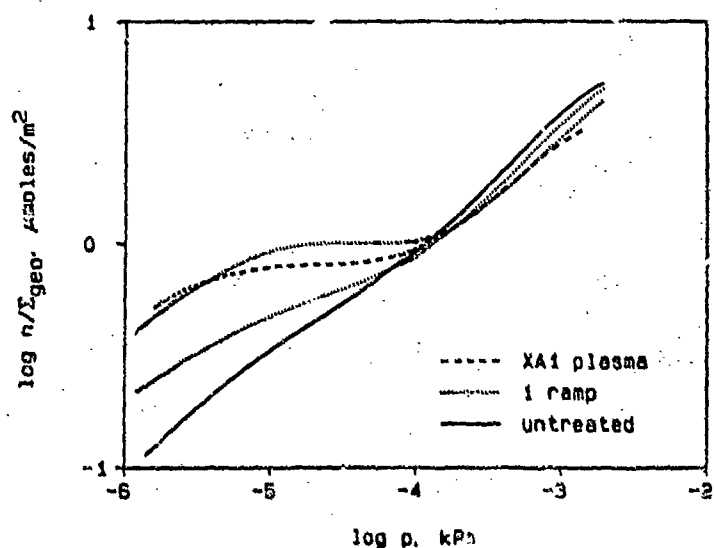
<u>Inverse Gas Chromatography</u>

Diffuse profiles of chromatograms were transformed to isotherms [3]. Adsorption volumes are expressed as n/Σ_{geo} (μmoles/m^2) to normalize the isotherms for all experimental conditions except differences in adsorption energetics. Figure 3 shows physical adsorption isotherms obtained by eluting untreated silicon carbide fiber with 2 μl injections of t–butylamine, a Lewis base. The solid curve shows adsorption on untreated fiber, as received. The adjacent dotted curve shows adsorption on untreated fiber after thermal treatment to 300°C. Dashes denote the isotherm on plasma treated fiber; the adjacent dotted curve is the isotherm after heat treatment.

Adsorption isotherms obtained with 0.5 μl injections of t–butanol, a Lewis acid, are presented in Figure 4. The solid line denotes untreated fiber; plasma treated fiber is shown with dashes; dotted curves indicate heat treated specimens.

DISCUSSION

The dotted desorption polytherms in Figures 1 and 2 show that plasma treatment scours organic contaminants from the fiber surface. The chemisorptive capacity for both the acidic and basic probes increases significantly upon plasma treatment (see Table V). The desorption temperature for the basic probe increased from 60°C to 75°C, evincing stronger solid/vapor interaction with the plasma treated surface. Heating to 300°C activates the untreated fiber surface, but not to the extent achieved by the plasma. Heating deactivates plasma treated surfaces slightly, perhaps because of readsorption of contaminants onto the highest energy sites.

Physical adsorption isotherms confirm the trends shown by thermal desorption. All of the isotherms in Figure 3 show substantial adsorptive capacity below 10^{-4} kPa; adsorption at low pressures results from the basic probe interacting with strongly acidic sites. Plasma treatment increases the adsorptive capacity in the low pressure sector of the isotherm; the effect of thermal treatment is minor. Analagous trends are seen when a Lewis acid is used as the probe vapor (Figure 4). The net effect of plasma treatment is to render the surface more acidic, and more basic, by removing surface contaminants.

Wet chemical titrations (Table III) corroborate the increased surface acidity indicated by adsorption experiments. (Diphenyl phosphate interacts anomalously with silica surfaces, obviating the basic site determination).

Wetting measurements in Table IV are insensitve to changes in surface energetics shown by other techniques. All of the values for formamide and ethylene glycol (the basic and acidic probe, respectively) are near the upper limit imposed by spreading. This demonstrates the limitations of wetting for characterizing high energy substrates.

Plasma treatment increases the surface silicon concentration, as shown by the XPS results in Table I. It is likely that enhanced acidity results from a larger surface concentration of silanol groups, since the hydroxyl and carboxyl components of the C_{1s} photopeak diminish with plasma treatment (Table II). The higher hydrocarbon content seen on plasma treated surfaces (Table II) is attributed to adventitiously adsorbed contaminants on the activated substrate. The net effect of plasma treatment is to remove oxidised carbon residues, activating the surface to behave as a getter for ambient aliphatics. The origin of the basicity of silicon carbide fiber is unclear, but may arise from silone or geminal hydroxyl functionality. The amphoteric nature of this substrate may be explained in more detail with high resolution analysis of the Si_{2p} photopeak.

REFERENCES

1.   Y. Hasegawa and K. Okamura, J. Mater. Sci. 21, 321, (1986).

2.   R.A. Petrisco and G.L. Stark, 33rd Int. SAMPE Exh. Proc., 13, (1987); SAMPE Eng. Series 33, 1015, (1988).

3.   S.P. Wesson and R.E. Allred, in <u>Inverse Gas Chromatography</u>, edited by D.R. Lloyd, T.C. Ward and H.P. Schreiber (ACS Symposium Series 391, Washington DC, 1989), p.203.

SPREADING OF LIQUID DROPLETS ON CYLINDRICAL
SURFACES: ACCURATE DETERMINATION OF CONTACT ANGLE.

H. DANIEL WAGNER, E. WIESEL, H. E. GALLIS
Polymeric Composites Laboratory, Materials Research Department, The
Weizmann Institute of Science, Rehovot 76100, Israel

ABSTRACT

The wetting of cylindrical monofilaments by liquid polymers is a
problem of much scientific and technological importance. In particular,
the characterization of the physicochemical nature of interfaces is a key
problem in the field of advanced fibrous composites. The macroscopic
regime contact angle, which reflects the energetics of wetting at the
solid-liquid interface, is difficult to measure by usual methods in the
case of very thin cylindrical fibers.

In the present article a numerical method is proposed for the
calculation of macroscopic regime contact angles from the shape of a
liquid droplet spread onto a cylindrical monofilament. This method, which
builds on earlier theoretical treatments by Yamaki and Katayama [1], and
Carroll [2], very much improve the accuracy of the contact angle obtained.
Experimental results with high-strength carbon, para-aramid, and glass
fibers, are presented to demonstrate the high degree of accuracy of the
method proposed.

INTRODUCTION

The characterization of the physicochemical nature of interfaces is a
key problem in the field of advanced fibrous composites. The macroscopic
regime contact angle, which reflects the energetics of wetting at the
solid-liquid interface, is difficult to measure by usual methods in the
case of very thin cylindrical fibers. Indirect measurement of contact
angles by means of a wetting microbalance apparatus has some
disadvantages. A method for determining the contact angle of liquid
droplets on cylindrical surfaces was developed simultaneously and
independently by Yamaki and Katayama [1], and Carroll [2]. Unfortunately,
measurements of the contact angle based on this method are, so far, unable
to provide an accuracy of better than about 5 degree. In the present
article a simple extension of the method of Yamaki and Katayama, and
Carroll, is presented, from which highly accurate values of the contact
angle may be obtained. This is demonstrated experimentally from the
spreading of glycerol droplets on carbon fibers, and epoxy droplets on
aramid and glass fibers.

PROFILE OF A LIQUID DROPLET ON A MONOFILAMENT

The Method of Yamaki, Katayama, and Carroll

Yamaki and Katayama [1] and Carroll [2] have derived an analytical
expression for the reduced droplet length L as a function of the reduced
maximum droplet thickness T and of the macroscopic contact angle θ (see
Figure 1), as follows:

$$L = 2[a \, F(\phi, \, k) + T \, E(\phi, \, k)] \tag{1}$$

where L=(droplet length/cylinder radius), T=(droplet half-thickness/cylinder radius), and a is given by

$$a = \frac{T\cos\theta - 1}{T - \cos\theta} \tag{2}$$

F and E are Legendre's standard incomplete elliptic integrals of the first and second kind, respectively, which are tabulated. The arguments ϕ and k are calculated by using the expressions:

$$\sin\phi = \left(\frac{1}{k^2}\left(1 - \frac{1}{T^2}\right)\right)^{\frac{1}{2}} \tag{3}$$

and

$$k^2 = 1 - \frac{a^2}{T^2} \tag{4}$$

(In the above analysis, the effect of gravity is neglected and the droplet is assumed to be in thermodynamic equilibrium). Since the dependence on the contact angle in Equation 1 is complex this expression cannot be inverted and the contact angle must be obtained by reading from a plot of L against T where lines corresponding to various values of θ are drawn. This involves a great deal of reading error, as observed in our laboratory as well as by other researchers [3, 4]. This will be illustrated in an example later.

We have developed a simple numerical algorithm by which the contact angle may be determined with very high accuracy [5]. This algorithm, now described, helps exploit to its full extent the method proposed by Yamaki and Katayama, and Carroll.
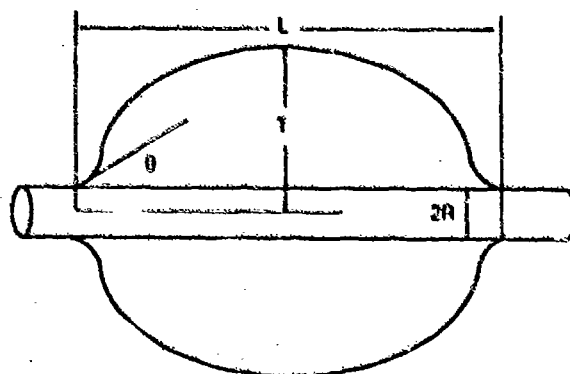

Figure 1: Liquid droplet on a cylindrical monofilament.

Accurate Contact Angle Determination

First Equation 1 is modified as follows. Rather than Legendre's form, the symmetrised variants [6] of the incomplete elliptic integrals of the first and second kind are preferred for computational purposes:

$$R_F(x,y,z) = \frac{1}{2}\int_0^\infty \frac{d\xi}{\sqrt{(\xi+x)(\xi+y)(\xi+z)}} \tag{5a}$$

$$R_D(x,y,z) = \frac{3}{2}\int_0^\infty \frac{d\xi}{\sqrt{(\xi+x)(\xi+y)(\xi+z)^3}} \tag{5b}$$

Then it can be shown that Legendre's standard integrals can be expressed in terms of R_F and R_D as follows:

$$F(\phi,k) = (\sin\phi)\, R_F(\cos^2\phi,\ 1-k^2\sin^2\phi,\ 1) \tag{6a}$$

$$E(\phi,k) = (\sin\phi)\, R_F(\cos^2\phi,\ 1-k^2\sin^2\phi,\ 1)$$
$$- \frac{1}{3}k^2\sin^3\phi\, R_D(\cos^2\phi,\ 1-k^2\sin^2\phi,\ 1) \tag{6b}$$

In view of equation 3, useful simplifications arise as follows: (i) The first argument (i.e. $\cos^2\phi$) of R_F and R_D in equations 6a and 6b is calculated in a straightforward manner; (ii) The second argument (i.e. $1-k^2\sin^2\phi$) of R_F and R_D in equations 6a and 6b may be immediately replaced by $1/T^2$.

Equation 1 is now rewritten in terms of R_F and R_D by means of equations 6a and 6b:

$$L = 2[\sin\phi\, (a+T)\, R_F - \frac{1}{3}Tk^2\sin^3\phi\, R_D] \tag{7}$$

Based· on equation 7 the following scheme was adopted for accurate determination of θ (the values L^* and T^* are measured experimental readings):

(1) A first guess θ_1 of the contact angle is chosen (using Carroll's plot), and a value T_1 is calculated using Equations 1 to 4, and T^*.

(2) A second guess θ_2 is made (close to the first one), and a second value L_2 is calculated as in (1);

(3) A value θ_3 is obtained by the interpolation (with i=3)

$$\theta_i \approx \frac{\theta_{i-2} - \theta_{i-1}}{L_{i-2} - L_{i-1}} L^* + \frac{L_{i-2}\theta_{i-1} - L_{i-1}\theta_{i-2}}{L_{i-2} - L_{i-1}} \tag{8}$$

(4) The value of the contact angle obtained is then compared to the previous one and if the difference between these is larger than a predetermined threshold value the process is continued (with i=4, 5,...) until a satisfactorily accurate value is obtained.

A Fortran 77 program was prepared based on the scheme proposed above, which proved to be simple, accurate and reliable. In [5] we plotted the contact angle (in the range $0° \leq \theta \leq 90°$) as calculated from the above method, against the reduced droplet length for reduced droplet thicknesses ranging between 1.5 and 5. The accuracy of the contact angle obtained from this plot was found to be better than that obtained from Figure 2 in Carroll's paper [2]. However the use of the Fortran program in an interactive mode yields much more accurate values of θ than those read from the plot in [5], and this is the preferred method.

Experimental Example

To illustrate the method, we use some results recently obtained in our laboratory (at room temperature) with (i) droplets of glycerol spread on ex-polyacrylonitrile extra high strength carbon fibers (ACIF-XHT, diameter of 6.8 μm, from Afikim Carbon Fibers, Israel), (ii) droplets of epoxy resin (CY 223 from Ciba Geigy, no hardener used) spread on single para-aramid filaments (Kevlar 49, diameter of 11.9 μm, from du Pont de Nemours, Inc.), and (iii) droplets of epoxy resin (DER 331 from Dow Chemical, no hardener used) spread on glass fibers (E-glass 5139, diameter of 18 μm, from Vetrotex International). For the carbon/glycerol system the average contact angle from 9 droplets is 55.8° with a coefficient of variation of 14.7 pc. This result is very close to the one obtained by Chang et al. [7] for the same system by using the Wilhelmy (electrobalance) technique, namely 58.9°. For the aramid/epoxy system the average contact angle from 14 droplets is 15.8° with a coefficient of variation of 19.3 pc. For the glass/epoxy system the average contact angle from 27 droplets is 19.7° with a coefficient of variation of 8.5 pc.

The scheme presented here for the measurement of the contact angle of each droplet gives much more accurate results for the contact angle than the evaluations from Carroll's plot (Figure 2 in Reference 2). For example, a range of 45-50° is found from Carroll's plot for a glycerol droplet on carbon fiber, with reduced droplet length equal to 10 and reduced thickness equal to 4, whereas an accurate value of 48.42° is found with our method.

Note that with very thin fibers (such as carbon) the droplet-to-droplet variability in contact angle is relatively large, whatever the method, and that the improvement in accuracy on the contact angle is very clear on a per droplet basis only. The fibers tested here had an epoxy-based surface sizing, and it is probable that inhomogeneities on the fiber surface due to the application of the sizing are partly responsible for this variability. Contact angle results currently obtained in our laboratory with unsized carbon fibers show a much lower droplet-to-droplet variability (coefficients of variation of about 8 percent with 15 fibers tested). Possible inaccuracies in the experimental measurements (mainly

of droplet length) may constitute another source of variability in the contact angle results, but this is substantially reduced by using the largest droplets only. With thicker fibers, such as E-glass, the method is very efficient as the droplet-to-droplet variability in contact angle is much reduced, as seen in our results.

CONCLUSION

A simple method is proposed, based on ideas advanced earlier by Yamaki and Katayama [1], and Carroll [2], to determine with high accuracy the apparent contact angle of a liquid droplet formed on a thin cylindrical monofilament. Based on this method a plot may be constructed [5] which gives the apparent contact angle against the reduced droplet length for a variety of values of the reduced thickness of the droplet. However, the highest accuracy results are obtained by means of an interactive Fortran program based on the iteration scheme proposed. Because of its simplicity and high accuracy, the method proposed can be used with great advantage in studies of wettability of reinforcing filaments by liquid resins in advanced composites, which provide a necessary criterion for optimization of mechanical properties.

ACKNOWLEDGMENTS

REFERENCES

1. J. Yamaki, Y. Katayama, J. Appl. Polym. Sci. 19, 2897 (1975).

2. B. J. Carroll, J. Coll. Interf. Sci. 57, (3), 488 (1976).

3. A. Gilbert (private communication).

4. M. Nardin, I. M. Ward, Mater. Sci. Technol. 3, 814 (1987).

5. H. D. Wagner, J. Appl. Phys., in press (1990).

6. B. C. Carlson, Special Functions of Applied Mathematics, (New York, Academic Press, 1977).

7. H. W. Chang, R. P. Smith, S. K. Li, A. W. Neumann, in Molecular Characterization of Composite Interfaces (Polymer Sci. & Technol. Ser.: Vol. 27), H. Ishida and J. Kumar, Eds., (New Jersey, Plenum Press, 1985), p. 413.

Interface Reactions in Ceramic and Metal Systems

INTERFACIAL REACTIONS OF REFRACTORY METALS
NIOBIUM AND TANTALUM WITH CERAMICS SILICON CARBIDE AND ALUMINA

A. Joshi, H.S. Hu, and J. Wadsworth
Lockheed Research and Development Division, Lockheed Missiles and Space Company, Inc., 3251 Hanover Street, Palo Alto, CA 94304

ABSTRACT

Recent interest in the development of advanced metal matrix composites has prompted research on interfacial reactions of Nb and Ta with candidate reinforcements such as silicon carbide and alumina. Formation of reaction layers as small as 0.1 µm can be detrimental to composite strength and ductility and in some instances to the corrosion behavior, which suggests the importance of understanding the early stages of interfacial reactions. Thin films of Nb and Ta were sputter deposited on single crystal and polycrystalline silicon carbide and on sapphire substrates, and the nature and extent of reaction evaluated using Auger depth profiling and electron microscopy. In the Nb/SiC system, NbC_x is the first reaction product to form, but the overall extent of the reaction is dominated by the formation of the more stable NbC_xSi_y ternary phase. Little or no interfacial reaction was observed in the Nb/Al_2O_3 system for up to 4 hours at 1100°C, which also suggests that Al_2O_3 may be a potential diffusion barrier to minimize reactions in the Nb/SiC system. Similar interesting observations were made in the Ta/SiC and Ta/Al_2O_3 systems.

INTRODUCTION

Low density materials with substantially improved high temperature mechanical properties and oxidation resistance are required for advanced aerospace systems. Metal matrices with ceramic reinforcements offer such potential. From a structural viewpoint, the metal/ceramic interface controls the transfer of load between a metallic matrix and its ceramic reinforcement and thereby influences the mechanical properties of a composite. Ideally, such an interface should be a mechanical continuum, but a chemical discontinuum, implying no interdiffusion between the matrix and the reinforcement. In most practical situations, compound formation occurs at the interface and results in some loss in mechanical strength [1]. Improved design of metal/ceramic materials is limited by the lack of understanding of fundamental interaction mechanisms between metal matrices and ceramic reinforcements. Such an understanding is highly desired to establish a scientific basis for the future selection of metal/ceramic systems.

Although matrix/reinforcement systems may be separated into several different classes [2], the vast majority of metal/ceramic systems of interest for aerospace structural applications are those in which the reinforcement and matrix chemically react to form compounds at the interface. In general, the various metal species which possess low density and high ductility (eg., Al and Ti), have a thermodynamic tendency towards compound formation with the most desirable reinforcement species. As a result, carbides, borides, or silicides are usually encountered in the interfacial reaction zone. Often, the formation of such layers degrades mechanical behavior.

To date, most investigations on metallic matrices and ceramic reinforcements have been empirical and have emphasized bulk engineering materials. Furthermore, they have concentrated on reaction layer thicknesses which are convenient for study, i.e., in excess of 3-5 µm, but that are not necessarily appropriate for understanding fundamental metal/ceramic interactions. Reaction layer thicknesses on the order of only 0.3-0.5 µm can lead to significant degradation in both strength and ductility. For example, thin (0.4 µm) titanium diboride (TiB_2) reaction layers in commercial purity titanium (TI-40A), reinforced with 25 vol% B filaments) lead to significant degradation in room temperature strain to fracture of the filament [3] and a TiB_2 layer thickness of only 0.7 µm can be tolerated before significant degradation in the ultimate tensile strength. Thus, an understanding and control of interfacial reactions is essential to obtaining good mechanical properties in metal/ceramic systems.

The present paper emphasizes the use of sophisticated surface analytical techniques, which make it possible to characterize reaction layers of less than 0.1 µm thickness, thereby providing a fundamental understanding of the early stages of the reaction kinetics between metal matrices (Nb and Ta) and certain candidate ceramic reinforcement materials (SiC, Al_2O_3) at high homologous temperatures

(>0.5 T$_m$). An ultimate goal of this research [4] is to understand these processes sufficiently well that diffusion barriers can be selected to control such interactions.

EXPERIMENTAL

Both single crystal and polycrystalline substrates of SiC were obtained from Carborundum Company. The single crystal orientation was determined to be (0001) using Laue back reflection. The polycrystalline substrates were Hexoloy SA SiC Tiles in which the SiC content is typically 99.2 wt%. Sapphire crystals were obtained from Crystal Systems, Inc. Crystal orientations of the substrates were (0001) and (1010) and the starting material had a nominal purity of 99.996 weight percent. Nb and Ta metal films with a nominal thickness of 1μm were sputter deposited from 99.9 wt% pure metal targets. After deposition, the substrates were annealed in vacuum with a base pressure of 5×10^{-6} torr at temperatures ranging from 800 to 1200° C for 2 to 8 hours.

Thin film metal/ceramic diffusion couples were characterized using Auger electron spectroscopy (AES), transmission electron microscopy (TEM), optical metallography, and scanning electron microscopy (SEM). Specimens for optical metallography and SEM were prepared by low angle cross-sections, which provided enlarged (4:1) images of the thin film/substrate interface region. All the AES studies reported herein were conducted using a Perkin Elmer Corporation model PHI 560 ESCA/SAM system. The surface analysis results were obtained from a relatively large area (~ 250μm x 250μm) and thus represent an average in most instances. All the sputter profiling was conducted using 5 keV Ar ion bombardment and the sputter rates were expressed in Ta$_2$O$_5$ equivalents. TEM specimens were ion-milled prior to examination in a JEOL-2000FX (200kV) microscope.
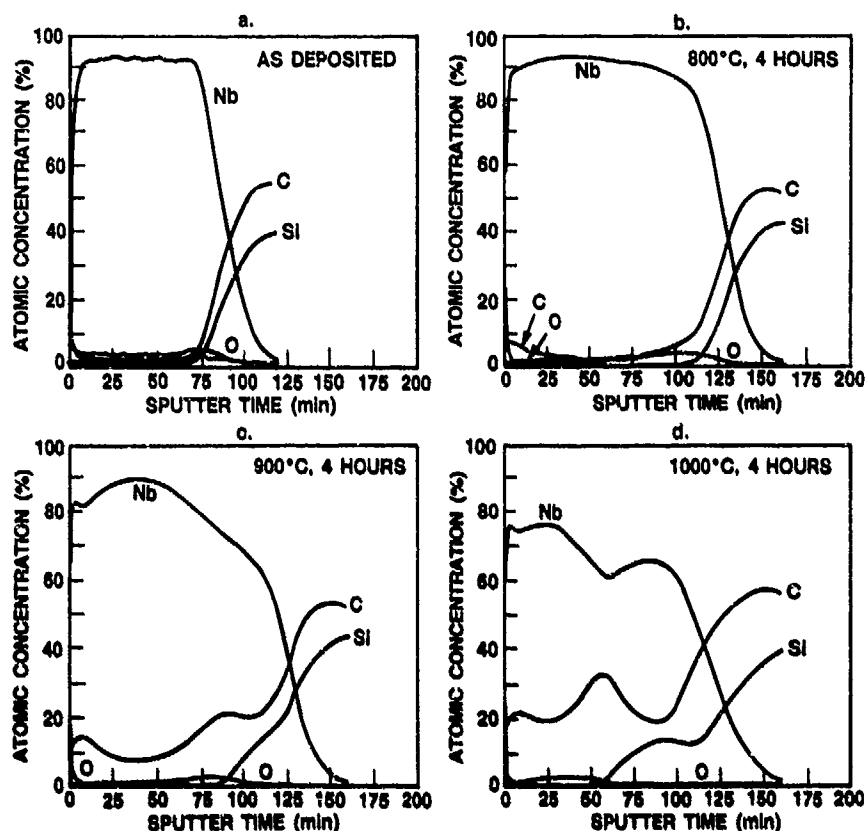

Fig. 1. AES depth profiles of Nb films (1.3 μm thickness) on polycrystalline SiC, in (a) the as-deposited condition, and after annealing for 4 h at (b) 800°C, (c) 900°C and (d) 1000°C.

RESULTS AND DISCUSSION

Interfacial reactions occurring in Nb/SiC, Nb/Al$_2$O$_3$, Ta/SiC, and Ta/Al$_2$O$_3$ were investigated but results from the Nb/SiC system are emphasized. Nb and Ta films in the as-deposited condition were noted to be relatively clean (i.e. below the AES detectability levels for O, C, and N, which are typically 0.1 at.%) as exemplified by the AES depth profile shown in Fig. 1a for a niobium film on a SiC substrate. Niobium thin films were deposited simultaneously on polycrystalline SiC, single crystal SiC (0001), and Al$_2$O$_3$ substrates. The thickness of the as-deposited niobium film was about 1.3 μm. These metal/ceramic specimens were vacuum treated for selected times at various temperatures and subsequently characterized by AES.

Nb/SiC System: The effect of annealing temperature on the interfacial reactions in the Nb/SiC system was studied by examining specimens annealed for 4 h at various temperatures. A specimen annealed at 600°C for 4 h showed little interdiffusion in comparison with the as-deposited specimen. The AES profile (shown in Fig. 1b) obtained upon heating to 800°C for 4 h, however, indicates some interdiffusion of Nb and C near the film/substrate interface. Also, during this anneal, the oxygen and carbon levels within the niobium film increased to the 2-3 at.% range. An examination of the nature of the profiles in various Nb/SiC thermally treated specimens, and consideration of all possible contamination sources, suggests that the elements C and O originate from the vacuum annealing system. After exposure at 900°C for 4 h, significant diffusion and reactions took place near the thin film interface, as shown in Fig. 1c. Formation of a distinct layer of carbon-rich niobium (possibly a NbC$_x$ phase) was observed after about 90 minutes of sputter time (0.96 μm depth) and a C- and Si-rich region (possibly NbC$_x$Si$_y$ phase) after about 110 minutes sputter time (1.14 μm depth). The oxygen contamination in the reacted region is very low indicating the possible rejection of oxygen from niobium during its reaction with C and Si. The reactions occurring after annealing at 1000°C for 4 h are shown in Fig. 1d. It is apparent that the NbC$_x$ region has moved further toward the surface of the film and the thickness of the NbC$_x$Si$_y$ region has increased.

The specimen annealed at 1000°C for 4 h was characterized in detail [5] by TEM, in order to understand the nature of reaction products. Two phases were observed in the first reaction layer adjoining SiC. Cubic NbC was present in some areas and hexagonal ternary phase Nb$_5$Si$_4$C in the other regions. The ternary phase was seen in all the specimens as the first or second layer, followed by tetragonal α-Nb$_5$Si$_3$ and the ordered hexagonal α-Nb$_2$C. Nb$_5$Si$_4$C formation is also consistent with the AES depth profiles from this specimen and various other annealed Nb/SiC (poly) and Nb/SiC (0001) specimens showed regions of compositional uniformity that contain Nb, Si, and C. The composition has an average value of approximately 64Nb-20C-16Si (in at.%). Based on the 1300°C section of the ternary phase diagram [6], the only ternary phase at this temperature is the T (hexagonal D8$_8$) phase with the stoichiometric formula Nb$_5$Si$_4$C. The carbon concentration in the NbC$_x$Si$_y$ region in most of the AES profiles is substantially higher than the 11% corresponding to the T phase. One possibility is that at lower temperatures (such as 1000 to 1200°C), the composition of this phase changes substantially or a new ternary phase becomes more stable. Also the AES sensitivity factors employed in atomic concentration calculations may not be accurate for application to these layered compounds. To avoid any misrepresentation, the designation NbC$_x$Si$_y$ will be used in the following discussions.

The extent of reaction of Nb with polycrystalline SiC at 1100°C is shown by the AES profile in Fig. 2a. This film consists of a layered structure that may be represented by NbC/Nb$_2$C/NbC$_x$Si$_y$/NbC/SiC. The surface compound is likely to be the result of the pick up of carbon from the vacuum environment. The silicon content at the interface is low compared to the 1000°C annealed specimen; this is probably because of the growth of the NbC$_x$Si$_y$ phase and the associated depletion of Si from the interfacial region. At temperatures of annealing higher than 1100°C, the reaction is completed in relatively short times. An AES spectrum from the surface of a specimen annealed at 1200°C for 2 h (Fig. 2b) reveals that the elements Nb, O, Si, and C (in its hydrocarbon form) are at the surface. Silicon migrated to the surface by diffusing through the entire film, an observation that is also demonstrated by the AES depth profile of the same specimen in Fig. 2c. The carbon Auger peak shapes and positions (not shown) indicate that the surface carbon (sputtering time=0) is hydrocarbon, the carbon in the film is similar to that of a metal carbide (eg., NbC$_x$), and is different from that of the SiC (corresponding to sputter time of 170 min). The silicon peak shapes indicate that surface silicon is present in the form of its oxide, silicon within the film is present in the form of a silicide or elemental silicon, and is different from that of the substrate SiC. The AES profile of this 2 h, 1200°C annealed specimen is consistent with a layered structure represented by NbC/Nb$_2$C/NbC$_x$Si$_y$/NbC/SiC.

The reaction rate as a function of time was studied for selected temperatures and times using AES depth profiles from Nb/SiC specimens. For example, at 900°C the overall reaction zone thickness of NbC_x + NbC_xSi_y increased from 0.47 μm (corresponding to 4 h annealing) to 0.65 μm after 8 h annealing. In particular, the thickness of the NbC_xSi_y layer increased, whereas the NbC_x layer thickness remained unchanged during this period.

Thin film specimens deposited on single crystal (SiC) substrates exhibited depth resolution (seen in the AES profiles) that was superior to the films deposited on polycrystalline SiC substrates. The improvement is readily seen in the as-deposited condition but is dominant in the annealed specimens. This is exemplified by the AES profile shown in Fig. 2d for the single crystal substrate and may be compared with Fig. 2a of the identically treated polycrystalline SiC substrate. In this case, the NbC_x layer forming within 4 h at 1100°C does not increase significantly in thickness upon further annealing, indicating the reaction is nearly complete. The surface has a layer of NbO_x mixed with NbC_x followed by layers of NbC_x, NbC_xSi_y, and NbC_x all on top of the SiC (0001) substrate.

Standard free energies of formation of various known binary compounds of Nb, C, and Si suggests that Nb_5Si_3 is the most stable reaction product over the entire temperature range of interest. The AES and TEM characterization results show that a ternary NbC_xSi_y is forming at the expense of several of the other products. In the Ta/SiC system, a similar compound of TaC_xSi_y forms readily at low temperatures and becomes the most dominant phase in specimens annealed at 1200°C for 4 h.
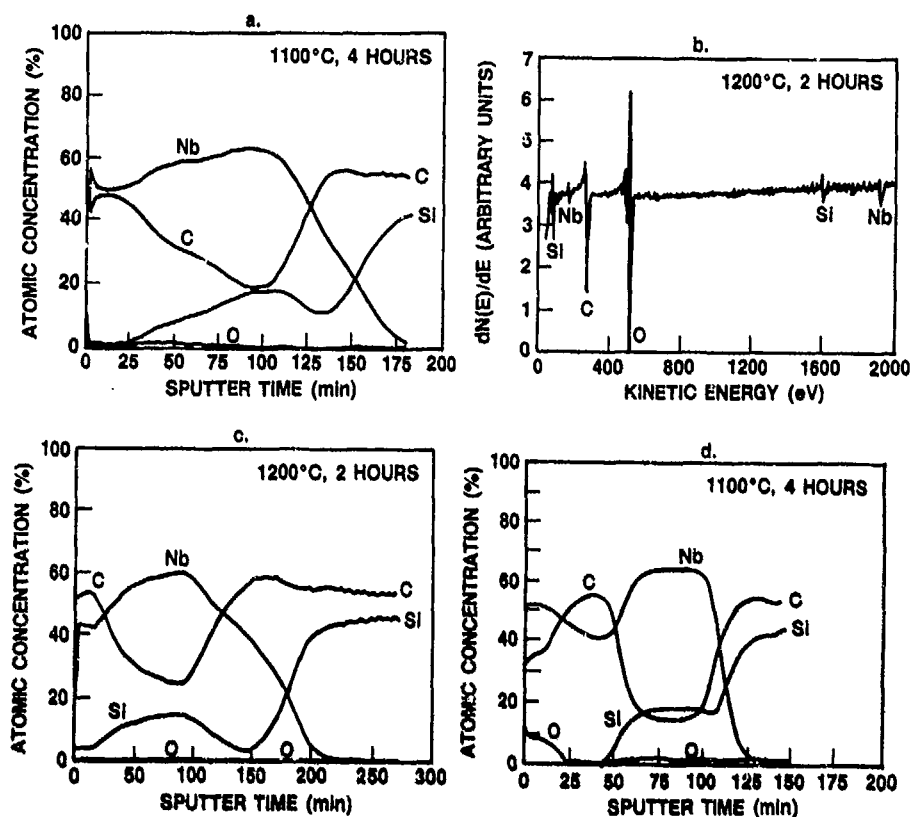

Fig. 2. AES data from Nb/SiC, (a) annealed 4 h at 1100°C, (b) annealed 2 h at 1200°C, (c) annealed 2 h at 1200°C and (d) Nb/SiC (0001) annealed 4 h at 1100°C.

The AES and TEM characterization described above has led to an improved understanding of the reaction sequence between Nb and SiC. TEM studies indicated the presence of NbC in regions adjacent to SiC. The NbC_xSi_y formation identified in the AES profiles is preceded by Nb_2C formation in most instances. Once this phase forms and grows to a certain thickness, it becomes self limiting, possibly because of the build-up of Si at the Nb_2C/SiC interface and associated formation of the NbC_xSi_y phase. The AES profiles also indicate that primarily the thickness of NbC_xSi_y region increases with continuing reaction (time or temperature). Thus the reaction appears to take a path Nb-Nb_2C-NbC_xSi_y-NbC-SiC. The portion of the path Nb_2C-NbC_xSi_y which is not obvious in the ternary phase diagram section at 1300°C may be understood if there is a thin region of NbC or Nb_5Si_3 between Nb_2C and NbC_xSi_y. The reaction path, in such an event, would be Nb-Nb_2C-NbC (or Nb_5Si_3)-NbC_xSi_y-NbC-SiC. In some specimens, the AES profiles indicated NbC-Nb_2C-NbC_xSi_y-NbC-SiC, which suggests surface carburization during annealing.

The thickness of reactions zones, as measured in the AES profiles, may also be utilized in determining the rates of reactions and the activation energy for the reaction may be determined through an Arrhenius plot. Such a determination indicates that the activation energy for NbC_xSi_y formation is 20.0 kcal/mole. Similar measurements obtained for NbC_x growth in Nb/SiC indicate an activation energy of 11.6 kcal/mole. Even though the limiting step in these reactions could not be identified, these relatively small activation energies indicate the ease of formation of NbC_x and NbC_xSi_y.

Nb/Al_2O_3 System: Interfacial reactions occurring at the interfaces of Nb films deposited on Al_2O_3 substrates were evaluated by thermal annealing followed by AES depth profiling. There was little or no evidence of reactions in specimens annealed for up to 4 h and 1100°C. Al_2O_3 is thermodynamically more stable than NbO, which is the most stable form of the various oxides of niobium. Thus no reaction would be expected between Nb and Al_2O_3.

The absence of a reaction between Nb and Al_2O_3 suggests that Al_2O_3 may be a promising diffusion barrier between Nb and SiC. A three layer system such as Nb/Al_2O_3/SiC, however, would also require that there be little or no reaction between Al_2O_3 and SiC. Calculated free energies of possible reactions between these compounds suggest that compounds such as Al_4C_3, SiO_2 or $3Al_2O_3 \cdot 2SiO_2$ are unlikely to form, since the free energies of these reactions are all positive and large in value.

Ta/SiC System: The reactions between Ta and SiC are, as anticipated, found to be similar to those between Nb and SiC. For example, AES data obtained from a Ta/SiC (0001) specimen annealed at 1100°C for 4 h indicated formation of TaC_x, TaC_xSi_y, and a depleted Si region above the substrate, in a manner similar to Nb/SiC. When the Ta/SiC (0001) specimen was annealed at 1200°C for 2 h, a Ta-C-Si region enriched in carbon formed at about 0.4 μm depth, with a composition different from the TaC_xSi_y identified at about 0.6 μm depth. This occurrence of a Ta-C-Si region is either a result of inhomogeneity of phase distributions in-plane, or a result of the formation of a separate layer of another ternary TaC_mSi_n phase. Further work utilizing TEM characterization is needed to elucidate fully these reactions. As with Nb/SiC specimens, the chemical state of carbon in the reacted film is indicated to be similar to a carbide. Upon longer time (4 h) annealing at 1200°C, the entire tantalum film reacted, leading to a relatively uniform TaC_xSi_y phase.

Ta/Al_2O_3 System: Tantalum did not react with Al_2O_3 in anneals up to 4 h at temperatures as high as 1200°C, as indicated by AES profiles showing little or no oxygen within the tantalum films following the reaction. Absence of reaction in this system suggests that an interfacial layer of Al_2O_3, applied between Ta and SiC, would be a promising diffusion barrier.

SUMMARY

Interdiffusion and reactions occurring in candidate metal matrix (Nb and Ta) and ceramic reinforcement materials (SiC and Al_2O_3) were evaluated using diffusion couple specimens, employing sputter deposited metal films. The reaction between Nb or Ta and SiC are complex and result in multilayered interfacial structures. The nature of these structures were evaluated using AES and TEM. Diffusion and reactions occurring at the interfaces of Nb and Ta films deposited on Al_2O_3, however, revealed little or no evidence of any significant reaction up to the highest temperature evaluated, 1100°C (4 h) for the Nb/Al_2O_3 system and 1200°C (4 h) for the Ta/Al_2O_3 system. These results suggest that Al_2O_3 may be a promising diffusion barrier between Nb and Ta metal matrices and SiC reinforcement.

154

ACKNOWLEDGMENT

REFERENCES

1. L.J. Ebert and P.K. Wright, "Mechanical Aspects of the Interface," in Interfaces in Metal Matrix Composites, edited by A.G. Metcalfe (Academic Press, New York, 1974), pp. 32-66.
2. A.G. Metcalfe, "Physical Chemical Aspects of the Interface", ibid., pp. 67-126.
3. A.G. Metcalfe, M.J. Klein, "Effect of Interface on Longitudinal Tensile Properties," in A.G. Metcalfe, op. cit., p. 151.
4. A. Joshi, H.S. Hu, L. Jesion, J.J. Stephens, and J. Wadsworth, "High Temperature Interactions of Refractory Metal Matrices with Selected Ceramic Reinforcements", to be published.
5. D.L. Yaney and A. Joshi, to be published.
6. C.E. Brukl, Ternary Phase Equilibria in Transition Metal-Boron-Carbon-Silicon Systems, Technical Report No. AFML-TR-65-2, Part II, Vol. VII, (Air Force Materials Laboratory, Wright Patterson Air Force Base, Ohio, 1966), p. 44.

SILICON-BASED COATINGS ON NIOBIUM METAL

P. D. STUPIK,[a] T. R. JERVIS,[b] M. NASTASI,[b] M. H. DONOVAN,[a]
AND A. R. BARRON[a*]

[a]Department of Chemistry, Harvard University, Cambridge,
MA 02138.
[b]Materials Science and Technology Division, Los Alamos National
Laboratory, Los Alamos, NM 87545.

ABSTRACT

Silicon coatings on niobium substrates were subjected to
thermal, ion beam and laser mixing, and the effectiveness of the
different methods for the synthesis of graded interfaces was
compared. The resulting metal/silicon interfaces were
characterized by X-ray photoelectron spectroscopy (XPS), Auger
electron spectroscopy (AES) and Rutherford backscattering (RBS).

INTRODUCTION

Niobium alloys have become important in applications which
require structural strength and high temperatures.[1] These alloys
are not oxidation resistant, and require protection, especially
in harsh environments. Silicon containing overlay coatings on
alloys of nickel and iron have been shown to dramatically
increase their resistance to oxidation and corrosion at high
temperature.[2] Unfortunately these types of coatings tend to fail
due to the formation of cracks induced by thermal stress at the
substrate-coating interface. These cracks then serve as pathways
for oxidation below the coating leading to catastrophic failure
of the protective coating.

We have been concerned with the formation of oxidation and
thermal-oxidation resistant coatings on niobium metal, as a model
for more complex niobium based alloy systems.[3] As part of this
study we have investigated the preparation of graded interfacial
layers between a niobium substrate and a silicon coating. A
graded interface shows a smooth variation in the niobium and
silicon concentrations, with the possibility of a constant
composition region. It is expected that these graded interfaces
will have greater thermal and mechanical stability than the
atomically sharp interfaces.

EXPERIMENTAL PROCEDURE

Elemental silicon (99.999% purity) was deposited by electron beam evaporation (background pressure $< 10^{-5}$ Torr) onto 2 mm thick polished niobium substrates. The substrates were sputtered with argon ions prior to and during the early stages of deposition to prevent the formation of native niobium oxide at the interface. The thickness of the coating (1800-2000 Å) was determined by RBS. One sample, A, was retained untreated while the remainder, B-H, were subjected to the following treatment. Two samples, B and C, were heated under dynamic vacuum ($< 3 \times 10^{-5}$ Torr), in a quartz tube furnace.[4] Sample B was heated for 18 hours at 550°C, while sample C was treated to a two step anneal at 550°C and 850°C, 18 hours for each step. Two samples, D and E, were subjected to ion beam mixing with 400 KeV krypton ions at pressures below 2×10^{-7} Torr. Sample D was ion beam mixed at room temperature, and sample E was mounted on a hot stage and mixed at 300°C. Both samples were given a total dose of 3×10^{16} ions cm^{-2} which took a total of 20 minutes each sample.

Samples F-H were laser mixed in air with an excimer laser of 248 nm.[5] A fixed spot size was used but different pulse energies produced fluences of 0.5 (F), 1.7 (G), and 2.5 (H) J cm^{-2} respectively.

The coatings were characterized by RBS, AES, XPS and low angle X-ray diffraction. RBS was carried out using 2.0 MeV He$^+$ ions at the Los Alamos Ion Beam Material Laboratory. AES were carried out on a Perkin-Elmer SAM-660. XPS spectra were acquired with a Surface Science Laboratories Model SSX-100 spectrometer with a monochromatized Al-K$_\alpha$ X-ray source ($10^{-8} - 10^{-9}$ Torr). A Guinier thin film diffractometer was used for low angle X-ray diffraction studies.

RESULTS AND DISCUSSION

The thermally annealed samples, B and C, were coloured blue (B) and purple (C). The Surface Scanning Electron Micrograph showed no significant difference between the thermally annealed samples and the untreated sample.

The AES sputter depth profiles of samples B-E and C are shown in Figure 1. The slightly broadened interfacial region in the low temperature (550°C) annealed sample, B (Figure 1b) as compared to the untreated sample, A (Figure 1a) is consistent with the slow diffusion of Nb and Si at temperatures below 800°C. Sample C not only shows a more pronounced diffusion region.
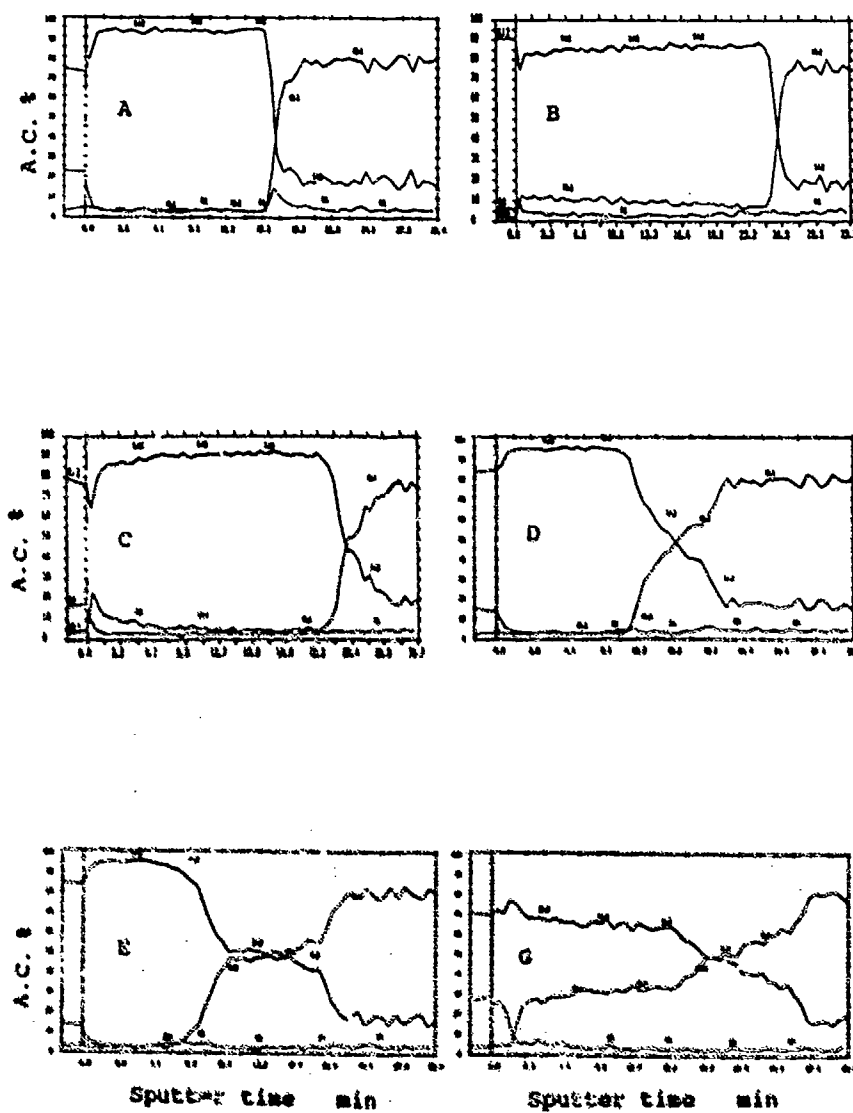
Figure 1. AES depth profile of silicon layers on niobium substrates: see text for sample description.

The AES data shows that the room temperature ion mixed
sample (Figure 1d) has a wider interface layer than that obtained
from the one and the two step anneals but with similar
composition profiles. Samples B, C and D do not show interface
layers with well defined composition regions. The sample given
the ion beam mixing at 300°C (E) has a nearly uniform interfacial
layer composition (Figure 1e). No NbSi$_2$ could be detected by X-
ray diffraction.

RBS spectra of samples D and E, subjected to ion beam mixing
at room temperature and 300°C respectively, are shown in Figure
2. The spectra clearly show that more mixing takes place in the
sample mixed at 300°C as compared to room temperature.

Figure 2. RBS spectra of the ion beam mixed samples, D and E, as
compared to the as deposited sample, A.
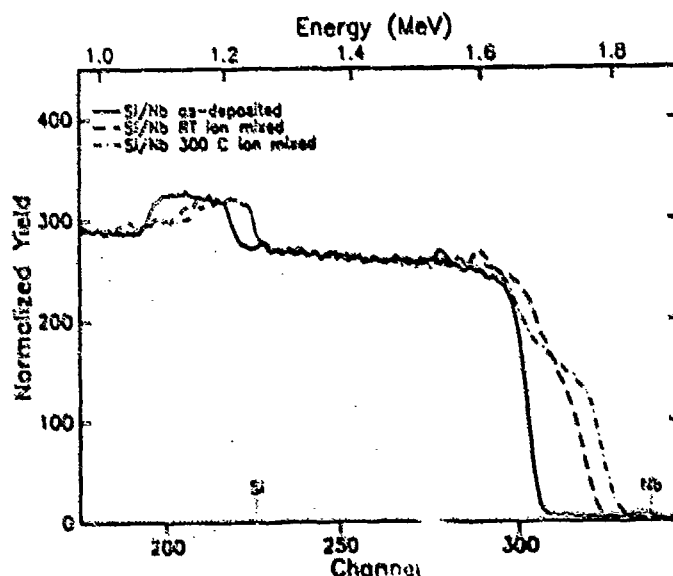
The RBS spectra of the laser mixed samples F-M are shown in
Figure 3 along with that of the as deposited sample (A). Sample F
mixed with a fluence of 0.5 J cm^{-2} does not show an obvious
constant phase region, but shows mixing on a scale comparable to

the 300°C ion mixed sample. By contrast the samples mixed at
1.7 Jcm^{-2} and 2.5 Jcm^{-2} show substantial mixing as well as regions
of nearly constant composition. AES depth profile analysis of
sample G (Figure 1f) is consistent with the RBS data, while the
XPS spectrum (Figure 4) and X-ray diffraction (ϕ=5°)[6] of H
confirm that the mixed zone to consist of polycrystalline $NbSi_2$.

Figure 3. RBS spectra of the laser mixed samples, F, G and H.
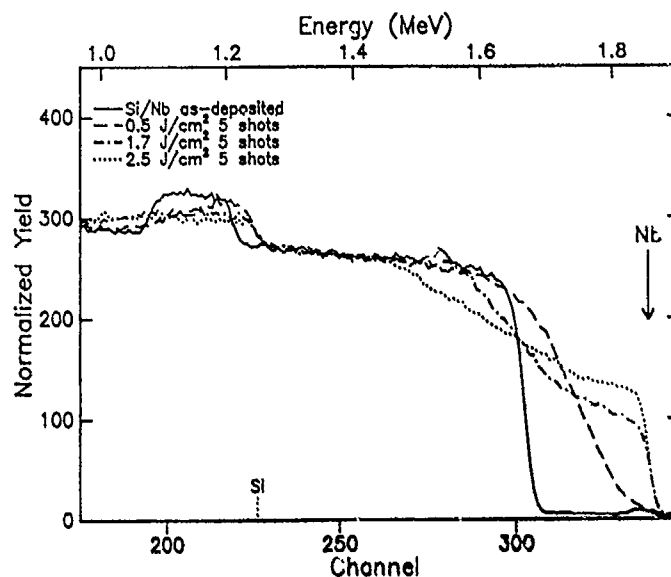
Figure 4. In 3d, curve fitted XPS spectral components for sample
H. Peak positions and assignments are included (eV).
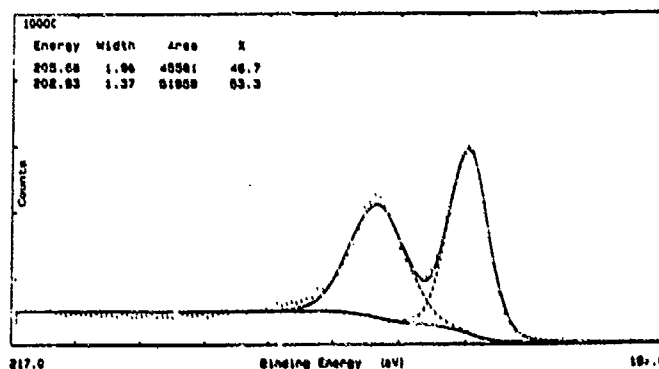
CONCLUSION

It is clear that ion beam and laser mixing are more
effective than thermal annealing, @ 850°C, for the preparation of
wide graded interfacial layers between niobium metal substrate
and silicon coatings. In addition to a broad interfacial region,
an essentially constant composition mixed zone is produced by
high energy laser mixing.

ACKNOWLEDGEMENT

REFERENCES

1.   H. Inouye, Niobium, Ed. H. Stuart, AIME 1981, p. 615.

2.   J. Daimer and E. Fitzer, High Temp. High Pressures, 14,
     549 (1982).

3.   P.D. Stupik, P.E. Laibinis and A.R. Barron, Industry and
     University Advanced Materials Conference II, AMI, Colorado
     (1989) Proceedings, in press.

4.   J.M. Poate, K.N. Tu, and J.W. Mayer, Thin Films-
     Interdiffusion and Reaction. J.Wiley and Sons, London, 1978,
     p. 360-402.

5.   T.R. Jervis, J.P. Hirvonen and M. Nastasi, J. Mater. Res.
     1, 1104 (1988).

6.   ASTM X-ray powder data file #8-450.

EFFECT OF AMBIENT ATMOSPHERE ON THIN FILM
REACTION OF Si_3N_4 WITH Ti

SESHU B. DESU* and J. ASHLEY TAYLOR**
* Department of Materials Engineering, Virginia Polytechnic Institute and State University, Blacksburg VA 24061
** AT&T Bell Laboratories, 555 Union Boulevard, Allentown, PA 18103

ABSTRACT

The reaction of sputtered deposited Ti films of 100 nm thick with low pressure chemical vapor deposited Si_3N_4 films (300 nm thick) was studied in N_2 or Ar, in a rapid thermal annealer. Reactions are followed using x–ray diffraction, Auger electron spectroscopy, and transmission electron microscopy. In argon, the Si_3N_4 and Ti reaction at low temperatures led to the product formation of two layer structure (TiN/Ti_5Si_3), with some contaminant oxygen and nitrogen released from the reaction uniformly dissolved throughout the remaining unreacted Ti. At higher temperatures, a three layer structure, $TiN/Ti_xSi_y/TiN$, on unreacted Si_3N_4 was developed. With increasing temperature the value of x and y decreased from 5 to 0 and 3 to 1, respectively. Reactions in N_2 ambient, irrespective of temperature, always produced the three layer structure, but the thickness of Ti_xSi_y layer was much smaller than that produced in argon ambient for the corresponding temperatures. The reaction mechanism can be explained in terms of relative diffusion coefficients and the stability of the interfaces.

INTRODUCTION

Advanced ceramic–metal braze joints, for critical applications such as heat engines, require optimized coatings on ceramics in order to obtain good wetting and adhesion between the chemically dissimilar components. Since Si_3N_4 is one of the ceramic materials being considered for the development of advanced heat engines, there is a considerable interest in reactive coatings such as Ti, Zr, Hf, and Ta [1–2]. For the optimization of ceramic–metal braze joints the understanding of interactions between the coating (e.g. Ti) and the ceramic (e.g. Si_3N_4) is essential. Understanding of the interactions between Ti and Si_3N_4 is also important for the development of advanced metallization technologies, such as self–aligned silicide contacts and interconnects and self–aligned diffusion barriers, for very large scale integrated (VLSI) circuits.

Borisov et al. [3] in 1978, investigated the solid–phase reactions in Ti and Si_3N_4 powder mixtures by high temperature differential thermal analysis. Based on the data of powder mixtures [3] and from the available free energy data, Beyers et al. [4] calculated a ternary phase diagram for the Ti–Si–N phase. Thin film reactions between Ti and Si_3N_4 were also studied [5–7]. Since, these studies [5–6] concentrated on much thinner layers of Si_3N_4 (e.g. 50 to 75 nm) interpretation became complicated because of interactions with the underlying substrate (e.g Si and SiO_2). Consequently, in the present study we have investigated thermal reactions of relatively thick Si_3N_4 (e.g. 300 nm) with sputter deposited Ti films under rapid thermal annealing conditions at temperatures between 600 to 1100°C.

EXPERIMENTAL

The thick Si_3N_4 films were prepared by depositing the following structure:
Ti(100 nm)/Si_3N_4(300 nm)/SiO_2(70 nm)/Si<100>(substrate). The Ti was sputter deposited at 300°C in Ar using a Varian model 3180 sputtering system. The Si_3N_4 layer was deposited by low pressure chemical vapor deposition at 800°C using ammonia and dichlorosilane as precursors. The index of refraction of the films was typically 2.01 at 632.8 nm, and the N/Si ratio was within experimental error of 1.33 as measured by electron microprobe (EMP). Typically 0.2 wt% Cl was detected by EMP in the Si_3N_4 films. The

SiO_2 layer was thermally grown on the Si<100> wafers before the Si_3N_4 was deposited. Rapid thermal annealer (AG Associates) was used for all the annealing in nitrogen or argon ambient over a temperature range of 600–1100°C for 20 to 120 sec.

Concentration versus depth profiles of the annealed films were obtained using Auger electron spectroscopy (AES) in conjunction with Ar ion milling. Some of the films were analyzed with Rutherford backscattering (RBS) and electron microprobe in order to calibrate the Auger peak heights. The instrumental parameters and Auger sensitivity factors used in this study were same as those listed in Reference [8]. Because the N KVV line interferes with the Ti LMM line and because the Ti LMM/Ti LMV ratio changes for different Ti compounds, both Ti lines were followed in the Auger profiles along with the Si LVV and O KVV. A depth profile using x–ray photoelectron spectroscopy (XPS), for which no interference for nitrogen exist, also was obtained for reaction in Ar at 700°C. For our case, XPS profiles are much slower because of the large sample area that is imaged; thus most of the profiles were obtained using AES. The crystal phases present in the film were determined by x--ray diffraction using a Philip's model XRG–5000 powder diffractometer with a Cu $K\alpha$ radiation. A cross section of the Si_3N_4 film annealed at 1000°C was obtained using Philip's model 400T transmission electron microscope (TEM).

RESULTS

Auger analysis of as–deposited Ti films showed a thin passivating TiO_2 layer on the outer surface, very little oxygen in the bulk of the film, and a small increase at the Ti/Si_3N_4 interface. The oxide on the outer surface of the Si_3N_4 layer was removed using buffered HF prior to the Ti deposition. However, some oxygen contamination (although slight) was expected at the interface as indicated by Auger depth profile. XRD investigation indicated a preferred orientation of the Ti <001> with the basal plane parallel to the Si<100> substrate. A lattice parameter for C_0 of 0.468 nm was calculated. These data were typical for all the as–deposited Ti films.

Table 1. lists the various phases formed after rapid thermal annealing in argon at various temperatures. The annealing of the films in argon from 600–800°C resulted in the formation of a two layer structure, very thin TiN/Ti_5Si_3, on unreacted Si_3N_4, while some oxygen and nitrogen were found uniformly dissolved throughout the rest of the unreacted α–Ti layer. This structure is demonstrated by the Auger profile (see Table 1). For the outer unreacted Ti layer, the ratio Ti LMM/Ti LMV lines, taken from the Auger depth profile, agreed with those for metallic titanium. O/Ti atomic ratios were found to be 0.04 to 0.08. The amount of oxygen in the Ti layer remained more or less constant over this temperature range. This oxygen originated most likely from oxygen contamination at the Ti/Si_3N_4 interface, dissolution of the TiO_2 passivating layer, or oxygen contamination in the Ar ambient.

Table 1. Ti/Si_3N_4 reaction products at various RTA temperatures in Ar.

Rapid Thermal Annealing Temperature

600–800°C	900°C	1000°C	1100°C
Ti(O,N)	TiN_2O_{1-2}	TiN_2O_{1-2}	TiN_2O_{1-2}
Ti_5Si_3	Ti_5Si_3	$TiSi_2$	Si
TiN	TiN	TiN	TiN
Si_3N_4	Si_3N_4	Si_3N_4	Si_3N_4

The N/Ti ratio, especially for small amounts of nitrogen, was difficult to measure precisely with AES because of the N KVV and Ti LMM interference. However, the Ti

LMM/Ti LMV ratio was found to increase after annealing, and an XPS depth profile of the film annealed at 700°C showed uniform distribution of nitrogen throughout the Ti film with a N/Ti ratio of about 0.13. Strong lines were still observed for the 002 and 004 reflections of α–Ti, but a significant increase in the d–spacings was observed after annealing. This increase has been correlated with the amount of oxygen and nitrogen randomly dissolved in α–Ti [9]. For the films annealed in Ar up to 800°C, we found no evidence from XRD for Ti_2N or TiN phases. However, the Auger depth profiles indicated the possibility of a TiN layer at the Ti_5Si_3/Si_3N_4 interface. The layer would be too thin to be observed by XRD.

The films annealed at temperatures grater than 800°C in argon exhibited a distinct three–layered structure: TiN_2(outer surface)/Ti_xSi_y/TiN on unreacted Si_3N_4. This three layer structure is clearly shown in the Auger profiles (Figure 1 & 2). The composition of the sandwiched layer (Ti_xSi_y) varied with the heat treatment temperature: Ti_5Si_3, $TiSi_2$ (C54), and Si for 900, 1000, and 1100°C, respectively. The N/Ti ratio for the TiN layer at the Si_3N_4 interface was close to 1.0 irrespective of temperature in the range 900–1000°C. However, for the outer titanium nitride layer the N/Ti ratios were 0.51, 0.88, and 0.91 for 900, 1000, and 1100°C anneals respectively. The outer titanium nitride layer contained some oxygen (O/Ti ratio $\cong$ 0.09). The XRD data indicated a preferred orientation of TiN<111>.

A drawing taken from a TEM cross section for the film annealed at 1000°C is illustrated in Figure 3. Again, three–layered structure could be clearly seen. The relative thickness of layers agreed well with the Auger depth profile. According to the reaction $11Ti + Si_3N_4 = 3TiSi_2 + 8TiN$, for complete reaction of 100 nm of titanium one would expect 66 nm of $TiSi_2$ and 81 nm of TiN. Thus, it can be clearly seen that the calculated thicknesses agree well with the total thickness of titanium nitride layers and thickness of $TiSi_2$ layer as determined from TEM (Figure 2). The grain size of the outer TiN layer was much finer than the layer at the Si_3N_4 interface. Microelectronic diffraction patterns showed spots with no evidence of an amorphous ring. The few d–spacings obtained from electron diffraction spots agreed with the XRD data.

Table 2. lists the Ti/Si_3N_4 reaction products in nitrogen ambient for various rapid thermal annealing temperatures. For all the investigated temperatures, a Ti_xSi_y layer and two TiN layers (one outer layer and one at Si_3N_4 interface) were formed. For low temperature (e.g. 600°C), a thin outer layer of TiN was formed; but mostly unreacted Ti remained; and Ti_5Si_3 and TiN were formed at the Si_3N_4 interface. The Auger profile indicated that the TiN layer (at the Si_3N_4 interface) was more prominent for N_2 annealing compared to argon annealing at the same temperature.

Table 2. Ti/Si_3N_4 reaction products at various RTA temperatures in N_2.

Rapid Thermal Annealing Temperature

600–800°C	900°C	1000°C	1100°C
TiN	TiN	TiN	TiN
Ti(O,N)	TiSi₂	Si	Si
Ti₅Si₃	TiN	TiN	TiN
TiN	Si₃N₄	Si₃N₄	Si₃N₄
Si₃N₄			

As the annealing temperature increased, progressively more Ti reacted with ambient nitrogen to form TiN at the outer surface. As the TiN layer thickened, the oxygen, which was uniformly dissolved in the unreacted Ti, was displaced toward the TiN/Ti_xSi_y
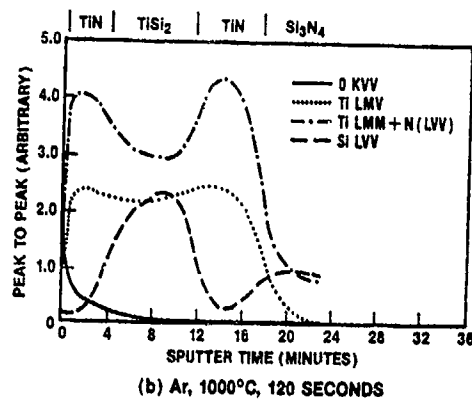
164

| TIN | TISi₂ | TIN | Si₃N₄ |

Figure 1 Auger Depth Profile After Annealing In Argon at 1000°C for 120 seconds.

(b) Ar, 1000°C, 120 SECONDS
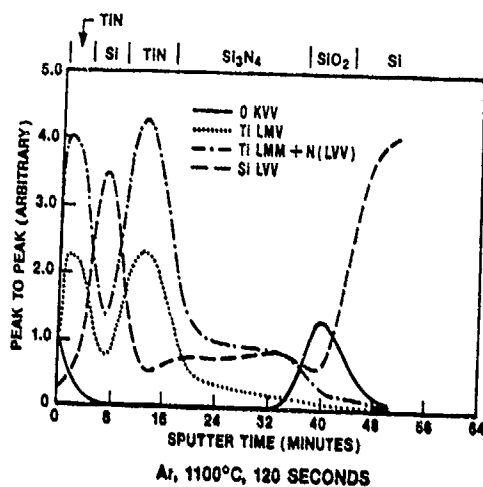
Figure 2 Auger Depth Profile After Annealing in Argon at 1100°C for 120 seconds.

Ar, 1100°C, 120 SECONDS
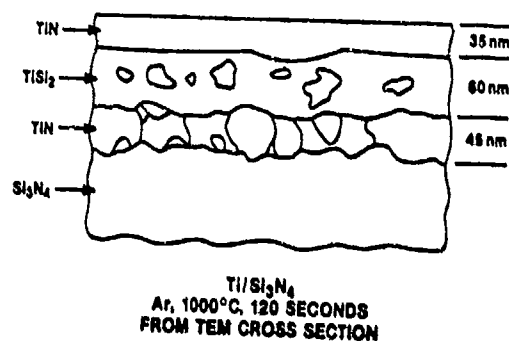
Figure 3 Drawing Taken From TEM Cross Section of the Film Annealed at 1000°C for 120 seconds in Argon.

Ti/Si₃N₄
Ar, 1000°C, 120 SECONDS
FROM TEM CROSS SECTION

interface. In contrast with the reactions in argon, lower amount of Ti_xSi_y was formed for reactions in nitrogen ambient.

The XRD data indicated that unreacted Ti remained in the films annealed up to 800°C. The expansion of the lattice parameter C_0 (up to 0.4785 nm) was significantly greater than for the Ar annealing, indicating the presence of the maximum amount of dissolved nitrogen. Weak peaks for the TiN(111) and (222) reflections were seen after the 600°C anneal; these lines became quite strong for subsequent annealing at higher temperatures. The weak lines for the Ti_5Si_3 were not observed for annealing below 900°C as they were for Ar, but the Auger line shapes for Si LVV for the silicide layer were similar to those in the Ar annealing. Thus, we assumed that the silicide formed at the interface was Ti_5Si_3.

DISCUSSION

Based on the nature of the products, the reactions between Ti and Si_3N_4 can be broadly classified into three groups (Table 3): I) reactions involving the formation of titanium silicides with the evolution of nitrogen, II) reaction involving the formation of titanium nitrides with free silicon, and III) reactions resulting in the formation of both titanium silicides and titanium nitrides. These reactions (1–7) are represented in Table 3 along with the mole ratios (thickness ratios) of the starting materials and heats of reaction per mole of titanium at room temperature. As can be seen from Table 3, that the group I reactions are thermodynamically unfavorable (neglecting the entropy contribution, which is reasonable for solid state reactions). In accordance with expectation, group I reactions were not observed. Thus, only reactions 4 to 7 need to be considered for further discussion.

Table 3. Possible Reactions in the Ti–Si_3N_4 System

#	Reaction	Ti/Si_3N_4 Mole Ratio	Ti/Si_3N_4 Thickness Ratio	ΔH_{298}/Ti mole KJ/mole
Group I				
1)	$1.5Ti+Si_3N_4 = 1.5TiSi_2+2N_2$	1.5	0.392	356
2)	$3.0Ti+Si_3N_4 = 3.0TiSi+2N_2$	3.0	0.783	116
3)	$5.0Ti+Si_3N_4 = Ti_5Si_3+2N_2$	5.0	1.305	31
Group II				
4)	$4.0Ti+Si_3N_4 = 4TiN+3Si$	4.0	1.044	−150
Group III				
5)	$5.5Ti+Si_3N_4 = 1.5TiSi_2+4TiN$	5.5	1.436	−146
6)	$7.0Ti+Si_3N_4 = 3TiSi+4TiN$	7.0	1.827	−142
7)	$9.0Ti+Si_3N_4 = Ti_5Si_3+4TiN$	9.0	2.349	−132

Of all the possible reactions, Reaction 4 which results in the formation of TiN and Si is thermodynamically the most favorable one. The final phase formation is determined not only by heat of reaction, but also on parameters such as starting composition, substrate material, ambient atmosphere, and kinetic phenomena. For the case of unreactive substrate and ambient atmospheres, the preferred reaction would vary smoothly from reaction 7 to 4 (Table 3) as the Ti/Si_3N_4 ratio in the starting material decreases. This can also be followed by rapid thermal annealing by imposing kinetic conditions on the reaction of a fixed Ti/Si_3N_4 ratio, in other words only allowing limited reaction. We have started with 300 nm of Si_3N_4 overlayed with 100 nm of Ti. This structure was heat treated for a fixed time (less than 120 sec.) at progressively increasing temperatures, thus allowing the percent completion of reaction to increase.

Although for our specimens the starting Ti/Si_3N_4 ratio is less than 1, the effective ratio will be a function of temperature because of the kinetic limitations imposed by the rapid thermal annealing conditions used in this study. At lower reaction temperatures (e.g. 600–900°C) the effective ratio will be very high since only a small amount of Si_3N_4 takes part in the reaction, and thus one expects the formation Ti_5Si_3 and TiN (Reaction 7 in

Table 3). As the temperature increases the effective ratio approaches towards the starting ratio, and a smooth transition from reaction 7 to 4 is expected. The results presented in Table 1 are in very good agreement with the above expectation. One deviation that was observed is that the TiSi phase was not identified experimentally which may be attributed to the inability to detect it or to the finite number of annealing temperatures that were investigated.

For the case of Ti–Si_3N_4 interactions in reactive ambient (e.g. N_2), one has to consider the relative reaction rates of Ti–Si_3N_4 and Ti–N_2 reactions. Because of the N_2 interaction with Ti, the formation of the TiN outer layer was observed even for the low reaction temperatures. Because of the consumption of Ti by N_2, the effective Ti/Si_3N_4 ratio was smaller for nitrogen reactions, at similar temperatures, when compared with the reactions in argon. This resulted in the formation of Si at 1000°C for nitrogen ambient in contrast with 1100°C for argon ambient (compare Tables 1 and 2).

The intriguing aspect of the reaction between thin films of Ti and Si_3N_4 is the formation of three layered structure for annealing in argon ambient. It is worthwhile to present a model for the formation of this structure in terms of thermodynamics and kinetics of the reactions. As can be seen from the Ti–Si–N phase diagram [4], TiN is stable with al of the titanium silicides or Si and Si_3N_4, but Si_3N_4 is not stable with any of the titanium silicides. This explains the absence of Si_3N_4–titanium silicide interface in the products and the presence of TiN always sandwiched between Si_3N_4 and titanium silicide. At the beginning of the reaction between Si_3N_4 and Ti, we assume that Si_3N_4 decomposes. Reaction of Si and nitrogen with Ti results in the formation of silicide and nitride layers. Since the silicide layer is not stable in contact with Si_3N_4, the layer structure at Si_3N_4 interface will be Si_3N_4/TiN/Ti_xSi_y. As the reaction continues the unreacted titanium layer will become saturated with dissolved nitrogen, finally resulting in the formation of the outer TiN layer, because the nitrogen diffuses much faster through the titanium products than Si. The concentration of Si increases in the silicide layer and results in the compositional transition from Ti_5Si_3 to Si (y/x value from 3/5 to 1).

SUMMARY

The reaction of Ti with Si_3N_4 is influenced not only by temperature but also by the composition of ambient atmosphere. Under rapid thermal annealing conditions, the composition of final phases is determined by the effective Ti/Si_3N_4 ratio rather than the starting ratio. The effective ratio decreases with increasing temperature and reactive gas concentration in the ambient. Products represented by reactions 4 to 7 of Table 3 were only observed under the experimental conditions used. The formation of the three layered structure was explained by assuming initial decomposition of Si_3N_4 and faster diffusion of nitrogen through the product layer. The effectiveness of rapid thermal annealing for imposing kinetic limitations on thin film reactions was clearly demonstrated.

REFERENCES

1) M.Santella, Adv.Ceram.Mater., 3, 457 (1988).
2) S.Kang, E.M.Dunn, J.H.Silverman, and H.J.Kim, Am.Ceram.Soc.Bull., 68, 1608 (1989).
3) Yu.S.Borisov, A.L.Borisova, Yu.A.Kocherzhinskii, and E.A.Shishkin, Poroshkovaya Metallurgiya 183, 63 (1978).
4) R.Beyers, R.Sinclair, and M.E.Thomas, J.Vac.Sci.Technol. B2, 781 (1984).
5) A.E.Morgan, E.K.Broadbent, and D.K.Sadana, Appl.Phys.Lett., 49, 1236 (1986).
6) J.C.Barbour, A.E.Kupier, M.F.C.Willemsen, and A.H.Reader, Appl.Phys.Lett., 50, 953 (1987).
7) S.B.Desu and J.A.Taylor, J.Am.Ceram.Soc., in press.
8) J.A.Taylor and S.B.Desu, J.Am.Ceram.Soc., 72, 1947 (1989).
9) B.Holmberg, Acta.Chem.Scand., 16, 1245 and 1255 (1962).

CHEMICAL INTERACTIONS IN THE ALUMINUM-CARBON AND ALUMINUM-SILICON CARBIDE SYSTEMS

Benji Maruyama*, Fumio S. Ohuchi** and L. Rabenberg***

*NRL-NRC Research Associate, Naval Research Laboratory Code 6371 Wash. D.C. 20375-5000, Formerly Center For Materials Science, University of Texas at Austin.

**E.I. du Pont de Nemours Exp Station, Box 80365 Wilmington, DE 19898

***Center For Materials Science, The University of Texas at Austin, Austin, TX 78712

ABSTRACT

X-ray Photoelectron Spectroscopy (XPS) was used to investigate the influence of O_2 and H_2O on the formation of aluminum carbide at aluminum-carbon and aluminum-silicon carbide interfaces. It was determined that dosing the interfaces with H_2O catalyzed the formation of aluminum carbide in both the aluminum-carbon and aluminum-silicon carbide systems. This result is consistent with the oxidation model of carbide formation [1], previously developed to understand the kinetics of aluminum carbide formation at graphite-aluminum interfaces. These results imply that the formation of aluminum carbide in graphite and silicon carbide reinforced metal matrix composites, which severely degrades the composite mechanical properties by degrading the fiber and interface strength [2], is catalyzed.

INTRODUCTION

Both aluminum-carbon and aluminum-silicon carbide couples react to form aluminum carbide upon heat treatment. The formation of aluminum carbide is a severe problem in aluminum-carbon and aluminum silicon carbide metal-matrix composites. In these composites, the carbide degrades the mechanical properties of the composite by weakening the interface and by producing stress concentrations in the fiber. Our oxidation model of carbide formation [1] predicted the reaction between aluminum and carbon was catalyzed by oxygen in a chemically active state.

The oxidation model of carbide formation predicted active oxygen present at the aluminum-carbon interface would catalyze carbon-carbon bond breakage and subsequent carbide formation. Briefly stated, the oxidation model of carbide formation states that the process of dissociation of carbon atoms from bulk carbon is analogous to the dissociation of carbon atoms during the oxidation of carbon in oxygen-containing gases. XPS of composite interfaces was chosen as the best technique to study carbide formation, and thereby test the model.

EXPERIMENTAL

Glassy-carbon and CVD ß-SIC sample surfaces were prepared by polishing with 0.05μ alumina powder. Samples were out-gassed prior to Al deposition. The silicon carbide samples were sputtered with 2.5keV argon ions at 800°C.

Aluminum deposition and H_2O- and O_2-dosing were performed in-situ concurrent with photoemission spectra acquisition. The gas dosing procedures are described in more detail in reference [4]. Approximately 2 nm of aluminum were deposited as estimated by relative peak intensities. Gas exposure was 500 Langmuirs of H_2O or O_2, 1×10^{-6} Torr for 500 seconds. Heat treatments were performed either in front of the analyzer or in an antechamber. Heat treatments were performed at 410°, 600 or 800°C for 10 minutes. Binding energies were determined by peak fitting, and were in agreement with those found in the literature [3].

RESULTS

H_2O Catalysis of Al_4C_3 Formation in Al-Glassy Carbon

Aluminum carbide formation was measured by analysis of C(1s) photoelectron spectra taken from heat treated samples. Samples were heat treated for 410°C, 10 minutes, and dosed with 500 Langmuirs H_2O or O_2, or left un-dosed prior to heat treatment. In Figure [1], the H_2O-dosed sample clearly exhibits enhanced carbide formation as compared to the O_2- and un-dosed samples, inferring H_2O dosing catalyzes aluminum carbide formation.
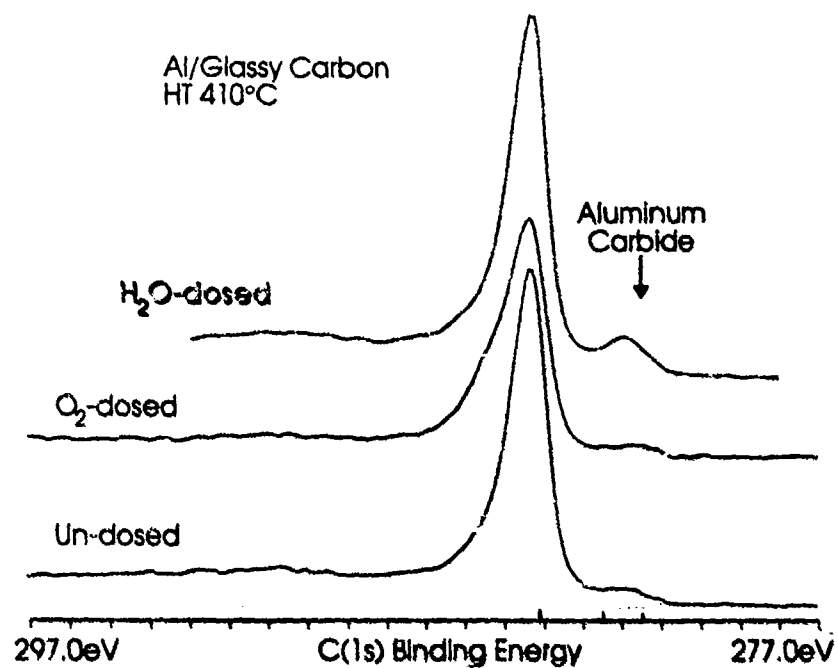
Figure [1]. Glassy Carbon Binding Energy 284.1eV,
Al₄C₃ 281.5eV, Al-O-C 282.5eV
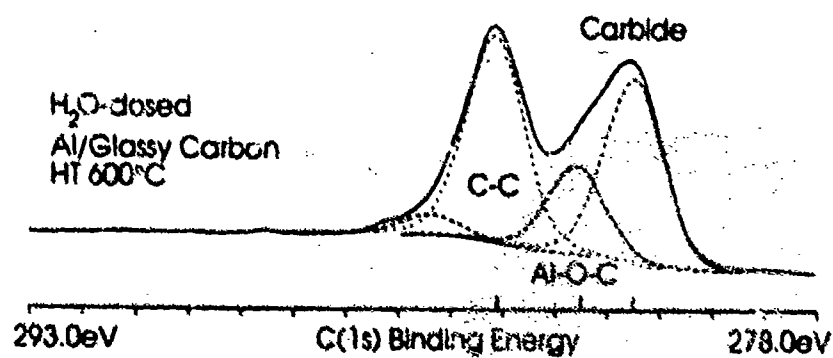
Figure [2]. Values for C(1S) photoelectron binding energies are as follows: Al₄C₃, 281.5eV, aluminum oxycarbide, 282.5eV. These are 2.6 and 1.6eV below glassy carbon C-C peak at 284.1eV. Peak at 285.4 is due to photoelectrons from oxidized carbon atoms.

Al₄C₃ and Aluminum Oxycarbide Peak Positions

One sample was completely reacted (600°C, 10 min) so that the peak positions of the reaction products could be clearly determined. Figure [2] shows a C(1s) spectrum from $H_2O/Al/C$, heat treated at 600°C for 20 minutes, until fully reacted. This spectrum clearly shows peaks corresponding to the binding energy of C(1s) photoelectrons from Al_4C_3, 281.5eV and aluminum oxycarbide, 282.5eV, which are 2.6 and 1.6eV, respectively, below the glassy carbon C-C peak at 284.1eV.

H_2O Catalysis of Al_4C_3 Formation in Aluminum-SiC

The success of the Al-carbon experiments led us to test the effect of H_2O on the formation of aluminum carbide in the aluminum-SiC system. The motivation for this experiment was the presumption that strong bonding of oxygen to SiC surfaces also weakens Si-C bonds, allowing catalytic dissociation of carbon and silicon, and subsequent formation of aluminum carbide and free silicon.

Aluminum carbide formation in aluminum-SIC couples was measured by analysis of Al(2p) photoelectron spectra taken from heat treated samples. H_2O-dosed and un-dosed samples of 2 nm Al on SIC, HT 600°C 10 minutes were analyzed. Figure [3] shows Al_4C_3 formation is much larger in the H_2O-dosed sample than in the un-dosed sample. These data indicate H_2O catalyzes aluminum carbide formation at aluminum-silicon carbide interfaces.

Formation of Free Silicon Upon Al_4C_3 Formation

The Si(2p) spectra in Figure [4] are from the same Al-SiC samples as in Figure [3]. The H_2O-dosed sample shows enhanced free silicon formation as compared to the un-dosed sample. This is expected as a product of the reaction:

$$4Al+3SiC \leftrightarrow Al_4C_3 + 3Si$$
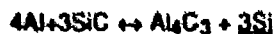
That is, mass balance requires enhanced free silicon formation in the H_2O-dosed sample occur in proportion to its enhanced aluminum carbide formation.
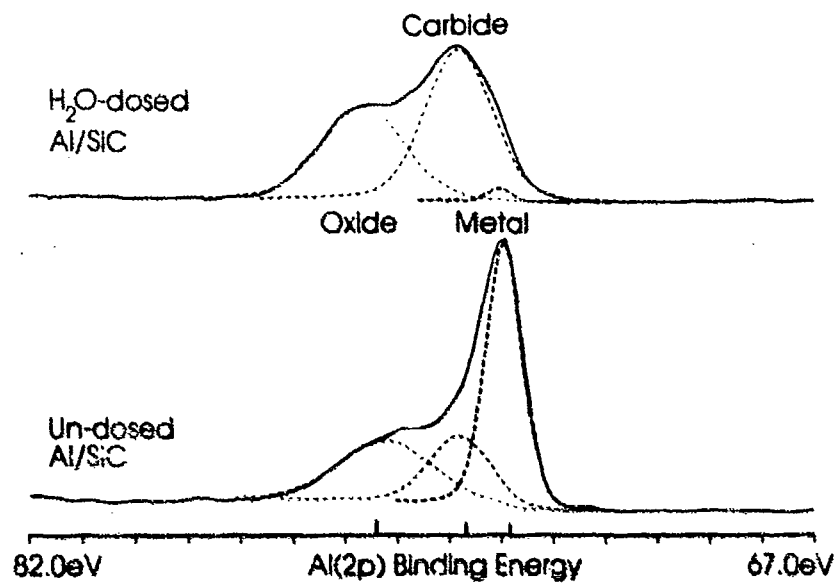
Figure [3]. Al₄C₃ Al(2p) photoelectron binding energy: 73.7eV
Aluminum Oxide: 75.4eV, Aluminum Metal: 72.8eV
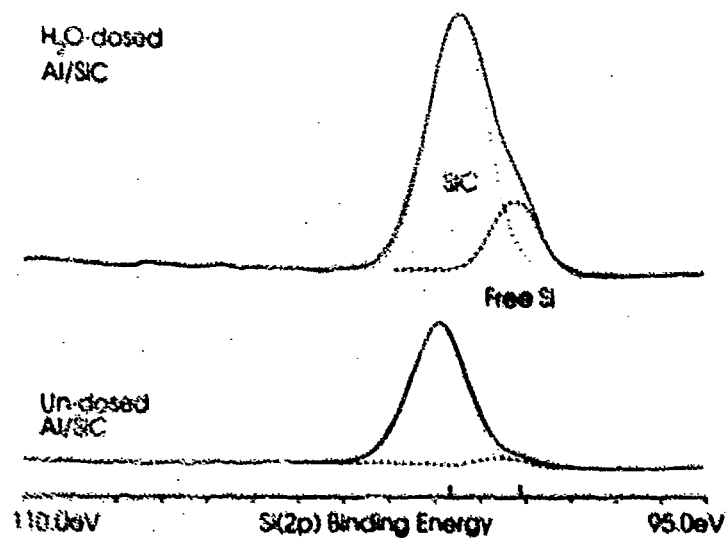
Figure [4]. Free silicon Si(2p) photoelectron binding energy: 99.1eV
SiC Si(2p) binding energy: 100.7eV

DISCUSSION

Currently, aluminum carbide formation in Al-Carbon and Al-SiC metal-matrix composites is avoided by coating the carbon or SiC reinforcement with a diffusion barrier. The current work suggests other means of controlling carbide formation, i.e. removing or deactivation the source of the catalyzing substance, H_2O. The results also confirm the usefulness of the oxidation model in describing the atomic structure of carbon reinforced metal-matrix composite systems, as well as the utility of the in-situ interface reaction/XPS technique developed by Ohuchi and Zhong [4]

This line of investigation, using in-situ XPS technique and the oxidation model, is being extended to other systems. We are currently considering Al-diamond, Ti-Carbon, Ti-SiC and Fe-Carbon as candidates for further investigation.

REFERENCES

1   B. Maruyama, L. K. Rabenberg, in Interfaces in Metal Matrix Composites, edited by A. K. Dhingra and S. G. Fishman eds (AIME Warrendale, 1986) p. 233.

2   V. M Bermudez. J. Appl. Phys. 63 (10), 15 May 4951 (1988).

3   T. W. Chou, A. Kelly and A. Okura. Composites, 16 (3) 187 July (1985).

4   Q. Zhong and F. S. Ohuchi in Interfaces Between Polymers, metals and Ceramics, edited by B. M. DeKoven, R. Rosenberg and A. J. Gellman, (Mater. Res. Soc. Proc. 153, Pittsburgh, PA 1989) p.71 Proc. Spring 89 MRS Conference, April 24-29, San Diego, CA.

STABILITY AND REACTIONS AT COMPOSITE INTERFACES OF TITANIUM ALUMINIDES WITH POTENTIAL FIBER MATERIALS

J. A. DEKOCK, Y. A. CHANG, M.-X. ZHANG AND O. Y. CHEN*
Department of Materials Science and Engineering, 1509 University Avenue, Madison, WI 53706.
*United Technologies, Pratt Whitney, E. Hartford, Connecticut

ABSTRACT

The Ti-Al-O and Ti-Al-B phase diagrams at 1100°C were estimated using thermodynamic data available in the literature assuming no ternary phases in either of the systems. Diffusion experiments consisting of a matrix of titanium aluminide with 2 at% Ta in contact with both Al_2O_3 and TiB_2 were carried out at 1100°C for up to 192 hours.

INTRODUCTION

Composite materials used as structural components at high temperatures are becoming an important class of emerging engineered materials. The ultimate performance of these materials depends a great deal on the stabilities at the composite interfaces. In the present study, we wish to study the interfacial stabilities between titanium aluminide and the two potential fibers Al_2O_3 and TiB_2. These and other ceramic fibers may be needed to improve the creep behavior of titanium aluminide at high temperatures.

The study was carried out using a combined computational/experimental approach. In addition to having compatible coefficients of thermal expansion between titanium aluminide and the ceramic fibers, there must also be thermodynamic stability at the interfaces. Kinetic barriers are unlikely to exist since these materials are to be used at high temperatures. Our approach is to first compute the phase equilibria of Ti-Al-O and Ti-Al-B using known and estimated thermodynamic data for all the binary phases. Assuming no ternary phases are present, the calculations were carried out using the program SOLGASMIX [1]. Based upon these calculations diffusion experiments involving titanium aluminide and the ceramic particles were performed.

APPROACH

Thermodynamic Calculation

The phase diagrams of Ti-Al-O and Ti-Al-B at 1100°C were calculated using the data available in the literature [2,3,4,5,6] and the program SOLGASMIX [1]. In this program, a Gibbs energy minimization technique is used.

Sample Preparation and Evaluation

Samples were prepared by hot pressing powder mixtures at 1288°C and 15 ksi for 2 hours. Two samples with a matrix composition of Ti-35.4 wt.%Al-9.14 wt.%Ta (Ti-52.1 at% Al-2.0 at% Ta) each containing 5 wt.% Al_2O_3 and TiB_2 respectively, were heat treated at 1100°C for 192 hours. Samples were coated with Y_2O_3 and vacuum sealed in quartz capsules. Heat treatment was performed in a resistance furnace. At the end of the heat treatment the samples were removed from the furnace and quenched in water. Each sample, together with a hot pressed (as received) sample for comparison purposes, was

Ti-Al-O Phase Equilibria @ 1100 °C
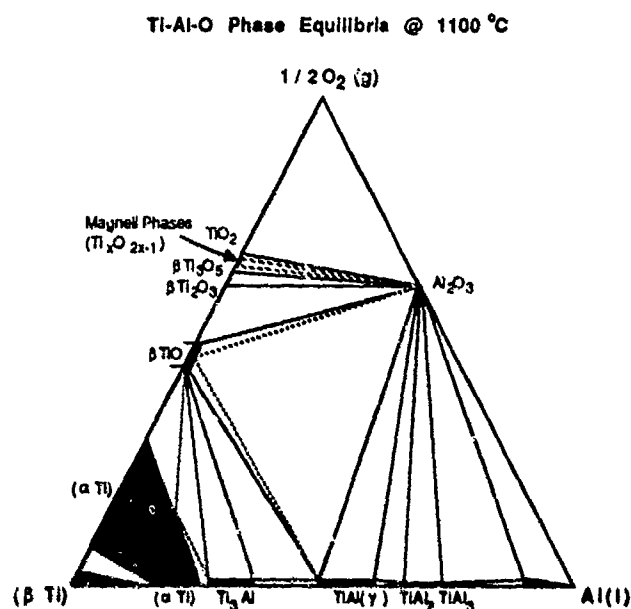
Fig. 1 Estimated phase equilibria for ternary system Ti-Al-0 at 1100° C.

then mounted, ground and polished. Comparisons between samples in the as received and heat treated conditions were made for each composite, both qualitatively by optical microscopy and quantitatively by electron probe microanalysis (EPMA). Microprobe analysis was done by traversing the matrix/particle interface in 2 micron increments perpendicular to the interface. Pure standards of Ti, Al, and Ta were used for calibration. Concentrations of 0 and B were determined by difference.

RESULTS AND DISCUSSION

The Ti-Al-O System

The estimated phase diagram at 1100° C is shown in Fig. 1. According to this diagram TiAl(γ, $L1_0$) is in equilibrium with Al_2O_3 and TiO, and Ti_3Al(α_2, DO_{19}) is in equilibrium with TiO. Tressler, Moore and Crane [7] carried out a phase equilibrium study at 871° C. On the basis of their investigation, two possible phase diagrams of Ti-Al-O at 871° C were proposed. In both of the proposed diagrams, TiAl is in equilibrium with Al_2O_3 and Ti_2O_3. However, in one of these proposed diagrams TiAl is in equilibrium with TiO but in the second it is not. Since not all of their samples reached equilibrium, it is difficult to interpret their experimental results. Until further experiments are performed, the 1100° C isotherm given in Fig. 1 must be considered tentative. It is noteworthy to point out that Tressler et al. also carried out diffusion couple experiments consisting of Ti and Al_2O_3 at 981° C for 940 hrs. They found the formation of Ti_3Al(α_2) and TiO between Ti and Al_2O_3. These data are consistent with the calculated phase equilibria in Fig. 1.

In addition to the isothermal section given in Fig. 1, a stability diagram, (i.e. log p_{O_2} versus $x_{Al}/(x_{Al} + x_{Ti})$), is also given in Fig. 2. This diagram gives the stabilities of the various phases as a function of oxygen pressure, while the isothermal section gives

Ti-Al-O Stability Diagram @ 1100 °C
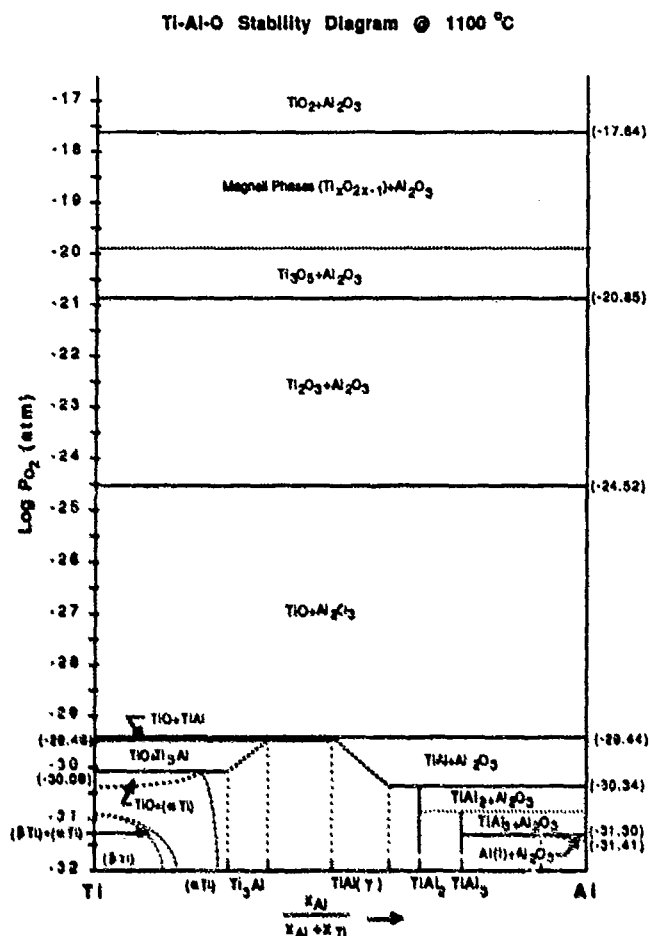
Fig. 2 Stability diagram for ternary system Ti-Al-0 at 1100° C.

information on the compositions of the co-existing phases.

Although the γ-phase used in the samples contained 2 at% Ta, the results obtained can be interpreted in terms of the Ti-Al-O phase diagram. Titanium aluminide is known to dissolve more than 2 at% Ta [8]. Since the oxides of Ta are less stable than those of Ti [2], the γ-phase with 2 at% Ta must be also in equilibrium with Al_2O_3, as shown in Fig. 1.

Remy et al. [9] reported the existence of the ternary phase $Al_2Ti_7O_{15}$, which has been omitted from Figs. 1 and 2 due to the inavailability of thermodynamic data. If included, minor changes would result, indicating $Al_2Ti_7O_{15}$ in two phase equilibrium with the phases Ti_3O_5, Ti_xO_{2x-1} and Al_2O_3.

Figure 3 shows the photomicrographs of a hot-pressed γ/Al_2O_3 sample (as received) and a sample heat treated at 1100° C for 192 hours. There is no evidence of any reaction at the interfaces. The composition profiles obtained by EPMA are shown in Fig. 4. It is noteworthy to point out that the compositions of γ determined by EPMA are 46.4±0.4 at% Ti, 51.6±0.4 at% Al and 2.0±0.05 at% Ta. The uncertainties are obtained from the

deviations of individual experimental points from the average values. However, we estimate the uncertainties for all three component elements to be ±0.5 at%. The concentrations determined by EPMA are in good agreement with the chemically analyzed values of 46.0 at% Ti, 52.1 at% Al and 2.0 at% Ta. As shown in Figs. 4A,B the

Fig. 3 Al_2O_3 particle in Ti-52.1 at% Al-2.0 at% Ta matrix: A) as received, b) heat-treated at 1100° C for 192 hours.
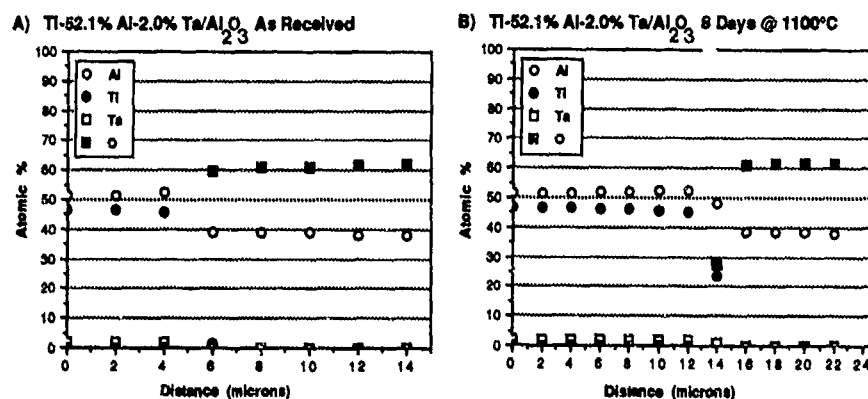
Fig. 4 EPMA results showing composition change across matrix/Al_2O_3 interface: A) as received, B) heat treated at 1100° C for 192 hours.

concentrations of Al in Al_2O_3 as determined by EPMA are the same, 38.9 at%, with the concentrations of oxygen obtained by difference. The microprobe results are consistent with the observation from the photomicrographs in that no reaction occurs at the interfaces.

The Ti-Al-B System

The calculated phase diagram of Ti-Al-B at 1100° C is shown in Fig. 5. According to this calculated diagram, γ is not in equilibrium with TiB_2. This calculated result is in contradiction to the experimental results shown in Figs. 6 and 7. As shown in Figs. 6A,B,

there is no evidence of any reaction at the γ/TiB$_2$ interfaces, for either the hot-pressed sample or the sample heat treated at 1100° C for 192 hours. The EPMA results given in Figs. 7A,B were in agreement with these observations. The concentrations of Ti determined by EPMA were 33 at% for the the hot-pressed and annealed samples. The concentrations of B are obtained by difference. It is interesting to note that the Ta concentration increases slightly at the γ/TiB$_2$ interfaces. This is quite reasonable since Ti

Ti-Al-B Phase Equilibria @ 1100 °C
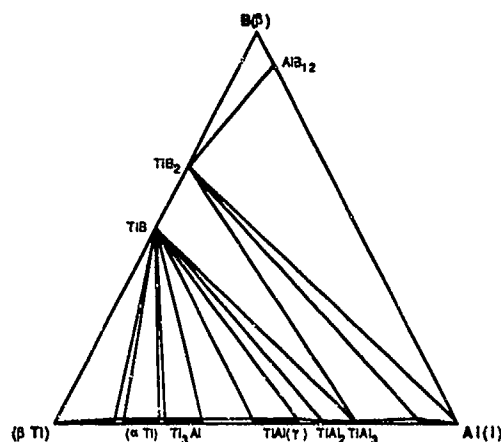
Fig. 5 Calculated phase equilibria for ternary system Ti-Al-B at 1100° C.
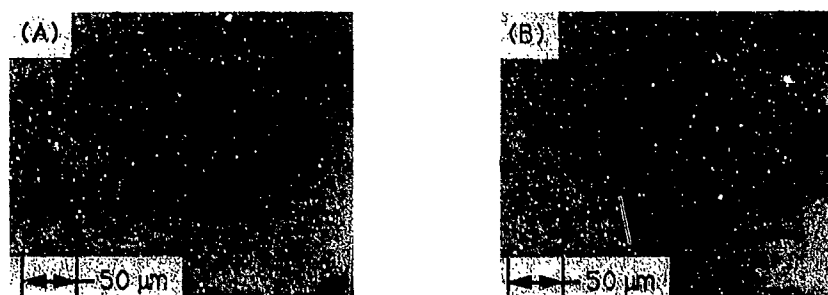
Fig. 6 TiB$_2$ particle in Ti-52.1 at% Al-2.0 at% Ta matrix: A) as received, B) heat treated at 1100° C for 192 hours.

is in the same family as Zr, and that ZrB$_2$ and TaB$_2$ form solid solutions [10].

The discrepancy between the calculated phase diagram and the experimental results may be due to two reasons. The first is that thermodynamic data available for the system Ti-B is inaccurate. The second is that there is a kinetic barrier between γ and TiB$_2$. Further experiments are being conducted in order to resolve this discrepancy.
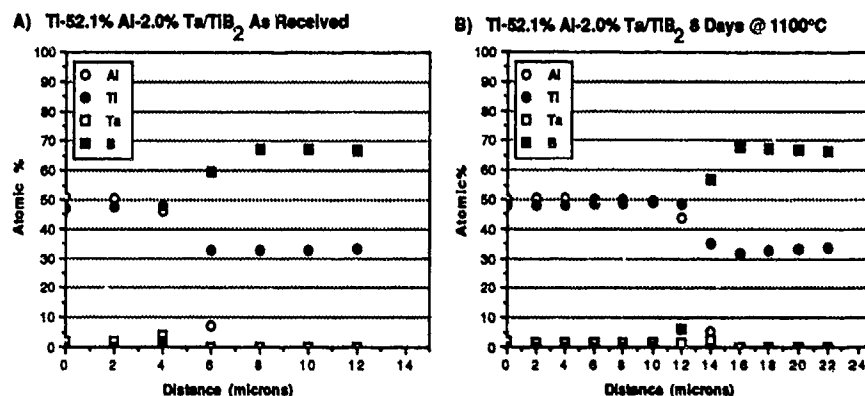
Fig. 7 EPMA results showing composition change across matrix/TiB$_2$ interface: A) as received, B) heat treated at 1100° C for 192 hours.

ACKNOWLEDGEMENTS

REFERENCES

1. G. Eriksson, SOLGASMIX (computer program), Chemica Scripta 8, 100-103 (1975), adapted for the IBM-PC by P. K. Liao and K. E. Spear, Pennsylvania State University.
2. L. B. Pankratz, Thermodynamic Properties of Elements and Oxides, Bulletin 672, United States Bureau of Mines, 1982.
3. I. Barin, O. Knacke and O. Kubaschewski, Thermochemical Properties of Inorganic Substances (Springer-Verlag Publishers, New York, 1973).
4. J.-C. Lin, T. Jewett, J. C. Mishurda, Y. A. Chang and J. H. Perepezko, "Materials Processing/Thermodynamics and Reactions at Interfaces", Second Annual Report ONR Contract (0014-86-K-0753), 1988.
5. D. R. Lide, J. Physical and Chemical Reference Data 4(1), 138 (1975).
6. J. L. Murray, P. K. Liao and K. E. Spear, Bulletin of Alloy Phase Diagrams 7, 6 (1986).
7. R. E. Tressler, T. L. Moore and R. L. Crane, J. Materials Science 8, 151-161 (1973).
8. S. Sridharan and H. Nowotny, Z. Metallkunde, 74, 468 (1983).
9. F. Remy, O. Monnereau, A. Casalot, F. Dahan and J. Galy, J. Solid State Chemistry 76, 167-177 (1988).
10. E. Rudy, "Compendium of Phase Diagram Data", AFML-TR-65-2, Part V, 1969.

THE EFFECT OF TEMPERATURE ON THE CHEMISTRY AND MORPHOLOGY OF THE INTERPHASE IN AN SCS6/Ti-6Al-4V METAL MATRIX COMPOSITE.

C.JONES^; C.J.KIELY^*, and S.S.WANG
National Centre for Composite Materials Research, University of Illinois, Urbana, Illinois 61801;*Materials Research Laboratory, University of Illinois, Urbana, Illinois 61801.
(^Now at Liverpool University, England)

ABSTRACT

The changes in chemistry and morphology within the interphase region of an SCS6/Ti-6Al-4V metal matrix composite upon exposure to varying heat treatments have been studied. It is thought that changes such as the formation of small TiC particles at one interface, and the narrowing of a protective pyrocarbon layer at another, induce fracture to occur at different places within the interphase upon heating. Evidence for a phase change on heat treatment of a $Ti_xSi_y(C)$ layer to the more thermodynamically stable silicide phase, Ti_5Si_3 is also presented.

INTRODUCTION

In the past decade there has been a great interest in developing composite materials based on embedding silicon carbide fibres in titanium alloy matrices. In such instances the silicon carbide fibres are usually coated with a protective layer to prevent abrasion and improve handling properties as well as inhibit interfacial reactions between fibre and matrix which may be detrimental to the mechanical properties of the fibres themselves. Many such protective coatings have been studied [1,2,3] each resulting in a variety of chemical reactions with the titanium matrix. However, none of these coatings proved successful in protecting the SiC filaments from matrix interaction. In 1982 Debolt et al at AVCO [4] developed an SCS coating which has been modified in recent years to overcome such problems. The latest form is an SCS6 coating which consists of a thin layer of pure pyrocarbon surrounding the filament followed by an SiC/C mixture in which the Si:C ratio increases towards the surface. In our previous study [5], a thorough investigation of the interface between SCS6 and Ti-6Al-4V in an "as received sample" was carried out. A schematic diagram of the complex interphase region observed is shown in Fig.1(a) together with an SEM image of an angle lapped sample (shown in Fig.1(b)). It can be seen that the interphase region consists of numerous layers most of which originate from the SCS6 coating itself. However, reaction has taken place between the outermost layers of the coating and the matrix to form a region of titanium carbide and a continuous layer of a carbon containing titanium silicide phase $Ti_xSi_y(C)$.

In this paper, we report a systematic study of the effect of prolonged exposure to elevated temperature on the interfacial chemistry and morphology of this composite. The microstructural and chemical changes occurring are thought to play dominant role in the fracture surfaces obtained from these samples.

EXPERIMENTAL PROCEDURE

A set of SCS6/Ti-6Al-4V metal matrix composite samples prepared from the same initial "as received" sample, were subjected to 100°C, 200°C, 300°C and 600°C anneals in air for 8 hours. Cross section samples for Auger and SEM analysis were mechanically cut 10° from the fibre axis. The machined surfaces were then mechanically polished progressing from 600 grade SiC paper to 6 μm and then 1 μm diamond paste until highly polished surfaces were achieved.

TEM samples were prepared by cutting 0.5mm thick perpendicular sections , then
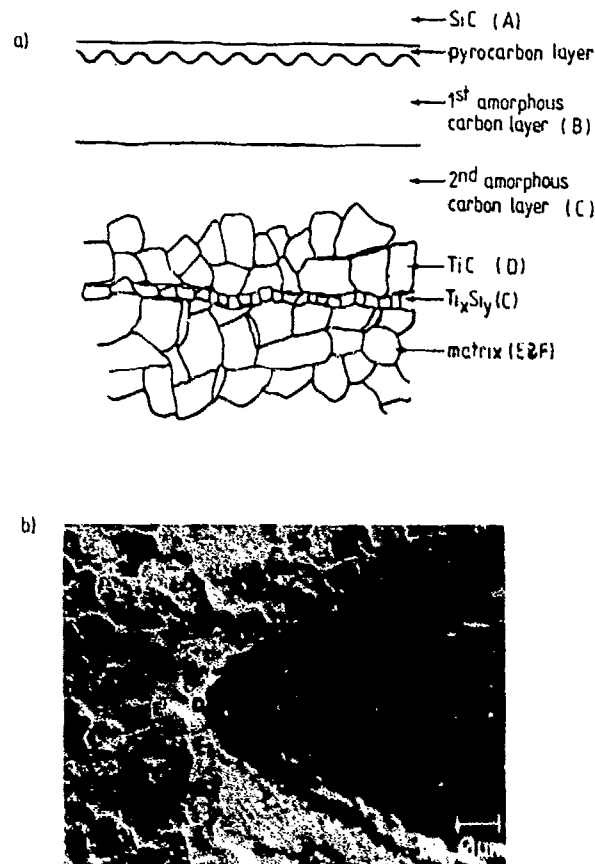
Figure 1 Schematic diagram and SEM micrograph of SCS6/Ti-6Al-4V Interphase.

mechanically polishing down from both sides to a total thickness of 80 μm. These sections were then ion milled to perforation with 6kV Ar+ ions at an incidence angle of 25°. TEM was carried out in a Phillips EM430 operating between 150 and 300kV.

Auger analysis was performed on PHI 660 and PHI 595 scanning Auger spectrometers, the latter being equipped with an *insitu* fracture stage enabling the chemistry of the fracture surface to be studied at pressures <10^{-9} Torr. These fracture surfaces were then further examined in a JEOL 35C scanning electron microscope. Line profiles and other Auger data were taken after each sample had been sputtered with 3kV Xe+ ions for 30 minutes (or until all the surface oxygen was removed).

RESULTS AND DISCUSSION

The Silicide Layer

In our previous study[5], it was noted that the continuous silicide layer (shown in Fig.1(a)) did not have a crystal structure corresponding to any of the previously reported titanium silicide phases. From Auger analysis it was shown that this layer contained appreciable but varying amounts of carbon. Fig.2(a) shows the convergent beam pattern from a prominent zone axis of one of these silicide grains. Similar convergent beam
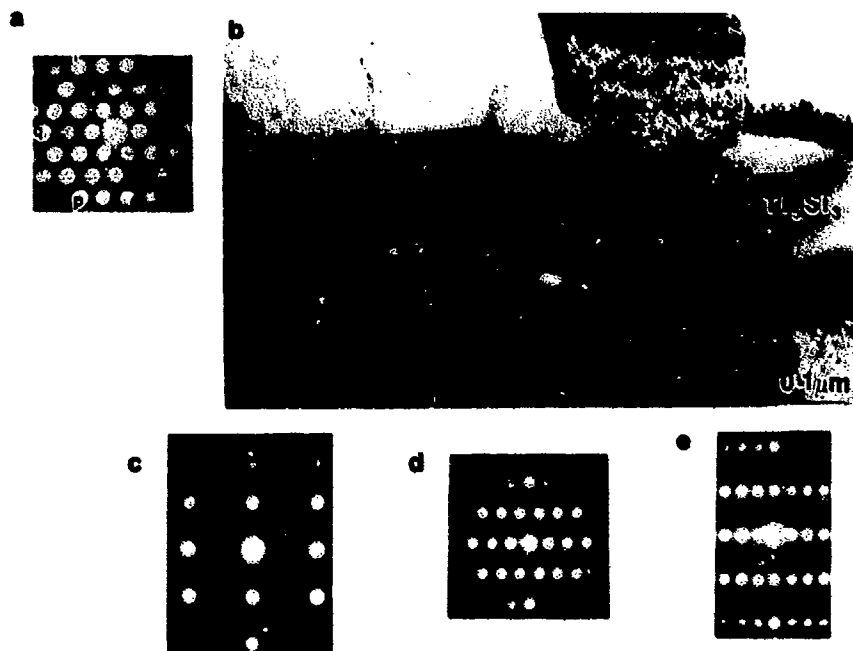
Figure 2 (a) CBP of one major zone axis in a $Ti_xSi_y(C)$ grain, (b) TEM micrograph of silicide layer in a sample heated to 300°C; (c) $(01\bar{1}0)$ (d) $(1\bar{2}13)$ (e) $(1\bar{2}10)$zone axes from the Ti_5Si_3 layer.

patterns from a large number of such crystals have been analysed and it has been found that g_R spacings vary from grain to grain in the range 0.177 to $0.182Å^{-1}$, with $g_P = g_Q$ $=0.177Å^{-1}$. Hence some of the patterns are perfectly hexagonal and others show a slightly distorted hexagonal implying that the composition and structure from grain to grain is slightly variable in this silicide layer. However, the inferred plane spacings of $d_P=d_Q=5.64Å$ and $5.63>d_R>5.55Å$ are not consistent with the expected Ti_5Si_3 $(10\bar{1}0)$ spacings of 6.45Å.

However, in all the heat treated samples examined, this layer has transformed to the more thermodynamically stable Ti_5Si_3 phase as indicated by the $(0\bar{1}10)$, $(1\bar{2}13)$, and $(1\bar{2}10)$ CBPs (shown in Figs 2c,d and e). The overall thickness of this layer (shown in Fig2b) remained unchanged.

The SiC/Carbon Coating

A series of Si line profiles through the first carbon layer (C) taken from the "as received"and heat treated samples is presented in Fig.3. The Si signal, in all cases, was normalised to that of the SiC itself. It can be seen that Si has diffused to some extent in all these heat treated samples. The amount of Si diffusion is seen to increase with increasing temperature to which the samples had been exposed. TEM examination of this layer reveals that the elongated SiC crystals within this layer increase in size and number density with increasing temperature, from an average of 50 x 150Å in the as received sample to 150 x 400Å in the sample heat treated at 600°C.

As noted previously, the SCS coating is designed to protect the SiC filament against damaging interfacial reactions with the matrix and also acts to relieve stress concentration at the surface of the SiC filament itself. The layer most responsible for this
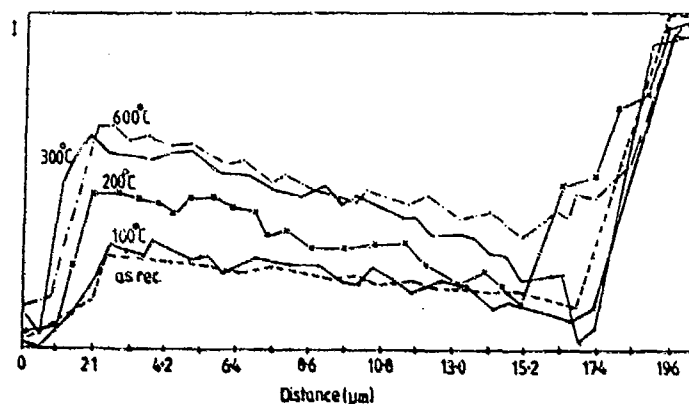
Figure 3 Si Auger line profiles through the amorphous carbon layer (B)

latter characteristic is the pyrocarbon layer (see Fig.4a and b) which is directly adjacent to the SiC filament [6]. It was found that the thickness of this layer decreased significantly with increasing temperature to which the sample had been exposed (from 0.15 µm in the as received sample to 0.038 µm in the sample heated to 600°C).

The SCS6/matrix Reaction Zone

Titanium is also known to diffuse into the SCS coating. On processing the composite, the Ti first reacts with the outer shell of SiC surrounding the fibre to form a thin but continuous layer of silicide (as described above). It then further diffuses through this layer (probably via the grain boundaries) into the carbon layers of the SCS6 coating to form TiC. At first the TiC crystals formed are small , but during processing they anneal and recrystallise to form much larger grains (approximately 0.3-0.5 um in size). Upon heat treating these samples two processes occur. Firstly, Ti diffuses further into the SCS coating to react with the carbon layer forming TiC microcrystals hence advancing the TiC layer deeper into the amorphous carbon layer. Secondly, some grain growth of buried TiC crystals occur. Fig.5 shows the TiC interphase layer for the sample heat treated to 200°C. A distinct gradation in grain size from one side of the layer to the other is seen. Adjacent to the silicide layer, the TiC grains are "tooth" shaped with typical diameters of 0.6 µm. This is followed by a layer of intermediate sized TiC crystals about 600Å which have a
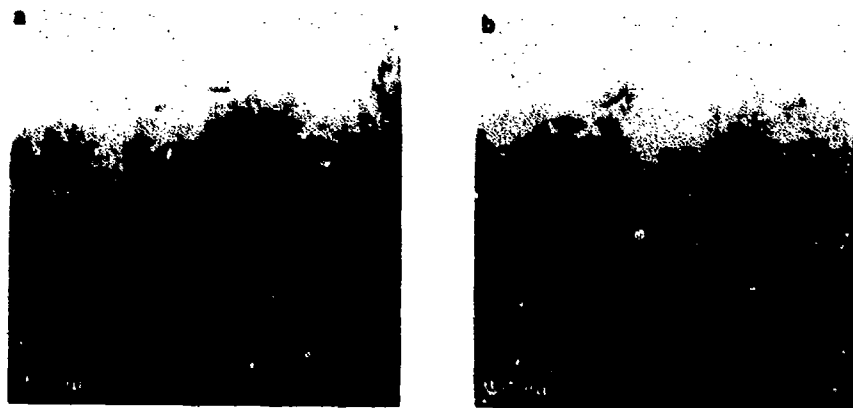
Figure 4 TEM micrograph of SiC/pyrocarbon/main carbon layer (B) region (a)"as rec. (b)300oC samples

Figure 5 TEM micrograph of the TiC layer in a sample heated to 300°C

less defined shape. Finally, the microcrystalline layer is found adjacent to the amorphous carbon layer.

<u>Fracture Surface Analysis</u>

Fig. 6 shows a series of SEM images from the fracture surfaces of the "as received" as well as the 300°C and 600°C samples. As shown previously [5], fracture takes place in the "as received" sample between the TiC layer and the second amorphous carbon layer (C). However, we have noted in previous sections that microstructural changes have occurred within the interphase region as a result of heat treatment. The two dominant changes effecting where fracture takes place are the following. Firstly, the increasing number of small TiC grains at the TiC/C interface would tend to lead to a strengthening of this interface (due to intermixing and the increased interface area). Furthermore, large grains at the interface on the other hand, are likely to be stress concentrators which would be detrimental to interfacial strength. Secondly, the decreasing thickness of the stress absorbing pyrocarbon layer closest to the SiC filament may weaken the SiC/C interface. The effect of the former effect is apparent in the sample exposed to 300°C (Fig.6(a)). Fracture in this case has taken place within the amorphous carbon layers instead of at the TiC/C interface as in the "as received" sample. The Auger analysis of this fracture surface reveals that oxygen has diffused and reacted with the SiC filament to form silicon oxide at the edges of the sample which were exposed to air during heating. Where this edge effect has occurred, fracture has taken place between this oxidised layer and the adjacent carbon layer. For the sample exposed to 600°C (Fig.6(b)), a significant number of broken fibres were observed on the fracture surface, suggesting that the pyrocarbon layer has lost most of its stress relieving properties.

CONCLUSIONS

The coating on the SiC fibres in the above samples is in fact a double pass of the SCS coating described by Debolt et al [4] with an outer shell of stoichiometric SiC. This would explain the interfacial formation of a continuous layer of silicide formed during processing which does not appreciably change in thickness upon heating. A phase change from $Ti_xSi_y(C)$ to the more thermodynamically stable hexagonal Ti_5Si_3 phase occurred upon annealing in air.

The changes in chemistry and morphology which occur as a result of prolonged heat treatment in air have been found to play an important role in determining the precise position where fracture occurs within the interphase and will affect the overall
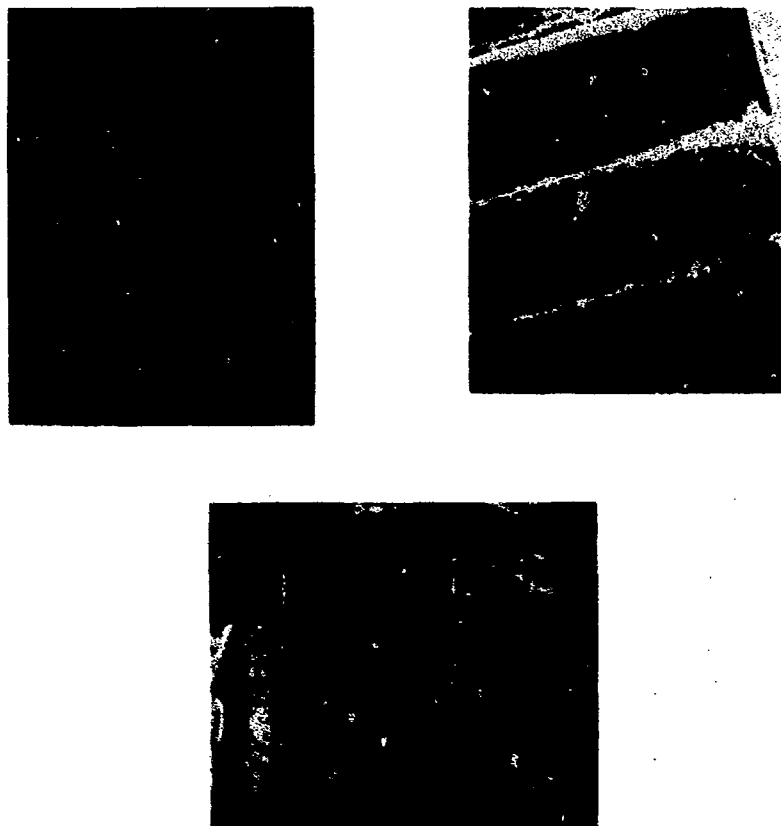
Figure 6   SEM images of a fracture surface from (a)"as rec.", (b) 300 °C, and (c) 600 °C samples.

performance of the composite at various temperatures. Diffusion of both Ti and Si was observed to occur during heat treatment. The diminishing thickness of the pyrocarbon layer adjacent to the SiC filament may be responsible for the fibre breakage observed on the fracture surfaces of samples heated to 600°C. The formation of numerous small TiC particles is thought to strengthen the bonding at the TiC/C interface and leads to fracture within the amorphous carbon layers in the 300°C sample instead of at the TiC/C interface itself observed for the "as received" sample.

REFERENCES

[1]   P.Martineau, M.Lahaye, R.Pailler, R.Naslain, M.Couzi and F.Cruege, J. Mater. Sci., 19, 2731, (1984).
[2]   P.Martineau, R.Pailler, M.Lahaye and R.Naslain, J.Mater.Sci, 19, 2749, (1984).
[3]   R.Pailler, P.Martineau, M.Lahaye and R.Naslain, Revue de Chime Minerale, 18 520 (1981).
[4]   H.E.Debolt, R.J.Suplinskas, J.A.Cornie, T.W.Heinze and W.Hauze, US Patent 4340636, July 20 (1982).
[5]   C.Jones, C.J.Kiely and S.S.Wang, J.Mater.Res., 4, No.2, 327, (1989).
[6]   S.R.Nutt and F.E.Wawner, J.Mater.Sci., 20, 1953, (1985).

SOLID STATE REACTIONS IN MECHANICALLY DEFORMED COMPOSITES IN THE NI-ZR AND THE NI-TI SYSTEMS

B. E. White, M. E. Patt and E. J. Cotts
Department of Physics, Applied Physics and Astronomy
State University of New York at Binghamton, Binghamton, NY 13901

ABSTRACT

Differential scanning calorimetry and x-ray diffraction analysis were utilized to monitor solid state reactions in mechanically deformed Ni/Ti multilayered composites. Solid state reactions at temperatures less than ≈ 650 K result in the formation of a highly disordered phase which is apparently amorphous.The subsequent nucleation and growth at higher temperatures of intermetallic compounds from the amorphous phase is examined. The relatively small thickness of amorphous material (less than 100 Å) which can be grown by solid state reaction in our Ni/Ti samples, combined with the indication that a disordered interface such as that produced by mechanical deformation facilitates these reactions in the Ni-Ti system, may provide some explanation for the relatively high degree of success experienced in the production of amorphous Ni-Ti by means of ball milling. Comparisons are made to results obtained in the Ni-Zr system.

Introduction

Single phase amorphous alloys can form in diffusion couples at relatively low temperatures (approximately half pertinent melting temperatures) by means of interdiffusion of pure, polycrystalline elements [1-12]. A number of requirements have been proposed for a successful solid state amorphization reaction (SSAR). The two metals which form the diffusion couple must possess a large, negative heat of mixing in the amorphous phase in order to drive the reaction. There must be a dominant moving species , i. e. one constituent of the diffusion couple should exhibit a much greater mobility than the other [4-6]. Such a disparity in the mobility of the atoms in the diffusion couple provides a constraint on the formation of equilibrium intermetallic compounds in a given temperature range and time frame, i. e. a kinetic constraint. The movement of both constituents is apparently required to nucleate and grow crystalline material while the mobility of only one constituent is required to grow an amorphous alloy. It has also been indicated that initially (in the as-prepared composite) a certain degree of disorder must be present at the interface between the polycrystalline metals , if not an amorphous interfacial region, in order for the metastable amorphous material to grow. Without such existent disorder at the interface, the nucleation and growth of equilibrium intermetallic compounds may be favored [7,8].

Experimental observations in the Ni/Zr system have been performed supporting these hypotheses. Various diffusion studies indicate that Ni is the dominant moving species in the SSAR in Ni/Zr diffusion couples [5,6,9]. Differential scanning calorimetry (DSC) measurements have been utilized to establish that a negative difference in free energy between the pure elements and the amorphous phase (8-10 kCal/mol) drives these solid state amorphization

reactions in the Ni/Zr system [10-12]. Anneals of Ni/Zr diffusion couples consisting of Ni deposited on single crystal Zr fail to produce amorphous material, while with a more disordered interface a similar anneal results in the growth of amorphous material[7,8].

The present study concerns a comparison of solid state reactions in deformed composites from the Ni-Ti system and the Ni-Zr system. As both Zr and Ti are IVB elements, these systems are considered to be chemically and thermodynamically similar [13-18]. But while amorphous material has been observed to grow to thicknesses of up to 1000Å at Ni/Zr interfaces [2,10-12,19-24], such prodigious growth has not been observed in Ni/Ti composites [13,21,23,25]. In fact, the growth of only equilibrium intermetallic compounds has been observed in some Ni/Ti diffusion couples[13,21]. In the present work we sought to investigate the difference in the reaction kinetics in these two systems by means of differential scanning calorimetry (DSC) measurements [26] on mechanically deformed [27], multilayered composites of Ni/Zr and Ni/Ti. It has been previously suggested that either differences in the growth rates of the amorphous phase, or differences in the kinetic constraint on formation of equilibrium intermetallic compounds, are the cause of the difference in reaction product in these two systems[13]. The initial growth of amorphous material in our Ni/Ti composites is apparently facilitated by the relatively large degree of disorder induced in the metal layers, and therefore at the interfaces, by the mechanical deformation process. There is strong indication that in mechanically deformed composites in both the Ni-Ti and the Ni-Zr systems there exists a similar kinetic constraint on the formation of crystalline intermetallic compounds. We find that any growth of amorphous material is significantly slower in the Ni-Ti system than in the Ni-Zr system. This difference in growth rates severely limits the amount of amorphous material that can be grown by means of solid state amorphization reactions in the Ni-Ti system.

Samples utilized for this study were composites of multilayered elements, prepared by means of mechanical codeformation of polycrystalline foils in a rolling mill. The structures and phases of the samples in the as-prepared state as well as at various degrees of reaction are characterized by means of x-ray diffraction analysis and transmission electron microscopy. A Rigaku x-ray diffractometer with Ni-filtered, Cu K_α radiation was utilized to obtain x-ray diffraction profiles of samples. Reactions in diffusion couples of the Ni-Ti system or the Ni-Zr system are initiated as the samples (hermetically sealed in aluminum pans) are heated at a constant rate above room temperature in the DSC. The rate of heat release is measured by means of DSC through the course of a reaction. Each DSC scan was followed by a second scan (identical thermal conditions) of the same sample; the data from the second scan were subtracted from the data of the first scan. A Perkin-Elmer DSC-4 interfaced to a Compaq Deskpro 286 computer was utilized for DSC measurements.

Solid state reactions in Ni/Zr and Ni/Ti composites

A comparison of solid state reactions in Ni/Zr and Ni/Ti multilayered composites of similar average stoichiometries (near equiatomic), geometries and degrees of deformation was performed (Fig. 1). The DSC traces indicate that the
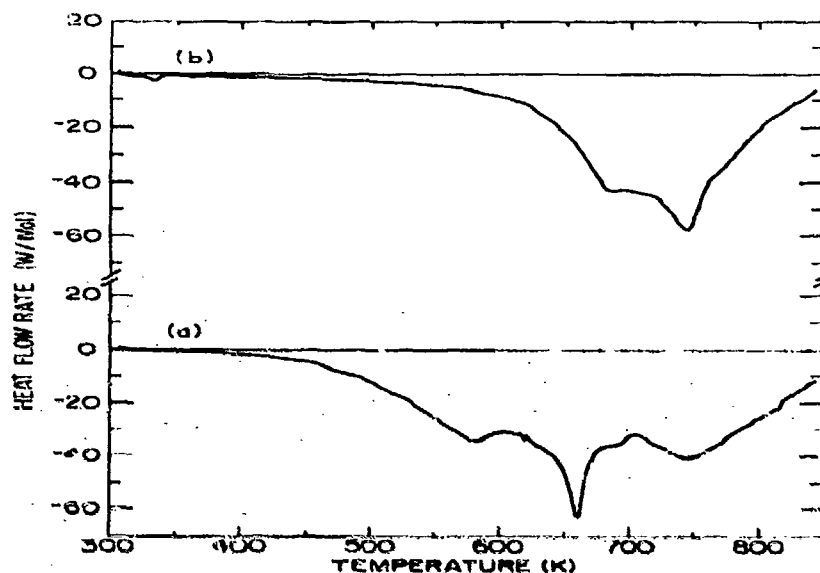
FIG. 1 The heat-flow rate as a function of temperature for a constant scan rate of 20 K/min, measured by means of differential scanning calorimetry. The samples were multilayered composites of average stoichiometry $Ni_{50}Ti_{50}$ and $Ni_{57}Zr_{43}$ produced by co-deformation of the two metals. The initial thicknesses of the polycrystalline foils was 10 μm for Ni and 20 μm for Zr and Ti. Both composites were deformed similar amounts with a deformation of about 99.9%. The data are for: (a) Ni/Zr system and (b) Ni/Ti system. The small downward going peak in the beginning of the trace in Fig. 1b reflects an endothermic signal observed in the second scan corresponding to the martensitic transition in $Ni_{50}Ti_{50}$.

- - - - - - - -

solid state reaction in the Ni/Zr composite is significantly faster than the solid state reaction in the Ni/Ti composite. Upon heating a Ni/Ti diffusion couple from 300 K to 850 K at 20 K/min in a differential scanning calorimeter (Fig. 1) a significant rate of heat release is first observed at about 580 K (this is in contrast to the reaction rate observed in the Ni/Zr diffusion couple of similar geometry[24]). Above a temperature of 580 K in the DSC scan of the Ni/Ti composite the reaction rate increases monotonically until a temperature of approximately 670 K. At this temperature a small, distinct peak is observed in the DSC scan followed by a marked decrease in the reaction rate and a series of peaks. X-ray analysis of similar samples heated to temperatures of 660 K and rapidly cooled to room temperature reveal Bragg peaks corresponding to the elements Ni and Ti, and a broad peak centered at $2\theta \approx 43.5$ degrees (Fig. 2b). Such a broad peak in x-ray scans is indicative of amorphous material[18,25], and the angle of its maximum corresponds to that of liquid quenched metallic glass of composition near $Ni_{63}Ti_{37}$. X-ray analysis of similar samples heated to temperatures of 670 K and rapidly cooled to room temperature reveals Bragg peaks corresponding to the elements, Ni and Ti, a broad peak centered at $2\theta \approx 43.5$ degrees and a new Bragg peak corresponding to

the intermetallic compound $Ni_{50}Ti_{50}$ with a CsCl structure, and perhaps some small peaks corresponding to hcp Ni_3Ti, indicating that a small amount of

crystalline material has been formed[28,29] (Fig. 2c). Similar samples heated to slightly higher temperatures and rapidly cooled to room temperature revealed x-ray diffraction patterns with additional new, small Bragg peaks corresponding to the CsCl structure of $Ni_{50}Ti_{50}$ and some small peaks corresponding to hcp Ni_3Ti. Upon examining numerous such Ni/Ti composites utilizing DSC and x-ray analysis we are able to correlate such a distinct change in the kinetics of the solid state reaction (as evidenced by a peak at a temperature near 670 K in DSC scans) with the presence of a small amount of crystalline material in the sample. Similar specimens examined in plane-view geometry with an Hitachi 7000 transmission electron microscope operated at 125 keV provide selected area diffraction patterns which indicate the same correlations between heat treatments and phase formation. Although in the absence of complete amorphization it is difficult to positively identify the phase initially formed in the Ni-Ti composites upon heating from room temperature, the evidence indicates that a highly disordered material which is either nanocrystalline or amorphous has formed.

Previous experiment [31] at temperatures near 1000 K has indicated that Ni atoms diffuse one or two orders of magnitude more rapidly in α-Zr than in α-Ti. Utilizing a means developed earlier[10-12], we attempt to calculate the rate of interdiffusion of Ni and Ti in amorphous Ni/Ti diffusion couples from the present DSC measurements. Assuming that we are observing diffusion limited,
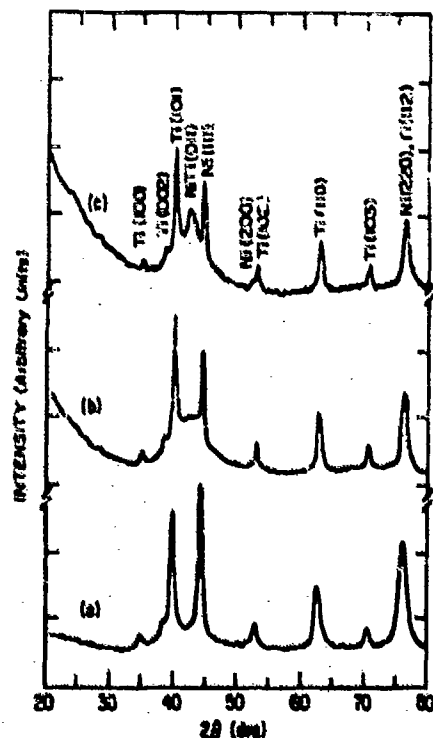
FIG. 2 X-ray diffraction profiles (Cu Kα radiation) for a multilayered composite of Ni and Ti of average stoichiometry Ni50Ti50.
(a) The as-co-deformed sample.
(b) The sample after being heated at 10 K/min to a temperature of 660 K and quenched to room temperature in the differential scanning calorimeter. (c) The sample after being heated at 10 K/min to a temperature of 670 K and quenched to room temperature in the differential scanning calorimeter.

one dimensional growth of amorphous material in the Ni-Ti system (cf. Fig. 1b at temperatures below 660 K) we examine the DSC data at temperatures from 620 K to 660 K. The integrated enthalpy release multiplied by the rate of enthalpy release as a function of reciprocal temperature for this data is fit to a straight line. We find an averaged interdiffusion constant $D = D_0 \exp(-E/kT)$, with activation energy $E =$ 1.35 ± 0.1 eV and D_0 within an order of magnitude of 8.1×10^{-5} cm^2/sec. A similar fit performed on the DSC data for the Ni/Zr composite of Fig. 1 results in an activation energy of 0.97 ± 0.1eV, and D_0 within an order of magnitude of 1.4×10^{-6} cm^2/sec. The large error in the determination of the prefactor D_0 is due to the difficulty in estimating the interfacial area in the deformed composites. At 600 K the calculated average interdiffusion constant in growing Ni-Ti amorphous interlayer is $D_{NiTi} = 3.5 \times 10^{-16}$ cm^2/s, as compared to $D_{NiZr} = 9.5 \times 10^{-15}$ cm^2/s at 600 K. The observed activation energy for the initial interdiffusion of Ni and Ti through the amorphous phase is significantly greater than that for the initial interdiffusion of Ni and Zr through the amorphous phase (1.35 versus 0.97). These activation energies are similar to those observed for diffusion of Ni atoms in α-Ti and in α-Zr[30-32].

The observed difference in growth rates in the Ni/Zr composites and the Ni/Ti composites appears to severely limit the amount of amorphous material that can be grown by means of solid state amorphization reactions in the Ni-Ti system. Utilizing our calculation of the averaged interdiffusion constant, we estimate the maximum thicknesses of amorphous material which could be grown in our Ni/Ti composites before the formation of equilibrium compounds (e.g. grown upon heating to 660 K in Fig. 1b) to be less than approximately 70 Å, more than an order of magnitude smaller than the limiting thickness (1000 Å) experimentally observed in Ni/Zr composites. The relatively small thickness of amorphous material which can be grown by solid state reaction in the Ni-Ti system, combined with the indication that a disordered interface such as that produced by mechanical deformation facilitates these reactions, may provide some explanation for the relatively high degree of success experienced in the production of amorphous Ni-Ti by means of ball milling[33-37]. Mechanically deforming powders by means of ball milling would most probably produce disordered interfaces. The continual creation of new Ni/Ti interfaces, and the relatively low temperatures produced in the ball mill, allows for short diffusion distances. Thus solid state amorphization reactions may run under these conditions while being frustrated in a more ordered geometry with an interlayer thickness greater than approximately 100 Å.

We have investigated solid state reactions in mechanically deformed composites in both the Ni-Ti system and the Ni-Zr system. We find indications that upon heating these composites from room temperature at a constant rate that amorphous material is the first phase to grow in both systems. Amorphous material grows much more slowly in Ni/Ti composites than in Ni/Zr composites. The maximum thickness of amorphous Ni-Ti layers that was successfully grown was determined to be less than approximately 70 Å, an order of magnitude smaller than that observed for Ni/Zr diffusion couples. This disparity appears to stem from the difference in mobilities of Ni atoms in these two systems.

Acknowledgements

References

1. R. B. Schwarz and W. L. Johnson, Phys. Rev. Lett. **51**, 415 (1983).
2. W. L. Johnson, Prog. Mater. Sci. **30**, 80 (1986) .
3. K. Samwer, Phys. Rep. **161**, 1 (1988).
4. R. B. Schwarz and W. L. Johnson, J. Less-Common Met. **140**, 1 (1988) .
5. Y. T. Cheng, W. L. Johnson, and M. -A. Nicolet, Appl. Phys. Lett.**47**,800 (1985).
6. H. Hahn and R. S. Averback, Phys. Rev. B **37**, 6537 (1988).
7. A. M. Vredenberg, J. F. M. Westendorp, F. W. Saris, N. M. van der Pers and Th. H. de Keijser, J. Mater. Res. **1**, 774 (1986).
8. W. J. Meng, C. Nieh, E. Ma, B. Fultz,and W. L.Johnson,J. Mater. Sci. Eng.**97**, 87(1988)
9. H. Hahn, R. S. Averback, and S. J. Rothman, Phys. Rev. B **33**, 8825 (1986).
10. E. J. Cotts, W. J. Meng, and W. L. Johnson, Phys. Rev. Lett. **57**, 2295 (1986).
11. L. Schultz, in *Rapidly Quenched Metals*, edited by S. Steeb and H. Warlimont (North-Holland, Amsterdam, 1984) p.551; L. Schultz, in Proceedings of the Sixth International Conference on Liquid and Amorphous Metals, in Z. Phys. Chem., 156 (1987).
12. R. Highmore, J. Evetts, A. L. Greer and R. E. Somekh, Appl. Phys. Lett. **50**, 566 (1987).
13. W. J. Meng, B. Fultz, E. Ma, and W. L. Johnson, Appl. Phys. Lett. **51**, 661 (1987).
14. J. C. Gachon and J. Hertz, CALPHAD **7**, 1 (1983).
15. A. W. Weeber, P. I. Loeff, and H. Bakker, J. Less-Common Met.**145**, 293 (1988).
16. K. H. Buschow, J. Phys. F. **14**, 593 (1984).
17. Z. Altounian, Tu Guo-hua, and J. O. Strom-Olsen, J. Appl. Phys. **54**, 3111 (1983).
18. K. H. Buschow, J. Phys. F **13**,563 (1983).
19. K. Hoshino, R. S. Averback, H. Hahn, and S. J. Rothman, J. Mater. Res. **3**, 55 (1988).
20. W. J. Meng, E. J. Cotts, and W. L. Johnson in Interfaces. Superlattices and Thin Films, edited by J. D. Dow, I. K. Schuller, J. Hillard, Materials Research Society Symposia Proceedings, Vol. 77 (Materials Research Society, Pittsburgh, 1987).
21. B. M. Clemens, J. Appl. Phys. **61**, 4525 (1987).
22. B. M. Clemens, Phys. Rev. B **33**, 7615 (1986).
23. B. M. Clemens and J. G. Gay, Phys. Rev. B **35** 9337 (1987).
24. G. C. Wong, W. L. Johnson and E. J. Cotts, to be published in J. Mat. Res..
25. J. F. Jongste, M.Hollanders, B.Thijsse, and E. Mittemeijer, Mat. Sci. Eng.**97**, 101 (1988).
26. E. J. Cotts, G. C. Wong and W. L. Johnson, Phys. Rev. B **37**, 9049 (1988).
27. M. Atzmon,J. Verhoeven,E. Gibson and W. L. Johnson, Appl. Phys. Lett. **45**,1052(1984)
28. S. Enzo, L. Schiffini, L. Battezzati,and G. Cocco, J. Less-Common Met.**140**. 129 (1988).
29. C. M. Jackson, H. J. Wagner, and R. J. Wasilewski, NASA Technology Utilization Pub. SP5110 (National Aeronautics and Space Administration, Washington, D. C. , 1972).
30. H. E. Kissinger, Anal. Chem. **29**, 1702 (1957).
31. G. M. Hood and R. J. Schultz, Phil. Mag. **26**, 329 (1972).
32. H. Nakajima, M. Keiwa, Y. Minonishi, and S. Ono, Trans. Jpn. Inst. Met. **24**,655 (1983).
33. R.B. Schwarz and C. C. Koch, Appl. Phys. Lett. **49**, 146 (1986).
34. R. B. Schwarz and R. R. Petrich, J. Less-Common Met. **140**, 171 (1988).
35. R. B. Schwarz, R. R. Petrich, and C. K. Saw, J. Non-Cryst. Solids **76**, 281 (1985).
36. E. Hellstern and L. Schultz, Appl. Phys. Lett. **48**, 124 (1986).

Interface Effects in Ceramic- and Metal-Matrix Composites

THE EFFECT OF WEAK INTERFACE ON TRANSVERSE PROPERTIES OF A CERAMIC MATRIX COMPOSITE

R. A. SHIMANSKY*, H. T. HAHN and N. J. SALAMON
The Pennsylvania State University, Department of Engineering Science and Mechanics,
University Park, PA 16802

ABSTRACT

Experimental studies conducted at the NASA Lewis Research Center on silicon carbide reaction-bonded silicon nitride composite system (SiC/RBSN) led to a significant observation regarding their unidirectional tensile properties. It was found that transverse stiffness and strength were much lower than those predicted from existing analytical models based on good interfacial bonding. Since the composite system was designed to have weakened interfaces to improve toughness, it was believed that these weakened interfaces were responsible for the decrease in transverse properties.

To support this claim, a two dimensional finite element analysis was performed for a transverse representative volume element. Specifically, the effect of fiber/matrix displacement compatibility at the interface was studied under both tensile and compressive transverse loadings. Interface debonding was represented active gap elements connecting the fiber and matrix.

The analyses show that the transverse tensile strength and stiffness are best predicted when a debonded interface is assumed for the composite. In fact, the measured properties can be predicted by simply replacing the fibers by voids. Thus, the following two conclusions are drawn from the present study: (1) little or no interfacial bonding exists in the SiC/RBSN composite; (2) an elastic analysis can predict the transverse stiffness and strength.

INTRODUCTION

Background

Ceramics and glasses are both inherently brittle materials that tend to be weak in tension but strong in compression. Fiber reinforcements have been used to improve the strength of these materials. Ceramic matrix composites (CMC) were first introduced over fifteen years ago by Phillips and his coworkers [1-3] when carbon fibers were imbedded in several glass matrix materials. In these early composite systems the stiffness and, more importantly, the ultimate strength were significantly higher than those of the monolithic matrix. Since the chemical reaction between fiber and matrix resulted in a strong interface, no change in the toughness (work-to-fracture) of these materials was observed.

To improve longitudinal toughness of CMC, mechanisms including fiber debonding and fiber pullout have been employed. These toughening mechanisms require a weak interface and strong fibers so that fiber/matrix debonding occurs at the matrix crack tip and matrix cracks propagate around instead of through the fibers. If the product of the fiber strength and fiber volume fraction is sufficient to support the additional load transferred by the failed matrix, the composite will continue to support load under a reduced stiffness, without catastrophic failure. This type of increased toughness has been observed by Prewo and Brennan [4-6] resulting in toughened glass-ceramic composites. The development of these composites showed that weakening the interface can significantly increase the toughness of these composites. A modified or weakened interface is obtained by preventing fiber-matrix chemical interactions by either (1) chemically treating the fiber surface or (2) natural formation of a carbon-rich interface from excess carbon in the fiber. With these modified interfaces, many new composite systems with enhanced longitudinal toughness and ultimate strain have been developed [7-9].

* Presently, Bucknell University, Mechanical Engineering Department, Lewisburg, PA 17837

Since structural applications of ceramic composites will invariably involve multiaxial loading, the transverse behavior of these materials must also be considered. In nearly all laminate designs, individual plies are subjected to loads parallel and perpendicular to the fiber direction.

Recently, the development of some CMC has included experimentally evaluation of transverse strength and stiffness of unidirectional laminates. These test results show a significant decrease in transverse properties from those expected for well-bonded fiber and matrix. It is believed that a weak or debonded interface condition is responsible for the reduction of transverse properties.

To obtain a comprehensive design methodology applicable to CMC, a means to estimate the transverse strength and stiffness of each ply is necessary. Models that predict the effects of debonded interface on composite behavior are vital to the development of structural components made from ceramic composites. However, for this project, the immediate needs require composite models that assume a weakened or debonded interface so that the observed reduction in transverse strength and stiffness may be confirmed.

PREDICTIVE MODELS

Closed-Form Models for Well-Bonded Interface

The elastic properties can be predicted from the constituent properties using micromechanics applied to a representative volume element (RVE). These approaches provide closed-form algebraic estimates for the composite elastic properties assuming that the fiber and matrix are perfectly bonded. The effective properties of fiber reinforced composites were initially formulated using the RVE approach by Hashin and Rosen [10]. Variations on this technique have been derived by Tsai and Hahn [11], and Christensen [12]. According to Tsai and Hahn, the equations to predict the elastic moduli of composite can be summarized as

$$P = \frac{1}{c_f + \eta_p c_m} \left(c_f P_f + \eta_p c_m P_m \right) \tag{1}$$

where P, P_f and P_m are the composite, fiber and matrix properties, respectively. C_f and C_m are fiber and matrix volume fractions, respectively. The stress partitioning parameter, η_p, is dependent on the desired composite property. These variables are summarized in Table I, where the fiber is assumed to be isotropic.

Table I - Variables for Equation 1.

Composite Property	P	P_f	P_m	η_p	Eq.
E_{11}	E_{11}	E_f	E_m	1	2a
ν_{12}	ν_{12}	ν_f	ν_m	1	2b
G_{12}	$1/G_{12}$	$1/G_f$	$1/G_m$	$\frac{1}{2}\left(1 + \frac{G_m}{G_f}\right)$	2c
k_2	$1/k_2$	$1/k_f$	$1/k_m$	$\frac{1}{2(1-\nu_m)}\left(1 + \frac{G_m}{k_f}\right)$	2d
G_{23}	$1/G_{23}$	$1/G_f$	$1/G_m$	$\frac{1}{4(1-\nu_m)}\left(3 - 4\nu_m + \frac{G_m}{G_f}\right)$	2e

$$k_i = \frac{E_i}{3(1-2\nu_i)} = \frac{G_i}{1-2\nu_i} \; ; \quad i = f, m$$

Note that Eqs 2a and 2b above are identical to the rule-of-mixtures formulation. The elastic constants of Eqs. 2a-2e can be used to calculate the transverse modulus and transverse Poisson's ratio as

$$E_{22} = \frac{4\,k_2\,G_{23}}{k_2 + G_{23}\left(1 + \frac{k_2 v_{12}^2}{E_{11}}\right)}$$

(2f)

$$v_{23} = \frac{E_{22}}{2G_{23}} - 1$$

(2g)

Another popular method for estimating the transverse modulus has been developed by Halpin and Tsai [13]. This closed-from semi-empirical equation is an approximation to a more rigorous micromechanics analyses. It has been shown to work especially well for low fiber volume fraction composites. The Halpin-Tsai equation for transverse modulus is given as

$$E_{22} = E_m\left(\frac{1 + \xi\,\eta\,c_f}{1 - \eta\,c_f}\right)$$

(3a)

where

$$\eta = E_m\left(\frac{\dfrac{E_f}{E_m} + 1}{\dfrac{E_f}{E_m} - \varsigma}\right)$$

$\xi = 2$ for cylindrical fibers

(3b)

In comparison to actual composite data, the Halpin-Tsai equation usually overestimates the transverse modulus. [13]

In general, existing micromechanics models agree reasonably well with experimental results for composites having well-bonded interfaces. For composites with debonded interfaces the existing models may not accurately predict the effective elastic properties due to the loss of displacement continuity between fiber and matrix. For example, when Eqs 2 and 3 are applied to the SiC/RBSN system that has a weakly bonded interface, the experimental transverse elastic properties are not accurately estimated, as illustrated in Table II. While it is assumed that frictional forces maintain interface continuity under longitudinal loadings, the debonded interface has a significant effect on the transverse load-displacement behavior.

When the interfaces are well-bonded, the transverse load-displacement behavior and effective elastic properties can be formulated in closed form by application of classical elasticity theory. However, when the interface is debonded, the problem is much more complex: In addition to the elastic behavior of the fiber and matrix, the loss of fiber-matrix displacement continuity results in a finite-area contact problem. The problem is also compounded when the effects of friction are included at the region of fiber-matrix contact. A schematic representation of this problem is depicted in Figure 1. The purpose of this analysis is to re-evaluate the transverse load-displacement behavior of the RVE, assuming a debonded interface, and a corresponding loss of fiber-matrix compatibility.

Finite Element Model for Debonded Interface

While it may be possible to derive an analytical solution to the debonded interface problem, the resulting equations would be non-linear and not in closed-form, requiring an iterative numerical solution to obtain the final load-displacement behavior. To efficiently solve this problem, a finite element approach has been used to determine the transverse load-displacement behavior. In this analysis, transverse ply strength and stiffness for the SiC/RBSN composite system are studied to verify if debonded interfaces are responsible for the loss of transverse properties.

elastic constant	experiment [14]	stress part. Eqs.2,3
E_{11} (GPa)	193	197.0
v_{12}	0.21	0.205
G_{12} (GPa)	31	64.2
E_{22} (GPa)	69	138.9
		163.9*

* Halpin-Tsai estimate for E_{22}, Eq. 3

Table II - Experimental vs. predicted elastic moduli for SCS-6/RBSN composite.

(a) well bonded tension   well bonded compression

(b) debonded tension   debonded compression
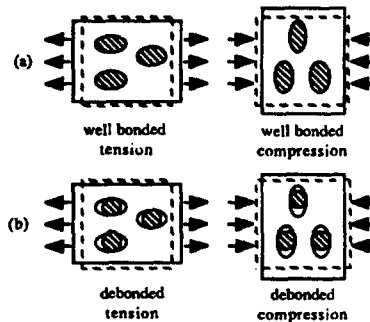
Figure 1 - Composite behavior under transverse loads.

A representative volume element was developed based on the fiber and matrix properties, reinforcement geometry and the type of load-displacement behavior to be studied. To model transverse behavior, the cross-section of the composite shown in Figure 2a is considered. This distribution may be idealized as a perfectly square packed fiber array (Figure 2b) [10-12] and the corresponding RVE geometry is given by Figure 2c. This RVE of unit depth employs a circular fiber embedded in a square of matrix material. Transverse loading is applied by a uniform horizontal displacement applied along the vertical boundaries of the RVE. Adjacent RVE compatibility is ensured by coupling both vertical displacements of the horizontal boundary surfaces and horizontal displacements of the vertical boundary surfaces to a uniform value in each direction, respectively. This coupling will cause the RVE boundaries to remain straight and square during the applied loading. From the resulting load-displacement behavior, the effective transverse modulus can be extracted. Under the same loadings, the principal stresses developed in the matrix can be used to predict the transverse strength.

(a)   (b)   (c)
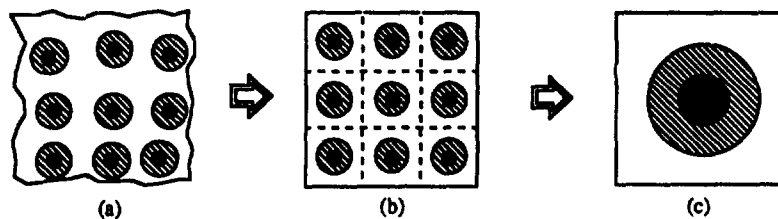
Figure 2 - Idealization of SiC/RBSN fiber array.

Constituent Properties

TABLE III - Constituent\ properties for SiC/RBSN system.

property	Avco SCS-6 SiC fiber	Reaction bonded Si₃N₄ matrix
E (GPa)	400 420 (sheath) 134 (core)	110
ν_{12}	0.2	0.22
α_{11} (10^{-6}/C°)	4.3	4.5
σ^{ult}_{11}(MPa)	3800	84

The fiber used in the SiC/RBSN composite is an Avco SCS-6 silicon carbide fiber. The fiber mechanical data, presented in Table III, has been either provided by the manufacturer [15] or estimated from other material data sources [16]. The matrix used in the model composite system is made of reaction-bonded silicon nitride. This composite fabrication process, described elsewhere [14,17-18]. The matrix strength and stiffness has also been reported by tensile testing of monolithic reaction-bonded Si₃N₄ [14]. These data are included in Table III. For this composite, little has been reported on the mechanical behavior of the interface. Since the macroscopic tensile test of the unidirectional laminate indicates a definite matrix cracking behavior, it is assumed that the interface can debond during stressing.

Finite Element Model Development

The RVE geometry in Figure 2c has been selected to model the mechanical behavior of the SiC/RBSN composite. All phases in the RVE have a unit depth in the fiber direction, and the stress analysis is performed under conditions of plane strain. To exploit symmetry of the problem, the RVE is divided into four quadrants as a result of the symmetry of geometry and applied load. The RVE quadrant is shown in Figure 3. The quadrant is composed of three distinct regions representing the fiber core, fiber sheath and matrix, where each has different material constants.

The ANSYS finite element package is used to generate the RVE model. The mesh for the RVE model is illustrated in Figure 4. The solid portions of the model that include the fiber core, fiber sheath and matrix regions are represented by four node, 2-D isoparametric plane strain elements.

A series of coincidental node pairs were generated along the interface to model the discontinuous displacement behavior of the fiber and matrix under transverse loads. Each pair of coincidental nodes are connected by a 2-D gap element which characterizes the behavior of the debonded interface. This element is defined by two nodes, which are initially coincident, and an angle which defines the tangential direction of the slip plane. When the nodes are in contact, compressive nodal force components normal to the slip surface are transferred across the element. When not in contact, no loads are transferred through the element. Loads parallel to the defined
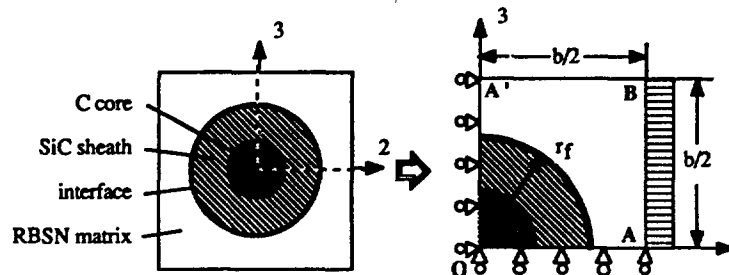
Figure 3 - RVE quadrant for SiC/RBSN composite.

slip surface may also be transferred between gap element nodes by Coulomb friction when a non-zero friction coefficient is defined as an element material property. The final step of the FE

modeling process required definition of three RVE boundary conditions. Since quarter-symmetry was assumed for the finite element mesh, special displacement boundary conditions must be generated along the symmetry surfaces OA and OA' of Figure 3. This symmetry condition prevents nodal displacements in directions normal to the respective surfaces. For example, nodes along boundary OA were fixed against u_3 displacements, but free to move in the 2 directions. Likewise, nodes along boundary OA' were fixed against u_2 displacement but free to translate in the 3 direction. The second applied boundary condition insured material compatibility with adjacent RVE by maintaining the outer boundaries as straight lines. This is accomplished by coupling of the u_3 displacements of all nodes along the boundary A'B and coupling of u_2 displacements of all nodes on the boundary AB, each to a common free value, respectively. The last boundary condition is used to apply transverse loads to the RVE. Transverse loads are applied by a uniform u_2 displacement (strain) of nodes along the vertical outer boundary AB. Transverse tensile loads are generated by a positive u_2 displacement (to the right), while compressive loads are accomplished by negative u_2 displacements (to the left).

Figure 4 -Finite element mesh for RVE

RESULTS

Transverse Modulus

Stresses, displacements and element areas from the finite element analysis were generated and used to predict E_{22} and v_{23} using Eqs 4. Since the unidirectional composite is transversely isotropic, it was assumed that the transverse modulus in the 2 and 3 directions are equivalent (i.e., $E_{22} = E_{33}$). The average strains in the 1, 2 and 3 directions are then expressed in terms of the average stresses

$$\bar{\varepsilon}_1 = \frac{1}{E_{11}} \bar{\sigma}_1 - \frac{v_{12}}{E_{22}} \bar{\sigma}_2 - \frac{v_{12}}{E_{22}} \bar{\sigma}_3 \tag{4a}$$

$$\bar{\varepsilon}_2 = \frac{1}{E_{22}} \bar{\sigma}_2 - \frac{v_{12}}{E_{11}} \bar{\sigma}_1 - \frac{v_{23}}{E_{22}} \bar{\sigma}_3 \tag{4b}$$

$$\bar{\varepsilon}_3 = \frac{1}{E_{22}} \bar{\sigma}_3 - \frac{v_{12}}{E_{11}} \bar{\sigma}_1 - \frac{v_{23}}{E_{22}} \bar{\sigma}_2 \tag{4c}$$

where the over bar indicates the value averaged over the volume of the RVE .

For the condition of plane strain ($\bar{\varepsilon}_1 = 0$) and a uniaxial transverse load applied in the x_2 direction ($\bar{\sigma}_3 = 0$), Eqs. 4 can be solved for E_{22} and v_{23}:

$$E_{22} = \left(1 + v_{23}\right) \frac{\bar{\sigma}_2}{\bar{\varepsilon}_2 - \bar{\varepsilon}_3} \tag{5a}$$

$$v_{23} = \frac{\bar{\varepsilon}_2 - \bar{\varepsilon}_3 - \bar{\sigma}_1 v_{12} / E_{11}}{\bar{\varepsilon}_2 + \bar{\sigma}_1 v_{12} / E_{11}} \tag{5b}$$

The normal stresses averaged over the RVE volume were calculated using the ANSYS post-processor. The average stresses are required because uniform displacements imparted to the

boundary of the heterogeneous RVE will result in non-uniform tractions along the boundary surface. Average stress in three dimensions is given by the following integral

$$\bar{\sigma}_{ij} = \int_V \sigma_{ij}(x_i)\, dv \qquad (6)$$

where the v and V represent the incremental and total volume of the applied stresses along the boundary surface, respectively. Since the finite element modeling process discretely divides the model into a series of homogeneous elements, the integral of Eq. 6 is approximated by a summation of stresses over all the elemental volumes of the RVE model.

In Eqs. 5, E_{11} and ν_{12} are approximated by the rule-of-mixtures formulation, as expressed by Eqs. 2. The average strains $\bar{\varepsilon}_2$ and $\bar{\varepsilon}_3$ are calculated by the applied uniform displacements u_2^0 and u_3^0 on the boundaries AB and A'B, respectively

$$\varepsilon_2 = \frac{u_2^0}{b/2} \quad \text{and} \quad \varepsilon_3 = \frac{u_3^0}{b/2} \qquad (7)$$

The tensile stress-strain behavior of the RVE finite element model was obtained by imparting a uniform, positive u_2^0 displacement at all nodes along the boundary AB to obtain a ε_2 strain of ±0.001. The u_3^0 displacement was generated by the Poisson effect of the u_2^0 load. To obtain a uniform u_3^0 displacement, the u_3 displacements of all nodes were coupled in the finite element program. This coupling faces boundary A'B to remain straight ensuring displacement compatibility with neighboring RVE's. These results were processed by Eqs. 4 to obtain the effective transverse modulus under tensile loading. Both well-bonded and debonded interfaces were considered.

The case of a perfectly bonded interface was evaluated as a benchmark for checking the accuracy of the finite element mesh and the validity of Eqs. 5 by comparing results to the existing micromechanics models. The compatibility of the fiber and matrix displacements was ensured by merging the interface gap elements. The fiber volume fraction was varied from 10 to 50% by adjusting the location of the corner nodes A, B and A'. Load-induced displacements of the RVE are schematically shown in Figure 5. The calculated transverse modulus is compared with results estimated by other models in Table IV. The present results fall in between the predictions by the two closed-form approximations, thereby assuring the accuracy and validity of this model.

Table IV - Transverse modulus (in GPa) of well-bonded composites under tensile load.

fiber vol %	Eqs. 2	Eqs. 3	RVEFEA Results
10	112.9	126.2	121.9
20	125.2	144.1	135.3
30	139.2	163.9	150.4
40	155.5	186.0	167.9
50	174.7	210.7	188.5

It has been noted in the previous experimental study of SiC/RBSN that the measured transverse modulus under tensile load is considerably lower than that predicted by assuming a perfectly bonded interface [14,18]. It is believed that this loss in transverse modulus is a direct result of debonding between the fiber and matrix. The case of a debonded interface was evaluated by using active interface gap elements to model the decoupled displacements of the fiber and matrix. The fiber volume fraction was varied from 10 to 50% by adjusting the location of the corner nodes A, B and A'. A plot of the debonded RVE displacements under tensile loads is shown in Figure 6.

Bhatt and Phillips have proposed that the transverse modulus can be estimated using the micromechanics relation, Eqs. 3, where the fiber modulus E_f is zero [14]. The calculated transverse elastic modulus with a debonded interface is compared to the estimate by Eqs. 3 with $E_f = 0$ as well as with the experimental value in Table V. The prediction by the RVE finite element model is even lower than that by the modified Halpin-Tsai equation, indicating that a debonded interface can completely nullify the load carrying capability of the fibers. Moreover both predictions are not too far from the measured value. This it is concluded that the unexpectedly low transverse modulus of SiC/RBSN is the result of interfacial debonding in the composite.
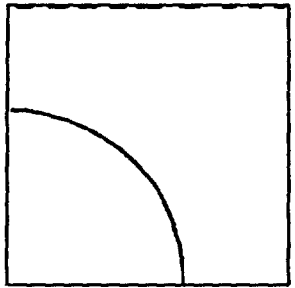
Figure 5 - RVE displacements for well-bonded interface under normal tensile loads transverse to fiber (dashed lines define unloaded shape).
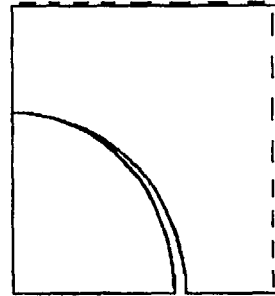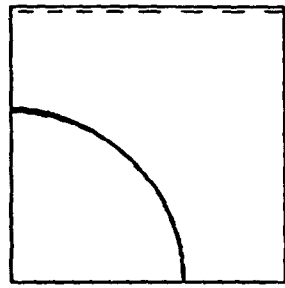

Figure 6 - RVE displacements for debonded interface under normal tensile loads transverse to fiber (dashed lines define unloaded shape).

Table V - Transverse modulus (in GPa) of debonded composite under tensile loads.

fiber vol %	Eq. 3.6, ($E_f = 0$)	RVEFEA Results	Exp. meas[14]
10	94.3	87.3	--
20	80.0	70.3	--
30	67.0	56.9	69
40	55.0	45.4	--
50	44.0	34.9	--

The RVE finite element model was used again to calculate the effective transverse modulus under compressive loading. Since the modulus would be the same in both tension and compression when the interface bonding is perfect, only the case of a debonded interface was considered to be of importance. Although experimental data for transverse compressive modulus was not available, the modeling was performed to estimate the performance of the composite under transverse compressive loading. As illustrated by both experiment and analysis, the transverse modulus under tension is reduced greatly in the presence of debonding between the fiber and matrix. Under a tensile load, the fiber separates from the matrix at the interface location having a tangent perpendicular to the applied load and the contribution of the fiber to the composite transverse modulus becomes negligible. Under a compressive load, however, the fiber and matrix are still in contact at this point, allowing the fiber stiffness to contribute to the transverse modulus. Therefore, the transverse modulus under compression is expected to be higher than under tension, Table VI. RVE displacements under compression are schematically shown in Figures 7 and 8 for well-bonded and debonded interfaces, respectively.

In the actual SiC/RBSN composite system, the effects of thermal mismatch and interfacial friction coefficient may influence the predicted transverse modulus if a debonded interface is present. For example, when the CTE of the fiber is less than that of the matrix, as in the SiC/RBSN composite, cooldown from the processing (stress-free) temperature will result in compressive normal stresses due to fiber-matrix mismatch. This interference will cause the fiber and matrix to remain in contact until a sufficient boundary displacement is applied to overcome the mismatch. This condition may result in a transverse modulus that is dependent upon the magnitude of the applied load. When the fiber and matrix are in contact, the matrix load is transferred to the fiber by shear stresses that result from Coulomb friction. Conversely, load transfer from the matrix to the fiber under compressive composite loadings may be accomplished by both normal and shear stresses developed at the interface. In both load cases, the degree of load transfer by shear is dependent upon friction coefficient, load magnitude and direction, and contact area.

Variations of thermal expansion mismatch and interface friction coefficient were studied using the finite element model. The details of this work are presented elsewhere [19]. These results indicate that transverse modulus under both tensile and compressive loads are not significantly influenced by either thermal mismatch or friction coefficient, Table VII.

Figure 7 - RVE displacements for well-bonded interface under normal compressive loads transverse to fiber (dashed lines define unloaded shape).

Figure 8 - RVE displacements for debonded interface under normal compressive loads transverse to fiber (dashed lines define unloaded shape).

Table VI - Transverse modulus (in GPa) for debonded composite under compressive loads.

fiber vol %	Eq. 4 ($E_f = 0$)	Eq. 4 ($E_f \neq 0$)	RVEFEA Results
10	94.3	126.2	115.0
20	80.0	144.1	119.5
30	67.0	163.9	123.7
40	55.0	186.0	127.4
50	44.0	210.7	130.4

Finally, the effects of interface on transverse Poisson's ratio of SiC/RBSN were studied. In this analysis only tensile loads were applied to the RVE with debonded interfaces. Values of v_{23} were calculated using Eq. 5b applied to the FEA results are given in Table VIII. The well-bonded interface FE results agree with the close-form predictions, ($v_{23} = 0.228$ to $v_{23} = 0.22$, respectively), the debonded interface will result in a Poisson's ratio that decreases with increasing fiber volume fractions. At present, no data is available to confirm these numerical results.

Table VII - Transverse Modulus (in GPa) for debonded interfaces as a function of interface friction coefficient.

friction coef.	RVE FEA results (tension)	RVE FEA results (compression)
0.0	56.9	123.7
0.2	57.0	127.3
0.5	57.1	137.2
1.0	57.2	147.2

Table VIII - Transverse Poisson's ratio for debonded SiC/RBSN under tension as a function of volume fraction.

volume fraction	RVE FEA debonded
10	.273
20	.251
30	.219
40	.184
50	.146

Transverse Ultimate Strength

Transverse ultimate strength of CMC cannot be predicted using a simple rule-of-mixtures based expression like that of Eqs. 2 or 3. Unlike longitudinal strength, transverse strength is controlled by numerous properties that include constituent properties, interface bond strength and residual stresses. To estimate transverse strength, the total contribution of these properties must be considered.

If the fiber and matrix are weakly bonded or debonded, the transverse strength can be estimated by assuming the debonded fibers to be cylindrical holes in the matrix. Based upon this assumption, a closed-form expression for transverse strength [20] may be given as

$$\sigma_2 = \sigma\,{}^{ult}_{matrix} \left[1 - 2\sqrt{\frac{c_f}{\pi}} \right] \tag{8}$$

This equation has been applied to the SiC/RBSN composite, where $c_f = 0.3$ and $\sigma\,{}^{ult}_{matrix}$ = 84 MPa, obtaining a transverse ultimate strength of σ_2 = 32 MPa. This agrees closely with the experimental strength of 27 MPa. While Eq. 8 provides a reasonable estimate of the transverse strength of weak interface composites under tensile loads, the effects of strong interfacial bonding and compressive loadings are not well understood. It is not possible to derive a simple, closed form solution for the stress state in a transverse RVE with debonded interface.

A finite element model of the RVE is used to determine the transverse strength of the SiC/RBSN composite. The transverse strength of the SiC/RBSN composite is predicted under tensile and compressive loads for well-bonded and debonded interfaces. The results from the debonded interface case under tension were compared to the experimentally measured tensile strength of the unidirectional 30% SiC/RBSN composite to confirm that debonded interfaces are present. The other interface and loading conditions are included without correlation for completeness.

Analysis of all four interface/loading conditions employed a maximum principal stress failure criterion for the matrix phase. After the load is applied, the maximum principal stress, S^1, developed at each element in the matrix was evaluated. The maximum principal tensile stress value generated in the matrix, S^1_{max}, was then divided by the nominal composite transverse stress to obtain a stress scaling factor, $K = S^1_{max} / \sigma_2$. It is proposed that when S^1_{max} is equal to the ultimate tensile strength of the matrix, the composite fails. Therefore, the transverse strength of the composite is given by

$$\sigma_2 = \frac{\sigma\,{}^{ult}_{matrix}}{K} = \sigma\,{}^{ult}_{matrix}\frac{\sigma_2}{S^1_{max}} \tag{9}$$

The stresses generated from the transverse modulus analysis were used to predict the transverse tensile strength. The transverse strengths predicted by the RVE finite element results and Eq. 9 are given in Table IX.

Table IX. Predicted transverse strength.

interface condition/load	predicted strength, σ_2 (MPa)
well-bonded/tension	63.6
debonded/tension	23.2
well-bonded/compression	420
debonded/compression	56.5

For a well-bonded interface under transverse tension the predicted value is more than twice the measured strength of 27 MPa. Therefore, the interfaces are probably not well-bonded. When a debonded interface under transverse tension was modeled the predicted transverse strength is only 23.2 MPa. This prediction is in close agreement with the measured strength of 27 MPa. Therefore it is concluded that the interfaces are debonded and that the present modeling approach appears to predict transverse tensile strength reasonably well. Transverse compressive loads were also considered. Using the stress results from the transverse modulus prediction for compressive loads, the same maximum principal stress failure criterion was applied to the matrix. The compressive strengths of both matrix and the composite have not been measured to date, therefore the predictions for compressive loading cannot be verified. However, the results can be used to estimate the likely effect of interface debonding on transverse compressive strength.

For compressive transverse loads applied to a composite with a well-bonded interface, the predicted transverse compressive strength is 420 MPa. Failure of the composite under compressive loading is the result of *tensile* failure in the matrix. Under the same loading, the transverse strength of a debonded interface was 189.8 MPa, providing a stress scaling factor of 1.48, and hence result in a transverse compressive strength of 56.5 MPa. This compressive strength is about twice the measured transverse tensile strength of 27 MPa.

CONCLUSIONS

The transverse elastic modulus is accurately predicted by the RVE finite element analysis fall within the range predicted by some of the existing micromechanical models when interfacial bonding is good. Therefore, the RVE finite element model is properly configured and the analysis is valid. When the interface is debonded, the analysis indicates that the direction of loading will influence the transverse modulus. Under tensile loads normal to the RVE, the fiber and matrix separate along a line through the RVE center parallel to the load. This discontinuity prevents fiber-matrix interactions, and renders the transverse modulus to be dependent mostly on the matrix. The predicted tensile transverse modulus for a debonded interface is 15 to 70% of that for well-bonded interface, with the difference increasing with increasing fiber volume fraction. In fact, the Halpin-Tsai Equation with $E_f = 0$ agrees reasonably well with the RVE finite element results, and may be used to estimate the transverse modulus under tensile loads in composites with debonded interfaces.

When compressive transverse loads are applied to the composite, the fiber and matrix maintain contact over most of the interface. Hence, the fiber carries much more load, and the predicted transverse modulus is significantly higher than that under tension. In fact, E_{22} of a debonded interface composite is up to 60 to 90% of that for the same composite having a well-bonded interface. Again, the difference increases with increasing fiber volume fraction.

The effect of thermal mismatch appears to have little effect on both the tensile and compressive transverse modulus of debonded interface composites. This is apparently due to the small differences in the fiber and matrix CTEs. If the CTEs are significantly different, it is expected that thermal mismatch will have more effect on the transverse modulus. The value of interface friction coefficient does not change the predicted transverse modulus under tensile loads. However, E_{22} under compressive loads shows some dependence on friction coefficient. Changing the friction coefficient from 0.0 to 1.0 increases the predicted transverse modulus by about 15% in the SiC/RBSN system.

Like the results obtained for E_{22}, the RVE finite element model predicts a significant decrease in transverse Poisson's ratio when the interface is debonded. Reductions down to 60% of v_{23} from the well-bonded case are predicted. Although the present predictions seem reasonable, experimental correlation is needed to verify their validity for the SiC/RBSN composite under compressive loads.

Transverse tensile strength of CMC with debonded interfaces can be estimated by a simple closed-form solution. This model cannot predict the effect of well-bonded interfaces, nor the strength under compressive loads. To resolve this, a finite element model has been used to predict the RVE stress-state under transverse loads. Transverse strength has been predicted using a maximum principal stress criteria (based on the bulk matrix strength) applied to the finite element model. When compared to the limited experimental data, the finite element approach predicts the experimental transverse tensile strength with good accuracy, provided a debonded interface is assumed. The results indicate that debonded interfaces will reduce the transverse tensile strength by about 60% to 23.2 MPa, from 63.6 MPa. Likewise, the transverse compressive strength will also decrease by nearly 86%, to 56.5 MPa, from 20 MPa. From these analytical estimates, it is clear that there are significant reductions in transverse strengths when the interfaces are weakened. These reductions of transverse strength must not be neglected when weakened interfaces are used to improve the longitudinal toughness of fiber reinforced CMC.

ACKNOWLEDGMENTS

REFERENCES

1. Sambell, R.A.J, Briggs, A., Phillips, D.C. and Bowen, D.H., "Carbon Fiber Composites with Ceramic and Glass Matrices, Part 2 - Continuous Fibers," J. Mater. Sci., 7 (6) 676-681 (1972).

204

2. Phillips, D.C., "Interfacial Bonding and the Toughness of Carbon Fiber Reinforced Glass and Glass Ceramics" *J. Mater. Sci.*, 9 [11] 1847-54 (1974).

3. Phillips, D.C., "The Fracture Energy of Carbon-Fiber Reinforced Glass" *J. Mater. Sci.*, 7 [10] 1175-91 (1972).

4. Prewo, K.M. and Brennan, J.J., "High Strength Silicon Carbide Fiber Reinforced Glass Matrix Composites," *J. Mater. Sci.*, 15 [2] 463-468 (1980).

5. Prewo, K.M. and Brennan, J.J., "Silicon Carbide Yarn Reinforced Glass Matrix Composites," *J. Mater. Sci.*, 17 [4] 1201-06 (1982).

6. Brennan, J.J. and Prewo, K.M., "Silicon Carbide Fiber Reinforced Glass-Ceramic Matrix Composites Exhibiting High Strength and Toughness," *J. Mater. Sci.*, 17 [8] 2371-83 (1982).

7. Singh, R.N. and Brun, M.K., "Effect of Boron Nitride Coating on Fiber-Matrix Interaction," *Ceram. Eng. Sci. Proc.*, 8 [7-8] 636-643 (1987).

8. Singh, R.N. and Gaddipati, A.R., "Mechanical Properties of a Uniaxially Reinforced Mullite-Silicon Carbide Composite," *J. Am. Ceram. Soc.*, 71 [2] C-100-C-103 (1988).

9. Bender, B., Shadwell, D. Bulik, C., Incorvati, L. and Lewis, D., "Effect of Fiber Coatings and Composite Processing on Properties of Zirconia-Based Matrix SiC Fiber Composites," *Am. Ceram. Soc. Bull.*, 65 [2] 363-369 (1986).

10. Hashin, Z. and Rosen, B.W., "The Elastic Moduli of Fiber Reinforced Materials," *J. Appl. Mech.*, 31, 223 (1964).

11. Tsai, S. W. and Hahn, H.T., "Introduction to Composite Materials," Technomic Publishing Co., Lancaster, Pa, 1980.

12. Christensen, R.M., "Mechanics of Composite Materials," John Wiley and Sons, New York, 1979.

13. Halpin, J.C. and Tsai, S.W., "Effects of Environmental Factors on Composite Materials," AFML-TR 67-423, June 1969.

14. Bhatt, R.T., "Properties of Silicon Carbide Fiber Reinforced Silicon Nitride Matrix Composites," NASA Technical Memorandum 101356, June 1988.

15. AVCO SCS-6 Fiber data sheet, Textron Corporation, Waltham, MA, 1986.

16. DiCarlo, J.A., "Fibers for Structurally Reliable Metal and Ceramic Matrix Composites," *Journal of Metals*, 37 [7] 44-49, (1985).

17. Bhatt, R.T. and Phillips, R.E., "Laminate Behavior for SiC Fiber-Reinforced Reaction-Bonded Silicon Nitride Matrix Composites," NASA Technical Memorandum 101350, October 1988.

18. Bhatt, R.T. and Phillips, R.E., "Thermal Effects on the Mechanical Properties of SiC Fiber Reinforced Reaction Bonded Silicon Nitride Matrix (SiC/RBSN) Composites," NASA Technical Memorandum 101348, October 1988.

19. Shimansky, R. A., "Effect of Interfaces on Continuous Fiber Reinforced Brittle Matrix Composites," Ph.D. Thesis, The Pennsylvania State University, University Park, PA, December, 1989.

20. Whitney, J.M., Daniel, I.M. and Pipes, R.B., "Experimental Mechanics of Fiber Reinforced Composite Materials," SEM Monographs No.4, Prentice-Hall, NJ, 1982.

THE EFFECT OF FIBER COATINGS ON INTERFACIAL SHEAR STRENGTH AND THE
MECHANICAL BEHAVIOR OF CERAMIC COMPOSITES

RICHARD A. LOWDEN AND KARREN L. MORE
Oak Ridge National Laboratory, P. O. Box 2008, Oak Ridge, TN 37831-6063

ABSTRACT

Thin coatings deposited on ceramic fibers prior to densification
employing chemical vapor infiltration techniques have been used to limit
fiber-matrix bonding. This has resulted in improvements in strength and
toughness at room and elevated temperatures in Nicalon® fiber-
reinforced/SiC matrix composites. The properties of the fiber-matrix
interface in fiber-reinforced ceramic composites have been examined
utilizing an indentation method in which a standard microhardness
indentor is used to push on fibers embedded in the ceramic matrix.
Compositions and microstructures at the interface have been characterized
employing analytical electron microscopy. Correlations between
interfacial phenomena and observed mechanical behavior have been made.

INTRODUCTION

In evaluating the mechanical behavior of Nicalon/SiC composites
fabricated during the development of the forced-flow, temperature-
gradient chemical vapor infiltration process (FCVI), both brittle failure
and ductile composite fracture were observed in specimens produced under
similar conditions. A thorough analysis of the fracture surfaces of the
composite specimens employing scanning and transmission electron
microscopy revealed a thin film at the fiber-matrix interface of
specimens that exhibited fiber pull-out. No film could be detected in
the specimens that failed in a brittle manner.[1]
Auger electron spectroscopic (AES) analysis of the fracture surfaces
of the composites exhibiting fiber pull-out, showed the fiber pull-out
grooves to be oxygen rich and the fiber surfaces to be coated with a thin
carbon film.[2] In comparison, it has been shown that a carbon-rich layer
forms on the fiber surface in Nicalon-reinforced lithium aluminosilicate
(LAS) glass-ceramic composites during processing.[4,5] The carbon-rich
layer weakens bonding at the fiber-matrix interface resulting in a
composite with high toughness. The layer could not be detected in
samples with low strength and low toughness.[5]
To improve the reproducibility of the properties of Nicalon/SiC
composites, a thin pyrolytic carbon layer was deposited on fibrous
preforms prior to densification to provide a uniform interface. The
carbon deposition conditions were chosen to produce a graphitic coating
with a laminar structure that lies parallel to the fibers.[6,7] (Fig. 1)
The coatings were found to prevent chemical damage of the fibers during
processing, as well as weaken the fiber-matrix interface, enhancing fiber
pull-out and slip.[5,6] The coating of the fibers with carbon resulted in
an increase in the toughness and the ultimate strength of the composite
materials; however, the usefulness of pyrolytic carbon is limited by its
low resistance to oxidation. Therefore, other fiber coatings with
similar mechanical properties but improved oxidation resistance were
examined.

Boron nitride has been employed as a modifying interlayer in various composite systems.[9,10] Submicrometer boron nitride coatings have proved to be valuable in controlling fiber-matrix bonding and interaction in zircon and zirconium titanate composites, as well as in other glass matrix systems. Boron nitride is relatively inert and has a greater resistance to oxidation than carbon.[11] These properties combined with its graphite-like structure make it a potentially excellent alternative to carbon as an interlayer in ceramic composite materials for service at elevated temperatures.

This report describes a study of fiber coatings used to alter the fiber-matrix bond and change the mechanical behavior of a ceramic fiber-reinforced ceramic matrix composite. The strength of the fiber-matrix bond was determined using established indentation methods[12]. Room and elevated temperature flexure strengths and resulting fracture behavior were used to qualitatively compare the effects of the various fiber pretreatments. Scanning and transmission electron microscopy have been used to characterize the structure and composition of the interface coatings.
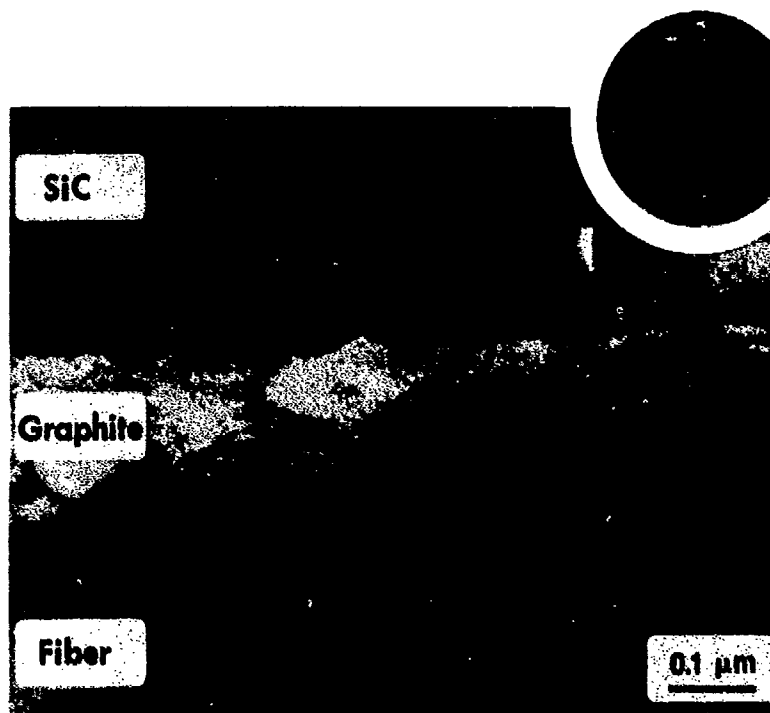
Fig. 1. TEM micrograph of the graphitic carbon layer at the interface of a Nicalon/SiC composite.

EXPERIMENTAL PROCEDURES

Composite Fabrication

Fibrous preforms were fabricated by stacking multiple layers of Nicalon plain-weave fabric rotated in a 0°± 30° sequence within the cavity of a graphite holder. The layers were hand compressed to produce a preform with a nominal loading of 40 vol. % fiber and were held in place by a perforated graphite lid pinned to the holder. The cloth sizing was removed through multiple washings with acetone. Two sizes of fibrous preforms were constructed, small disks, 45 mm in diameter and 12.5 mm thick, and larger disks, 75 mm diameter by 16 mm thick.

Selected preforms were next precoated with thin layers of carbon. The coatings were deposited from an argon/propylene mixture at 1375 K and 3 KPa pressure. The thickness of the carbon layer was varied by changing the concentration of the propylene and was measured using polarized-light optical microscopy of cross-sections. All coating times were two hours. Control samples of uncoated fibers were prepared for comparison.

The boron nitride coatings were applied to fabric samples prior to preform fabrication. The coated fabric was prepared by the CVD Department of Comhurex, Pierrelatte, France. BN layers were deposited on plain weave cloth from a mixture of boron trichloride, ammonia, and hydrogen utilizing proprietary processing conditions. Fibrous preforms were produced from the cloth as previously described.

The preforms were densified using the FCVI process developed at ORNL.[13-16] The composites were infiltrated with SiC produced by the decomposition of methyltrichlorosilane (MTS) in hydrogen at a hot-surface temperature of 1473 K and atmospheric pressure.

Flexure Testing

Bars were cut from the samples parallel to the 0°-90° orientation of the top layer of cloth using a diamond saw, and tensile and compression surfaces were ground parallel to the long axis of the specimen. The average dimensions of the test bars from the composite samples were 2.5 × 3.3 × 40 mm for the small samples and 3 × 4 × 55 mm for the larger composites. All specimens were measured and weighed to determine densities.

Room temperature flexural strengths were measured using four-point bending methods, with a support span of 25.4 mm, a loading span of 6.4 mm, and a crosshead speed of 0.051 cm/min. The larger bend bars were used for elevated temperature flexure testing. The specimens were first coated with a 35 μm SiC layer prior to testing. The elevated temperature flexure strengths were measured in four-point bending, with a support span of 40 mm, a loading span of 20 mm, and a loading rate of 1.0 kg/sec. The tests were performed using alumina fixtures at 298, 773, 1023, 1273, and 1473 K. All specimens were loaded perpendicular to the layers of cloth. The fracture surfaces of the specimens were examined using a Hitachi S-800 scanning electron microscope. Specimens that did not completely part during flexure testing were broken by hand so that the fracture surfaces could be examined.

Fiber-Matrix Bond Measurements

Several methods have been developed to quantify the strength of interfacial bonding in fiber-reinforced composites.[12,16,17] Such tests permit a semiquantitative determination of interfacial stresses derived from relatively simple load and displacement relationships. A common technique is the indentation method, which has been thoroughly examined.[12,16] This technique involves using a microhardness indentor to apply a force to the end of a fiber embedded in a matrix. Interfacial shear stresses can be evaluated from the applied load and the displacement of the fiber.

A 6.0-mm thick cross-sectional specimen was cut from each completed composite sample to be used for indentation testing. The specimens were cut along the 0-90° orientation of the top layer of cloth to ensure that a portion of the exposed fibers would be oriented perpendicular to the cut surface. This alignment is essential for proper implementation of the indentation mechanics. The specimens were mounted and polished using standard metallographic techniques. Loads were applied to fiber ends using a Vickers diamond indentor and a Shimadzu Type M instrument. Loading to the fiber ends was progressively increased until debonding was observed and continued until contact of the indentor with the edge of the fiber cavity was evident. Loads of up to 3.0 N were required to displace the fibers. Indents were also placed in longitudinally polished fibers to determine fiber hardness values.

RESULTS

Interfacial Stresses and Mechanical Behavior

Room temperature flexure strengths, densities, and interfacial frictional stress measurements are summarized in Table 1. The difficulties in interpreting flexure test results for continuous fiber-reinforced composites are recognized and the results are reported only for intercomparison. Load-crosshead displacement curves were recorded and were used to characterize fracture phenomena.

Table 1. The influence of fiber coatings on the properties of Nicalon/SiC composites.

Precoat	Thickness* (microns)	Frictional Stress (MPa)	Matrix Fracture Stress (MPa)	Ultimate Flexure Strength (MPa)	Observed Behavior
Uncoated	—	49 ± 15	82 ± 10	82 ± 10	Low strength, brittle
Carbon	0.07	11 ± 6	257 ± 29	344 ± 20	Moderate strength, low pull-out
Carbon	0.17	4.3 ± 1.2	193 ± 28	420 ± 36	High strength, improved pull-out
Carbon	0.26	0.6 ± 0.4	160 ± 16	390 ± 13	Moderate strength, pull-out
Carbon	>0.5	—	—	352 ± 33	Lower strength, high pull-out
Boron Nitride	0.15	6.6 ± 1.7	—	350 ± 40	Moderate strength, pull-out

*Calculated from weight gain.

The composites prepared from uncoated fibers exhibited low flexure strength and displayed brittle failure, with no signs of toughening (Table 1). The lack of fiber pull-out and the flat, smooth fracture surfaces of test specimens suggest a high degree of bonding between fiber and matrix and/or complete failure of the reinforcement. Indentation measurements confirmed the high interfacial frictional stresses and in some cases the loads were enough to cause splitting of the fiber and extensive cracking of the surrounding matrix (Fig. 2).

The influence of the thickness of the carbon layer on the mechanical behavior of the composites was investigated. The concentration of reactant propylene was varied to produce films that ranged in thickness from 0.10 to > 0.5 μm. The thickness of the interfacial film had a significant effect on the matrix fracture stress, ultimate strength, and toughness of the specimens. (Table 1) The influence of carbon interlayer thickness on the fracture of the composites is shown in the load-displacement curves in Figure 3. A single matrix crack was observed in all tests and can be seen as the sudden drop in the curve and subsequent deviation from linearity. Matrix cracking stress and interfacial frictional stress decreased with increasing interlayer thickness. The decrease in frictional stress was also accompanied by an increase in the degree of fiber pull-out.

Fig. 2. Indent impressions on uncoated Nicalon fibers in a SiC matrix. (interfacial frictional stress, τ_i = 49 ± 15 MPa).
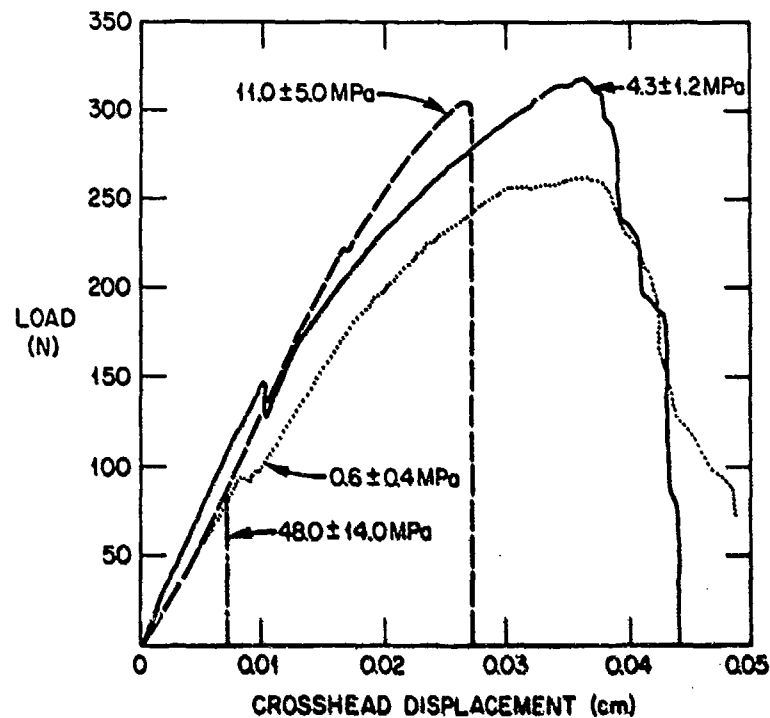
Fig. 3. The effect of carbon interface coating thickness on the flexure behavior of Nicalon/SiC composites. Indentation frictional stresses for the curves are indicated.

Composites produced with boron nitride-coated fibers exhibited strength values and fracture behavior comparable to composites with carbon interfacial layers. Transmission electron microscopic analysis of the interface in the composites found the BN coatings to be ~0.2 μm thick and composed of extremely fine grains of hexagonal BN. The graphitic structure of the hexagonal BN grains was evident in high resolution TEM micrographs of the interface layer. (Fig. 4)

The ultimate strength of the composites increased slightly with temperature up to 1273 K where degradation of fiber properties results in a reduction in composite strength. (Fig. 5) The composites exhibited good strengths and gradual failure in all tests. No differences in the performance of specimens containing fibers with similar thicknesses of carbon and boron nitride (~0.2 μm) were observed.
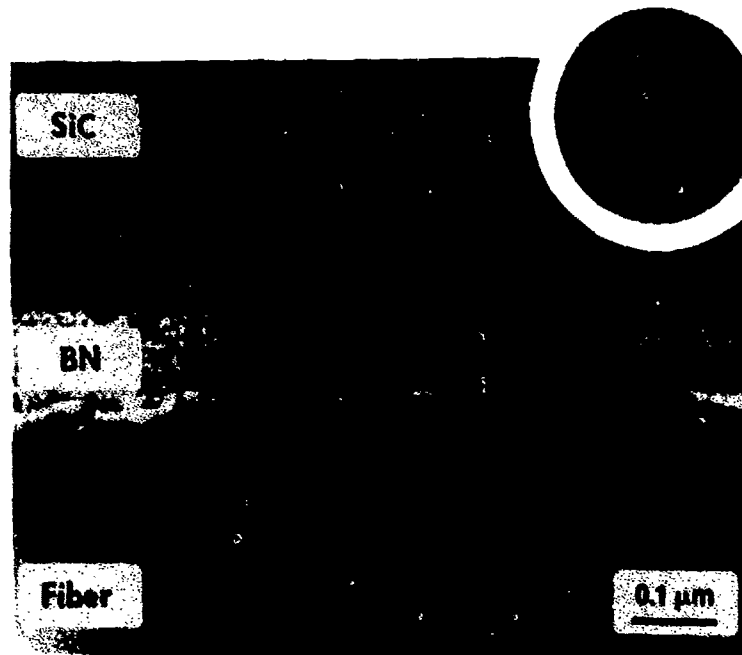
Fig. 4. TEM micrograph of the polycrystalline BN interlayer in a Nicalon/SiC composite. Inserted high resolution TEM micrograph shows graphitic structure of the coating.
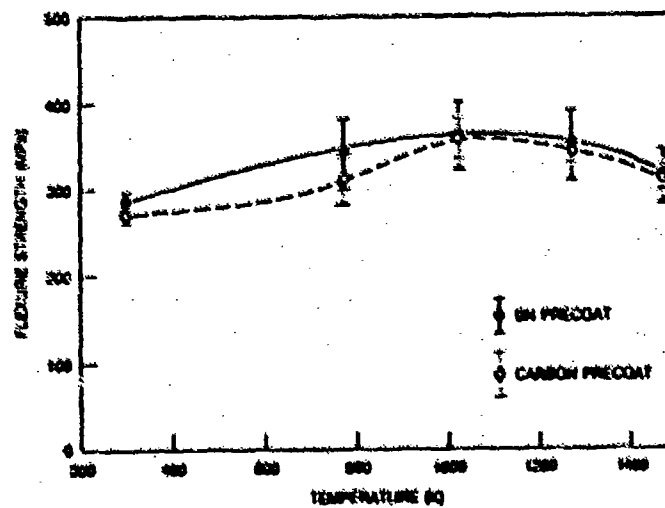
Fig. 5. High temperature flexure strengths for Nicalon/SiC composites with ~ 0.2 μm carbon and BN interface coating.

DISCUSSION

Precoating and Fracture Behavior

Pyrolytic carbon and boron nitride layers deposited on fibrous preforms prior to densification improved the mechanical properties of Nicalon/SiC composites fabricated using FCVI techniques. Precoating fibers prior to matrix deposition not only reduced interfacial stresses, but may have also provided protection from chemical attack during processing. The values for interfacial frictional stress for the samples containing uncoated fibers were relatively high; 49 ± 15 MPa as calculated from indent measurements. In comparison, reported shear numbers for Nicalon/glass composites are ~ 2.0 MPa.[13] The high values for Nicalon/SiC composites fabricated from uncoated fibers are consistent with observed behavior, for these composites exhibited brittle, catastrophic failure. Carbon coatings at the fiber-matrix interface significantly reduced interfacial frictional stresses in the Nicalon/SiC composites. Composites with carbon interlayers had measured interfacial stresses of <1 to ~10 MPa. Specimens with thicker carbon layers, thus lower interfacial stresses, exhibited a high degree of pull-out, comparable to the degree observed in the aforementioned glass matrix composites.

Polycrystalline hexagonal BN possesses structure and properties very similar to those of graphite and a coating of this material deposited on the fibers produced results comparable to those of carbon interfacial coatings. The room and elevated temperature mechanical properties and fracture behavior of the Nicalon/SiC composites with graphitic carbon and polycrystalline boron nitride coatings of the same thickness were identical. Interfacial frictional stress measurements were virtually the same for the carbon and BN interlayers, 4.3 ± 1.2 and 6.6 ± 1.7 MPa, respectively. Thus it is indicated that BN can be used as an alternative to carbon in this system for applications in oxidizing environments and elevated temperatures.

CONCLUSIONS

The fiber-matrix interface in fiber-reinforced ceramic composites controls the mechanical behavior of these materials. An extremely strong bond does not allow for crack deflection or debonding at the fiber-matrix interface therefore a crack propagating in the matrix simply passes through the fibers undisturbed resulting in brittle fracture. Conversely, an extremely weakened interface leads to a low matrix fracture stress and low ultimate strength, for as the composite is stressed, load is not transferred efficiently from the matrix to the fibers, thus the properties of the reinforcement are not utilized. Therefore, interfacial forces must be controlled to produce a composite material with good matrix failure stress and ultimate strength that also exhibits gradual composite failure through effective fiber pull-out.

Carbon has been shown to be an effective interfacial coating for the Nicalon/SiC system. The deposition of a graphitic carbon coating on the fibers prior to infiltration improved the ultimate strength and toughness of the material. The thickness of the coating affects the properties of the interface and thus can be varied to produce material with different mechanical properties. Boron nitride, which possesses properties similar to carbon, produced room and high temperature strengths identical to those of the carbon layers. BN coatings may provide improved elevated temperature stability through improved oxidation resistance.

ACKNOWLEDGEMENTS

REFERENCES

1. M. H. Rawlins, T. A. Nolan, D. P. Stinton, and R. A. Lowden, "Interfacial Characterization of Fiber-Reinforced SiC Composites Exhibiting Brittle and Toughened Fracture Behavior," *MRS Symposium Proceedings*, Vol. 78, Advanced Structural Ceramics (November 1986).

2. R. A. Lowden, "Characterization and Control of the Fiber-Matrix in Fiber-Reinforced Ceramic Composites," ORNL/TM-11039, March 1989.

3. J. J. Brennan, "Interfacial Chemistry and Bonding in Fiber Reinforced Glass and Glass-Ceramic Composites," Ceramic Microstructures '86: Role of Interfaces, University of California, Berkeley (July 1986).

4. J. J. Brennan, "Interfacial Characteristics of Glass-Ceramic Matrix/SiC Fiber Composites," Interface Science and Engineering '87, Lake Placid, New York (July 1987).

5. J. J. Brennan, "Interfacial Characteristics of Glass and Glass-Ceramic Matrix/Nicalon SiC Fiber Composites," Proceedings of "Tailoring Multiphase and Composite Ceramics," Ed. by R. E. Tressler, et al., Penn. St. Univ., 549-560 (July 1985).

6. W. V. Kotlensky, "Deposition of Pyrolytic Carbon in Porous Solids," *Chem. Phys. Carbon* 9, 173-262 (1973).

7. H. O. Pierson and M. L. Lieberman, "The Chemical Vapor Deposition of Carbon on Carbon Fibers," *Carbon* 13, 159-66 (1975)

8. D. P. Stinton, A. J. Caputo and R. A. Lowden, "Synthesis of Fiber-Reinforced SiC Composites by Chemical Vapor Infiltration," *Am. Ceram. Soc. Bull.* 65(2), 347-50 (1986).

9. R. W. Rice, et al., "The Effect of Ceramic Fiber Coatings on the Room-Temperature Behavior of Ceramic-Fiber Composites," *Ceram. Eng. Sci. Proc.* 2(7-8), 661-701 (1981).

10. B. Bender, et al., "Effect of Fiber Coatings and Composite Processing of Properties of Zirconia-Based Matrix SiC Fiber Composites," *Am. Ceram. Soc. Bull.* 65(2), 363-9 (1986).

11. A. J. Caputo, D. P. Stinton, R. A. Lowden, and T. M. Besmann, "Fiber-Reinforced SiC Composites with Improved Mechanical Properties," *Am. Ceram. Soc. Bull.* 66(2), 368-72 (1987).

12. D. B. Marshall, "An Indentation Method for Measuring Matrix-Fiber Frictional Stresses in Ceramic Components," *Comm. Amer. Ceram. Soc.* C259-60 (December 1984).

13. A. J. Caputo, R. A. Lowden, and D. P. Stinton, *Improvements in the Fabrication of Ceramic-Fiber-Ceramic-Matrix Composites by Chemical Vapor Deposition*, ORNL/TM-9652, June 1985.

14. D. P. Stinton, A. J. Caputo, and R. A. Lowden, "Synthesis of Fiber-Reinforced SiC Composites by Chemical Vapor Infiltration," *Am. Ceram. Soc. Bull.* 65(2), 347-50 (1986).

214

15. R. A. Lowden, A. J. Caputo, D. P. Stinton, T. M. Besmann, and M. K. Morris, *Effects of Infiltration Conditions on the Properties of SiC/Nicalon Composites*, ORNL/TM-10403, May 1987.

16. J. F. Mandell, "Modified Microdebonding Test for Direct In Situ Fiber/Matrix Bond Strength Determination in Fiber Composites," Composite Materials: Testing and Design (Seventh Conference), ASTM STP 893, J. M. Whitney, Ed., American Society for Testing and Materials, Philadelphia, 1986, pp. 87-108.

17. D. B. Marshal and W. C. Oliver, "Measurement of Interfacial Mechanical Properties in Fiber-Reinforced Ceramic Composites," *J. Am. Ceram. Soc.* 70(8), 542-8 (1987).

IMPROVED PERFORMANCE IN MONOFILAMENT FIBER REINFORCED GLASS MATRIX COMPOSITES THROUGH THE USE OF FIBER COATINGS

WILLIAM K. TREDWAY AND KARL M. PREWO
United Technologies Research Center, Silver Lane, East Hartford, CT 06108

ABSTRACT

The mechanical performance of glass matrix composites reinforced with large diameter (140 μm) monofilaments has been investigated. Strong interfacial adhesion between uncoated boron monofilaments and the borosilicate glass matrix resulted in composites exhibiting low failure strain and brittle fracture. The use of coated monofilaments improved composite performance considerably by reducing fiber-matrix interfacial adhesion. Auger analysis of the interface indicated that a carbon-rich layer had formed between the monofilament coating and the matrix during composite fabrication.

INTRODUCTION

Fiber reinforced glass matrix composites have been investigated over the past two decades due to their potential for high strength and stiffness, excellent toughness, low density, and fabricability [1-4]. United Technologies Research Center (UTRC) has been active in this area for many years, investigating the use of a variety of carbon, silicon carbide, and oxide fibers and yarns in a host of different glass and glass-ceramic matrices for many aerospace and industrial applications [4-10]. The use of large diameter monofilaments (100-140 μm diameter) to reinforce glass and glass-ceramic matrices has been pursued recently at UTRC because of the excellent strength and stiffness characteristics of these fibers in both tension and compression. These studies have shown that the "translation efficiency" of properties from these monofilaments to the composite can be quite high, especially for glass-ceramic matrix composites [11].

This paper reports the results of a recent program designed to develop monofilament reinforced glass matrix composites for structural applications in space. In this investigation, a variety of monofilaments with and without fiber coatings were used to reinforce borosilicate glasses. This paper will describe the strength and fracture characteristics of these glass matrix composites as well as microscopic and chemical analysis of the fiber-matrix interfacial region.

EXPERIMENTAL PROCEDURE

Uncoated and coated monofilaments used to reinforce the composites are listed in Table I. The matrix composition for all the composites was a commercially available borosilicate glass*. Carbon fiber yarn** was also included in the composites to fill in the glass-rich regions between monofilaments so as to toughen the matrix and provide additional structural integrity to the composite.

* Code 7740, Corning Glass Works
** Thornel P-100, Amoco Performance Products

TABLE I - Monofilaments Used as Composite Reinforcements

Monofilament	Coating	Trade Name	Manufacturer
Boron	---	---	Textron
Boron	B_4C	---	Textron
Boron	SiC	Borsic	Textron
Boron	SiC	Sicabo	Textron (monofilament) Composites, Inc. (coating)
SiC	C/SiC	SCS-6	Textron

Uniaxially reinforced laminated composites containing the monofilaments and carbon fibers were prepared using a proprietary process. Consolidation of the composites was achieved by hot-pressing in an inert atmosphere at 1250°C at a pressure of 6.9 MPa. This procedure resulted in nearly fully-densified composites containing 1-2 % porosity.

Tensile testing of the composites was performed using straight-sided specimens at a crosshead speed of 0.13 cm/min. In all cases the gage length was 2.54 cm. Composite strain was monitored using glued-on strain gages on both sides of the tensile specimen.

Fracture behavior was observed using both optical and scanning electron microscopy (SEM) techniques. SEM samples were sputter-coated with gold to prevent charging in the microscope. Electron microprobe analysis was performed on monofilament cross-sections using samples that were polished using standard metallographic techniques. Composition analysis of the monofilament coatings in the as-received state as well as of the monofilament-matrix interfacial region after composite fabrication was performed using a scanning Auger multiprobe (SAM). For the interfacial analyses, composites were split interlaminarly (parallel to the monofilament laminae) so that both a monofilament and a matrix trough (where a monofilament had pulled away during fracture) could be analyzed. In this manner, a composition profile of the interfacial region could be constructed.

RESULTS AND DISCUSSION

In general, the microstructures of all the composites were similar, with fairly uniform distribution of the monofilaments throughout the matrix. The carbon fiber was also distributed uniformly throughout the matrix and in between the monofilaments. A few regions of isolated porosity were found in some of the composites, but they were not believed to be of any significance in terms of composite performance.

Uncoated Monofilaments

The tensile fracture surface of the composite containing uncoated boron monofilaments is shown in Figure 1. The ultimate tensile strength (UTS) of the composite, 276 MPa, represents only about 28% of the theoretical strength based on a simple rule-of-mixtures calculation. The failure strain of the composite was also quite low. Examination of the fracture surface of the composite indicated that the composite failed in a brittle manner, with no evidence of monofilament pullout (refer to Figure 1). Close examination reveals that while some toughness is provided to the composite via pullout of the small carbon fibers, the boron monofilaments appear to be bonded very strongly to the glass. It appears that the crack propagating through the matrix experienced no deflection at the monofilament-matrix interface, resulting in continued propagation directly through the boron monofilament.
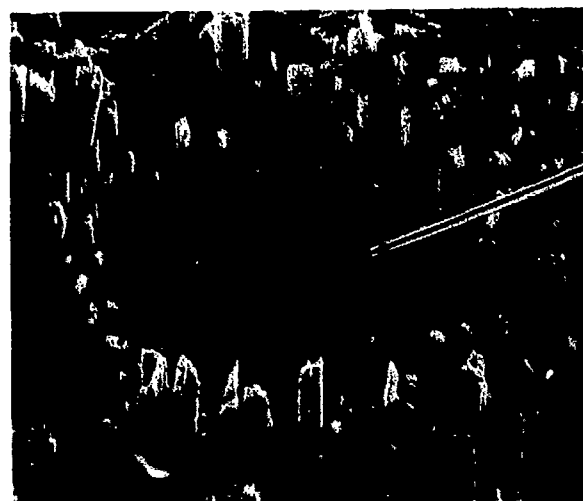
Boron
monofilament

FIGURE 1 - Fracture
morphology of boron
monofilament reinforced
composite, with no pullout
of the boron
monofilaments due to
strong fiber-matrix
interfacial adhesion.

Tungsten core   **50 μm**

Also evident in Figure 1 is some type of reaction at the interface between the core of the monofilament (tungsten) and the boron monofilament itself. While it is not known exactly what led to this reaction, it is clear from examination of the tungsten-boron phase diagram that it was not due to a reaction between the two metals. It is believed that the degradation of the tungsten core was most likely caused by diffusion of some chemical species from the glass through the boron to the tungsten-boron interface. Electron microprobe analysis of the region from the matrix through the boron into the tungsten core indicated the presence of significant amounts of carbon, silicon, and oxygen in the region between the tungsten core and the boron monofilament. Any of these species could have easily reacted with the tungsten to produce the degraded core evident in Figure 1.

Coated Monofilaments

Concern over the brittle fracture behavior resulting from the strong monofilament-matrix adhesion in the boron reinforced composites led to the use of coated monofilaments in the hope that the fiber coating would prevent strong adhesion and improve composite fracture toughness and overall tensile performance. Several different coated monofilaments were utilized, as shown in Table I. The different coating materials evaluated were B_4C, SiC, and a mixture of carbon and SiC. The B_4C and SiC coatings were applied to boron monofilaments, while the C/SiC mixed coating was over a SiC monofilament. Two different SiC-coated boron monofilaments were used in the study. One of these coated monofilaments, known as Borsic, was manufactured entirely by Textron Specialty Materials. In the case of the other fiber, known as Sicabo, the SiC coating was deposited by Composites, Inc. over boron monofilaments that had been purchased from Textron.

The tensile performance of the composites reinforced with the coated monofilaments as well as the uncoated boron monofilament is summarized in Table II. The B_4C-coating did not

TABLE II - Tensile Performance of Monofilament Reinforced Glasses

Monofilament	Vol %	Ultimate Tensile Strength (MPa)	Percent Theoretical Strength	Failure Strain (%)	Fracture Morphology
Boron	28	276	28	0.10	Brittle
B_4C/Boron	20	220	31	0.13	Near-brittle
Borsic	21	413	56	0.38	Fibrous
Sicabo	23	524	65	0.36	Fibrous
SCS-6	20	655	93	0.27	Fibrous

improve tensile strength to any significant extent, with the fracture surface exhibiting very little pullout of the monofilaments (average pullout length < 10 µm). The tungsten core-boron interface again showed some signs of degradation, although not to the same extent as seen in the uncoated boron monofilaments. Electron microprobe analysis in this case did not indicate any significant levels of carbon, silicon, or oxygen in the core-monofilament interfacial region.

The Borsic, Sicabo, and SCS-6 monofilaments all resulted in significantly enhanced tensile performance, with high tensile strengths and substantial amounts of monofilament pullout. The SCS-6 reinforced composite exhibited especially good tensile strength, with 93% translation of the monofilament strength to the composite. Figure 2 shows SEM micrographs of the fracture morphology demonstrated by the Sicabo reinforced composite. These pictures indicate that there was no degradation of the tungsten core during fabrication, suggesting that the SiC coating prevented the diffusion of species from the glass into the boron monofilament. It is also evident from these micrographs that the coating is still intact on the boron monofilament, with fracture and debonding occurring between the coating and the matrix, rather than within the coating or between the coating and the monofilament.

(a)   (b)
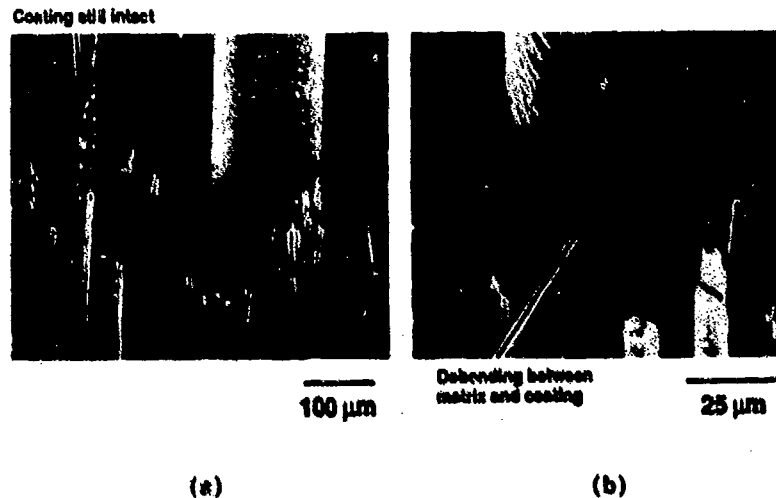
FIGURE 2 - Fracture morphology of the Sicabo reinforced composite. Figure 2(a) shows that the SiC coating is still intact on the boron monofilament, and also illustrates that there was no degradation of the tungsten core during fabrication. Figure 2(b) shows that debonding occurred between the SiC coating and the matrix during fracture.

Auger analysis was performed on the coating-matrix interfacial regions of the Borsic, Sicabo, and SCS-6 reinforced composites to establish the chemical composition across the interface. This procedure has been used extensively at UTRC in recent years in the analysis of interfacial chemistry in NICALON™ SiC yarn reinforced glass-ceramics with considerable success [8]. Figure 3 shows the interfacial composition profile obtained from the Sicabo reinforced composite. It is evident from this profile that a thin carbon-rich layer (< 500Å thick) exists between the matrix and the fiber coating. Also present between the carbon layer and the coating is a region containing significant levels of silicon (~15 at%) and oxygen (~30 at%), with small amounts of boron and sodium that have diffused in from the matrix. The Si:O ratio suggests that SiO_2 may exist in this region. Studies of the fiber-matrix interfacial region in these composites using TEM techniques are currently underway. Profiles obtained from the Borsic and SCS-6 composites were very much similar to that shown in Figure 3 with respect to the existence of a thin carbon-rich layer and a SiO_2 layer between the matrix and the coating. It is believed that this carbon-rich layer between the matrix and the monofilament coating is responsible in large part for the extensive monofilament pullout observed in these composites.

Auger analysis of the as-received Sicabo and Borsic monofilaments indicated that they contained ~53-55 at% carbon and ~45-47 at% silicon in the interior of the fiber, with small amounts of oxygen (8-10 at%) near the surface of the fiber. This indicates that the coating is not stoichiometric SiC, but rather a carbon-rich SiC. The coating on the SCS-6 monofilament is also a mixture of carbon and SiC, though much richer in carbon the the coating on the Borsic
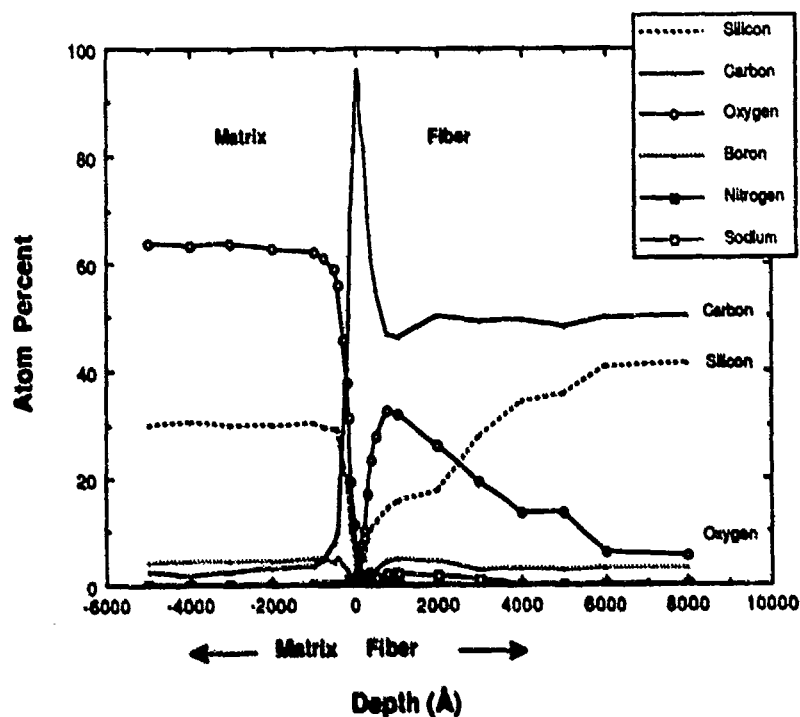
FIGURE 3 - Auger analysis of the fiber-matrix interfacial region in the Sicabo reinforced composite. Note the carbon-rich layer at the interface and the SiO_2 interlayer between the carbon and the SiC coating.

and Sicabo monofilaments. It is proposed here that the carbon layer formation in the composites reinforced with the Borsic, Sicabo, and SCS-6 monofilaments is the result of a solid-state reaction between the SiC in the coating and oxygen from the glass and the fiber surface. This reaction was first described by Cooper and Chyung [12] in an investigation of carbon layer formation at the fiber-matrix interface in NICALON™ SiC yarn reinforced glass-ceramics, and can be given as [12]

$$SiC(s) + O_2(g) \rightarrow SiO_2(s) + C(s) \tag{1}$$
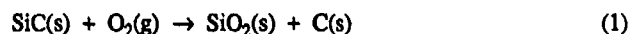
The SiO_2 interlayer that was observed to form between the carbon layer and the SiC coating can also be explained as being a product of the reaction described in equation (1). Of all the chemical equilibria pertaining to the oxidation of SiC, equation (1) has been determined to have the most negative Gibbs free energy and the most rapid reaction kinetics since it does not require the diffusion of gaseous reaction products away from the interface [12]. It seems reasonable, then, that this equation would most accurately explain the oxidation mechanism operative at the SiC-matrix interface within these composites.

It has been suggested that the interfacial carbon layer that forms in NICALON™ reinforced glass-ceramic matrix composites consists not only of the carbon that forms from the reaction described by equation (1), but also is made up of the free condensed carbon that is inherently a part of the fiber [12]. This seems very plausible in light of additional observations made in SiC whisker reinforced composites [13] where it was found that interfacial carbon layer formation was much more prevalent in composites containing SiC whiskers that were nonstoichiometric (carbon rich) than in composites reinforced with very pure, stoichiometric SiC whiskers. This corresponds well with the observations made in this investigation, since all of the monofilament coatings were found to be carbon-rich rather than stoichiometric SiC. In light of all these observations, it seems reasonable to conclude that the formation of the carbon layer at the interface between SiC and the glass matrix is enhanced significantly by the presence of excess condensed carbon in the SiC.

SUMMARY

Glass matrix composites reinforced with uncoated boron monofilaments demonstrated low tensile strengths and brittle fracture behavior. The use of a carbon-rich SiC coating on the boron monofilaments resulted in much improved composite tensile properties and substantial fiber pullout. Similar results were obtained through the use of C/SiC-coated SiC monofilaments (SCS-6). The fiber pullout characteristics were attributed to a carbon-rich layer that was found to form at the interface between the monofilament coating and the glass matrix during composite fabrication. This carbon layer was believed to form largely as the result of an oxidation reaction between the SiC in the coating and oxygen from the glass.

ACKNOWLEDGEMENTS

REFERENCES

1. I. Crivelli-Visconti and G. A. Cooper, Nature 221, 754 (1969).
2. R. A. J. Sambell, D. H. Bowen and D. C. Phillips, J. Mater. Sci. 7, 663 (1972).
3. D. C. Phillips, J. Mater. Sci. 9, 1847 (1974)
4. K. M. Prewo, UTRC Internal Report No. R79-111330-6, 1979.
5. K. M. Prewo, J. F. Bacon and D. L. Dicus, SAMPE Quart. 10, 42 (1979)
6. K. M. Prewo, J. Mater. Sci. 17, 3549 (1982).
7. K. M. Prewo, J. Mater. Sci. 21, 3590 (1986).
8. J. J. Brennan, in Interfacial Characterization of Glass and Glass-Ceramic Matrix/Nicalon SiC Composites, edited by R. E. Tressler, G. L. Messing, C. G. Pantano and R. E. Newnham (Plenum Press, New York, 1986) pp. 549.
9. V. C. Nardone and K. M. Prewo, J. Mater. Sci. 23, 168 (1988).
10. K. M. Prewo, B. Johnson and S. Starrett, J. Mater. Sci. 24, 1373 (1989).
11. D. C. Jarmon and K. M. Prewo, ONR Report No. R86-917054-1, 1986.
12. R. F. Cooper and K. Chyung, J. Mater. Sci. 22, 3148 (1987).
13. J. J. Brennan, AFOSR Report No. R89-917894-1, 1989.

CREEP PROPERTIES AND INTERFACIAL MICROSTRUCTURE OF SiC WHISKER
REINFORCED Si_3N_4

HÅKAN A. SWAN AND COLETTE O'MEARA
Department of Physics, Chalmers University of Technology, S-412 96 Göteborg, Sweden

ABSTRACT

Preliminary creep tests were performed on SiC whisker reinforced and matrix Si_3N_4 material fabricated by the NPS technique. The material was extensively crystallised in the as received material, leaving only thin amorphous films surrounding the grains. No improvement in the creep resistance could be detected for the whisker reinforced material. The deformation mechanisms were found to be that of cavitation in the form of microcracks, predominantly at the whisker/matrix interfaces, and the formation of larger cracks. Extensive oxidation of the samples, as a result of high temperature exposure to air, was observed for the materials tested at 1375°C.

INTRODUCTION

In recent years SiC whiskers have been added to Si_3N_4 based ceramic materials in order to improve the mechanical properties of the material. Evidence exists for an increase in the room temperature fracture toughness [1,2], but no improvement in the creep resistance at elevated temperatures has as yet been observed [3,4]. The strength of Si_3N_4 materials degrades at elevated temperatures due to the presence of an intergranular glassy phase, which is a residue of the liquid phase sintering medium. This glassy phase strongly affects the creep rate at elevated temperatures, where the dominant creep mechanism is that of grain boundary sliding resulting in extensive cavitation [5,6]. At lower temperatures, creep rates rapidly decrease due to a strain hardening effect [6].

The objective of this investigation was to perform preliminary creep testing of SiC whisker reinforced Si_3N_4 materials using a 4-point bending test. The creep mechanisms of the whisker reinforced Si_3N_4 material as well as the matrix material were investigated. The microstructures of the as-received material and the crept material were characterised, as was the oxide scale which formed during creep testing.

EXPERIMENTAL

Materials processing

The material was fabricated by the nitrided pressureless sintering technique (NPS) [7] using 10 wt-% Y_2O_3 and 6 wt-% Al_2O_3 as sintering aids. One parameter, the whisker content, was varied (0 and 30 vol-%). The NPS technique involves the nitridation and subsequent pressureless sintering of compacts of submicron Si and Si_3N_4 powders formed with sintering aids and whiskers. The whiskers were not subjected to any surface treatment. From earlier work [2] it was found that the whisker containing material did not compact sufficiently when pressed prior to sintering. This resulted in large crack-like porosity of the sintered composites. The fully sintered whisker reinforced Si_3N_4 material was therefore hot isostatically pressed (HIP) for one hour at

224

1600°C using a pressure of 200MPa. The HIPing resulted in a fully dense material.

Creep Testing

Creep tests were performed using 4-point bending in air at 1200, 1300 and 1375°C. Both the whisker reinforced and the matrix material were tested using different loads. The outer span of the testing rig was 40 mm and the inner span 20 mm. The specimen size was 3.5x4x45 mm. The deflection was measured as a function of the load directly on the loading rod. The deformation effects of the HIP SiC rollers and the total loading system was thus included in the deformation measurements. The applied bending moment is given as the elastic outer fibre stress and the strain as the outer fibre strain [8]. The deformed samples were cooled down under stress.

Microstructural Characterisation

The microstructure of the samples was studied using analytical electron microscopy (SEM, TEM, STEM and EDS) in combination with X-ray diffractometry (XRD). The TEM specimens were prepared by cutting, grinding, dimpling and ion beam thinning of the samples. Specimens for electron microscopy were prepared from the as-received material as well as from material which had been subjected to bend testing at elevated temperatures. Samples were taken both from the strained region and the unstrained regions of the specimens. The latter were considered as pure heat treated specimens. The major crystalline phases were identified by X-ray diffractometry (XRD) of polished sections. Oxidation of the samples as a result of high temperature exposure to air during testing was studied by X-ray diffractometry (XRD) and scanning electron microscopy (SEM) of the surface and polished transverse sections. A TEM specimen of the oxide scale was prepared by ion beam thinning from the matrix side only, thereby leaving only the oxide scale to be studied.

RESULTS AND DISCUSSION

Creep Testing

A strain vs time creep curve for the different materials tested at 1200°C is shown in Fig. 1. The primary creep region is followed by a region with decreasing creep rate, strain hardening behaviour, and no steady state creep region was observed. An increase of the load shifted the curve slightly due to the elastic strain of specimen and the testing rig and the settlement of the loading rollers into the specimen. No consistent change of strain rate due to the increased load could be detected since the strain hardening contribution dominated the creep curve behaviour.

The traditional creep parameters such as the creep exponent (n) and the creep activation energy (Q) cannot be determined directly from a creep curve of this type. Other methods of creep characterisation have been developed by Evans et al.[9], and Fett et al.[10] for this type of behaviour. However the testing rig proved to be inadequate in obtaining data which was accurate enough and also in obtaining a sufficient amount of data for quantitative analysis according to the methods proposed by the latter authors. The deflection of the specimen needs to be measured directly on the specimen with a high degree of precision in order to obtain quantitative results.
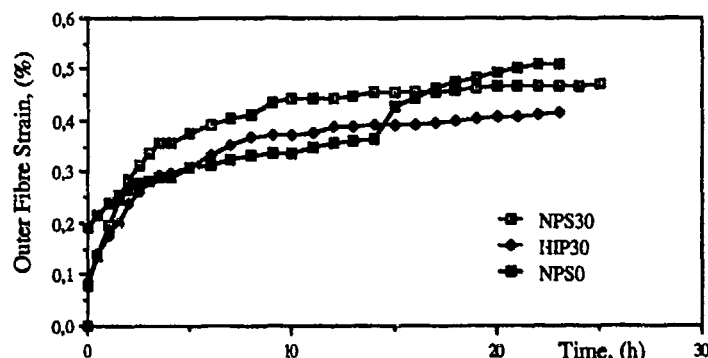
Fig. 1. Strain vs time diagram for the different composites tested at 1200°C. An outer fibre stress of 100MPa was used. NPS0 = Si_3N_4 matrix material, NPS30 = 30% SiC whisker reinforced Si_3N_4, and HIP30 = 30% SiC whisker reinforced Si_3N_4, which was HIPed to full density.

A number of mechanisms have been proposed to explain this strain hardening behaviour in Si_3N_4 materials: 1). Cation diffusion during creep testing results in a high viscosity glassy phase, which reduces the creep rate. In our materials, this could partially explain the strain hardening, as a high concentration of sintering additive cations were detected in the oxide scale, resulting in a cation depletion zone below the scale. 2). Oxidation induced crystallisation of the glassy phase which results in a decrease in the volume of the glassy phase. However, the material subjected to testing in this investigation was already extensively crystallised in the as-received state. Furthermore, strain hardening behaviour has been observed in creep experiments performed in a nitrogen atmosphere [1]. Therefore the effect of oxidation may not completely account for the strain hardening behaviour. 3). Microcracking induced strain hardening. Microcracks were observed in this work, however this effect has not as yet been fully evaluated.

When the temperature during creep testing was raised to 1375°C the appearance of the creep curve changed to that of steady state behaviour. However, this creep region was not studied further due to specimen failure. The strength of the material was considerably decreased at this temperature. These results may indicate that the test temperature was above the eutectic temperature for the material composition, therefore changing the creep mechanism as well as the specimen strength. Other studies have reported similar behaviour, where a eutectic in the region of 1350°C to 1375°C is recorded. The strength above this temperature degrades significantly while the oxidation rate increases, thus limiting the application of these materials to temperatures below ~1350°C.

Microstructure

The general microstructure of the as received materials is shown in Fig. 2 a-b. XRD analysis showed the presence of a major β-Si_3N_4 phase and secondary crystalline phases, while no α-Si_3N_4 was detected. The main secondary phase was identified as α-$Y_2Si_2O_7$. Small peaks, which were of low intensity compared with the main phases were observed on the diffractograms. These peaks however could not be identified with precision and it is concluded that small quantities of other phase(s) were present. As observed by TEM, the major phase, β-Si_3N_4, was mainly present as rod shaped grains with the diameter less than 1 μm. The β-Si_3N_4

grains were surrounded by predominantly crystalline secondary phases. Intergranular glassy phases were only observed as thin interfacial films of 1-10nm in thickness surrounding the grains. Dislocations were only observed in large grains and regions of local high stress concentration. The effect of HIPing upon the microstructure of the whisker reinforced Si_3N_4 was examined and, apart from a fully dense body, no major microstructural changes were observed. The whiskers were randomly oriented and from 1-10 μm in length. The whiskers were not homogeneously dispersed and clusters of up to 5 whiskers were observed. The whisker/Si_3N_4 and whisker/secondary crystalline phase interfaces always contained amorphous material.

The large amount of sintering additives used with the NPS technique increases the amount of liquid phase during sintering and decreases the fraction of silica in the melt. These factors promote the crystallization of secondary phases during cooling as was observed in these materials. This is a major microstructural difference between this and other work on creep of SiC whisker reinforced materials, where the intergranular phase was predominantly amorphous [6,7]. The increased crystallinity of this material may strongly influence the role of the whiskers during creep deformation.

Fig. 2. TEM image of the whisker reinforced material before post HIPing. a) Bright field image and b) Dark field image showing extensive secondary phase crystallisation.

The microstructure of the material crept at 1375°C is shown in Fig. 3a-b. Fig. 3a shows the microstructure of the material below the oxidation scale in the region of maximum strain. Secondary crystalline phases were found to be present, and thin amorphous films were observed surrounding the grains. No change in the volume of secondary crystalline phase could be detected. Dislocations were observed in both the secondary phase crystals and the Si_3N_4 grains. Debonding and microcracking/cavitation at the whisker/matrix interface was commonly observed (Fig. 3a.). Furthermore, a number of large cracks of up to ~50 μm were observed, as shown in Fig. 3b. The specimen taken from the unstrained region had similar microstructural features but did not contain either large cracks, or debonding of the whisker/matrix interfaces. The non-reinforced Si_3N_4 material tested at 1200°C was observed to have the same general microstructure as the material crept at 1375°C. Microcracks and larger cracks were also found.

The creep results indicated that a creep temperature of 1375°C may have been above that of the eutectic, however this was not confirmed by the microstructural examination. No increase in glass volume was observed, and cavitation was only observed in the form of elongated interfacial cracks (microcracks). This suggests that the liquid was of high viscosity and therefore brittle, enabling fracture along its length. Alternatively, the secondary phases present remained crystalline during testing.
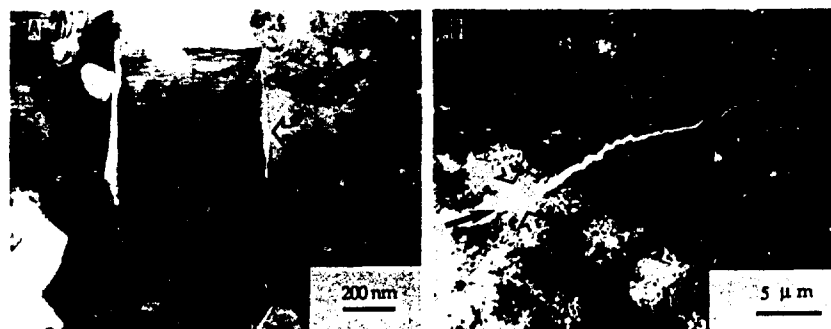
Fig. 3. TEM images of the whisker reinforced post HIPed material after creep testing at 1375°C, taken from the zone of maximum deformation. a) Bright field image of a whisker (W) debonded from the matrix, and b) Bright field image of a large crack.
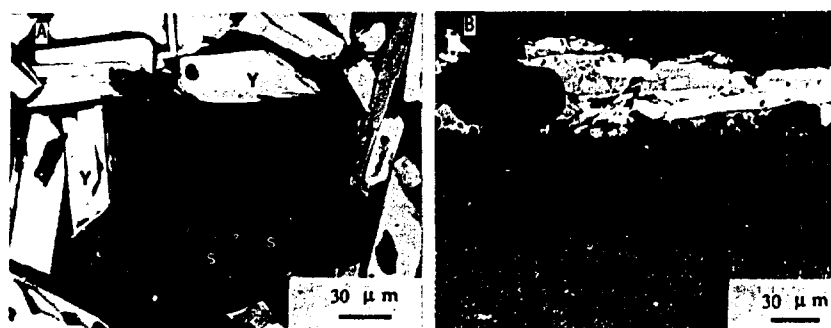
Fig. 4. SEM backscattered electron image of the oxide scale forming on whisker reinforced Si_3N_4 material creep tested at 1375°C for 40h. a) The oxide surface showing an yttrium rich phase (Y) and a Si-rich phase (S) in an amorphous phase which was rich in Al, Y, Si and O. Cracks and pores were frequently observed in the scale. b) Transverse section indicating the formation of a cation depletion zone, resulting from the outward diffusion of the cations to the scale during oxidation.

Oxidation

The extent of oxidation of the samples was observed to change considerably with temperature and time. Very little scale growth was observed in the material tested at 1200°C indicating a slow rate of oxidation. For specimens tested at 1375°C an oxide scale of about 30-50 μm was observed with SEM, see Fig. 4a-b. Fig. 4a-b shows the characteristics of the oxide scale for the material tested at 1375°C. An yttrium rich phase (bright) and a Si-rich phase (dark) are seen in an amorphous phase which was rich in Al, Y, Si and O. Cracks and pores were frequently observed in the scale. A zone of dark contrast of ~50 μm was found below the oxide scale indicating the formation of a cation depletion zone, resulting from the outward diffusion of the cations to the scale during oxidation. TEM examination of the bottom part of the oxide scale showed the presence of Si_2N_2O crystals dispersed in amorphous material (Fig. 5). In this layer

of Si_2N_2O and amorphous phase, partially dissolved (or oxidised) Si_3N_4 grains and SiC whiskers were detected.

Fig. 5. TEM bright field image of the oxide scale of whisker reinforced Si_3N_4 material creep tested at 1375°C for 40h showing the presence of Si_2N_2O (S) and other crystalline phases in an amorphous layer (A).

CONCLUSIONS

* No improvement was detected in the creep resistance of whisker reinforced Si_3N_4 material.
* The deformation mechanisms were found to be cavitation in the form of microcracking, and the formation of large cracks extending ~50 µm.
* The microcracks were observed predominantly at the whisker/matrix interface.
* Extensive oxidation of the samples, as a result of high temperature exposure to air, was observed for the materials tested at 1375°C.

REFERENCES

1. P.F. Becher, C.H. Hsueh, P. Angelini and T.N. Tiegs, J. Am. Ceram. Soc., 71 (12), 1050-61 (1988).
2. A.H. Swan, E. Olsson, R. Lundberg and G.L. Dunlop, presented at the IIB-89 Conference, Paris, France, 1989 (to be published).
3. J.R. Porter, F.F. Lange and A.H. Chokshi, in Processing and Creep Performance of Silicon Carbide Whisker-Reinforced Silicon Nitride, edited by P.F Becher, M.V. Swain, and S. Sômiya (Mat. Res. Soc. Symp. Proc. 78, Pittsburgh, PA 1987) pp. 289-294.
4. M. Backhaus-Ricoult, J. Castaing and J.L. Routbort, Rev. Phys. Appl. 23, 239-249 (1988).
5. A.G. Evans and W. Blumenthal, in Fracture Mechanics of Ceramics, edited by R.C. Bradt, A.G. Evans, D.P.H. Hasselman and F.F. Lange (Plenum, New York, 1983) 6, pp. 423-448.
6. D.R. Clarke, in Progress in Nitrogen Ceramics, edited by F.L. Riley (Martinus Nijhoff, The Hague, 1983) pp. 341-358.
7. R. Pompe, L. Hermansson and R. Carlsson, Sprechsaal, 115, 1098 (1982).
8. G.W. Hollenberg, G.R. Terwilliger and R.S. Gordon, J. Am. Ceram. Soc. 54, 196 (1971).
9. R.W. Evans, T. Murakami and B. Wilshire, Br. Ceram. Trans. J. 87 (2), 54-57 (1988).
10. T. Fett, K. Keller and D. Munz, J. Mater. Sci. 23, 467 (1988).

R-CURVE BEHAVIOR OF SiC WHISKER / Al_2O_3 MATRIX COMPOSITES

JOSEPH HOMENY* AND CHRISTOPHE MANGIN*
*University of Illinois, Department of Materials Science and Engineering - Ceramics Division, 105 South Goodwin Avenue, Urbana, IL 61801

ABSTRACT

The R-curve behavior of SiC whisker / Al_2O_3 matrix composites was evaluated. Composites were fabricated with Silar SC-9 and Tateho SCW-1-S SiC whiskers. The properties of the two SiC whiskers were similar in all aspects, except for significant differences in surface chemistry. These differences were found to be a key factor in determining the R-curve behavior.

BACKGROUND

In whisker reinforced ceramics, the reinforcements are primarily utilized to enhance the fracture toughness. Essentially, the whisker reinforcement prevents catastrophic brittle failure by providing mechanisms that dissipate energy during the fracture process. The operation of various toughening mechanisms, such as crack deflection [1-2], whisker pullout [3-7], and whisker bridging [8-10], to a large extent depends on the the degree of chemical and / or mechanical bonding at the whisker / matrix interface. The chemical bonding is primarily affected by the matrix chemistry, the whisker surface chemistry, and the fabrication parameters, while the mechanical bonding is primarily affected by the whisker morphology and whisker / matrix thermal expansion mismatches. It is generally believed that a strong interfacial bond results in a composite exhibiting brittle behavior. These composites are characterized by high strengths and low fracture toughnesses. If the interfacial bond is weak, then the composite will not fail in a catastrophic manner, due to the activation of various energy dissipation mechanisms. These composites are characterized by high fracture toughnesses and low strengths. Thus, it is necessary to control the interfacial bond in order to optimize the overall mechanical behavior of the composite.

Recent work by Homeny and Vaughn [11] and Homeny et al. [12] on 30 volume percent SiC whisker / Al_2O_3 matrix composites illustrates the

effect of whisker surface chemistry on the fracture toughness and strength. Two whiskers, Silar SC-9* and Tateho SCW-1-S**, similar in all aspects except for surface chemistry, were used to reinforce polycrystalline Al_2O_3. As determined by X-ray photoelectron spectroscopy, the surfaces of the Tateho SCW-1-S whisker were found to consist essentially of SiC, while those of the Silar SC-9 whisker contained a substantial amount of SiO_xC_y and SiO_2, in addition to the expected SiC. Table I summarizes the mechanical properties of the composites, along with a polycrystalline Al_2O_3, of identical grain size. The Silar SC-9 SiC whisker / Al_2O_3 matrix composite exhibited a significant increase in fracture toughness, while the Tateho SCW-1-S SiC whisker / Al_2O_3 matrix composite exhibited only a modest increase. Both composites, however, exhibited increases in strength. Scanning electron microscopy examination of fracture surfaces and crack / microstructure interactions revealed a combination of inter-granular and intra-granular fracture for all specimens. However, the Silar SC-9 SiC whisker / Al_2O_3 matrix composite also exhibited extensive whisker pullout and bridging, on the order of 2 to 4 whisker diameters. A minor amount of crack deflection was also seen in both composites.

Table I - Summary of mechanical properties of 30 volume percent SiC whisker / Al_2O_3 matrix composites.

	Polycrystalline Al_2O_3	Composite (Silar SC-9)	Composite (Tateho SCW-1-S)
Theoretical Density (%)	99.2	100.0	99.2
Grain Size (μm)	<2.5	<2.5	<2.5
Strength (MPa)	456±40	641±34	606±146
Fracture Toughness (MPa$\sqrt{m}$)	3.3±0.2	8.7±0.2	4.6±0.2

* ARCO Metals Company, Greer, SC.
** Tateho Chemical Industries Company, Hyogo-Ken, Japan.

Consideration of the SiC whisker / Al_2O_3 matrix property mismatches revealed the following:

(1) Thermal Expansion Mismatch - Since the thermal expansion coefficient of SiC ($4.7 \times 10^{-6}/^{\circ}C$) is less than that of Al_2O_3 ($8.8 \times 10^{-6}/^{\circ}C$), hoop tension and radial compression existed in the matrix, while radial compression existed in the whisker. Along the axis of the whisker there was axial compression, while the matrix was in axial tension. This residual stress state allowed crack deflection toughening mechanisms to operate, as cracks were attracted to the whiskers and propagated parallel or at right angles to them. Interfacial compressive stresses were also created, which increased the mechanical bonding at the whisker / matrix interface. The resultant effective interfacial shear stress, τ_i, was estimated at 800 MPa by Becher et al. [13]. The critical whisker length, l_c, was calculated as follows:

$$l_c = (\sigma_{fw} r) / \tau_i \tag{1}$$

where r = whisker radius (0.3 μm) and σ_{fw} = whisker tensile strength (7 GPa). Using equation (1) yielded a critical length of approximately 2.5 μm, in agreement with observed pullout lengths for the Silar SC-9 SiC whisker / Al_2O_3 matrix composite, suggesting a lack of chemical bond formation. In this composite, apparently the thin surface layer, i.e. 20 to 40 Å, of SiO_xC_y and SiO_2 prevented a strong chemical bond from occurring. In the Tateho SCW-1-S SiC whisker / Al_2O_3 matrix composite, there apparently was an enhancement of the interfacial shear strength due to combined mechanical and chemical bonding.

(2) Young's Elastic Modulus Mismatch - Since the $E_{whisker}/E_{matrix}$ ratio was approximately 2, the observed strength increases were due to the load transfer mechanism. Apparently the interfacial shear stress was sufficient in both composites to enhance the strengths.

The research reported in this article deals specifically with the R-curve behavior of the composites described above. It was performed to determine if the differences in toughening behavior, due to whisker surface chemistry, would be reflected in the R-curve behavior. An increase in fracture toughness as a function of crack growth, i.e. rising R-curve behavior, reveals that the resistance to crack propagation increases with increasing crack growth. From the engineering point of view, rising R-curve behavior is an important consideration in designing a composite for optimum mechanical behavior.

EXPERIMENTAL

The specimens evaluated for R-curve behavior were identical to those described in Table I. Specimen fabrication details are described by Homeny et al. [14]. R-curve evaluation was performed using 3 mm x 4 mm x 60 mm chevron-notched bars cut from hot pressed billets. All surfaces were finished with a 320 grit diamond wheel and the chevron notch was cut with a 0.228 thick diamond saw so as to produce an angle of 45° at the base of the triangle. Room temperature load-displacement curves were measured in four point bending on a stiff mechanical test machine. The test was performed at a crosshead speed of 0.015 mm/min, so as to achieve stable crack propagation.

The R-curves, i.e. fracture toughness versus crack length, were calculated using the modified model of Bluhm [15-20]. The fracture toughnesses, K, were calculated from the maximum load, P_{max}, and the minimum geometric correction factor, Y^{*}_{min}, as follows:

$$K = (P_{max} / B W^{1/2}) Y^{*}_{min} \qquad (2)$$

where B = specimen thickness and W = specimen width.

RESULTS AND DISCUSSION

Load-Displacement Curves

For composites fabricated with the two types of SiC whiskers, typical load-displacement curves are shown in Figure 1. For the Tateho SCW 1-S SiC whisker / Al_2O_3 matrix composite, the load-displacement curves showed a quasi-continuous shape. The only singularity was at the end of the linear portion of the curve at the limit of elastic behavior, which represented the point of load transfer from the matrix to the whiskers. For the Silar SC-9 SiC whisker / Al_2O_3 matrix composite, the load-displacement curves showed irregularities in the decreasing load portion, in addition to the point of load transfer. Figure 2 shows the details of the saw tooth shape, specifying the points of crack initiation and crack arrest. To each point of initiation corresponded a point of arrest, until the last initiation, where the crack propagated catastrophically. This saw tooth behavior is strong evidence for the operation of a crack wake toughening mechanism, e.g. whisker pullout and bridging.
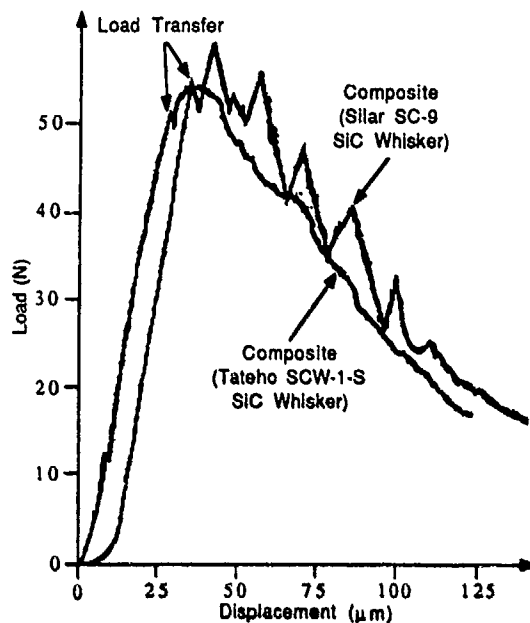
Figure 1. Influence of SiC whisker type on load-displacement curve for 30 volume percent SiC whisker / Al$_2$O$_3$ matrix composites.
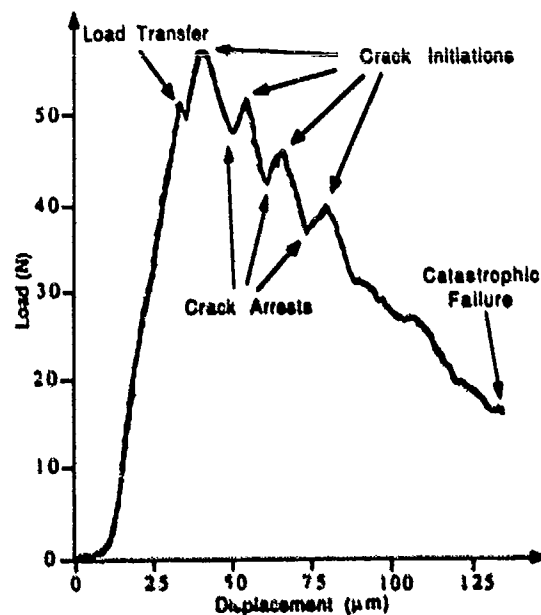
Figure 2. Saw tooth shape of load-displacement curve for 30 volume percent Silar SC-9 SiC whisker / Al$_2$O$_3$ matrix composite.

R-Curves

In the case of the Tateho SCW-1-S SiC whisker / Al_2O_3 matrix composite, the R-curve was flat (see Figure 3). The composite exhibited a fracture toughness slightly higher than that of the unreinforced polycrystalline Al_2O_3, 4.2 MPa√m compared to 3.9 MPa√m. The flat R-curves indicate that no crack wake toughening mechanisms were activated during crack propagation.

. Opposite to the previous case, the Silar SC-9 SiC whisker / Al_2O_3 matrix composite generated rising R-curves. The saw tooth shape allowed for the calculation of two R-curves; one for crack initiation and one for crack arrest. In agreement with the derivation of the R-curve calculation, the initiation curve was associated with the higher values of fracture toughness than the arrest curve (see Figure 4). The composite exhibited a fracture toughness range significantly higher than that of the unreinforced polycrystalline Al_2O_3, 8.3 to 9.3 MPa√m compared to 3.9 MPa√m (see Figure 5). Scanning electron microscopy examination of fracture surfaces and crack / microstructure interactions revealed extensive whisker pullout and bridging in the crack wake.
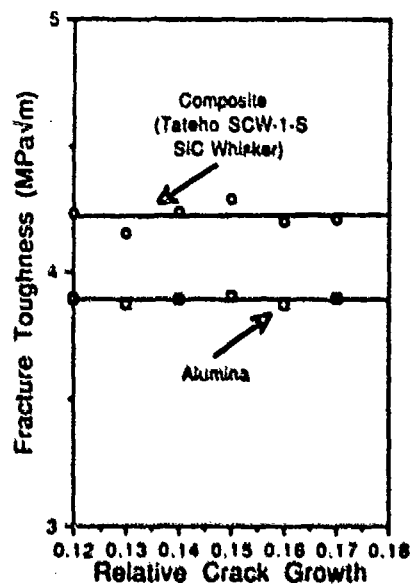
Figure 3. R-curves for 30 volume percent Tateho SCW 1-S SiC whisker / Al_2O_3 matrix composite and unreinforced polycrystalline Al_2O_3.
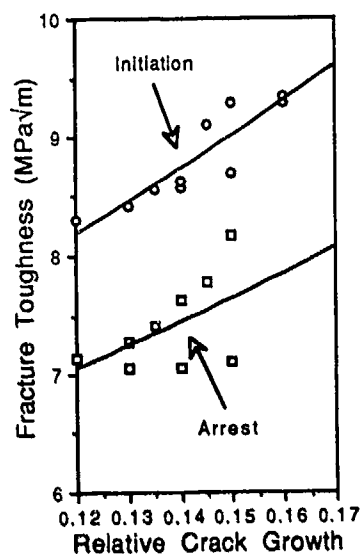
Figure 4. Crack initiation and arrest R-curves for 30 volume percent Silar SC-9 SiC whisker / Al_2O_3 matrix composite.
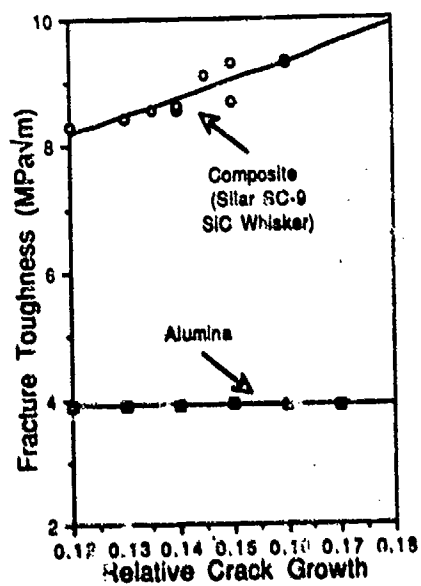
Figure 5. R-curves for 30 volume percent Silar SC-9 SiC whisker / Al_2O_3 matrix composite and unreinforced polycrystalline Al_2O_3.

CONCLUSIONS

The main differences between composites fabricated with Silar SC-9 and Tateho SCW-1-S whiskers were related to the shape of the R-curves and the ultimate values of the fracture toughness. The Silar SC-9 SiC whisker / Al_2O_3 matrix composite exhibited rising R-curves, while the Tateho SCW-1-S SiC whisker / Al_2O_3 matrix composite showed flat R-curves. The Silar SC-9 SiC whisker / Al_2O_3 matrix composite also exhibited significant increases in fracture toughness compared to the unreinforced polycrystalline Al_2O_3, while the Tateho SCW-1-S SiC whisker / Al_2O_3 matrix composite showed little improvement over the unreinforced polycrystalline Al_2O_3. This observation was not related to the physical or mechanical properties of the whiskers, since they were basically equivalent, but rather to the surface chemistry differences. The presence of SiO_xC_y and SiO_2 on the surfaces of the Silar SC-9 whiskers was a critical factor in allowing crack wake toughneing mechanisms, i.e. whisker pullout and bridging, to operate in the composites fabricated with these whiskers. These wake toughening mechanisms were responsible for the enhanced fracture toughness and rising R-curves for this composite.

REFERENCES

1. K. T. Faber and A. G. Evans, Acta. Metall. 31, 565 (1983).
2. K. T. Faber and A. G. Evans, Acta. Metall. 31, 577 (1983).
3. R. W. Rice, Ceram. Eng. and Sci. Proc. 2, 661 (1981).
4. R. W. Rice, Ceram. Eng. and Sci. Proc. 6, 589 (1985).
5. R. W. Rice, Chem. Tech. 4, 230 (1983).
6. D. K. Shetty, Current Awareness Bulletin, Metals and Ceramics Information Center, Battelle Columbus Laboratories 118 (1982).
7. A. Kelly, Proc. Roy. Soc. Lond. A 319, 95 (1970).
8. M. G. Jenkins, A. S. Kobayashi, K. W. White, and R. C. Bradt, J. Am. Ceram. Soc. 70, 393 (1987).
9. M. R. Piggot, J. Mater. Sci. 5, 669 (1970).
10. D. Lewis III, in Processing of Advanced Ceramics, edited by J. S. Moya and S. D. Aza (Sociedad Espanola de Ceramica Y Vidro, Madrid, Spain, 1987) pp. 49-72.
11. J. Homeny and W. L. Vaughn, Mat. Res. Soc. Bull. 7, 66 (1987).
12. J. Homeny, W. L. Vaughn, and M. K. Ferber, J. Am. Ceram. Soc., accepted for publication.

13. P. F. Becher, T. N. Tiegs, J. C. Ogle, and W. H. Warwick, in Fracture Mechanics of Ceramics. Vol. 7: Composites. Impact. Statistics. and High-Temperature Phenomena, edited by R. C. Bradt, D. P. H. Hasselman, A. G. Evans, and F. F. Lange (Plenum, New York, NY, 1986) pp. 61-73.

14. J. Homeny, W. L. Vaughn, and M. K. Ferber, Am. Cer. Soc. Bull. 66, 333 (1987).

15. D. Munz, R. T. Bubsey, and J. E. Srawley, Int. J. of Frac. 16, 359 (1980).

16. M. Sakai and K. K. Yamasaki, J. Am. Ceram. Soc. 66, 371 (1983).

17. M. G. Jenkins, A. S. Kobayashi, K. W. White, and R. C. Bradt, Eng. Frac. Mech. 30, 505 (1988).

18. D. Munz, R. T. Bubsey, and J. L. Shannon, Jr., J. Am. Ceram. Soc. 63, 300 (1980).

19. A. H. Cottrell, The Mechanical Properties of Matter (Krieger, Huntington, NY, 1981) pp. 124-130.

20. M. Sakai and K. Yamasaki, J. Am. Ceram. Soc. 66, 376 (1983).

MECHANICAL PROPERTIES AND GRAIN GROWTH INHIBITION IN THE SYSTEM
$Al_2O_3:c-ZrO_2$

J. D. French, H. M. Chan, M. P. Harmer and G. A. Miller
Department of Materials Science and Engineering, Lehigh
University, Bethlehem, PA 18015.

ABSTRACT

The grain coarsening in a 50:50 volume percent $Al_2O_3:c-ZrO_2$
composite is shown to be severely limited even after long heat
treatments at high temperatures (100 hours at 1650°C). The
strength behavior, measured by an indentation-strength-in-
bending (ISIB) method, shows a "rule-of-mixtures" type behavior.
The microstructural stability at high temperatures yields
reliability in the mechanical properties which has important
implications with regard to fiber-reinforcement technology.

INTRODUCTION

Duplex interconnected microstructures have been used for
many years in the metals field for the generation of fine-grained
materials suitable for superplastic forming.[1] However, this
technique has not been exploited in the field of ceramics for
producing microstucturally stable materials. Microstructural
stability implies reliability of mechanical properties, since
grain growth would be limited during high temperature service.

To study the microstructural development and mechanical
properties of dual phase interconnected microstructures, a
suitable system must be chosen in which there is (a) limited
solid solubility of the two phases, and (b) no intermediate
compounds between phases. The system $Al_2O_3:c-ZrO_2$ was selected
since it fulfils both these criteria. Although there has been a
fair amount of previous work in this system [2,3], the emphasis
has been on highly alumina-rich and zirconia-rich compositions.
Very little study has been carried out with compositions near
50:50 volume percent.

EXPERIMENTAL PROCEDURE

Commercial, high purity powders* were mixed in 200-proof
ethanol and ball milled for 24 hours then air dried on a hot
plate. After crushing the dried cake, specimens for mechanical
testing (25 mm diameter, 3 mm thickness) were produced by die
pressing/isostatic pressing (30 MPa/350 MPa). Single-phase
specimens were fabricated using the same pressing schedule. The
pellets were calcined in air for 16 hours at 1000°C followed by
sintering. Table I shows the sintering times and temperatures
for the three compositions. The sintering schedule was chosen

*Sumitomo AKP-HP Al_2O_3, Japan; Tosoh 8Y-ZrO_2, Japan.

to produce a final average grain size of ~5 μm. Pellets 12 mm
diameter, 5 mm thickness were also produced for microstructural
development studies. Polished cross-sections were characterized
using scanning electron microscopy (SEM), and average grain
sizes were determined using a lineal intercept technique. Room
temperature strength was measured using an indentation-strength-
in-bending (ISIB) technique. [4,5]

TABLE I. Sintering schedule for single phase and dual-phase
specimens for mecanical testing.

Composition	Temperature, °C	Time, hours
Al_2O_3	1650	3
AZ50	1650	9
$c-ZrO_2$	1500	2

RESULTS AND DISCUSSION

Figure 1 shows the grain growth behavior of single phase
Al_2O_3, single phase ZrO_2, and the duplex AZ50 as a function of
sintering time at 1650°C. The sintering kinetics were modelled
using the relation:

$$G^n - G_0^n = Kt \tag{1}$$

where G is the average grain size at time t, n is the grain
growth kinetic exponent, G_0 is the grain size at t = 0 and K is
a constant. The growth rate constants, for n = 3, appear in
Table II.
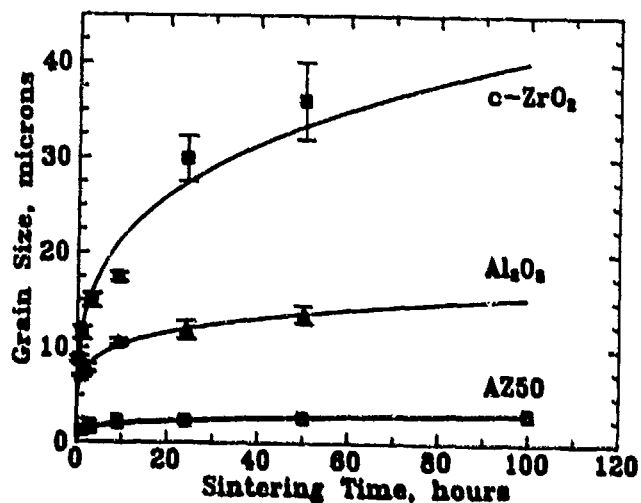
FIGURE 1. Effect of time, at 1650°C, on the average grain size
of single phase $c-ZrO_2$(■), single phase Al_2O_3(▲) and AZ50 -
Al_2O_3 phase(△) and $c-ZrO_2$ phase(□).

TABLE II.   Grain growth constants, for n = 3, for single phase
            Al_2O_3, single phase $c-ZrO_2$, and each phase in AZ50.

	Composition	$Kx10^{23}$, m^3/s
single phase	Al_2O_3	1200
	$c-ZrO_2$	27000
AZ50	Al_2O_3	7.3
	$c-ZrO_2$	7.6

It can be seen that the presence of 50 vol% $c-ZrO_2$ (AZ50),
lowers the grain growth constant of Al_2O_3 by a factor of 160.
It should be noted that kinetic exponents from 2 to 6 all
provided a reasonable fit (accounted for >90% of the variation)
to the data. However n = 3 was chosen to allow comparison with
the effect of MgO on the grain growth of Al_2O_3 [6] , where K was
observed to decrease by a factor of 50 at 1600 C. A typical
microstructure of the AZ50 composition can be seen in Figure 2,
where the dark phase is Al_2O_3 and the light phase is $c-ZrO_2$.
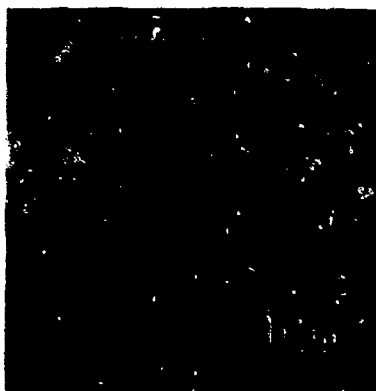
FIGURE 2. Typical microstructure of AZ50 after 100 hours at
1650°C.

Clearly the AZ50 duplex structure exhibits dramatic inhibition
of grain coarsening relative to the constituent phases. The
underlying physical mechanisms for this, together with grain
growth data on other AZ compositions will be discussed in future
work. [7]
     The strength-indentation load results, Figure 3, show a
"rule-of-mixtures" like behavior, i.e. the the AZ50 graph of log σ
- log P is linear with a slope of -1/3, and falls midway between
the single phase data. This result suggests that grain boundary
stresses due to the thermal expansion mismatch between Al_2O_3 and
$c-ZrO_2$ play a relatively minor role in the mechanical properties
of the composite at these grain sizes.
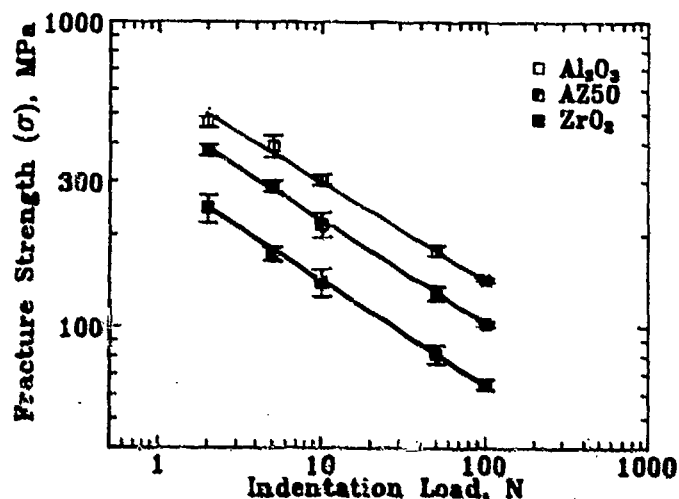
FIGURE 3. The effect of composition on the strength behavior of
Al_2O_3:c-ZrO_2 composites.

SUMMARY

1) AZ50 shows dramatic coarsening resistance even after 100
   hours at 1650°C.
2) The strength data (logσ - log P) shows a "rule-of-
   mixtures" type behavior with the strength of the AZ50
   intermediate between that of the single phases.
3) The microstructural stability of a dual-phase
   microstructure, such as AZ50 could be applicable to fiber
   technology, where fiber coarsening could be controlled or
   possibly eliminated.

ACKNOWLEDGEMENTS

REFERENCES

1. J. Pilling and N. Ridley Superplasticity in Crystalline
   Solids, The Institute of Metals, London, 1989, pp.6-47.

2. F. F. Lange and M. Hirlinger, J. Am. Ceram. Soc. $\underline{70}$ (8) 243-249 (1987).

3. F. F. Lange and M. Hirlinger, J. Am. Ceram. Soc. $\underline{70}$ (11) 827-830 (1987).

4. J. B. Wachtman, Jr., W. Capps and J. Mandel, J. Mater., $\underline{7}$ (1972, 188-94.

5. G. de With and H. H. M. Wagemans, J. Am. Ceram. Soc., $\underline{72}$ (8) 1538-41 (1989).

6. S. J. Bennison and M. P. Harmer, J. Am. Ceram. Soc. $\underline{68}$ (1) C22-C24 (1985).

7. J. D. French, M. P. Harmer, H. M. Chan and G. A. Miller, Communication to be published in J. Am. Ceram. Soc.

THE ROLE OF CRYSTALLIZATION OF AN INTERGRANULAR GLASSY PHASE IN DETERMINING GRAIN BOUNDARY RESIDUAL STRESSES IN DEBASED ALUMINAS

NITIN P. PADTURE[1], HELEN M. CHAN[1], BRIAN R. LAWN[2] and MICHAEL J. READEY[3]

[1]Department of Materials Science and Engineering, Whitaker Lab # 5, Lehigh University, Bethlehem, PA 18015

[2]Ceramics Division, Bldg. # 223, National Institute of Standards and Technology, Gaithersburg, MD 20899

[3]Coors Ceramics Company, 17750, 32nd Avenue, Golden, CO 80401

ABSTRACT

The influence of microstructure on the crack resistance (R-curve) behavior of a commercial debased alumina containing large amounts of glassy phase (28 vol %) has been studied using the Indentation-Strength test. The effect of two microstructural variables, viz. grain size and the nature of the intergranular second phase (glassy or crystalline) has been evaluated. Crystallization of the intergranular glass was carried out in order to generate residual stresses at the grain boundaries, which have been shown to enhance R-curve behavior in ceramic materials. Enhancement of the R-curve behavior was observed with the increase in grain size. However, no effect of the nature of the intergranular second phase on the R-curve behavior, in small and large grain materials, was observed. The results from characterization of these materials using various analytical techniques is presented, together with possible explanations for the observed effects.

INTRODUCTION

Recently several researchers [1 to 4] have reported considerable increase in toughness of debased (liquid-phase-sintered) aluminas, containing 10 to 30 vol % intergranular glass, by crystallization of the glass via simple heat-treatments. However, it should be noted that the toughness measurements in the above studies were performed at single crack length values, whereas recent work has shown that many alumina ceramics show increase in toughness with crack length, i.e. crack resistance or R-curve behavior [5 to 10]. The effect of crack resistance has been attributed to the phenomenon of microstructural grain-localized bridging of the crack, in the wake of its tip, and is very sensitive to the microstructure of the material [5, 11]. In the present study we have set out to evaluate the effect of grain size and crystallization of the intergranular glass on the mechanical properties (R-curve behavior) of these materials over a wide range of crack lengths.

The grains bridging the crack, in non-cubic polycrystalline ceramics, have been postulated to be clamped in the matrix by compressive residual stresses generated during cooling from processing temperatures, due to thermal expansion anisotropy present in these materials [12]. These residual stresses play an important role in the bridging phenomenon. The grain size of the polycrystalline ceramic is also known to influence R-curve behavior of these materials [7,13].

Indentation-strength [7, 8] is a very convenient way of monitoring R-curve behavior in ceramic materials. Bending over of the fracture stress versus indentation load curve at the low indentation load end is a direct consequence of R-curve behavior exhibited by the material, and gives rise to a region where the fracture stress is independent of the indentation load (and hence crack size) [15, 16]. An important implication of R-curve behavior, therefore, is that it suggests a degree of flaw tolerance, which is very useful in terms of engineering design. R-curve behavior also has great significance in the wear properties of materials, since this is governed by fracture characteristics at low flaw sizes. More recently it has been postulated that R-curve behavior increases the Weibull modulus of ceramic materials which exhibit such behavior [17,

18].

The purpose of this study was to determine the separate and combined influence(s) of grain size and second phase crystallinity on the R-curve behavior of debased ceramics. The material chosen was Coors AD85 alumina containing about 28 vol % glass. This material was subjected to carefully designed heat-treatments so as to increase the grain size and increase residual stresses at the grain boundaries by crystallization of the intergranular glass. It was envisaged that in doing so, it would be possible to enhance R-curve behavior in these materials.

EXPERIMENTAL

About 300 samples of AD85 alumina in the form of disks (25mm dia x 3mm) were obtained from Coors Ceramic Company. A series of heat-treatments was carefully devised in order to produce four sets of samples of differing microstructures. Tables I and II show the details of the heat-treatments and the resulting microstructures respectively. The denotation S or L refers to small or large grain size respectively, and C or G refers to crystalline or glassy second phase respectively.

Table I Various heat-treatments, AD85 subjected to.

Material	Heat-treatments	Purpose
AD85-S-G	a) As-received	-
AD85-S-C	a) 1400°C for 6 hours, quenched	Homogenize intergranular glass
	b) 1150°C for 130 hours	Crystallize intergranular glass
AD85-L-G	a) 1550°C for 250 hours	Increase grain size
AD85-L-C	b) 1200°C for 130 hours	Crystallize the intergranular glass

Table II Microstructural aspects of AD85 after the heat-treatments.

Material	Grain size	Intergranular phase
AD85-S-G	3μm	Glassy
AD85-S-C	3μm	80% crystalline
AD85-L-G	18μm	Glassy
AD85-L-C	18μm	80% crystalline

Specimens for Transmission Electron Microscopy (TEM) were prepared from the above samples using a dimpler and then ion-beam milling until perforation. TEM investigation was performed on a Phillips EM 400T at an accelerating voltage of 120 keV. Chemical composition of the intergranular glass was determined using Scanning Transmission Electron Microscopy (STEM) and Energy Dispersive Spectroscopy of x-rays (EDS) on the same instrument. Samples were prepared for Scanning Electron Microscopy (SEM) by polishing sections to 1μm grade followed by thermal etching at 1500 °C for 15 minutes.

Mechanical testing of AD85-S-G, AD85-S-C, AD85-L-G and AD85-L-C was carried out as follows. About 50 disk samples of each were polished to 1μm grade on the prospective tensile side. A Vickers indentation was made at the center of the polished surface with loads varying from 2 to 300 N. Some samples were left unindented. The samples were broken in biaxial flexure using the 3-point support and punch fixture. Details of this particular method of mechanical testing have been described elsewhere [7].

RESULTS AND DISCUSSION

Table III shows the composition of the intergranular glass of AD85-S-G samples after homogenization heat-treatment, as determined by STEM and EDS. This is an average of many different spectra obtained from different regions of the sample. The compositions were observed to be fairly consistent, which implies that the glassy phase is homogeneous. The composition obtained agrees closely with that determined by Weiderhorn et al. [19] for AD85 with the same heat-treatment. Using this composition as the basis, the heat-treatment given in table I was devised. Figure 1 show SEM micrographs of AD85-S-G (grain size 3μm) and AD85-L-G (grain size 18μm). Figures 2 and 3 show TEM micrographs of AD85-S-G and AD85-S-C showing glassy and crystalline intergranular phases respectively. The grain size did not change appreciably during crystallization heat-treatment. The crystalline intergranular phase in AD85-S-C was observed to be mostly anorthite. With this composition it was not possible to achieve 100% crystallinity, thus pockets of residual glassy phase were observed at the triple points.

Table III Average composition of the intergranular glass in AD85.

Oxide	SiO_2	Al_2O_3	MgO	CaO	BaO
Wt%	56.5	27.5	2.1	8.6	5.3
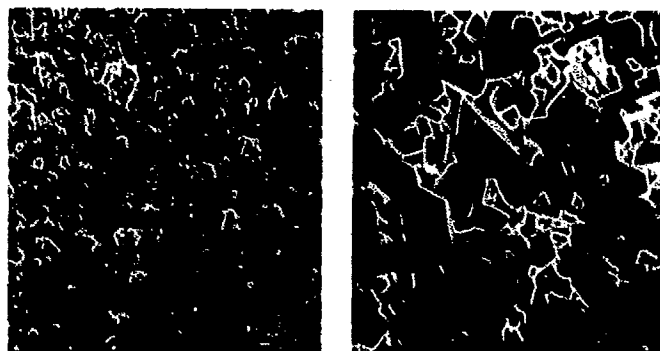
Figure 1 SEM Secondary electron images of polished and etched sections of AD85 aluminas a) AD85-S-G (fine grained material) , b) AD85-L-G (coarse grained material).
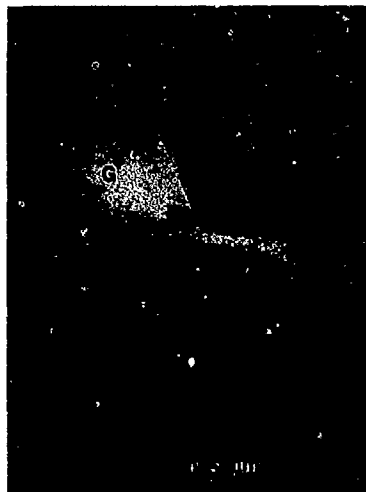
Figure 2 TEM bright field image of AD85-S-G showing intergranular glassy pockets (A-Alumina, G- Glass).

Figure 3 TEM bright field image of AD85-S-C showing crystalline intergranular phase (A-Alumina, C- Crystalline).
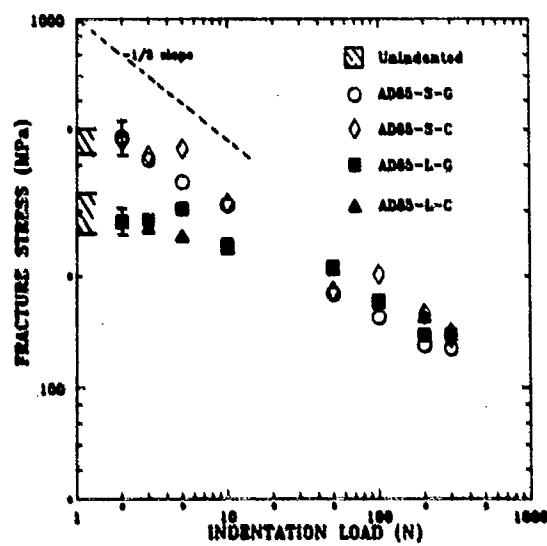
Figure 4 Plot of indentation load versus fracture stress for four different materials, derived from AD85. The error bars for all the data are shown in the left. The hatched region represents failures from natural flaws.

Figure 4 shows indentation load versus fracture stress for AD85-S-G, AD85-S-C, AD85-L-G, and AD85-L-C. It can be seen that all the data essentially falls on two graphs corresponding to 1) fine grained materials (AD85-S-G and AD85-S-C) and 2) coarse grained materials (AD85-L-G and AD85-L-C). It can be clearly seen that coarse grain aluminas show much more pronounced R-curve behavior than fine grain aluminas.

Because the curves for materials with glassy and crystalline intergranular phases show similar behavior, this indicates marginal or no effect of crystallization on the R-curve properties of these materials. The effect of grain size on the R-curve behavior, however, is much more marked, and this is in agreement with results obtained by Cook et al.[7] for single phase aluminas, and Bennison et al. [20] for debased aluminas. Given that grain-bridging processes must be dependent on the residual stresses in the grain boundary regions, the lack of effect of crystallization on the R-curve behavior is somewhat surprising.

Possible explanations for the lack of effect of crystallization of the intergranular glass are thought to be as follows:

1. Stress relaxation by residual glass
2. Fracture through the residual glass
3. Stress relaxation by high temperature deformation (twinning) of anorthite.

Work is currently underway to determine which of the above mechanisms (if any) are correct [21].

CONCLUSIONS

The major conclusions from the above study can be summarized as follows:

1. The effect of grain size on the R-curve behavior predominates.
2. Crystallization of the intergranular glass has relatively little or no effect on the R-curve behavior of AD85. Possible explanations attributing to the observed behavior have been described above.
3. An important conclusion can however be drawn form the observed behavior. Coors AD85 can be subjected to prolonged heat-treatment cycles up to 1200°C without having any significant effect on room temperature mechanical properties (pertaining to fast crack growth). This property of AD85 can be very useful in prolonged high temperature structural applications and in metallization applications imparting heat-treatment tolerance along with flaw tolerance.

ACKNOWLEDGEMENTS

The authors wish to thank Dr. S. J. Bennison for many useful discussions.

REFERENCES

1. N.A. Travitzky, D.G. Brandon and E.Y. Gutmanas, Mater. Sci. Eng., 71, 65-70 (1985).
2. N.A. Travitzky, D.G. Brandon and E.Y. Gutmanas, Mater. Sci. Eng., 71, 77-86 (1985).
3. Y. Yeshurun, Z. Rosenburg, N.A. Travitzky and D.G. Brandon, Mater. Sci. Eng., 71, 71-75 (1985).
4. W.A. Zdaniewski and H.P. Kirchner, Adv. Ceram. Mater., 1, 99-103 (1986).
5. R. Knehans and R. Steinbrech, J. Mater. Sci. Letters, 1, 327-329 (1982).
6. R.W. Steinbrech, R.Knehans and W. Schaarwachter, J. Mater. Sci., 18, 265-270 (1983).

7. R.F. Cook, B.R. Lawn and C.J. Fairbanks, J. Amer. Ceram. Soc., 68, 604-615 (1985).
8. R. F. Cook, B. R. Lawn, and C. J. Fairbanks, J. Amer. Ceram. Soc. 68, 616-623, (1985).
9. M. V. Swain, J. Mater. Sci. Letters, 5, 1313-1315 (1986).
10. F. Duerler, R. Knehans and R. W. Steinbrech, J. de Physique, C1, 617-621 (1986).
11. P.L. Swanson, C.J. Fairbanks, B.R. Lawn, Y-W. Mai and B.J. Hockey, J. Amer. Ceram. Soc., 70, 279-289 (1987).
12. S. J. Bennison and B. R. Lawn, Acta Metall., 37, 2659-2671, (1989).
13. P. Chanikul, S. J. Bennison and B. R. Lawn, J. Amer. Ceram. Soc., to be published.
14. Y-W. Mai and B. R. Lawn, J. Amer. Ceram. Soc., 70, 289- 294 (1987).
15. R.F. Cook, C.J. Fairbanks, Y-W. Mai and B.R. Lawn, J. Mater. Res., 2, 345-356 (1987).
16. S. J. Bennison and B. R. Lawn, J. Mater. Sci. 9 , 3169-3175 (1989).
17. R. F. Cook and D. R. Clarke, Acta Metall., 36, 555-562 (1988).
18. D. K. Shetty and J-S. Wang, J. Amer. Ceram. Soc., 72, 1158-1162 (1989).
19. S.M. Wiederhorn, B.J. Hockey and R.F. Krause Jr., Ceramic Microstructures '86, edited by J. Pask and A.G. Evans (Plenum Publishing Company, New York, 1988) pp. 795-806.
20. S.J. Bennison, H. M. Chan and B.R. Lawn, J. Amer. Ceram. Soc., 72, 677-679 (1989).
21. N. P. Padture, H. M. Chan, B. R. Lawn and M. J. Readey, J. Amer. Ceram. Soc., to be published.

IMPROVED INTERFACIAL ADHESION IN METAL MATRIX/METALLIC GLASS COMPOSITES

UWE KÖSTER and MARGRET BLANK-BEWERSDORFF
University of Dortmund, Dept. of Chemical Engineering,
D-4600 Dortmund 50, Federal Republic of Germany

ABSTRACT

Interfacial adhesion in metal matrix/metallic glass composites can be improved by two methods: either by shifting the original interface into the glassy material by interface induced crystallization or by creating new crystalline/amorphous interfaces during glass formation by solid state reactions between two crystalline materials.

INTRODUCTION

Within the last decades the economic importance as well as the technological development of metal matrix composites has shown a strong increase. This led to the development of new types of composite materials. An interesting new, in literature nearly unknown kind of composite is the combination of metallic glasses within a metallic matrix.

Metallic glasses are amorphous materials. Due to their amorphous state they often exhibit extraordinary properties such as high strength (up to 4000 MPa) along with good ductility [1] or good corrosion resistance [2]. Using the melt spinning technique metallic glasses can be directly produced as a ribbon with a high surface-to-volume ratio at low production costs.

Beside the melt spinning technique metallic glasses can be formed by solid state reactions from crystalline materials. This amorphisation technique has been developed by Schwarz and Johnson [3] in the La-Au system. Between thin, alternating layers of two crystalline components an amorphous interphase will grow during annealing. Schultz [4] modified this thin film technique by using Ni and Zr foils which were rolled into one another, cold welded and subsequently annealed. This treatment led again to the formation of an amorphous interphase. Using this method Schultz was even able to obtain amorphous wires.

Good adhesion between fibre and matrix is the main determinating factor for any technical application of composites. Previous efforts [5-7] of incorporating metallic glass ribbons into a metallic matrix usually failed due to a severe lack of adhesion. Our previous investigations [8] have shown that good adhesion can only be obtained with clean, e.g. oxide free, surfaces of both components. There are two ways to produce amorphous/crystalline composites with improved adhesion at the interface:
- shifting the former amorphous/crystalline interface into the glassy material by interface induced crystallization,
- creating new amorphous/crystalline interfaces during glass formation by solid state reactions.

The mechanisms of both methods are shown schematically in fig. 1 and will be explained in more detail later. In this investigation microstructural changes in the interfacial region of the composites as produced by both methods have been studied systematically by microscopical analysis.

by primary crystallization

Ni
$a - Fe_{42} Ni_{42} B_{16}$
Ni

$\Longrightarrow$ 1h 350°C

Ni
$\gamma - (Fe, Ni)$
Ni

(Blank-Bewersdorff, Koster, Mat Sci Lett, 1989)
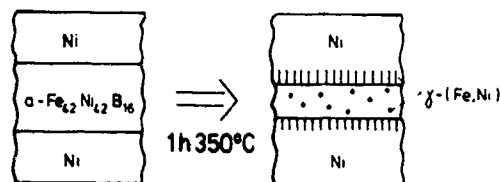
by amorphization due to solid state reactions (crystalline / crystalline)

Co
Zr
Co
Zr
Co

$\Longrightarrow$ 2h 210°C

Co
Zr
Co
Zr
Co

$\alpha - Co_{80} Zr_{20}$

(Schroder, Sommer, Koster, Phys Rev Lett, 1985)

by amorphization due to solid stat reactions (crystalline / amorphous)

Ni
$a - Ni_{30} Zr_{70}$
Ni

$\Longrightarrow$?

Ni
$a - Ni_{30} Zr_{70}$
Ni
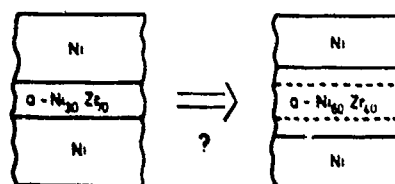
Fig. 1: Formation (schematically) of metal matrix/metallic glass composites with improved interfacial adhesion: (a) by interface induced crystallization; (b),(c) by solid state reactions.

RESULTS AND DISCUSSION

Shifting the amorphous/crystalline interface into the glassy material by interface induced crystallization

The primary crystallizing glass $Fe_{42}Ni_{42}B_{16}$ was produced by melt spinning under 30 hPa helium giving a ribbon with a thickness of 20-25 μm and a width of 1-1.5 mm. On these ribbons nickel was electrolytically deposited using Watt's bath [9]. To obtain reasonable adhesion, the oxide layer on the ribbon surfaces had to be removed by etching prior to the electrolytic deposition of nickel. These composites were annealed between 1 and 5 h under high vacuum at temperatures between 300-400°C. Adhesion was indirectly measured by tensile tests, while the interfacial reactions were studied by means of microscopical methods (OM, SEM, TEM), in particular by cross-sectional TEM.

The adhesion between the components was relatively poor in the unannealed composites. Looking at the fracture surface after tensile testing, a separation of the components was observed due to a lack of adhesion between fibre and matrix. The adhesion was improved by annealing. Fig. 2 shows the fracture surface of an annealed composite (30 min at 350°C). No gaps can be

observed. Whereas the fracture surface of an unprocessed ribbon after the same heat treatment exhibits the typical vein pattern, the fracture surface of the ribbon embedded in the metallic matrix shows a quite different appearance with a less developed pattern of very fine veins, running rectangular from the interfaces accumulating into the middle of the ribbon.
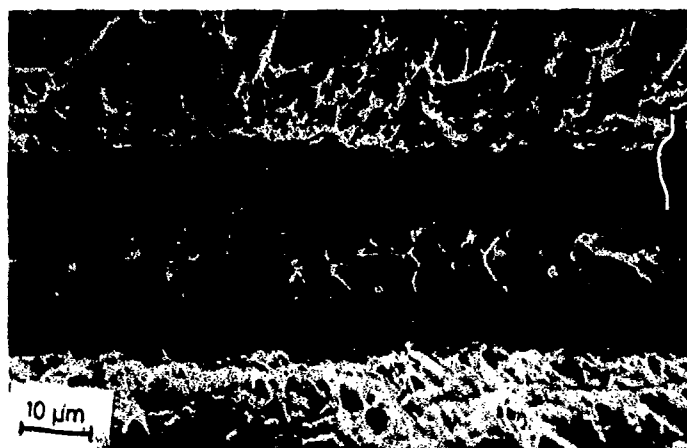
Fig. 2: Fracture surface after tensile testing of an $Fe_{42}Ni_{42}B_{16}/Ni$ composite (annealed for 30 min at 350°C).

The primary crystallizing glass $Fe_{42}Ni_{42}B_{16}$ was chosen for this experiment, because after early annealing embrittlement of the amorphous structure it is known to regain strength and ductility during further annealing into the partially crystallized state [10]. Fig. 3 shows the tensile strength as a function of annealing time at 360°C for the primary crystallizing glass $Fe_{84}B_{16}$ as well as for the eutectic crystallizing glass $Fe_{80}B_{20}$. With increasing annealing time the amount of free volume, which is responsible for the localized ductility, will be reduced by relaxation processes and the material becomes brittle. In the $Fe_{84}B_{16}$ glass, however, further annealing leads to primary crystallization of α-Fe accompanied with an increase in strength and ductility. The reason for the reductilization is probably an increase of free volume at or near the interfaces of the soft α-Fe crystals. Internal stresses due to the different thermal expansion coefficients of the amorphous and the crystalline phase will build up during cooling down from annealing temperature and might also cause such an effect. In contrast, the eutectic crystallizing glass $Fe_{80}B_{20}$ as well as polymorphic crystallizing glasses exhibit only annealing embrittlement. Similar reductilization effects have been observed for the primary crystallizing glasses when embedded in a metallic matrix.

To obtain further information about the reason behind the improved adhesion, cross-sectional transmission electron microscopy has been performed. Fig. 4 shows the influence of annealing at 350°C on the microstructure of the interfacial region in a $Fe_{42}Ni_{42}B_{16}/Ni$ composite. Nickel crystals are deposited as columnar grains perpendicular to the ribbon surface. From these crystalline Ni-layers, fine γ-(Fe,Ni) crystals grow epitaxially into the
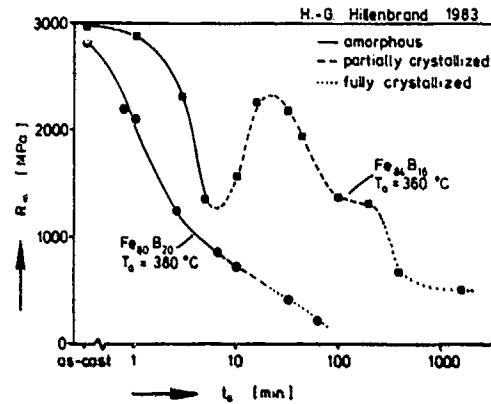
Fig. 3: Influence of annealing on tensile strength for $Fe_{80}B_{20}$ and $Fe_{84}B_{16}$ ribbons [10].

amorphous ribbon and shift the crystalline/amorphous boundaries into the original glass (see fig. 1). After short annealing (30 min) in the bulk as well as at the interface the first few very small γ-(Fe,Ni) crystals were formed. Along the interface a number of very small holes can be seen. Because surface as well as interface induced crystallization usually starts earlier than the crystallization of the bulk, we can assume that some regrowth of the deposited nickel crystals may have occurred. On further annealing these crystals form a crystallization front and after 150 min the original amorphous/crystalline interface has been shifted by 70 to 80 nm on each side into the ribbon. The growth rate of the crystallization front is time-dependent. Using the activation energy for growth of γ-(Fe,Ni) crystals in the bulk of the same glass [11] a thickness of 60 nm can be calculated, which is in good agreement to our experimental results.

Fig. 4: Influence of annealing at 350°C on the microstructure of the interfacial region in $Fe_{42}Ni_{42}B_{16}$/Ni composites: (a) 30 min; (b) 150 min.

By measuring the mechanical properties the improved adhesion between the glassy ribbon and the matrix could be confirmed. Stress-strain diagrams show that due to the embedding in a ductile metallic matrix, the glassy ribbon was able to withstand plastic deformation up to 2% without rupture; the metallic glass itself exhibits only elastic elongation under similar conditions. Optical micrographs of longitudinal sections exhibit that the plastic deformation of the ribbon did not take place homogeneously, but on several activated shear bands.

Formation of Metal Matrix/Metallic Glass Composites by Solid State Reactions

After careful cleaning and etching Ni- and Zr-foils (Ni: d = 0.5 mm; Zr: d = 0.11 mm) were alternatingly packed and subsequently cold-rolled. The thickness reduction was about 70 %. Unannealed this composite shows a reasonable adhesion just due to the formation of clean metallic surfaces. After annealing at temperatures between 250 and 380°C for 0.25 to 100 h the interfacial regions have been analyzed by cross-sectional TEM.

Fig. 5 shows a TEM micrograph of a Ni/Zr composite after annealing for 25 h at 270°C. Between the crystalline Ni- and Zr-layers an amorphous interphase (see fig. 1) has been formed. Such a reaction can proceed by interdiffusion if the free energy of the amorphous phase is lower than that of the crystalline sandwich. The time-dependent growth of the amorphous layer indicates that the reaction is diffusion controlled with an activation energy for diffusion of Q_D = 100 kJ/mole, which is in good agreement to measurements by Meng [13] in Ni/Zr thin film diffusion couples. The formation of the amorphous interphase led to a strong increase of adhesion between the components; only a few Kirkendall voids could be observed. After the amorphous phase has reached a critical thickness of about 0.1 μm [12,13] further annealing leads to the formation of a crystalline phase, probably NiZr.

Fig. 5: Amorphous interphase between cold-rolled Ni- and Zr-foils after annealing for 25 h at 270°C [12].

258

The method of producing amorphous/crystalline metallic composites by solid state reactions should also work using Zr-rich Ni-Zr metallic glasses instead of the pure Zr-foils in contact with Ni-foils. Thermodynamically it should be possible to enlarge the amorphous section by moving the interface into the crystalline layer, i.e. by formation of an amorphous phase with less Zr content due to interdiffusion of the nickel at elevated temperatures (see fig. 1). However, as yet this has not proved successful. Only the formation of a thin crystalline interphase with unknown structure was observed.

ACKNOWLEDGEMENT

REFERENCES

[1] H.-G. Hillenbrand, E. Hornbogen, U. Köster, Metall 36, 1059 (1982)

[2] M. Naka, K. Hashimoto, T. Masumoto, Corrosion 32, 146 (1976)

[3] R.B. Schwarz, W.L. Johnson, Phys.Rev.Lett. 51, 415 (1983)

[4] L. Schultz, Proc. Rapidly Quenched Metals 5 (1984), 1585

[5] S.J. Cytron, Proc. Rapidly Quenched Metals 5 (1984), 145

[6] S.J. Cytron, J.Mat.Sci.Lett. 1, 211 (1982)

[7] G. Nussbaum, D. Ast, J.Mat.Sci. 22, 23 (1987)

[8] M. Blank-Bewersdorff, U. Köster, G. Steinbrink, J.Mat.Sci.Lett. 8, 796 (1989)

[9] J.W. Oswald, in Heavy Electrodeposition of Nickel, The International Nickel Company Ltd., London 1962

[10] H.-G. Hillenbrand, PhD thesis, Ruhr-Universität, Bochum 1983

[11] U. Herold, PhD thesis, Ruhr-Universität, Bochum 1982

[12] R. Pries, B. Schuhmacher, U. Köster, to be published

[13] W.C. Meng, C.W. Nieh, W.L. Johnson, Appl.Phys.Lett. 51, 1693 (1987)

THE INFLUENCE OF INTERFACIAL MODIFICATION ON TENSILE STRENGTH OF Gr/Al COMPOSITES

CHENG HE, GUODING ZHANG AND RENJIE WU
Institute of Composite Materials, Shanghai Jiao Tong University
Shanghai 20030, People's Republic of China

ABSTRACT

Varying the composition of the matrix alloy was a useful technique for tailoring the interfacial structure of MMC. In this paper, the influence of different interfacial states on the tensile strength of Gr/Al composites were investigated. Three aluminum alloys, pure Al, Al-Ti alloy (Ti oversaturated) and LY12 (an Al-Cu-Mg alloy) were chosen as the matrix materials. The results showed that the composites with Al-Ti matrix had excellent tensile properties, even after heat-treatment at 600°C, while with LY12 matrix exhibited poor properties compared with pure Al matrix. Microanalysis revealed that the interfacial structures of the composites with the above matrices were different. In addition, an initial study of mechanism of these matrix effects on the properties of the composites was also carried out.

INTRODUCTION

Graphite fiber reinforced aluminum matrix composites are candidate materials for aerospace applications because of both the high specific strength and modulus. However, major problems encountered in the fabrication of such composites include wetting, bonding and interfacial reaction at the fiber-matrix interface [1-4]. So, surface treatment of the fiber with coatings and matrix alloying are widely used to improve wettability and inhibit the reaction at interface, and then, to modify the interfacial state and affect the final mechanical properties of the composites [5-7].

In this paper, we were dealing with the influence of three aluminum matrices, pure Al, Al-Ti alloy and LY12 (an Al-Cu-Mg alloy), on the tensile properties of the Gr/Al composite wires with Ti-P coating on the fibers. The interfacial structure of the composites and the mechanism of the effects of these matrices were also studied initially.

EXPERIMENTAL PROCEDURE

The composite wires, with commercialy pure aluminum (99.9wt%Al), Al-Ti binary alloy (0.40wt%Ti) and LY12 (an aluminum alloy with 3.8-4.9wt%Cu, 1.2-1.8wt%Mg and 0.3-0.9wt%Mn) matrices, were produced by Ti-B CVD coating and infiltration with molten aluminum matrix. All composite wires contained approximately 50 vol% of continuous and unidirectional Toray graphite fiber M40 (its tensile strength was about 1860 MPa, modulus of elasticity was about 3.6×10^5 MPa and diameter was about 6.5 μm).

The composite wires, M40/Al, M40/Al-Ti and M40/LY12, were examined in as-received and heat-treated conditions. Heat treatment was carried out at 400°C, 490°C, 550°C, 580°C and 600°C for 1 hour in a vacuum environment (less than 5×10^{-4} Torr). Tensile tests of the composites and the fibers after the matrix was leached away were performed at room temperature by XLL-50 universal testing maching at a 25 mm/min crosshead speed. The fracture surfaces of the composites were observed by SEM.

Microanalyses were carried out by TEM, SAM and XPS. The TEM specimens of the composites were prepared by ion milling and examined in a Hitachi H-700 transmission electron microscope with a beam size of approximately 100 nm. The fracture surfaces of M40/Al and M40/Al-Ti fractured in-situ were examined by a Perkin-Elmer PHI-610 scanning Auger microscope in vacuum environment (about 5×10^{-10} Torr) with a beam size of approximately 500

nm. Specimens for XPS were prepared by leaching away the matrix carefully and the surfaces of the fibers which were extracted from the composites were examined using a NP-1 X-ray photoelectron spectroscope.

RESULTS AND DISCUSSION

Tensile Strength of Composites

The effects of temperature on the tensile strength of the composites and the graphite fibers after the matrix was leached away are shown in Table I.

Table I. The effects of temperature on the strength of the composites and the leached fibers.

	A.R.*	400°C	490°C	550°C	580°C	600°C	ROM
			tensile strength (MPa)				
M40/Al	948.6	997.6	1051.5	1020.2		824.2	1078.2
	(1960.0)	(1996.3)	(1996.3)	(1976.7)		(1670.9)	
M40/Al-Ti	934.1	1095.6	1131.9	1086.8		1002.5	1078.2
	(1965.9)	(2034.5)	(2005.1)	(2037.4)		(1970.8)	
M40/LY12	523.3	619.3	583.1	610.5	493.9	351.8	1193.1
	(1949.2)	(2023.7)	(2012.9)	(2028.6)	(1793.4)	(1612.1)	

* : as-received
( ): the strength of the fibers after the matrix was leached away

Tensile strength of M40/Al-Ti almost reached the value calculated by the rule-of-mixtures (ROM) even after heat-treatment at 600°C, while the strength of M40/LY12 was much lower than the ROM UTS value. Below 550°C, the strength of the fibers in M40/LY12 after the matrix was leached away was unchanged compared with the original fibers, which meant no fiber deterioration occurred. The change in extensive pull-out fracture morphology in M40/Al-Ti even at 600°C to flat fracture across fibers in M40/LY12 suggested that M40/LY12 had a much higher interfacial bonding strength [Figure 1(a) and 1(b)]. Comparatively, M40/Al also exhibited pull-out fracture surfaces below 550°C. After heat-treatment at 600°C, the tensile strength of both M40/Al and the fibers after the matrix was leached away was reduced and the pull-out length of the fibers in composite fracture surfaces decreased greatly. This was due to the chemical reaction at the interface and the increase of the interfacial bonding.

Microanalysis and Mechanisms of the Matrix Effects

The in-situ fracture of both M40/Al and M40/Al-Ti as-received occurred along the fiber-matrix interface, making it possible to examine the composition of both matrix troughs and fiber surfaces by SAM. Spectra taken from a matrix trough and the surface of a fiber in M40/Al-Ti are presented in Figure 2(a) and 2(b). The difference of elements in trough and fiber surface suggested that the fracture path was between the fiber surface and the interfacial zone. SAM spectra of M40/Al as-received were very similar. The existence of original oxygen at the interface may relate to the fabrication process of composites or residue in the original graphite fibers. Initial XPS study of the fiber surface revealed some chemical compounds such as Al_2O_3, AlO_x, TiO_2 and TiB_2 existing at the interface, among which the TiB_2 was the original surface coating. From the observation by TEM, it was evident that the thickness of this original interface was thin and the structure seemed looser than the matrix; no chemical reaction products were observed in both M40/Al and M40/Al-Ti as-received. After heat-treatment at 600°C, M40/Al-Ti still retained this interfacial structure to a large extent, but for M40/Al, most of this interfacial layer disappeared and
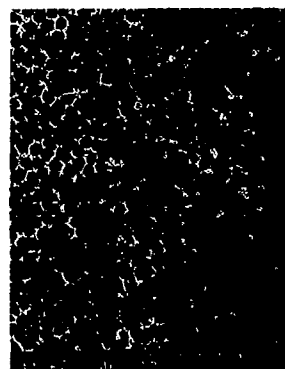
1(a)   1(b)

Fig.1   Fractographs of M40/Al-Ti as-received 1(a);and
         M40/LY12 as-received 1(b).
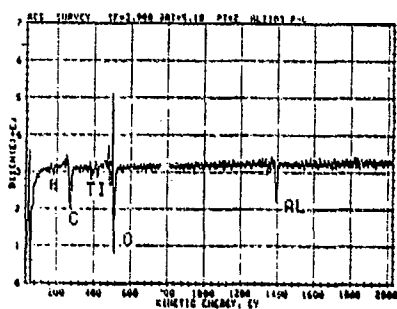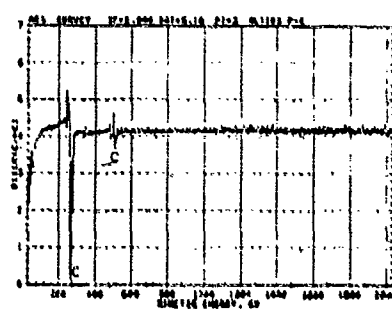
2(a)   2(b)

Fig.2   SAM spectra of M40/Al-Ti as-received: 2(A), from a
         matrix trough; 2(b), from the surface of a fiber.

some reaction products could be observed (Figure 3(a) and 3(b)). EDS results (Table II) showed the content of Ti at the interface in M40/Al decreased after heat-treatment at 600°C.

| 3(a) | 3(b) |
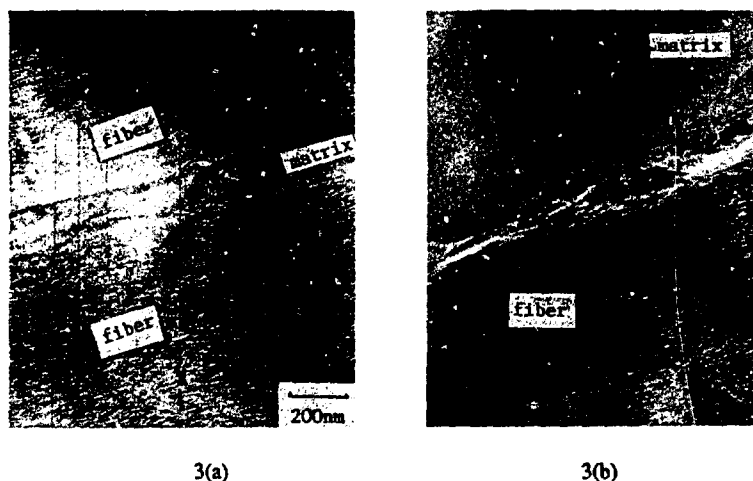
Fig. 3   Transmission electron micrograph of composites
3(a) M40/Al-Ti after heat-treatment at 600°C showing interfacial layer remaining;
3(b) M40/Al after heat-treatment at 600°C showing some reaction products appearing.

Table II. EDS results of Ti content in the near-interface region of the composites as-received and after heat-treatment at 600°C.

| | Amounts (wt%) of Ti | |
	as-received	600°C
M40/Al	1.16	0.76
M40/Al-Ti	1.21	1.18

So, it could be postulated that the interfacial layer of M40/Al and M40/Al-Ti as-received consisted of TiO_2, TiB_2, Al_2O_3 and AlO_x. The stability of this interface, which could prevent excessive interfacial reaction and provide a suitable interfacial bonding, was probably related to the high content of Ti at the interface. Ti oversaturated in the matrix could inhibit the diffusion of Ti from interface to matrix, thus protecting this interfacial state. Therefore, excellent properties of M40/Al-Ti even at high temperature were obtained. The further study of this hypothesis is presently underway.

In M40/LY12, no such original interfacial structure was observed but some Cu-rich phases including $CuAl_2$ existed at the interface or between the fibers; additionally, the accumulation of Cu around fibers was also found. This caused the strong interfacial bonding and deteriorated the strength of the composites [8].

Therefore, the interfacial states had a significant effect on the mechanical properties of Gr/Al composites. It was very useful for obtaining high-performance composites to choose a suitable matrix and tailor the interfacial structure of the composites. In addition, from the above results, we found the interfacial bonding strength of M40/Al-Ti which exhibited excellent properties was rather weak compared with M40/LY12. This phenomena may support the principle of the weak bonding theory, that mechanical properties of MMC could be improved by appropriately weakening the bonding strength to meet an optimal bonding state.

CONCLUSIONS

1. Matrix alloying has a significant influence on the interfacial state of Gr/Al composite and consequently on the final properties of the composite. It is very important for obtaining high-performance Gr/Al composite to tailor the interfacial state.

2. Aluminum matrix with 0.4 wt%Ti can improve the longitudinal tensile properties, especially at high temperatures of about 600°C, while LY12, with high Cu content, greatly deteroriates the properties of the composites

ACKNOWLEDGMENT

REFERENCES

1. M. F. Amateau, J. Compo. Mater. 10 (1976) 279.
2. G. Blankenburgs, J. Aus. Inst. Met. 14 (1969 No. 4) 236.
3. I. H. Khan, Met. Trans. 7A (1976) 1281.
4. S. J. Baker, J. Mater. Sci. 13 (1978) 1329; 1822.
5. W. J. Renton, ed. Hybrid and Selected Metal Matrix Composites (AIAA, 1977) p. 162.
6. S. Towata, Trans. Jpn. Ins. Met. 26 (1985) 563.
7. T. A. Chernyshova et al., J. Mater. Sci. 20 (1985) 3524.
8. C. He et al., unpublished paper.

Interface Effects in
Polymer Matrix Composites

TAILORED INTERPHASES IN FIBRE
REINFORCED POLYMERS

MICHAEL R. PIGGOTT

Advanced Composites Physics & Chemistry Group, Department of Chemical Engineering and Applied Chemistry, University of Toronto,Toronto, Ontario M5S 1A4, Canada

ABSTRACT

The use of fibre coatings to enhance adhesion between fibres and polymers normally means that, in the fibre composite, some residue of the coating is present at the fibre-matrix interface. This constitutes the interphase. The mechanical properties of this material may be measured using simple fibre pull out tests. These tests have the advantage of revealing the interphase failure mode (i.e. brittle or ductile) as well as providing such data as work of fracture, yield stress, interfacial pressure and the coefficient of friction for post-debonding slip. Results obtained so far indicate some ductility and yielding with thermoplastic interphases, although final failure is brittle. Thermoset interphases appear to be universally brittle, with small works of fracture (10-200 Jm^{-2}). The change in Young's modulus across the interphase may be a factor influencing brittle fracture, the biggest change giving the most brittle interphase.The ideal interphase should probably have a modulus intermediate between that of the fibre and the polymer, together with moderate yield stress, to give the composites adequate shear strength and good impact resistance through promotion of fibre pull outs.

INTRODUCTION

The main objective of fibre treatments has been to provide good adhesion between the fibre and matrix. For example, coatings developed for glass fibres have a silane group which interacts strongly with the glass, to provide a water resistant bond, and another group that reacts with the polymer, with thermosets at least, to form a strong bond with the polymer [1]. Another function of the fibre treatment is to facilitate processing, and protect the fibre from damage during handling. The net result of this is to introduce an interphase between fibres and matrix with properties which are different from each of the other two phases, i.e. fibre and polymer.

Since most reinforced polymers are not ductile there have been many attempts to increase toughness by modifying the interphase. Harris et al [2] showed that a weak interface improved toughness, but at the expense of loss of shear strength. Since then many fibre coatings have been investigated: rubbers [3,4], soft epoxies [5], other deformable polymers [6] and also viscous layers [7]. They all improved toughness but decreased shear strength.

In this paper we discuss measurements made on the interface/interphase, and their implications for reinforced polymers. In particular the possiblity of designing an interphase will be examined.

2. MECHANICAL PROPERTIES OF THE INTERPHASE AND INTERFACE

In experiments to measure interphase/interface properties, a fibre or the polymer is manipulated so that very high shears develop at the fibre surface. Failure of the interphase can occur by yielding and/or by brittle fracture. After failure, further shearing may be governed by further yielding or by friction across the failed surfaces.

Thus we can recognize at least five possible parameters which govern the process: 1) the yield strength τ_{iy}, 2) the ultimate strength, τ_{iu}, and 3) the work of fracture of the interphase, G_i; also 4) the friction coefficient of μ and 5) the pressure P across the interface.
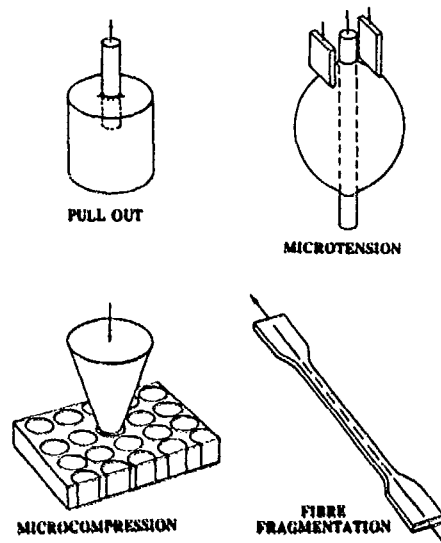
Fig. 1. Methods presently used for measuring properties of fibre-matrix interphases

In principle, the simplest way to introduce a known amount of shear into the interphase is the pull out test, see fig. 1. With thermosetting polymers the plot of force, F, applied to the fibre vs distance, x, moved by the system pulling the fibre is as shown in fig. 2. [8]. The force increases approximately linearly as the fibre is stretched. At some maximum force, F_A, the interphase fails. Subsequent sliding is governed by friction. Using fig. 2 as our model, we will discuss the five parameters.
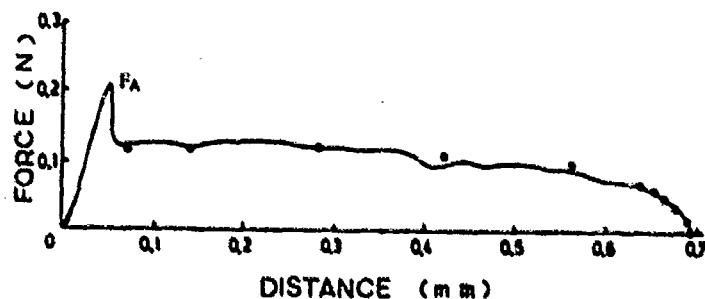
Fig. 2. Pull out curve for Kevlar-epoxy. Solid circles indicate curve fitting for frictional sliding

2.1 Yielding and Shear Stress Failure

If the matrix is elastic-perfectly plastic the pull out curve would have no frictional part. Once F_A is reached, uniform yielding takes place along the whole fibre surface, and F then decreases linearly with x. Thus

$$F_A = 2\pi r L \tau_{iy} \qquad (1)$$

and after $F = F_A$

$$F = 2\pi r L \tau_{iy}(L-x)/(L-x_a) \qquad (2)$$

where $2\,r$ is the fibre diameter, L is the embedded length, and x_a is the value of x for $F = F_A$. (The value of x_a depends mainly on the stiffness of the testing machine, including its grips, and the free length of fibre, i.e. the length not embedded in the matrix, or held by the grip of the testing machine.) A plot of F_A vs L should thus be a straight line. Such plots have been obtained with metals [9]; see fig. 3.
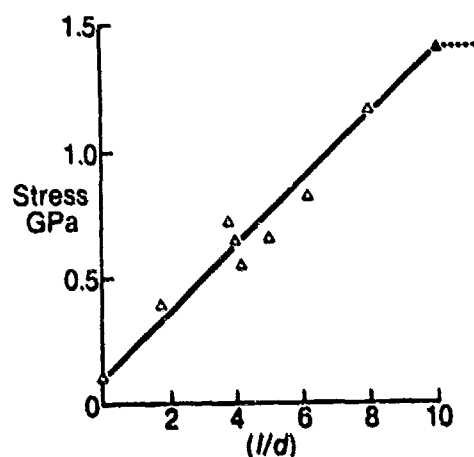
Fig. 3. Stress required to pull a tungsten wire out of copper
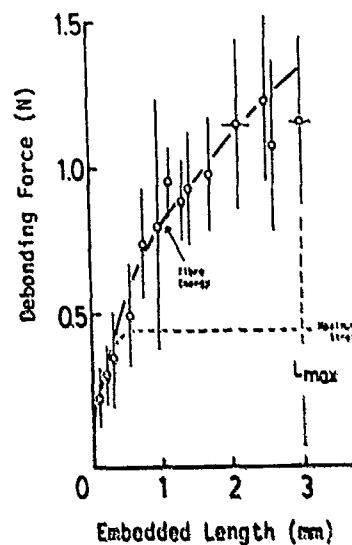
Fig. 4. Debonding force vs embedded length for glass fibres in polyester resin

If the matrix work hardens, so that $\tau_{iu} > \tau_{iy}$ we expect equation 1 to be obeyed with τ_{iy} replaced by τ_{iu}.

If failure occurs when the maximum interfacial shear stress exceeds the shear strength of the interphase, then [10]

$$F_A = 2\pi r^2 \tau_{iu} \tanh(ns)/n \qquad (3)$$

A plot of F_A vs L will thus have the asymptote

$$F_A = 2\pi r^2 \tau_{iu}/n \qquad (4)$$

and so long as τ_{iu} (or τ_{max}) $< n\sigma_{fu}/2$, pull out of indefinitely long lengths of fibre should be possible, unless some other shear resistance is activated.

2.2 Work of Fracture

When the interphase fails by brittle fracture the F_A vs L plot is not expected to be linear. An equation which has been found to fit many results obtained with glass, carbon and Kevlar fibres in thermosets very well [11] is

$$F_A = 2\pi r \sqrt{E_f G_i r} \sqrt{n s \tanh(n s)} \qquad (5)$$

where $s = L/r$ and

$$n^2 = E_m/E_f (1+\nu_m) \ln(R/r) \qquad (6)$$

Here E_m and ν_m are the Young's modulus and Poisson's ratio of the polymer, and 2R is the diameter of the polymer bar in which the fibre was embedded. Fig. 4 shows an example of such a fit.

Equation 5 was based on the strain energy in the embedded fibre and immediately adjacent polymer being enough to cause complete fibre debonding. However, no mechanism for crack initiation was suggested. A more recent analysis [12], based on an initial crack at the polymer surface propagating down the fibre gives

$$F_A = 2\pi r \sqrt{E_f G_i r} \tanh(n s) \qquad (7)$$

The similarity of equation 7 and equation 3 should be noted.(Note: it was given in a different form in the paper; this form is equivalent to that.)

Both equations 3 and 5 reduce to

$$F_A = 2\pi L \sqrt{E_m G_i r/(1+\nu_m) \ln(R/r)} \qquad (8)$$

for small embedded lengths (up to about 0.1 mm for glass, carbon and Kevlar fibres). At lengths of about 1 mm or more equation 3 gives $F_A \approx \sqrt{L}$, i.e.

$$F_A = 2\pi r \sqrt{E_m G_i L/(1+\nu_m) \ln(R/r)} \qquad (9)$$

while equation 7 gives F_A independent of L, i.e.

$$F_A = 2\pi r \sqrt{E_f G_i r} \qquad (10)$$

Equation 5 appears to fit some results for carbon qualitatively at least, since a plateau region was often observed [12]. Equation 10 was first obtained by Outwater and Murphy [13] for fibres bridging cracks.

Results for G_i in table 1 were estimated using equation 5. It will be observed that they are low, especially with Kevlar and carbon fibres.

2.3 Pressure and Friction

The high stresses applied to fibres with moderate Young's moduli, such as glass and Kevlar, cause significant Poisson's shrinkages. This is a disadvantage of fibre pull out type tests. However, it can be put to good use for estimating the cure and thermal shrinkage stress P_0.

After debonding at F_A, as shown in fig. 2, F decreases non linearly, and the greatest slope in this part of the curve is at the instant when the fibre emerges from the polymer. This slope gives the frictional shear stress, τ_f, where

$$\tau_f = \mu P_0 \tag{11}$$

Before the fibre has pulled out, the pressure, and hence the frictional shear stress is reduced;

$$P = P_0 - \nu_s \sigma_f \tag{12}$$

where

$$\nu_s = \nu_f E_m / (1 + \nu_m) E_f \tag{13}$$

and σ_f is the fibre stress, i.e. $F/\pi r^2$

An analysis of the pull out process, when the free length is small [14], gives

$$F = (\pi r^2 P_0 / 4\nu_s)(1 - \exp(2\nu_s \mu(L-x)/r)) \tag{14}$$

Thus a curve fit [8] using equation 14 yields both P_0 and μ. The solid circles in fig. 2 are the results of such a curve fit.

2.4 Estimated Values of Parameters

There is a great deal of evidence that debonding is often a brittle fracture process. 1) In pull out tests F_A is not a linear function of embedded length, see fig. 4. 2) In pull out tests with glass in polyester, for the longer embedded lengths (2-3 mm), F_A exceeds the value estimated from equation 3 with $\tau_{iu} = \tau_{mu}$ by more than a factor of 2 [15]. 3) In other debonding tests, values of τ_{iu} estimated from the results are often too high. For example, in some work with glass in epoxy, fragmentation tests gave τ_i values ranging from 33 to 51 MPa, according to fibre surface treatment when τ_{iu} was 29 MPa [16]. These results were shown to be compatible with $G_i = 180 \pm 5$ Jm^{-2}. In the literature, values of τ_i of as much as 100 MPa can be found [17] in cases where the shear strength of the polymer is highly unlikely to exceed 40 MPa.

Representative values for G_i estimated from pull out tests are given in table 1. Recent results obtained with polyethylene are included. Although the force-distance plot was not linear in this case, and yielding appeared to take place before complete bond failure, F_A vs L was not linear. It was therefore fitted to equation 3 to get the results shown.

The only test which gives data on μ and P_0 separately is the pull out test carried out with a short free length (~ 1mm) and with the fibres embedded only a short distance in a solid

block of polymer. The microtension and microcompression tests may be used to estimate τ_f (see equation 9) but P should be corrected for the fibre Poissons effect (see equation 10: note that the microcompression test overestimates τ_f ($\sigma_f < 0$) while the microtension test underestimates it ($\sigma_f > 0$): also the long free length normally used in the microtension test means that the fibre pulls through the bead for a considerable distance when the fibre stress suddenly drops after debonding; this could well damage the interphase and reduce friction still further.)

Representative values for μ and P_0 estimated from pull out tests are given in table 1.

Table 1.
Interphase/Interface Data From Pull Out Tests

Fibre	Polymer	Post Cure Temp (°C)	Time (h)	G_i[1] (Jm^{-2})	μ	P_0 (MPa)	ε_{1i}[2] (%)
	Epoxy		none	50	0.83	23	1.6
	Epoxy	60	24	80	0.86	26	2.0
	Epoxy	130	6	140	2.4	23	2.7
Glass	Polyester		none	60	0.55	11	1.7
	Polyester	80	6	190	0.54	21	3.1
	Polyester[3]	80	12	45	0.6	17	1.5
	Polyethylene		none	95	-	-	2.2
	Polyethylene[4]		none	50	-	-	1.6
	Epoxy[5]		none	14	9	7	-
Kevlar	Epoxy[6]	80	24	42	3	14	-
	Polyethylene		none	28	-	-	-
	Epoxy		none	25	-	-	1.0
Carbon	Epoxy	60	24	25	-	-	1.0
Steel	Epoxy	40	36	200	-	-	..

Notes:
1 Estimated using equation 3.
2 Estimated using equation 15; ε_{fu} values: Glass; 5%; Carbon 1.4%.
3 23,000h immersion in water at 60°C reduced G_i to 25 Jm^{-2}, P to 9 MPa and μ to 0.6
4 Fibre pyrolysed to remove silane coating and processing aids, etc.
5 Fibre immersion in water at 20°C reduced G_i to 7 Jm^{-2}.
6 Fibre immersion in water at 20°C reduced G_i to 20 Jm^{-2}.

3. Implications for Fibre Composites

3.1 Fibre composite stress-strain curves

Brittle fracture debonding occurs at higher values of F_A than would have been estimated based on equation 3. Thus the interphasial yielding criterion used for the analysis of stress-strain curves [18] is probably not valid. Consequently we expect debonding to occur at higher applied stresses. So, for aligned short fibre composites, the linear part of the stress-strain curve is expected to be much longer.

We can estimate the composite strain ε_{1i} at the instant of debonding from the equation

$$\varepsilon_{1i} \cong 2\sqrt{G_i/E_f r} \qquad (15)$$

at least when ns ≥ 5, i.e. for fibre lengths greater than about 0.5 mm. The derivation of equation 15 is given in the appendix. (A more approximate equation was given previously [15])

Values of ε_{1i} are given in table 1. Although G_i values are small ε_{1i} can be as much as one half of the fibre breaking strain, ε_{fu} at which point most composites will break anyway. Thus debonding is probably not such an important contributor to failure in well made composites as was previously thought [19], at least for high modulus fibres.

3.2 Across-the-grain toughness

When an aligned fibre composite is fractured with the fibres normal to the fracture plane, fibres fracture some distance from the plane, and pull out. To do this they must first debond. We may use the value of G_i to estimate the contribution of debonding energy to the fracture energy.

For brittle fibres, we may estimate the work of fracture (on the assumption that debonding can take place) from the average fibre pulled out length [20].

$$x_b \cong \frac{mr\,\sigma_{fu}}{2\mu(P_o - v_s)} \tag{16}$$

where the fibre strength σ_{fu} is measured on a moderate fibre length (a few cm) and m is a parameter representing the decrease in fibre strength with lengths tested [21]. (This equation is only valid for $P_o > v_s\sigma_{fu}$). The work of fracture due to frictional pull out is

$$G_{1p} = V_f\mu P_o\, x_b^2/r \tag{17}$$

for a composite having a fibre volume fraction of V_f. The work of fracture due to debonding is

$$G_{1d} = V_f x_b G_i/r \tag{18}$$

and so

$$G_{1d}/G_{1p} = 2(P_o - v_s\sigma_{fu})G_i/P_o mr\sigma_{fu} \tag{19}$$

Values for G_{1d}/G_{1p} estimated from this formula, using data from table 1, range from about 0.8% for carbon to 2% for glass. (For Kevlar equation 16 is not valid.) For carbon and glass, therefore, debonding work is usually only a small fraction of pull out work. For Kevlar, if we assume x_b is ~ 1 mm, or longer as observed in practice [22] we find G_{1d}/G_{1p} ~ 1%

3.3 The Tailored Interphase

Since our measurements suggest that the interphase is brittle, and with carbon and Kevlar, much more brittle than the polymer, the first step in tailoring the interphase is to make it tougher.

The use of rubber layers has not been entirely successful because the rubber has a low shear modulus, and so reduces the shear strength of the composite. Thermoplastic interphases tested so far have not been notably successful either.

It will be observed that the works of fracture of the interphases are less for carbon than for glass fibres, see table 1. Yet in both these cases, some sort of chemical bonding is postulated [23, 24]. This suggests that there could be a Young's modulus effect. (Kevlar does not fit this pattern very well, probably because chemical bonding is more difficult to achieve in this case [25]) The degree of stress concentration depends on the change in Young's modulus across the interphase, being greater for a greater modulus change. Thus, there is possibly a correlation between stress concentration and work of fracture.

It is therefore suggested that interphases be developed which have Young's moduli intermediate between that of the fibre and the polymer. They should have moderate yield stresses, so that fibre pull out is not suppressed in across-the-grain fracture. At the same time the yield stress should be high enough to ensure adequate yield strength.

CONCLUSION

The interphase between fibres and thermosetting polymers is brittle, and normally fails by fracture rather than yielding. With thermoplastics there is some indication of yielding, but this also is followed by brittle fracture. Thus, to improve interphases they should be less prone to fracture. There is a possibility that using material with a much higher Young's modulus may inhibit brittle failure by reducing stress concentrations. If this is the case, materials should be sought which have Young's modulus $E_i \sim \sqrt{E_f E_m}$. At the same time the material should be ductile.

ACKNOWLEDGEMENTS

REFERENCES

1. E.P. Plueddemann, Silane Coupling Agents (Plenum Press, New York 1982), Chapter 2
2. B. Harris, P.W.R. Beaumont, E. M. de Ferran, J. Mater. Sci. 6, 238 (1971).
3. E. P. Plueddemann, 29th Ann. Tech. Conf. SPI Section 24A, (1974).
4. N.L. Hancox and H. Wells, Fib. Sci. Tech. 10, 9 (1977)..
5. L.D. Tryson and J.L. Kardos, 36th Ann. Conf., SPI, section 2E, (1981).
6. A. Crasto, S.H. Own and R.V. Subramanian, Proc. ICCI., (Elsevier, New York, Ed., H. Ishida and J.L. Koenig, 1986), p. 133.
7. N.H. Sung, T.J. Jones and N.P. Suh, J. Mater. Sci., 12, 239 (1977).
8. M.R. Piggott and M. Reboredo, Proc. 34th Int. SAMPE Symp., 1913 (1989).
9. A. Kelly, Strong Solids, (Second edition; Clarendon Press, Oxford, 1973), p. 203.
10. L.B. Greszczuk, ASTM STP, 452, (1968), 42.
11. M.R. Piggott, Comp. Sci. Tech., 30, 295 (1987).
12. L.S. Penn and S.M. Lee, Comp. Tech. Res. 11, 23 (1989).
13. J.O. Outwater and M.C. Murphy, 24th Ann. Techn. Conf. SPI, Section 11C, (1969).
14. P.S. Chua and M.R. Piggott, Comp. Sci. Tech. 22, 33 (1985).
15. M.R.Piggott and P.S. Chua, Ind. Eng. Chem. Product, Res. Dev. 26, 672 (1987).
16. A.T.Di Benedetto, G. Haddad, C. Schilling and F. Osterholtz, Proc. Int. Conf. on Interfacial Phenomena in Composite Materials (Ed. F.R. Jones, Butterworths, London, 1989), p.181.
17. M.R. Piggott, Advances in Composites: Chemical and Physicochemical Effects (Eds. T.L. Vigo & B.J. Kinzig Amer. Chem. Soc., 1989).
18. M.R. Piggott, J. Mater Sci. 13, 1709 (1978).
19. A. Kelly, Strong Solids (Second edition; Clarendon Press, Oxford, 1973), p. 180.
20. M.R. Piggott, Proc. ICF5, 465 (1981).
21. A.G. Metcalf and K.G. Schmitz, ASTM Proc. 64, 1075 (1974).
22. M. Reboredo; Monthly Report, University of Toronto, July 25, (1989).

23. H. Ishida, Polym. Comp. 5, 101 (1984).
24. J.B. Donnet, S. Dong, G. Guilpain and M. Brendel, Proc. ICCI2 (Ed. H. Ishida, Elsevier, 1988), p 35.
25. L.S. Penn, T.J. Byerley and T.K. Liao, Adhesion International (Proc. 10th Ann. Mtg. Adhesion Soc.) 631 (1987).
26. M.R. Piggott, Load Bearing Fibre Composites, (Pergamon, Oxford, 1980) Chapter 5.

APPENDIX

Debonding in Fibre Composites

We estimate the strain energy due to the fibre tensile stress, and that associated with the shears in the polymer adjacent to the fibre. The treatment given here follows that in the Chapter 5 of writers book [26] to whom the reader is referred for the development of the expressions used for fibre stress (σ_f) and matrix shear stress (τ_e). The unit of composite considered is a fibre, length 2L, surrounded by polymer over the whole of its length, having diameter 2R. The origin of the x axis is the fibre centre, see fig. A1.
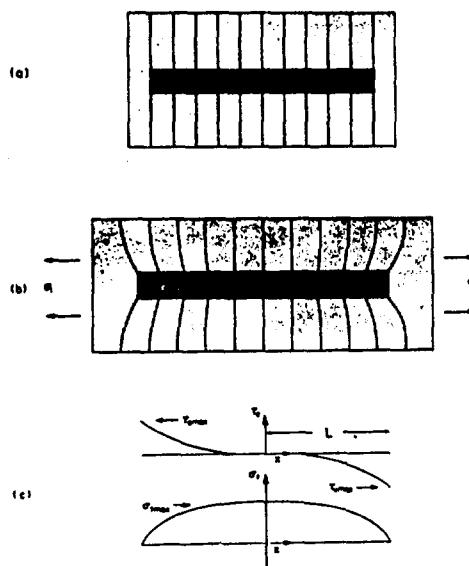
Fig. A1. Unit of composite used for elastic analysis.

The strain energy in the fibre U_f is

$$U_f = \frac{\pi r^2}{2E_f} \int_0^L \sigma_f^2 \, dx$$

$$= \frac{\pi r^2}{2E_f} \int_0^L \left[E_f e_1 \{1 - \cosh(nx/r)/\cosh(ns)\} \right]^2 dx$$

$$= \tfrac{1}{2}\pi r^2 E_f \varepsilon_1^2 \{L(1+1/2\cosh^2(ns)) - 3r\tanh(ns)/2n\}$$

To estimate the shear strain energy in the polymer, U_m, we use [15, equation 22] with $l = dx$ and

$$\tau_e = nE_f \varepsilon_1 \sinh(nx/r)/2\cosh(ns)$$

so that

$$U_m = (2\pi r^2 (1+\nu_m)\ln(R/r)/E_m) \int_0^L \tau_e^2 dx$$

which on substitution and integration gives

$$U_m \tfrac{1}{4}\pi r^2 E_f \varepsilon_1^2 \left[r\tanh(ns)/n - L/\cosh^2(ns) \right]$$

Since the total energy, U_t, is the sum of U_f and U_m

$$U_t = \tfrac{1}{2}\pi r^2 E_f \varepsilon_1^2 \left[L - r\tanh(ns) \right]$$

The condition for a crack to grow is

$$d(2\pi r L G_i - U_t)/dL \leq 0$$

which gives

$$2\pi r G_i \leq \tfrac{1}{2}\pi r^2 E_f \varepsilon_1^2 \left[1 - 1/\cosh^2(ns) \right]$$

Thus the critical strain for the initiation of debonding is ε_{1i}, obtained by re-arranging the above equation:

$$e_{1i} = 2\sqrt{G_i/E_f r} / \sqrt{1 - 1/\cosh^2(ns)}$$

For $ns = 3$, corresponding to a fibre length of about 0.3 mm, the denominator comes to 0.99. Thus we write

$$e_{1i} \cong 2\sqrt{G_i/E_f r}$$

for fibre lengths greater than 0.3mm.

INTRINSIC MATERIAL LIMITATIONS IN USING INTERPHASE MODIFICATION TO ALTER FIBER-MATRIX ADHESION IN COMPOSITE MATERIALS.

LAWRENCE T. DRZAL
Department of Chemical Engineering and Composite Materials and Structures
Center, Michigan State University, East Lansing, MI 48824-1326

ABSTRACT

A very large percentage of studies seeking to improve fiber-matrix adhesion to alter composite properties are directed at the formation of primary chemical bonds between the reinforcement surface and the matrix. The dynamic events that occur when the fiber-matrix interface is formed lead to the creation of an interphase which can have properties quite different from the matrix in addition to any chemical bond formation.

This study has been directed at elucidating the role of these interphase properties themselves on fiber-matrix adhesion. A reinforcement (AS-4 carbon fiber) with a quantifiable surface chemistry and an epoxy matrix have been kept constant through a series of experiments in which the distance between crosslinks of the matrix has been changed. The wettability of the fiber and the degree of chemical bonding to the fiber have not changed but the interfacial shear strength measured for each of these systems has decreased with decreasing matrix modulus. It will be shown that the properties of the matrix and the residual stresses created during processing limit the maximum interfacial shear stress that can be supported by the fiber-matrix interphase.

BACKGROUND

The subject of adhesion between fiber and matrix and how the degree of adhesion affects composite properties has been the subject of continuing study since the early 1960's. At first, "acceptable" adhesion between fiber and matrix was a "necessary" criterion for producing a composite with "acceptable" mechanical properties. Many of the early micromechanical attempts at describing composite behavior relied on the assumption that perfect adhesion existed between fiber and matrix. As the potential use of composite materials expanded however, the advent of new polymeric matrices and new higher performance reinforcing fibers led to the need for fundamental investigation of the mechanisms of adhesion between fiber and matrix and its effect on composite properties.

The literature is full of proposed models of adhesion but none are effective in predicting the type of fiber surface treatment required for a given fiber-matrix combination or coupling the degree of adhesion to observed composite properties [1]. The major reason for this lack of theoretical development lies in the oversimplification of the fiber-matrix interface. Undue attention has been given to single mechanisms which were reputed to be solely responsible for fiber-matrix adhesion. Attempts at explaining adhesion solely by chemical forces, electrostatic interactions, surface energetic considerations, etc. are largely unsuccessful. A review of the model proposed compared against the growing experimental evidence of the structure and composition of the region including and near to the fiber-matrix interface leads to the conclusion that the interrelationships between fiber, interface and matrix create a complex region not easily amenable to predictive analysis based solely on a single mechanism approach.

The concept of a two-dimensional interface between fiber and matrix has given way to the evolution of a three-dimensional region more properly termed an interphase [2]. **Figure 1** is a schematic representation of an interphase illustrating some of the possible components. This interphase

includes the two dimensional region of contact between fiber and matrix (the
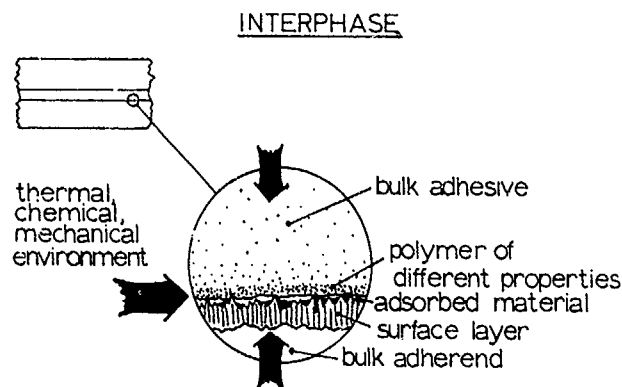
INTERPHASE

Figure 1. A schematic diagram showing a magnified view of a
cross-section of the fiber-matrix interface and all of its components.
The entire region is taken as the "interphase".

interface) but also must incorporate a region of some finite thickness
extending on both sides of the interface. The boundaries are defined as
being the point in the matrix where the local properties start to change
from the bulk properties moving in a direction toward the interface. This
region includes matrix that may have chemical and morphological features
different from the bulk matrix. It can include impurities, unreacted
polymer components, non-polymerized matrix additivies, etc. At the
interface, not only can there be chemical and physical interactions between
fiber and matrix, but also voids, adsorbed gases and surface chemical groups
can be concentrated. On the reinforcement side, morphological and chemical
features can be different from the bulk. Imposed on this region are the
processing conditions which allow chemical reactions, volumetric changes and
stresses to be generated. The resultant "interphase" can be a very complex
material which does not easily lend intself to analysis by single parameter
models.

Recent studies on the effect of the fiber surface treatment [3] and the
effect of fiber finish [4] on adhesion between graphite fibers and epoxy
matrices has shown that the interphase concept provides a conceptual
framework in which the phenomena of adhesion should be studied. In
particular, recent results have shown that it is the properties of the
matrix region in close proximity to the fiber surface that seem to control
the level of fiber-matrix adhesion and the failure mode of the interphase
region. The research reported in this paper is part of an on-going effort
to investigate the role of the composition and structure of polymer matrix
interphases in order to provide the underpinnings for a predictive
description of fiber-matrix adhesion and its relation to composite
performance [14][15][16]. In this study, attention was directed at
elucidating the effect of the matrix properties itself on fiber-matrix
adhesion. Since the matrix functions as a stress transfer agent between
fibers, its stress transfer capability could be expected to affect a
mechanical measurement of fiber-matrix adhesion independent of the
interphase structure. Knowledge of an explicit dependence of this type
could define the intrinsic limitations of coatings and finishes used to
control and improve fiber-matrix adhesion.

EXPERIMENTAL MATERIALS AND METHODS

Reinforcing Fiber

One carbon fiber representative of the majority of polyacrylonitrile based carbon fibers was chosen for this study. It is an AS-4 fiber (Hercules, Inc.) whose fiber tensile modulus is 238 GPa and tensile strength is 3.6 GPa when measured at a 25mm gage length. The fiber was surface treated by the manufacturer with an oxidation process which optimizes the adhesion to epoxy matrices. The surface chemistry and energetics of PAN based carbon fibers have been studied and reported previously [6]. This AS-4 fiber is is circular in cross-section and has a microscopically smooth surface.

Polymeric Matrices

An amine-epoxy matrix system was selected for this study. This chemistry is the foundation for the majority of aerospace applications [7]. The reactants can be processed at low temperatures and the properties of the resultant matrix are typical for a high performance matrix. A di-functional epoxy, diglycidyl ether of Bisphenol-A (DGEBA) (Epon 828, Shell Chemical Co.) and a tetra-functional epoxy, tetraglycidylmethylenedianiline (TGMDA) (MY720, Ciba-Giegy Co.) were processed at stoichiometric conditions with any of a series of difunctional amines. The amines were selected to provide a series with increasing distance between amine groups ranging from the small aromatic meta-phenylene diamine (MPDA) and diamino, diphenyl sulphone (DDS) to linear polyether amines (Jeffamines, J-230, J400, J403 and J700, Texaco, Co.). This series of diamine curing agents created an epoxy crosslinked
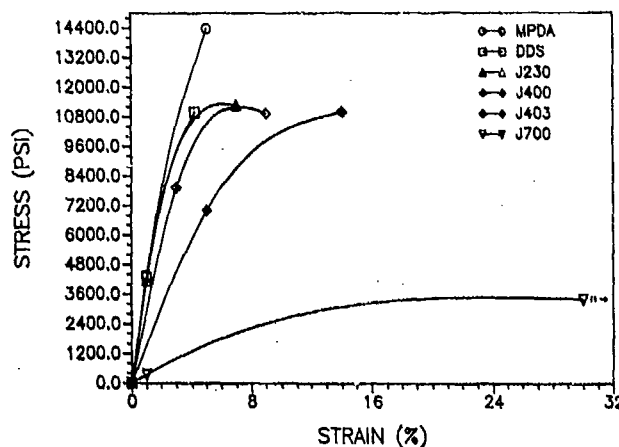
Figure 2. Stress-Strain Behavior for Di- and Tetra- Functional Epoxy Systems Cured with Diamines of Various Chain Lengths.

network with increasing length between crosslinks thereby providing matrices with increasing compliance. **Figure 2** is a plot of the stress-strain behavior of these materials showing the progression of properties attainable. An important factor in selecting to increase the polyether amine length as opposed to the epoxy length is the preservation of epoxy-amine chemistry throughout the series by the use of the polyether diamines. If epoxy oligomers are selected, additional hydroxyl functional groups are

present along the oligomer backbone. These hydroxyls could interact with each other and complicate the analysis.

Because of the complexity of the state of stress applied in most composite testing protocols, a single fiber method was selected to evaluate adhesion at the fiber-matrix interphase. In this technique, the fiber is totally encapsulated in a matrix coupon, a tensile load is applied to the coupon, and an interfacial shear stress transfer mechanism is relied upon to transfer the coupon tensile forces to the encapsulated fiber through the interface.[8][9] As the load is increased on the specimen, shear forces are transmitted to the fiber along the interface. The fiber tensile strength (σ_f) increases to the point where the fracture strength is exceeded and the fiber breaks inside of the matrix. This process is repeated producing shorter and shorter fragments until the remaining fragment lengths are no longer sufficient in size to produce further fracture through this stress transfer mechanism. The fragment critical length-to-diameter ratio (lc/d) is measured. A shear-lag analysis is completed on the fragments in order to calculate an interfacial shear strength (τ). In practice, there is a distribution of critical lengths and Weibull statistics are used to fit the data.

$$\tau = \frac{\sigma_f}{2}(\frac{d}{l_c}) \tag{1}$$

The embedded single fiber technique has several advantages. A large number of data points can be gathered in each observation, the failure process itself can be observed in transmitted polarized light, the locus of failure is identified and the process replicates the in-situ events in the actual composite itself. A large amount of experimental data has been generated with this method and published elsewhere [3][4][9].

RESULTS AND DISCUSSION

Wettability

The surface free energy of the AS-4 carbon fibers and the epoxy amine matrix has been measured and reported [6]. The thermodynamic criterion for wetting of the fiber by the matrix is in general that the surface free energy of the fiber surface must be greater than that of the matrix. This condition was achieved for all of the fiber matrix combinations. Since the matrix materials also possess low viscosity, and the viscosity also decreases with increasing temperature before the crosslinking reaction has progressed early in the processing cycle, fiber wettability is will be achieved and is not a concern in this study.

Chemical Bonding

Modern surface analytical techniques allow the chemical nature of the carbon fiber surface to be determined. Xray Photoelectron Spectroscopy in particular provides not only atomic information but molecular information about the surface sites. Of far more importance than the surface composition of the fiber surface is the determination of the type and extent of chemical bonding between the matrix and the reinforcing fiber. Solid state analysis of the actual fiber-matrix interface is impossible. However, selection of appropriate model compounds may be useful in defining the upper bounds on the extent of chemical interaction.

In a series of experiments, monofunctional epoxy compounds, amines and epoxy-amine adducts were dissolved in an inert aromatic solvent and placed

in contact with carbon fibers under the same temperature conditions experienced in the solid state processing of the composite [5][10]. Afterwards, the fibers werc extracted in the pure solvent, dried and then their surface composition was determined with XPS analysis. Comparison of the carbon fiber spectra before and after this exposure to the matrix constituents ccnfirmed that chemical adsorption had taken taken place. Both the epoxy group and the amine group can chemically react with the surface oxygen groups. Chemical bonding would be expected to create a stronger interaction than physical bonding. On an absolute basis only about 4% of the surface sites of the carbon fiber are involved in chemical bonding. The magnitude of the bond strength for chemical bonds is very high but the quantity of bonds is low resulting in a small difference.

For the epoxy-amine-carbon fiber system studied here, it is expected that chemical bonding would be identical for all systems and because of the small number of chemical bonds formed, it is expected that the role of chemcial bonding between the fiber and the matrix would be small. At most, under the processing conditions of this study, 4-5% of the available carbon fiber surface sites can chemically react with the epoxy matrix. Indeed, another study has shown that chemical bond formation between fiber and matrix is of itself a minor component in promoting increased fiber-matrix adhesion . In that study, the surface of a similar carbon fiber was stripped of all functional groups. The reduction in interfacial shear strength attributed to removal of chemical bonding per se amounted to less than 10 percent of the attainable level of interfacial shear strength [3].

Interfacial Shear Strength

Table 1 contains the material properties (i.e. tensile and shear modulus of the various matrices) and the measured interfacial shear strength of each matrix with the AS-4 carbon fiberusing the embedded single fiber technique. The matrix properties were measured as 0.5 mm/min crosshead

Table 1. Tabulation of the Matrix Tensile Modulus, Shear Modulus, and Interfacial Shear Strength for the AS-4 Fiber.

Resin	Curing Agent	Tensile Modulus	Shear Modulus	Interfacial Shear Strength
DGEBA	mPDA	3.30 GPa	1.17 GPa	77.9 MPa
	DDS	3.40 GPa	1.30 GPa	64.3 MPa*
	J230	2.95 GPa	1.09 GPa	56.7 MPa
	J400	2.73 GPa	1.01 GPa	51.3 MPa
	J403	2.31 GPa	0.85 GPa	46.9 MPa
	J700	0.67 GPa	0.23 GPa	38.6 MPa
TGMDA	J700	1.26 GPa	0.45 GPa	40.8 MPa
	J700/J403	2.67 GPa	0.99 GPa	48.8 MPa
	J700/J400	2.92 GPa	1.08 GPa	53.8 MPa

displacement. Poisson's ratio was measured with a strain gage and the shear modulus was computed by the relationship $G=E/2(1+v)$ where E is the tensile modulus and v is the Poisson's ratio. There are statistically significant differences in the interfacial shear strength for each fiber-matrix combination even though the interfacial chemistry has been kept constant. In general the interfacial shear strength decreases with decreasing matrix stiffness. Since stress transfer between matrix and fiber occurs in shear, there should be a dependency on the shear modulus of the matrix. Figure 3 is a plot of the average interfacial shear strength as a function of the matrix shear modulus. It can be seen that all of the matrix formulations

fall on a single smooth curve which shows an increasing interfacial shear strength with increasing shear modulus of the matrix.
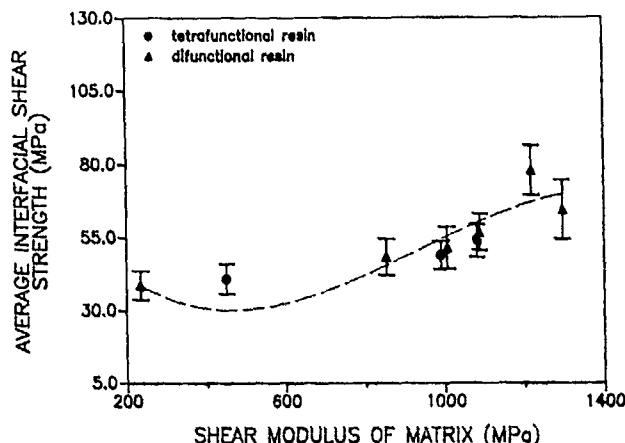
Figure 3. Plot of the Interfacial Shear Strength Versus the Matrix Shear Modulus.

Rosen [11], Cox [12] and others have predicted that a dependency of interfacial shear stress on matrix properties should exist. They developed micromechanical models of the interfacial stress around a single fiber fragment as a function of position along the fragment length, as well as the fiber and matrix properties. Cox proposed the following equation assuming perfect bonding of a fiber fragment, 1, embedded in an elastic matrix, under a general strain, e.

$$\tau = E_f \epsilon_m \left(\frac{G_m}{2E_f \ln(\frac{R}{r})} \right)^{0.5} \frac{\sinh\beta(0.5L-x)}{\cosh\beta\frac{L}{2}} \quad (2)$$

This relationship expresses the interfacial shear stress distribution around the fiber fragment as a function of position. The E's are tensile moduli of the fiber and matrix, G is the shear modulus of the matrix, R is the fiber radius and r is the distance in the radial direction, and B is a scaling factor. Examination of this relationship shows that in general it consists of three components. There are matrix dependent material terms denoted by the subscript (m), fiber dependent material terms denoted by the subscript (f) and geometry dependent terms. The geometrical and fiber dependent terms are constant for this set of experiments where the fiber remains the same throughout all of the experiments. Therefore a plot of the product of the square root of the shear modulus of the matrix times the strain-to-failure of the matrix against the interfacial shear stress should produce a montonic relationship.

Figure 4 is a modified version of such a plot. Since the matrix undergoes a strain only up to the point of the last fiber fragment fracture, a plot of the product of the square root of the shear modulus times the strain of the matrix at last fiber fragment fracture has been made against the interfacial shear strength. It is obvious that this formulism successfully models the variation of the interfacial properties with matrix properties down to values of interfacial shear strength of 35 MPa. The lack of dependence detected at values of interfacial shear strength below about 35MPa is attirbuted to the plastic nature of the matrices below this point.

These matrices have very large elongations at failure and very low shear
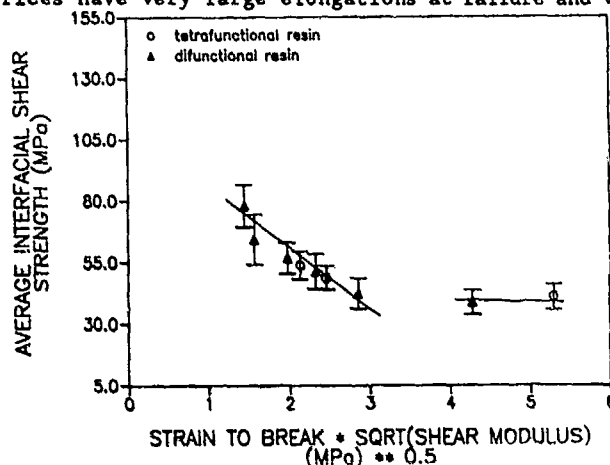
Figure 4. A plot of the single fiber interfacial shear strength against the product of the square root of the matrix shear modulus times the matrix strain at the critical length.

moduli. Necking of the specimen has also been observed.

Residual Stresses

In addition to chemical and structural considerations, the state of stresses which result from the processing of the material itself can influence the degree of fiber-matrix adhesion. In the case of carbon fibers, the coefficient of thermal expansion is quite small and can actually
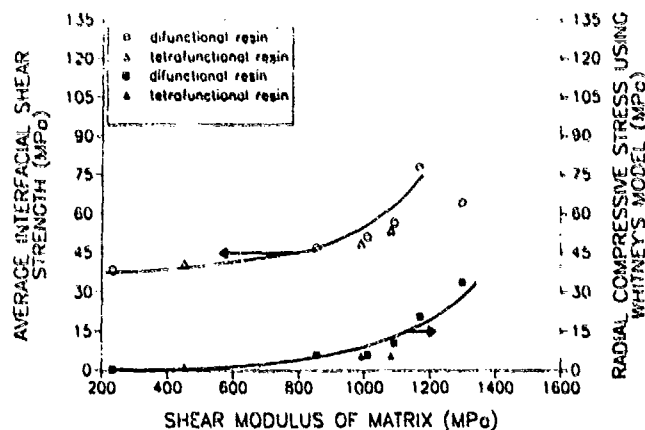
Figure 5. A plot of the single fiber interfacial shear strength and the radial component of the interfacial shear stress against the shear moduli of various epoxy-amine matrices.

be negative. The fiber itself is anisotropic and the radial and longitudinal thermal expansions can be quite different. The matrix is isotropic but has a factor of thirty larger coefficient of thermal expansion

than the fiber. This mismatch becomes increasingly significant as higher processing temperatures are reached. The absolute difference between the glass transition temperature and use temperature determines the magnitude of these stresses.

Epoxy matrices also reduce their volume as they crosslink. This volumetric shrinkage contributes to the state of stress at the fiber-matrix interphase. For fibers surrounded by matrix, the resulting cure shrinkage produces a compressive interfacial force while for matrix confined between an array of fibers, a net tensile interfacial state of stress may exist. The resulting state of stress can reduce the level of adhesion attainable between fiber and matrix. **Figure 5** also contains the calculation of the interfacial stress for the fiber-matrix combinations used in this study. [13] It can be seen that the radial component of the stress changes in the same manner as the measured interfacial shear stress. The change in the radial component of the stress changes in an identical manner to the change in the interfacial shear stress. While there does seem to be a one-to-one correspondance between the data, it is not possible to state at this time that the changes in radial compressive stress are entirely responsible for the increase in the interfacial shear strength.

A more important extrapolation can be made by viewing the results of this study in light of the interphase between fiber and matrix. When "coatings" or "finishes" are used to modify the adhesion between fiber and matrix, a layer of material is placed at the interphase. The results of this study suggest that it is the properties of this interphase region which will provide a limitation to the degree of adhesion which can be obtained from this fiber-finish-matrix combination.

CONCLUSIONS

The conclusions which can be drawn as a result of this work are:

First, there are intrinsic material limitations in the maximum level of shear strength attainable for a given fiber-matrix combination. This level depends on the shear modulus of the interphase material itself.

Second, the formulation presented by Rosen which is based on linear elastic mechanics appears to adequately describe the interfacial dependency on matrix properties.

Third, the results presented here indicate that it is possible to develop a predictive methodology for interfacial performance based on some intrinsic properties of the interphase material. This implies that when "coatings" or "finishes" are placed at the interface to alter fiber-matrix adhesion, the properties of the coating itself may be the limiting factor.

REFERENCES

1. L. T. Drzal, "The Epoxy Interphase in Composites," Review Chapter in **Advances in Polymer Science II, Vol. 75**, K. Dusek, ed., Spring-Verlag, (1985).

2. L. T. Drzal, **SAMPE Journal, 19**, 7 (1983).

3. L. T. Drzal, M. Rich, and P. Lloyd, J. **Adhesion, 16**, 1-30, (1983).

4. L. T. Drzal, M. Rich, M. Koenig, and P. Lloyd, J. Adhesion, **16**, 133-152, (1983).

5. R. Agrawal, and L. T. Drzal, (accepted for publication in J. **Adhesion**).

6. G. Hammer, and L.T. Drzal, **Appl. Surf. Sci., 4**, 340 (1980).

7. **Engineered Materials Handbook**, Vol.1, ASM International (1987)

8. A. Kelly and W. R. Tyson, **Journal of Mechanics and Physics of Solids, 10**, 199 (1963).

9. M. J. Rich, and L.T. Drzal, J. **Rein. Plast. Comp. 7**, 145 (1988).

10. K. Hook, R. Agrawal, and L. T. Drzal, submitted to J. Adhesion.

11. B. W. Rosen, **Fibre Composite Materials**, Amer. Soc. for Metals, Metals Park, OH (1965)

12. H. L. Cox **British Journal of Applied Physics, 3**, 72 (1952).

13. J. M. Whitney and L.T. Drzal, **Toughened Composites**, ASTM STP 937, 179-196, American Society for Testing and Materials, Philadelphia (1987).

14. V. Rao and L. T. Drzal, **Polymer Composites**, accepted for publication.

15. L. T. Drzal, **Materials Science and Engineering**, accepted for publication.

16. L. T. Drzal, **Vacuum**, submitted for publication.

ELASTIC MODULUS OF THE INTERPHASE IN ORGANIC MATRIX COMPOSITES

J.G. WILLIAMS[i], M.E. DONNELLAN[ii], M.R. JAMES[iii], AND
W.L. MORRIS,[iii]
(i)Michigan Technological University, Houghton, MI 49931
(ii)Naval Air Development Center, Warminster, PA 18976
(iii)Science Center, Rockwell International Corp., Thousand
Oaks, CA 91360

INTRODUCTION

In organic matrix composites the properties of the matrix
in the vicinity of the reinforcing fiber are of interest [1].
It has been suggested that a volume of material surrounding
the fiber is significantly different from the bulk matrix [2-
6]. Recent work has indicated that the interphase layer may
be softer than the normal matrix material [6]. For a model
composite with a single fiber embedded in an epoxy/amine
matrix this layer was observed to be about 500nm thick and the
material had an average elastic modulus of about 1/4 of that
of the normal matrix material. The objective of the present
work is to observe the effect of fiber treatment on the
elastic properties of the interphase.

EXPERIMENTAL PROCEDURE AND RESULTS

Material

The resin used in this work was Epon 828 cured with the
stoichiometric weight of meta phenylene diamine. The resin
was commercial grade material and the amine was laboratory
grade material and they were mixed in stoichiometric amounts.
The specimens were cured at 100°C for 1 hr in the presence of
a small quantity of free amine. This was placed so as to
saturate the local environment with amine to reduce the
possibility of loss of amine through volatalization.
The fiber was commercial carbon fiber, Fiberite AS-4,
purchased from Hercules in the surface-treated condition. One
sample was supplied coated with an epoxy compatible size and
one sample was unsized. One sample of fiber was coated with a
phenolic resin (Karbon 941 from Fiberite: elastic modulus 3.9
GPa) from toluol solution. The coating thickness was
determined from a scanning electron micrograph to be about
100nm. The process for application of this coating and the
characterization of the phenolic coated fiber have been
described [7].
Typical properties for the matrix resin [8,9] and fiber [10]
are shown in Table I.

TABLE I

Properties of the Matrix Resin and Fiber

Resin: Epon 828 (100 pt wt)-meta Phenylene Diamine(15.5 pt wt)
Fiber: Fiberite AS4-G (Surface treated)

Property	Matrix Value	Fiber Value
Glass transition temperature	$160^{o}C$	-
Specific Gravity	1.165	1.80
Tensile Strength (MPa)	85	3795
Young's Modulus (GPa)	3.3	235
Elongation to failure (%)	6.1	1.53
Diameter (μ)	-	7
Coef of expansion (m/m/^{o}C)	4.8×10^{-5}	5.5×10^{-7}

Tensioned Fiber Method
Sample Preparation

The tensioned fiber method is a technique for measurement of surface displacements in a disk of resin containing a single fiber when the fiber is loaded in tension. The resin is supported by a holder illustrated in Figure 1. The upper surface was polished by hand using 4000# SiC paper and the surface decorated with 5μ MgO smoke. A gold coating was applied to prevent charging in the microscope.
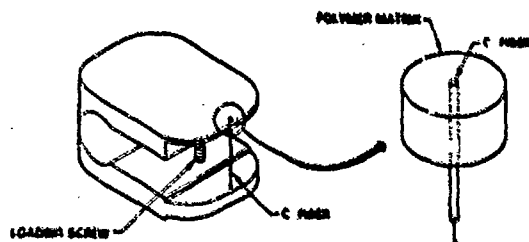
Fig. 1 Diagram of in-situ loading frame. The polymer matrix sample has a diameter of 500μ and a thickness of 180μ.

High Spatial Resolution Displacement Measurement Techniques

Stereoimaging displacement analysis was used to obtain sub-micron spatial resolution and high displacement sensitivity. With this technique, differential displacement is measured using pairs of SEM or optical micrographs, one taken before and one taken after the application of a mechanical load [6,11,12].

During development of the technique large time dependent, transient displacements were observed in the specimens [6]. The present studies exposed the samples to six cycles of load to 0.6% fiber strain in order to relax out the time dependent component of the displacements. After the total of six loading cycles were completed, the dominant matrix movement within 3μ of the fiber was positive with respect to the fiber surface, and was essentially reversed on unloading.

Interface micrographs were recorded at 20,000X at a 30° viewing angle to obtain the out-of-plane displacements at 0.4% fiber strain. The surface displacements shown in Figure 2 were obtained along typical fiber diameters.
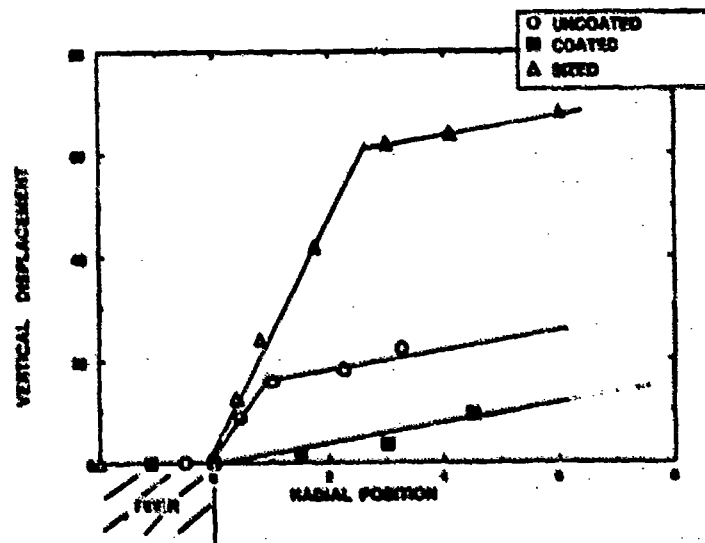
Fig. 2 Out-of-plane, elastic displacements of the matrix (nm) relative to the distance from the fiber (μ) after elimination of the time dependent deformation. Data shown as points. Also shown are the predicted surface displacements.

DISCUSSION

A recent publication has described the use of a shear lag
model for calculation of surface deformations in the sample
used here [13]. Shear lag analysis predicts that the surface
displacement relative to the fiber surface should be linear
with distance from the fiber if the matrix has a constant
modulus. The predicted displacements for a uniform modulus
matrix with properties shown in Table 1 is similar to the line
drawn for the coated fiber displacements in Figure 2. For the
treated and unsized fiber and for the treated and sized fiber,
at all points the observed displacement is higher than the
predicted displacement. For the fiber coated with the
phenolic resin the displacements observed are very similar to
those predicted by the shear lag model without interface. At
a distance from the fiber the slope of the predicted and
observed displacement lines are approximately equal for all
specimens. The slope is proportional to the elastic modulus.
If it is assumed that the fiber is surrounded by an interphase
of constant modulus it is possible to estimate values for the
modulus and thickness of the interphase material. Best fit
values for the treated/unsized fiber indicate a modulus of 1/4
of the modulus of the quoted value for the matrix and a
thickness of about 500 nm. For the treated/sized specimen the
modulus was about 1/5 of the quoted value and the thickness of
the layer was about 3000nm. The phenolic coated fiber
specimen did not show the presence of an interphase with
material properties different from the quoted data.

This data suggests that the fiber is surrounded by a region
of matrix which is capable of high, viscoelastic deformation.
The observations indicate that the application of a commercial
sizing agent to the fiber enhances the formation of the
interphase. The application of a thin, cured phenolic
material appears to eliminate the formation of the soft
interphase material.

The observation of a soft interphase is consistent with the
analysis of fiber push-out tests reported in the literature
(6) and with the observations of Piggott [3]. Large matrix
deformations have been reported in other work [12,14,15,16].

The dependence of the interphase properties on the surface
treatment of the fiber is consistent with a mechanism of
formation of the interphase through modification of the matrix
cure mechanism near the fiber as a result of the fiber surface
treatment. It has been postulated earlier (6,17) that the
interphase is formed due to the interference of the surface-
active fiber in the polymerization of the matrix during the
cure. The carbon surface is oxidized during manufacture to
improve adhesion of the fiber to the matrix. The chemical
functionality on the surface is primarily acidic in nature
(carboxylic and hydroxyl groups)(18,19). It has the effect of
adsorbing amine from the mixed resin onto the fiber surface
and interfering with the cure chemistry of the matrix. The
interaction must be complex, however, as the concentration of
acidic groups on the fiber surface is insufficient to cause
such a reduction in modulus (18,20). The commercial size
added to the fiber appears to enhance the formation of the
interphase. A similar soft interphase does not appear to be

formed when a single fiber is coated with phenolic resin, possibly due to the action of the phenolic coating as a barrier between the free acidic groups on the surface of the fiber and the free amine in the uncured matrix.

CONCLUSIONS

1. In model polymer composites made with a single carbon fiber and Epon 828 cured with metaphenylene diamine there exists an interphase region between the fiber and the matrix.
2. The formation of the interphase is dependant on the fiber surface and is negligible if the fiber surface is coated with a protective phenolic coating. Surface oxidized and oxidized and sized fibers show pronounced interphase layers. The interphase thickness was about 500 nm for the unsized fiber and about 1000nm for the sized fiber.
3. At this time it cannot be determined if a similar interphase would exist in a normal composite where the interfiber distance is about 1.2µ (65% resin volume fraction). Consequently, the significance of these observations for normal composites is unknown.

ACKNOWLEDGMENTS

REFERENCES

1. See for example Interfaces in Polymer, Ceramic, and Metal Matrix Composites, edited by Hatsuo Ishida (Elsevier Publ., New York, 1988).

2. Lawrence T. Drzal, Tough Composite Materials: Recent Developments (Noyes Publ., Park Ridge, NJ, 1985) pp. 207-222.

3. M.R. Piggott, Polymer Composites 8 (5), 291-296 (1987).

4. Andrew Garton and John H. Daly, Polymer Composites 6 (4), (1985).

5. C.G. Shelton and P.R. Marks, Journal of Material Science Letters 7 (6) 673-675 (1988)

6. J.G. Williams, N.E. Donnellan, M.R. James, and W.L. Morris, J. Material Science (in press).

7. R.E. Allred, L.A. Harrah and R.M. Salas, Development of Model Composites with Controlled Interfaces, PDA Technical Report, PDA-IR-1823-00-01, 1989.

8. Vidya B. Gupta, Lawrence T. Drzal, W. Walter Adams and Charles Y. Lee, Proc 29th National Conf SAMPE, 1984, pp. 901-912.

9. Shell Chemical Co. Technical Literature

10. Fiberite Co. Technical Literature

11. Brian N. Cox, Winfred L. Morris and Michael R. James, Proc. Nondestructive Testing and Evaluation of Advanced Materials and Composites. Colorado Springs, CO (August 1986) pp. 25-39

12. Winfred L. Morris, R.V. Inman and Brian N. Cox, J. Materials Science (in press).

13. Kai Chin Tsai, A.M. Arocho and L.W. Gause, J. Material Science (in press).

14. Roger J. Morgan, E.T. Mones and W.J. Steele, Polymer 23, 295 (1982).

15. L. Lorenzo and H.T. Hahn, Polymer Engineering and Science 26, 274 (1986).

16. S. Yamini and R.J. Young, Journal of Material Science 15, 1833 (1980).

17. Andrew Garton, William T.K. Stevenson and S.F. Wang, Journal of Polymer Science, Pt A: Polymer Chemistry, 26 (5), 1377-1391 (1988).

18. J.E. Castle and J.F. Watts, Interfaces in Polymer, Ceramic, and Metal Matrix Composites, edited by Hatsuo Ishida, (Elsivier Publ., New York, 1988) pp. 57-76.

19. P. Denison, F.R. Jones and J.F. Watts, Interfaces in Polymer, Ceramic, and Metal Matrix Composites, edited by Hatsuo Ishida, (Elsivier Publ., New York, 1988) pp. 77-85.

20. S. Chwastiak and R. Bacon, Symposium on Advances in Composite Materials, Polymer Division, 182nd ACS Meeting, 1981.

THE PRODUCTION OF MODULUS GRADIENTS AT INTERFACES

ANDREW GARTON, GAUTAM HALDANKAR AND EDWARD SHOCKEY
Polymer Program and Chemistry Department, University of
Connecticut, Box U-136, Storrs, CT 06269-3136

ABSTRACT

We have developed a range of "antiplasticizing" additives
for epoxy and polyimide resins which can increase the modulus of
the cured polymers by > 40%, increase their tensile and shear
strengths, modify their fracture behavior, and decrease their
water uptake. These additives may be used alone or in conjunc-
tion with rubber modifiers. The optimum additive formulations
are complex mixtures, but we describe here two relatively pure
model systems. The epoxy additive is the reaction product of
4-hydroxyacetanilide (HAA) and vinylcyclohexene dioxide (VCD),
while the polyimide additive is the reaction product of epoxy-
phenoxypropane (EPP) and HAA . These additives are mixed with
the epoxy resin and curing agent (or polyamic acid solution in
the case of polyimides), before curing, and the mixture is then
cured in the conventional fashion. We describe here some
physical properties of the modified epoxies and polyimides and
their use in adhesive formulations. These materials offer the
potential for constructing modulus gradients at interfaces
through their use as primers, so as to allow testing of the many
hypotheses concerning desirable interphase properties. Some
initial experiments in this area are described.

INTRODUCTION
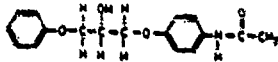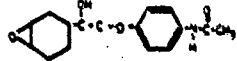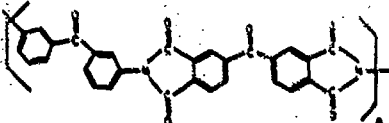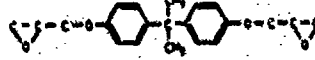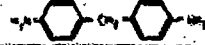
We have decribed previously a range of low molecular weight
additives for epoxy resins, given the descriptive name "epoxy
fortifiers" [1-4]. These additives increase the modulus of
cured epoxy formulations through a decrease in the free volume
of the crosslinked network. The occurrence of a surprising
degree of localized yielding during tensile testing of modified
epoxies was attributed to an anomalously high increase in free
volume with strain [3-5]. A commercial variant of these
materials is produced by Polysar Ltd., of Sarnia, Ontario,
Canada. The purpose of this communication is to describe some
mechanistic studies involving relatively pure model systems, and
their relevance to the concept of "controlled interphases". We
demonstrate that it is possible to produce an interphase with a
modulus exceeding that of the bulk polymer. The occurrence of a
high modulus interphase has been postulated as a mechanism for
improved stress transfer across matrix-reinforcement interfaces
[6,7]. We realize that the opposite, i.e. flexible, ductile,
interphases, has also been proposed to improve composite and
adhesive performance [8,9]. The use of modulus-modifying
additives of the type described here provides one route to test
these conflicting hypotheses.

EXPERIMENTAL SECTION

The epoxy and polyimide resins and the additive structures
are described in Table I. The epoxy formulation is a well known
amine-cured diglycidlyl system on which comparative data have
been obtained for at least twenty years. The polyimide data
were obtained on a commercial variant of LARC-TPI (Durimid 100,
Rogers Corporation), but qualitatively similar data have been

obtained with the Pyralin series of resins (2540 and 2545,
Dupont, based on pyromellitic dianhydride/oxydianiline). The
additive EPPHAA was prepared by reacting epoxyphenoxypropane
with 4-hydroxyacetanilide at 1.1:1 mole ratio [5]. The additive
VCDHAA was prepared by reacting vinylcyclohexene dioxide with
4-hydroxyacteanilide at 1.5:1 mole ratio [5]. Both materials
were purified by solvent extraction and reprecipitation, and
their structures confirmed by infrared spectroscopy, liquid
chromatography and nuclear magnetic resonance spectroscopy. The
additive EPPHAA is >95% pure, while VCDHAA contains >65% of the
listed structure, with the major impurities being oligomeric
species (e.g. VCD_2HAA). No claim is made that the additive
formulations described here are optimized. In particular, we
recognize that additives containing methylene functionality will
be insufficiently thermally stable for use in polyimides for
high temperature applications. Instead, we intend only to
illustrate the magnitude of property variation obtainable by
this route, and to explore the molecular mechanism.

Table I

Resin or Additive	Structure
EPPHAA	
VCDHAA	
Durimid 100	
EPON 828	
MDA	

Polyimide films (2.5-6 mils final thickness) were prepared
from the polyamic acid solutions by casting on glass plates
using a doctor blade. The films were allowed to dry overnight
in a glove box. Thermal imidization then took place at 100°C
for 1h followed by 200°C for 30 minutes (low temperature cure
system), and in some cases an additional 30 minutes at 300°C
(high temperature cure system). The epoxy system is relatively
conventional and has been described previously [5]. For some
epoxy adhesive formulations, the resin was prereacted with 15phr
(parts per hundred of resin) of a carboxy-terminated nitrile
rubber (B.F.Goodrich 1300X8), so as to improve the fracture
toughness of the adhesive, in accordance with conventional
practice. Adhesive bonding characteristics were determined
using a steel torsional joint geometry decribed by Bell [10].
The steel surfaces were degreased and treated with citric acid.
Tensile moduli were determined at 1Hz in a nitrogen
atmosphere using a Polymer Laboratories Dynamic Mechanical
Analyzer (DMA). Water uptake data were determined gravimet-

rically. Attempts were made to modify interphase moduli by the use of the epoxy additive as a primer (relying on interdiffusion of the resin and additive to set up a gradient), and by casting thin layers of resin/additive mixtures on metal surfaces, then allowing them to partially cure before applying the unmodified adhesive.

RESULTS AND DISCUSSION

We have shown previously that additive EPPHAA increases the room temperature modulus of the epoxy system by > 40%, lowers the T_g and suppresses the low temperature relaxations (3,4). Figures 1 and 2 show that a similar phenomenon occurs with a polyimide resin. We note that although the magnitude of the effect is similar for the two cure conditions, other data for the Pyralin polyimides points to a greater effect at lower cure temepratures. We attribute this to the volatility and poor thermal stability at 300°C of the additive, which contains an unstable methylene sequence. It should also be noted that although the modulus of the polyimide was increased, the tear strength was in some cases decreased, which would limit the usefulness of these materials as free standing thin films. The additive EPPHAA was shown to be almost totally unreacted with the epoxy resin (i.e. it was solvent extractable), and experiments are underway to determine the chemical reactivity of EPPHAA with the polyimide.
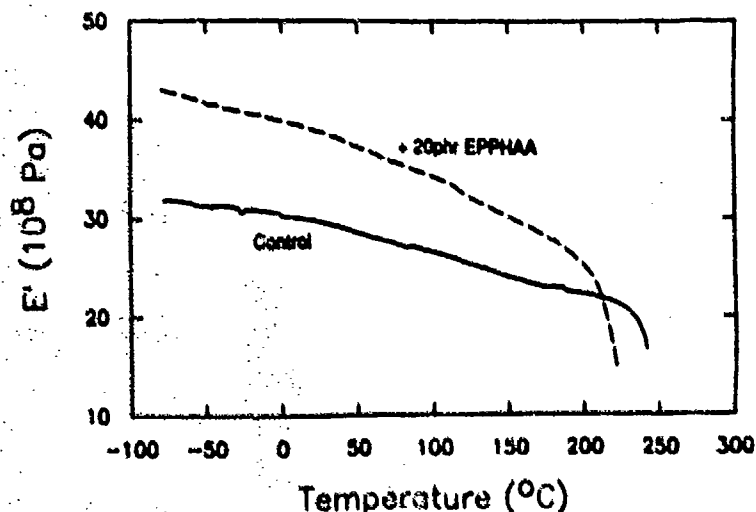
Figure 1. DMA at 1Hz of polyimide film (300°C cure)

Figure 3 shows that in addition to modifying the modulus of the epoxy system, the additive VCDHAA can also reduce the water uptake, consistent with the proposed reduction in free volume. The reduction in the magnitude of the effect with increasing temperature implies that there is a balance between the reduction in free volume associated with VCDHAA addition, and the increase in hydrophilicity associated with the incorporation of the polar additive. However, these results indicate that these materials should allow us to test the hypothesis that hygothermal durability can be improved by restricting diffusion of water to the interface.

294
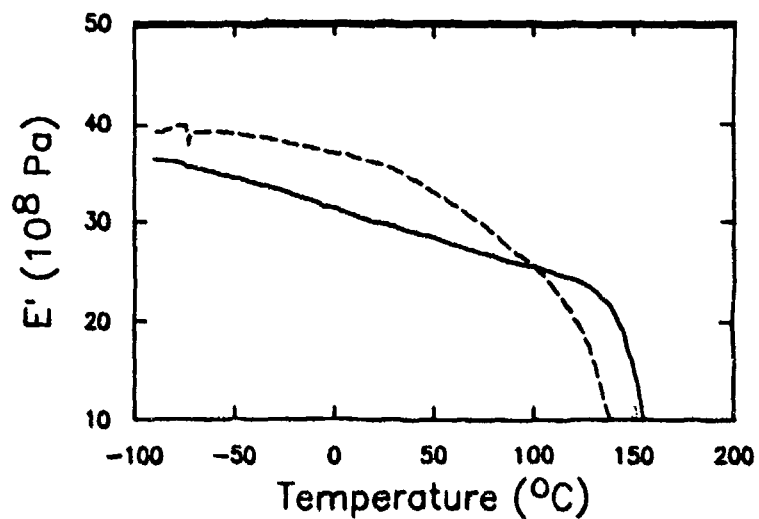
Figure 2. DMA at 1Hz of polyimide film (200°C cure)
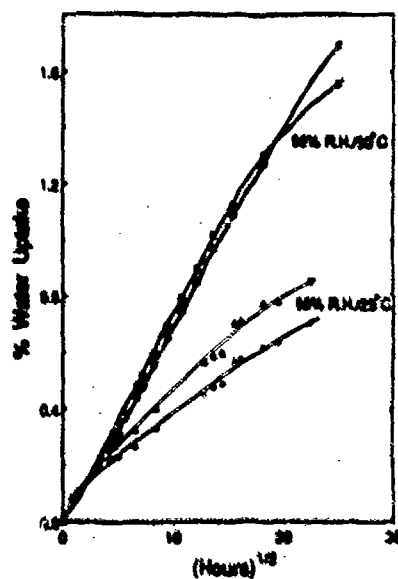
Figure 3. Water uptake for cured epoxy resin

☐ ▲   control
● ◆   +20phr VCDHAA

Table II summarizes some adhesive joint data we have reported in detail elsewhere (5). The shear stresses at failure are close to the shear strength of the resin, and so order of

magnitude improvement cannot be expected. However, the table
shows that adhesive bond strength can be improved by incorpora-
tion of VCDHAA and EPPHAA into the bulk of the adhesive.   One
interesting point not immediately apparent from the table is
that the rubber modified epoxy shows the greatest potential for
improvement.   The addition of the rubber improves the fracture
properties but decreases the shear strength and modulus.   The
addition of 20phr (parts per hundred of resin) VCDHAA to the
rubber modified epoxy increases the shear strength appreciably,
and improves the modulus to about that of the unmodified
control.   A further point described elsewhere (5) is the
catalytic effect of VCDHAA and EPPHAA which allows these high
strengths to be achieved with cure temperatures as low as 80°C.
The joint properties should therefore really be compared to
conventional low temperature cure systems, where the improvement
is much more noticeable (e.g. the same joint prepared with Epon
828/DETA has a normalized shear strength of less than half those
reported here).

Table II Properties of Adhesive Joints
(normalized shear strengths under torsional loading, average of
at least six specimens)

150°C cure		80°C cure		rubber modified	
control	100	control	<10	control	74
+20phr EPPHAA	120	+30phr EPPHAA	106	+20phr VCDHAA	89
+30phr EPPHAA	117				
+20phr VCDHAA	128				
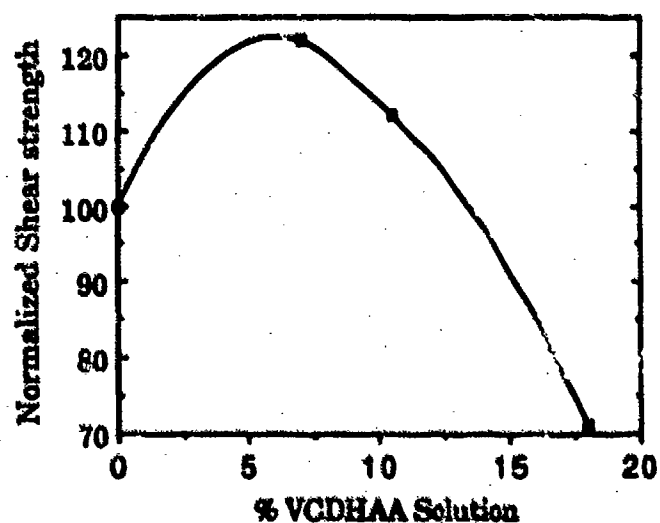
Figure 4. Shear strength (normalized) of torsional joints
           vs concentration of primer solution. Primer applied
           by dipping steel joint into acetone solution of primer

Figure 4 shows some initial data for the use of these additives as interphase modifiers. The form of the gradient was controlled by interdiffusion of the VCDHAA primer and the epoxy, and so this is a poorly controlled experiment, but there appears to be an optimum at which the joint shear strength is improved, but then too thick a layer of primer forms a weak boundary and the joint strength falls. We are presently performing a series of more controlled experiments where an interphase gradient is produced by casting (and partially curing) layers of polymer with different additive concentrations. It is necessary to optimize the extent of cure of these layers (if the preceding layer is over-cured then the next layer will adhere poorly. If the preceding layer is under-cured, then the additive will equilibrate between the two layers). Using this technique we have obtained improvements in joint strength comparable with those produced by modification of the bulk adhesive, but until we have better control over the variables mentioned above it would be unwise to present quantitative data. We also recognize that the optimum interphase structure will probably depend on the parameter which is being tested (e.g. peel test vs shear test), but feel that, despite these difficulties, some experimental verification would be of value to the continuing debate over polymer interphases.

REFERENCES

1.   P.D.McLean, A.Garton, R.F.Scott and S.E.Gransden, US Patent 4,480,082
2.   P.D.McLean, A.Garton and R.F.Scott, US Patent 4,739,028
3.   J.Daly, A.Britten, A.Garton and P.D.McLean, J.Appl.Polym.Sci., 29,1403 (1984)
4.   A.Garton, P.D.McLean, W.Stevenson, J.N.Clark and J.H.Daly Polym.Eng.and Sci.,27,1620 (1987)
5.   A.Garton, G.Haldankar and P.D.McLean, J.Adhesion, 29,13 (1989)
6.   L.T.Drzal, M.J.Rich, M.F.Koenig and P.F.Lloyd, J.Adhesion, 16,133 (1983)
7.   H.Schonhorn and F.W.Ryan, Adv.Chem.Ser., 87,140 (1968)
8.   J.Chang, J.P.Bell and R.Joseph, SAMPE Quarterly, 18,39 (1987)
9.   M.R.Piggott, Polymer Composites, 8,291 (1987)
10.   W.McCarvill and J.P.Bell, J.Adhesion, 6,185 (1974)

THERMOMECHANICAL STABILITY OF INTERPHASES IN GLASS REINFORCED COMPOSITES

A.T. DIBENEDETTO*, JAIME A. GOMEZ**, C. SCHILLING**, F. OSTERHOLTZ** AND
G. HADDAD***
   *University of Connecticut, Department of Chemical Engineering, Institute of Materials Science, Storrs, CT 06269-3136
   **Specialty Chemical Division, Union Carbide Corp., Tarrytown, NY
***Monsanto Chemical Co., Springfield, MA

ABSTRACT

The thermomechanical stability of organosilane surface treatments for E-glass fibers used in fiber reinforced composites was evaluated. The effect of molecular structure of 40 to 80 nanometer coatings on the force transmission across the fiber/matrix interface was measured as a function of temperature and exposure to water using a fiber fragmentation test. It was found that phenyl-substituted amino silanes exhibited better thermal stability, but were less resistant to boiling water, than the commerically available γ-amino propyl silanes. A bis-trimethoxy γ-amino propyl silane showed an increase in both the hydrolytic and thermal stability when compared to the commercial product. A good balance of thermal and hydrolytic stability was also obtained with a methylaminopropyltrimethoxy silane coating.

The strain energy released from the glass fibers upon decoupling from the epoxy matrix or silane coating was found to be in the range of 145 to 186 ^{9}/m^2 and varied no more than 20 percent over a temperature range of 25 to 75°C or when exposed to boiling water and then redried. It also varied very little with the silane coating used. In addition, the average shear stress attained at the fiber-matrix interface in an imbedded single fiber test at 25°C was as much as two times higher than the shear strength of the epoxy matrix and as much as five times higher at elevated temperature. These data lead one to the conclusion that the interphase failure in these composites is controlled by a plane strain fracture in the constrained region of the organic phase, near the fiber surface, rather than by the maximum shear strength in the interphase.

INTRODUCTION

The properties of glass fiber reinforced composites are dependent upon the stability of the interfacial region between the matrix and the fiber surfaces. The primary function of the fiber/matrix interface is to transmit stress from the polymer matrix to the high strength reinforcing fibers. The ability to transmit stress depends upon the mechanical properties of the matrix, the load bearing ability of the fibers and the strength of the fiber/matrix interface. A strong chemically stable interface can be obtained by application of a coupling agent on the fiber surface which interacts either chemically or physically with both the fiber and matrix. The most widely used coupling agents for glass are the organosilanes having the general formula X_3SiR, where the R is an alky or aromatic functional group and the X are readily hydrolyzable groups that react in the presence of water to form both siloxane linkages and polysiloxane coatings on the glass surfaces.

Considerable evidence suggests that rather than a monomolecular interface, a coating of polysiloxane, as much as 40 to 80 monometers thick, forms an interphase between the fiber and the matrix material. The stress transmission characteristics of this interphase are critical to the mechanical performance of the composite. After many years of study there is still speculation as to whether it is better to leave an interphase

with graded properties as a buffer between fiber and matrix or to have a monolayer of a reactive coupling agent to strongly bond the fiber to the matrix. In this study we report results on the effect of the molecular structure of silane agents on the stress transmission characteristics of polysiloxane interphases as a function of temperature and exposure to boiling water.

EXPERIMENTS

The thermal and hydrolytic stability of a series of commercial and experimental silane coupling agents for glass fiber reinforced composites were evaluated using an imbedded single fiber composite tension test [1]. A series of silane coupling agents were synthesized at the Specialty Chemical Division of Union Carbide Corp. in Tarrytown, NY [2,3]. All were variations of the widely used compound 3-aminopropyltrimethoxy silane (APS). The materials used in this study are 3-(phenyl amino) propyltri-methoxy silane (PAPS), 3-(4 hydroxy-3 methoxyphenyl) propyltrimethoxy silane (HMPS), 3-(methyl amino) propyl trimethoxy silane (MAPS), 3-(amino ethylamino) propyl trimethoxy silane (AAPS) and a bis(3-trimethoxy silyl-propyl) amine (BTA). The reactive groups were systematically changed to provide either wet strength retention (as with BTA) or high temperature stability (as with HMPS). The E-glass fibers were spun from the melt at 2200°C and water washed. The silanes were applied as a primer solution of 5% silane and 5% water in either methanol or toluene, as appropriate. After 5 minutes of contact with the primer solution the fibers were air-dried for 5 minutes, heated in vacuum at 100°C for 30 minutes, boiled in water for one hour and then redried in vacuum at 100°C for another hour. FTIR was used to confirm the presence of silane on the surface and scanning electron microscopy was used to observe the topography of the coating. After the final water washing the coating appeared to be smooth and uniform. Thermogravimetric analysis indicated that its weight was of the order of 0.5 to 1.0 percent, signifying average coating thicknesses of 40 to 80 nanometers.

Fiber tensile strength distributions were obtained using ASTM Standard D3379-5 at a crosshead speed of 0.51mm per minute. As reported previously [3], the distribution of fiber breaking strengths conformed to a double box distribution over wide ranges of fiber length. At fiber gauge lengths of 0.2 to 2.0 mm, which covers the range of measured critical lengths, the fiber strength can be represented within ± 10% by the following equation:

$$\sigma_f(\ell_c) = 400 + \frac{1,815,000[1-(0.998)^{58.8\ell_c+1}]}{[58.8\ell + 1]} + 6050(0.998)^{58.8\ell_c} \qquad (1)$$

where $\sigma_f(\ell_c)$ and ℓ_c are in units of MPa and millimeters respectively.

Single filaments were selected at random from the coated bundles and mounted in a silicone rubber mold. Epon 828 epoxy resin and 100pph Versamide 125 amine curing agent were mixed and poured into the cavities. The samples were cured for two hours at 100°C followed by a two hour postcure at 150°C, left in the oven overnight to cool and then stored in a dessicator until used. The single fiber composite samples were loaded in tension on an MTS 880 servohydraulic loading machine at 0.51 mm per minute to elongations of up to 10 percent. Fragmentation was complete at about 7 percent elongation. The samples were observed and photographed under a microscope equipped with cross polarizers. The lengths of the fiber fragments were measured using a micrometer eyepiece. Enough samples were tested to obtain 80 to 100 fragments for each fiber type.

Upon tensile deformation, stress is transferred through shear at the

interface to the fiber fragments. At some point either a shear or a tensile component will reach a limiting value and cause either a debonding at the interface, a shear yielding of the matrix or crack propagation in either phase. The purpose of the fiber fragmentation test is to measure quantitatively the maximum load transfer and to determine optically, if possible, the limiting fracture mechanism.

The maximum load per unit of circumference, (F), transferable to a fiber of critical length can be calculated from a force balance as:

$$F = \frac{1}{\pi d_f} [\sigma_f(\ell_c) \frac{\pi}{4} d_f^2] = \frac{\sigma_f(\ell c) d_f}{4} = \int_0^{\ell_c/2} \tau(x) dx \qquad (2)$$

where $\sigma_f(\ell_c)$ is the strength of the fiber at the critical length and d_f is the fiber diameter. The shear stress at the fiber/matrix interface, $\tau(x)$, is integrated from the center to the end of the fiber. The shear stress distribution is determined by the mechanical properties of the silane coating and the matrix material near the interface and the maximum attainable value of $\tau(x)$ is determined by the state of stress and the mechanism of failure. In certain ideal situations the stress distribution can be determined [4,5], but in most cases it is necessary to evaluate numerically the multiaxial stress field around the fiber ends. A mean value of $\tau(x)$ can be estimated by assuming uniform shear along the fiber surface and integrating equation (2).

RESULTS AND DISCUSSION

A typical fragment length distribution for coated E-glass fibers in the epoxy resin is shown in Figure 1. The mean critical lengths were used to calculate the maximum force transferable per unit of circumference, F, and an "average" interfacial shear transmission parameter, $<\tau>$. Also, a minimum debonding energy per unit of surface area, G, was obtained by estimating the elastic strain energy released from the fiber end upon debonding:

$$G = \frac{(\frac{\pi}{4} d_f^2) (\ell_{c/2}) (\frac{\sigma_f \ell_c}{2})^2}{E_f(\pi d_f) (\ell_{c/2})} = \frac{F^2}{d_f E_f} \qquad (3)$$

where E_f is the elastic modulus of the fiber.

The force transmission properties as a function of temperature are shown in Table I. At room temperature, F is equal to 13.6 ± 0.2 kN/m, the minimum energy release G is 180 ± 5 J/m², and both are insensitive to the silane coating used. On the other hand, the average shear transmission varies inversely with the critical aspect ratio, with HMPS promoting the highest value (51.2MPa) and the absence of silane resulting in the lowest value (32.9MPa). The phenyl substituted silanes support higher shear stress at room temperature, probably indicating a higher rigidity of these coatings. All values of $<\tau>$ are higher than the shear strength of the bulk epoxy (25.1MPa), which indicates that either the shear strength of the interphase material is higher than that of the bulk epoxy or the force transmission is not limited by yielding of the material near the interface. While in all cases the shear stress transmission decreases substantially with temperature, the minimum strain energy release drops only slightly (7% to 21% maximum). Values of G in the range 145 to 186 are of the order of the plane strain energy release rates G_{Ic} of epoxy type materials which leads one to the conclusion that the mechanism of "inter-
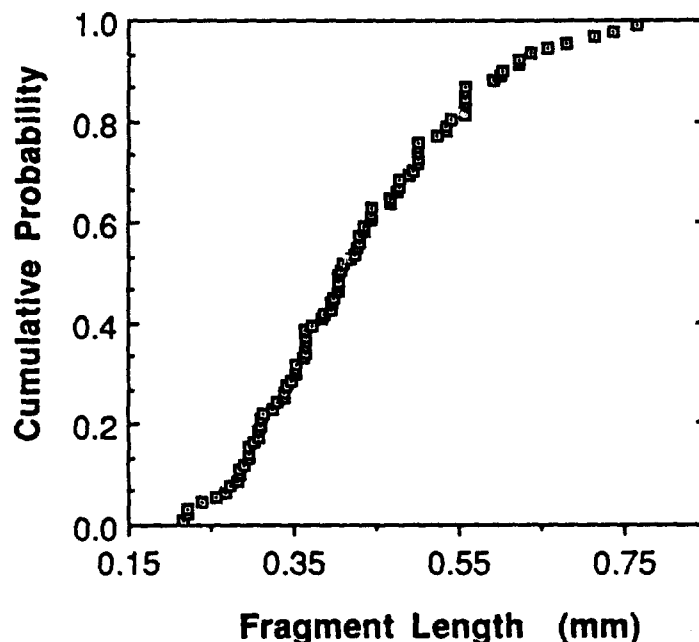
Figure 1. Fragment length distribution for HMPS coated E-glass fibers.

phase" failure is probably a plane strain fracture somewhere on the matrix side of the interface.

One can see substantial differences in the thermal stability of the coatings. It appears, for example, that the substitution of phenyl groups on the polysiloxane promotes thermal stability. The HMPS coating, and to a lesser extent the PAPS coating, retains much of its ability to transmit load even 30° above the glass transition temperature of the bulk epoxy. The uncoated and the APS coated fiber material show the poorest thermal stability, while the BTA and MAPS silane coatings exhibit a thermal stability intermediate to the others.

The single fiber composite samples were also exposed to boiling water for periods of 2 and 24 hours. Samples were tested both wet and after drying for 48 hours in vacuum at 100°C. Table II illustrates the effect of boiling water treatment on the force transmission properties. After 2 hours exposure the critical lengths of all samples tested wet were higher than the initial values, indicating a degradation of the force transmission ability of the interfaces. The material with uncoated fibers showed the most degradation, while the BTA and AAPS coated fibers showed the most resistance to boiling water. The increased functionality of these two coupling agents appears to provide slightly better initial hydrolytic stability. Upon drying, the uncoated, BTA and MAPS coated samples recovered nearly completely their force transmission characteristics, while the APS and HMPS coated samples showed clear signs of permanent deterioration.

After 24 hours of exposure to boiling water none of the materials exhibited any interfacial strength when tested wet. Upon loading, the fibers merely slip in the matrix and cannot be broken in tension. This indicates penetration of water into the epoxy resin and probably the interface. The swelling of the bulk epoxy and the interphase material results in very high swelling stresses that could easily rupture the

TABLE I: FORCE TRANSMISSION PROPERTIES OF VARIOUS SILANE COATINGS
ON E-GLASS FIBERS - EFFECT OF TEMPERATURE

TEMPERATURE	25°C				50°C				75°C			
COATING	t_c/d_f	f_b^{kN}	$<\tau>$MPa	G J/m^2	t_c/d_f	f_b^{kN}	$<\tau>$MPa	G J/m^2	t_c/d_f	f_b^{kN}	$<\tau>$MPa	G J/m^2
MMPS	40.0	13.8	51.2	185	46.6	13.6	43.4	181	66.8	13.3	29.5	172
PAPS	39.9	13.8	51.3	186	52.2	13.5	38.5	178	94.6	12.9	19.8	163
BTA	45.9	13.6	44.2	182	49.5	13.5	40.7	180	96.3	12.9	19.9	163
MAPS	44.5	13.7	45.6	182	61.4	13.4	32.3	174	91.0	13.0	21.2	164
AAPS	55.5	13.6	36.0	177	57.0	13.4	35.0	175	118.0	12.7	16.0	157
APS	55.5	13.6	36.0	177	63.3	13.2	31.3	174	148.0	12.4	12.4	149
Uncoated	60.4	13.4	32.9	175	70.9	13.1	27.7	171	167.0	12.2	10.9	143
$(\tau_i)_{freey}$		25.1				6.9				5.0		

TABLE II: FORCE TRANSMISSION PROPERTIES OF VARIOUS SILANE COATINGS
ON E-GLASS FIBERS - EFFECT OF BOILING WATER EXPOSURE*

COATING	2Hr WATER BOIL				2 HR WATER BOIL/48 HR DRY				24 HR WATER BOIL/48 HR DRY			
	t_c/d_f	f_b^{kN}	$<\tau>$MPa	G J/m^2	t_c/d_f	f_b^{kN}	$<\tau>$MPa	G J/m^2	t_c/d_f	f_b^{kN}	$<\tau>$MPa	G J/m^2
MMPS	60.0	13.4	33.1	174	43.6	13.7	46.6	183	42.0	13.7	46.5	184
BTA	55.0	13.5	36.4	177	42.4	13.6	42.6	181	51.0	13.5	36.3	178
MMPS	64.0	13.3	30.9	173	49.0	13.6	41.7	181	48.6	13.6	41.4	181
PAPS	60.0	13.2	29.2	171	-	-	-		67.5	13.6	22.0	181
AAPS	60.0	13.4	33.1	175	-	-	-		61.5	13.1	23.0	168
APS	60.2	13.3	29.0	172	67.0	13.3	29.1	173	61.4	13.3	30.7	173
Uncoated	141.7	12.8	10.0	161	64.0	13.3	30.9	163	64.4	13.3	30.7	173
$(\tau_i)_{freey}$		6.9				22.1				25.1		

* Tested @ 25°C

interface. Water in the interphase region will also cause hydrolysis of the silane coatings. Either factor could cause interphase failure. After drying, the material with uncoated fibers recovered nearly completely, indicating little permanent damage to either the epoxy matrix or the fibers. The epoxy also recovered its initial yield strength. Of the silane coated materials, those containing methyl substituted silane coated fibers (MAPS) appear to have recovered completely their load transmitting ability. The bis-methoxy compound BTA was also reasonably stable, losing only 11% of its shear transmission capability. The phenyl substituted coatings PAPS and HMPS lost 57% and 19% respectively of their shear transmission capability and the amine compounds APS and AAPS lost 15% and 34% respectively. Incomplete recovery indicates a degree of irreversibility in the integrity of the interphase and perhaps the hydrolysis of the polysiloxanes.

The fiber fracture at the fiber-matrix interface was observed under cross polarized light revealing stress birefringence patterns around the coated fibers [2,3]. At room temperature both the interface and the matrix are stable and can sustain the strain concentration around the broken fiber ends. At higher temperature the matrix and/or interface weaken and the fibers appear to slip in the matrix. As the force transmission at the interface diminishes as a result of exposure to boiling water, the birefringence patterns decrease in intensity as slippage of the fibers in the matrix becomes apparent, confirming the conclusions drawn from the data of Tables I and II.

REFERENCES

1. W.A. Fraser, F.H. Ancker, A.T. DiBenedetto and B. Elbirli, Polymer Composites, 4, 238 (1983).
2. A.T. DiBenedetto, G. Haddad, C. Schilling and F. Osterholtz, in Interfacial Phenomena in Composite Materials '89, Edited by F.R. Jones, (Butterworths, 1989) pg. 181.
3. A.T. DiBenedetto and P.J. Lex, Polymer Engineering and Sciences, 29, No. 8, 543 (1989).
4. A. Kelly and W.R. Tyson, J. Mech. Phys. Solids, 13, 329 (1965).
5. B.W. Rosen, A.I.A.A.J., 2, 1985, (1964).

INTERFACIAL INTERACTIONS IN SILICA REINFORCED SILICONES

MIRTA I. ARANGUREN, CHRISTOPHER W. MACOSKO, BIMAL THAKKAR and
MATTHEW TIRRELL
University of Minnesota, Dept of Chemical Engineering and
Materials Science,421 Washington Ave.SE., Minneapolis, MN 55455

INTRODUCTION

The study of the type and strength of the filler-polymer linkages is of great importance in understanding the reinforcement of elastomers. Silicone rubbers are weak elastomers and the addition of reinforcing fillers is essential in order to obtain useful, strong materials. The best reinforcing filler for these elastomers are fumed silicas. These fillers, like reinforcing carbon blacks, have very complex structures. Both have fractal characteristics, small particles fused together forming open aggregates that can cluster by physical forces. Silicas have sometimes more complex structures than carbon blacks, but have a better understood surface chemistry. Interactions between polydimethylsiloxanes and silica surfaces have been studied using heat of adsorption measurements of mostly low molecular weight analogs or inferring the strength of the adsorption by the shift of particular peaks in the infrared spectrum [1]. Here we will present a new technique that measures directly the strength of the adsorption of the polymer segments onto glass and between themselves. It also allows for comparison of the strength of such bonds with the strength of a polymer entanglement "link".

MATERIALS

The polydimethylsiloxanes used in this work are vinyl terminated and have molecular weights ranging from $Mn = 8900$ to 146000 (Table I), thus below and above the critical molecular weight for entanglements ($Mc = 25000$, [2]). PDMS2 and PDMS3 are from Dow Corning (Midland, MI) and PDMS1 was bought from Petrarch.

Table I
Molecular Weights and Polydispersity of the PDMS Used in This
Work.

	PDMS1	PDMS2	PDMS3	PDMS4*
Mn	146,000	66,400	8,900	22600
Mw/Mn	2.2	1.8	1.9	3.9

(*) mixture 70 to 30 by weight of PDMS2 and PDMS3

Fumed silica (Aerosil 130, Degussa) and chemical modifications of it were used in this work, in order to keep approximately the same structure and surface area. Table II presents the silicas used, their surface area and the type of surface treatment.

Fumed silicas are manufactured using a flame process that produces droplets of SiO_2 of about 7 to 30 nm that fuse together to form aggregates. These aggregates are of colloidal size (less than 1μ) and can agglomerate in the dry state due to physical forces (van der Waals or hydrogen bonding).

304

<div align="center">

Table II
Fumed Silicas Treatment and Surface Area

</div>

	Aerosil 130	Aerosil R972	Modified Silica 1	Modified Silica 2
Surface Area (m²/g)	133	108	112	114
Surface Treatment	none	dimethyl dichlorosilane	hexamethyl disilazane	tetramethyldivinyl disilazane (30%wt.) + hexamethyldisilazane (70% wt)
Fraction of Silanols *	1	0.08	0	0

* The hydroxilated area of Aerosil 130 is taken to be 1 as reference (measured using the methyl red technique).

The FTIR spectra of the silicas show that commercial Aerosil R972 is a partially treated silica, the peak corresponding to isolated silanols (3750 cm^{-1}) is small but noticeable. The other two modified silicas were treated in our laboratory using the technique detailed by Maxson and Lee [3] and the spectra showed complete treatment. This degree of treatment was also confirmed more quantitatively by adsorption of a dye such as methyl red, that is adsorbed only onto hydroxylated surfaces. These results are shown in Table II.

EXPERIMENTAL

The composites were prepared by mechanical mixing of the polymer and filler without the addition of any mixing aids. The apparatus used was a Rheomixer Haake 600 with a chamber capacity of 60 to 80 cm^3. The mixing was done at room temperature using sigma blades at 35 rpm. The addition of silica to the polymer took about 30 minutes to form a master batch of 20 to 40 phr (parts of silica per hundred parts of polymer) depending of how stiff the material became. The torque signal reached a constant value about 30 minutes after the silica incorporation , but the total time of mixing was 3 hours. The composite made from Aerosil R972 and PDMS4 was prepared in a Baker Perkins mixer (1ℓ capacity) using the same procedure as above.

Diffuse reflectance infrared spectroscopy (DRIFT) was used to characterize the silica surfaces before and after the polymer adsorption. We used an IBM IR44 spectrometer with a diffuse reflectance cell from Harrick (Praying Mantis model). The samples for the IR study were prepared by mixing 1 part (by volume) of silica that had been dried for 1 hour at 105°C with 7 to 10 parts of NaCl (previously dried for 1 hour at 120°C). The spectra were obtained at room temperature, as the average of 500 scans with 2 cm^{-1} resolution. The spectra were later modified using the Kubelka-Munk correction.

Bound rubber is defined as the amount of polymer that is not dissolved by a good solvent in the uncured material. We measured this quantity at room temperature with chloroform. In this way, only the strongly adsorbed chains remain after the extraction and any entangled free chains or polymer occluded inside of the aggregates is probably washed out. 2 g of uncured silicone rubber were put into contact with 20 ml of chloroform for 2 to 3 days. The supernatant was separated and the solids left behind were subject to the above procedure a couple of times. The separation of the solid from the polymer solution was attained by centrifugation at 13000 rpm for 45 minutes.

The surface force measurements were done using the technique described by Israelachvili and Adams [8], but replacing mica by smooth glass surfaces [9]. A glass bubble was formed by blowing a heated sealed Pyrex glass tube. The bubble is later broken. Pieces of about 1 cm^2 and 2 to 3 μ thickness are silvered and glued onto glass lenses with the silvered side down. The polymer was later adsorbed onto either one or on both the surfaces by immersing the lenses into a solution of PDMS2 in toluene (0.05g/ml) for 12 hours. Then, the surfaces were washed in toluene and used for the measurements. A spot was considered suitable for the test if after the surfaces jump into adhesive contact, further compression resulted in no movement of the fringes indicating smooth surfaces. At this spot the surfaces were kept in contact under no compressive load for different time intervals between measurements. When the gradient of the attractive portion of the force vs. distance profile exceeded the spring constant the surfaces jumped apart to a distance which when multiplied by the spring constant of the dou'le plate cantilever leaf spring yielded the adhesive force. This force was measured by separating the surfaces in air, whereas the radius of curvature of the undeformed surface was measured by immersing the surfaces in toluene. The adhesive force as measured in the experiment was divided by $3\pi R$ in order to obtain γ, the surface energy.

RESULTS

.he DRIFT spectra of the untreated silica Aerosil 130 before and after compounding with the PDMS is shown in Figure 1. The peak at 3750 cm^{-1} disappears indicating that adsorption is strongly related to the presence of isolated SiOH on the silica surface. This single observation, however, is not enough to determine if the adsorption is physical or chemical in nature. Previous work published in the area [4] indicates that a chemical reaction involving the surface SiOH takes place at temperatures above 130 c. In fact an irreversible increment in the modulus of the uncured composites was detected after heating a composite at 153°C. [5] The measurement was done using a Rheometrics System IV by measuring the storage modulus, G', vs. frequency at small deformations. No changes were detected at
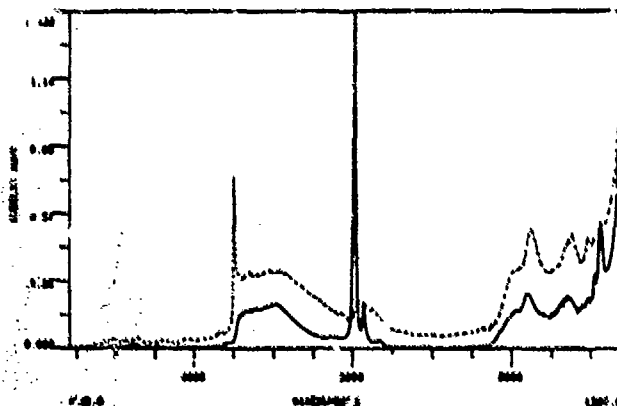
Figure 1 DRIFT spectra of Aerosil 130 before (dashed line) and after (continuous line) adsorption of PDMS4

temperatures $\leq 110°C$. Thus, we think that the adsorption is mainly physical and due to the H bonding of the PDMS chains to the isolated silanols of the silica.

The results from the bound rubber measurements are limited by the way in which the solids separation is done. Table III shows these results. The higher the PDMS molecular weight the larger the amount of adsorbed polymer. Problems arise in the solid separation at Mn= 146000, because during the centrifugation step, part of the free chains also sediment. The trend, however, is valid. We also noticed that the larger the OH concentration in the silicas, the larger the amount of adsorbed polymer. Again some problems appear during the centrifugation of completely treated silica. The centrifugation is not strong enough to sediment some small clusters and the results show zero or negative amounts of adsorbed polymer indicating that some silica is lost in the supernatant.

Table III
Bound Rubber Results

Silica: Aerosil R972

PDMS Mn	$PDMS_{ads}/PDMS_{total}*100$	$PDMS_{ads}/silica$	ϕ
146000	(high)		
66400	6.9	0.219	0.12
22600	5.3	0.263	0.12
8900	1.8	0.064	0.08

Polymer: PDMS (Mn= 22600)

Modified Silica 1	(~ 0)	(~ 0)	0.08
Aerosil R972	5.3	0.263	0.08
Aerosil 130	8.1	0.407	0.08

where ϕ is the volume fraction of silica, calculated using $\rho_{sil.}$ = 2.2 g/cm^3 and ρ_{PDMS} = 0972 g/cm^3. ϕ= 0.12 corresponds to 30 phr and ϕ=0.08 to 20 phr.

The results could be later improved using elemental carbon determination for both, the silicas in the dry state and the silicas onto which the polymer is adsorbed. Using similar materials, Cohen-Addad observed the same trends as those seen here. Further, based on the assumption that the whole silica surface is wetted by the polymer, they observed that the amount of polymer adsorbed per unit of weight of silica is independent of the silica concentration (6).

Figure 2 shows the preliminary results of the direct measurement of the forces between the Pyrex glass surfaces, and PDMS (Mn=66400). In the first case, the polymer was adsorbed only onto one of the surfaces, hence facilitating bridge formation when the two surfaces were put into contact. The surface on which the polymer was adsorbed was washed for only 1 hour with solvent after the adsorption, thus some free polymer may have remained as well as weakly adsorbed chains.

In the second case, the polymer was adsorbed up to saturation on both glass surfaces. After adsorption the surfaces were washed three times with pure solvent for a total of 24 hours and then put into contact in the surface forces
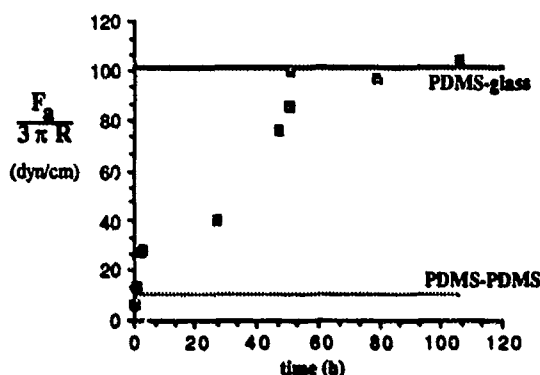
Figure 2. Surface Forces measurements. PDMS-PDMS is the case in which the polymer was adsorbed on both surfaces, PDMS-glass is the case in which the polymer was initially adsorbed on one surface.

apparatus. The predominant type of linkages possible is the entanglement of chains adsorbed on different surfaces. Without any applied load the force seems to remain constant and low in the time interval observed.

The important result is the large increment of the forces when bridges are present in comparison to the case where the interactions are between PDMS adsorbed on two different surfaces.

DISCUSSION

The physical picture which emerges from our studies is illustrated schematically in Figure 3. Bound rubber and FTIR results indicate that there exists a strong adsorption of the polymer onto the silica surface and at the same time, extensive agglomeration occurs at small deformations[5]. Aggregates of different sizes have adsorbed polymer and thus, agglomeration takes place through silica-polydimethylsiloxane-silica linkages. Figure 3 (not at scale) shows the type of attachments that are possible:

   a) entanglements with intermediate free chains,
   b) entanglements of chains adsorbed onto different
   aggregates, and
   c) direct bridging of two aggregates by the same chain.
While the three types of linkages are expected to increase the modulus of the rubber, the first one should not change greatly the relaxation behavior of the material, while the existence of the other two should broaden the spectrum of the relaxation times which is a experimental feature in reinforced elastomers[7].

The use of the surface forces apparatus offers a new tool to study the interfacial forces in these systems. In this preliminary work we have compared the forces required to pull apart two surfaces on one of which the polymer is adsorbed, hence facilitaitng bridge formation (linkages of type c) and the forces required to pull apart two surfaces with polymer adsorbed on each of them, hence allowing for contribution due to entanglements between polymer chains (linkages of type b).

308
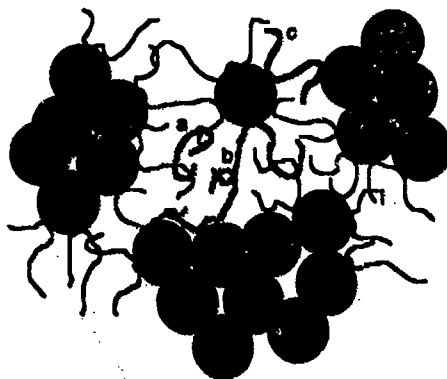
Figure 3. Different types of silica-PDMS-silica attachments.

The forces measured separating a polymer layer from glass
evolved slowly during the time of measurement up to values about
10 times larger than in the case of polymer adsorbed on the two
surfaces. We believe that bridges were formed from the very
first contact, but with
time, weakly adsorbed chains as well as free entangled chains
were squeezed out from the gap, which was seen to decrease with
increasing time of contact. This preliminary measurement
resulted in larger forces than those found for glass-glass
surfaces measured wii the same technique, 40 to 60 dyn/cm,[9]
but more experiments are needed before we can discuss these
results in absolute terms. The results obtained with this
technique supports our proposition on the importance of filler-
polymer attachments since it suggests that polymer bridging can
be a strong force for agglomeration, not usually suspected. The
results obtained with this last technique are encouraging enough
to continue the study with polymers of different molecular
weights and treated glass surfaces.

REFERENCES

1. K.I. Brebner, R.S. Chahal, L.E.St-Pierre, Polymer, 21, 533
   (1980).
2. W.W. Graessley and S.F. Edwards, Polymer, 22, 1329 (1981).
3. M.T. Maxson and L.J. Lee, Rubber Chem. Technol., 58, 436
   (1982).
4. G. Berrod, A. Vidal, E. Papirer, J.B. Donnet, J. App. Polym.
   Sci., 26, (1981).
5. M. Aranguren, PhD thesis, University of Minnesota, 1989.
6. J.P. Cohen-Addad, C. Roby, M. Sauviat, Polymer, 26, 1231
   (1985).
7. N.J. Mills, J. App. Polym. Sci., 15, 2791 (1971).
8. J.N. Israelachvili and G.E. Adams, J.Chem.Soc.Faraday Trans.
   I., 74, 975 (1978).
9. B. Thakkar, H. Watanabe, M. Tirrell, D.J. David, MRS
   Proceedings, 16.1 (1989).

INTERFACIAL EFFECTS OF PLASMA TREATMENT
ON FIBER PULL-OUT

UMESH GAUR* and THEODORE DAVIDSON**

*TRI/Princeton, P.O. Box 625, Princeton, NJ 08542
**Center for Surface & Interface Research,
University of Connecticut, Storrs, CT 06269

INTRODUCTION

Surface modification of organic reinforcement fibers by exposure to certain plasmas appears to have considerable potential as a means for improving the performance of composites. Such treatments can change fiber surface properties, leaving the core of the fiber virtually unaffected so that the mechanical properties of the fibers remain unaltered. Previous studies [1-5] have shown that plasma treatment of polymeric fibers can modify surface energetics and that the acid/base characteristics of a fiber surface can be altered by exposure to plasmas of acidic or basic gases. Although several publications [6,7] have reported that the mechanical properties of composites reinforced with plasma-treated fibers are enhanced, there has been no direct evidence to show the impact of fiber surface plasma treatment on interfacial shear strength.

In this paper we report the effect of plasma treatment on interfacial shear strengths as measured by the microbond pull-out technique [8,9]. This technique provides a direct measurement of interfacial adhesion between a fiber and resin matrix. It involves the application of microdroplets of resin (30-200 μm long) onto a single fiber, followed by measurement of the force required to pull out or debond the fiber from each droplet. This technique has been found to be sensitive enough to differentiate among various fiber/resin combinations [8-12]. In this study, the effects of plasma treatment on aramid and high modulus polyethylene fiber have been investigated by measuring their interfacial shear strength in conjunction with epoxy resin.

EXPERIMENTAL DETAILS

Fiber Treatment

Aramid fiber (Kevlar® 49, DuPont), washed in acetone, and high modulus polyethylene fiber (finish-free Spectra® 1000, Allied/Signal) were treated in yarn form with four types of plasmas. The ionized gases used in the treatments can be broadly classified into four types: oxidizing plasma, reducing plasma, neutral plasma, and hydrophilic plasma. It was expected that each of these plasmas would impart a corresponding functionality on the fiber surface.

The plasma treatments were done in a gas flow reactor at low powers and ambient temperature. Excitation at 13.56 MHz was used at power levels of 50 watts for ten minutes. Gas flow rates were typically 20 sccm; system pressure was 500 mTorr. Plasma was excited in a tee-shaped reactor by means of an external coil on the stem of the tee. The yarns were wound around an open glass bobbin located just downstream of the glow region.

The TRI Microbond Experiment

The microbond technique involves depositing a small amount of resin onto the surface of a fiber in the form of a droplet which forms concentrically around the fiber in the shape of an ellipsoid. After appropriate hardening or curing, the fiber diameter and the droplet length are measured with the aid of an optical microscope to determine the embedment area. The fiber is pulled out of the resin droplet using a special device to grip the droplet bonded to the fiber (Fig. 1). This device consists of two adjustable plates that form the slit of a microvise that is attached to a vertical drive system. The plates are positioned just above the droplet and the slit is narrowed symmetrically until the plates just make contact with the fiber. As the plates move downward, an initial frictional force between the fiber and the shearing plates is registered, indicating that the slit is touching the fiber so that the droplet has little chance of slipping through. As the shearing plates continue to move downward, they encounter the droplet and exert a downward shearing force on it. Upon debonding, the pull-out force is recorded. Debonding force is calculated by subtracting the initial frictional force from the measured force. Interfacial shear strength is calculated by taking the ratio of debonding force and embedment area.

FORCE CELL

JAWS OF MICROVISE
(moving downward)

EMBEDDED
LENGTH (ℓ)
(~30-200 μm)

MICRODROPLET

FIBER DIAMETER (d)
(~10 μm)
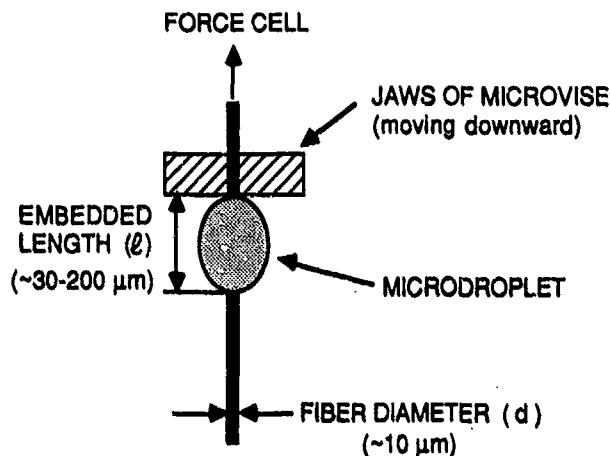
Figure 1.   Schematic of the TRI microbond arrangement.

In a typical experiment, 10-50 specimens are measured. The collection of individual shear strength values form a Gaussian type of distribution. Considerable evidence has been obtained to establish that these shear strength distributions are real variations in bond strength and not a reflection of systematic experimental errors [9]. The distributions are believed to be due to fiber surface hoterogeneity [13]. The distributions may be used to provide comparisons between differing fiber/resin systems, or the data points may be used as an aggregate to calculate and compare average shear strengths.

RESULTS AND DISCUSSION

Our preliminary characterization of the treated fiber surfaces involved scanning electron microscopy (SEM). Figure 2 shows a representative comparison of untreated Kevlar 49 with plasma-treated fibers. The surfaces of the treated fibers are coarse and grainy, due either to chemical surface modification or to surface deposition. Figure 3 compares Spectra 1000 with and without plasma treatment. With these fibers it seems that, in addition to surface modification and/or surface deposition, microcavitation of the surface has also taken place. The SEM micrographs also show that for Spectra 1000 fibers the surface treatment is quite uniform, while for Kevlar 49 the surface is not uniformly treated. Although further analysis of the fiber surface is needed to identify the nature of the fiber surface modification, these micrographs clearly establish that the fiber surface has indeed been modified.
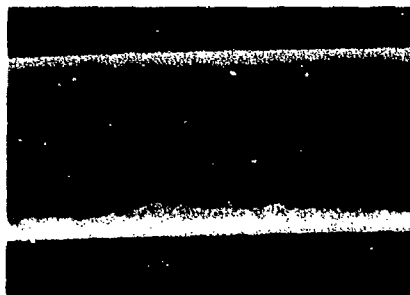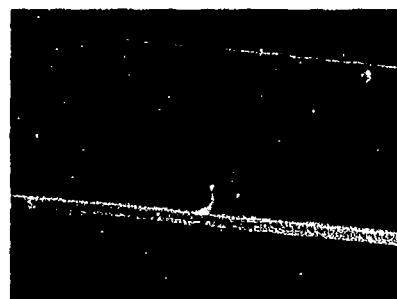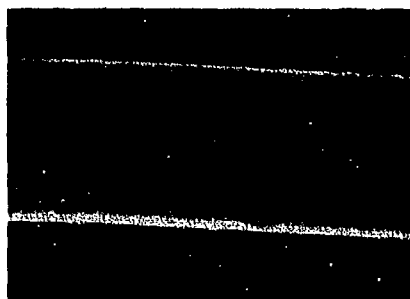
Figure 2. SEMs of Kevlar 49 filaments (2280x).

Top: Untreated.
Bottom: Treated, acid plasma.

Figure 3. SEMs of Spectra 1000 filaments.

Top: Untreated (760x).
Bottom: Acid plasma (1420x).

To determine the efficacy of the surface treatments in improving fiber adhesion with epoxy resin, we measured interfacial shear strengths between Epon 828 and both untreated and plasma-treated Kevlar 49 and Spectra 1000. Kevlar 49/Epon 828 microdroplets were cured, using methylenedianiline as the curing agent, at 80°C for two hours and 150°C for three hours. Due to the lower melting temperature of Spectra fibers, the Spectra/Epon 828 specimens were cured at 70°C for 16 hours; we did control experiments to establish that full interfacial bond strength can also be attained by curing Epon 828 at this lower temperature under these conditions.

Shear strength distributions normalized with respect to the average shear strengths are shown in Figure 4 for untreated and typical plasma-treated Kevlar 49 and Spectra 1000 filaments with Epon 828. The width of the shear strength distributions for the controls are somewhat narrower than those for the plasma-treated fibers, implying that the treated fibers have a greater degree of surface heterogeneity. This is consistent with the SEM observations.
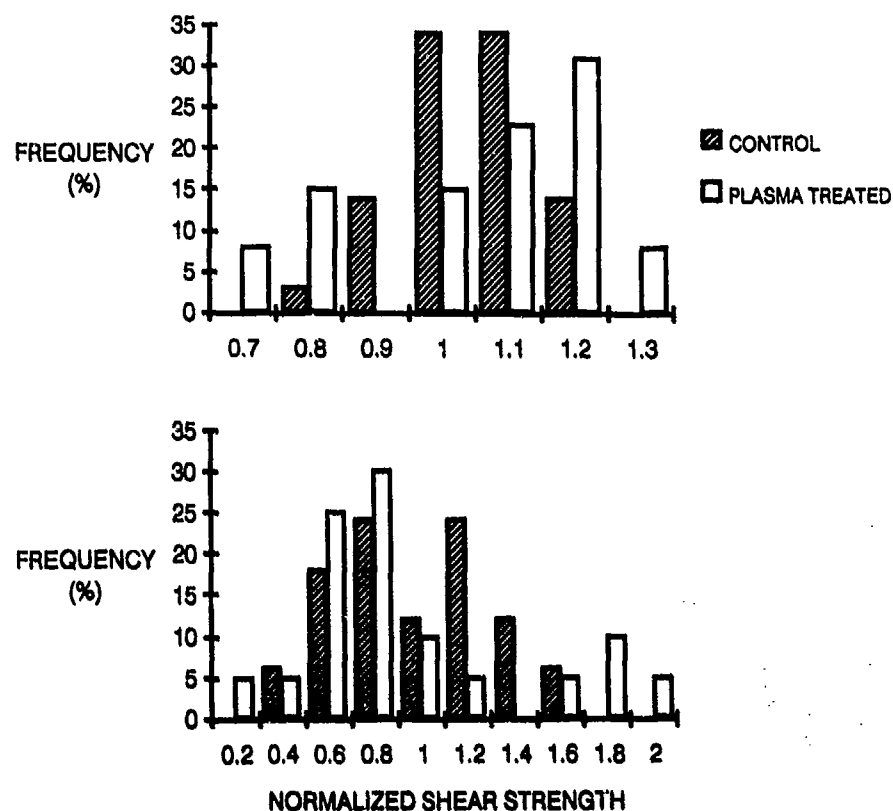
Figure 4. Normalized shear strength distributions for untreated and plasma-treated filaments.

Top: Kevlar 49. Bottom: Spectra 1000.

Average interfacial shear strengths for untreated and plasma-treated Spectra 1000 and Kevlar 49 are summarized in Table I. The bond strengths with Spectra 1000 clearly show a very significant improvement in interfacial adhesion for all the plasma treatments. For neutral plasma-treated fiber, the bond strength has increased several-fold. Shear strength data for Kevlar 49 also show a consistent significant improvement in interfacial bonding as a result of plasma treatment. It should be pointed out that the increases in bond strength, for both Kevlar and Spectra, are higher than we have observed for any other type of fiber surface treatment.

It is important to note that significant increases in interfacial shear strength were observed for all the plasma-treated fibers irrespective of the chemical nature of the ionized gas. Based upon this observation, it may be hypothesized that the adhesive bond strength was improved due to texturing of the fiber surface. Some roughening of the surface is observed in the SEM and might account for increased frictional resistance or bonding between the fiber and resin.

TABLE I

MICROBOND DATA FOR PLASMA-TREATED SPECTRA 1000 AND KEVLAR 49 FIBER WITH EPON 828 MATRIX RESIN

Treatment	Average interfacial shear strength τ $\pm$ 95% confidence interval, MPa	τ (plasma-treated)/ τ (untreated)
Spectra 1000/Epon 828		
Untreated (control)	1.09 ± 0.29	-
Oxidizing plasma	8.15 ± 2.20	7.5
Reducing plasma-I	7.07 ± 1.86	6.5
Reducing plasma-II	5.20 ± 1.30	4.8
Neutral plasma	8.61 ± 1.86	7.9
Hydrophilic plasma	4.33 ± 1.10	4.0
Kevlar 49/Epon 828		
Untreated (control)	29.66 ± 1.14	-
Oxidizing plasma	57.47 ± 5.45	1.9
Reducing plasma-I	53.91 ± 5.30	1.8
Reducing plasma-II	53.50 ± 4.95	1.8
Hydrophilic plasma	45.41 ± 5.21	1.5

Alternatively, although different gas mixtures were used to create oxidizing, reducing, and neutral plasmas, the action of any plasma results in the formation of very active surface species. When the fiber is brought out of the reactor and contacts ambient air, oxidation could occur. This might render even the reduced surfaces oxidized. A relevant observation has been made by Gerenser [14]: polyethylene treated in an argon plasma showed no C_{1s} broadening toward higher binding energies nor any detectable O_{1s} signal when XPS analysis was performed without breaking vacuum. Brief exposure to air caused the plasma-treated polyethylene surface to show 2% oxygen. Further study of our fibers will be needed to sort out the cause of the observed increases in interfacial shear strength.

ACKNOWLEDGEMENTS

REFERENCES

1. R. E. Allred, Sc.D. Thesis, Massachusetts Institute of Technology, Cambridge, Mass., February 1983.
2. R. E. Allred, E. W. Merrill, and D. K. Roylance, "Molecular Characterization of Composite Interfaces," edited by H. Ishida and G. Kumar, (Plenum Press, New York, 1985), pp. 333-375.
3. T. Yasuda, N. Gazicki, and H. Yasuda, J. Appl. Polym. Sci., Appl. Polym. Symp. 38, 201 (1984).
4. T. Yasuda, K. Yoshida, T. Okuno, and H. Yasuda, J. Polym. Sci., Polym. Physics Ed. 26, 2061 (1988).
5. S. P. Wesson and R. E. Allred, ACS Preprint - Polym. Mat. Sci. Eng. 58, 650 (1988).
6. S. L. Kaplan, P. W. Rose, H. X. Nguyen, and H. W. Chang, Proc. 33rd International SAMPE Symposium, 1988, p. 551.
7. H. X. Nguyen, C. C. Weedon, and H. W. Chang, Proc. 34th International SAMPE Symposium, 1989, p. 1603.
8. B. Miller, P. Muri, and L. Rebenfeld, Comp. Sci. Tech. 28, 17 (1987).
9. U. Gaur and B. Miller, Comp. Sci. Tech. 34, 35 (1989).
10. U. Gaur, G. P. Desio, and B. Miller, Proc. of SPE ANTEC '89, 1513 (1989).
11. K. P. McAlea and G. J. Nusio, Polym. Comp. 9, 285 (1988).
12. L. S. Penn, G. C. Tesoro, and H. X. Zhou, Polym. Comp. 9, 184 (1988).
13. U. Gaur and B. Miller, Proc. of Third International Conference on Comp. Interfaces, Cleveland, OH, May 1990 (to be published).
14. L. J. Gerenser, J. Adhesion Sci. Tech. 1 (4), 303 (1987).

EFFECT OF Ti+, Ar+, N+ AND He+ ION IMPLANTATION ON ARAMID FIBER ADHESIVE PROPERTIES

J. Kalantar*, D. S. Grummon**, L. T. Drzal*, I. H. Loh‡ and R. A. Moody‡‡

* Department of Chemical Engineering, Michigan State University
   East Lansing, Michigan 48824.
** Department of Metallurgy, Mechanics and Materials Science, MSU
‡ Advanced Surface Technology, Incorporated, Waltham MA 02154
‡‡ Spire Corporation, Patriots Park/Bedford, MA 01730.

INTRODUCTION

Composites made with high performance polymer fibers can achieve axial properties comparable to those which use inorganic reinforcements, but with somewhat inferior interfacial properties. A high degree of chain alignment in polyaramids, such as Kevlar, produces weak interactions between adjacent polymers, resulting in poor transverse strength in the fiber, and low interfacial shear strength in composite systems. The latter controls many composite properties, such as transverse, shear and flexural strengths. Also, by reducing the tendency to form weak interfacial boundary layers, good fiber-matrix adhesion can enhance environmental stability. For these reasons, modifications to reinforcement fiber surfaces that promote fiber-matrix adhesion are frequently used to improve the performance of composites.

In this study, direct ion implantation has been investigated as a fiber surface modification technique to enhance the interfacial properties between aramid polymer fibers and epoxy matrices. Though the technology of ion implantation has been extensively developed for doping of semiconductors, and has found some use for enhancing wear and corrosion resistance of metals, the high cost of the process has admittedly discouraged extensive study of ion beam processing of *structural* materials, especially when large surface areas are involved. The use of the technique on polymer-fiber and polymer-metal adhesion problems has however, been successful in some systems [1,2], and could eventually become cost-effective if processes could be developed which used low dose irradiations at high beam current and moderate accelerating potential.

Puglisi [3] has reviewed some of the effects of ion beams on polymeric substrates. Nuclear and electronic interactions stop energetic incident ions within the target, or cause it to recoil, and usually sputter material from the surface. In polymers, low molecular weight fragments may also be lost as volatiles. The spatial distribution of implanted matter and deposited energy are determined by accelerating potential, ion mass, ion flux, and the polymer target chemistry. As a class, polymeric materials display substantial variability in their response to excitation by ion beams, and nuclear and electronic interactions may be difficult to distinguish. Ion doses greater than 10^{14} cm^{-2} may begin to produce amorphous carbonized products, leaving affected regions with only partial memory of their original composition. At these moderate to high doses, nuclear interactions generate many random atomic displacements, producing large, highly excited metastable defect complexes, while electronic interactions tend to drive the system back toward chemical stability. At doses lower than 10^{13} cm^{-2}, nuclear and electronic interactions can produce both scission (bond-breaking to products such as H_2 and C_2H_2), and aggregation reactions (which increase molecular weight). The relative extent of scission or aggregation depends on the chemistry of the target; for example, scission reactions dominate for polymethylmethacrylate, but for polystyrene the aggregation reactions

prevail [3]. Though much has been learned, ion implantation of macromolecular substrates is of relatively recent interest and fundamentals of ion-polymer interactions are not yet well established.

This study has been undertaken to understand the ways in which the effects of ion irradiation can be exploited to modify fiber-matrix interfacial properties in aramid-epoxy composites. The versatility of the technique, the ability of ion implantation to produce non-equilibrium conditions in shallow, controllable surface layers without sharp interfacial gradients, and the capacity of irradiation to alter the physical morphology of the free surface, all contribute to the attractiveness of the process. Previous work on polyethylene [1,2], in which adhesion problems are severe, has demonstrated that ion implantation has substantial potential for improving adhesion performance of the fiber-matrix interface. Here, we report experimental findings on polyaramid fibers, with particular focus on the effects of ion implantation on surface composition, fiber-matrix interfacial shear strength, epoxy composite failure modes, and failure morphologies. The studies include experiments with 30 to 400 KeV Ti^+, Ar^+, He^+ and N^+ ions implanted in polyaramid fibers to doses ranging from 10^{12} to 10^{15} ions/cm^2. Though our results are not particularly encouraging with respect to the achievement of large improvements in polyaramid interfacial shear strength properties, the findings reveal additional detail in the complex picture of the fiber-matrix interphases in materials, such as Kevlar, which have a pronounced skin-core structure. It is shown that fiber-matrix adhesion may be enhanced *without* concomitant improvement in interfacial shear strength, when the result of the surface modification is simply to drive the locus of failure into the interior of the fiber.

EXPERIMENTAL METHODS

Kevlar-49, in both fiber and fabric forms, from E.I. duPont de Nemours, Wilmington, DE was soxhlet extracted in absolute ethanol for 24 hours and dried overnight at 400K to eliminate interference by fiber sizing. Individual fibers were laid up on a 75 mm square aluminum frame which held them in contact with a chilled aluminum heat sink. In this way, several hundred lengths of fiber (or about 60 cm^2 of fabric) could be irradiated on both sides by inverting the frame between separate implantations. Irradiations were performed at Spire Corporation, Bedford MA, in a medium current implanter. Ion species, doses and energies, together with computed projected ranges for each of the implantations, are summarized in Table 1. Beam currents ranged between 0.2 to 5 μA, and irradiation temperatures were held to below 375 K. Subsequent XPS studies showed no presence of re-sputtered aluminum on any of the irradiated samples. After irradiation, the fibers were left on their carriers and sealed in nitrogen-purged bags to prevent absorption of atmospheric moisture. Most of the implanted fibers were composited within four days after irradiation. Others were allowed to age prior to interfacial shear strength testing to look for any time decay in the irradiation effects.

Table I: Schedule of Implantations

Ion	Energy keV	Dose ions/cm	Ion Projected Range, nm
N+	30	1×10^{14}	102
N+	30	5×10^{14}	102
N+	30	1×10^{15}	102
Ar+	75	1×10^{15}	100
Ti +	100	1×10^{15}	111
N+	100	2×10^{13}	320
N+	100	1×10^{14}	320
N+	390	2×10^{12}	937
N+	400	5×10^{12}	954
N+	400	2×10^{13}	954
N+	400	1×10^{14}	954
N+	390	2×10^{14}	937
He+	390	1×10^{13}	1550

Single-fiber dog-bone specimens for interfacial shear strength studies were prepared according to procedures described elsewhere [4]. D.E.R. 331 DGEBA epoxy from Dow Chemical Co., Midland, MI, was chosen for

the matrix to enable comparison with established baseline data from a previous study [5]. Two curing agents, m-phenylenediamine (Aldrich, Milwaukee, WI), and diethyltoluenediamine (Ethyl Corp., Baton Rouge, LA) were combined with the epoxy resin and the system cured for 3 hours at 448K. In addition, single fiber curved neck specimens were fabricated for use in compression tests as described in reference [6].

Fiber-matrix interfacial morphology was examined by transmission electron microscopy (TEM) of ultramicrotomed thin sections cut normal to the fiber long-axis. Chemical characterization of the surface treated fibers was obtained by X-ray photoelectron spectroscopy (XPS) using fabric specimens.

Determinations of interfacial shear strength were made by a critical length measurement technique [4,5] in which a single fiber composite specimen was deformed in tension until multiple fiber breaks were observed by optical microscopy. The interfacial shear strength, τ, is inversely proportional to the the average length between breaks in the fiber (the critical length, l_c) according to:

$$\tau = \sigma_f \cdot d \; / \; [\; 2 \, l_c] \qquad (1)$$

where σ_f is the fiber tensile strength and d is the fiber diameter ($12.5 \; ^{+}/_{-} \; 0.6 \; \mu m$ for the fibers used in this study). Single fiber compressive strengths were determined by recording loads which produce fiber kinks in single fiber curved-neck specimens. In this case, compressive strength, σ_c, is a function of failure load (P), the fiber and matrix cross-sectional areas (A_f and A_m), and the ratio of the elastic modulii (E_m and E_f), according to [6]:

$$\sigma_c = P \; / \; [\; A_f + E_m \cdot A_m \; / \; E_f \;] \qquad (2)$$

RESULTS AND DISCUSSION

Fibers implanted with nitrogen at doses at or above 1×10^{14} ions/cm^2 show contrast effects in transmission electron micrographs which appear as a darkening in the fiber surface region, corresponding roughly to the ion projected range. Figure 1 is an example showing this darkened region in a composited fiber[1] prepared by ultramicrotomy. Such surface zones have also been reported in ion irradiated polyethylene [7] and were attributed to the formation of pregraphitic or graphitic particles containing stabilized free radicals. At doses at or below 10^{13} cm^{-2} of 400 keV N$^+$, this near surface darkening is absent in irradiated Kevlar, as can be seen in Figure 2. The effect of irradiation on elemental composition, determined by XPS experiments, is shown in Figure 3 for fibers (in fabric form) implanted with various doses of 400 keV nitrogen For nitrogen implants, increased carbon concentration at the surface of irradiated specimens occurs for doses corresponding to the onset of surface darkening in TEM foils, i.e, about 10^{14} ions/cm^2. This compositional shift is supportive evidence that the surface darkening in TEM foils is, in fact, due to carbonization. Doses of 10^{13} ions/cm^2 and below do not show significant surface composition changes, again in agreement with the TEM observations, indicating that significant carbonization occurs only when doses exceed 10^{13} N$^+$/cm^2. Implants of the less massive He$^+$ ions at 1×10^{13} ions/cm^2 produce smaller

---

[1] The darkened zone on this fiber appears only on the left side due to accidental shielding by an adjacent fiber. The falloff of the darkening effect seen at the center of the left hand edge of the fiber corresponds to a region where the incident ion beam was tangent to the fiber for both the obverse and the reverse irradiations, producing less efficient implantation.

composition shifts, consistent with the findings of Venkatesan et al [8] for less massive projectiles.
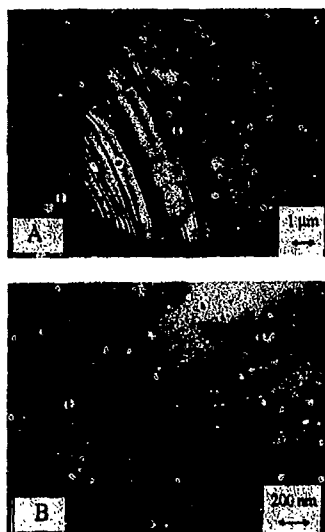
Fig. 1. Kevlar fiber irradiated with 10^{14}cm^{-2} of N$^+$ showing darkened surface zone. Above: whole fiber (K) in matrix (E). Detail below.
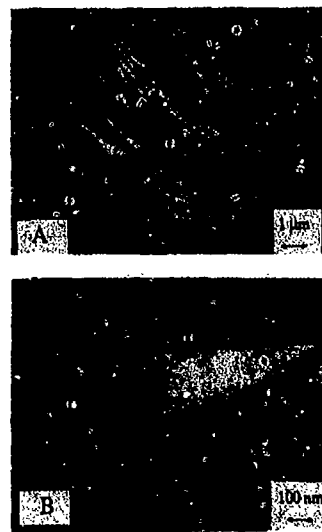
Fig. 2. Similar irradiation with at dose of 10^{13} cm^{-2}: surface darkening is absent. Arrows show microtoming direction.

Failure mode of the interphase is also affected when higher dose irradiations produce apparent carbonization. In general, untreated aramid fibers in epoxy matrices will show interfacial fiber-matrix failure with some surface cohesive fibrillations on the fiber [5]. The TEM image in Figure 4, for example, shows an untreated aramid fiber composite in which the interfacial separations are parallel to the sectioning direction. Cohesive fiber failures are seen to occur near the fiber-matrix parting areas. A similar failure mode was observed for the low dose (<10^{13} ions/cm^2) implanted fibers in this study. In contrast, for carbonizing implantations (>10^{13} N$^+$/cm^2), the fiber-matrix failure mode is more cohesive. That is, the fiber-matrix interface remains largely intact and shear failure occurs deeper within the fiber. TEM micrographs of a composited fiber implanted with 10^{14} N$^+$/cm^2 at 400 keV, made after failure in interfacial shear strength tests, show this behavior in Figure 5. Here, the implanted fiber exterior has adhered well to the matrix and the locus of failure has shifted toward the fiber interior. Shear failure occured within the implanted surface layer of
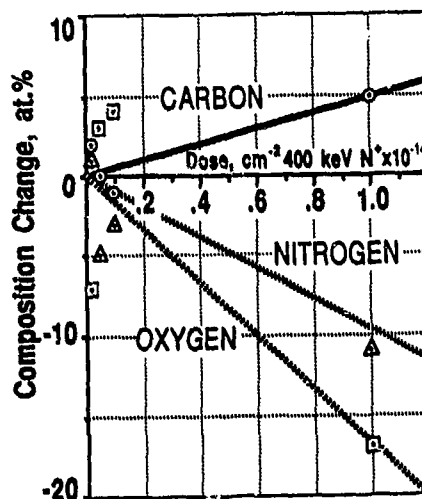
Fig. 3. Elemental composition shifts for N$^+$ implanted Kevlar as a function of ion dose.

the fiber. Irradiation with 1×10^{15} cm^{-2} of 400 keV Ti$^+$ produced similar results.
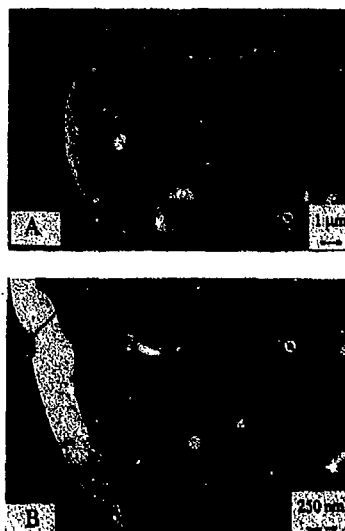
Fig. 4. Untreated Kevlar fiber showing interfacial separations and cohesive fibrillations.

Fig. 5. Kevlar fiber (K) irradateiad with 10^{14} N$^+$ cm^{-2} at 400 keV·: the locus of failure has been shifted to the fiber

This apparent difference between the failure modes of high-dose carbonizing implantations and the lower dose implantations may be a result of increased microscopic porosity of the carbonized surface. This is consistent with the relative insensitivity of ISS levels to aging of the fibers, evident in the data shown Figure 6. Here, the effect of ion irradiation on interfacial shear strength is given for fibers implanted with 10^{14} N$^+$/cm^2 at 30, 100, and 390 keV, which were composited either within 4 days of irradiation, or aged in air for one month. There is little apparent effect of aging beyond four days. Implantations of 1×10^{14} ions/cm^2 produced some degradation of interfacial shear strength which occured even though subsequent TEM study showed fiber-matrix adhesion levels to have improved. It is possible that carbonization may degrade the fiber's near surface mechanical properties sufficiently to account for the shift in the locus of failure to the fiber weakened interior when there is an improved interfacial bond. Strength measurements on implanted fibers show that ion irradiation degrades tensile properties even at doses lower than those which produce pronounced polymer carbonization. Table II shows tensile strength data for fibers with various ion beam surface modifications.

Fig. 6. Interfacial shear strength of Kevlar-epoxy composites for fibers implanted with 10^{14} N$^+$ cm^{-2} as a function of energy.

along with rough subjective indications of their extent of carbonization observed by TEM. In general, ion implantation produces tensile strength losses that increase with the implantation depth (energy) and dose. Loss of interfacial shear strength, however, levels off at implantation energies above 100 keV. For the low dose irradiations, all fibers implanted at 400 keV (~1 to 1.5 μm implantation depth) show a loss of tensile strength, despite the absence of the surface layer carbonization. This suggests that scission reactions dominate the chemistry of ion-target interactions in polyaramids, as they reportedly do in the case of ion irradiated polymethylmethacrylate [8].

Compressive strengths are also listed for various irradiation conditions in Table II. Though the measurement technique is approximate, it appears that compressive strengths, which are poor to begin with in polyaramid fibers, are not greatly affected by irradiation at doses below 1×10^{15} ions/cm^2. Since compressive properties are largely controlled by the shear resistance of the fiber [9], aggregation reactions which produce extensive cross-linking ought to improve compressive strength. If scission reactions do indeed dominate ion interactions with polyaramids, as the compressive strength and carbonization data suggest, then mechanical property improvements which depend on cross-linking by aggregation reactions may be difficult to achieve using ion irradiation.

Table II

Tensile and Compressive Strengths of Irradiated Kevlar

Species	Dose	Energy keV	Compressive Strength, GPa	Tensile Strength, GPa	Comments
CONTROL			.752 +/-.168	2.88 +/-.31	
N+	1x10^{14}	30	.746 +/-.164	2.51 +/-.34	
N+	5x10^{14}	30	.743 +/-.140	2.82 +/-.30	Carbonized
N+	1x10^{15}	30	.706 +/-.128	2.98 +/-.31	Carbonized
Ar+	1x10^{15}	75	.690 +/-.096	2.74 +/-.20	Carbonized
N+	2x10^{13}	100	.820 +/-.084	2.77 +/-.36	
N+	1x10^{14}	100	.777 +/-.107	2.59 +/-.30	Carbonized
Ti+	1x10^{15}	100	.745 +/-.161	3.00 +/-.26	Carbonized
N+	2x10^{12}	390	.728 +/-.061	2.67 +/-.27	
N+	5x10^{12}	400	.750 +/-.070	2.72 +/-.25	
N+	2x10^{13}	400	.785 +/-.104	2.46 +/-.17	
Ho+	1x10^{13}	390	.713 +/-.133	2.50 +/-.32	
N+	1x10^{14}	400	.748 +/-.083	2.28 +/-.13	Carbonized
N+	2x10^{14}	390	.376 +/-.066	2.27 +/-.13	Carbonized

CONCLUSIONS

Results of this study indicate that surface carbonization of polyaramid fibers takes place at ion doses above 10^{14} ions/cm^2. Carbonization improves aramid-epoxy interfacial adhesion but at the same time produces a weaker boundary layer within the fiber. As a result there is little, if any, net increase in interfacial shear strength in the composite. Loss of strength in the fiber surface probably results from the domination of scission reactions over aggregation reactions during ion-polyaramid interaction. Increased adhesion, which is relatively insensitive to the atmospheric aging of the fiber, may arise from morphological changes at the fiber surface. In addition, surface reactivity and surface energy may play a role, and are currently under study.

REFERENCES

1. A Ozzello, D.S. Grummon, J. Kalantar, L.T. Drzal, I.H. Loh and R.A. Moody, MRS Proc. 153, p. 217 (1989).
2. P. Bodo and J.E. Sundgren, J. Appl. Phys. 60, p. 1161 (1986).
3. O. Puglisi, Mater. Sci. Eng., B2, p. 167 (1989).
4. L. T. Drzal, M. J. Rich, J. D. Camping and W. J. Park, Proc. 35th Ann. Tech. Conf., Reinf. Plastics and Composites Inst. (Soc. of the Plastics Indus.) Paper 20-C (1980).
5. J. Kalantar and L.T. Drzal, J. Mater. Sci. (in press).
6. L. T. Drzal, AFWAL-TR-86-4003 (1986).
7. M. Schaible, H. Hayden and J. Tanaka, IEEE Trans. on Elec. Insulators, EI-22, No. 6, pp. 699-708 (1987).
8. T. Venkatesan, L. Calcagno, B.S. Elman and G. Foti, Ion Beam Modification of Insulators, Elsevier, New York, p. 301 (1987).
9. S. J. Deteresa, "The Axial Strength of High Performance Polymer Fibers", Ph.D. dissertation, Univ. of Massachusetts, 1985.

THE EFFECTS OF FIBER SURFACE TREATMENTS BY A COLD PLASMA IN CARBON FIBER/BISMALEIMIDE COMPOSITES

Tao C. Chang and B. Z. Jang
Composites Research Labs, 201 Ross Hall
Materials Engineering Program
Auburn University, AL 36849

ABSTRACT

The effects of plasma treatments on the physical and chemical characteristics of carbon fiber surface and on the mechanical properties of carbon fiber/bismaleimide (BMI) resin composites were investigated. Scanning tunneling microscopy (STM), scanning electron microscopy (SEM), X-Ray Photoelectron Spectroscopy (XPS), and wettability measurements were applied for fiber surface characterization. Oxygen plasmas were found to be effective in enhancing the interfacial adhesion between carbon fiber and BMI matrix. Possible mechanisms of interfacial adhesion promotion were suggested and discussed.

INTRODUCTION

The mechanical properties of a fiber-resin composite depend not only on the properties of its constituents, but also on the fiber-matrix interfacial adhesion. An adequate interfacial bonding is required to ensure the effective load transfer between fiber and matrix to effectively utilize the great strength and stiffness of the fibers. However, the adhesion between untreated graphite fibers and resins is usually poor. A variety of surface treatment techniques have been developed to improve the interfacial bonding in carbon fiber-reinforced epoxy composites [1]. Much less work has been done on the interface between fiber and other resin systems. The increasing demand for higher temperature matrix resins has motivated us to choose a two-component bismaleimide system as the matrix material in this work.

Cold-plasma technology has been extensively applied in the fields of semiconductor and other material surface treatments. In composite applications, plasma treatments of ultrahigh modulus polyethylene fibers [2] and aramid fibers [3] have been used to improve the adhesion of fibers to resins. Plasma coatings of propylene [4], acrylonitrile [5], and styrene [5] have also shown positive effects on the properties of composites and reinforcements. In this study, oxygen plasma was used to treat the surface of graphite fibers since this technique is effective and yet relatively simple and inexpensive. The primary goal of this research was to explore the advantages and limitations of utilizing the plasma reaction technique for modifying interfacial adhesion in composites. Emphasis is placed on the determination of the changes in chemical and physical states of the graphite fiber surface in response to plasma treatments and the effects of these changes on the composite properties.

EXPERIMENTAL

Materials

PAN-based untreated and unsized high-strength graphite fibers (Hercules, AU4-12K) were used throughout this investigation. A two-component

bismaleimide resin (CIBA-GEIGY, Matrimid™ 5292) was used as the matrix material. These two components are 4,4'Bismaleimidodiphenyl-methane (component A) and O,O'-Diallyl Bisphenol A (component B), respectively. The ratio of A to B was 113/85 parts by weight (pbw), as recommended by the manufacturer [6].

Sample Preparation

Graphite fiber yarns were carefully wrapped around a stainless steel frame with inside dimensions of 7.62cm x 10.16cm x 0.1cm. The frame along with the fiber yarns were then placed inside the chamber of a plasma reactor (Technic West Inc., PEII-A). The reactor is composed of a 40 KHz radio frequency generator with two parallel plate electrodes. The plasma treatment was conducted typically at an input power of 50 watts under a pressure of 53.3 Pa with an oxygen flow rate of 1.076×10^{21} molecules per minute. Treatment periods range from a few seconds to an hour.

Upon completion of the plasma treating process, the fiber-wrapped frame was removed from the reaction chamber. The yarns which were laid up parallel to each other on the steel frame were then impregnated with a well mixed BMI resin to produce a small prepreg layer. Four prepreg layers for each treatment time were stacked into a mold, which were then compression molded under a contact pressure with the temperature being increased from room temperature to 177 °C at a rate of 3 °C/min. The mold was held at 177 °C for 10-15 minutes under a light contact pressure, then a pressure of 0.69 Mpa was applied and held for 1 hour. The mold was then cooled to room temperature under this pressure. The de-molded laminate was post-cured in an air circulating oven at 200 °C for 2 hrs, then at 250 °C for 6 hrs.

Mechanical Testing

Each laminate was fabricated into three transverse tensile specimens each with the dimensions of 10cm x 2cm x 0.1cm. Transverse tensile testing was found [4] to be one of the more sensitive techniques for assessing the relative interfacial adhesion strength in composites. The tensile strength of each filament sample was obtained by testing at least 20 specimens. This single-filament tensile test was conducted to determine if and when plasma treatments would become detrimental to the fiber strength.

Fiber Surface Characterization

The surface texture of fibers, before and after plasma treatments, were examined by using a scanning electron microscope (SEM) and a scanning electron tunneling microscope (STM). XPS (Kratos, model XSAM 800) analysis was also conducted to study the variations of functionality on the carbon fiber surface. Elemental surface concentrations can be calculated using the corrected XPS peak areas.

The surface energy of the graphite fibers was determined by measuring the contact angles of a variety of liquids according to the method proposed by Kaelble [7]. Using the Wihelmy plate technique [8], the contact force ΔM (μgm) between a single fiber of C circumference and a liquid of surface tension r_{Lv} is described by the following equation

$$\Delta M = \frac{C \ r_{Lv} \cos\theta}{g} \qquad (1)$$

where θ is the advancing liquid-solid contact angle and g= 980.6 dyne/cm. Since M, r_{Lv} and C can be evaluated independently, $\cos\theta$ can be calculated from Eq.1. In this study, M is measured by using an electrobalance (Cahn, model 2000), and C by microscopy. The apparatus for the Wilhemy technique is shown in Figure 1 [8]. The surface energies of solids and liquids are considered to be the sum of separate dispersive (London-d) and polar (Keesom-p) contributions, which can be calculated from a two-component model discussed elsewhere [7]. Table 1 lists surface tension properties of test liquids used in this study.

RESULTS AND DISCUSSION

Test Liquid	r_{LV}	r_{LV}^d	r_{LV}^p	$2a_L$	$b_1/a_L^{1/2}$
			dyn/cm		(dyn/cm)
Water	72.5	21.8	51.0	9.34	1.53
Glycerol	64.0	34.0	30.0	11.66	0.94
Formamide	58.3	32.3	26.0	11.37	0.90
Ethylene glycol	48.3	29.3	19.0	10.83	0.81
Octane	21.3	21.3	0.00	9.23	0.00

Table I.
Surface tension properties of test liquids at 20 °C

Figure 2 indicates that, as the treatment time increases, the transverse tensile strength increases gradually from 2.20 MPa (untreated) to 4.71 MPa (20 minute treated). Since the transverse tensile strength of a composite is a resin- and fiber-dominated property, this observed increasing trend with the same resin is obviously due to the improvement of interfacial adhesion provided for by the plasma treatments. The technique of oxygen plasma reaction does provide an effective means to enhance the adhesion between graphite fibers and the BMI resin. Nevertheless, since a plasma consists of various highly energetic species, exposure of fibers to the plasmas for an extended period of time could produce a negative effect. As shown in Fig 3, the average tensile strength of fibers was slightly degraded from 3.8 GPa (untreated) to 3.01 GPa (20 minute treated). At given plasma reaction conditions, there appears to exist an optimal treatment time where the interfacial adhesion can be significantly improved without a reduction in filament strength. This is consistent with some of our previous research results [4].

Representative topographic features of carbon fiber surface, as revealed by SEM, are shown in Figure 4. When the treatment time was short (e.g. less than half a minute), the fiber surface seemed to become slightly smoother, possibly exhibiting the cleaning effect of a plasma. Removal of the contaminants on the fiber surface may facilitate a better resin-fiber contact (wettability) and promote stronger van der Waal's forces. The fiber surface becomes increasingly rougher when the treatment time further increases. The increased fiber roughness, in the form of porosity, should promote mechanical keying or interlocking mechanism between the fiber and the matrix. Although the results of the fiber surface topology study by using STM should be considered preliminary at the present time, the observations appear to support the above findings of SEM. Three line-printed diagrams showing the surface profile of carbon fibers after 0, 5, and 60 minutes of treatments are presented in Fig 5.

X-ray photoelectron and Auger spectroscopic analyses of graphite fiber surfaces have shown the presence of oxygen on the surface of graphite fibers [9]. A semi-quantitative comparison of relative atomic concentration of oxygen and carbon on the fiber surface is shown in Table 2. Apparently, the oxygen concentration on the surface of fibers has been increased by oxygen plasma treatment.

From Kaelble's method [7], a best fit straight line is obtained for each data set using linear regression analysis. The slope and the intercept of this straight line therefore can be used to determine the r_{sv}^p, r_{sv}^d, and r_{sv} for each treatment case. In Table 3 are listed the average values of fiber surface tension for varying treatment time. Close scrutiny of the polar and dispersive components of the surface free energy indicates that the dispersive portion decreases to certain extent then levels off. But the polar component increases with treatment time up to 5 minutes then decreases afterward, so does the total energy. The reason for the decreasing polar part after 10 minutes treatment is still unknown. A smooth substrate

STRENGTH (GPa)

OXYGEN PLASMA TREATMENT TIME (min)
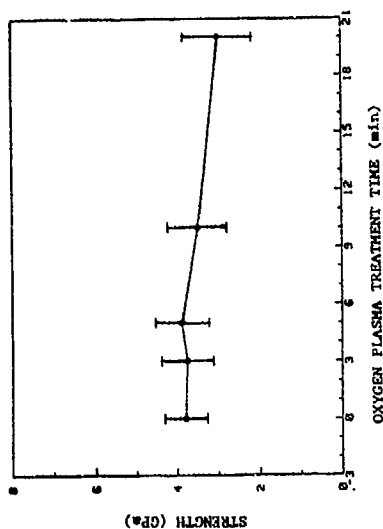
Figure 3. The results of single filament tensile test.

STRENGTH (MPa)

OXYGEN PLASMA TREATMENT TIME (min)
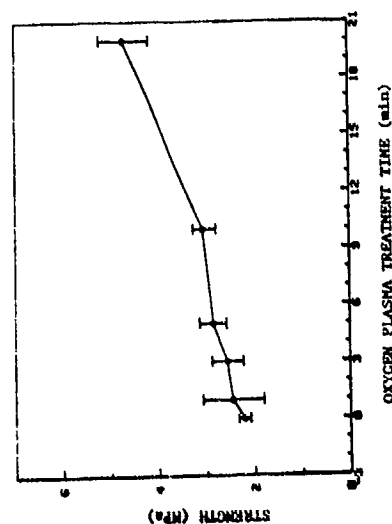
Figure 2. The results of transverse tensile test.

(b)

Figure 4.
The SEM micrographs of fiber surface for
(a) untreated and (b) 20 min. treated.

RECORDER

ELEVATOR

BALANCE

FIBER

LIQUID

Figure 1. The apparatus for Wilhemy technique.

(a)

1μm

1μm
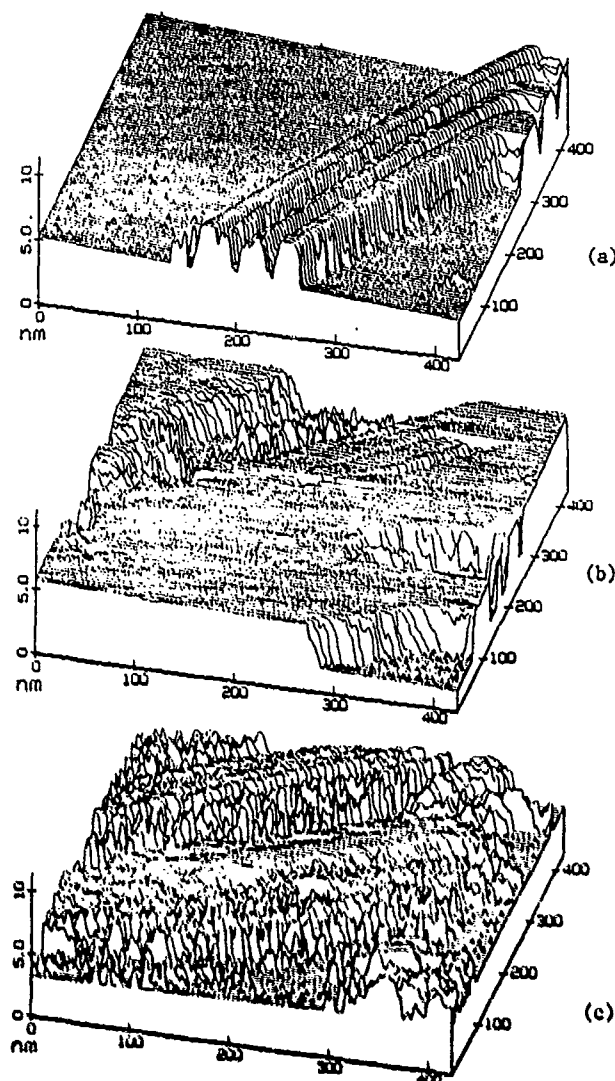
Figure 5. The STM lineplots of fiber surface profile for (a) untreated
(b) 5 min. treated and (c) 60 min. treated.

surface was usually assumed in contact angle measurements [10]. This
assumption may become unjustifiable for the samples treated for more than
five minutes that contain a high level of surface porosity. In general,
oxygen plasma treatment increases the oxygen content (by XPS) and the
polarity (by contact angle measurement) of the fiber surface despite the
lack of proportionality between these two results.

CONCLUSIONS

The effectiveness of plasma treatments in improving the interfacial
adhesion between the graphite fibers and the BMI resin has been
demonstrated. Given the same plasma reaction conditions, there appears to
exist an optimal time for balanced interfacial adhesion and tensile strength

Table III. Summary of fiber surface tension properties

Time of Plasma Treatment	$r_{sv}^d \pm s^d$ (dyn/cm)	$r_{sv}^p \pm s^p$ (dyn/cm)	$r_{sv} \pm s$ (dyn/cm)
Untreated	20.31±2.10	9.22±1.73	29.53±2.10
1 Min Treated	16.82±2.23	22.33±1.00	39.15±2.23
3 Min Treated	14.41±1.57	30.79±4.74	45.20±4.74
5 Min Treated	15.35±1.15	38.95±6.72	54.30±6.27
10 Min Treated	19.22±6.01	21.54±5.21	40.76±6.01
20 Min Treated	16.62±3.44	23.52±6.45	40.14±6.45

Table II. The relative oxygen and carbon atomic concentrations of various fibers by XPS.

Atomic Conc. %	Untreated	1 min.	3 min.	5 min.	10 min.	20 min.
O1s	19.6	20.22	20.27	22.27	23.27	25.71
C1s	80.38	79.78	79.73	77.23	76.73	74.29

of carbon fibers. The best plasma reaction conditions for improved composite properties have yet to be determined. The improvement in the interfacial adhesion strength as induced by the oxygen plasma treatments may be ascribed to: (a) the enhanced mechanical keying between fiber and matrix because of the increased roughness on the fiber surface, (b) the increased surface free energy which would promote the wettability of fiber by matrix, and (c) the possible removal of weak boundary layer on the fiber surface by plasma which provides a better fiber-resin contact for a greater van der Waals force and the possible chemical interaction between the fiber and the BMI resin.

REFERENCES

1. J. Delmonte, in Technology of Carbon and Graphite Fiber Composites, Ch.6, (Van Nostrand Reinhold Company, 1980).
2. N. H. Ladizesky, J. M. Ward and L. N. Phillips, Progr. Sci. Eng. Composi. Mater. 4th. 1, 203-210(1982).
3. R. E. Allred, E. L. Merril and D. K. Roylance. Polym. Prep. (ACS Div. Polym. Chem.), 24 (1), 223-224 (1983).
4. B. Z. Jang, H. Das, L. R. Hwang and T. C. Chang, in Interfaces in Polymer, Ceramic, and Metal Matrix Composites, edited by H. Ishida (Elsevier Science Publishing Co., Inc.,1988), pp. 319-333.
5. G. Dagli and N.-H. Sung, Polym. Compos., 10, 109-116(1989).
6. CIBA-GEIGY Corp. data sheet, 1985.
7. D. H. Kaelble, P. J. Dynes and E. H. Cirlin, J. Adhesion, 6, P. 23(1974).
8. A. W. Neumann, and R. J. Good, in Surface and Colloid Science, Vol. 11, pp. 31-91 (Plenum Press, New York, 1979).
9. F. Hopfgarten, Fiber Sci. Technol. 11(1978) P. 67.
10. J. D. Andrade, L. M. Smith, and D. E. Gregonis, in Surface and Interfacial Aspects of Biomedical Polymers, Ed. by J. D. Andrade (Plenum Press, New York, 1985), Vol. 1, p.249.

CORRELATION BETWEEN FIBRE SURFACE ENERGETICS AND FIBRE-MATRIX ADHESION IN CARBON FIBRE REINFORCED PEEK COMPOSITE

D J HODGE, B A MIDDLEMISS AND J A PEACOCK

ICI Wilton Materials Research Centre, PO Box 90, Wilton, Middlesbrough, Cleveland, UK

Abstract

Surface energies of carbon fibres at different levels at surface treatment have been determined by a wetting force technique and related to fibre-matrix adhesion in carbon fibre reinforced PEEK composite. The effect of oxidative surface treatment on the surface free energy is detailed, along with the changes in surface oxygen and nitrogen content, as determined by X-ray photoelectron spectroscopy (XPS). The work of adhesion has been calculated for the carbon fibres and thermoplastic, which correlate well with experimental determination of interfacial strength. The technique can therefore be used to predict adhesion levels in fibre reinforced composites.

Introduction

The fibre surface chemistry is an important parameter in influencing the adhesion between a fibre and polymeric matrix in a composite. The exact nature of the surface chemistry of carbon fibres is difficult to analyse quantitatively, but the elemental composition of the top 35A of fibre surface can be accurately determined using XPS (ESCA). Although useful in characterising fibre surfaces, the disadvantage of XPS is that the 35A sampling depth inevitably means that many of the atoms detected may not take part in the adhesion process to a matrix material. The logic which suggests

that an increase in oxygen and nitrogen content, as determined by XPS, increases the likelihood of interaction with the matrix is therefore only likely to be true up to a point.

Some progress has been made with XPS derivitisation techniques [1], to show the presence of specific functional groups.

A separate, but related, approach involves determination of the "effectiveness of the fibre surface chemistry" in forming adhesive bonds. Such information can be obtained through an appreciation of the surface energetics of the fibre surface.

This paper describes the determination of the polar and dispersive components of the surface energies of carbon fibres with non-optimised surface (A), controlled surface (B) and with additional surface treatment (C), using the method described by Faelble [2, 3] for analysing angles. The surface energies of a freshly extruded PEEK fibre were determined and the work of adhesion, W_a, between each carbon fibre and PEEK calculated. The W_a values can be compared to the value for the work of cohesion, W_c, for PEEK and related to the level of adhesion found in a corresponding CF-PEEK composite.

Theory

Measurement of Contact Angles

The contact angle, θ, when a liquid of surface energy γ_l wets a fibre of diameter d, can be determined from measurement of a wetting force, F, using the equation (4):

$$F = \pi d \, \gamma_l \cos \theta \tag{1}$$

Determination of Polar and Dispersive Components of Fibre Surface Energy

Surface energetic analyses of the fibres used in this study were
determined by measuring the contact angle of a variety of liquids having known
polar and dispersive components of their total surface free energy and
analysing the results according to Kaelble [2, 3]. This method assumes that
the total surface free energy across an interface γ^T can be split into
components corresponding to the non-polar or dispersive interactions γ^d and
the polar interactions γ^p

$$\gamma^T = \gamma^p + \gamma^d \tag{2}$$

The assumption generally holds for low surface energy solids such as
polymers.

The work of adhesion W_a between a fibre of surface energy γ_f and a liquid
of surface energy γ_l is defined by

$$W_a = \gamma_f + \gamma_l - \gamma_{fl} \tag{3}$$

Where γ_{fl} is the surface energy of the fibre-liquid interface. Using the
substitutions

$$\gamma_l = \gamma_l^d + \gamma_l^p = \alpha_l^2 + \beta_l^2 \tag{4}$$

and

$$\gamma_f = \gamma_f^d + \gamma_f^p = \alpha_f^2 + \beta_f^2 \tag{5}$$

the following equation can be obtained

$$\frac{W_a}{2\alpha_l} = \alpha_f + \beta_f \left[\frac{\beta_l}{\alpha_l} \right] \tag{6}$$

where $W_a = \gamma_l (1 + \cos \theta)$ $\tag{7}$

hence, if γ_1, γ_1^p and γ_1^d are known and θ, the contact angle, is measured for a range of liquids then a plot of $W_a/2\alpha_1$ versus β_1/α_1 will yield a straight line with the slope and intercept providing a solution to γ_f^p and γ_f^d.

Experimental

Fibre surface energies were determined using a Cahn Contact Angle Analyser: essentially a computer controlled microbalance. A single fibre was carefully cut and attached onto the end of a wire hook using double sided tape. The fibre/hook was then attached to the arm of the microbalance directly above a container containing the probe liquid. The force on the fibre was determined as a function of a liquid height as the liquid container was raise· at a rate of 40 μm/sec until at least 2 mm of fibre was immersed. The advancing contact angle was calculated from the wetting force obtained. A typical force- displacement graph which includes both the advancing wetting force and the receding force obtained when the fibre is removed from the liquid is shown in Figure 1. The Analar Grade liquids used in the experiment and their surface free energies are listed in Table I.

Table I Surface Free Energy Components for the Probe Liquids used in this Study [5]

Liquid	γ_1^T	γ_1^d (mJ/m^2)	γ_1^p
n-hexadecane	27.6	27.6	0.0
ethanediol	48.3	29.3	19.0
dimethylsulphoxide	43.5	38.9	8.7
formamide	58.2	39.5	18.7
water	72.8	21.8	51.0

A PEEK fibre was freshly prepared using a melt extruder, SEM examination showed the fibre to be smooth with a diameter of 643 μm (Figure 2). At least four wetting force measurements were carried out for each fibre and liquid combination. A fresh fibre was used for each run.

Carbon fibre reinforced PEEK composites of 61% fibre volume fraction were prepared from fibres A, B and C and transverse flexural strengths (TFS) measured on unidirectional laminates (ASTM D790).

Results

The results of the wetting force determinations of contact angles on the carbon and PEEK fibres are listed in Table II.

Table II Mean Contact Angles for Carbon and PEEK Fibres (standard deviations shown in brackets)

Fibre	Liquid	Wetting Angle (θ)	
A	n-hexadecane	20	(5.3)
Non-optimised	ethanediol	37.8	(3.7)
	DMSO	14	(3.6)
	formamide	58.7	(1.9)
	water	76.5	(6.0)
B	n-hexadecane	19.7	(2.7)
Controlled Surface	ethanediol	26	(11)
	DMSO	10	(0)
	formamide	39.4	(7)
	water	52	(6.8)

Figure 1 Typical wetting force versus distance
trace of fibre B with ethanediol
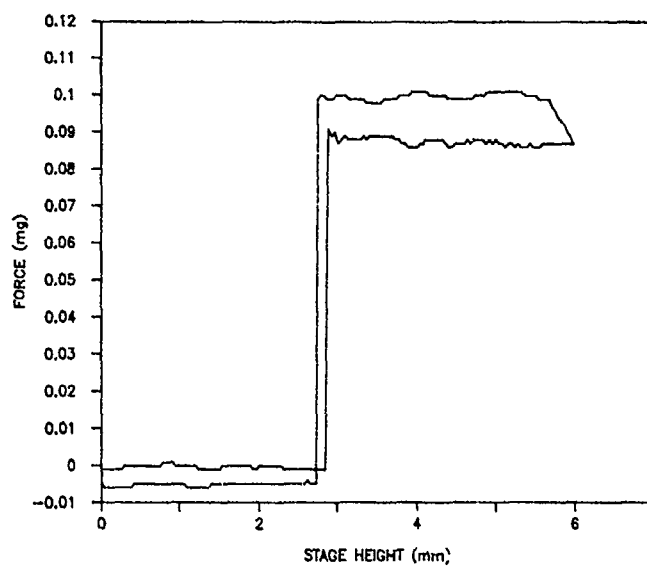
Figure 2 SEM of 643 μm PEEK fibre
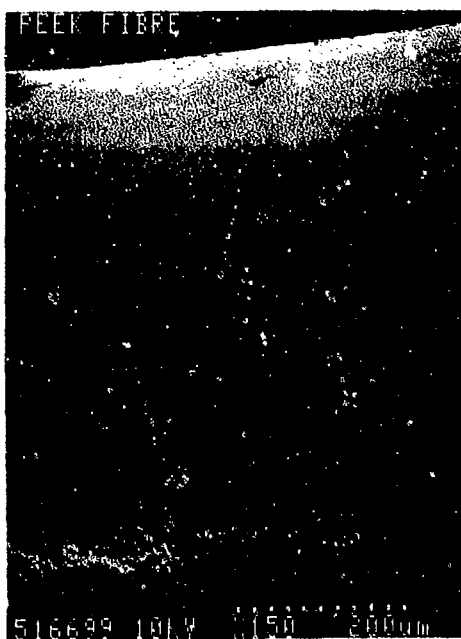
Fibre	Liquid	Wetting Angle (θ)	
C	n-hexadecane	13.7	(6)
Additional Surface	ethanediol	23	(5.8)
Treatment	DMSO	37.6	(1.7)
	formamide	24.2	(2)
	water	67.8	(4.2)
PEEK	n-hexadecane	19	(0)
	ethanediol	43.8	(6.9)
	DMSO	33.8	(5.3)
	formamide	58.3	(0.6)
	water	70.5	(7.7)

Plots of ($W_a/2\alpha$) versus (β_1/α_1) for the non-optimised fibre and for the fibre with controlled surface are shown in Figure 3 and 4 respectively: each point plotted represents an individual contact angle measurement. A best fit straight line was determined for each data set using linear regression analysis and the slope and intercept used to determine α_f and β_f. The results are shown in Table III.

Table III Polar, Dispersion and Total Surface Free Energy of Carbon and PEEK Fibres

Fibre	α	β	γ_f^d	γ_f^p	γ_f^T
A	5.21	2.92	27.15	8.51	35.7
B	5.11	4.72	26.1	22.3	48.4
C	4.90	4.64	24.0	21.5	45.5
PEEK	4.51	4.29	20.3	18.4	38.7

Figure 3 $W_a/2\alpha_1$ versus β/α and best fit straight
line for fibre A (non-optimised)

alpha fibre=5.21 beta fibre=2.92
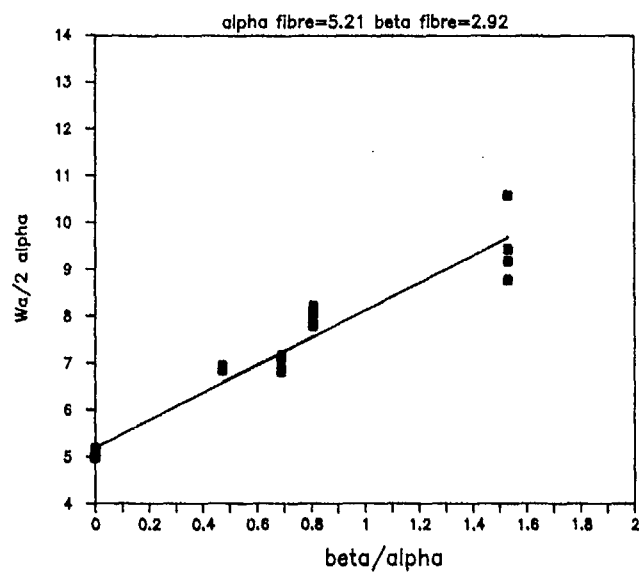
Figure 4 $W_a/2\alpha_1$ versus β/α and best fit straight
line for fibre B (controlled surface)

alpha fibre=5.11 beta fibre=4.72
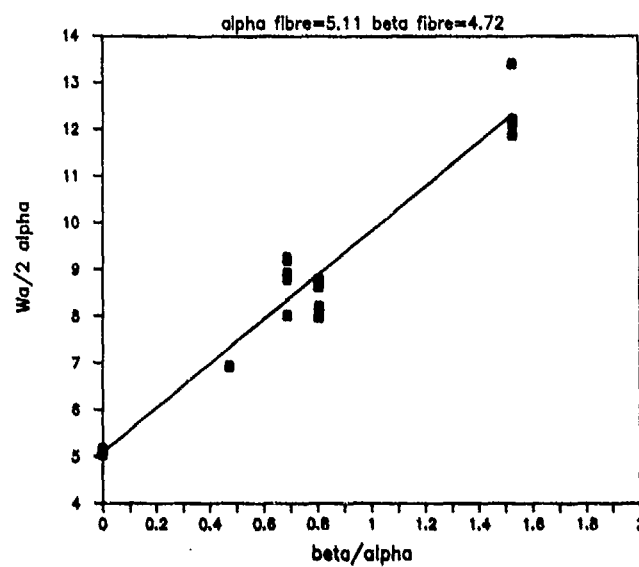
XPS analysis of the fibres and transverse flexural strengths of the corresponding PEEK composites are shown in Tables IV and V respectively.

Table IV XPS Analysis of Fibres

Fibre	XPS Analysis of Fibres		
	C	O	N
A	95.5	2.2	2.1
B	88.5	7.3	4.0
C	83.0	11.9	4.8

Table V Transverse Flexural Strengths in PEEK Composite

Fibre	TFS (MPa)
A	53.6
B	152.5
C	157.6

Discussion

There is more than threefold increase in the surface oxygen content and a doubling of the surface nitrogen content when comparing the non-optimised (A) fibre with the controlled surface (B) fibre. Additional surface treatment of the fibre leads to a further increase in oxygen (11.9%) and nitrogen (4.8%) content. Contact angle analysis reveals that the polar component of the surface free energy, γ_f^P, increases almost threefold when moving from fibre A to fibre B. This is accompanied by a slight reduction in the dispersive component γ_f^d. γ_f^P does not increase further for the fibre with additional surface treatment. This is perhaps an indication that XPS detects some functionality which is just beneath the fibre surface and therefore does not contribute to the surface energy, or in any adhesion process.

The transverse flexural strength of fibre B/PEEK composite is considerably higher than that for the composite made with fibre A. Additional surface treatment (fibre C) results in no significant increase in the TFS for the PEEK composite, as predicted by the similarity in the total surface free energy (γ_f^T) for fibre B (optimised) and C. These results imply that the polar component of the fibre surface energy is the major factor in influencing the fibre-PEEK adhesion.

W_a Calculation for Carbon-Fibre PEEK Interface

During the process of making composite laminates, carbon fibres are placed in contact with either solutions or melts of polymers or monomer mixes, probably at elevated temperatures, and then cooled (or cured and cooled in the case of thermosets) to solidify the composite. In addition to simple dispersive or polar interactions, this whole process may result in additional interactions across the fibre-matrix interface such as covalent bonding, mechanical interlocking or shrinkage stresses arising from thermal contractions of the matrix which could give rise to frictional adhesive contributions. Calculation of the work of adhesion in a composite is therefore a complex process.

Naively, however, we have used the room temperature surface energies of carbon fibres and solid PEEK fibre, listed in Table III, to calculate works of adhesion for carbon fibre-PEEK using the following equations:

$$W_a = \gamma_f + \gamma_m - \gamma_{fm} \tag{8}$$

$$\gamma_{fm} = (\alpha_m - \alpha_f)^2 + (\beta_m - \beta_f)^2 \tag{9}$$

where subscripts f, m refer to fibre and matrix respectively. The results of these calculations are shown in Table VI.

Table VI Calculated Work of Adhesion for Carbon Fibre Reinforced PEEK Composites

Fibre	γ_f (mJ/m^2)	γ_m (mJ/m^2)	γ_{fm} (mJ/m^2)	W_a $mJ/m^2)$
A	35.6	38.7	2.4	71.9
B	48.4	38.7	0.5	86.6
C	45.5	38.7	0.3	84.0
				W_c (mJ/m^2)
PEEK	--	38.7	--	77.4

The W_A values for the different fibre surface treated composite are required to be compared with the work of cohesion of PEEK itself, W_C, that is,

$$W_C = 2\gamma_m \tag{10}$$

The W_A for the fibre-matrix bond between PEEK and fibre B is larger than W_C for PEEK hence, in the composite, the interface should remain intact and failure should occur in the PEEK matrix. Similarly for the fibre with additional treatment, $W_A > W_C$ and cohesive (matrix) failure occurs. For the composite from fibre A, however, the interface is weakest and adhesive failure should occur. This is exactly what happens in the composite as shown in the TFS results. Subsequent examination of the TFS fracture surface reveals bare carbon fibre in the case of the fibre A/PEEK composite and fibre well covered with ductile polymer in both fibre B/PEEK and fibre C/PEEK composites. This indicates adhesive failure at the fibre-matrix interface for the non-optimised fibre composite and cohesive failure in the PEEK matrix in the latter two composites. In carbon-PEEK composites therefore, surface energetics can be used to predict the level of fibre matrix adhesion.

Note: Comparison of W_a and W_C values calculated above with fracture energies, G_c, determined from mechanical tests.

338

Equation (10) used above is the fracture energy required to break only secondary bonds in the polymer eg. Van der Waals, dipolar etc. However, G_c includes the energy to fracture covalent bonds, cause plastic deformation of the polymer and so on. Hence

$$G_c \gg 2\ \gamma_m \tag{11}$$

In the case of PEEK, typical G_cs are around $5kJ/m^2$.

Acknowledgements

References

1   P Denison, F R Jones and J F Watts, J. Mat. Sci. 20, 4647 (1985).

2   Kaelble, D H, Dynes, D.J and Cirlin, E H, J. Adhesion, 6, 23 (1974).

3   Dynes, P J and Kaelble, D H, J. Adhesion, 6, 195 (1974).

4   Drzal, L T, Mescher, J A and Hall, D T, Carbon, 17, 375 (1979).

5   D G Rance, in Industrial Adhesion Problems, edited by D M Brewis and D Briggs (Orbital Press, 1985), p48.

6   Fife, B, Barlow, C Y, and Peacock, J A, Sixth International Conference for Composite Materials (ICCM-VI), 3, 439 (1987).

EFFECT OF SURFACE OXYGEN ON ADHESION OF CARBON FIBER REINFORCED COMPOSITES

P. W. YIP and S. S. LIN
Army Materials Technology Laboratory, Watertown, MA 02172

ABSTRACT

Five carbon fibers from different precursors were surface treated by various chemical reagents for the elucidation of the mechanism involved in interfacial adhesion. SEM, ESCA and SAM techniques were used to characterize morphology as well as surface constituents of the treated fibers. The transverse tensile strengths of the composites made from the treated fibers and epoxy resin were also obtained. The result indicated that the interlocking mechanism by surface roughness seemed to play a major role in the fiber-epoxy adhesion.

INTRODUCTION

Over past 15 years, carbon fibers (CF) have evolved into a major reinforcing substance for structure materials [1,2]. The strength and the extent of the reinforcement are dependent on nature of resin matrix, fiber strengths as well as fiber-resin interfaces. The mechanical properties and ultimate performances of composites tie intimately with surface morphologies of the fibers. Three different adhesive mechanisms are known to exist at the interfaces [3]: mechanical interlocking, chemical binding and weak attracting forces such as dipole-dipole, Van der Waals, and electrostatic interactions. However, the extent of these interactions between the fiber surface and the matrix component is not clearly understood.

In this paper, the investigation was made to elucidate the reinforcing mechanism involved in the fiber epoxy composites. Five carbon fibers of different origins are treated by various chemical reagents to modify surface characteristics. The surface morphology and chemistry are examined by scanning electron microscope (SEM) [4], X-ray photoelectron spectroscopy (XPS or ESCA) [4,5] and scanning Auger microprobe (SAM) [6] techniques, and the interfacial adhesive strength by transverse tensile stresses (TTS) of the fiber epoxy composites. The effects of these chemical treatments are compared and the major reinforcing mechanism involved in the interfacial adhesion are discussed.

EXPERIMENTAL

Fiber samples

Five CF are used in this experiment: Three pitch based carbon fibers, one (PCF) made by Tonen Oil Co. and two (OCF1 & CCF5) by Osaka Gas Co. Japan, and two polyacrylonitrile (PAN) based CF, Magnamite IM6 (HCF) and Besfight IM600 (TCF), made by Hercules, USA and Toho Rayon, Japan respectively. The physical data provided by the manufacturers are shown in Table 1.

Surface treatments

The conditions and procedures of the oxidative treatments are described below. Owing to wide chemical reactivities of these fibers, the reaction times are slightly different for each fiber in these treatments.
(1) Acid solution: Treated with 60% concentrated nitric acid at a boiling and refluxing condition for a period of 24 hours for PCF, 12 hours for OCF, and 4 hours for TCF and HCF.
(2) Peroxide solution: Treated with a 15 % hydrogen peroxide solution near boiling for a period of 14 hours

(3) Gas oxidation: Pre-soaked in concentrated phosphoric acid at the boiling point for one hour followed by heating in a muffle furnace under oxygen atmosphere at 400 $^{\circ}$C: 14 hours for PCF and OCF, 6 hours for TCF and one hour for HCF.

(4) Hydrogen reduction: Hydrogen reduction of the acid treated fiber (Process #1) at in a muffle furnace at 1000 $^{\circ}$C: 14 hours for PCF, 12 hours for OCF, 6 hours for HCF and 5 hours for TCF.

The fibers after the wet treatments (1) and (2) were rinsed with distilled water three times followed by acetone and distilled water. After the five washings, the samples were dried in an oven at 100-120 $^{\circ}$C overnight before the analyses. The fibers from the dry processes (3) and (4) were used directly without washing.

Table 1 Physical and Mechanical data of Fibers

| Symbol | Source | Precursor | Physical data | | | | |
			Size	Tow	Diameter (μm)	Strength (GPa)	Modulus (GPa)
PCF	TONEN HM3131	Petroleum pitch	no	3K	10	3.4	491
OCF1	Osaka Gas F180	Coal tar pitch	no	3K	10-11	1.8	180
OCF5	Osaka Gas F500	Coal tar pitch	no	3K	10-11	2.8	500
HCF	Hercules IM6-U-12K	PAN	no	12K	6	4.77	250
TCF	TOHO RAYON 707642E31	PAN	yes	12K	4.7	5.78	297

Specimens for Transverse Tensile Strength (TTS)

The composite test specimens [7] for TTS are prepared with the treated fibers and epoxy resin. The epoxy resin consists of 100 parts EPON 828 resin and 40 parts EPON V-40 curing agent, supplied by Miller Stephenson Chemical Co. The unidirectional composites were made by impregnating the fiber tows into epoxy resin under pressure followed by curing in an oven at 100 $^{\circ}$C overnight. The thickness of the resulting composite is about 4-12 mils. This composite sheet is then made into the test specimens of 38-88 mil width by slicing across the fiber direction with a diamond wafer blade.

The digital tensile test instrument, Model 1000 made by Tinius Olson Co., was used to measure the transverse tensile strength. The measurement was made with a ten-pound load cell and a cross-head speed of 0.8"/min. A statistical average was obtained from thirty or more measurements.

Surface Oxygen Concentration

The ESCA/Auger instrument, made by Physical Electronic Ind., PHI-548 with a double pass cylindrical analyzer and Mg K X-ray radiation was employed in the determination of surface oxygen concentrations. In the preparation of the specimen, a bundle of fibers were densely packed and aligned to give approximately an area of 1/2 inch square. The excessive lengths of the fibers were trimmed and the cut ends were glued to a conductive adhesive copper tape. Two surface properties were readily obtainable from ESCA spectra: (a) Atomic oxygen concentration: calculated from the integrated area under the O_{1s} and C_{1s} peaks, and (b) Oxidized carbon to carbon ratio: obtained from the proportions of oxygen linked carbons (including hydroxyl, ether, ester, carbonyl and carboxyl functional groups) to carbons without oxygen linkages. This ratio was calculated from the deconvolution [8] of the C_{1s} peak profile.

RESULTS

After the oxidative treatments, significant changes are observed by SEM on the surfaces of the carbon fibers. The extent of surface morphological alterations is strongly dependent on the fiber precursors as well as surface microstructure. The appearance of striations in the well oriented pitch based CF with large crystallites is not affected by the treatments, while the fibers with smaller crystallites having a high degree of random orientation are oxidized readily showing various shades along the fiber length in SEM images. In the solution treatments, the diameters of the fibers appeared to increase in size due to the formation of oxide layers. The extent of the oxide formation was less for pitch and more for PAN CF. Moreover, the oxidized layers were not distributed evenly throughout, but were formed on some preferred locations, such as large bumps, deep crevices, cracks and surface flaws, swellings and delaminations. In the gaseous treatments, more bumps and pits were observed in the PAN based CF which has no striation. Many inclusions, foreign impurities, cracks and bumps were especially noticeable in these fibers. The oxidation appeared to take place preferentially at surface defects, cracks, bumps, and pits.

The peak shapes [9,10] of carbon and oxygen in the ESCA spectra are plotted in Figure 1. The carbon peak profiles change substantially from the untreated one to the treated ones. The left shoulder of the carbon peak increases asymmetrically indicating the presence of carbon oxygen functional groups. Moreover the carbon peak widths at half height also increase for the oxidized fibers. In the sized fiber (TCF), two overlapping peaks are observed in the C_{1s} core peak (not shown). This highly asymmetric profile is derived from the sizing compound containing a significant amount of alcohol and ether functional groups. For those peaks obtained after the hydrogen reduction treatment, the left shoulder decreased considerably indicating lesser amounts of the carbon-oxygen functional groups on the surfaces. In the oxygen peak lineshapes, the treated fibers always give broader peak widths than those of the sized and untreated ones. This is caused by the formation of a wide variety of singly and doubly bound oxygen on the surfaces.

The highest surface oxygen concentrations are observed in the treatments come from concentrated nitric acid solution and/or gas oxidation at high temperatures as shown in Table 2. The oxygen concentration increase several folds. However, in general, the oxygen concentrations after the hydrogen treatment of the acid treated surfaces decrease to a few atomic % approximately a half to one quarter of the original untreated concentrations.

The strength of interfacial adhesion can be obtained by a variety of measurements, such as, interlaminiar shear stress (ILSS), interfacial shear stress (IFSS) and transverse tensile stress (TTS). Interpreting data from ILSS are complicated due to many interacting forces such as flexural, compressive and tensile stresses during the testing of unidirectional composites. IFSS would be an excellent choice, but the technique is time consuming. Eventually, the choice was made on TTS due to simplicity as well as good representation. In properly prepared specimens, the adhesive strength should compose more than 85% of the TTS magnitude in the high fiber density composites [11].

Generally, the transverse tensile strength (TTS) as shown in Table 2 increases drastically after all treatments except for TCF and OCF1. The TTS magnitudes which are about 1 % of the uni-directional composite strength for the untreated fiber, generally increase after the chemical treatments. However, TTS of the fiber reinforced epoxy composites shows no clear variation with the chemical etching agents in the treatments. In the treatments of OCF1 and the sized PAN based TCF, no substantial improvement is observed. Unexpectedly, the fibers after the hydrogen treatment yield approximately the same magnitudes of TTS as other treatments.

Table 2   Transverse Tensile Strength of Fiber Composites
and Oxygen Concentrations on Fiber Surfaces.

Chemical Agents**		Untreated	Acid Conc HNO_3	Peroxide H_2O_2	Oxidation O_2	Hydrogen H_2
PCF	TTS(MPa)	8.8	25.4	19.3	16.3	18.3
	Oxygen(at %)	6.3	14.3	8.6	11.1	1.4
OCF1	TTS(MPa)	23.6	22.1	21.8	24.5	22.6(20.9)***
	Oxygen(at %)	1.9	19.1	12.3	8.4	7.9
OCF5	TTS(MPa)	15.2	22.3	17.2	26.8	25.1
	Oxygen(at %)	0.9	11.5	6.4	7.1	1.1
HCF	TTS(MPa)	13.4	19.4	20.09	31.55	30.4
	Oxygen(at %)	3.0	15.1	9.7	12.9	1.4
TCF	TTS(MPa)	19.74	20.26	25.13	20.52	27.16
	Oxygen(at %)	12.8*	15.5	9.7	11.5	2.7

*   Sizing agent on the surface
**   Treatment times and Conditions vary
*** Parentheses: Hydrogen reduction of untreated fiber only.

DISCUSSION

The structure of carbon fiber [1,12] is an array of carbon ribbons consisting of turbostratic graphite crystallites running along the fiber length. The fiber surface is composed of basal planes and prismatic edges of the crystallites. There are many mis-matches on the surfaces, such as cracks, notches, pits, crevices, foreign particle inclusions, and dislocations. Furthermore, numerous loose delaminated layers and fibrils exist.

Two kinds of surface chemical reactivities exist: low energy sites of basal planes and reactive prismatic edges [13]. The oxidation occurs predominantly toward disorganized or edge carbons. The initial step of the oxidative treatments is to smooth the surface and to eliminate loose surface layers, followed by the reaction leading to the formation of graphitic (lamellar) oxides and the evolution of carbon dioxide. The degree of the graphitic oxide formation depends on the alignment of carbon crystallites along the fiber. Thus, more oxygen is found on less oriented carbon layer surfaces.

The oxidative treatment produces more active sites by the formation of chemically active carbon-oxygen functional groups, but also increases the surface roughness by etching. The extent of increased roughness or enlarged surface area, depends on the nature, temperature and the degree of the treatment. In the nanometer scale, the increases are attributed to the formation of micropores, cracks, etch pits, lamellar oxide layers, the elimination of trapped carbonization products and weakly absorbed oxygen. The extended oxidation is followed by coalesce of pits into channels, and or enlargement of pit dimensions. Therefore, the two adhesive forces, chemical binding and mechanical interlocking, are formed simultaneously after the oxidative treatments.

The interfacial adhesion can be formed by the low energy surfaces which are bound with resin matrix through dispersion, dipole-dipole, dipole-induced dipole, electrostatic, pi-bonding, hydrogen bonding, or donor acceptor interaction. Also the chemical bindings are possible by carbon-oxygen functional groups at prismatic edges. The mechanical interlocking of the two

mating surfaces is also an important sour ｜ of the interfacial strength. The pits, crevices, cracks and the topology or the surface are the essential forms of the interlocking. However, the matrix liquid must seep into micro spaces of these flaws for effective mechanical anchoring.

In the present experiments, the surface oxygen concentrations was clearly established from ESCA spectra. Regardless of fiber surface morphologies, the oxygen concentrations increase to about 15 atomic % after etching in concentrated nitric acid, change to about 10% under peroxide solution and oxidation atmosphere, and reduce to 2-4% in the hydrogen stream. It is interesting to note that the trends of these five sets of data are similar.

The magnitudes of TTS increase substantially after the treatments except for sized TCF and OCF1 which show marginal improvements. TTS after the peroxide, oxidation and hydrogen treatments improves at least twice the strength of the resulting composite. This improvement could derived from either increased surface oxygens or enlarged surface ruggedness. The improvement is found independent on the fiber precursors.

From the analysis of the data between TTS and oxygen concentrations, the result indicates that increased amounts of oxygen have no direct correlation with the enhanced TTS. Especially in the hydrogen treatment, the high TTS data are associated with minimum amounts of surface oxygen. This behavior is observed in all fibers regardless of the different fiber origins. Evidently, surface oxygen has little to do with TTS. Since the hydrogen treated fibers are those obtained after the acid treatments in which the reduction probably takes place only on surface oxides, the surface morphologies of the two should be similar. Therefore, the major role of the oxidative treatments on CF adhesion is not chemical in nature.

In the sized PAN based fiber of TCF, no significant improvement of TTS is observed. This could be caused by the presence of the sizing compound on the fiber surface, which yields a high TTS before the treatments. The effect of sizing on fiber adhesion is not clear at this time, but it is certainly more beneficial than detrimental. The pitch based fiber of OCF1 also shows no TTS enhancement, probably due to the nature of fiber. The fiber is found to compose of small crystallites which provide numerous rugged terrains and maximum roughness. The present oxidation apparently yields about the same magnitude of roughness. Therefore, no further improvement of TTS is observed.

CONCLUSION

The present observations are inconsistent with the postulate [1,14,15] that chemical binding is an essential part of the fiber-resin interface. One of three interfacial adhesive strengths is the chemical binding which comes from the oxygen containing functional groups on the carbon fiber surface. Particularly, these functional groups, -OH,)C=O, -OC=O are major binding forces of the interfacial adhesion. Thus, surface oxygen is needed for improved performance of the fiber reinforced composites.

The important role of the oxidative treatment seems to be the creation of more rugged surface terrains by etching than the formation of chemical linkages. Thus, the treatment creates more roughness which in turn promotes physical surface anchoring. The mechanism involving mechanical interlocking between CF and epoxy resin appear to surpass the significance of the chemical bindings formed by the carbon oxygen functional groups in the present CF-epoxy interfaces. Therefore, it is expected that the etching by fluorination of CF would promote the fiber resin adhesion similar to that of the oxidative treatment.

In short, the following observations are made from the present experiments: (1) The extent of oxidation on the carbon fiber surface is more dependent on the chemical reagents than the surface structures and the precursors of the fibers in the present treatment condition. (2) The degree of adhesion is not promoted by the amount of oxygen or carbon oxygen functional groups on the

fiber surface. (3) The chemical treatments not only increase the oxygen surface concentration, but also enhance surface roughness. The increased roughness provides more adhesion due to enhanced mechanical interlocking and physical mating.

REFERENCES:

1. J. Delmonte, Technology of Carbon and Graphite Composites, Chapter 6, (Van Nostrand Reinhold Co., NY, 1980)
2. E. P. Plueddemann, Composite Materials, Vol 6, Chapter 7 (Academic Press, NY, 1974)
3. E. Fitzer, Carbon Fibers and Their Composites, (Springer-Verlag, Berlin, NY, Tokyo 1983)
4. S. S. Lin and P. W. Yip, MTL TR 87-49, 1987 & JANNAF-CMCS meeting report, 1988
5. S. S. Lin, and P. W. Yip, 19th Bienniel Conference on Carbon, Extended abstract p244, June 1989
6. S. S. Lin, presented at AVS Oct. 1989 & JVST A, 8, [3] (1990)
7. ASTM D3552-77 1982
8. D. Briggs & M. P. Seah, Practical Surface Analysis (John Wiley & Sons, NY 1983)
9 A. Ishitani, Carbon, 19, 269 (1981)
10. F. Hopfgarten, Fiber Scie. Technol., 12, 283 (1979)
11. G. A. Cooper and A. Kelly, in Interfaces in Composite, ASTM STP 452 pp90-106 1969
12. M. Guigon, A. Oberlin & G. Desarmot, Fiber Scie. Technol., 20, 177, (1984)
13. J. B. Donnet, Carbon, 20, 267, (1982)
14. L. T. Drazel, Carbon, 15, 129-138 (1977)
15. E. Fitzer and R. Weiss, Carbon 25, 455 (1987)

Figure 1

XPS Peak Profiles of Carbon and Oxygen from Treated Surfaces of Tonen HM Pitch based Carbon Fibers

ELECTRON BINDING ENERGY (ev)
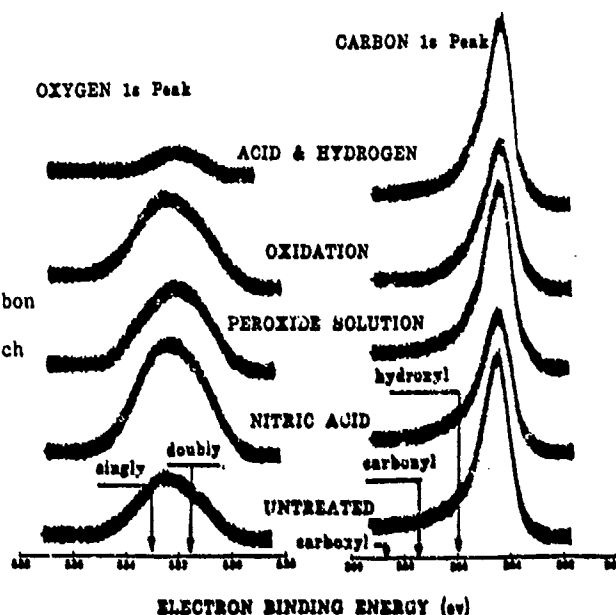
INTERPHASE BEHAVIOR IN CYCLIC FATIGUE OF MONOFILAMENT COMPOSITES.

LINDA S. SCHADLER*, JUAN C. FIGUEROA**, CAMPBELL LAIRD*
* U. of Pennsylvania, Philadelphia, PA.
**E.I. Du Pont de Nemours and Co., Wilmington, Delaware

ABSTRACT

Macroscopic properties of fiber reinforced composites are dependent on the micromechanics of the filament-matrix interphase. We present here some preliminary results of our studies aimed at understanding the behavior of the interphase when the composite is subjected to cyclic tensile loading. We have used carbon/polycarbonate mono-filament composites as a model system for studying the effects of loading direction (axial and transverse), frequency, and amplitude. The interphase was varied by etching the filament surface. Damage was characterized by fiber matrix debonding, reduction in interphase stress transfer efficiency, and changes in the locus of failure as determined by SEM fractography.

INTRODUCTION

A controlling factor in the fatigue life of fiber reinforced composites is the fiber-matrix interphase behavior because the interphase controls the load transfer from the matrix to the strengthening fibers. Although there is a large fatigue data base, the role of the interphase in fatigue failure is not well understood. The goal of this work is to improve the understanding of filament-matrix interphase micromechanical behavior in cyclic fatigue. Fatigue tests were carried out in two loading directions (axial and transverse), at several frequencies and several amplitudes.

The approach we took to isolate the effects of the interphase was to use monofilament composites, and to alter the fiber surface in a controlled manner to determine the effects of treatment [1]. Using mono-filament composites the interphase strength or the ability of the interphase to transfer load (stress transfer effectiveness, STE) can be determined [2-10]. Space does not allow a thorough review of the techniques, but readers are referred to reference 9. Instead, the technique used for measuring STE in this work is presented as follows.

As a monofilament composite is loaded in the axial direction, the filament will begin to fracture. Load is then transfered from the matrix to the fiber through shear at the interphase (see Figure 1). Kelly [3] derived a simple expression using a force equilibrium analysis that relates the shear stress at the interface near the end of the filament fragment to the length over which load is transfered, and the stress in the filament. Assuming a constant shear stress in the interphase, the expression reduces to:

$$\tau = \frac{\sigma r}{2 Z} \tag{1}$$

where σ is the stress in the filament, τ is the shear stress, r is the radius of the filament, and Z is the distance along the filament.

By using a birefrigent transparent matrix and viewing the fragmentation phenomena in cross polarization, λ, the region over which load is transferred, is optically active and its length can be measured. STE is then calculated by replacing Z with λ, and σ with E*ϵ (where E is the Young's modulus of the filament (assumed to be constant), and ϵ is the strain measured in the composite). In addition matrix cracking and interphase cracks can be seen. Using an apparatus described previously [11], we measured λ at several filament breaks and at several composite strains. The growth of λ with strain for a typical filament is shown in Figure 2, and is seen to be linear at low strains. This linear growth implies that there is no interaction between λ regions, and the non-linear growth, which occurs at high

strains, implies that the λ regions are overlapping. All calculations were done using values in the linear region to ensure that the fiber was carrying as much load as possible.

$$\tau_{rz}^{*} = \frac{E \cdot d \cdot \varepsilon}{4 \lambda}$$

E : Fiber Modulus
d : Fiber diameter
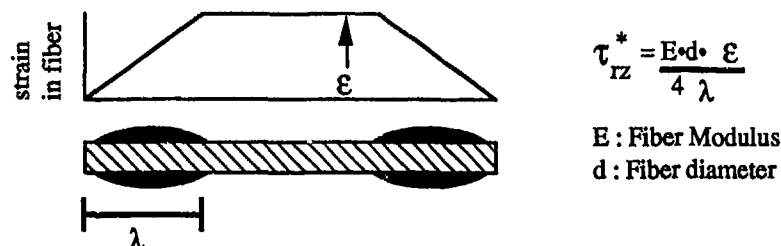
Figure 1.   Schematic of filament fragment in cross polarization to define Stress Transfer Zone (STZ) and its length, λ.

This tool was used to investigate the change in interphase STE due to cyclic fatigue.   However, because only the composite strain is measured, the exact strain in the filament is not known.   Therefore, we calculate the relative values of STE for different interphase strengths rather than the absolute values of STE.   In addition, it has been shown that the interfacial shear stress is not constant throughout the STZ [12];   this technique measures the average STE in a stress transfer zone.
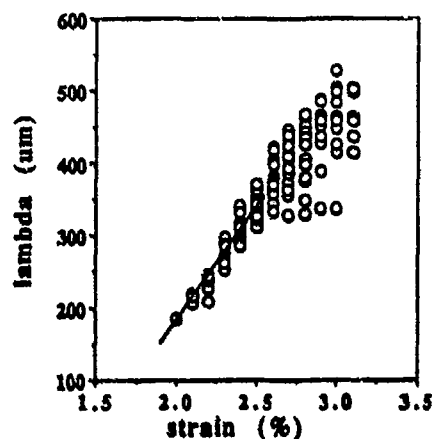
Figure 2. Lambda (the length of the Stress Transfer Zone) vs applied Composite Strain for a typical fiber showing linear behavior at low strains.
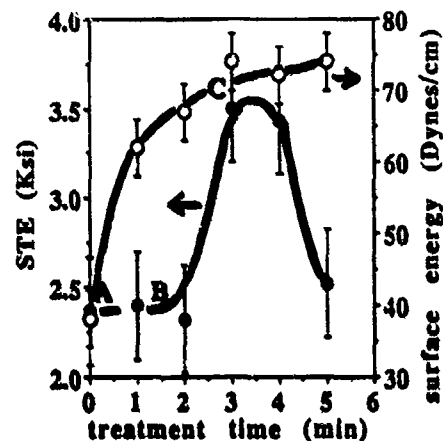
Figure 3. Change in Stress Transfer Efficiency   and surface energy with treatment time. Labels indicate three types of fibers tested.

EXPERIMENTAL PROCEDURE

Sample Preparation

Samples were made from Polycarbonate (a thermoplastic with a Young's modulus of 2.4Gpa) and from Hercules AU4 graphite filaments (Young's Modulus in the axial direction of 170-200Gpa).   Details of the molding procedure were presented earlier [11].   The fiber surface was altered by etching the fiber surface.   The effects of surface treatment on filament properties are presented in a companion

paper [1]. Figure 3. shows the effect of surface treatment on the surface energy and the STE. We elected to study an as received fiber (A), a fiber treated for one minute (B), and a fiber treated for three minutes (C) because of the the available range in STE and surface energy. The error bars represent the scatter in the data. The samples cycled in the transverse direction had A,B, and C filaments. Samples cycled in the axial direction had A and C filaments.

Fatigue loading

Fatigue tests were carried out on an INSTRON 1331 servohydraulic fatigue machine. Special grips were built to hold the samples and care was taken to ensure good alignment. The specimens did not have a reduced gage length, and strain was measured with an extensometer attached to the grips. Tests were run under load control with R=0.1 Creep during testing was less than 5% of the total strain, and the change in residual modulus was small. The wave form was triangular to maintain a constant loading rate during the test. The transverse samples were 65mm X 90mm X 0.5mm. The axial samples were 3mm X 90mm X .5mm. Loading schedules are presented in Table I. After cycling, a smaller sample was cut from the cycled specimen for fragmentation testing.

Table I. Loading schedules for transverse and axial cyclic fatigue tests.

Transverse Cyclic loading schedule

Amplitude \ frequency	.01 Hz	.05Hz	0.1 Hz	0.5 Hz	1.0 Hz
2%	*	•	@	#	@
2.35%	•	+	•	@	#
2.7%	•		•		•

- • up to 1000 cycles
- * up to 1500 cycles
- + up to 3000 cycles
- # up to 5000 cycles
- @ up to 10000 cycles

Axial Cyclic loading schedule

Amplitude	.1%	.2%	1%	2%
up to n cycles	10^4	10^4	10^6	10^3

Determination of Cyclic Damage

For purposes of this paper, damage was defined as the reduction in STE. Two halves of the same monofilament, one cycled, one not cycled, were compared using the fragmentation technique described above. In addition the shape of the stress transfer zones as seen in cross polarization were compared.

In order to obtain further information on how damage occurs, fractography was carried out on fiber pull out samples. Pulled out fibers were prepared by notching and straining to failure representative samples.

RESULTS AND DISCUSSION

Transverse loading

Since PC yields at 7% and since a fiber oriented transverse to the load direction has regions of high stress concentration, strain amplitudes in the low range of 2-2.7% were employed for transverse cyclic tests. In order to reduce edge effects the samples were 90 mm wide.
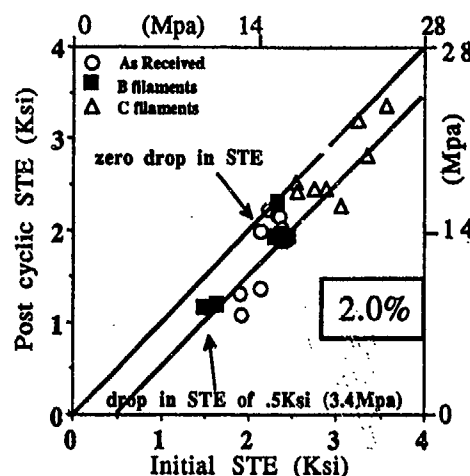
Figure 4. Stress Transfer Efficiency after cycling in the transverse direction at 2%vs initial Stress Transfer Efficiency
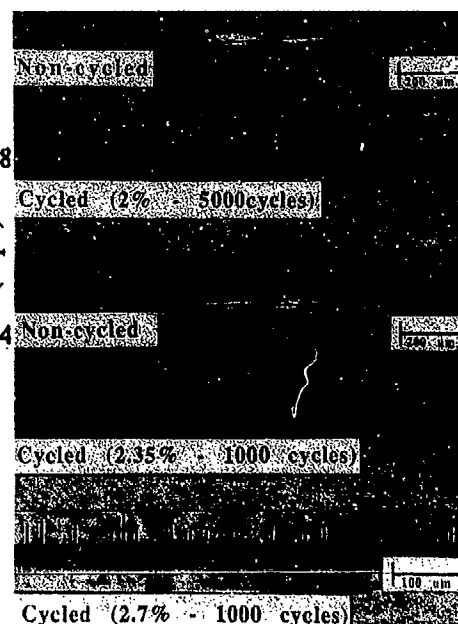
Figure 5. Photoelastic patterns for samples cycled at (a) 2%, (b) 2.35% (c) 2.7% Intensity information is masked because it is reproduced from a color photograph.

After cycling at 2% there was a slight reduction in STE. We did not observe an effect of frequency or number of cycles on damage. Figure 4 shows a plot of the initial STE versus the final STE for all three filament types. The upper line represents zero damage. The lower line represents a drop in STE of 3.4Mpa. Although the absolute value of STE is different for the three filament types, the amount of damage (or the drop in STE) is the same. This indicates that the damage is not a function of interphase properties, but of matrix properties. There seems to be no debonding as evidenced by similar photoelastic patterns (Figure 5) and by similar SEM fractographs (a fractograph of a non-cycled sample is shown in Figure 6) for cycled and non-cycled samples. Since the deformation of polycarbonate is not frequency dependent at room temperature, but does undergo cyclic softening, we believe that the drop is STE for all filament types is due to matrix softening in the interphase region.

At 2.35%, in spite of the large width of the sample, a crack grew from the edge of the sample at the poles of the filament during the first few cycles partially delaminating the interphase. This delamination and subsequent damage caused a large drop in the STE. During the fragmentation test, we believe that the load was transferred partly by friction between the matrix and the fiber; the resulting photoelastic patterns were more elongated, and less intense as shown in Figure 5. Figure 7 shows the increase in damage with cycles, and the frequency dependence of damage for filament types A, B and C. Damage occurs more rapidly at lower frequency. Again, the damage accumulation of the change in STE is indistinguishable for filament types A,B and C even though the absolute values of STE do differ, again indicating that the damage is matrix dominated.

After cycling at 2.7% there was a visible interphase crack, and several filament failures had occured during cycling. SEM of the pulled out filaments reveals polycarbonate on the side of the filament indicating that the crack grew

partly through the matrix (see Figure 6). The fragmentation test yielded no noticeable load transfer from the matrix to the filament, and above 2.5% longitudinal strain, matrix cracks that nucleated at the filament surface propagated perpendicular to the filament (see Figure 5). These cracks did not usually grow longer than about 30um, and the number of cracks increased with applied strain.

(a) Control Sample   (b) Cycled 2.7% 1000 cycles
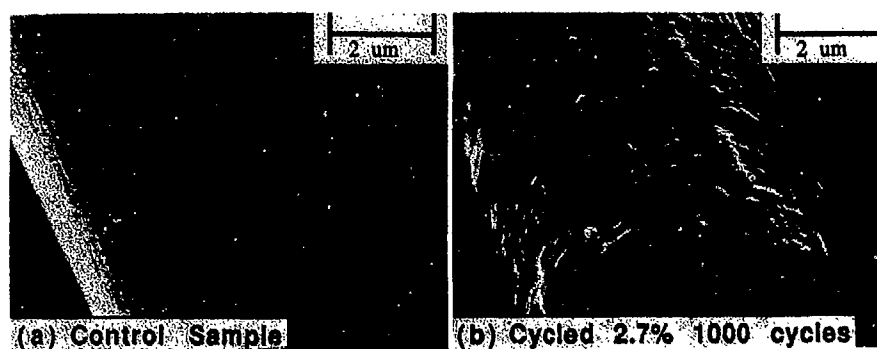
Figure 6. SEM of a control sample and a sample cycled at 2.7% for 1000 cycles at 20,000 X.
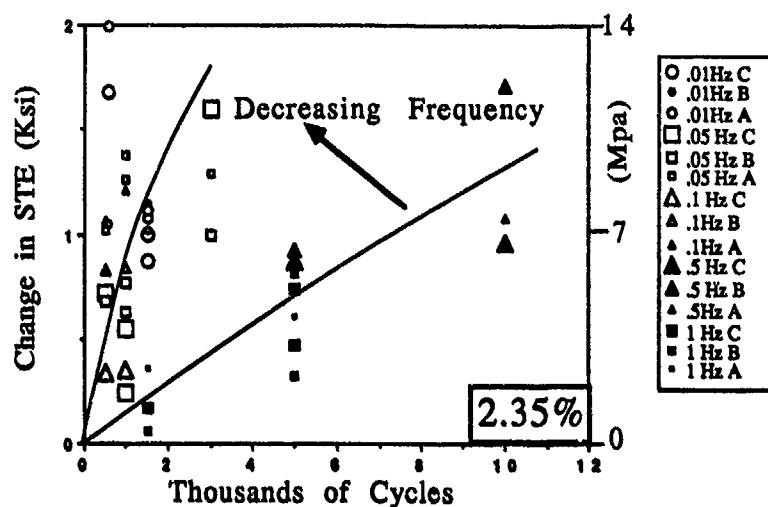
Figure 7. Damage due to cycling at 2.35%as a function of cycles for 5 frequencies and filaments A,B,C. Lines are chosen to show that damage increases faster at low frequency

Axial loading

It was found that the interphase STE was not altered by cycling in the axial direction at strains below the failure strain of the filament. Damage was not observed until the strain amplitude was large enough to fracture the filament during cycling. This is not a surprising result because the shear far from the filament ends (in this case the filament ends were in the grips) is almost zero, and the strains imposed are low cyclic strain for polycarbonate. At strain amplitudes

above the filament failure strain, damage can be described in the following manner: the filament fractures during the first cycle, the number of breaks being dependent on the strain imposed; subsequently there is fiber-matrix debonding observed by a lengthening of the stress transfer zone. (Figure 8) The kinetics of debonding may be interphase dependent, and work is planned to understand this behavior.
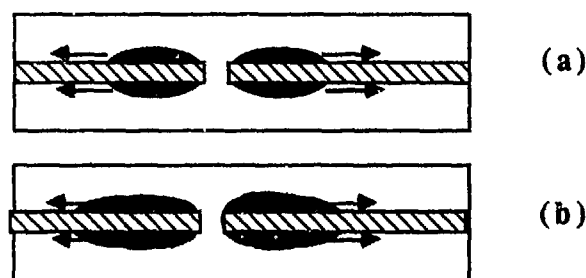
Figure 8. Schematic of damage during axial fatigue. (a) fiber fails during first cycle. (b) subsequent cycling lengthens stress transfer zone.

CONCLUSIONS

(1) The fatigue behavior of the interphase in a mono-filament composite in the transverse direction is matrix dominated, but is mediated by the fiber surface.

(2) The fatigue behavior of the interphase in a mono-filament composite in the axial direction is dependent on the filament strength until the filament fractures. After filament fracture occurs, cyclic damage is matrix dominated. The fatigue behavior of short filament composites should therefore always be matrix dominated.

REFERENCES

1. J.C. Figueroa, L.S. Schadler, C. Laird, presented at the 1989 MRS Fall Meeting, Boston, MA, 1989 (in press)
2. A.T. Dibenedetto, L. Nicolais, L. Ambrosio, J. Groeger in Composite Interfaces edited by H. Ishida, and J.L. Koenig (Proc. first International Conference on Composite Interfaces (ICCI-I), Cleveland, OH 1986) pp. 47-55
3. A. Kelly, Proc. R. Soc., London, 282 63 (1964)
4. L.T. Drzal, Adv. Polym. Sci. 75, 1, (1986)
5. W.D. Bascom and R.M. Jensen, J. Adhesion, 19 ,219 (1986)
6. M.R. Piggot, Failure of Plastics. (Hanser Publishers, New York, 1986) pp. 443-461
7. N. Ikuta,Z. Maekawa, H. Hamada, S. Yoshioka, E. Nishio, T. Hirashima in Interfaces in Polymer, Ceramic, and Metal Matrix Composites edited by H. Ishida (Proc. 3rd International Conference on Composite Interfaces, 1988) pp. 611
8. L. Di Landro, M. Pegoraro, J. Mat. Sci. 22 1980 (1987)
9. M. Narkis, E.J.H. Chen, and R.B. Pipes, Polymer Composites, 9, 245 (1988)
10. E.I.M. Asloun, M. Nardin, J. Schultz, J. Mat. Sci. 24 1835 (1989)
11. L.S. Schadler, J.C. Figueroa, C. Laird (Proc. Advanced Materials Conference, Denver, CO, 1989) still in press.
12. C. Galiotis J. Mat. Sci. 19 3640 (1984)
13. Beardmore, Treatise on Materials Science and Technology. Vol 6. (Academic Press, New York (1975).

INTERLAMINAR FRACTURE IN CARBON FIBER/
THERMOPLASTIC COMPOSITES

J. A. Hinkley,* W. D. Bascom** and R. E. Allred***
*NASA Langley Research Center, Mail Stop 226, Hampton, VA 23665-5225
**Department of Materials Science and Engineering, University of Utah, Salt Lake City, UT 84112
***PDA Engineering, 3754 Hawkins, NE, Albuquerque, NM 87109

ABSTRACT

The surfaces of commercial carbon fibers are generally chemically cleaned or oxidized and then coated with an oligomeric sizing to optimize their adhesion to epoxy matrix resins. Evidence from fractography, from embedded fiber testing and from fracture energies suggests that these standard treatments are relatively ineffective for thermoplastic matrices. This evidence is reviewed and model thermoplastic composites (polyphenylene oxide/high strain carbon fibers) are used to demonstrate how differences in adhesion can lead to a two-fold change in interlaminar fracture toughness.

The potential for improved adhesion via plasma modification of fiber surfaces is discussed. Finally, a surprising case of fiber-catalyzed resin degradation is described.

INTRODUCTION

Although the fiber-dominated properties of continuous-fiber composites are outstanding, transverse and out-of-plane loads can cause problems. Transverse cracks and delaminations resulting, for example, from impacts, can seriously degrade in-plane compressive properties [1]. The potential of tougher matrix materials to improve resistance to cracking under these conditions is one of the motivations in the development of thermoplastic matrix resins [2].

In order to optimize a composite system, however, one must consider the fiber, the matrix and the interfacial region. Although much is known about the effects of surface treatments and sizings in carbon fiber/epoxy systems [3], almost nothing has been published on optimizing carbon fiber/thermoplastic bonding.

The present report brings together chemical characterization, fiber surface modification, adhesion testing and composite data on some thermoplastic systems. It will be shown that significant improvements in properties can be achieved by interface modification.

CHARACTERIZATION OF FIBER/MATRIX BONDING

Fractography

If a unidirectional composite is split and peeled apart at the midplane, an examination of the fracture surface provides some indication of the mode of failure. Figure 1, from an AS4/polysulfone laminate, is typical of amorphous thermoplastic composites. Although the visible resin is highly deformed, fracture seems to have occurred at or near the fiber/resin interface. Even at high magnification, almost no resin can be found clinging to the bare fibers. Very similar fracture surfaces have been observed at LaRC for at least seven thermoplastic resins on unsized or epoxy sized, conventionally treated carbon fibers. In sharp contrast, the fracture of carbon fiber/epoxy laminates occurs in the resin and fibers in the fracture surface are well-coated with resin.
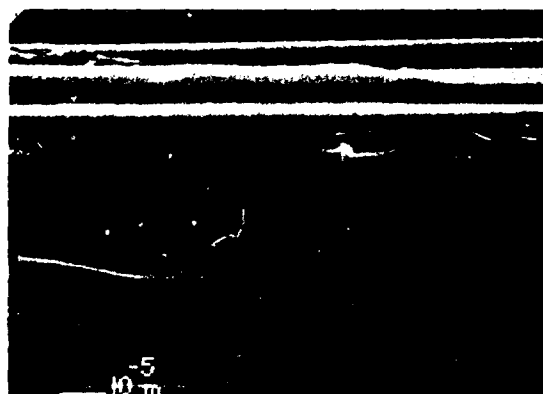
Figure 1.   SEM of interlaminar fracture surface AS4/Polysulfone

Embedded-Fiber Tests

In order to obtain a more quantitative measure of fiber/matrix adhesion, single carbon fibers were embedded in thermoplastic resins using solvent casting techniques [4]. When such microcomposites are strained in tension, the limiting fiber fragment lengths obtained are inversely related to the limiting interfacial stresses. Furthermore, the stress birefringence patterns at fiber breaks allow one to distinguish interfacial slipping ("poor" adhesion) from matrix yielding ("good" adhesion). The data in Table I clearly indicate the problems with thermoplastics.

Table I

Embedded Single Fiber Test Results

Resin	AS4		XAS	
	l_c, mm	Adhesion	l_c, mm	Adhesion
polyphenylene oxide	0.83	poor	0.37	good
epoxy	0.38	good	0.21	good

Composite Tests

Hunston has observed [5] that the Mode I interlaminar fracture toughness, G_{Ic}, values of thermoplastic composites are lower than might have been expected from these inherently tough resins. He speculated that a weak interfacial bond lowers interlaminar toughness. Data presented in the next section confirm this. On the other hand, Kinloch and Kodokian [6] point out that the tendency of a material to delaminate away from a pre-existing crack is correlated not with toughness, but with interlaminar tensile strength (or transverse tensile strength). Very tough resins may exhibit weak interfacial bonding and produce poor composite strengths.

MODEL COMPOSITE STUDIES

Fiber/Matrix Adhesion

A comparision of unsized, surface treated commercial fibers using embedded filament tests showed that they differed significantly in their adhesion to a number of thermoplastic resins. To determine the effect of this difference on interlaminar toughness, 24-ply unidirectional composites were prepared and tested as double cantilever beams [7]. Data were reduced by the compliance calibration method and the initial crack growth resistance from a thin insert used to avoid complications from fiber bridging [8]. The results are shown in Table II.

Table II

Interlaminar Fracture Toughness of PPO Composites

	AS4	XAS
G_{Ic}, J/m^2	240	440

Interface strength clearly affects composite toughness. The difference in adhesion also shows up clearly in electron micrographs of the fracture surfaces (Figure 2).
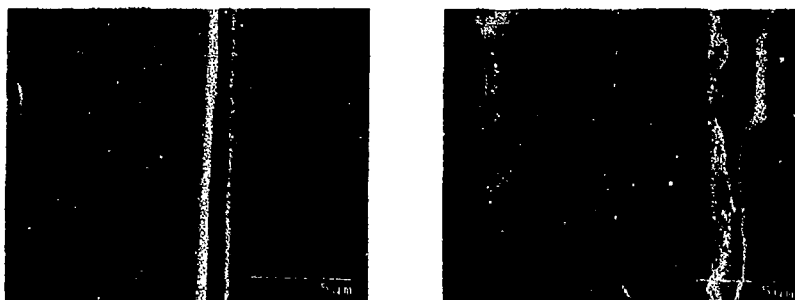
Figure 2.   SEM of interlaminar fracture surfaces a) AS4/PPO, b) XAS/PPO

Elemental analysis of the surface compositions of these and other fibers suggests that the nitrogen/oxygen ratio, which probably depends on the manufacturer's surface treatment, may be decisive in adhesion to thermoplastics (Table III).

Table III

XPS Analysis of Fiber Surfaces

	Atomic Composition (%)			
	C	O	N	N/O
AS4	90	5.7	4.3	0.75
XAS	84	7.6	8.4	1.1

Plasma Treatment

The ability to manipulate chemical species, as well as to functionalize graphite basal planes, makes RF plasma treatment an attractive approach to fiber surface modification. Table IV summarizes data on polycarbonate composites made from unsized IM7 fiber treated in a continuous plasma treatment/impregnation facility. Evidently plasma treatment can give improvements in adhesion. The translation of these improvements into composite properties is harder to characterize, for reasons that will be touched on in the next section. It appears from Table IV that the degree of fiber/matrix bonding may influence transverse strength more sensitively than it does interlaminar toughness. The last column in Table IV illustrates the role of the interface in water uptake. Water at the interface severely degrades composite strength.

Table IV

Polycarbonate Composite Properties

Fiber	G_{Ic} (initiation),[a] kJ/m^2	Transverse Flexural Strength,[b,c] MPa	Water Weight Gain,[d] Percent
IM7 (control)	----	93 ± 23	3.1
IM7 (treatment 1)	----	108 ± 26	0.6
IM7 (treatment 2)	----	140 ± 9	0.2
AS4 (control)	0.54 ± 0.11		
AS4 (treatment 2)	0.66 ± 0.14		

[a]Average of 3 specimens
[b]Average of at least 6 specimens
[c]Tested at room temperature, dry
[d]80°C immersion, 2300 hours

Resin-Fiber Interactions

During an earlier study [9], it was noticed that composites made from the same matrix resin (polycarbonate) differed in interlaminar toughness by 60%, depending on the choice of fiber. Careful gel permeation chromatography of resin extracted from these composites has revealed that a significant loss in resin molecular weight occurred with one fiber [10]. Apparently at the processing conditions (250°C, 200 psi) the fiber surface catalyzes degradation reactions. This observation also explains the more brittle appearance of the fractured resin in this composite.

SUMMARY

All of the thermoplastic composites studied fail predominantly near the interface. Somewhat improved adhesion has resulted in 50-100% increases in matrix-dominated properties, so it appears that there is room for further improvement if bonding can be optimized.

REFERENCES

1. J. G. Williams and M. D. Rhodes, in Composite Materials: Testing and Design (Sixth Conference) ASTM STP 787, I. M. Daniel, ed. American Society for Testing and Materials, Philadelphia, 1982, pp. 450-480.

2. N. J. Johnston, T. K. O'Brien, D. H. Morris and R. A. Simonds, 28th Nat'l SAMPE Symp. and Exhib. 28, 502 (1983).

3. For Example L. T. Drzal, M. J. Rich and P. F. Lloyd, J. Adhesion 16, 1 (1983); L. T. Drzal, M. J. Rich, M. F. Koenig and P. F. Lloyd, ibid. 16, 133 (1983).

4. W. D. Bascom, R. M. Jensen and L. W. Cordner, Int'l Conf. on Composite Matls. (6th: 1987, London) F. L. Mathews, ed. Elsevier, London, 1987 p. 5.424.

5. D. Hunston and R. Dehl, SME Technical Paper EM 87-355, Autocom '87 (1987).

6. A. J. Kinloch and G. K. A. Kodokian, Final Technical Report, Contract DAJA-45-86-C-0037 European Research Office of the U.S. Army, September 1989.

7. J. A. Hinkley, J. Reinf. Plast. Comp. (in press).

8. A. J. Russell and K. N. Street, in Delamination and Debonding of Materials, ASTM STP 876, W. S. Johnson, ed. American Soc. for Testing and Materials, Philadelphia, 1985, p. 349.

9. J. A. Hinkley, N. J. Johnston and T. K. O'Brien, in Advances in Thermoplastic Matrix Composite Materials, ASTM STP 1044, G. M. Newaz ed., ASTM. Philadelphia, 1989, p. 251.

10. J. A. Hinkley, in Composites, T. L. Vigo, ed., ACS Advances in Chemistry Series (in press).

Author Index

Subject Index

MATERIALS RESEARCH SOCIETY SYMPOSIUM PROCEEDINGS

MATERIALS RESEARCH SOCIETY SYMPOSIUM PROCEEDINGS

MATERIALS RESEARCH SOCIETY SYMPOSIUM PROCEEDINGS

MATERIALS RESEARCH SOCIETY SYMPOSIUM PROCEEDINGS

MATERIALS RESEARCH SOCIETY SYMPOSIUM PROCEEDINGS

Recent Materials Research Society Proceedings listed in the front.

MATERIALS RESEARCH SOCIETY CONFERENCE PROCEEDINGS